METHODS FOR SYNAPTIC INTERROGATION

EDITED BY: Dirk Feldmeyer, John F. Wesseling and P. Jesper Sjöström
PUBLISHED IN: Frontiers in Synaptic Neuroscience

frontiers Research Topics

frontiers

ISSN 1664-8714
ISBN 978-2-88963-864-2
DOI 10.3389/978-2-88963-864-2

About Frontiers

Frontiers is more than just an open-access publisher of scholarly articles: it is a pioneering approach to the world of academia, radically improving the way scholarly research is managed. The grand vision of Frontiers is a world where all people have an equal opportunity to seek, share and generate knowledge. Frontiers provides immediate and permanent online open access to all its publications, but this alone is not enough to realize our grand goals.

Frontiers Journal Series

The Frontiers Journal Series is a multi-tier and interdisciplinary set of open-access, online journals, promising a paradigm shift from the current review, selection and dissemination processes in academic publishing. All Frontiers journals are driven by researchers for researchers; therefore, they constitute a service to the scholarly community. At the same time, the Frontiers Journal Series operates on a revolutionary invention, the tiered publishing system, initially addressing specific communities of scholars, and gradually climbing up to broader public understanding, thus serving the interests of the lay society, too.

Dedication to Quality

Each Frontiers article is a landmark of the highest quality, thanks to genuinely collaborative interactions between authors and review editors, who include some of the world's best academicians. Research must be certified by peers before entering a stream of knowledge that may eventually reach the public - and shape society; therefore, Frontiers only applies the most rigorous and unbiased reviews.
Frontiers revolutionizes research publishing by freely delivering the most outstanding research, evaluated with no bias from both the academic and social point of view. By applying the most advanced information technologies, Frontiers is catapulting scholarly publishing into a new generation.

What are Frontiers Research Topics?

Frontiers Research Topics are very popular trademarks of the Frontiers Journals Series: they are collections of at least ten articles, all centered on a particular subject. With their unique mix of varied contributions from Original Research to Review Articles, Frontiers Research Topics unify the most influential researchers, the latest key findings and historical advances in a hot research area! Find out more on how to host your own Frontiers Research Topic or contribute to one as an author by contacting the Frontiers Editorial Office: researchtopics@frontiersin.org

METHODS FOR SYNAPTIC INTERROGATION

Topic Editors:
Dirk Feldmeyer, Julich Research Center, Helmholtz Association of German Research Centers (HZ), Germany
John F. Wesseling, Institute of Neurosciences of Alicante (IN), Spain
P. Jesper Sjöström, McGill University, Canada

Citation: Feldmeyer, D., Wesseling, J. F., Sjöström, P. J., eds. (2020). Methods for Synaptic Interrogation. Lausanne: Frontiers Media SA.
doi: 10.3389/978-2-88963-864-2

Table of Contents

frontiers in Synaptic Neuroscience

EDITORIAL
published: 10 June 2020
doi: 10.3389/fnsyn.2020.00023

Editorial: Methods for Synaptic Interrogation

Dirk Feldmeyer[1,2]*, *John F. Wesseling*[3]* and *P. Jesper Sjöström*[4]*

[1] Institute of Neuroscience and Medicine 10 (INM-10), Research Centre Jülich, Jülich, Germany, [2] Department of Psychiatry, Psychotherapy and Psychosomatics, Medical School, RWTH Aachen University Hospital, Aachen, Germany, [3] Instituto de Neurociencias, CSIC-UMH, San Juan de Alicante, Spain, [4] Centre for Research in Neuroscience, Brain Repair and Integrative Neuroscience Program, Department of Medicine, Department of Neurology and Neurosurgery, The Research Institute of the McGill University Health Centre, Montreal General Hospital, Montreal, QC, Canada

Keywords: synapse, plasticity, electrophysiology, microscopy, optogenetics, methods

Editorial on the Research Topic

Methods for Synaptic Interrogation

INTRODUCTION

Synapses are the specialized junctions that transmit information between neurons and that connect them into circuits. Synapses are often plastic and can be modulated to process information in the short term as well as to store information in the long term (Zucker and Regehr, 2002; Abbott and Regehr, 2004; Markram et al., 2012; Maheux et al., 2016). They play fundamental roles in biological computation and memory formation—key tasks of the brain. Yet precisely how this occurs remains unknown at levels ranging from molecules to systems.

A wealth of powerful techniques for interrogating synaptic function has emerged in recent years, and yet important studies continue to additionally rely on methods in use decades ago. Training new researchers in the state of the art is a time-consuming bottleneck that is often hampered by the lack of easy-to-understand descriptions of best practices. Here we provide a collection of straightforward, accessible papers on a range of methods for exploring synaptic function, written by experts.

METHODS DESCRIBED IN THIS COLLECTION

Finding Synaptic Connections

To analyze synaptic transmission, it is paramount to use clearly identified synaptic connections. Deep insight has previously been obtained by studying classic preparations such as neuromuscular junctions of many species, the Mauthner cell in fish, and the calyx of Held in the mammalian brain stem (e.g., Del Castillo and Katz, 1954; Korn and Faber, 2005; Neher, 2017). In this collection, four articles describe how new neuronal connections can be identified and investigated at the levels of structure and function.

Cultured neurons forming autaptic synapses, i.e., those established by a neuron onto itself, provide an elegant tool allowing the study of synaptic transmission under tightly controlled conditions. Bekkers describes the procedures to prepare and record from autaptic cultures as well as several applications, such as the study of vesicular release, the role of synaptic proteins, and the neuromodulation of synaptic release.

Qi et al. review several applications of the *in-vitro* slice preparation to investigate structure-function aspects of synaptic transmission at connections between identified neurons, e.g., synaptic efficacy and release probability, as well as the location of synaptic contacts. Due to ease of drug

OPEN ACCESS

Edited by:
Maxim Volgushev, University of Connecticut, United States

Reviewed by:
Kurt Gottmann, Heinrich Heine University of Düsseldorf, Germany

***Correspondence:**
Dirk Feldmeyer
d.feldmeyer@fz-juelich.de
John F. Wesseling
johnfwesseling@gmail.com
P. Jesper Sjöström
jesper.sjostrom@mcgill.ca

Received: *06 May 2020*
Accepted: *12 May 2020*
Published: *10 June 2020*

Citation:
Feldmeyer D, Wesseling JF and Sjöström PJ (2020) Editorial: Methods for Synaptic Interrogation. Front. Synaptic Neurosci. 12:23. doi: 10.3389/fnsyn.2020.00023

application compared to *in-vivo* studies, acute slices are also useful to study neuromodulation of neurotransmitter release. It is also the method of choice to study synaptic transmission in human brain tissue.

Jouhanneau and Poulet describe sophisticated experimental procedures they developed to study monosynaptically connected neurons in superficial layers of intact rodent brain. Using two-photon microscopy for multiple targeted patching, they are able to characterize how excitatory and inhibitory neuronal microcircuits act *in vivo*, under realistic physiological conditions and behavioral states. The use of multiple electrodes additionally permits the study of connectivity profiles in intact neuronal microcircuits.

Besides local connections, identification of long-range monosynaptic connections is an important step to unravel paths across brain areas. In their original paper, Lavin et al. report procedures for labeling monosynaptic connections of a specific neuron population using modified rabies virus injection in combination with a preceding injection of helper viruses (also see Wickersham et al., 2007). They found that the helper virus concentration was a key determinant for the quality of tracing results.

Exploring Plasticity and Synaptic Release

Long-term potentiation and depression are widely thought to underlie learning and memory, yet the locus of plasticity expression is still a matter of debate (Costa et al., 2017). Four articles in this Research Topic describe a range of electrophysiological and optical imaging techniques and analytic frameworks that enable the elucidation of the locus of expression. Glasgow et al. review the strengths and pitfalls of a range of methods, including classical tools such as spontaneous release, paired-pulse ratio, and NMDA:AMPA ratio, to more novel optical tools including calcium indicators and optical actuators. Brock et al. delve deeper into CV analysis, providing a detailed but straightforward how-to guide to this classical method, including derivation of formulas, computer simulations, and potential pitfalls. Although paired recordings may alleviate some of the pitfalls, even monosynaptic inputs typically arise at multiple sites, which can complicate the analysis. However, in two complementary methods papers, MacDougall and Fine and Padamsey et al. show how key complications can be avoided by combining electrophysiology with two-photon microscopy of transmission at single sites in acute slices.

A better understanding of short-term plasticity is needed for understanding how biological computation works, but remains a complicated effort. Bykowska et al. review new analytic procedures for using underlying principles to help infer both release statistics and synaptic dynamics from data ranging from unitary connections to *in-vivo* network recordings. However, a complication is that the underlying principles have never been completely resolved.

For example, many models assume that individual synapses can only release transmitter from a single vesicle at a time. However, a seemingly contradictory concept that is also widespread is that individual synapses maintain a readily releasable pool of multiple synaptic vesicles. And indeed, Barros-Zulaica et al. present a detailed analysis of monosynaptic connections indicating that at least some types of synapses can and often do release transmitter from multiple vesicles within this pool simultaneously, in agreement with several other studies (Rudolph et al., 2015). Soares et al. reach a similar conclusion from a complementary study using the glutamate detector iGluSnfr to circumvent caveats associated with electrophysiological and less direct optical imaging techniques. Soares et al. also introduce a new method to eliminate measurement biases related to failures of neurotransmission that may be adaptable to a broad range of techniques.

Furthermore, even models that allow for multivesicular release often assume uniform release probability among the vesicles within the readily releasable pool. However, Gustafsson et al. review their own early evidence from neonatal hippocampus that many vesicles typically categorized as readily releasable only undergo exocytosis after persistent repetitive stimulation. The phenomenon is likely related to the current concept of reluctant or slowly releasing subdivisions of readily releasable pools, now reported at a wide range of synapse types. By themselves, the results do not necessarily contradict assumptions about uniform release probability because the delayed exocytosis may involve post-primed vesicles that were not actually readily releasable at the beginning of stimulation. Nevertheless, as part of a review of complications that can interfere with measurements of vesicle recruitment to the readily releasable pool, Wesseling summarizes evidence from calyx of Held that seems incompatible (also see Maschi and Klyachko, 2020).

Two-Photon Neurotransmitter Uncaging

Neurotransmitter uncaging can act within milliseconds, making it a powerful method for elucidating synaptic function, but with traditional light sources such UV lamps or violet lasers, uncaging is not spatially confined. With two-photon excitation, however, the uncaged volume is smaller than a μm^3, providing biological realism and excellent experimental control.

Ellis-Davies—a pioneer of uncaging—describes the state of the art of two-photon glutamate uncaging. He compares the pros and cons of using different cages and provides historical background. Building on this work, the Araya team describes in detail a cost-effective custom-built microscope for cutting-edge combined two-photon uncaging and imaging (Mitchell et al.). Relying on a single ultrafast laser to save cost, this cutting-edge setup can still activate multiple dendritic spines with near simultaneous calcium imaging.

Combining Genetics and Optics

Optogenetics is a powerful technique for interrogating neural circuits, yet its implementation is not always straightforward. In a practical how-to paper, Gruver and Watt show how to optimize optogenetic activation of cerebellar Purkinje cell axons to interrogate inputs to the deep cerebellar nuclei. The concept of optogenetics is often extended to include the monitoring of cellular compartments, e.g., using genetically encoded calcium indicators. Brockhaus et al. coupled GCaMP6f to synaptophysin to create synGCaMP6f, which enriches the calcium indicator

in boutons, resulting in excellent signal to noise in small axonal compartments.

It is also possible to combine optical and genetic methods to explore synaptic architecture. Reshetniak and Rizzoli provide a detailed review of approaches for visualizing synaptic organelles and cytoskeletal protein complexes, such as styryl dyes, cypHer5E-labeled antibodies, quantum dots, toxins, etc. Finally, Ebner et al. provide a detailed protocol for how to optically induce calcium-dependent gene activation and labeling of active neurons using CaMPARI and Cal-Light. Because CaMPARI acts in seconds but Cal-Light requires several days, these powerful tools can serve different purposes on different timescales.

CONCLUDING REMARKS

This collection of papers provides the current state of a sampling of useful methods for interrogating synaptic function. We gathered these papers to make accessible a range of techniques, by disseminating a set of how-to descriptions written by the experts themselves. Our hope is that this collection will serve as a useful foundation for future synaptic neuroscience research, and a new generation of important discoveries about the nature of brain function.

AUTHOR CONTRIBUTIONS

DF, JW, and PS wrote the manuscript.

FUNDING

DF was supported by the Helmholtz Society and the European Union's Horizon 2020 Research, Innovation Programme under Grant Agreement No. 785907. JW was supported by the Consejo Superior de Investigaciones Científicas and Ministry of Science (BFU2016-80918R) of Spain, and the Generalitat Valenciana (PROMETEO 2019/020). PS was supported by FRQS Chercheurs-Boursiers Senior 9 Award #254033.

ACKNOWLEDGMENTS

We are deeply thankful to all the authors who contributed articles to this Research Topic. We would also like to thank Alanna Watt for help and useful discussions.

REFERENCES

Abbott, L. F., and Regehr, W. G. (2004). Synaptic computation. *Nature* 431, 796–803. doi: 10.1038/nature03010

Costa, R. P., Mizusaki, B. E. P., Sjöström, P. J., and van Rossum, M. C. W. (2017). Functional consequences of pre- and postsynaptic expression of synaptic plasticity. *Philos. Trans. R. Soc. B Biol. Sci.* 372:20160153. doi: 10.1098/rstb.2016.0153

Del Castillo, J., and Katz, B. (1954). Quantal components of the end-plate potential. *J. Physiol.* 124, 560–573. doi: 10.1113/jphysiol.1954.sp005129

Korn, H., and Faber, D. S. (2005). The Mauthner cell half a century later: a neurobiological model for decision-making? *Neuron* 47, 13–28. doi: 10.1016/j.neuron.2005.05.019

Maheux, J., Froemke, R. C., and Sjöström, P. J. (2016). "Functional plasticity at dendritic synapses," in *Dendrites, 3th Edn,* eds G. Stuart, N. Spruston, and M. Häusser (Oxford: Oxford University Press), 465–498. doi: 10.1093/acprof:oso/9780198745273.003.0018

Markram, H., Gerstner, W., and Sjöström, P. J. (2012). Spike-timing-dependent plasticity: a comprehensive overview. *Front. Synaptic Neurosci.* 4:2. doi: 10.3389/978-2-88919-043-0

Maschi, D., and Klyachko, V. A. (2020). Spatiotemporal dynamics of multivesicular release is determined by heterogeneity of release sites within central synapses. *eLife* 9:e55210. doi: 10.7554/eLife.55210

Neher, E. (2017). Some subtle lessons from the calyx of held synapse. *Biophys. J.* 112, 215–223. doi: 10.1016/j.bpj.2016.12.017

Rudolph, S., Tsai, M. C., von Gersdorff, H., and Wadiche, J. I. (2015). The ubiquitous nature of multivesicular release. *Trends Neurosci.* 38, 428–438. doi: 10.1016/j.tins.2015.05.008

Wickersham, I. R., Finke, S., Conzelmann, K. K., and Callaway, E. M. (2007). Retrograde neuronal tracing with a deletion-mutant rabies virus. *Nat. Methods* 4, 47–49. doi: 10.1038/nmeth999

Zucker, R. S., and Regehr, W. G. (2002). Short-term synaptic plasticity. *Annu. Rev. Physiol.* 64, 355–405. doi: 10.1146/annurev.physiol.64.092501.114547

Conflict of Interest: The authors declare that the research was conducted in the absence of any commercial or financial relationships that could be construed as a potential conflict of interest.

frontiers in Synaptic Neuroscience

REVIEW
published: 09 January 2019
doi: 10.3389/fnsyn.2018.00048

Two-Photon Uncaging of Glutamate

*Graham C. R. Ellis-Davies**

Department of Neuroscience, Mount Sinai School of Medicine, New York, NY, United States

Two-photon microscopy produces the excited singlet state of a chromophore with wavelengths approximately double that used for normal excitation. Two photons are absorbed almost simultaneously, via a virtual state, and this makes the excitation technique inherently non-linear. It requires ultra-fast lasers to deliver the high flux density needed to access intrinsically very short lived intermediates, and in combination with lenses of high numerical aperture, this confines axial excitation highly. Since the two-photon excitation volume is similar to a large spine head, the technique has been widely used to study glutamatergic transmission in brain slices. Here I describe the principles of two-photon uncaging of glutamate and provide a practical guide to its application.

Keywords: Glu = glutamate, 2-photon, uncaging, quanta, plasticity, dendritic spikes

OPEN ACCESS

Edited by:
Per Jesper Sjöström, McGill University, Canada

Reviewed by:
Brenda L. Bloodgood, University of California, San Diego, United States
Won Chan Oh, University of Colorado, United States
Tommaso Fellin, Fondazione Istituto Italiano di Technologia, Italy

****Correspondence:***
Graham C. R. Ellis-Davies
graham.davies@mssm.edu

Received: *02 November 2018*
Accepted: *11 December 2018*
Published: *09 January 2019*

Citation:
Ellis-Davies GCR (2019) Two-Photon Uncaging of Glutamate. Front. Synaptic Neurosci. 10:48. doi: 10.3389/fnsyn.2018.00048

Caged compounds are, by definition, biological molecules which have been rendered inert by covalent attachment of a photochemical protecting group (Ellis-Davies, 2000). Originating in 1978 with caged ATP (Kaplan et al., 1978), all important biological signaling molecules and cations have been controlled by uncaging (Ellis-Davies, 2007). Conceptually simple in its design, the strategy is to block a crucial functionality of the biomolecule that is required for its activity with the "caging chromophore." Irradiation cuts this bond, releasing the caged substrate. The term "caged compounds" was coined by a physiologist (Joe Hoffman) who was unaware of the term "caged" was used in chemistry to mean box-like structures. And we should not forget, of course, those involved in animal husbandry use the term in a literal way. The simplicity of term remains attractive, so I use it in the way Hoffman did, to mean a *functional* cage.

After the initial success of caged ATP in the study of the Na,K-ATPase (Kaplan and Hollis, 1980), other biologists became interested in caged compounds. Henry Lester, George Hess, David Trentham and Roger Tsien and their co-workers all made seminal contributions to the field with the development of caged cGMP (Lester et al., 1979), carbamoylcholine (Walker et al., 1986), IP_3 (Walker et al., 1987), and Ca^{2+} (Tsien and Zucker, 1986) in the 1980–86 period. All these caged compounds were designed for photolysis with near-UV light using the *ortho*-nitrobenzyl photochemical protecting group introduced by Barltrop et al. (1966). As an interesting aside I would like to point out that Barltrop was a natural product chemist who did a sabbatical with Melvin Calvin in the 1950s, with whom he must have started to think about using light for synthetic organic chemistry, and that Barltrop's work eventually lead to the gene chip revolution (McGall et al., 1997). For neuroscience, the work of the Hess group was crucial, as they developed the first caged neurotransmitters (Wilcox et al., 1990; Wieboldt et al., 1994a,b; Niu et al., 1996; Breitinger et al., 2000). And so laser uncaging of neurotransmitters became a topic of active research for neurophysiologists using one-photon (1P) photolysis (Eder et al., 2004). Beyond low-resolution functional mapping of receptors (Eder et al., 2004), 1P uncaging has been widely used for studying circuit connectivity by many laboratories (Shepherd, 2012). Such studies will not be discussed here.

The challenge for using 1P uncaging of glutamate for high-resolution functional mapping is that normal excitation must release the neurotransmitter wherever light hits the solution of caged compound. Of course lenses with a high numerical aperture will produce focused light, thus

glutamate concentrations will be maximal at the focal point. But the same quantity of glutamate will be released in every plane above and below this point because of linear excitation. Thus, in complex biological preparations, such as brain slices this can lead to large clouds of glutamate release outside the site of interest. One can immediately appreciate that 2P uncaging is potentially very advantageous for glutamate neurophysiology, as uncaging becomes pin-point due the nature of non-linear excitation (**Figure 1A**).

A SHORT HISTORY OF 2-PHOTON EXCITATION

Quantum theory says that absorption of light occurs when the transition moment between the ground state and the excited state is non-zero. This is only true when there is an inversion of orbital symmetry during the transition (Electronic states have symmetries that are either even, *gerade* or "*g*" states, or uneven, *ungerade,* or "*u*" states). This principle is formalized in the parity selection rule for light absorption: transitions from *g* to u or from *u* to *g* are allowed; transitions from *g* to *g,* or from *u* to *u* are forbidden. Two-photon excitation gives rise to "virtual" states in which the electronic wave function remains unchanged when the Cartesian coordinate system of the molecule is inverted through the center of symmetry, and so this process is strictly "geometrically forbidden" by the parity selection rule. Göppert-Mayer (1931) realized that Paul Dirac's dispersion theory could apply to 2P *excitation* as well as light transmission. She developed the idea of an "intermediate electronic excited state" (K in **Figure 1B**) that must have opposite symmetry of the ground and final excited state (so the parity rule for light absorption still applies), but overall the selection rule for 2P transitions is the exact opposite of 1P: *g* to *g* is allowed but *g* to *u* is forbidden (Friedrich, 1982).

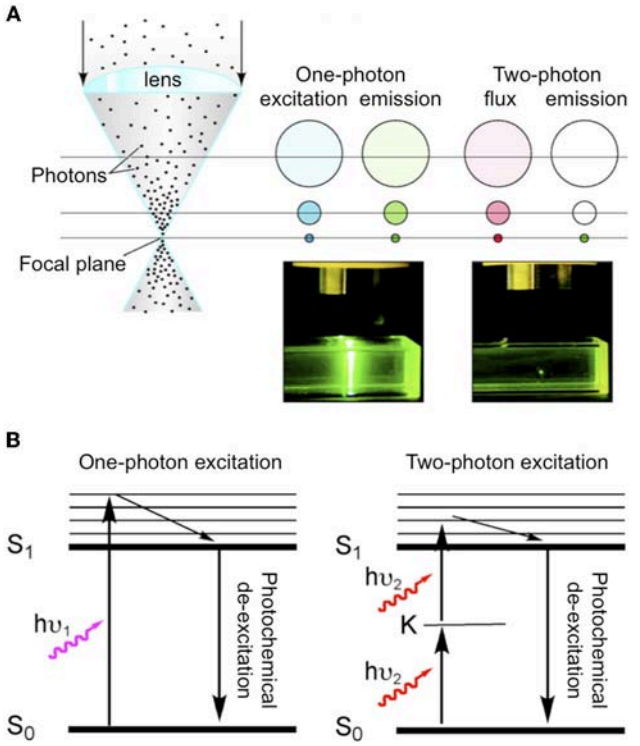

FIGURE 1 | Comparison of one-and two-photon excitation. **(A)** Cartoon illustrating the fundamental differences between normal (i.e., one-photon) absorption and two-photon absorption. As blue light is focused by a lens during one-photon excitation of a chromophore the concentration of excited molecules increases but the same number of molecules are excited in each z section. Whereas, during two-photon irradiation with NIR the total flux in each z section is constant (red), but excitation only occurs at the focus (green). Hence, for fluorescence emission can be seen throughout the light path for one-photon, but is pin-point for two-photon. Adapted from Ellis-Davies (2011b), by permission of the American Chemical Society. **(B)** Simple Jablonski diagram illustrating the absorption of light from the ground state (S_0) to excited state (S_1) occurs directly with one-photon absorption (hu_1), and goes via a "virtual state" K in the case of two-photon excitation (hu_2).

The development of lasers revolutionized molecular spectroscopy, and in the 1960s and 70s 2P excitation was used to study electronic excitations that had only been known theoretically [i.e., the forbidden *g* to *g* transitions, and especially *gerade* excited state energy levels (Friedrich, 1982)]. Birge et al were the first to use 2P excitation to study biological chromophores, such as rhodopsin (Birge, 1986). In 1978 Sheppard and Kampfner suggested 2P excitation might be used for non-linear scanning microscopy (Sheppard and Kampfner, 1978). But it was not until the pioneering work of Denk et al. (1990) that this idea was realized (Denk et al., 1990). Of course since that time 2P imaging has become a standard optical method (Denk and Svoboda, 1997; Soeller and Cannell, 1999; Zipfel et al., 2003; Helmchen and Denk, 2005; Ellis-Davies, 2011b; Crowe and Ellis-Davies, 2014). In the abstract of their seminal study Denk also observed that: "This technique also provides unprecedented capabilities for three-dimensional, spatially resolved photochemistry, particularly photolytic release of caged effector molecules" (Denk et al., 1990).

In fact, uncaging was starting to mature as a technique by 1990, however uncaging of neurotransmitters was essentially nascent at that point, so Denk's observation proved to be extremely prescient. Glutamate was not uncaged in brain slices until 1993 (Callaway and Katz, 1993). Denk himself published the first proof of principle 2P uncaging experiment a year later (Denk, 1994). Until 1999 no further reports of 2P photolysis in living cells appeared. Lipp and Niggli uncaged Ca^{2+} by irradiation of DM-nitrophen (Kaplan and Ellis-Davies, 1988) to mimic Ca^{2+} sparks to initiate Ca^{2+} waves in cardiac myocytes (Lipp and Niggli, 1998). Their work suggested to me that the electron donating groups of the DM-nitrophen chromophore conferred sufficient absorptivity upon of the *ortho*-nitrobenzyl chromophore to make it reasonably sensitive to 2P excitation and useful for highly localized uncaging. This discovery lead to the synthesis of DMNPE-4 (Ellis-Davies, 1998) and DMCNB-glutamate (**Figure 2**), both of which are 2P sensitive (DelPrincipe et al., 1999; Ellis-Davies, 1999).

Starting in 1999 several new caged glutamate probes were developed by organic chemists. I give brief survey of these, starting with Roger Tsien's contribution to this field, which was

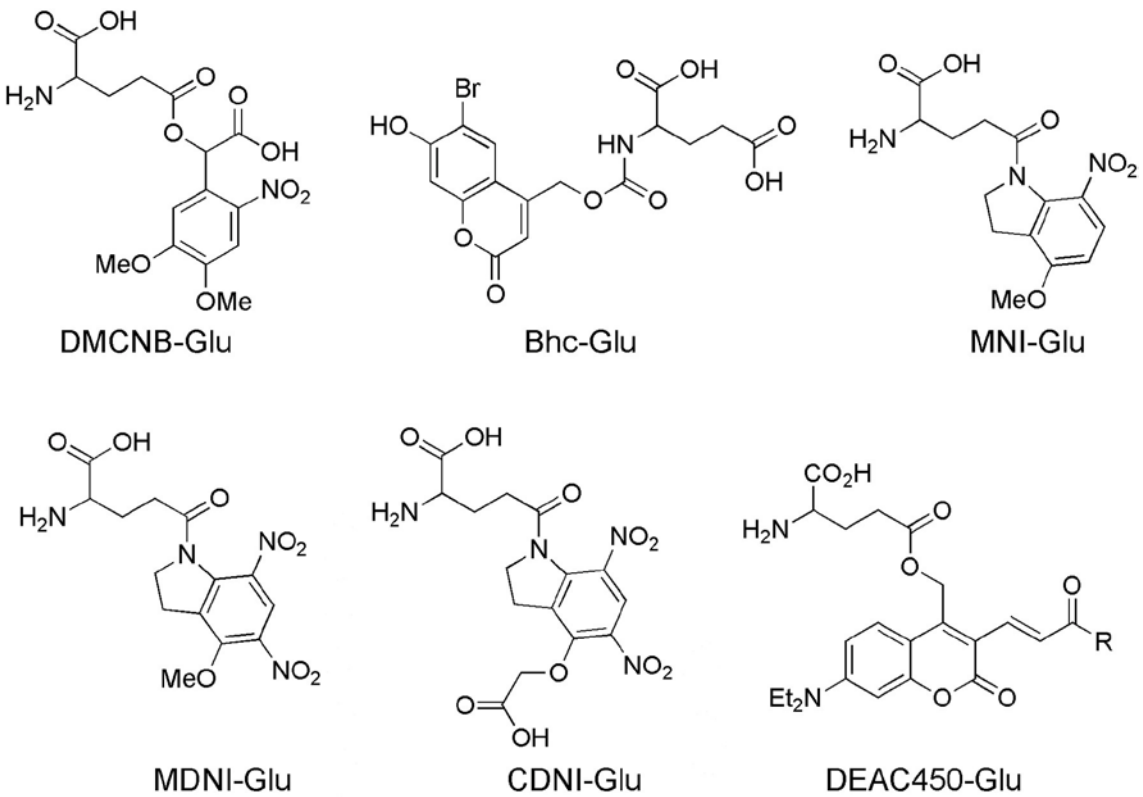

FIGURE 2 | Caged glutamate probes designed for 2P photolysis. Structures of caged glutamate probes used for 2P photolysis. DMCNB, (Ellis-Davies, 1999), Bhc, (Furuta et al., 1999); MNI, (Matsuzaki et al., 2001); MDNI, (Fedoryak et al., 2005); CDNI, (Ellis-Davies et al., 2007a); DEAC450, (Olson et al., 2013b).

his inaugural paper to *PNAS* on his election to US National Academy of Sciences.

Bhc-Glu

The bromo-hydroxycoumarin (Bhc) probe that was specifically designed for 2P photolysis of glutamate (Furuta et al., 1999). Based around the coumarin photochemical protecting group which had first been used for uncaging cAMP (Furuta et al., 1995) with near-UV, Bhc-Glu (**Figure 2**) has a 2P cross-section of 50 GM, and a quantum yield of photolysis of 0.019, giving a probe with photochemical properties of great potential. However, actually caged via the carbamate, the known (Corrie et al., 1993) slow rate of hydrolysis of the photoproduct (which is *not* glutamate) meant Bhc-Glu eventually released the neurotransmitter on a slow time scale of 10 ms. The residence time of excited molecules on the 2P focal volume is 0.3 ms (Brown et al., 1999). Furthermore, the chromophore itself is quite lipophilic causing severe solubility issues for practical use in brain slices. Never the less, Bhc-Glu was important for the field as it pointed the way for future developments, and highlighted the difficulties in making an "ideal cage" for neurophysiology.

MNI-Glu

The first caged glutamate that worked well for 2P uncaging was 4-methoxy-7-nitroindolinyl-glutamate (MNI-Glu, **Figure 2**). Independently synthesized by myself (Matsuzaki et al., 2000) and the Corrie laboratory in 2000 (Papageorgiou and Corrie, 2000). Built on knowledge gained from DM-nitrophen and DMCNB-Glu (Ellis-Davies, 1999), that electron-rich nitroaromatic chromophores were able to undergo efficacious 2PE, I reasoned that adding such substituents to nitroindolines would probably allow effective 2P uncaging in brain slices. Such proved to be the case. In 2001 my collaboration with Kasai and co-workers set the foundations for the use of 2P uncaging of MNI-Glu (Matsuzaki et al., 2001) by many other neurophysiologists (see below). MNI-Glu has proved useful as it possesses a unique set of properties in terms of a caged Glu probe: (1) It is biologically inert toward AMPA-R. Remarkably, even at 12 mM there is no antagonism apparent. It was also reported initially that MNI-Glu was inert toward GABA-A receptors (Canepari et al., 2001), but this proved not to be the case subsequently. (2) It is highly stable at physiological pH. Solutions used for 1 day at 25–37°C also show no hydrolysis, and stored at 4°C for 4 days also show no hydrolysis (Huang et al., 2005). (3) It is highly soluble in physiological buffer, solutions of at least 200 mM can be made. (4) It is photolyzed with good efficiency by near-UV light, with a quantum yield in the 0.065–0.085 range (Papageorgiou and Corrie, 2000; Corrie et al., 2016). (5) It absorbs light well in the near-UV (extinction coefficient 4,500 mM cm at 336 nm), and can be photolyzed with violet lasers that are standard on

confocal microscopes as the absorption in about 10% of the maximum. (6) It has a 2P uncaging cross-section of 0.06 GM at 730 nm (Matsuzaki et al., 2001), a value sufficient to allow many experiments without apparent phototoxicity (see below). (7) These absorptions make MNI-Glu optical compatible with other chromophores used for fluorescence imaging, such as GFP, YFP, most Ca^{2+} dyes, and dyes, such as Alexa-594. (8) Glutamate is released quickly, as judged by the rapid rise times of photo-evoked currents produced by 50 ms flashes (Matsuzaki et al., 2001). (9) 2P uncaging at single spines shows excellent 3D resolution (**Figure 3**) (10) MNI-Glu can be made easily in five steps from readily available starting material. After the initial success of MNI-Glu for 2P uncaging experiments in brain slices in 2001 (Matsuzaki et al., 2001), the probe became commercially available from Tocris in about 2003. It should be noted that we used the trifluoroacetic acid (TFA) salt in 2001 (Matsuzaki et al., 2001), and zwitterionic MNI-Glu (i.e., desalted, non-TFA compound) in 2003 (Smith et al., 2003), and it was the latter that was commercialized by Tocris. Of course, once in solution the TFA counter ion freely dissociates from the caged compound as it is dissolved in physiological buffer.

With MNI-Glu having such a nice combination of chemical, photochemical and pharmacological properties, what scope for probe development remained? Three properties were open to chemical ingenuity: (a) increase in quantum yield, allowing less light for photolysis, potentially enabling longer term experiments; (b) improvements in GABA-A receptor pharmacology; and (c) photolysis at longer wavelengths, allowing 2-color uncaging of two biomolecules with chromatic independence.

MDNI-Glu

4-Methoxy-5,7-dinitroindolinyl-glutamate (MDNI-Glu) was the probe that first attempted to improve the quantum yield of uncaging (Fedoryak et al., 2005). We found that this probe was photolyzed with a quantum yield of about 0.5. We also found that in a cuvette 2P photolysis of MDNI-Glu was about 5–6 times more effective than MNI-Glu suggesting the second nitro group merely increases the quantum yield. Uncaging MDNI-Glu with a violet laser enabled extremely efficacious photo-evoked Ca^{2+} signals in astrocytes in brain slices (Fedoryak et al., 2005). Recently our probe has been remade in Hungary, with the claim that it was a "novel invention," with exactly same molecule was called "DNI-Glu" (Chiovini et al., 2014).

CDNI-Glu

We found there were some practical issues of solubility with MDNI-Glu, so addressed these by adding one carboxylate to methoxy group. Thus, 4-carboxymethoxy-5,7-dinitroindolinyl-glutamate (CDNI-Glu) was introduced in 2007. This probe maintained (Ellis-Davies et al., 2007a) the chemical properties of MDNI-Glu. In collaboration with the groups of Bergles and Kasai we showed it performed well on neurons photochemically. The Bergles group tested CDNI-Glu against MNI-Glu "blind," with solutions of both probes bath-applied to brain slices in succession to same neuron multiple times, the dramatic difference in current responses was striking. The Kasai group tested the same compounds by local perfusion of each probe to neurons in brain slices, 2P uncaging revealed that CDNI-Glu was about five times larger than MNI-Glu. The Bergles group saw similar results in their 2P experiments (Ellis-Davies, 2011b). Interestingly, conditions for 2P uncaging could be found where multiple uncaging events on single spines with MNI-Glu were phototoxic, but not for CDNI-Glu as less energy was required to evoke the same current in the latter case (Ellis-Davies et al., 2007a).

CDNI-GABA

In 2010 we introduced the CDNI-caged version of GABA (Matsuzaki et al., 2010). This was the first compound used for efficient and effective 2P uncaging of GABA on neurons in brain slices. The quantum yield of uncaging of photolysis is slightly

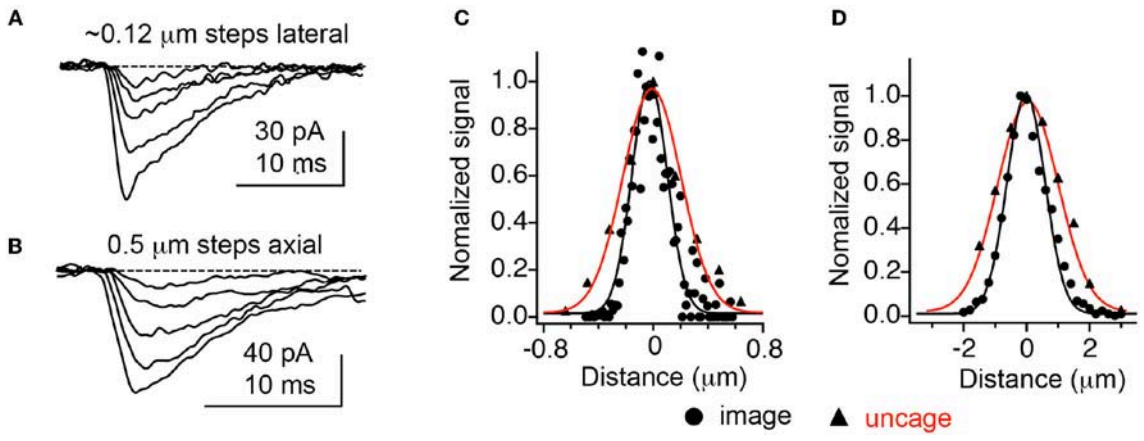

FIGURE 3 | Optical resolution compared with 2P uncaging currents at single spines. **(A,B)** Currents decrease at an isolated spine on a CA1 neuron as the uncaging laser is moved away from the cell laterally and axially. **(C,D)** Comparison of currents evoked by 2P uncaging of MNI-Glu (red curves) with diffraction-limited 2P imaging of 0.1 mm fluorescent beads. Adapted from Smith et al. (2003), by permission of the Physiological Society.

higher than CDNI-Glu, being 0.6. It is useful to note that both compounds were made with no silica gel chromatography being required. However, the last synthetic step, addition of the crucial second nitro group, requires quite harsh conditions, so the final reaction mixture requires HPLC purification with TFA, leading to the isolation of the TFA salt of the CDNI cage (Ellis-Davies, 2011a). While a detailed discussion of caged GABA is beyond the scope of a review on 2P uncaging of glutamate, I would note that CDNI-GABA has proved quite useful in several reports (Chiu et al., 2013; Gross et al., 2013; Oh et al., 2016; Villa et al., 2016). In particular, in a very elegant study by Kwon and co-workers on synaptogenesis during development induced by GABA (Oh et al., 2016).

DEAC450-Glu

Simple nitroaromatic caged compounds, such as DM-nitrophen and CDNI-Glu are best photolyzed with a Ti:sapphire laser at red wavelengths around 720–740 nm. They are much less sensitive to photolysis at longer wavelengths, such as 800–830 nm range (Kantevari et al., 2010, **Figure 4**), imply that at 900 nm these probes are photostable. This longer wavelength "optical window" provides an opening for uncaging biomolecules with second, complementary wavelength of 2P light. Thus, we synthesized a 7-diethylaminocoumarin (DEAC) derivative that absorbs visible light maximally around 450 nm, and is uncaged by 2P excitation best at double this wavelength (Olson et al., 2013b). Crucially the near-UV absorption minimum around 350 nm leads to a very low 2P absorption at 720 nm, the region that is ideal for simple nitroaromatic caged compounds. Thus, when DEAC450-Glu is partnered with CDNI-GABA, or CDNI-Glu with DEAC450-GABA, two-color uncaging experiments with 720 nm and 900 nm are possible (Amatrudo et al., 2015). An example of the latter is shown in **Figure 4**. In this experiment each compound was bath applied at similar concentrations, irradiation with 720 and 900 nm light independent in current clamp were used to fire/block action potentially with excellent chromatic selectivity using dual 2P uncaging. I would note that DEAC450 is fluorescent in the green range, so is more difficult to use with GFP than MNI, CDNI or RuBi. We have found that normal red dyes (e.g., Alexa-594) are excited in the NIR (**Figure 4** uses 1,070 nm for imaging).

Like MNI-Glu and CDNI-Glu, DEAC450-Glu, and DEAC450-GABA antagonize GABA-A receptors (Olson et al., 2013b; Amatrudo et al., 2014). Indeed all caged Glu and GABA probes we have tested are antagonistic. Interestingly, the rutheniumbipyridials RuBi-Glu and RuBi-GABA have very similar IC-50 values (7.8 and 4.4 mM, **Table 1**), providing clue to the origin of the antagonism, namely that a carboxylate of each probe can enter the GABA binding cleft and act as a competitive antagonist to GABA. The amino acid carboxylate of Glu is probably too close to RuBi to influence binding much, whereas for DEAC450 it has more influence (**Table 1**). These data suggested that to reduce antagonism dramatically one probably needed to "cover" both ends of the amino acids, thus we developed the concept of "cloaked caged compounds" to deliver biologically inert caged neurotransmitters (Richers et al., 2017).

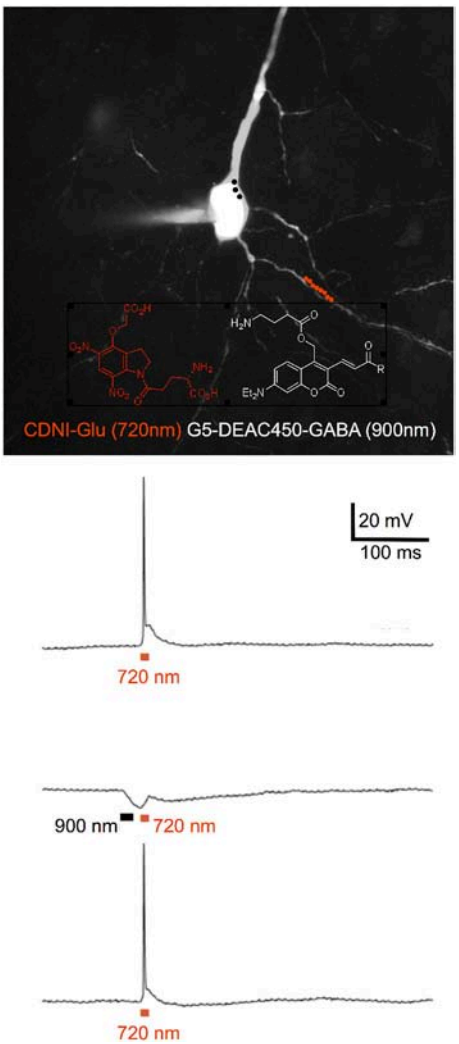

FIGURE 4 | Two-color 2P uncaging of glutamate and GABA. CDNI-Glu (1 mM) and G5-DEAC450-GABA (0.6 mM) were bath applied to a brain slice. The red and black dots indicate the location for irradiation at 720 nm along a dendrite (red) and 900 nm around the soma (black). Uncaging at 720 nm (10 × 1 ms, 50 mW) fired an action potential (top trace), which could be blocked (middle trace) by prior uncaging at 900 nm (3 × 3 ms, 50 mW). Such blockade was found to be reversible (lower trace). Adapted from Richers et al. (2017), by permission from Wiley-VCH.

Cloaked Caged Neurotransmitters

The initial pharmacological characterization of MNI-Glu by Corrie and Ogden in 2001 suggested that this probe was inert toward both AMPA and GABA-A receptors (Canepari et al., 2001). We did not evaluate inhibitory pharmacology for the simple reason that we did not expect any off-target issues for caged Glu. Around the same time, the first report of caged GABA antagonism appeared (Molnár and Nadler, 2000), but this important study was largely ignored by the field for many years. Much to our surprise we discovered subsequently that MNI-Glu did indeed antagonize GABA-A receptors (Ellis-Davies et al., 2007b). It is now widely agreed that all the most widely used

TABLE 1 | GABA-A receptor antagonism of caged neurotransmitters.

Caged NT	IC_{50} (μM)
MNI-Glu	105
CDNI-GABA	110
CDNI-Glu	243
DEAC450-Glu	33
DEAC450-GABA	0.5
PEG-DEAC450-GABA	11
RuBi-Glu	7.7
RuBi-GABA	4.4
G5-DEAC450-GABA	900

All IC-50s were measured by bath application of the probe to brain slices acutely isolated from adult mice. L2/3 neurons in the PFC were patch-clamped and a stimulation pipette was used to evoke GABAergic input in the presence of AMPA-and NMDA-receptor blockers (Olson et al., 2013b; Amatrudo et al., 2014; Richers et al., 2017).

caged Glu and GABA probes do show some antagonism toward GABA-A receptors, *especially at concentrations required for 2P uncaging*. We have recently introduced what we think is a general solution to this pervasive problem, namely attaching large neutral or anionic dendrimers to the caged neurotransmitters (Richers et al., 2017). Starting with the strongly antagonistic DEAC450-GABA, we have found that a neutral fifth generation dendrimer reduces the IC-50 90-fold. I would suggest that our cloaking method could provide a general solution to a problem that bedeviled the caged neurotransmitter field since 2000.

Other Caging Chromophores for 2P Photolysis

The low 2P uncaging cross-section of simple nitroaromatic chromophores has lead chemists to seek to improve the ability of caged Glu to undergo 2P photolysis. The strategy adopted has been to follow rules outlined in 1998 by Marder (Albota et al., 1998) and Reinhardt (Reinhardt et al., 1998), where the size of extended p-electron systems was studied systematically in relation to the 2P absorption cross-section. Goeldner and co-workers pioneered the application of this insight, with several publications. In particular their 2008 description of a large polyaromatic system called BNSF (Gug et al., 2008a), which had a 2P cross-section of 20 GM, was important. Unfortunately the caged glutamate derivative made with the BNSF photochemical protecting group was not very buffer soluble, so no biology was reported with this probe. In contrast, a much smaller aromatic antennae (a methoxybiphenyl) allowed a reasonably soluble caged with a 2P cross-section of 4.5 GM (Gug et al., 2008b). Even with such a promising value compared to MNI-Glu, no 2P biology was reported. We found that a side-by-side biological comparison of a more buffer soluble version of the probe with MNI-Glu reveled that the cuvette properties did not lead to expected improvements in 2P neurobiology, suggesting caution in being able to translate simple chemical measurements to practical physiology (Passlick and Ellis-Davies, 2017). The final chromophore in this series was used to cage GABA in 2012. Electron rich amino-nitrobiphenyls (ANBP) were reported to have 2P cross-section up to 73 GM. But even this exceptional value still required 25 ms irradiation to produce currents of 6 pA from layer 2/3 neurons in brain slices (Donato et al., 2012).

RuBi-Glu also appears to undergo effective 2P uncaging in brain slices (Fino et al., 2009). This probe has been commercially available for many years, but relatively few studies have utilized it (Fino and Yuste, 2011). In contrast, it is RuBi-GABA that has proved popular for visible light (i.e., 1P) uncaging of GABA. Indeed, as noted below, this probe proves a very useful optical partner to MNI-Glu for two-color uncaging using blue and 720 nm 2P light for RuBi and MNI, respectively.

Chemists have reported the development of several other extended p-electron systems for potentially caging neurotransmitters (Korzycka et al., 2015; Cueto Diaz et al., 2016). But like BNSF these all seem to suffer a solubility problem, one which must be inherent to large lipophilic organic molecules. Thus, no neurophysiology has yet been reported using these chromophores.

PRACTICAL CONSIDERATIONS FOR 2P UNCAGING OF GLUTAMATE

Storage

MNI-Glu

As noted above, MNI-Glu is exceptionally stable. Solids either as the TFA salt or zwitterion seem indefinitely stable. Solutions at neutral pH can be used after at least 1 year (Amatrudo et al., 2015). Usefully, ACSF solution may be frozen and used subsequently, after filtration, testing for pH and osmolarity. In the case of solutions for local perfusion, Hepes-buffered solutions may be made, frozen in small aliquots, and used very effectively. Solutions of pH > 8 must be avoided as the amide bond can hydrolyze (Kantevari et al., 2016).

CDNI and MDNI-Glu

These probes are freely soluble in physiological buffer, solutions of 20 mM are easily made. However, the probes cannot be stored at this pH as they are slightly unstable. There is a similar problem for MDNI-Glu. Thus, solutions must be slightly acidic (ca. pH 4) and frozen for long-term storage. HPLC analysis of solutions frozen for over 2 years at pH 4 show no change (Amatrudo et al., 2015). The probes are easily stored safely as solids for many years. Small aliquots may be made by dissolving in methanol with 0.1% TFA, followed by solvent evaporation on a speedvac.

RuBi-Glu

The chemical bond that cages Glu in this probe is not base labile. So solutions of 20 mM can be made and used without any worries over hydrolytic stability. A bigger concern for RuBi-Glu is handling with ambient white light. While MNI-Glu is relatively stable under normal fluorescent lights (these lack much violet light, and have no near-UV), such light readily and rapidly

TABLE 2 | Photochemical properties of caged glutamate probes.

Caged Glu	ε (λ_{max})	QY	ε.QY	Time of release (ms)	2PuCS (GM/nm)	Stability at pH 7.4	Commercially available
CNB	500 (350)	0.14	20	0.021	NR	Slow hydrolysis	Y
MNI	4,500 (336)	0.065	293	NR*	0.06 (740)	Stable	Y
Bhc	17,500 (368)	0.019	329	3–10	1.0 (740)	Stable	N
RuBi	5,600 (450)	0.13	728	0.05	0.14 (800)	Stable	Y
MDNI	6,400 (330)	0.5	3,200	NR*	0.06 (720)	Slow hydrolysis	Y
CDNI	6,400 (330)	0.5	3,200	NR*	0.06 (720)	Slow hydrolysis	N
DEAC450	43,000 (450)	0.39	16,800	NR*	0.5 (900)	Stable frozen	N

*ε, extinction coefficient; λ_{max}, absorption maximum; QY, quantum yield; 2PuCS, two-photon uncaging cross section; NR, not reported. *Biology with these p robes implies fast release.*

photolyzes RuBi-Glu, so caution must be paid to handling this probe. We use Roscolux filters 13 and 25 to protect MNI and RuBi.

Methods of probe application to brain slices

The simplest method is, of course, bath application of a known concentration of probe. However, given that most probes cost >$100 for 10 mg, this can seem prohibitively expensive for many studies. However, it does allow certain types of studied to be performed which other methods do not (Higley and Sabatini, 2008). Notably, if one requires precise pharmacology to be performed across many samples and days, it is the most reliable way to carry out such experiments. A minimum volume for recirculation is about 7 mL, thus care must be taken to monitor solvent evaporation over the period of experimentation.

The simplest alternative to bath application is use of a picospritzer fitted with a normal patch pipette. I recommend Hepes buffered solutions, as opposed to normal ACSF, as this seems the best way to control the pH of the application solution. Very small volumes of solution can last days, leading to substantial cost savings. In the case of any TFA salt, care must be taken to test the pH of the application solution. Here the non-TFA salt of MNI-Glu is quite advantageous, as high concentrations of a zwitterion will not place undue demands on the buffer capacity of solutions that typically only contain 10 mM Hepes. A distinct disadvantage of this method is that local perfusion is indeed quite local, so if one wants to study a large neuron, such as CA1 principal cells the puffing pipette may have to be moved. An elegant alternative has been described by Wang and co-workers who developed a simple "large bore" local perfusion system which we have also used extensively (Civillico et al., 2011). While requiring slightly more material, perhaps 0.2–0.5 mL for a day, this method delivers caged compounds very effectively. And even allows a double barrel application system for side by side comparison of two caged compounds on the same cell (Passlick and Ellis-Davies, 2017).

An elegant method for uncaging power calibration was developed by Sabatini. Concerned about the light scattering nature of brain tissue, they found that one could calibrate the local power dosage at spine head by using the bleaching of Alexa-594 at a known concentration. They found that 40% bleach at any depth below the slice surface would in practice give consistent currents with MNI-Glu uncaging (Bloodgood and Sabatini, 2007). A summary of the chemical properties of important caged glutamate probes is shown in **Table 2**.

KEY EXPERIMENTS USING 2P UNCAGING OF GLUTAMATE

The first study using 2P uncaging was carried out by Denk in 1994. With this work he established many, but of all, of the key aspects of the new method. Unfortunately his work was essentially limited by the reality that he had to use a probe (CNB-carbamoylcholine) that was originally developed for UV uncaging, and so was not very effective for 2P excitation. Uncaging periods of 30–40 ms were required to produce large ACH receptors currents from cultured cells. In spite of this limitation, Denk revealed that 2P uncaging showed excellent axial resolution, as would be expected for non-linear excitation (Denk, 1994). With the advent of caged glutamate probes designed for 2P neurophysiology, a diverse group of scientists have used the method to study the details of spine and dendritic physiology.

Optical Quanta

In 2001 Kasai and co-workers established that 2P uncaging of MNI-Glu on cultured neurons enabled diffraction-limited uncaging such that the photo-evoked currents (2pEPSCs) exactly matched individual mEPSCs. Cultured cells allowed staining of pre-synaptic terminals with FM1-43, such that we could visualize pre-synaptic elements which were opposite to AMPA receptor hotspots detected by uncaging, suggesting such receptor clusters were indeed synapses. The evoked currents were found to be correlated with the square of the incident power, imply a true 2P excitation effect (Matsuzaki et al., 2001). Importantly, the high resolution "functional mapping" technique described by Denk was implemented in brain slices with MNI-Glu. We found that APMA receptor currents were strongly correlated with spine head volume. In subsequent experiments it was established that these currents correlated not with a change in conductivity, but with receptor density itself (Tanaka et al., 2005). Furthermore, functional mapping was carried out at several z sections of the brain slice, with the photo-evoked currents showing excellent axial resolution (**Figure 3**). This set of experiments established for the first time that the very coin of communication in the brain, quantal release of glutamate, could be mimicked optically by neurophysiologists.

Optical LTP at Visually Designated Synapses

The development of the dual 2P laser microscope by Kasai was the next important advance in this field. Also having two galvanometers, this instrument allowed simultaneous, chromatically independent uncaging, and imaging. The key experiment with this microscope established that an increase in synaptic strength at small spines on CA1 neurons was accompanied by a long-term increase in spine head volume. In other words, LTP had a structural correlate (Matsuzaki et al., 2004). Such optical LTP is probably at a higher frequency (5–10x) than LFS in low Mg^{2+} solutions, yet since glutamatergic input was independent of the pre-synapse, we could select spines of various sizes to show that an increase in volume at individual, isolated was independent from other nearby spines. The photostimulation protocol required ∼60 (photochemical) quanta at 1 Hz at 0 mV, or the same input in "zero Mg^{2+}" solutions with GFP-labeled neurons that were not patch-clamped. Such experiments established a powerful method for LTP at visually designated spines, and suggested spines were physically isolated biochemical compartments, a reality that many other experiments showed was only partially true.

2pEPSCs and 2P Ca^{2+} Imaging

Using the second 2P laser for imaging function rather than structure is a second important application of the dual 2P laser microscope. Given the importance of intracellular Ca^{2+} signaling in neurons, use of low affinity fluorescent Ca^{2+} dyes was the obvious first port of call for this approach. Sabatini and Svoboda both published seminal studies imaging Ca^{2+} in spine heads in 2004 and 2005, respectively (Carter and Sabatini, 2004; Sobczyk et al., 2005). In parallel to these studies, Kasai also reported how the size of the spine neck controlled Ca^{2+} compartmentalization in spines (Noguchi et al., 2005). Sabatini and co-workers published a series of intense studies concerned with the modulation of $CaV_{2.3}$ on spine heads (Ngo-Anh et al., 2005; Bloodgood and Sabatini, 2007; Giessel and Sabatini, 2010). They have found that this voltage-gated ion channel is intimately linked in space to yet another channel on spine heads, the small conductance Ca^{2+}-activated potassium (or SK) ion channel. They found that increases in Ca^{2+} concentration via $CaV_{2.3}$ initiated hyperpolarisation, giving rise to apparently conflicting functions of spine Ca^{2+} when compared to NMDA receptors. Sabatini and co-workers concluded that the latter are in a privileged microdomain where large (ca. 10–20 μM), highly local increases in Ca^{2+} via $CaV_{2.3}$ activate adjacent SK channels and the SK channels hyperpolarize spine head membrane potential. The changes in spine head Ca^{2+} from NMDA receptors is only 1–2 μM, so it does not rise to sufficiently high levels to stimulate SK channels. Thus, depending on its origin, spine Ca^{2+} can have bidirectional effects on local potential. All of these studies illustrate the strength of dual 2P microscopy to define the details of the nature of Ca^{2+} signaling in spine heads as the experimenter can immediately link cause and effect at visually designated spine using a stereotypical input.

Spine LTP Is Local and Non-compartmentalized

The initial single spine studies by Kasai suggested spines were functionally isolated compartments (Matsuzaki et al., 2001). And even though some Ca does spill out of the stimulated spine during 2P uncaging of glutamate, the size and response of each spine in short dendritic segments (ca. 10 mm) are uncorrelated, suggesting spines were isolated biochemcially. However, a seminal study by Harvey and Svoboda revealed that this was an over simplification (Harvey and Svoboda, 2007). They found that spines within 10 mm of a LTP spine seemed to sensitize small, nearby spine to activation to a "sub" optical LTP protocol. Thus, about half the uncaging pulses could be used to induce structural LTP at such spines. In a follow up that appeared shortly after this, the same authors added 2P FRET-FLIM imaging to reveal that *ras* was the biochemical signal transferring input from the initial LTP spine to its neighbors (Harvey et al., 2008). This latter study was carried out in collaboration with Yasuda, who went on to develop and apply a series of FRET-FLIM probes to study in exquisite detail many of the key molecules involved in spine LTP (Lee et al., 2009; Murakoshi et al., 2011, 2017; Zhao et al., 2011; Hedrick et al., 2016; Colgan et al., 2018). Yasuda's work has showed that some molecules remain compartmentalized, whereas other spread to proximate spines with various length and time constants. Crucial to such studies is the continued development of novel FRET-FLIM probes (Zhao et al., 2011; Chu et al., 2016; Laviv et al., 2016). Of course, all of Yasuda's work is built upon the seminal optical LTP study using MNI-Glu by Kasai and co-workers published in 2004 (Matsuzaki et al., 2004).

Complementary to studies on structural LTP have been several reports using 2P uncaging of glutamate to induce structural LTD or synaptogenesis. For example, Kwon and Sabatini showed that 2P uncaging of MNI-Glu on dendritic shafts of L2/3 neurons in brain slices from young mice (P 10–15 days) could induce the growth of new spines. Subsequently the same group showed that neuroligin-1 was crucial for such synaptogenesis (Kwon et al., 2012). Interestingly these spines were always partnered by presynaptic cells, as local electrical stimulation revealed post-synaptic Ca transients in the new spine. Such data are consistent with earlier reports from the Svoboda group that when new spines appeared *in vivo* in adult mice they were found to have a presynaptic bouton with a PSD, which was detected *post-hoc* using EM. In 2012 the Sabatini laboratory used 2P uncaging of MNI-Glu to reveal that synaptogenesis in MSN was activity dependent by chemogenetic control of input onto MSN (Kozorovitskiy et al., 2012). In the same year Zito and co-workers used MNI-Glu to show that *de novo* 2P-induced spinogenesis in slice cultures was dependent on proteasome activity (Hamilton et al., 2012). Zito and co-workers have used 2P uncaging of MNI-Glu to induce LTD at single spines on neurons in slice culture. Starting in 2013, they have shown that "low frequency" 2P stimulation at 0.1 Hz can caused structural LTD. Uncaging power was adjusted to mimic quantal input, and 90 pulses caused spines to shrink in a manner that depended on NMDA, IP_3, and metabotropic receptors. Shortly after this study appeared,

we found that structural LTD was induced by pairing GABA uncaging around spines prior to 2P uncaging of CDNI-Glu in a spike-timing dependent way (Hayama et al., 2013). The latter study was also performed on slice cultures, but 2P input was at 1 Hz. Importantly, the study by Zito demonstrated that LTD was reversible, as MNI-Glu uncaging at 10 Hz not only restored spines to their previous size, but could induce LTP at the LTD spine. Follow up studies by Zito and co-workers showed that the LTD sensitivity could be conferred by local LTP (Oh et al., 2015), and does not always require NMDA receptors (Stein et al., 2015).

Clustered Spine Signaling Studied Using 2P Uncaging

The non-linear electrical response of neurons is the fundamental of their input-output function. Local non-linearities within branch segments were first reported by Llinas in 1980 (Llinás and Sugimori, 1980). Such dendritic spikes have been studied using local electrode stimulation and uncaging with focused UV lasers (Schiller et al., 2000). In 2006 Magee and co-workers pioneered the use of 2P uncaging to study dendritic spikes with two studies in 2006 (Gasparini and Magee, 2006; Losonczy and Magee, 2006). They established that the local integration of unitary excitatory post-synaptic potentials (uEPSPs[1]) was dependent on the number and distribution of uEPSPs. By patch clamp measurements along main apical dendrite of CA1 neurons the Magee laboratory showed that non-linear output was observed only when the number uEPSPs generated by two-photon uncaging of MNI-Glu at several sites were temporally clustered within a 20-micron dendritic segment. Spatial distribution of the same number of uEPSPs over more than 100 microns produced linear outputs locally (Gasparini and Magee, 2006). In both cases, when the uEPSPs were temporally asynchronous, linear output was recorded locally. Two-photon interrogation of radial oblique dendrites with MNI-Glu revealed that these thin neurites had a different input-output pattern from the main dendritic trunk. In radial oblique dendrites equal non-linear somatic outputs were observed for spatially clustered and distributed multiple uEPSPs (Losonczy and Magee, 2006). This study also provided an estimate of the number of uEPSPs required on average for dendritic spike by showing that two-photon uncaging at ∼20–25 spines (with a somatic potential of 0.25 mV per spine) could evoke a dendritic spike. Thus, 6–7 2pEPSPs of 0.75 mV can have approximately the same somatic output as 25 uEPSPs of 0.25 mV. Finally, the Magee laboratory established that if clustered inputs were positioned close the main trunk (ca. 20 microns), a significantly larger synaptic input was required to induce a dendritic spike when compared to that required for inputs positioned near the end (>90 microns from the trunk) of a dendrite. This is because the main trunk acts as a current sink for proximal inputs, whereas because the input resistance increases toward the terminus of the dendrite this prevents current loss and reduces the amount of synaptic input required for a dendritic spike. Following this, Hausser et al. used such patterned inputs to verify predictions from cable theory by Wilfred Rall, confirming that the direction of local dendritic input (toward the cell was stronger than away from it) conditioned the strength of the Ca^{2+} signal (Branco et al., 2010).

In 2008 the Magee laboratory explored the effects of clustered inputs on the *strength of the output*, and discovered that some branches were plastic. Significant differences between the non-linear electrical responses of individual dendrites were discovered. Stereotypical two-photon uncaging of MNI-Glu at spatially clustered groups of spine heads on almost 500 basal and proximal radial oblique dendrites of CA1 neurons revealed that non-linear responses could be categorized bimodally into "strong" and "weak" groups with a 10-fold difference in rate of change of potential (Losonczy et al., 2008). Interestingly they found that weak branches could be converted into strong ones by bath application of carbachol and local theta stimulation for about 20 min, and called this new form of synaptic plasticity "branch-strength potentiation." In Kv1.4 knockout mice such changes were not observed. Following this study, Tonegawa and coworkers used clustered multi-spine uncaging of MNI-Glu to determine if changes branch-strength potentiation were accompanied by local protein translation (Govindarajan et al., 2011). They found that when 10–20 spines were synchronously stimulated in the presence of forskolin a few spines (average 4) within this group underwent structural LTP that lasted for at least 240 min (sL-LTP). If forskolin was not present the initial volume change was not sustained beyond 150 min. Note, previous studies (Matsuzaki et al., 2004; Harvey and Svoboda, 2007; Harvey et al., 2008; Patterson et al., 2010) did not normally go beyond 100 min so did not detect this slow volume loss. There was also a small group of spines (average 1–2) from the initial group of unpotentiated spines that exhibited sL-LTP from a second round of clustered uncaging, but without forskolin present. This "local priming" is similar to that reported by Svoboda and coworkers for single spine structural LTP. Yasuda and co-workers have shown that induction of structural LTP at a few (3–7) spatial dispersed spines can initiate ERK translocation to the nucleus of CA1 neurons where the protein upregulated transcription factors (Zhai et al., 2013). This fascinating study revealed that a few spines on the same branch did not have this effect, whereas 7 spines distributed over as much as 200 microns could produce an integrated nuclear increase in ERK. Interestingly the "timing window" for these effects had to be >40 min. These recent studies by the Tonegawa and Yasuda laboratories suggest that CA1 pyramidal neurons can encode both clustered and distributed synaptic inputs to control protein translation and transcription in distinctly different ways.

These 2P studies were conducted on pyramidal cells in the cortex. What about neurons in other brain regions? Surmeier and co-workers have used multi-spine head uncaging of MNI-Glu on medium spiny neurons (MSN) to show that sustained upstates can be generated by targeting clustered groups of 10 spines more than 100 microns from the soma (Plotkin et al.,

[1]Note this standard notation for quantal signals is sometimes used for "uncaging EPSPs". I find such use in this context confusing, as photochemical "uEPSPs" are used to mimic quantal uEPSPs. For this reason we chose, in 2001, "2pEPSC" to denote the currents evoked by two-photon uncaging of glutamate. Laser energy can be tuned to evoke a postsynaptic signal that mimics either an uEPSC or uEPSP, or such signals can be made supraquantal by increasing the uncaging energy.

2011). Stimulation of clusters at a distance of 40–60 microns reduced the length of the upstate from 120 to 30 ms. T-type Ca channels and NMDA receptors were found to be responsible for these upstates, but other voltage gated dendritic ion channels had no role. Interestingly, direct and indirect pathway MSN had similar non-linear properties.

Two-Color Actuation: 2P Uncaging of Glutamate Paired With Blue-Sensitive Probes

Most of the studies using using 2P uncaging of glutamate used our original protocol with Ti:sapphire lasers mode-locked at about 720 nm to photolyze MNI-Glu. Since the absorbance of visible light above about 420 nm by MNI is low, and is zero in the blue region, this provides a chromatic channel to allow two-color actuation. Several studies have appeared using this approach. The first example of this approach was a very elegant study by Oertner and co-workers in 2008 (Zhang et al., 2008). This work took advantage of the poor response of ChR2 toward 2P excitation at 720 nm, thus expressing this light-gated ion channel in neurons allowed a 2-color induction of LTP at single spines. Blue light was used to initiate an action potential, with 2P uncaging of MNI-Glu timed to coincide with this in a form of spike-timing dependent plasticity (STDP). In the same year Kasai and co-workers presented a detailed study of the role of protein synthesis in STDP, but we used whole-cell patch-clamp in a more Classical approach (Tanaka et al., 2008). The use of blue light to induce spikes by Oertner circumvented the patch-clamp requirement, and in so doing allowed them to use FRET-FLIM imaging of CaMKII to quantify the time course of kinase action during plasticity at single spines.

More recently, Kasai and co-workers used the poor response of RuBi-GABA toward 2P activation to study effects of local inhibition of spine LTD and LTP (Hayama et al., 2013). Pairing blue photolysis of this probe with CDNI-Glu (uncaging at 720 nm), they concluded that local inhibition could condition the response of single spines to a STDP-like LTD protocol (but not LTP). Further, the LTD effect was not entirely local, as with about 15 microns induced by the spread of activated cofilin. Independent studies by Higley and co-workers revealed that using the same chemical probes, discovered that a subset of spines on L2/3 neurons in the PFC receive both glutamatergic and GABAergic synaptic inputs (Chiu et al., 2013). On disynaptic spines, inhibition was sufficient to sculpt spine Ca^{2+} transients, modeling suggested that the resistance of the spine neck was sufficient to isolate such spines from any local dendritic inhibition. Finally, the development of the blue-light responsive DEAC450 (Olson et al., 2013a; Agarwal et al., 2017) will enable the study of the symbiotic nature of intracellular signaling and excitatory input.

SUMMARY

Two-photon uncaging of glutamate is a well-established technique. It has been widely used to probe the electrical and biochemical properties of individual spines. Its spatial precision provides a powerful means of optical interrogation of these privileged domains. Further, the ability to address the physiological synergism amongst spines can be studied in a unique way by multi-spine stimulation using 2P uncaging. Chromatically complementary chromophores provide further opportunities for physiologists to probe parallel signaling pathways using 2-color photoactuation. Many genetically-encoded probes do not normally respond effectively to the short 2P wavelengths used for glutamate uncaging, thus "old" and "modern" optical methods could work together in an uniquely powerful way for many future experiments.

AUTHOR CONTRIBUTIONS

The author confirms being the sole contributor of this work and has approved it for publication.

ACKNOWLEDGMENTS

My laboratory has been supported by the NIH since 1995 by GM053395, funding that supported development of all our caged compounds discussed in this review. This review was also supported by NIH grant NS069720. I want to acknowledge the contribution of recent members of my group who helped develop two-color uncaging (Drs. Jeremy Olson, Joe Amatrudo, Matt Richers, and Stefan Passlick). Collaborations with Drs. Bernardo Sabatini and Mike Higley, and their co-workers, were also crucial to this project. Finally, I want to acknowledge the interactions with my long-term collaborators Drs. Ernst Niggli and Haruo Kasai, and their co-workers, without whom two-photon uncaging would not have been possible.

REFERENCES

Agarwal, H. K., Zhai, S., Surmeier, D. J., and Ellis-Davies, G. C. R. (2017). Intracellular uncaging of cGMP with blue light. *ACS Chem. Neurosci.* 8, 2139–2144. doi: 10.1021/acschemneuro.7b00237

Albota, M., Beljonne, D., Bredas, J., Ehrlich, J., Fu, J., Heikal, A., et al. (1998). Design of organic molecules with large two-photon absorption cross sections. *Science* 281, 1653–1656. doi: 10.1126/science.281.5383.1653

Amatrudo, J. M., Olson, J. P., Agarwal, H. K., and Ellis-Davies, G. C. R. (2015). Caged compounds for multichromic optical interrogation of neural systems. *Eur. J. Neurosci.* 41, 5–16. doi: 10.1111/ejn.12785

Amatrudo, J. M., Olson, J. P., Lur, G., Chiu, C. Q., Higley, M. J., and Ellis-Davies, G. C. R. (2014). Wavelength-selective one- and two-photon uncaging of GABA. *ACS Chem. Neurosci.* 5, 64–70. doi: 10.1021/cn400185r

Barltrop, J. A., Plant, P. J., and Schofield, P. (1966). Photosensitive protective groups. *Chem Commun*. 0, 822–823. doi: 10.1039/c19660000822

Birge, R. (1986). Two-photon spectroscopy of protein-bound chromophores. *Acc. Chem. Res.* 199, 138–146. doi: 10.1021/ar00125a003

Bloodgood, B. L., and Sabatini, B. L. (2007). Nonlinear regulation of unitary synaptic signals by CaV(2.3) voltage-sensitive calcium channels located in dendritic spines. *Neuron* 53, 249–260. doi: 10.1016/j.neuron.2006.12.017

Branco, T., Clark, B. A., and Häusser, M. (2010). Dendritic discrimination of temporal input sequences in cortical neurons. *Science* 329, 1671–1675. ‘

Breitinger, H. G., Wieboldt, R., Ramesh, D., Carpenter, B. K., and Hess, G. P. (2000). Synthesis and characterization of photolabile derivatives of serotonin for chemical kinetic investigations of the serotonin 5-HT(3) receptor. *Biochemistry* 39, 5500–5508. doi: 10.1021/bi992781q

Brown, E. B., Shear, J. B., Adams, S. R., Tsien, R. Y., and Webb, W. W. (1999). Photolysis of caged calcium in femtoliter volumes using two-photon excitation. *Biophys. J.* 76, 489–499. doi: 10.1016/S0006-3495(99)77217-6

Callaway, E. M., and Katz, L. C. (1993). Photostimulation using caged glutamate reveals functional circuitry in living brain slices. *Proc. Natl. Acad. Sci. USA*. 90, 7661–7665. doi: 10.1073/pnas.90.16.7661

Canepari, M., Nelson, L., Papageorgiou, G., Corrie, J., and Ogden, D. (2001). Photochemical and pharmacological evaluation of 7-nitroindolinyl-and 4-methoxy-7-nitroindolinyl-amino acids as novel, fast caged neurotransmitters. *J. Neurosci. Meth.* 112, 29–42. doi: 10.1016/S0165-0270(01)00451-4

Carter, A. G., and Sabatini, B. L. (2004). State-dependent calcium signaling in dendritic spines of striatal medium spiny neurons. *Neuron* 44, 483–493. doi: 10.1016/j.neuron.2004.10.013

Chiovini, B., Turi, G. F., Katona, G., Kaszas, A., Palfi, D., Maak, P., et al. (2014). Dendritic spikes induce ripples in parvalbumin interneurons during hippocampal sharp waves. *Neuron* 82, 908–924. doi: 10.1016/j.neuron.2014.04.004

Chiu, C. Q., Lur, G., Morse, T. M., Carnevale, N. T., Ellis-Davies, G. C. R., and Higley, M. J. (2013). Compartmentalization of GABAergic inhibition by dendritic spines. *Science* 340, 759–762. doi: 10.1126/science.1234274

Chu, J., Oh, Y., Sens, A., Ataie, N., Dana, H., Macklin, J. J., et al. (2016). A bright cyan-excitable orange fluorescent protein facilitates dual-emission microscopy and enhances bioluminescence imaging *in vivo*. *Nat. Biotechnol.* 34, 760–767. doi: 10.1038/nbt.3550

Civillico, C. F., Rickgauer, J. P., and Wang, S. H. H. (2011). "Targeting and excitation of photoactivatable molecules: design considerations for neurophysiology experiments," in *Photosensitive Molecules for Controlling Biological Function*, eds Chambers, J. J., and Kromer, R. H (New York City: Springer), 7–37. doi: 10.1007/978-1-61779-031-7_2

Colgan, L. A., Hu, M., Misler, J. A., Parra-Bueno, P., Moran, C. M., Leitges, M., et al. (2018). PKCalpha integrates spatiotemporally distinct Ca(2+) and autocrine BDNF signaling to facilitate synaptic plasticity. *Nat. Neurosci.* 21, 1027–1037. doi: 10.1038/s41593-018-0184-3

Corrie, J., Kaplan, J. H., Forbush, B., Ogden, D. C., and Trentham, D. R. (2016). Photolysis quantum yield measurements in the near-UV; a critical analysis of 1-(2-nitrophenyl)ethyl photochemistry. *Photochem. Photobiol. Sci.* 15, 604–608. doi: 10.1039/C5PP00440C

Corrie, J. E., DeSantis, A., Katayama, Y., Khodakhah, K., Messenger, J. B., Ogden, D. C., et al. (1993). Postsynaptic activation at the squid giant synapse by photolytic release of L-glutamate from a 'caged' L-glutamate. *J. Physiol.* 465, 1–8. doi: 10.1113/jphysiol.1993.sp019662

Crowe, S. E., and Ellis-Davies, G. C. R. (2014). Longitudinal *in vivo* two-photon fluorescence imaging. *J. Comp. Neurol.* 522, 1708–1727. doi: 10.1002/cne.23502

Cueto Diaz, E., Picard, S., Klausen, M., Hugues, V., Pagano, P., Genin, E., et al. (2016). Cooperative veratryle and nitroindoline cages for two-photon uncaging in the NIR. *Chem. Eur. J.* 22, 10848–10859. doi: 10.1002/chem.201601109

DelPrincipe, F., Egger, M., Ellis-Davies, G. C., and Niggli, E. (1999). Two-photon and UV-laser flash photolysis of the Ca cage, dimethoxynitrophenyl-EGTA-4. *Cell Calcium* 25, 85–91. doi: 10.1054/ceca.1998.0009

Denk, W. (1994). Two-photon scanning photochemical microscopy: mapping ligand-gated ion channel distributions. *Proc. Natl. Acad. Sci. U.S.A.* 91, 6629–6633. doi: 10.1073/pnas.91.14.6629

Denk, W., Strickler, J. H., and Webb, W. W. (1990). Two-photon laser scanning fluorescence microscopy. *Science* 248, 73–76. doi: 10.1126/science.2321027

Denk, W., and Svoboda, K. (1997). Photon upmanship: why multiphoton imaging is more than a gimmick. *Neuron* 18, 351–357. doi: 10.1016/S0896-6273(00)81237-4

Donato, L., Mourot, A., Davenport, C. M., Herbivo, C., Warther, D., Léonard, J., et al. (2012). Water-soluble, donor-acceptor biphenyl derivatives in the 2-(o-nitrophenyl)propyl series: highly efficient two-photon uncaging of the neurotransmitter γ-aminobutyric acid at $\lambda = 800$ nm. *Angew. Chem. Int. Ed.* 51, 1840–1843. doi: 10.1002/anie.201106559

Eder, M., Zieglgansberger, W., and Dodt, H. U. (2004). Shining light on neurons–elucidation of neuronal functions by photostimulation. *Rev. Neurosci.* 15, 167–183. doi: 10.1515/REVNEURO.2004.15.3.167

Ellis-Davies, G. C. R. (1998). Synthesis of photolabile EGTA derivatives. *Tetrahedron Lett.* 39, 953–956. doi: 10.1016/S0040-4039(97)10668-2

Ellis-Davies, G. C. R. (1999). Localized photolysis of caged compounds. *J. Gen. Physiol.* 114:1a.

Ellis-Davies, G. C. R. (2000). "Basics of photoactivation," in *Imaging Living Cells: A Laboratory Manual*, eds R. Yuste, and A. Konnerth (Cold Spring Harbor, NY: Cold Spring Harbor Press), 300–320.

Ellis-Davies, G. C. R. (2007). Caged compounds: photorelease technology for control of cellular chemistry and physiology. *Nat. Methods* 4, 619–628. doi: 10.1038/nmeth1072

Ellis-Davies, G. C. R. (2011a). A practical guide to the synthesis of dinitroindolinyl-caged neurotransmitters. *Nat. Protoc.* 6, 314–326. doi: 10.1038/nprot.2010.193

Ellis-Davies, G. C. R. (2011b). Two-photon microscopy for chemical neuroscience. *ACS Chem. Neurosci.* 2, 185–197. doi: 10.1021/cn100111a

Ellis-Davies, G. C. R., Matsuzaki, M., Paukert, M., Kasai, H., and Bergles, D. E. (2007a). 4-Carboxymethoxy-5,7-dinitroindolinyl-Glu: an improved caged glutamate for expeditious ultraviolet and two-photon photolysis in brain slices. *J. Neurosci.* 27, 6601–6604. doi: 10.1523/JNEUROSCI.1519-07.2007

Ellis-Davies, G. C. R., Meucci, O., and Shimizu, S. (2007b). *Two-Photon Uncaging of Glutamate in the Cortex of Living Mice*. Society for Neuroscience Annual Conference 480.6/S14 (Washington, DC).

Fedoryak, O. D., Sul, J. Y., Haydon, P. G., and Ellis-Davies, G. C. R. (2005). Synthesis of a caged glutamate for efficient one- and two-photon photorelease on living cells. *Chem. Commun.* 0, 3664–3666. doi: 10.1039/b504922a

Fino, E., Araya, R., Peterka, D. S., Salierno, M., Etchenique, R., and Yuste, R. (2009). RuBi-Glutamate: two-photon and visible-light photoactivation of neurons and dendritic spines. *Front. Neural Circuits* 3:2. doi: 10.3389/neuro.04.002.2009

Fino, E., and Yuste, R. (2011). Dense inhibitory connectivity in neocortex. *Neuron* 69, 1188–1203. doi: 10.1016/j.neuron.2011.02.025

Friedrich, D. M. (1982). Two-photon molecular spectroscopy. *J Chem Ed* 59, 472–481. doi: 10.1021/ed059p472

Furuta, T., Torigai, H., Sugimoto, M., and Iwamura, M. (1995). Photochemical properties of new photolabile camp derivatives in a physiological saline solution. *J. Org. Chem.* 60, 3953–3956. doi: 10.1021/jo00118a008

Furuta, T., Wang, S. S., Dantzker, J. L., Dore, T. M., Bybee, W. J., Callaway, E. M., et al. (1999). Brominated 7-hydroxycoumarin-4-ylmethyls: photolabile protecting groups with biologically useful cross-sections for two photon photolysis. *Proc. Natl. Acad. Sci. U.S.A.* 96, 1193–1200. doi: 10.1073/pnas.96.4.1193

Gasparini, S., and Magee, J. C. (2006). State-dependent dendritic computation in hippocampal CA1 pyramidal neurons. *J. Neurosci.* 26, 2088–2100. doi: 10.1523/JNEUROSCI.4428-05.2006

Giessel, A. J., and Sabatini, B. L. (2010). M1 muscarinic receptors boost synaptic potentials and calcium influx in dendritic spines by inhibiting postsynaptic SK channels. *Neuron* 68, 936–947. doi: 10.1016/j.neuron.2010.09.004

Goppert-Mayer, M. (1931). Über Elementarakte mit zwei Quantensprüngen. *Ann. Phys.* 401, 273–294.

Govindarajan, A., Israely, I., Huang, S. Y., and Tonegawa, S. (2011). The dendritic branch is the preferred integrative unit for protein synthesis-dependent LTP. *Neuron* 69, 132–146. doi: 10.1016/j.neuron.2010.12.008

Gross, G. G., Junge, J. A., Mora, R. J., Kwon, H. B., Olson, C. A., Takahashi, T. T., et al. (2013). Recombinant probes for visualizing endogenous synaptic proteins in living neurons. *Neuron* 78, 971–985. doi: 10.1016/j.neuron.2013.04.017

Gug, S., Bolze, F., Specht, A., Bourgogne, C., Goeldner, M., and Nicoud, J.-F. (2008a). Molecular engineering of photoremovable protecting groups for two-photon uncaging. *Angew. Chem. Int. Ed.* 47, 9525–9529. doi: 10.1002/anie.200803964

Gug, S., Charon, S., Specht, A., Alarcon, K., Ogden, D., Zietz, B., et al. (2008b). Photolabile glutamate protecting group with high one- and two-photon uncaging efficiencies. *Chembiochem* 9, 1303–1307. doi: 10.1002/cbic.200700651

Hamilton, A. M., Oh, W. C., Vega-Ramirez, H., Stein, I. S., Hell, J. W., Patrick, G. N., et al. (2012). Activity-dependent growth of new dendritic spines is regulated by the proteasome. *Neuron* 74, 1023–1030. doi: 10.1016/j.neuron.2012.04.031

Harvey, C., Yasuda, R., Zhong, H., and Svoboda, K. (2008). The spread of Ras activity triggered by activation of a single dendritic spine. *Science* 321, 136–140. doi: 10.1126/science.1159675

Harvey, C. D., and Svoboda, K. (2007). Locally dynamic synaptic learning rules in pyramidal neuron dendrites. *Nature* 450, 1195–1200. doi: 10.1038/nature06416

Hayama, T., Noguchi, J., Watanabe, S., Takahashi, N., Hayashi-Takagi, A., Ellis-Davies, G. C. R., et al. (2013). GABA promotes the competitive selection of dendritic spines by controlling local Ca signaling. *Nat. Neurosci.* 16, 1409–1416. doi: 10.1038/nn.3496

Hedrick, N. G., Harward, S. C., Hall, C. E., Murakoshi, H., McNamara, J. O., and Yasuda, R. (2016). Rho GTPase complementation underlies BDNF-dependent homo- and heterosynaptic plasticity. *Nature* 538, 104–108. doi: 10.1038/nature19784

Helmchen, F., and Denk, W. (2005). Deep tissue two-photon microscopy. *Nat. Methods* 2, 932–940. doi: 10.1038/nmeth818

Higley, M. J., and Sabatini, B. L. (2008). Calcium signaling in dendrites and spines: practical and functional considerations. *Neuron* 59, 902–913. doi: 10.1016/j.neuron.2008.08.020

Huang, Y. H., Sinha, S. R., Fedoryak, O. D., Ellis-Davies, G. C., and Bergles, D. E. (2005). Synthesis and characterization of 4-methoxy-7-nitroindolinyl-D-aspartate, a caged compound for selective activation of glutamate transporters and N-methyl-D-aspartate receptors in brain tissue. *Biochemistry* 44, 3316–3326. doi: 10.1021/bi048051m

Kantevari, S., Matsuzaki, M., Kanemoto, Y., Kasai, H., and Ellis-Davies, G. C. R. (2010). Two-color, two-photon uncaging of glutamate and GABA. *Nat. Methods* 7, 123–125. doi: 10.1038/nmeth.1413

Kantevari, S., Passlick, S., Kwon, H. B., Richers, M., Sabatini, B. L., and Ellis-Davies, G. C. R. (2016). Development of anionically decorated caged neurotransmitters: *in vitro* comparison of 7-nitroindolinyl- and 2-(p-phenyl-o-nitrophenyl)-propyl-based photochemical probes. *Chembiochem* 17, 953–961. doi: 10.1002/cbic.201600019

Kaplan, J. H., and Ellis-Davies, G. C. R. (1988). Photolabile chelators for the rapid photorelease of divalent cations. *Proc. Natl. Acad. Sci. U.S.A.* 85, 6571–6575. doi: 10.1073/pnas.85.17.6571

Kaplan, J. H., Forbush, B., and Hoffman, J. F. (1978). Rapid photolytic release of adenosine 5′-triphosphate from a protected analogue: utilization by the Na:K pump of human red blood cell ghosts. *Biochemistry* 17, 1929–1935. doi: 10.1021/bi00603a020

Kaplan, J. H., and Hollis, R. J. (1980). External Na dependence of ouabain-sensitive ATP:ADP exchange initiated by photolysis of intracellular caged-ATP in human red cell ghosts. *Nature* 288, 587–589. doi: 10.1038/288587a0

Korzycka, K. A., Bennett, A., Cueto-Diaz, E. J., Wicks, G., Drobizhev, M., Blanchard-Desce, M., et al. (2015). Two-photon sensitive protecting groups operating via intramolecular electron transfer: uncaging of GABA and tryptophan. *Chem. Sci.* 6, 2419–2426. doi: 10.1039/C4SC03775H

Kozorovitskiy, Y., Saunders, A., Johnson, C. A., Lowell, B. B., and Sabatini, B. L. (2012). Recurrent network activity drives striatal synaptogenesis. *Nature* 485, 646–650. doi: 10.1038/nature11052

Kwon, H.-B., Kozorovitskiy, Y., Oh, W.-J., Peixoto, R. T., Akhtar, N., Saulnier, J. L., et al. (2012). Neuroligin-1-dependent competition regulates cortical synaptogenesis and synapse number. *Nat. Neurosci.* 15, 1667–1674. doi: 10.1038/nn.3256

Laviv, T., Kim, B. B., Chu, J., Lam, A. J., Lin, M. Z., and Yasuda, R. (2016). Simultaneous dual-color fluorescence lifetime imaging with novel red-shifted fluorescent proteins. *Nat. Methods* 13, 989–992. doi: 10.1038/nmeth.4046

Lee, S.-J. R., Escobedo-Lozoya, Y., Szatmari, E. M., and Yasuda, R. (2009). Activation of CaMKII in single dendritic spines during long-term potentiation. *Nature* 458, 299–304. doi: 10.1038/nature07842

Lester, H. A., Krouse, M. E., Nass, M. M., Wassermann, N. H., and Erlanger, B. F. (1979). Light-activated drug confirms a mechanism of ion channel blockade. *Nature* 280, 509–510. doi: 10.1038/280509a0

Lipp, P., and Niggli, E. (1998). Fundamental calcium release events revealed by two-photon excitation photolysis of caged calcium in Guinea-pig cardiac myocytes. *J. Physiol.* 508, 801–809. doi: 10.1111/j.1469-7793.1998.801bp.x

Llinás, R., and Sugimori, M. (1980). Electrophysiological properties of *in vitro* Purkinje cell dendrites in mammalian cerebellar slices. *J. Physiol.* 305, 197–213. doi: 10.1113/jphysiol.1980.sp013358

Losonczy, A., and Magee, J. C. (2006). Integrative properties of radial oblique dendrites in hippocampal CA1 pyramidal neurons. *Neuron* 50, 291–307. doi: 10.1016/j.neuron.2006.03.016

Losonczy, A., Makara, J. K., and Magee, J. C. (2008). Compartmentalized dendritic plasticity and input feature storage in neurons. *Nature* 452, 436–441. doi: 10.1038/nature06725

Matsuzaki, M., Ellis-Davies, G. C. R., and Kasai, H. (2000). *Two-Photon Uncaging of Glutamate Reveals AMPA Receptors Density Expression at Single Spine Heads*. Society for Neuroscience Annual Conference 426.12 (Washington, DC).

Matsuzaki, M., Ellis-Davies, G. C. R., Nemoto, T., Miyashita, Y., Iino, M., and Kasai, H. (2001). Dendritic spine geometry is critical for AMPA receptor expression in hippocampal CA1 pyramidal neurons. *Nat. Neurosci.* 4, 1086–1092. doi: 10.1038/nn736

Matsuzaki, M., Hayama, T., Kasai, H., and Ellis-Davies, G. C. R. (2010). Two-photon uncaging of gamma-aminobutyric acid in intact brain tissue. *Nat. Chem. Biol.* 6, 255–257. doi: 10.1038/nchembio.321

Matsuzaki, M., Honkura, N., Ellis-Davies, G. C., and Kasai, H. (2004). Structural basis of long-term potentiation in single dendritic spines. *Nature* 429, 761–766. doi: 10.1038/nature02617

McGall, G. H., Barone, A. D., Diggelmann, M., Fodor, S. P. A., Gentalen, E., and Ngo, N. (1997). The efficiency of light-directed synthesis of DNA arrays on glass substrates. *J. Am. Chem. Soc.* 119, 5081–5090. doi: 10.1021/ja964427a

Molnár, P., and Nadler, J. V. (2000). gamma-Aminobutyrate, alpha-carboxy-2-nitrobenzyl ester selectively blocks inhibitory synaptic transmission in rat dentate gyrus. *Eur. J. Pharmacol.* 391, 255–262. doi: 10.1016/S0014-2999(00)00106-0

Murakoshi, H., Shin, M. E., Parra-Bueno, P., Szatmari, E. M., Shibata, A. C. E., and Yasuda, R. (2017). Kinetics of endogenous CaMKII required for synaptic plasticity revealed by optogenetic kinase inhibitor. *Neuron* 94, 37–47.e35. doi: 10.1016/j.neuron.2017.02.036

Murakoshi, H., Wang, H., and Yasuda, R. (2011). Local, persistent activation of Rho GTPases during plasticity of single dendritic spines. *Nature* 472, 100–4. doi: 10.1038/nature09823

Ngo-Anh, T. J., Bloodgood, B. L., Lin, M., Sabatini, B. L., Maylie, J., and Adelman, J. P. (2005). SK channels and NMDA receptors form a Ca2+-mediated feedback loop in dendritic spines. *Nat. Neurosci.* 8, 642–649. doi: 10.1038/nn1449

Niu, L., Gee, K. R., Schaper, K., and Hess, G. P. (1996). Synthesis and photochemical properties of a kainate precursor and activation of kainate and AMPA receptor channels on a microsecond time scale. *Biochemistry* 35, 2030–2036. doi: 10.1021/bi9516485

Noguchi, J., Matsuzaki, M., Ellis-Davies, G. C., and Kasai, H. (2005). Spine-neck geometry determines NMDA receptor-dependent Ca2+ signaling in dendrites. *Neuron* 46, 609–622. doi: 10.1016/j.neuron.2005.03.015

Oh, W. C., Lutzu, S., Castillo, P. E., and Kwon, H. B. (2016). De novo synaptogenesis induced by GABA in the developing mouse cortex. *Science* 353, 1037–1040. doi: 10.1126/science.aaf5206

Oh, W. C., Parajuli, L. K., and Zito, K. (2015). Heterosynaptic structural plasticity on local dendritic segments of hippocampal CA1 neurons. *Cell Rep.* 10, 162–169. doi: 10.1016/j.celrep.2014.12.016

Olson, J. P., Banghart, M. R., Sabatini, B. L., and Ellis-Davies, G. C. R. (2013a). Spectral evolution of a photochemical protecting group for orthogonal two-color uncaging with visible light. *J. Am. Chem. Soc.* 135, 15948–15954. doi: 10.1021/ja408225k

Olson, J. P., Kwon, H. B., Takasaki, K. T., Chiu, C. Q., Higley, M. J., Sabatini, B. L., et al. (2013b). Optically selective two-photon uncaging of glutamate at 900 nm. *J. Am. Chem. Soc.* 135, 5954–5957. doi: 10.1021/ja4019379

Papageorgiou, G., and Corrie, J. (2000). Effects of aromatic substituents on the photocleavage of 1-acyl-7-nitroindolines. *Tetrahedron* 56, 8197–8205. doi: 10.1016/S0040-4020(00)00745-6

Passlick, S., and Ellis-Davies, G. C. R. (2017). Comparative one- and two-photon uncaging of MNI-glutamate and MNI-kainate on hippocampal CA1 neurons. *J. Neurosci. Meth.* 293, 321–328. doi: 10.1016/j.jneumeth.2017.10.013

Patterson, M. A., Szatmari, E. M., and Yasuda, R. (2010). AMPA receptors are exocytosed in stimulated spines and adjacent dendrites in a Ras-ERK-dependent manner during long-term potentiation. *Proc. Natl. Acad. Sci. U.S.A.* 107, 15951–15956. doi: 10.1073/pnas.0913875107

Plotkin, J. L., Day, M., and Surmeier, D. J. (2011). Synaptically driven state transitions in distal dendrites of striatal spiny neurons. *Nat. Neurosci.* 14, 881–888. doi: 10.1038/nn.2848

Reinhardt, B., Brott, L., Clarson, S., Dillard, A., Bhatt, J., Kannan, R., et al. (1998). Highly active two-photon dyes: Design, synthesis, and characterization toward application. *Chem. Mater.* 10, 1863–1874. doi: 10.1021/cm980036e

Richers, M. T., Amatrudo, J. M., Olson, J. P., and Ellis-Davies, G. C. R. (2017). Cloaked caged compounds: chemical probes for two-photon optoneurobiology. *Angew. Chem. Int. Ed.* 56, 193–197. doi: 10.1002/anie.201609269

Schiller, J., Major, G., Koester, H. J., and Schiller, Y. (2000). NMDA spikes in basal dendrites of cortical pyramidal neurons. *Nature* 404, 285–289. doi: 10.1038/35005094

Shepherd, G. M. G. (2012). Circuit mapping by ultraviolet uncaging of glutamate. *Cold Spring Harb. Protoc.* 2012, 998–1004. doi: 10.1101/pdb.prot070664

Sheppard, C. J., and Kompfner, R. (1978). Resonant scanning optical microscope. *Appl. Opt.* 17, 2879–2882. doi: 10.1364/AO.17.002879

Smith, M. A., Ellis-Davies, G. C., and Magee, J. C. (2003). Mechanism of the distance-dependent scaling of Schaffer collateral synapses in rat CA1 pyramidal neurons. *J. Physiol.* 548, 245–258. doi: 10.1113/jphysiol.2002.036376

Sobczyk, A., Scheuss, V., and Svoboda, K. (2005). NMDA receptor subunit-dependent [Ca2+] signaling in individual hippocampal dendritic spines. *J. Neurosci.* 25, 6037–6046. doi: 10.1523/JNEUROSCI.1221-05.2005

Soeller, C., and Cannell, M. (1999). Two-photon microscopy: Imaging in scattering samples and three-dimensionally resolved flash photolysis. *Microsc. Res. Tech.* 47, 182–195. doi: 10.1002/(SICI)1097-0029(19991101)47:3<182::AID-JEMT4>3.0.CO;2-4

Stein, I. S., Gray, J. A., and Zito, K. (2015). Non-ionotropic NMDA receptor signaling drives activity-induced dendritic spine shrinkage. *J. Neurosci.* 35, 12303–12308. doi: 10.1523/JNEUROSCI.4289-14.2015

Tanaka, J., Horiike, Y., Matsuzaki, M., Miyazaki, T., Ellis-Davies, G. C., and Kasai, H. (2008). Protein synthesis and neurotrophin-dependent structural plasticity of single dendritic spines. *Science* 319, 1683–1687. doi: 10.1126/science.1152864

Tanaka, J., Matsuzaki, M., Tarusawa, E., Momiyama, A., Molnar, E., Kasai, H., et al. (2005). Number and density of AMPA receptors in single synapses in immature cerebellum. *J. Neurosci.* 25, 799–807. doi: 10.1523/JNEUROSCI.4256-04.2005

Tsien, R. Y., and Zucker, R. S. (1986). Control of cytoplasmic calcium with photolabile tetracarboxylate 2-nitrobenzhydrol chelators. *Biophys. J.* 50, 843–853. doi: 10.1016/S0006-3495(86)83525-1

Villa, K. L., Berry, K. P., Subramanian, J., Cha, J. W., Oh, W. C., Kwon, H. B., et al. (2016). Inhibitory synapses are repeatedly assembled and removed at persistent sites *in vivo*. *Neuron* 89, 756–769. doi: 10.1016/j.neuron.2016.01.010

Walker, J. W., McCray, J. A., and Hess, G. P. (1986). Photolabile protecting groups for an acetylcholine receptor ligand. Synthesis and photochemistry of a new class of o-nitrobenzyl derivatives and their effects on receptor function. *Biochemistry* 25, 1799–1805. doi: 10.1021/bi00355a052

Walker, J. W., Somlyo, A. V., Goldman, Y. E., Somlyo, A. P., and Trentham, D. R. (1987). Kinetics of smooth and skeletal muscle activation by laser pulse photolysis of caged inositol 1,4,5-trisphosphate. *Nature* 327, 249–252. doi: 10.1038/327249a0

Wieboldt, R., Gee, K. R., Niu, L., Ramesh, D., Carpenter, B. K., and Hess, G. P. (1994a). Photolabile precursors of glutamate: synthesis, photochemical properties, and activation of glutamate receptors on a microsecond time scale. *Proc. Natl. Acad. Sci. U.S.A.* 91, 8752–8756. doi: 10.1073/pnas.91.19.8752

Wieboldt, R., Ramesh, D., Carpenter, B. K., and Hess, G. P. (1994b). Synthesis and photochemistry of photolabile derivatives of gamma-aminobutyric acid for chemical kinetic investigations of the gamma-aminobutyric acid receptor in the millisecond time region. *Biochemistry* 33, 1526–1533. doi: 10.1021/bi00172a032

Wilcox, M., Viola, R., Johnson, K., Billington, A., Carpenter, B., McCray, J., et al. (1990). Synthesis of photolabile precursors of amino acid neurotransmitters. *J. Org. Chem.* 55, 1585–1589. doi: 10.1021/jo00292a038

Zhai, S., Ark, E. D., Parra-Bueno, P., and Yasuda, R. (2013). Long-distance integration of nuclear ERK signaling triggered by activation of a few dendritic spines. *Science* 342, 1107–1111. doi: 10.1126/science.1245622

Zhang, Y.-P., Holbro, N., and Oertner, T. G. (2008). Optical induction of plasticity at single synapses reveals input-specific accumulation of alphaCaMKII. *Proc. Natl. Acad. Sci. U.S.A.* 105, 12039–12044. doi: 10.1073/pnas.0802940105

Zhao, Y., Araki, S., Wu, J., Teramoto, T., Chang, Y.-F., Nakano, M., et al. (2011). An expanded palette of genetically encoded Ca2+ indicators. *Science* 333, 1888–1891. doi: 10.1126/science.1208592

Zipfel, W. R., Williams, R. M., and Webb, W. W. (2003). Nonlinear magic: multiphoton microscopy in the biosciences. *Nat. Biotechnol.* 21, 1369–1377. doi: 10.1038/nbt899

Conflict of Interest Statement: The author declares that the research was conducted in the absence of any commercial or financial relationships that could be construed as a potential conflict of interest.

frontiers in Synaptic Neuroscience

METHODS
published: 04 March 2019
doi: 10.3389/fnsyn.2019.00005

Optical Quantal Analysis Using Ca^{2+} Indicators: A Robust Method for Assessing Transmitter Release Probability at Excitatory Synapses by Imaging Single Glutamate Release Events

Zahid Padamsey[1], Rudi Tong[2] and Nigel Emptage[2]**

[1] Center for Discovery Brain Sciences, University of Edinburgh, Edinburgh, United Kingdom, [2] Department of Pharmacology, University of Oxford, Oxford, United Kingdom

OPEN ACCESS

Edited by:
Dirk Feldmeyer,
Forschungszentrum Jülich, Helmholtz Association of German Research Centers (HZ), Germany

Reviewed by:
Hartmut Schmidt,
Leipzig University, Germany
Eric Hanse,
University of Gothenburg, Sweden

***Correspondence:**
Zahid Padamsey
zahid.padamsey@ed.ac.uk
Nigel Emptage
nigel.emptage@pharm.ox.ac.uk

Received: 30 November 2018
Accepted: 14 February 2019
Published: 04 March 2019

Citation:
Padamsey Z, Tong R and Emptage N (2019) Optical Quantal Analysis Using Ca^{2+} Indicators: A Robust Method for Assessing Transmitter Release Probability at Excitatory Synapses by Imaging Single Glutamate Release Events. Front. Synaptic Neurosci. 11:5. doi: 10.3389/fnsyn.2019.00005

Despite evidence that presynaptic efficacy and plasticity influence circuit function and behavior *in vivo*, studies of presynaptic function remain challenging owing to the difficulty of assessing transmitter release in intact tissue. Electrophysiological analyses of transmitter release are indirect and cannot readily resolve basic presynaptic parameters, most notably transmitter release probability (p_r), at single synapses. These issues can be circumvented by optical quantal analysis, which uses the all-or-none optical detection of transmitter release in order to calculate p_r. Over the past two decades, we and others have successfully demonstrated that Ca^{2+} indicators can be strategically implemented to perform optical quantal analysis at single glutamatergic synapses in *ex vivo* and *in vitro* preparations. We have found that high affinity Ca^{2+} indicators can reliably detect spine Ca^{2+} influx generated by single quanta of glutamate, thereby enabling precise calculation of p_r at single synapses. Importantly, we have shown this method to be robust to changes in postsynaptic efficacy, and to be sensitive to activity-dependent presynaptic changes at central synapses following the induction of long-term potentiation (LTP) and long-term depression (LTD). In this report, we describe how to use Ca^{2+}-sensitive dyes to perform optical quantal analysis at single synapses in hippocampal slice preparations. The general technique we describe here can be applied to other glutamatergic synapses and can be used with other reporters of glutamate release, including recently improved genetically encoded Ca^{2+} and glutamate sensors. With ongoing developments in imaging techniques and genetically encoded probes, optical quantal analysis is a promising strategy for assessing presynaptic function and plasticity *in vivo*.

Keywords: optical quantal analysis, Ca^{2+} imaging, presynaptic plasticity, hippocampus, Schaffer-collateral, release probability

INTRODUCTION

The efficacy of synaptic input critically shapes circuit function and behavior. Synaptic efficacy is comprised of two main features: (1) postsynaptic potency (q), which refers to the amount of postsynaptic depolarization generated by a synapse in response to a single quantum of neurotransmitter and (2) presynaptic release probability (p_r), which refers to the likelihood a synapse will release a single quantum of neurotransmitter. Both pre- and postsynaptic efficacy impact cellular and circuit operations (Evans et al., 2018; Grillo et al., 2018), as well as undergo activity-dependent changes *in vivo* (Maren, 2005; Koga et al., 2015; Choi et al., 2018). Whereas several techniques can be employed to measure q, examination of p_r is often more challenging owing to the difficulties of assessing transmitter release in intact tissue. Although there are a number of electrophysiological approaches that can be employed to assess presynaptic efficacy, they are indirect and cannot readily resolve presynaptic release at single synapses (see Clements and Silver, 2000; Yang and Calakos, 2013 for a review of electrophysiological approaches to quantal analyses and their limitations). Such issues can be resolved by optical quantal analysis.

Optical quantal analysis is a means of assessing p_r based on the all-or-none optical detection of transmitter release. In principle this can be done with any fluorescent reporter of vesicular fusion or transmitter release, and at any synapse (see "Discussion"). The fluorescent reporter used for detecting transmitter release, however, must afford sufficient sensitivity to reliably detect quantal release at the chosen synapse, and in the chosen experimental preparation. Over the past two decades we have demonstrated that Ca^{2+} indicators provides one such means for robustly assessing transmitter release at glutamatergic synapses in *in vitro* and *ex vivo* slice preparations by enabling the detection of all-or-none, excitatory synaptically evoked postsynaptic Ca^{2+} transients [EPSCaTs; (Emptage et al., 1999)].

EPSCaTs are present at most central glutamatergic synapses [including hippocampal, neocortical, striatal, and amygdalar (Bloodgood and Sabatini, 2007)], though have been most extensively studied at hippocampal Schaffer-collateral synapses (**Figure 1**). Here, it has been well established that a single quantum of glutamate can trigger sufficient Ca^{2+} influx into a dendritic spine that can be detected by high affinity Ca^{2+} indicator dyes, such as Oregon Green BAPTA-1 (OGB-1) (Emptage et al., 1999). This Ca^{2+} influx is mediated by both NMDA receptors (NMDARs) and voltage-gated Ca^{2+} channels (VGCCs), activation of which is driven by AMPA receptor (AMPAR)-mediated depolarization (Ngo-Anh et al., 2005; Grunditz et al., 2008; Padamsey et al., 2017) (**Figure 1B**). The recruitment of these Ca^{2+} sources by uniquantal glutamate release likely reflects the strong electrical compartmentalization of the spine head (Harnett et al., 2012; Beaulieu-Laroche and Harnett, 2018). In spines containing endoplasmic reticulum (ER), which comprise approximately 10–20% of Schaffer collateral synapses, additional Ca^{2+} release is triggered reliably via RyR-gated stores, and also via IP_3R-gated stores, albeit with delayed kinetics and reduced probability (Emptage et al., 1999; Holbro et al., 2009; Padamsey et al., 2018) (**Figure 1C**). Because release of single quanta of glutamate can drive detectable levels of Ca^{2+} influx in dendritic spines, the probability of eliciting an EPSCaT with single presynaptic stimuli can be used as a proxy for p_r. Indeed, we have shown that the probability of evoking EPSCaTs is physiologically and pharmacologically similar to p_r: (1) both are stochastic all or none-events (Emptage et al., 1999) that (2) have similar means and distributions (Ward et al., 2006), and (3) similarly exhibit short-term facilitation (Emptage et al., 1999, 2003). Moreover, (4) EPSCaT probability, like p_r, scales with the size of the active zone (Holderith et al., 2012) and (5) can be decreased by baclofen and adenosine, which are known to decrease p_r (Emptage et al., 1999; Oertner et al., 2002; Chalifoux and Carter, 2010).

In this paper, we provide a detailed protocol for using Ca^{2+} dyes to measure p_r at Schaffer-collateral synapses in hippocampal slices. We describe extensions and applications of the technique, including its use for assessing activity-dependent presynaptic plasticity. The general technique we describe here can be used at other synapses, and with other sensors of glutamate release, including genetically encoded Ca^{2+} and glutamate sensors. We end by discussing the limitations of our method, and highlight the future potential of optical quantal analysis, especially in light of recent advancements in genetically encoded sensors and *in vivo* imaging techniques.

MATERIALS AND METHODS

We begin with the core technique, which involves (1) preparing brain slices, (2) loading a postsynaptic cell with Ca^{2+} indicator dye, (3) searching for a spine that generates EPSCaTs in response to electrical stimulation, and (4) calculating p_r from these responses.

Optical Quantal Analysis With Ca^{2+} Indicators

Brain Slice Preparation

In our labs, we focus on synaptic properties at CA3-CA1 synapses assessed in either acute or cultured hippocampal slices, which are prepared according to previously published methods (Emptage et al., 2003; Padamsey et al., 2017). Both acute and cultured slices have been shown to have very similar synaptic properties and forms of plasticity (De Simoni et al., 2003; Enoki et al., 2009; Padamsey et al., 2017). For acute slice preparation, coronal acute hippocampal slices (400 μm) are made from the brains of 2–3 week old male Wistar rats. Dissection and slice preparation is performed in an ice cold, sucrose-based ACSF solution (in mM: 85 NaCl, 65 sucrose, 26 $NaHCO_3$, 10 glucose, 7 $MgCl_2$, 2.5 KCl, 1.2 NaH_2PO_4, and 0.5 $CaCl_2$) that is bubbled with 95% O_2 and 5% CO_2. Slices are allowed to recover at room temperature for at least 1 h in normal ACSF (in mM: 120 NaCl, 2.5 KCl, 26 $NaHCO_3$, 11 glucose, 1 $MgCl_2$ 1.2 NaH_2PO_4, and 2 $CaCl_2$) prior to recording. Because of the thermal sensitivity of presynaptic release, recordings are done at near physiological temperatures 32–33°C (Pyott and Rosenmund, 2002).

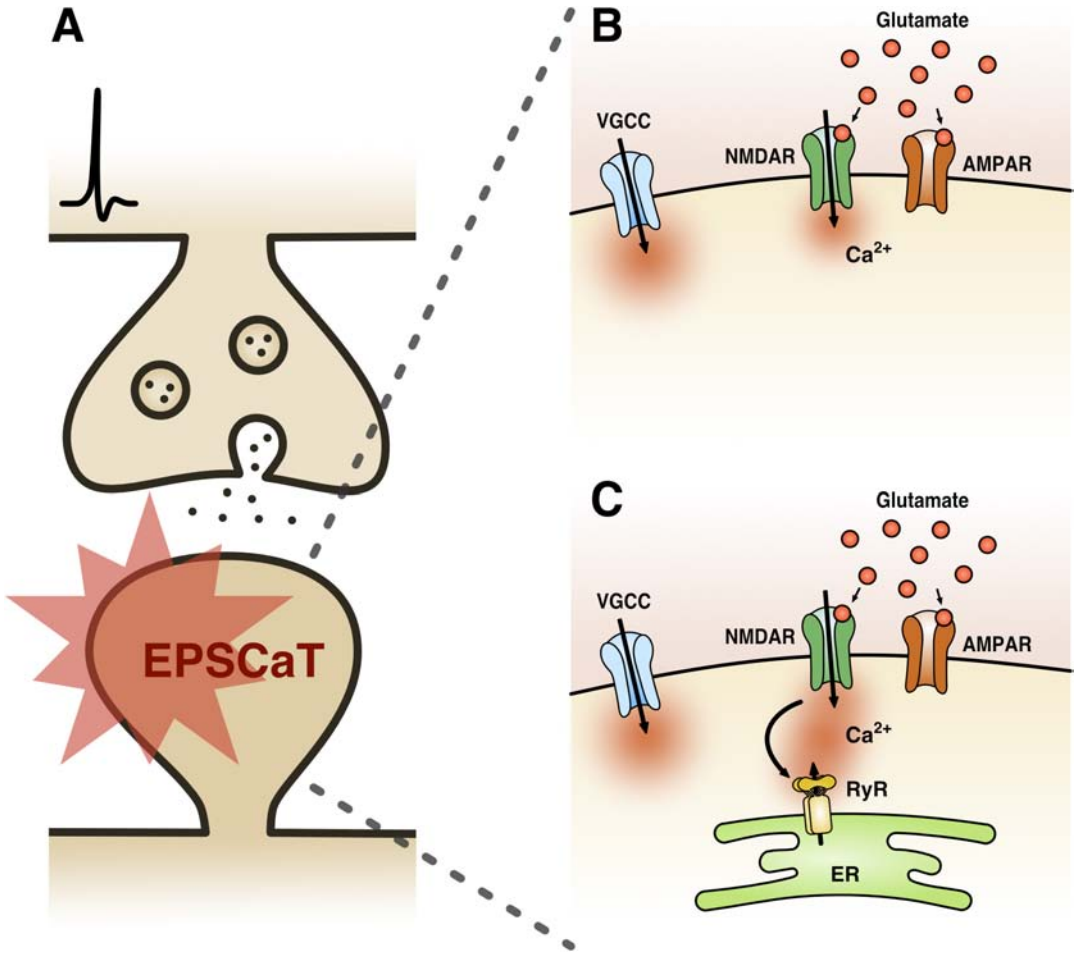

FIGURE 1 | Excitatory postsynaptic Ca^{2+} transient (EPSCaT) pharmacology. **(A)** Schematic of an EPSCaT-generating synapse responding to uniquantal glutamate release. **(B)** EPSCaT signals are derived from NMDAR- and VGCC-mediated Ca^{2+} influx, driven by AMPAR-mediated depolarization. **(C)** At synapses containing ER, EPSCaTs are additionally and reliably amplified by Ca^{2+} induced Ca^{2+} release (CICR), which is triggered by NMDARs and mediated by RyRs. In some instances, EPSCaTs will also show a delayed IP_3R-mediated Ca^{2+} component, triggered by group 1 metabotropic glutamate receptors (mGluRs) signaling (not shown).

Cultured hippocampal slices (350 μm), which offer excellent optical access to subcellular compartments, are prepared from male Wistar rats (P7–P8). Brains are dissected in ice cold Earle's Balanced Salt Solution (EBSS) with added glucose (+35 mM) and HEPES (+20 mM), and pH corrected to 7.2–7.4 using 5 M NaOH. Slices are placed on a membrane insert with growth media (50% Minimum Essential Media, 25% heat-inactivated horse serum, 23% EBSS, 2% B-27, and +35 mM of added glucose), and incubated at 36°C and 5% CO_2 for 7–14 days prior to use. During recordings, slices are perfused with ACSF (in mM: 145 NaCl, 2.5 KCl, 26 $NaHCO_3$, 11 glucose, 1–2 $MgCl_2$ 1.2 NaH_2PO_4, and 2–3 $CaCl_2$), bubbled with 95% O_2 and 5% CO_2, and heated to 32–33°C.

Ca^{2+} Imaging and Dye Loading

Historically, we and others have used sharp microelectrodes to simultaneously load cells with Ca^{2+} indicator dye and record from them (Emptage et al., 1999, 2003; Enoki et al., 2009). Sharp microelectrodes greatly minimize dilution of cytoplasmic contents which can otherwise impair synaptic plasticity (Malinow and Tsien, 1990; Padamsey et al., 2017). However, sharp microelectrode recordings are a challenging technique to perfect and have a lower success rate than patch microelectrodes. We therefore recommend the use of whole-cell patch recordings, which are much easier to perform.

Whole-cell patch recordings with low-resistance electrodes (4–8 MΩ) disrupt the intracellular *mileu* of cells and lead to loss of presynaptic long-term potentiation (LTP) within 10 min of break-in (Padamsey et al., 2017). In conditions where loss of plasticity is not an issue, such as in cases where only basal synaptic parameters are of interest, whole-cell recordings may be carried out with low-resistance (4–8 MΩ) patch electrodes loaded with 0.2 mM OGB-1 dissolved in standard internal solution (in mM: 135 KGluconate, 10 KCl, 10 HEPES, 2 $MgCl_2$, 2 Na_2ATP and 0.4 Na_3GTP; pH = 7.2–7.4).

For plasticity experiments, higher resistance patch electrodes should be used (18–25 MΩ) to reduce the rate of dilution of intracellular factors. In our hands, higher resistance electrodes

enable presynaptic LTP induction up to 15–20 min following break-in. These electrodes should be loaded with a higher concentration of OGB-1 (0.5–1 mM) to ensure adequate dye loading of the cell (Padamsey et al., 2017). Alternatively, our preferred method for plasticity experiments is to single-cell bolus load Ca^{2+} indicator dye into the target neuron, allowing EPSCaT imaging to proceed without electrophysiological recording or disruption of the intracellular *mileu*, and therefore without out any stringent time constraints (Padamsey et al., 2017). To perform single-cell bolus loading, we transiently patch (∼60 s) a cell with a low-resistance patch electrode (4–8 MΩ) containing a high concentration of OGB-1 (1 mM) dissolved in standard internal solution. Following loading, the patch is slowly retracted over the course of 5–10 s during which the plasma membrane rapidly reseals with very high success. We then allow 10–20 min for dye diffusion before imaging. After EPSCaT recording, which typically takes 15–20 min, the cell can be transiently re-patched to induce plasticity if required. Re-patching can be performed with very high success rates.

Regardless of the loading method, it is important that a sufficient concentration of Ca^{2+} indicator dye is present in the cell. Too little dye prevents measurement of Ca^{2+} signals with an adequate signal to noise ratio (SNR). In contrast, too much dye leads to excessive Ca^{2+} buffering within the cell, which reduces the magnitude of activity-dependent fluorescence changes, and alters the electrophysiological properties of the cell. The adequacy of loading can be assessed by triggering a back propagating action potential (bAP) and imaging fluorescence in the proximal dendrites (∼50–100 μm). We find that a resulting fractional change in fluorescence ($\Delta F/F$) of >0.80 is indicative of a sufficient amount of dye loading in CA3 and CA1 pyramidal neurons. Dye concentration and loading times can be adjusted to achieve suitable loading levels.

For imaging Ca^{2+} fluorescence we use a BioRad MRC-1000 scan head attached to a Zeiss Axioscope upright microscope equipped with an Olympus water immersion lens (60X NA 0.90). Laser excitation can either be provided by a 488 nm solid state laser in the case of confocal imaging in cultured slices, or a Ti:Sapphire laser in the case of two photon imaging in acute slices. Emitted fluorescence is detected with a photomultiplier tube. We use LaserSharp software (BioRad) to control the microscope and acquire images, and ImageJ to analyze the images.

Stimulating and Searching for EPSCaTs

For extracellular stimulation we use a glass electrode, comprising of a low-resistance patch pipette (4–8 MΩ) filled with ACSF. A tungsten electrode, which is connected to a constant current stimulator (e.g., Digitimer) (Padamsey et al., 2017), is inserted into the pipette. The tip of the glass can be coated with bovine serum albumin fluorescent conjugate (e.g., 0.05% bovine serum albumin-Alexa Fluor 488 dissolved in 0.1 M PBS with added 3 mM NaN_3 to maintain sterility) to aid visualization of the electrode during fluorescent imaging (Ishikawa et al., 2010; Padamsey et al., 2017). The electrode is then positioned close to an imaged dendritic branch (5–10 μm) (Yasuda et al., 2004; Padamsey et al., 2017) (**Figures 2– 4**). With this method, spines on the target branch have a high likelihood of responding to electrical stimulation. The dendritic branch can then be rapidly and efficiently searched during stimulation for responsive spines by using line scans (xt) that traverse as many spines as possible. During a line scan we deliver two stimulation pulses (100 μs duration) 70 ms apart in order to increase the likelihood of glutamate release via paired pulse facilitation. This is important to increase the likelihood of finding low p_r synapses, and therefore to prevent selection bias in favor of high p_r synapses. Stimulation intensity should be kept subthreshold for dendritic or somatic spiking, which will be evident during Ca^{2+} imaging. An EPSCaT, when triggered in the absence of dendritic or somatic spiking, should be restricted to the spine head; though some elevation in the dendrite may occur due to diffusion (Noguchi et al., 2005). The described technique typically allows 1–2 EPSCaT-generating spines to be rapidly found (1–2 min). If no responsive spines are found, the electrode can be moved a few microns, and the dendrite can be searched again. Once an EPSCaT is found, the stimulation intensity should be continually decreased until the probability of eliciting an EPSCaT is 0, after which the stimulation intensity should be increased by at least 20% to ensure that stimulation is suprathreshold for EPSCaT generation, and that any EPSCaT failures cannot be attributed to axonal stimulation failures (Emptage et al., 1999). If the EPSCaT cannot be stimulated by at least 20% above threshold intensity without eliciting a dendritic or somatic spike, then another spine should be identified.

Bringing the stimulating electrode closer than 5 μm to the imaged spine risks direct depolarization of voltage-gated channels in the dendrite or the associated presynaptic terminal. Direct depolarization of the dendrite typically results in branch-wide Ca^{2+} influx, whereas direct depolarization of the presynaptic terminal triggers spine-restricted EPSCaTs with highly inflated p_r measures (unpublished observations from our lab), presumably due to elevated Ca^{2+} influx in the terminal. Indeed, studies in which stimulating electrodes are <5 μm to the imaged synapse report higher basal p_r values (0.80) (Chalifoux and Carter, 2010) than those in which the electrodes are placed further from the spine (∼0.2–0.4) (Emptage et al., 2003; Ward et al., 2006; Enoki et al., 2009; Padamsey et al., 2017).

In previous studies, we and others have placed our stimulating electrode much further from the dendritic tree (>50 μm) (Emptage et al., 1999, 2003; Ward et al., 2006; Enoki et al., 2009). However, we find that with this technique it is typically more difficult to find EPSCaTs, since larger regions of the dendritic tree need to be searched for responsive spines.

For imaging EPSCaTs at postsynaptically silent synapses the Mg^{2+} block of NMDAR must be minimized to unmask EPSCaTs during synaptic stimulation. This can be achieved by either holding the postsynaptic neuron between −20 and 20 mV, or by removing extracellular Mg^{2+} from the bath solution (Ward et al., 2006).

Estimating p_r

Once an EPSCaT-generating spine has been identified, the response of the spine to repeated trials of electrical stimulation is imaged in order to accurately calculate p_r. During this time, the position of the stimulating electrode should be monitored

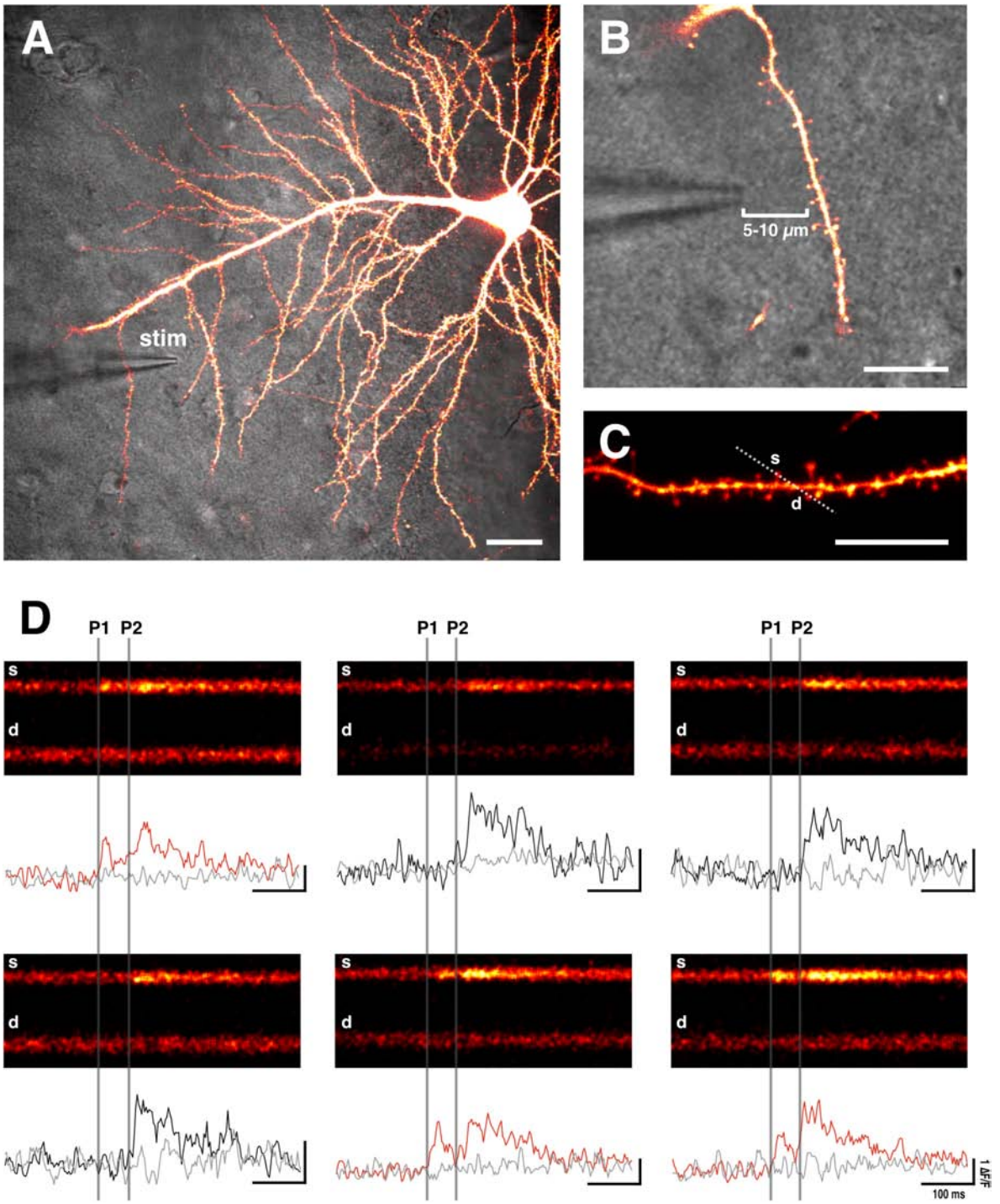

FIGURE 2 | Sample EPSCaTs recordings. **(A)** Image of a CA1 pyramidal neuron that has been bolus loaded with Ca^{2+} indicator dye (OGB-1). A glass stimulating electrode (stim) is placed within 5–10 μm of a target dendrite (scale bar: 20 μm). **(B)** Magnified image of the stimulating electrode and target dendrite (scale bar: 10 μm). **(C)** Laser scanning is restricted through a line across the target spine (s) and underlying dendrite (d) (scale bar: 10 μm). **(D)** Sample line scans in which paired pulse stimulation (two pulses 70 ms apart: P1 and P2, which are denoted by vertical gray bars) is delivered following a baseline period. Raw fluorescence is quantified ($\Delta F/F$) for both the spine (black and red traces) and dendrite (gray trace) below each line scan. Red traces show significant increases in spine fluorescence (i.e., EPSCaTs) in response to the first of the two pulses (P1); black traces fail to show spine fluorescence changes in response to P1 that are significantly different than noise. As is evident, EPSCaTs are probabilistic, restricted to the spine head, and are easily identified visually. EPSCaT probability is greater for the second of two pulses (P2), reflecting short-term facilitation. p_r is calculated as the EPSCaT probability for the first pulse (P1).

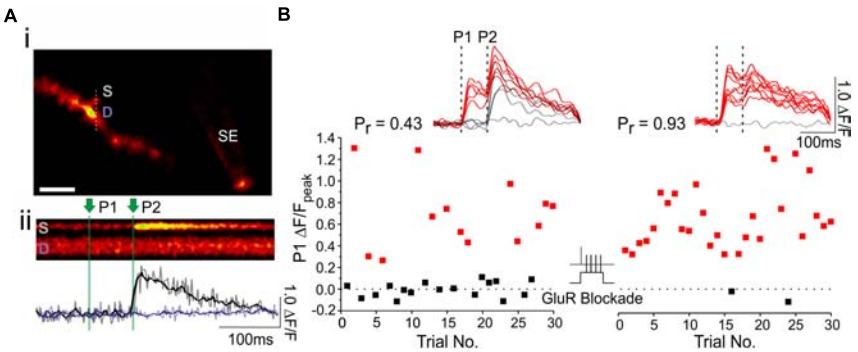

FIGURE 3 | Using optical quantal analysis to image presynaptic plasticity. **(Ai)** Image of a CA1 dendrite loaded with OGB-1 (white scale bar: 2 μm). A fluorescently coated glass stimulating electrode (SE) is positioned within 5–10 μm of the imaged dendrite, and an EPSCaT-generating spine is found. Laser scanning is restricted through the spine head (S) and the underlying dendrite (D). **(Aii)** Example line scan during paired pulse stimulation in which two stimuli (P1 and P2) are delivered 70 ms apart. The quantified, smoothed fluorescent transient ($\Delta F/F$) in the spine (black trace) and dendrite (purple trace) is shown below. **(B)** The spine is imaged during 30 stimulation trials at baseline, and another 30 stimulation trials 30 min after plasticity induction. The peak EPSCaT amplitude during the first pulse (P1) of each stimulation trial is plotted in the graph. Red points denote successful release events, in which EPSCaT amplitudes are significantly greater than noise; black points denote failures. Sample smoothed fluorescent transients from the stimulation trials are shown above, for both the baseline and post-induction periods, along with the estimates of p_r. In this experiment, plasticity was induced by Hebbian stimulation, consisting of pairing single presynaptic stimuli with postsynaptic complex spikes (60 pairings repeated at 5 Hz; see text for further details). Pairing was delivered in a glutamate receptor blockade (GluR Blockade: 100 μM D-AP5, 10 μM NBQX, 500 μM R,S-MCPG, and 10 μM LY341495) designed to block all glutamate receptors. After pairing, the blockade was washed out and EPSCaTs were imaged 30 min post-induction. p_r increased following paired stimulation. The experiment shows that the induction of presynaptic plasticity does not require glutamate signaling. Figure adapted from Padamsey et al. (2017) under the terms of the Creative Commons Attribution License (CC BY).

carefully to ensure mechanical drift, which can affect EPSCaT probability, is minimal. Images are acquired as line scans (xt) through the spine and underlying dendrite (**Figures 2**, **3**). This enables rapid acquisition of frames (500 Hz) while minimizing photobleaching. Simultaneous imaging of the spine and dendrite is important for distinguishing bona fide EPSCaTs from Ca^{2+} influx associated with local dendritic spikes or bAPs. For a given imaging trial, we typically acquire 200 successive lines at 500 Hz, for a total of 400 ms of imaging; though this will vary depending on the experiment. Single or paired pulse stimulation (70 ms interstimulus interval) is delivered 50–200 ms following the start of the scan, to enable sufficient time for baseline imaging. We prefer to use paired pulse stimulation as it makes it easier to monitor the quality and presence of EPSCaTs throughout the experiment, especially at low p_r synapses. If paired pulses are used, p_r is only ever calculated on the basis of the Ca^{2+} influx associated with the first of the two pulses.

Several imaging trials are required to accurately estimate EPSCaT probability, and thus p_r. However, it is important to minimize imaging to minimize phototoxicity and indicator bleaching. We highly recommend including the antioxidants Trolox (1 mM) and ascorbic acid (0.2 mM) in the ACSF to help preserve the health of the spine and dendrite during imaging. When photodynamic damage is sufficient to compromise the integrity of the membrane, the dendritic compartment will rapidly brighten, and eventually bleb. A reliable estimate of p_r typically requires 20–30 imaging trials, though this will depend on the actual value of p_r. From the binomial theorem, the standard error (SE), and therefore the uncertainty associated with a measure of p_r is:

$$\mathrm{SE} = \sqrt{\left[\left(1 - p_r\right)\left(p_r\right)/N_{\mathrm{trials}}\right]}$$

where N_{trials} is the total number of imaging trials. Note the SE is minimal when p_r is 0 or 1, and maximal as p_r approaches 0.5. Because of this, we often have at least 30 imaging trials when imaging synapses with $p_r \sim 0.5$, and 20 trials, when synapses have a p_r of approximately <0.2 or >0.8; rough estimates of p_r for these purposes can be derived online, during image acquisition.

Following imaging, p_r is formally calculated offline as the proportion of imaging trials in which the spine exhibited a significant and selective increase in fluorescence in response to electrical stimulation. Fluorescence is calculated as:

$$\Delta F/F = \left(F - F_{\mathrm{baseline}}\right) / \left(F_{\mathrm{baseline}} - F_{\mathrm{background}}\right)$$

where F is the fluorescence at any given point in time, F_{baseline} is the mean fluorescence at baseline, prior to stimulation, and $F_{\mathrm{background}}$ is the mean fluorescence of the background associated with regions of the image devoid of fluorescent structures. To calculate the $\Delta F/F$ associated with the putative Ca^{2+} transient (i.e., $\Delta F/F_{\mathrm{transient}}$), we average the $\Delta F/F$ over a 50 ms time window starting from the point of stimulation. For a transient to be considered a successful release event, we require its $\Delta F/F_{\mathrm{transient}}$ to be at least 2.5 times greater than noise, which is measured as the SE of the $\Delta F/F$ calculated during the last 50 ms of baseline imaging. The total proportion of trials in which the $\Delta F/F_{\mathrm{transient}}$ is significantly greater than baseline noise is taken as a measure of p_r.

If EPSCaT recordings are contaminated by dendritic spikes or bAPs, then it is imperative to characterize $\Delta F/F_{\mathrm{transient}}$ for both the dendrite and spine. Dendritic spikes and bAPs generate synchronous Ca^{2+} events of similar amplitude and kinetics in both spine and dendrite, provided that both compartments are in the same plane of focus and have baseline fluorescences that are

clearly distinguished from background. Consequently, EPSCaTs that co-occur with dendritc spikes or bAPs result in higher fluorescent levels in the spine than in the dendrite. In this case, a successful trial would require the $\Delta F/F_{spine}$ significantly exceed the $\Delta F/F_{dendrite}$ (Nevian and Helmchen, 2007).

Extensions and Applications of Optical Quantal Analysis

Here, we describe extensions of optical quantal analysis, including how it can be used (1) to assess activity-dependent changes in p_r, (2) to examine the impact of local synaptic signaling on p_r.

Assessing Activity-Dependent Changes in p_r

Optical quantal analysis can be conducted before and after plasticity protocols to examine activity-dependent changes in p_r (**Figure 3**). Several protocols can be used to induce long-term changes in synaptic efficacy, though not all protocols induce presynaptic changes (Padamsey and Emptage, 2014). Presynaptic LTP induction typically requires greater levels of postsynaptic depolarization than postsynaptic LTP induction. This is because presynaptic LTP is driven by L-type voltage gated Ca^{2+} channels (L-VGCCs), which have higher voltage activation thresholds than postsynaptic NMDARs, which instead drive postsynaptic LTP (Padamsey and Emptage, 2014; Padamsey et al., 2017).

To this end, we have used several protocols successfully to induce presynaptic LTP at Schaffer-collateral synapses.

(i) The first protocol uses high-frequency stimulation (HFS) consisting of three bursts of 20 presynaptic pulses at 100 Hz, delivered 1.5 s apart. Critically, during stimulation, the postsynaptic cell should be sufficiently depolarized (5–10 mV) by current injection to ensure that the presynaptic stimulation evokes APs (Emptage et al., 2003; Enoki et al., 2009).

(ii) A spike-timing dependent plasticity (STDP) protocol can also be used. Indeed, we have recently found that pairing presynaptic stimuli with postsynaptic complex spikes provides a robust way of driving presynaptic LTP (Padamsey et al., 2017). Complex spikes are triggered by a 2–3 nA postsynaptic current injection with a 7–10 ms rising phase, a 20 ms plateau phase, and a 30–33 ms falling phase in order to emulate the kinetics of complex spikes recorded *in vivo* (Grienberger et al., 2014). During pairing, a complex spike follows the evoked presynaptic stimulus by 7–10 ms. Complex spikes can also be evoked by a conventional current injection (square pulse: 2–3 nA for 100 ms); however, spike timings are less reliable with this method. Pairing is performed 60 times at 5 Hz.

(iii) Alternatively, Enoki et al. (2009) have induced presynaptic LTP using a STDP protocol in which single presynaptic stimuli are paired with a standard burst of postsynaptic spikes (3 at 100 Hz), where each spike is generated by a 2–10 ms current depolarization. The first postsynaptic spikes follows the presynaptic stimulus by 10 ms. Pairing is repeated 100 times at 0.33 Hz in a $GABA_A$ receptor blockade.

Presynaptic long-term depression (LTD) can also be induced at Schaffer-collateral synapses with several protocols.

(1) We have recently found that presynaptic LTD at these synapses is reliably triggered by autocrine activation of presynaptic NMDARs, driven by glutamate release (Padamsey et al., 2017). Consequently, protocols that strongly drive glutamate release in the absence of postsynaptic depolarization potently induce presynaptic LTD. For example, delivery of a pair of stimuli (5 ms apart), which emulates CA3 burst firing *in vivo* (Kowalski et al., 2016), 60 times at 5 Hz reliably depresses p_r. Alternatively, 60–120 single presynaptic stimuli delivered at 5 Hz also induces presynaptic LTD, though only at high p_r (>0.5) synapses. The postsynaptic neuron should be hyperpolarized (<-90 mV) in either case to prevent postsynaptic spiking (Padamsey et al., 2017).

(2) A STDP protocol can also be used to induce presynaptic LTD, which also depends on presynaptic NMDAR activation (Andrade-Talavera et al., 2016; Bouvier et al., 2018), likely driven by glial glutamate release (Min and Nevian, 2012). Here, three postsynaptic APs, each elicited by a 2–10 ms current injection, is followed (Δt = 50 ms from the first postsynaptic AP) by a single presynaptic stimulus. Pairing is repeated 100 times at 0.33 Hz (Enoki et al., 2009).

Examining the Impact of Local Synaptic Signaling on p_r

A key advantage of spine Ca^{2+} imaging is that it yields the spatial location of stimulated synapses, which enables spatially targeted manipulations of local synaptic signaling with photolytic uncaging (**Figure 4**). Previously, we have combined optical quantal analysis at single spines with MNI-glutamate uncaging to examine the impact of elevated glutamate release on presynaptic LTP and LTD (Padamsey et al., 2017). To do so, an EPSCaT-generating spine is first found. The associated spine head is then targeted for single or multi-photon glutamate spot photolysis. To deliver caged glutamate we use a local glass pipette (4–8 MΩ) connected to a picospritzer and placed within 100 μm of the imaged spine. The pipette is filled with 10 mM MNI-Glutamate dissolved in Tyrodes solution (in mM: 120 NaCl, 2.5 KCl, 30 glucose, 2 $CaCl_2$, 1 $MgCl_2$, and 25 HEPES; pH 7.2–7.5) and filter sterilized. We limit laser exposure to 1–2 ms using a TTL controlled shutter (LS6; Uniblitz). The laser power is adjusted so as to produce a Ca^{2+} transient with similar amplitude and kinetics as recorded EPSCaTs. In this way uncaging can be made to mimic uniquantal evoked glutamate release (**Figure 3**). Using this technique, we found that during presynaptic stimulation, artificially elevating glutamate release impaired presynaptic LTP induction, and promoted long-lasting decreases in p_r. These effects were mediated by presynaptic NMDARs (Padamsey et al., 2017).

In addition to glutamate, we have also photo-released nitric oxide (NO) at EPSCaT producing synapses to evaluate its role in LTP induction. For this technique, caged NO ($RuNOCl_3$; 0.5–1 mM) is bath applied prior to photolysis. We set the photolysis

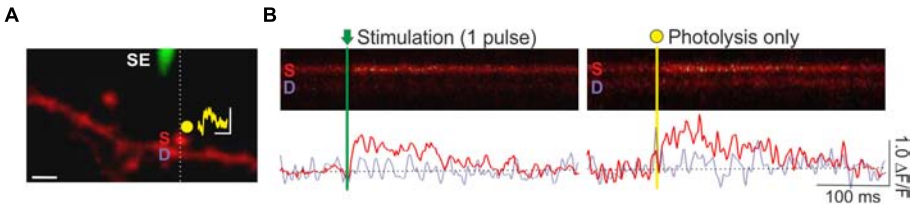

FIGURE 4 | Combined optical quantal analysis with glutamate photolysis. **(A)** Image of a CA1 dendrite loaded with OGB-1 (white scale bar: 2 μm). A fluorescently coated glass stimulating electrode (SE) is positioned within 5–10 μm of an imaged dendrite, and an EPSCaT-generating spine is found. The spine is then targeted for glutamate photolysis (yellow spot). Photolysis laser power is adjusted to trigger a Ca^{2+} transient of similar amplitude and dynamics as stimulation. The resulting synaptic potential evoked by glutamate photolysis is shown above the spine head (yellow trace; scale bar: 1 mV by 100 ms). To image Ca^{2+} responses, laser scanning is restricted to a line across the imaged spine (S) and underlying dendrite (D). **(B)** Sample line scans during stimulation and glutamate photolysis. Fluorescent changes in the spine (red trace) and dendrite (purple trace) are quantified as $\Delta F/F$ in the smoothed traces below each line scan. Ca^{2+} transients evoked by stimulation and by photolysis are similar. Figure adapted from Padamsey et al. (2017) under the terms of the Creative Commons Attribution License (CC BY).

duration to 50 ms. To titrate laser power we use the NO-indicator DAF-FM (Invitrogen). The dye is first loaded into a cell by transiently patching it (60 s) with a patch electrode containing 250 μM DAF-FM dissolved in standard internal solution. After the dye reaches diffusional equilibrium (10 min), the soma is targeted for photolysis while line scan imaging. The intensity of photolysis is changed to produce an average $\Delta F/F$ increase of ∼0.07 (averaged across trials) in DAF-FM fluorescence, which amounts to 10 nM of NO based on the manufacturer's supplied data. This concentration of NO has previously been shown to produce LTP at hippocampal synapses (Arancio et al., 1996). We calibrate laser power only once for a set of experiments. Once the intensity of uncaging is set, an EPSCaT producing spine can be targeted for spot photolysis. We have previously paired NO photolysis at the spine head with single presynaptic stimuli (30 pairings at 5 Hz). We found that presynaptic LTP was induced only when NO photolysis followed, but not preceded, the presynaptic stimulus by 7–10 ms. This suggests that NO signaling at the presynaptic terminal follows the same timing rules as traditional STDP (Padamsey et al., 2017).

DISCUSSION

Limitations

We have described how to use optical quantal analysis to assess p_r using Ca^{2+} sensitive dyes at single synapses in brain slice. This method is not without its limitations. Firstly, it is important to note that the selection of synapses for optical quantal analysis may incur a bias in favor of large spines producing large Ca^{2+} transients, which are more likely to catch the experimenter's eye. Such spines may, for example, have larger number of AMPARs and/or have a higher likelihood of containing ER. Selection bias can be limited by careful and systematic scans of spines during the initial search procedure for EPSCaT-generating synapses. We find that systematic searches are easier when the stimulating electrode is placed in close vicinity of a dendrite, since the search is spatially limited. Consequently, the experimenter can spend more time carefully examining the spines in a small region of the cell, rather than attempting to assess large regions of dendrite for synaptic responses, as is the case when the electrode is placed at a distance (>10 μm) from the soma.

A second limitation of optical quantal analysis with Ca^{2+} indicator dyes is that the technique uses a postsynaptic measure to infer presynaptic function. This means that postsynaptic changes could in principle, by altering EPSCaT amplitude, impact the probability of EPSCaT detection. However, because of the excellent SNR provided by Ca^{2+} indicator dyes, EPSCaT amplitudes lie well above detection threshold. Indeed, we have shown that twofold increases or decreases in EPSCaT amplitude, induced by pharmacological alterations of postsynaptic NMDARs, do not affect estimates of EPSCaT probability, suggesting that assessment of presynaptic efficacy is unlikely to be confounded by postsynaptic factors, at least at CA3-CA1 synapses (Padamsey et al., 2017). Moreover, estimates of p_r using Ca^{2+} indicators are consistent with estimates generated by other independent techniques, such as paired pulse ratio analysis (Padamsey et al., 2017).

The optical quantal analysis, as described here, considers a quantum to be any release event at the imaged dendritic spine. In practice, the vast majority of release events will be comprised of single vesicles, though a small proportion of events may consist of multiple vesicles, particularly at synapses with high basal release probabilities (Balaji and Ryan, 2007). In principle, multivesicular release may be quantified using Ca^{2+} imaging provided that EPSCaT amplitude scales with the number of vesicles of glutamate released; this could be verified, for example, by examining Ca^{2+} transient amplitudes evoked by varying intensities of glutamate photolysis at the imaged synapse. Nonetheless, p_r as measured by conventional optical quantal analysis represents the probability that a synapse will release any neurotransmitter in response to an AP, regardless of whether it's uni- or multivesicular in nature.

Another limitation of optical quantal analysis, as described here, is that it cannot be used to assess vesicular release probability (p_v), which is, the probability a given vesicle will be released from the synapse. Calculation of p_v requires knowledge of the total number of vesicles in the readily releasable pool of the synapse, in addition to the number of vesicles released per AP.

Such measurements can be made using FM dyes and pHlourins in dissociated cultures (Ariel and Ryan, 2010; Ermolyuk et al., 2012).

Recent experimental evidence suggests that neurotransmitter release at a synapse is mediated by multiple, independent presynaptic release modules (Tang et al., 2016; Biederer et al., 2017). Conventional postsynaptic Ca^{2+} imaging cannot readily measure release probability at individual release modules, nor can other live-cell imaging techniques unless applied to reduced preparations (ex. dissociated cultures) where optical access is much improved (Midorikawa and Sakaba, 2015). p_r measurements made with Ca^{2+} imaging in intact tissue will therefore reflect an integrated measure of release probability across all potential release modules associated with the imaged dendritic spine. As a consequence, observed changes in p_r may reflect either an increase in average release probability across sites, or an addition of more release sites to the synapse. In the case of perforated synapses, in which dendritic spines form multiple synapses with independent boutons, estimates of p_r at the spine may be confounded if more than one such bouton is recruited by electrical stimulation. This confound is unlikely to have a major impact on experimental results since perforated synapses comprise only a minority of central synapses [10–15% of mature CA1 synapses; (Harris and Stevens, 1989)].

Wider Applicability of Optical Quantal Analysis

Although we have focussed on the application of optical quantal analysis at Schaffer-collateral synapses, it is important to note that the technique can and has been used to measure p_r to other central synapses, including those of the neocortex (Reid et al., 2001; Koester and Johnston, 2005; Chalifoux and Carter, 2010; Kwon and Sabatini, 2011; Chun et al., 2014). Moreover, optical quantal analysis does not strictly require synthetic Ca^{2+}-sensitive dyes. In principle, a number of probes that are able to report on transmitter release could be used to assess p_r and presynaptic plasticity using the general technique we describe here. Such probes include fluorescent lipophilic dyes (e.g., FM dyes) and pH sensors (e.g., pHlourins) which report vesicular fusion, glutamate sensors which report cleft glutamate concentration, and voltage sensors, which like Ca^{2+} sensors, report the postsynaptic response of transmitter release. The only requirement for optical quantal analysis is that the chosen probe robustly and reliably detect single trial uniquantal glutamate release events with good SNR at the chosen synapse, and in the chosen experimental preparation. Optical quantal analysis with FM dyes and pHlourins is currently only possible in dissociated cultures, where optical access is optimal (Tokuoka and Goda, 2008; Ariel and Ryan, 2010). Voltage sensors are not currently sensitive enough to robustly detect single trial uniquantal glutamate release at individual synapses (Platisa and Pieribone, 2018). By contrast, recent improvements in genetically encoded Ca^{2+} (GCaMP6/7 variants) and glutamate sensors (iGluSnFR variants) make them particularly well suited for non-invasive optical quantal analysis in slice preparations with cell-type specificity (Chen et al., 2013; Marvin et al., 2017; Dana et al., 2018; Helassa et al., 2018; Jensen et al., 2018).

Despite the advantages afforded by genetically encoded sensors, they are not without limitations. Genetically encoded probes require the additional effort of sparsely transfecting tissue weeks before hand; Ca^{2+}-sensitive proteins also have slow kinetics and run the risk of impacting cellular physiology due to long-term Ca^{2+} buffering. By contrast, synthetic Ca^{2+} indicators have faster kinetics and are easier to use. Dye loading via a patch pipette also naturally provides electrophysiological control of the postsynaptic cell, which would be required for most plasticity experiments during LTP or LTD induction. Moreover, postsynaptic access to the cell enables infusion of intracellular reagents and control over intracellular ion concentrations and voltage, which may be useful for examining the effects of cellular and receptor signaling on presynaptic function (Padamsey et al., 2017). Because of the ease and convenience of the technique, we would therefore highly recommend the use of Ca^{2+} indicator dyes for optical quantal analysis in brain slice experiments in which cell-type specificity is not strictly required.

Future Outlook and Conclusion

Unfortunately, optical quantal analysis is not yet possible *in vivo* as the SNR of existing optical techniques does not allow for robust and reliable detection of single quanta of glutamate in the intact brain. However, *in vivo* optical quantal analysis is becoming increasingly likely with ongoing improvements in genetically encoded sensors Ca^{2+} (Dana et al., 2018), voltage (Storace et al., 2016; Yang and St-Pierre, 2016), and glutamate sensors (Marvin et al., 2017; Helassa et al., 2018; Jensen et al., 2018). These are complemented by advances in imaging methodologies such as three photon microscopy (Rowlands et al., 2017), adaptive optics (Ji, 2017), and endoscopy (Miyamoto and Murayama, 2016), including the use of multi-mode fibers (Vasquez-Lopez et al., 2018), which promise greater optical access *in vivo*. In conclusion, optical quantal analysis offers researchers a simple and effective method for assessing transmitter release and plasticity *in vitro*, with potential for future applications *in vivo*.

AUTHOR CONTRIBUTIONS

ZP drafted the manuscript. RT designed the figures. NE provided funding and overall guidance. All authors revised the manuscript.

FUNDING

This work was funded by a grant from the Biotechnology and Biological Sciences Research Council (BBSRC; BB/P02730X/1). ZP is funded by a research fellowship from the Royal Commission for the Exhibition of 1851.

REFERENCES

Andrade-Talavera, Y., Duque-Feria, P., Paulsen, O., and Rodríguez-Moreno, A. (2016). Presynaptic spike timing-dependent long-term depression in the mouse hippocampus. *Cereb. Cortex* 26, 3637–3654. doi: 10.1093/cercor/bhw172

Arancio, O., Kiebler, M., Lee, C. J., Lev-Ram, V., Tsien, R. Y., Kandel, E. R., et al. (1996). Nitric oxide acts directly in the presynaptic neuron to produce long-term potentiation in cultured hippocampal neurons. *Cell* 87, 1025–1035.

Ariel, P., and Ryan, T. A. (2010). Optical mapping of release properties in synapses. *Front. Neural Circuits* 4:18. doi: 10.3389/fncir.2010.00018

Balaji, J., and Ryan, T. A. (2007). Single-vesicle imaging reveals that synaptic vesicle exocytosis and endocytosis are coupled by a single stochastic mode. *Proc. Natl. Acad. Sci. U.S.A.* 104, 20576–20581. doi: 10.1073/pnas.0707574105

Beaulieu-Laroche, L., and Harnett, M. T. (2018). Dendritic spines prevent synaptic voltage clamp. *Neuron* 97, 75–82.e3. doi: 10.1016/J.NEURON.2017.11.016

Biederer, T., Kaeser, P. S., and Blanpied, T. A. (2017). Transcellular nanoalignment of synaptic function. *Neuron* 96, 680–696. doi: 10.1016/j.neuron.2017.10.006

Bloodgood, B. L., and Sabatini, B. L. (2007). Ca2+ signaling in dendritic spines. *Curr. Opin. Neurobiol.* 17, 345–351. doi: 10.1016/j.conb.2007.04.003

Bouvier, G., Larsen, R. S., Rodríguez-Moreno, A., Paulsen, O., and Sjöström, P. J. (2018). Towards resolving the presynaptic NMDA receptor debate. *Curr. Opin. Neurobiol.* 51, 1–7. doi: 10.1016/j.conb.2017.12.020

Chalifoux, J. R., and Carter, A. G. (2010). GABABReceptors modulate NMDA receptor calcium signals in dendritic spines. *Neuron* 66, 101–113. doi: 10.1016/j.neuron.2010.03.012

Chen, T. W., Wardill, T. J., Sun, Y., Pulver, S. R., Renninger, S. L., Baohan, A., et al. (2013). Ultrasensitive fluorescent proteins for imaging neuronal activity. *Nature* 499, 295–300. doi: 10.1038/nature12354

Choi, J. H., Sim, S. E., Kim, J. I., Choi, D. I., Oh, J., Ye, S., et al. (2018). Interregional synaptic maps among engram cells underlie memory formation. *Science* 360, 430–435. doi: 10.1126/science.aas9204

Chun, S., Westmoreland, J. J., Bayazitov, I. T., Eddins, D., Pani, A. K., Smeyne, R. J., et al. (2014). Specific disruption of thalamic inputs to the auditory cortex in schizophrenia models. *Science* 334, 1178–1182. doi: 10.1126/science.1253895

Clements, J. D., and Silver, R. A. (2000). Unveiling synaptic plasticity: a new graphical and analytical approach. *Trends Neurosci.* 23, 105–113.

Dana, H., Sun, Y., Mohar, B., Hulse, B., Hasseman, J. P., Tsegaye, G., et al. (2018). High-performance GFP-based calcium indicators for imaging activity in neuronal populations and microcompartments. *bioRXiv* [Preprint]. doi: 10.1101/434589

De Simoni, A., Griesinger, C. B., and Edwards, F. A. (2003). Development of rat CA1 neurones in acute versus organotypic slices: Role of experience in synaptic morphology and activity. *J. Physiol.* 550(Pt 1), 135–147. doi: 10.1113/jphysiol.2003.039099

Emptage, N., Bliss, T. V. P., and Fine, A. (1999). Single synaptic events evoke NMDA receptor-mediated release of calcium from internal stores in hippocampal dendritic spines. *Neuron* 22, 115–124.

Emptage, N. J., Reid, C. A., Fine, A., and Bliss, T. V. P. (2003). Optical quantal analysis reveals a presynaptic component of LTP at hippocampal Schaffer-associational synapses. *Neuron* 38, 797–804.

Enoki, R., Hu, Y. L., Hamilton, D., and Fine, A. (2009). Expression of long-term plasticity at individual synapses in hippocampus is graded, bidirectional, and mainly presynaptic: optical quantal analysis. *Neuron* 62, 242–253. doi: 10.1016/j.neuron.2009.02.026

Ermolyuk, Y. S., Alder, F. G., Henneberger, C., Rusakov, D. A., Kullmann, D. M., and Volynski, K. E. (2012). Independent regulation of basal neurotransmitter release efficacy by variable Ca2+ influx and bouton size at small central synapses. *PLoS Biol.* 10:e1001396. doi: 10.1371/journal.pbio.1001396

Evans, D. A., Stempel, A. V., Vale, R., Ruehle, S., Lefler, Y., and Branco, T. (2018). A synaptic threshold mechanism for computing escape decisions. *Nature* 558, 590–594. doi: 10.1038/s41586-018-0244-6

Grienberger, C., Chen, X., and Konnerth, A. (2014). NMDA receptor-dependent multidendrite Ca2+spikes required for hippocampal burst firing invivo. *Neuron* 81, 1274–1281. doi: 10.1016/j.neuron.2014.01.014

Grillo, F. W., Neves, G., Walker, A., Vizcay-Barrena, G., Fleck, R. A., Branco, T., et al. (2018). A distance-dependent distribution of presynaptic boutons tunes frequency-dependent dendritic integration. *Neuron* 99, 275–282.e3. doi: 10.1016/j.neuron.2018.06.015

Grunditz, A., Holbro, N., Tian, L., Zuo, Y., and Oertner, T. G. (2008). Spine neck plasticity controls postsynaptic calcium signals through electrical compartmentalization. *J. Neurosci.* 28, 13457–13466. doi: 10.1523/JNEUROSCI.2702-08.2008

Harnett, M. T., Makara, J. K., Spruston, N., Kath, W. L., and Magee, J. C. (2012). Synaptic amplification by dendritic spines enhances input cooperativity. *Nature* 491, 599–602. doi: 10.1038/nature11554

Harris, K. M., and Stevens, J. K. (1989). Dendritic spines of CA 1 pyramidal cells in the rat hippocampus: serial electron microscopy with reference to their biophysical characteristics. *J. Neurosci.* 9, 2982–2997. doi: 10.1523/JNEUROSCI.09-08-02982.1989

Helassa, N., Dürst, C. D., Coates, C., Kerruth, S., Arif, U., Schulze, C., et al. (2018). Ultrafast glutamate sensors resolve high-frequency release at Schaffer collateral synapses. *Proc. Natl. Acad. Sci. U.S.A.* 115, 5594–5599. doi: 10.1073/pnas.1720648115

Holbro, N., Grunditz, A., and Oertner, T. G. (2009). Differential distribution of endoplasmic reticulum controls metabotropic signaling and plasticity at hippocampal synapses. *Proc. Natl. Acad. Sci. U.S.A.* 106, 15055–15060. doi: 10.1073/pnas.0905110106

Holderith, N., Lorincz, A., Katona, G., Rózsa, B., Kulik, A., Watanabe, M., et al. (2012). Release probability of hippocampal glutamatergic terminals scales with the size of the active zone. *Nat. Neurosci.* 15, 988–997. doi: 10.1038/nn.3137

Ishikawa, D., Takahashi, N., Sasaki, T., Usami, A., Matsuki, N., and Ikegaya, Y. (2010). Fluorescent pipettes for optically targeted patch-clamp recordings. *Neural Networks* 23, 669–672. doi: 10.1016/j.neunet.2010.02.004

Jensen, T. P., Zheng, K., Cole, N., Marvin, J. S., Looger, L. L., and Rusakov, D. A. (2018). Multiplex imaging of quantal glutamate release and presynaptic Ca^{2+} at multiple synapses *in situ*. *bioRxiv* [Preprint]. doi: 10.1101/336891

Ji, N. (2017). Adaptive optical fluorescence microscopy. *Nat. Methods* 14, 374–380. doi: 10.1038/nmeth.4218

Koester, H. J., and Johnston, D. (2005). Target cell-dependent normalization of transmitter release at neocortical synapses. *Science* 308, 863–866. doi: 10.1126/science.1100815

Koga, K., Descalzi, G., Chen, T., Ko, H.-G., Lu, J., Li, S., et al. (2015). Coexistence of two forms of LTP in ACC provides a synaptic mechanism for the interactions between anxiety and chronic pain. *Neuron* 85, 377–389. doi: 10.1016/J.NEURON.2014.12.021

Kowalski, J., Gan, J., Jonas, P., and Pernía-Andrade, A. J. (2016). Intrinsic membrane properties determine hippocampal differential firing pattern in vivo in anesthetized rats. *Hippocampus* 26, 668–682. doi: 10.1002/hipo.22550

Kwon, H. B., and Sabatini, B. L. (2011). Glutamate induces de novo growth of functional spines in developing cortex. *Nature* 474, 100–104. doi: 10.1038/nature09986

Malinow, R., and Tsien, R. W. (1990). Presynaptic enhancement shown by whole-cell recordings of long-term potentiation in hippocampal slices. *Nature* 346, 177–180. doi: 10.1038/346177a0

Maren, S. (2005). Synaptic mechanisms of associative memory in the amygdala. *Neuron* 47, 783–786. doi: 10.1016/j.neuron.2005.08.009

Marvin, J. S., Scholl, B., Wilson, D. E., Podgorski, K., Kazemipour, A., Mueller, J. A., et al. (2017). Stability, affinity and chromatic variants of the glutamate sensor iGluSnFR. *Nat. Methods* 15, 936–939.

Midorikawa, M., and Sakaba, T. (2015). Imaging exocytosis of single synaptic vesicles at a fast CNS presynaptic terminal. *Neuron* 88, 492–498. doi: 10.1016/j.neuron.2015.09.047

Min, R., and Nevian, T. (2012). Astrocyte signaling controls spike timing-dependent depression at neocortical synapses. *Nat. Neurosci.* 15, 746–753. doi: 10.1038/nn.3075

Miyamoto, D., and Murayama, M. (2016). The fiber-optic imaging and manipulation of neural activity during animal behavior. *Neurosci. Res.* 103, 1–9. doi: 10.1016/j.neures.2015.09.004

Nevian, T., and Helmchen, F. (2007). Calcium indicator loading of neurons using single-cell electroporation. *Pflugers Arch. Eur. J. Physiol.* 454, 675–688.

Ngo-Anh, T. J., Bloodgood, B. L., Lin, M., Sabatini, B. L., Maylie, J., and Adelman, J. P. (2005). SK channels and NMDA receptors form a Ca2+-mediated feedback loop in dendritic spines. *Nat. Neurosci.* 8, 642–649. doi: 10.1038/nn1449

Noguchi, J., Matsuzaki, M., Ellis-Davies, G. C. R., and Kasai, H. (2005). Spine-neck geometry determines NMDA receptor-dependent Ca2+signaling in dendrites. *Neuron* 46, 609–622. doi: 10.1016/j.neuron.2005.03.015

Oertner, T. G., Sabatini, B. L., Nimchinsky, E. A., and Svoboda, K. (2002). Facilitation at single synapses probed with optical quantal analysis. *Nat. Neurosci.* 5, 657–664. doi: 10.1038/nn867

Padamsey, Z., and Emptage, N. (2014). Two sides to long-term potentiation: a view towards reconciliation. *Philos. Trans. R. Soc. B Biol. Sci.* 369:20130154. doi: 10.1098/rstb.2013.0154

Padamsey, Z., Foster, W. J., and Emptage, N. J. (2018). Intracellular Ca 2+ release and synaptic plasticity: a tale of many stores. *Neuroscientist* doi: 10.1177/1073858418785334 [Epub ahead of print].

Padamsey, Z., Tong, R., and Emptage, N. (2017). Glutamate is required for depression but not potentiation of long-term presynaptic function. *eLife* 6:e29688. doi: 10.7554/eLife.29688

Platisa, J., and Pieribone, V. A. (2018). Genetically encoded fluorescent voltage indicators: are we there yet? *Curr. Opin. Neurobiol.* 50, 146–153. doi: 10.1016/j.conb.2018.02.006

Pyott, S. J., and Rosenmund, C. (2002). The effects of temperature on vesicular supply and release in autaptic cultures of rat and mouse hippocampal neurons. *J. Physiol.* 539(Pt 2), 523–535. doi: 10.1113/jphysiol.2001.013277

Reid, C. A., Fabian-Fine, R., and Fine, A. (2001). Postsynaptic calcium transients evoked by activation of individual hippocampal mossy fiber synapses. *J. Neurosci.* 21, 2206–2214.

Rowlands, C. J., Park, D., Bruns, O. T., Piatkevich, K. D., Fukumura, D., Jain, R. K., et al. (2017). Wide-field three-photon excitation in biological samples. *Light Sci. Appl.* 6:e16255. doi: 10.1038/lsa.2016.255

Storace, D., Sepehri Rad, M., Kang, B. E., Cohen, L. B., Hughes, T., and Baker, B. J. (2016). Toward better genetically encoded sensors of membrane potential. *Trends Neurosci.* 39, 277–289. doi: 10.1016/j.tins.2016.02.005

Tang, A. H., Chen, H., Li, T. P., Metzbower, S. R., MacGillavry, H. D., and Blanpied, T. A. (2016). A trans-synaptic nanocolumn aligns neurotransmitter release to receptors. *Nature.* 536:210. doi: 10.1038/nature19058

Tokuoka, H., and Goda, Y. (2008). Activity-dependent coordination of presynaptic release probability and postsynaptic GluR2 abundance at single synapses. *Proc Natl Acad Sci U.S.A.* 105, 14656–14661. doi: 10.1073/pnas.0805705105

Vasquez-Lopez, S. A., Koren, V., Ploschner, M., Padamsey, Z., Cizmar, T., and Emptage, N. J. (2018). Subcellular spatial resolution achieved for deep-brain imaging in vivo with a minimally invasive multimode fibre. *Light Sci. Appl.* 7:110.

Ward, B., McGuinness, L., Akerman, C. J. J., Fine, A., Bliss, T. V. P., and Emptage, N. J. (2006). State-dependent mechanisms of LTP expression revealed by optical quantal analysis. *Neuron* 52, 649–661. doi: 10.1016/j.neuron.2006.10.007

Yang, H. H., and St-Pierre, F. (2016). Genetically encoded voltage indicators: opportunities and challenges. *J. Neurosci.* 36, 9977–9989. doi: 10.1523/JNEUROSCI.1095-16.2016

Yang, Y., and Calakos, N. (2013). Presynaptic long-term plasticity. *Front. Synaptic Neurosci.* 5:8. doi: 10.3389/fnsyn.2013.00008

Yasuda, R., Nimchinsky, E. A., Scheuss, V., Pologruto, T. A., Oertner, T. G., Sabatini, B. L., et al. (2004). Imaging calcium concentration dynamics in small neuronal compartments. *Sci. Signal.* 2004:l5. doi: 10.1126/stke.2192004pl5

Conflict of Interest Statement: The authors declare that the research was conducted in the absence of any commercial or financial relationships that could be construed as a potential conflict of interest.

frontiers in Synaptic Neuroscience

REVIEW
published: 07 March 2019
doi: 10.3389/fnsyn.2019.00007

The Small and Dynamic Pre-primed Pool at the Release Site; A Useful Concept to Understand Release Probability and Short-Term Synaptic Plasticity?

Bengt Gustafsson, Rong Ma and Eric Hanse*

Department of Physiology, Sahlgrenska Academy, University of Gothenburg, Gothenburg, Sweden

Advanced imaging techniques have revealed that synapses contain nanomodules in which pre- and post-synaptic molecules are brought together to form an integrated subsynaptic component for vesicle release and transmitter reception. Based on data from an electrophysiological study of ours in which release from synapses containing a single nanomodule was induced by brief 50 Hz trains using minimal stimulation, and on data from such imaging studies, we present a possible modus operandi of such a nanomodule. We will describe the techniques and tools used to obtain and analyze the electrophysiological data from single CA3–CA1 hippocampal synapses from the neonatal rat brain. This analysis leads to the proposal that a nanomodule, despite containing a number of release locations, operates as a single release site, releasing at most a single vesicle at a time. In this nanomodule there appears to be two separate sets of release locations, one set that is responsible for release in response to the first few action potentials and another set that produces the release thereafter. The data also suggest that vesicles at the first set of release locations are primed by synaptic inactivity lasting seconds, this synaptic inactivity also resulting in a large heterogeneity in the values for vesicle release probability among the synapses. The number of vesicles being primed at this set of release locations prior to the arrival of an action potential is small (0–3) and varies from train to train. Following the first action potential, this heterogeneity in vesicle release probability largely vanishes in a release-independent manner, shaping a variation in paired-pulse plasticity among the synapses. After the first few action potentials release is produced from the second set of release locations, and is given by vesicles that have been recruited after the onset of synaptic activity. This release depends on the number of such release locations and the recruitment to such a location. The initial heterogeneity in vesicle release probability, its disappearance after a single action potential, and variation in the recruitment to the second set of release

OPEN ACCESS

Edited by:
John F. Wesseling, Institute of Neurosciences of Alicante (IN), Spain

Reviewed by:
Jeffrey Scott Diamond, National Institute of Neurological Disorders and Stroke (NINDS), United States
Daniel Gitler, Ben-Gurion University of the Negev, Israel

***Correspondence:**
Bengt Gustafsson
b.gustafsson@gu.se

Received: *02 November 2018*
Accepted: *20 February 2019*
Published: *07 March 2019*

Citation:
Gustafsson B, Ma R and Hanse E (2019) The Small and Dynamic Pre-primed Pool at the Release Site; A Useful Concept to Understand Release Probability and Short-Term Synaptic Plasticity? Front. Synaptic Neurosci. 11:7. doi: 10.3389/fnsyn.2019.00007

locations are instrumental in producing the heterogeneity in short-term synaptic plasticity among these synapses, and can be seen as means to create differential dynamics within a synapse population.

Keywords: hippocampus, synapse, nanomodule, release probability, plasticity, glutamate, vesicle, release site

INTRODUCTION

Recent work using various imaging techniques has begun to reveal the supramolecular organization of the presynaptic active zone and of its postsynaptic counterpart, the postsynaptic density. There are still uncertainties regarding the exact spatial relationship among structures vital to the release such as the readily releasable vesicles, the vesicle scaffold proteins, the voltage-gated calcium channels (VGCCs), as well as the postsynaptic receptors and their associated proteins. Nonetheless, a nanomodule organization within the synapse in which these components are brought together to constitute an integrated subsynaptic component for vesicle release and transmitter reception is starting to emerge (Biederer et al., 2017). Data regarding the distance requirements in the nm scale for effective interaction between the VGCCs and the vesicle Ca^{2+} acceptor (Nakamura et al., 2015) as well as for the release and AMPA receptor locations (MacGillavry et al., 2013; Tang et al., 2016; Haas et al., 2018) has also indicated the importance of such close spatial organization. All in all, such a nanomodule should cover an area of no more than $\sim$0.04 μm^2 (Hruska et al., 2018), which is about the active zone areas of the smallest Schaffer collateral synapses onto CA1 pyramidal cells (CA3–CA1 synapses; Schikorski and Stevens, 1997). Interestingly, after chemically induced long-term potentiation (LTP), synapses acquire additional such nanomodules (Hruska et al., 2018), indicating that synaptic strength is a function of the number of such nanomodules acquired by a synapse (Lisman and Raghavachari, 2006).

Some time ago two of the authors of this article examined, using minimal stimulation and whole-cell recording, the release from single CA3–CA1 synapses in the neonatal rat (Hanse and Gustafsson, 2001a,b,c,d, 2002). These are small synapses likely to contain only one such nanomodule (Fiala et al., 1998). An analysis of the release pattern during brief train activation of these synapses strongly suggested univesicular release from a small population of vesicles, indicating that this putative nanomodule operates as a single functional release site. The vesicle pool was found to be dynamic in that the number of vesicles available for release at stimulation onset (referred to as the pre-primed pool) varied from trial to trial. Moreover, the release probability (P_r) in response to the first action potential in the train (P_1) varied much among these synapses, and depended, in addition to vesicle pool size, on a large diversity in vesicle release probability at the onset of stimulation (P_{ves1}). This large diversity in P_{ves1} was instrumental in creating the large variation among the synapses in short-term plasticity behavior during train stimulation, from profound depression to large facilitation.

In this article we will describe in what manner and with which tools the experimental results from these neonatal synapses were acquired and processed, and discuss these results in the context of current understanding of the supramolecular structure of a nanomodule.

OUTLINE OF A NANOMODULE (THE FUNCTIONAL RELEASE SITE)

The distribution of active zone and PSD areas of CA3–CA1 synapses in adult animals varies from $\sim$0.01 to $\sim$0.18 μm^2, but is highly skewed with the vast majority of values between 0.02–0.04 μm^2 (Schikorski and Stevens, 1997). Based on combined pre- and post-synaptic imaging (of vesicle and PSD proteins, respectively) it would appear that active zone areas below $\sim$0.04 μm^2 correspond to synapses containing a single nanomodule, and those with larger areas multiples of such nanomodules (Biederer et al., 2017; Hruska et al., 2018). With respect to the spatial organization of proteins on the postsynaptic side, the AMPA receptors are present throughout the PSD but are specifically clustered in a small area (hot spot, $\sim$0.005 μm^2) within the central region of the nanomodule (MacGillavry et al., 2013). On the presynaptic side, VGCCs, docked vesicles and release locations can also be found distributed throughout the active zone, but not randomly (Scimemi and Diamond, 2012; Nakamura et al., 2015; Tang et al., 2016; Éltes et al., 2017; Maschi and Klyachko, 2017). As recently proposed, the nucleus of a release location could be a nanoassembly of Munc13–1 (together with some other active zone proteins) that by contacting syntaxin-1 builds a docking/priming location for a single vesicle (Sakamoto et al., 2018). It is then assumed, albeit not demonstrated, that such a nanoassembly comes into close contact with a small cluster of VGCCs. Such a nanoassembly would have a diameter of 60–80 nm in total, that gives a nanoassembly area of 0.003–0.005 μm^2, i.e., about one tenth of a nanomodule. Considering the number of docked vesicles that can be observed within an active zone area of $<$0.04 μm^2 (Schikorski and Stevens, 1997) there should be some 2–6 Munc13–1 nanoassemblies in a small, 1-nanomodule, synapse. The vesicle-associated protein RIM1/2 also displays a clustered organization within the active zone (Tang et al., 2016), but with seemingly smaller number of hot spots than Munc-13 (Tang et al., 2016). A RIM1/2 nanoassembly is also organized in approximate register with the AMPA receptor hot spot, indicating a transverse nanocolumn for synaptic release/reception (Tang et al., 2016).

The release machinery of a nanomodule might then consist of some 2–6 release locations (nanoassemblies) capable of binding a similar number of docked vesicles, distributed over an active zone area of about 0.02–0.04 μm^2 but preferentially towards the center

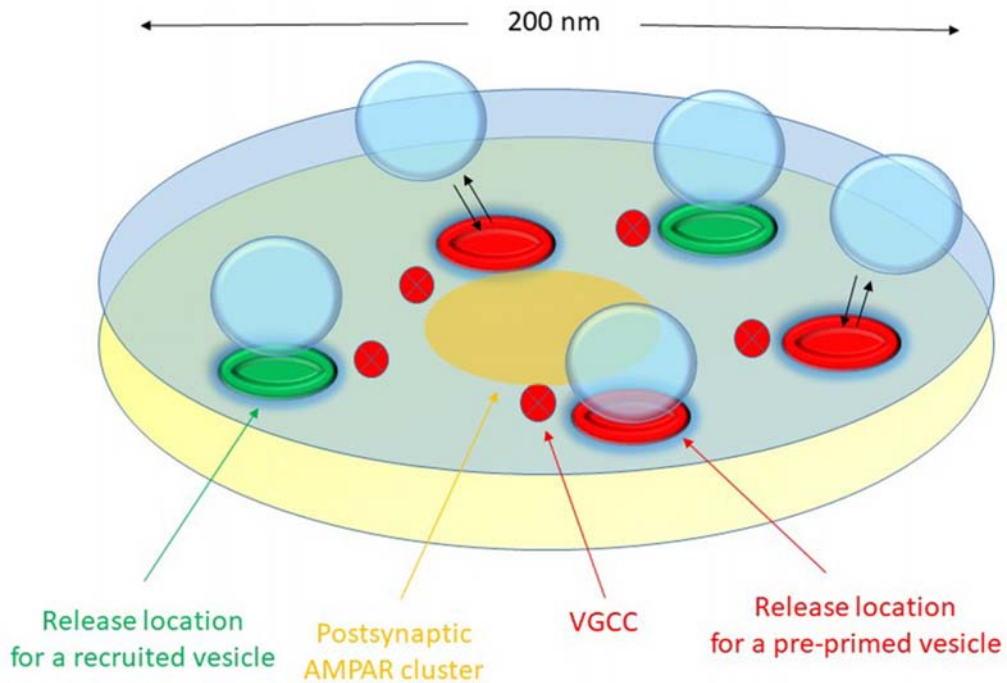

FIGURE 1 | Schematic drawing of a functional release site (nanomodule) at rest. The schematic release site contains five release locations. The three red release locations constitute the pre-primed source pool, responsible for phasic release. Here one of these release locations has a docked and pre-primed vesicle. The two green release locations are for recruited vesicles, responsible for tonic release. Voltage-gated calcium channels are indicated in the presynaptic membrane and a nanocluster of AMPA receptors are indicated in the postsynaptic membrane.

of the nanomodule opposite to the postsynaptic AMPA receptor hot spot. As indicated by the Munc13-1 vs. RIM1/2 discrepancy in number, there may be two functionally separate sets of release locations. A schematic drawing of such a nanomodule indicating these different sets of release locations (red vs. green) is shown in **Figure 1**.

MINIMAL STIMULATION TECHNIQUE

In our study the minimal stimulation technique (Raastad et al., 1992; Stevens and Wang, 1995) was used to activate a single synapse onto a single CA1 pyramidal cell (**Figure 2**). This technique is possible to use for these neonatal synapses since there is good evidence electrophysiologically that the axons stimulated only have a single connection to a given postsynaptic cell (Hsia et al., 1998; Groc et al., 2002). Using brief train stimulation as test stimulation, axon activation and synaptic release goes hand in hand (in parallel), allowing for an unbiased selection of the CA3–CA1 synapses. Thus, the P_1 values of the sampled synapses covered the full range of P_r values (in response to single action potentials) demonstrated for these synapses using population recordings (Wasling et al., 2004). In addition, the use of brief train stimulation as test stimulus also results in a sharp detection threshold for additional axon activations with variation in stimulation strength. The analysis of such single synapse activation experiments showed that the EPSCs, although varying substantially in amplitude, displayed a very narrow range of latency and time course (Hanse and Gustafsson, 2001c). If being an inclusion criterion such uniformity in EPSC time characteristics may cause a selection bias against synapses with multivesicular release. However, for our experiments this uniformity was a *post hoc* observation.

QUANTAL AMPLITUDE

For any given synapse the evoked EPSCs varied substantially in amplitude, the coefficient of variation (CV) being mostly between 30%–60% among the synapses, associated with both normal and skewed distributions (Hanse and Gustafsson, 2001c). There was among the synapses no positive correlation between CV and EPSC amplitude (excluding failures), or release probability (P_r), as might have been expected if multivesicular release contributes to the EPSC variation. To further examine whether multivesicular release contributes to the EPSC variation, the considerable change in P_r that can arise in a synapse during train activation was used. When selecting synapses with initial high P_r (>0.5) that displayed strong depression during the train stimulation, EPSC amplitude (excluding failures) was found to

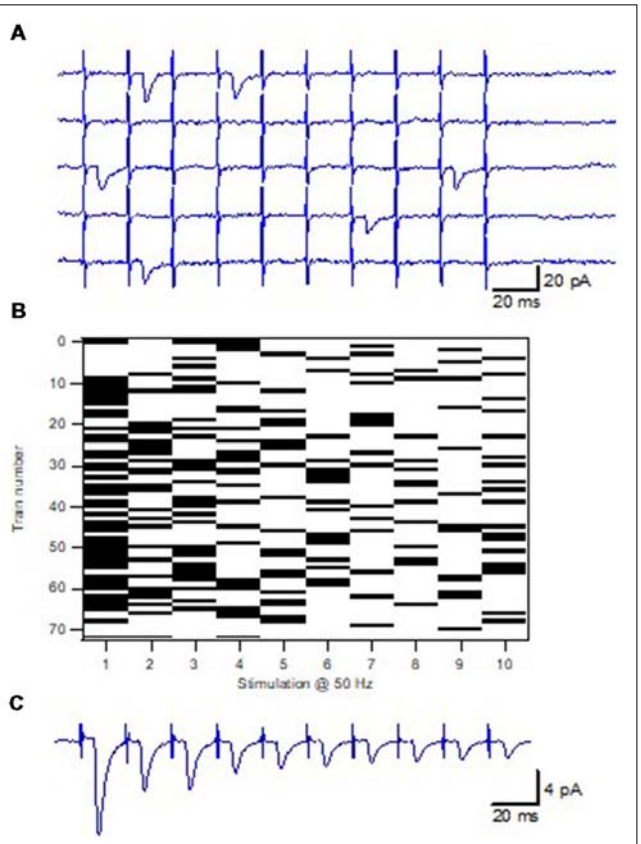

FIGURE 2 | Minimal train stimulation of a unitary synaptic input. **(A)** Five consecutive example sweeps from one synaptic input in response to minimal train stimulation, 10 impulses 50 Hz. **(B)** Release pattern for the synaptic input shown in **(A)**. Release is indicated with a black bar and failure is indicated by a white bar. **(C)** Average train response for the synaptic input shown in **(A,B)**. Adapted from Hanse and Gustafsson (2001a).

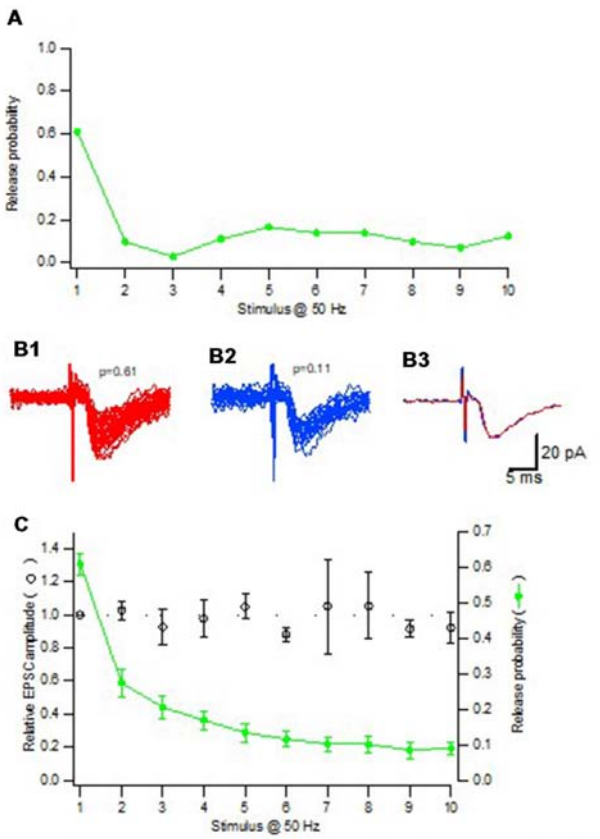

FIGURE 3 | Quantal size is independent of release probability. **(A)** Release probability for one synaptic input repeatedly activated with a train consisting of 10 impulses at 50 Hz. **(B1)** All EPSCs (n = 44) from the 1st position in the train where the release probability was 0.61. **(B2)** All EPSCs (n = 22) from the 2nd to the 10th position in the train where the release probability was 0.11. To minimize the risk for potential influence of desensitization only EPSCs that were not immediately preceded by another EPSC were included. **(B3)** Average of the EPSCs included in **(B1,B2)** superimposed. **(C)** Summary plot (n = 19 synaptic inputs) shows both the relative amplitude of the EPSCs (open black circles) and the average release probability (filled green circles) as a function of stimulus position in the train. Adapted from Hanse and Gustafsson (2001c).

be independent of P_r, thus seemingly excluding that the high P_r conditions result in multivesicular release (**Figure 3**). Such conclusion requires, however, that transmitter from a single vesicle does not come close to saturate the postsynaptic receptors. Experiments using cultured hippocampal neurons as well as 2nd postnatal week CA3–CA1 synapses in slice preparation have shown that the receptors are far from saturated, the median EPSC being <50% of the saturated response (Liu et al., 1999; McAllister and Stevens, 2000).

Given that the evoked EPSCs are generated from single vesicle releases, the variation in amplitude can result from the release of vesicles containing different amounts of transmitter either because of vesicle size variation (Sulzer and Edwards, 2000; Grabner and Moser, 2018) or of vesicle transmitter concentrations (Wu et al., 2007). In addition, vesicle release has been found to take place also outside the central region of the nanomodule where the AMPA receptors have their highest density (Maschi and Klyachko, 2017). Since a misalignment between release location and AMPA receptor hot spot of >100 nm can affect the EPSC amplitude (without obvious effects on the EPSC time course; Haas et al., 2018), such spatial mismatch may also contribute to the EPSC variability (Franks et al., 2003). However, creating such extra mismatch, using a truncated form of neuroligin that shifts the release locations away from the AMPA receptor hot spot, results in no more than ∼20% decrease in quantal EPSC amplitude (Haas et al., 2018). Nonetheless, these results (Haas et al., 2018) suggest that, given a central position of the AMPA receptor hot spot within a nanomodule, the surface area of a nanomodule should not be >∼0.04 μm^2 for optimal activation of the AMPA receptors. This is in line with the observation of an increased number of nanomodules when synapses are strengthened after chemically induced LTP (Hruska et al., 2018). These results also suggest that our observation that the quantal EPSC is unaffected by its position in the train indicates that vesicles released initially vs. late in the train are released from locations ∼equally close to the AMPA receptor hot spot.

PRE-PRIMED POOL

The P_r of a synapse is generally evaluated when activating the synapse at low frequencies, such as 0.2–0.033 Hz. The vesicle pool of interest for such release is the number of vesicles that are primed for release at just that instant of time when the action potential arrives, i.e., are pre-primed. The number of vesicles that can be released by prolonged stimulation of the synapses, or released by hypertonic treatment or other such means, may then not be very relevant. A common technique to evaluate this immediately releasable pool (but for a population of synapses) is to subject the synapses to a brief (10–20 impulses) high-frequency activation, and construct a cumulative synaptic response curve (Neher, 2015). After a few stimuli this curve becomes more or less linear, explained as the establishment of equilibrium between release and recruitment of vesicles. Extrapolation of this linear part to time zero then gives a measure of the vesicle pool available at stimulus onset. However, what is obtained is not the absolute pool size, but pool size expressed in units of the release probability. Moreover, the estimated value will depend on assumptions regarding when recruitment of new vesicles during the train stimulation actually begins. In addition, there is no way of knowing that this pool is fully depleted during the initial non-linear part of the cumulative curve.

Determining the Pre-primed Pool

Brief train activation at high frequency was also used in our study to evoke release but the focus was on the interaction between release events occurring later in the train vs. that occurring to the 1st stimulus in the train (Hanse and Gustafsson, 2001d). Using that novel procedure, taking advantage of the variability in the number of release events in the various trials (**Figure 2**), it was first examined when during the stimulation train the occurrence of a 2nd release event is associated with a larger value of P_1 (as compared to when only one release event had occurred). This analysis revealed that a 2nd release event that occurred within the first half of a 10-impulse train was associated with a larger P_1, and was thus given by a pre-primed vesicle. Importantly, this vesicle added to P_1 as if it acted independently of the vesicle that produced the 1st release event at that trial, and as if it had the same P_{ves} value. On the other hand, a 2nd release event that occurred in the second half of the train was not associated with a larger P_1, and had thus been recruited to a primed state during the train. The pool of pre-primed vesicles, determining the value of P_1, thus only constitutes a subpopulation of the vesicles released even during a 10-impulse 50 Hz stimulus.

To estimate the size of this subpopulation, we adopted a variation of the above procedure to examine the timing of release events during the train. To explain this procedure one can consider a single release location that acquires and releases a single vesicle (with a certain probability) one at a time at a certain rate, and expose it to repeated trials of train stimulation. Thereafter the relation between P_1 and train length is examined, selecting only trials in which one release event occurs (1-release trials). With a train length of 1, P_1 will of course be 1. With increasing train length, trials with the single vesicle released at later positions in the train will occur, and P_1 will successively decrease. Moreover, since the release occurs at a certain rate, trials in which the vesicle was released in position 1 tend to be the first to display a 2nd release event, and no longer be counted as 1-release trials. These trials will be 2-release trials, removing them (when a vesicle is released in position 1) from the calculation of P_1. Thus, the P_1-train length curve will continually decay and reach zero after a time reflecting the recruitment rate. Such P_1-train length relations were indeed also found when examining synapses lacking initial release (**Figure 4**), or when starting the analysis after the depletion of the pre-primed pool (Hanse and Gustafsson, 2001d).

Consider instead a release location that contains a single vesicle at the onset of stimulation, and onto which there is no new recruitment. The P_1-train length curve, selecting only 1-release trials, will initially look the same as in the above

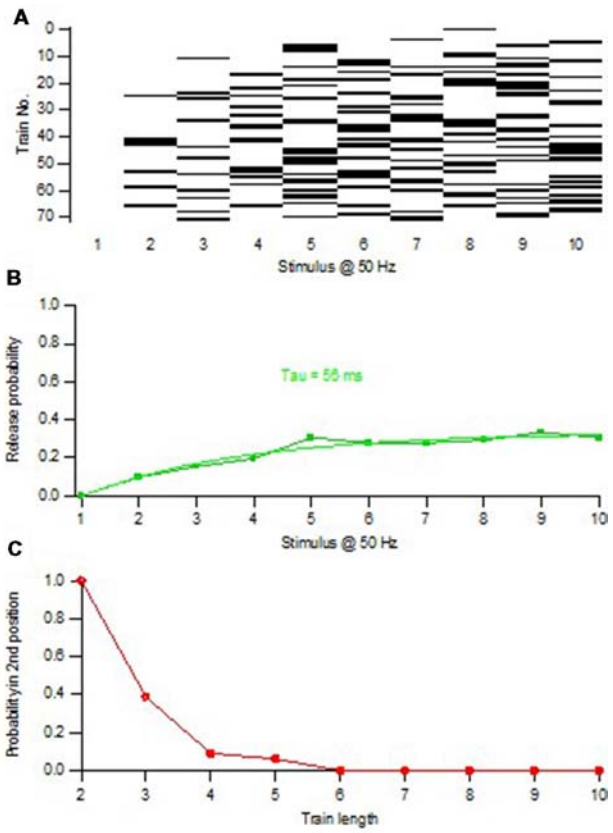

FIGURE 4 | Minimal train stimulation of a synapse lacking pre-primed pool. **(A)** Release pattern for one synaptic input repeatedly activated with a train consisting of 10 impulses at 50 Hz. Release is indicated with a black bar and failure is indicated by a white bar. Note the absence of release in the 1st position of the train. **(B)** Release probability plotted against the position in the stimulus train. The release probability curve is fitted with exponential function indicating a time constant of increased release probability of 56 ms. **(C)** Release probability in the 2nd position of the train as a function of train length (increasing from 2 to 10). Only trials that up to the train length had contained one release event were selected for the calculation of the release probability in the 2nd position. Note that this curve decays to zero within five stimuli showing that no 1-release trials remain after the 5th stimulus. Adapted from Hanse and Gustafsson (2001d).

example. However, at a train length corresponding to the maximum number of stimuli needed to release that vesicle, the curve will flatten out and reach a plateau level at a P_1 value that is equal to P_{ves1}. The reason for this plateau is that all trials will remain 1-release trials when train length becomes longer because there is no further release (due to lack of recruitment). If now recruitment is added to this release such that, as in the above scenario, trials in which the vesicle was released in position 1 will be the first to display a 2nd release event, the plateau will disappear and the curve decay to zero. If, on the other hand, the recruited vesicles are recruited/released at random with respect to the release of the 1st vesicle, 1-release trials used for the calculation of P_1 will disappear from the analysis regardless of the position in the train at which the 1st vesicle was released. The curve will thus flatten out and reach a plateau level at a P_1 value that is equal to P_{ves1}. Such P_1-train length relations with a plateau were indeed also invariably found when the synapses were examined starting from the 1st stimulus position in the train (**Figures 5B,C**).

The existence of such a plateau thus suggests that the pre-primed pool is a subpool separate from the recruited pool of vesicles, and that it should roughly correspond to the number of vesicles released before the plateau is reached. To further sharpen when during the train the pre-primed pool is used up, and the recruited pool has taken over, for each synapse the P_1-train length curve was also determined for 2-release trials. From the intersection of this curve with that obtained using 1-release trials, the position in the train at which a 2nd release event no longer affected P_1, i.e., no longer came from the pre-primed pool, could be determined (**Figure 5B**). The average pre-primed pool for a synapse was thereafter estimated as the cumulative release occurring prior to that position. Likewise, the pre-primed pool at each individual trial for a synapse was estimated as the number of release events in that trial occurring prior to that position (Hanse and Gustafsson, 2001b).

Trial-to-Trial Variation in Pre-primed Pool Size, and Pool Size Distribution

For any given synapse, the pre-primed pool was found to vary in size from trial to trial, mostly between zero and three. Thus, at some trials pre-primed vesicles were completely absent, the fraction of such trials varying between 10% and 50% among the synapses (see **Figure 5A**). Such a stochastic trial-to-trial variation in the number of vesicles released has also been noted by others (Trigo et al., 2012). To obtain a measure of the form of the pool size distribution, values from synapses of about equal average pre-primed pool size were compiled (Hanse and Gustafsson, 2001b). This procedure resulted in distributions that agreed with binomial ones with a probability of 0.3 of the primed state, independent of pre-primed pool size. This would suggest that the pre-primed pool is part of a three times larger pool (the pre-primed source pool) that in a dynamic fashion shapes the number of vesicles primed at stimulus onset. This partial priming of the pool is not a consequence of a very slow priming rate. In some experiments the trains were also evoked once every 30 s (instead of every 5 s; Hanse and Gustafsson, 2001d). This slowing

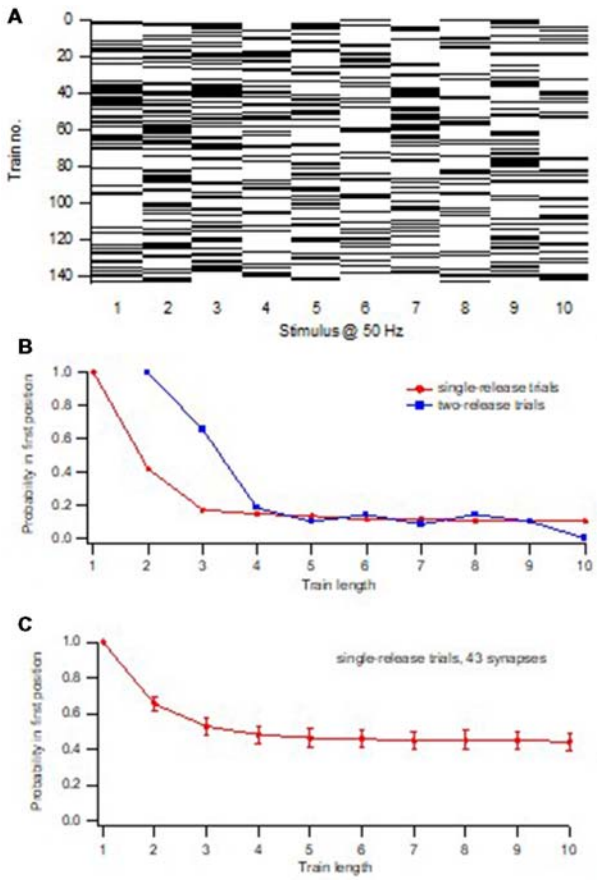

FIGURE 5 | Determination of the pre-primed pool and P_{ves1}. **(A)** Release pattern for one synaptic input repeatedly activated with a train consisting of 10 impulses at 50 Hz. Release is indicated with a black bar and failure is indicated by a white bar. **(B)** Release probability in 1st position of the train as a function of train length (increasing from 1 to 10). Red squares represent trials that up to the train length had only contained one release event, and those trials were selected for the calculation of the release probability in the 1st position. In other words, for each train-length x, all trials that contained a single release event in the first × positions were selected out from all trials in a given experiment, and P_1 was calculated. Note that this curve decays to a plateau within five stimuli indicating that no 1-release trials remain after the 5th stimulus. Blue squares represent trials that up to the train length had contained two release events, the second release event in the last position of the examined train length. **(C)** Summary graph of single release trials from 43 synaptic inputs. Adapted from Hanse and Gustafsson (2001d).

of repetition rate increased the pre-primed pool by only 15%, demonstrating that even at such slow stimulus rates most vesicles in the pool are not pre-primed at the arrival of an action potential. On the other hand, it also shows that the pre-priming rate is nevertheless quite slow, taking more than 5 s.

The P_{ves1} value for a synapse could thus be obtained from the P_1 value when only 1-release trials were used, and was found to vary among the synapses from <0.1 to almost 1.0, on average 0.43. Together with an average pre-primed pool of close to 1.0 (see below), the average P_1 should be ∼0.4, which agrees well with the average P_1 value of 0.42 for our synapse population (excluding synapses lacking initial release; Hanse and Gustafsson, 2001d). To examine this issue also

for the individual synapses, the estimated average pre-primed pool and P_{ves1} values were obtained for each synapse from the subgroups of 1- and 2-release trials, respectively. The pre-primed vesicles were then allowed to operate independently to cause the release of a single vesicle, according to the equation $P_1 = 1 - (1 - P_{ves})^{pool}$. The P_1 values calculated from these values of pre-primed pool and P_{ves1} were found to agree well with the experimentally obtained P_1 values observed using all the trials (Hanse and Gustafsson, 2001d).

Release Dependence Within a Paired Stimulus; Effect of a Dynamic Pre-primed Pool

The (average) pre-primed pool sizes estimated in the above manner varied among the synapses from 0.5 to 2.0 with a skew towards lower values, the average value among the synapses being 1.03 (Hanse and Gustafsson, 2001d). Such small pool values beg the question of how to explain the well-known fact for CA3–CA1 synapses that, using paired-pulse activation, the P_r to the 2nd stimulus (P_2) is the same whether or not there is release to the 1st stimulus ($P_{2\ release}/P_{2\ failure} \approx 1$; Stevens and Wang, 1994; Isaac et al., 1996; Hjelmstad et al., 1997; Hanse and Gustafsson, 2001c). Certainly, with such a small pool the release of 1 vesicle by the 1st action potential would be expected to affect P_2. However, simulating such release indicated, on average, little release dependence (Hanse and Gustafsson, 2002). This is because with a binomially distributed trial-to-trial variation in pool size, release in response to the 1st stimulus will preferentially occur on those trials in which more vesicles are primed, and *vice versa*. The number of pre-primed vesicles remaining for the 2nd stimulus can then be equal independent of whether release occurred, or not, in response to the 1st stimulus. Proper consideration of such a mechanism for release success or failure can be relevant for the interpretation of causes of paired-pulse plasticity (see "Discussion" section in Hanse and Gustafsson, 2002). Simulation also showed some deviation from a ratio of 1 depending on the value of P_1, the ratio being somewhat <1 at low P_1 and >1 at high P_1. Such deviation, which does not occur if multivesicular release is allowed in the simulations, was also observed for the experimentally observed values (Hanse and Gustafsson, 2002). It should be noted that a consequence of the dynamic pool is thus that the pre-primed pool size will actually appear to be reduced ("depleted") independently of whether release occurred, or not.

As will be discussed later in more detail (see "Multivesicular Release" section), other authors see the nanoassembly rather than the nanomodule as the quantal release site, implying several independent release sites within a nanomodule (Sakamoto et al., 2018). Since the number of release sites was found to be equal to the number of vesicles in the readily releasable pool, each of these release sites should at rest be fully occupied with a single vesicle. Following the release from such a site, this site will be replenished with a new vesicle which will subsequently be released. Such a release scenario is not consistent with our data. Thus, the P_1-train length relation will not display any plateau but decays to zero because of the cyclical manner of release (**Figure 4**). Moreover, release to the 1st stimulus will always be associated with a smaller P_2, i.e., ($P_{2\ release}/P_{2\ failure} < 1$). For example, in the case of a synapse with only a single release site, release to the 1st stimulus will always result in zero release to the 2nd stimulus.

P_{ves1},P_{ves} NORMALIZATION AND PAIRED-PULSE PLASTICITY

CA3–CA1 synapses activated at low frequency by single action potentials or by brief trains are very heterogeneous with respect to P_r and P_1, respectively, also in the neonatal rat. Note that while P_r and P_1 values both refer to release probabilities obtained in response to the 1st action potential following a period of rest, they may not be the exactly the same because of lingering effects of short-term plasticity. Nonetheless, both these release probabilities vary among the synapses from well below 0.1 to close to 1 with a distribution skewed towards the lower values (Dobrunz and Stevens, 1997; Hanse and Gustafsson, 2001d; Wasling et al., 2004). While the variation in P_r has generally been attributed to a variation in pool size among the synapses (Dobrunz and Stevens, 1997), our data suggested that a variation in P_{ves1} (<0.1–0.9) was an even more important factor for the P_1 heterogeneity. This dependence of P_1 on P_{ves1} is not in contrast to the previous notion of a dependence on pool size since no correlation was found between the size of the pre-primed pool and P_{ves1} (Hanse and Gustafsson, 2001d). Thus, the variation in P_{ves1} will not actually alter the overall effect of a variation in pool size on P_1.

Notably, this P_{ves} heterogeneity was only true with respect to the 1st stimulus in the train (P_{ves1}), the P_{ves} values computed for releases to the 2nd stimulus (P_{ves2}) displaying a much more narrow distribution (0.2–0.4; **Figure 6**) with no correlation between P_{ves1} and P_{ves2} (Hanse and Gustafsson, 2001a). For any

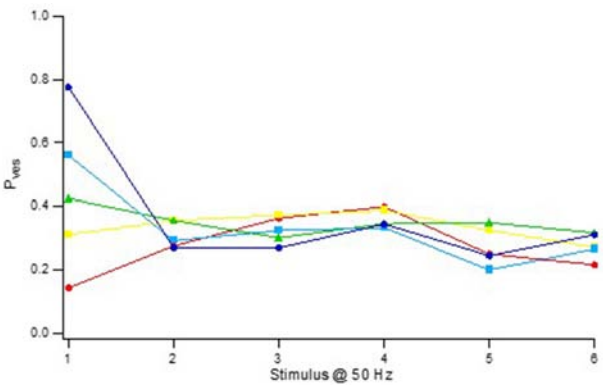

FIGURE 6 | Activity-dependent normalization of P_{ves}. Vesicle release probability (P_{ves}) as a function of stimulus position in a 50 Hz train. The synaptic inputs were divided into five groups according their P_{ves} in the 1st stimulus position. P_{ves} was calculated using the equation $P_{ves(n)} = 1 - (1 - P_{(n)})^{1/pool(n)}$, where $P_{(n)}$ is the release probability at stimulus position *n* and $pool_{(n)}$ is the size of the pre-primed pool at the nth stimulation. The pre-primed pool was estimated after subtraction of the average release probability curve for synapses lacking pre-primed pool ("Zero P_1" in **Figure 8C**). Adapted from Hanse and Gustafsson (2001a).

given synapse the P_{ves} value for later releases from the pre-primed pool stayed at the level of P_{ves2}. This P_{ves} normalization did not require release but was secondary to the action potential itself and/or its associated calcium influx.

Thus, during synaptic activity the P_{ves} heterogeneity among the synapses largely disappears, thereafter to become re-established by synaptic inactivity. This establishment of P_{ves1} heterogeneity by synaptic inactivity and its removal by activity makes many of the CA3–CA1 synapses rather unresponsive to sporadic arrivals of action potentials but more responsive after their arrivals, while other synapses are made very responsive to such arrivals but much less so thereafter. Since the P_{ves} normalization does not require release, high P_{ves1} and low P_{ves1} synapses are thus subjected to a release-independent depression and facilitation, respectively. The inactivity-induced establishment of P_{ves1} heterogeneity followed by a release-independent P_{ves} normalization is thus instrumental in producing the heterogeneity in facilitation/depression behavior among the synapses appearing during the first few stimuli (such as paired-pulse plasticity), and can be seen as a means to create differential dynamics within a synapse population.

A similar dissociation between a large heterogeneity in initial release and a more narrowly distributed later release has also been described in another well-studied synapse, the Calyx of Held synapse (Taschenberger et al., 2016). This behavior was interpreted by these authors as the presence in some proportion of the synapses of superprimed (high P_{ves}) vesicles. These vesicles will result in an initial high P_r, but they are rapidly used up, allowing vesicles with normal P_{ves} to decide later release. This interpretation does not agree with ours since what appears to be "superprimed" in the high P_r CA3–CA1 synapses is not the vesicle but the release location. Moreover, there should then not only be "superprimed" but also "subprimed" locations, creating high and low P_r synapses, respectively. Furthermore, while the superprimed state in Calyx of Held synapses is thought to disappear in a release-dependent fashion (depletion of the superprimed vesicles), the P_{ves} normalization occurs in a release-independent manner.

We have no explanation for the large P_{ves1} heterogeneity among the neonatal CA3–CA1 synapses. One factor that controls P_{ves} is the density of VGCCs contributing to the trigger calcium (Éltes et al., 2017). However, since a single action potential can switch P_{ves1} to a new value (P_{ves2}) that is completely unrelated to P_{ves1}, such a quantitative difference in VGCCs does not seem likely. Another important factor in deciding P_{ves} is the distance between the VGCCs and the vesicle calcium acceptor synaptotagmin-1. Should this distance exceed 100 nm, P_{ves} would be reduced to negligible levels (Nakamura et al., 2018). One may then speculate that during rest some synapses keep their docked/primed vesicles more distant from the VGCCs, this difference nullified by action potential-induced calcium entry. Finally, other important regulators of P_{ves} are the vesicle-related proteins Munc13–1 and Munc18 (Lai et al., 2017) and synaptotagmin-7 (Jackman et al., 2016). Since these proteins affect the energy barrier for fusion and can bind calcium, one can also envisage activity-dependent changes in their influence on P_{ves}.

MULTIVESICULAR RELEASE

Our analysis suggests that a single nanomodule, despite containing a number of docked vesicles and release locations, functions as a single release site releasing at most a single vesicle at the arrival of an action potential. As demonstrated a long time ago, release from a CA3–CA1 synapse is followed by a few ms of release refractoriness that may explain such univesicular release from a population of vesicles (Stevens and Wang, 1995; Dobrunz et al., 1997; Hjelmstad et al., 1997). While there is no existing explanation for such refractoriness, there are several manners in which such lateral inhibition of release following the exocytosis of one of the vesicles could occur (Nadkarni et al., 2010). Nonetheless, evidence for multivesicular release has been presented for a number of synapses, including the CA3–CA1 synapses (Oertner et al., 2002; Christie and Jahr, 2006; Ricci-Tersenghi et al., 2006), and the notion that each docking site is an independent release site is now considered the favored one (Rudolph et al., 2015; Pulido and Marty, 2017). However, even quite small synapses (active zone areas of 0.05–0.1 μm^2) may contain more than one nanomodule (Hruska et al., 2018), resulting in multivesicular release but from morphologically separate release regions (nanomodules) within an active zone, assuming that a possible lateral inhibition of release among the vesicles is restricted to vesicles within a nanomodule. On the other hand, should multivesicular release occur from a single nanomodule, there should be no lateral inhibition, and thus no release refractoriness. If such lack of refractoriness exists in such synapses remains to be demonstrated (Nadkarni et al., 2010). In addition, the time resolution in the method used to detect release must also be such that a 2nd release event is not explained by asynchronous release.

Nonetheless, a favored notion today is that release from an active zone is multivesicular (Rudolph et al., 2015; Pulido and Marty, 2017), and, importantly, that each docking site works as an independent release site. Recent evidence for this notion can be found in the study by Sakamoto et al. (2018) which combined examination of the release from individual hippocampal synapses using a glutamate imaging technique with studies of the nanoscale supramolecular organization of the active zone protein Munc13–1, thought to be important for vesicle priming. To estimate the number of independent release sites for the synapse examined, the authors used the multiple probability fluctuation analysis in which the variance of the synaptic response is estimated at various values of P_1 (Saviane and Silver, 2007) obtained e.g., by varying the extracellular Ca^{2+}/Mg^{2+} ratio. For the synapse population examined this estimated number of release sites was found to be correlated in an 1:1 relation with the number of Munc13–1 nanoassemblies, suggesting that a single such nanoassembly operates (together with some other active zone proteins) as an independent release site. Also the readily releasable pool of vesicles for each synapse was estimated, using the cumulative synaptic response curve given by brief high-frequency stimulation. This pool was also found to be correlated in a 1:1 relation to the number of release sites, indicating that, at rest, each release site (nanoassembly) is occupied by one vesicle each. These vesicles would then

constitute a readily releasable pool of vesicles that is depleted within a few high frequency stimuli. Release thereafter would come from the fast replenishment of these same release sites with vesicles docked/primed following the onset of stimulation.

While these results clearly appear to favor a release behavior quite distinct from that favored by our results, there are certain aspects that have to be considered. As noted above ("Release Dependence Within a Paired Stimulus; Effect of a Dynamic Pre-primed Pool" section), our results indicated a pre-primed pool that on average was close to 1 among the synapses. Thus, also a synapse that contains several nanomodules within an active zone, each nanomodule consisting of several nanoassemblies, would also on the average have an equal number of release sites and of readily releasable vesicles. In the Sakamoto et al.'s (2018) article there is no mention of either the active zone areas or the number of docked vesicles within these areas. Nonetheless, from their published records (see their Figure 4C), the active zones were at least 2–5 times larger than the 0.04 μm^2 area taken by us as the upper limit of a nanomodule. Thus, active zones of this size could at least explain the number of release sites (1–6) in the form of nanomodules found in the vast majority of the synapses examined by these authors.

The other aspect to be considered is the equal number of nanoassemblies and release sites reported in this article (Sakamoto et al., 2018), each nanoassembly believed to be occupied at rest by a docked/primed vesicle and serving as the quantal release site. However, no independent evidence for such a match between vesicle and nanoassembly number was provided. In fact, estimates of docked vesicle number in cultured hippocampal synapses (Schikorski and Stevens, 1997) would suggest a considerably higher number of such vesicles (for active zone areas comparable to those indicated in Figure 4C of Sakamoto et al., 2018) than the number of nanoassemblies reported by Sakamoto et al. (2018). The variation in size among the observed nanoassemblies (Figure 4C of Sakamoto et al., 2018) also begs the question of whether all of these represent discrete entities. In fact, in a similar recent study, using the *Drosophila* neuromuscular junction, release sites corresponding to a nanomodule in size appeared to contain several such assemblies (Reddy-Alla et al., 2017). Thus, while Sakamoto et al. (2018) make a rather strong case for multiple release sites within an active zone, they do not necessarily set aside our notion that a nanomodule, containing a number of docked vesicles and release locations, serves as the quantal release site.

Another form of experimental approach to demonstrate multivesicular release is the use of a weak AMPA receptor antagonist. Thus, when multivesicular release occurs, the glutamate concentration in the synaptic cleft will be higher and the weak antagonist will have less effect on the synaptic response. Using this technique onto third week hippocampal synapses, synaptic field responses evoked under conditions of high release probability (to increase the likelihood of multivesicular release) were found to be significantly less affected by such a receptor antagonist than responses observed under control conditions (Christie and Jahr, 2006). While such a result strongly suggests multivesicular release at those synapses, it does not necessarily invalidate our notion of nanomodule univesicular release. Postsynaptic subdomains of nanomodule dimensions, based on PSD-95, can be separated by less than about 200 nm (Fukata et al., 2013), and simulations have indicated that AMPA receptors can be activated from release locations several 100 nm away (Haas et al., 2018). Thus, one cannot exclude that glutamate released from one nanomodule may contribute to AMPA receptor activation at an adjacent nanomodule. Thus, we believe that a proper interpretation of studies using weak receptor antagonist has to await more knowledge regarding a possible cross-talk among the nanomodules within an active zone.

INITIAL VS. LATE RELEASE AND VESICLE RECRUITMENT

Our data suggest that the neonatal CA3–CA1 synapses have a pre-primed source pool that varies among the synapses from two to six vesicles, and which is responsible for the pre-primed pool (Hanse and Gustafsson, 2001d). The size of this source pool is thus in rough agreement with the number of docked vesicles and release locations in a nanomodule. The pre-primed pool averages one-third of the pre-primed source pool, but varies from trial to trial mostly from zero up to three vesicles (Hanse and Gustafsson, 2001b). During brief train stimulation only the pre-primed vesicles of that source pool can participate in the release (**Figure 1**). This is because, as indicated by the plateau phase of the P_1-train length curve, the vesicles released later in the train are released in a random manner with respect to those released from the pre-primed pool. They must therefore come from a separate pool of vesicles that are released at a separate set of release locations than those used by the pre-primed vesicles (**Figure 7**, green release locations). It may then be envisaged that the priming of the pre-primed source pool of vesicles (that occurs during rest and is slow) takes place at the actual release location and that the vesicles that are not in a primed state at stimulation onset hinder further release from these locations (release locations with black crosses in **Figure 7**). The vesicles released later in the train have then been recruited and primed ("post-primed") in an activity—dependent manner with a fast priming rate to the other set of locations (**Figure 7**, green release locations). If these recruited vesicles are docked prior to their priming, they would add a few additional docked vesicles/release locations to the 2–6 vesicles constituting the pre-primed source pool. It is tempting to associate the pre-primed source pool to the possible subgroup of release locations containing RIM1/2 nanoassemblies (Tang et al., 2016). Some support for this notion comes from experiments using RIM1α knock-outs in which the later release is left unaffected while the initial release is reduced (Calakos et al., 2004).

This distinction between a pre-primed source pool and a recruited pool deduced from the P_1-train length curves is also supported by the release behavior of some synapses that only show release to the first 2–3 stimuli of the train as well as of some synapses displaying no release until the 2nd or 3rd stimulus (Hanse and Gustafsson, 2001d), indicating an absence of a recruited and a pre-primed pool, respectively. Also synapses with a dip in the release at the 3rd–4th stimulus positions,

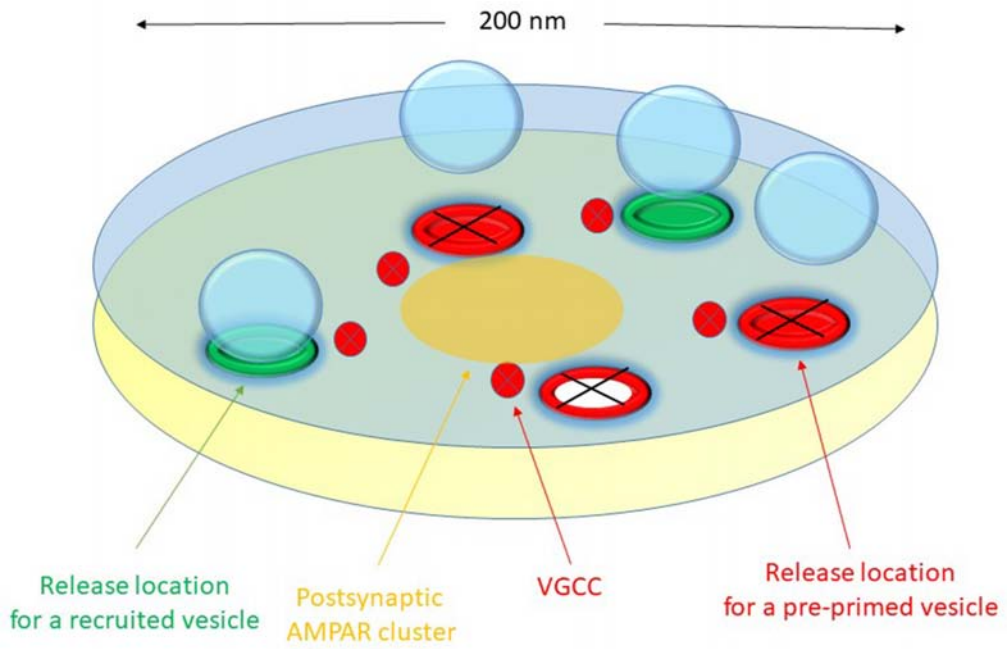

FIGURE 7 | Schematic drawing of a functional release site (nanomodule) during activity. The schematic release site contains five release locations. The three red release locations constitute the pre-primed source pool, responsible for phasic release. The two green release locations are for recruited vesicles, responsible for tonic release. During activity, priming and release occur at the release locations for recruited vesicles and the release locations for pre-primed vesicles do not contribute as indicated by black crosses. The red and white release location indicates recent exocytosis of a pre-primed vesicle. Voltage-gated calcium channels are indicated in the presynaptic membrane and a nanocluster of AMPA receptors are indicated in the postsynaptic membrane.

indicating a temporal separation between the releases from two distinct pools, were observed (Hanse and Gustafsson, 2001d). A further test of this two pool idea would have been to examine for each trial the correlation between release events belonging to the pre-primed and the recruited pool, respectively. That is, if the pools are distinct, the number of recruited release events should be the same whether a trial shows 2–3 pre-primed release events or no such events. Unfortunately, no such analysis was thought of at the time of the publication of our studies.

Another manner to demonstrate a difference between the pools would be to condition a 10-impulse train by either a brief train (such as a 3-impulse train that would release predominantly from the pre-primed pool) or by a 10-impulse tetanus producing release from both pools. In fact, such experiments have been done, showing that the brief train only reduces the initial part of the evoked response while the longer train affects also the later release (Andersson and Hanse, 2011).

Two Parallel Vesicle Pools in a Nanomodule for Initial (Phasic) and Later (Tonic) Release, Respectively

From the above it appears that the vesicles within a nanomodule can interact with two separate sets of release locations (**Figure 1**), possibly differing with respect to the type of molecules that constitutes the release location (see above). At one of these sets (**Figure 7**, green release locations), vesicles are released in a cyclical fashion, and the vesicles interacting with these release locations produce the later steady state, or "tonic," release during the stimulation train. These vesicles should not be able to become pre-primed, i.e., to be primed during inactivity. Instead they will become primed within 50–100 ms after onset of activity (post-primed) likely as a consequence of increased cytoplasmic Ca^{2+}. Whether these vesicles are docked prior to the onset of activity cannot be decided from our data. The P_{ves} of these vesicles is also unknown. While the P_{ves} of vesicles released from the pre-primed pool can be estimated to be ∼0.2–0.4 for stimulus positions beyond the first, it cannot be directly assumed that such P_{ves} values also hold true for this recruited pool of vesicles. However, considering that these vesicles are released in a cyclical manner, the main determinant of P_r in this part of the train would not be P_{ves}, but rather the recruitment to the release location, and the number of such locations within a nanomodule. At the other set of release locations (**Figure 7**, red release locations) the vesicles can become docked/primed during inactivity, i.e., become pre-primed, and following the onset of activity a given release location can only, at most, release one vesicle. Generally, only a subset of the vesicles in this pool is in a primed condition at the onset of activity, and the size of this subset varies from trial to trial. The vesicles interacting with these

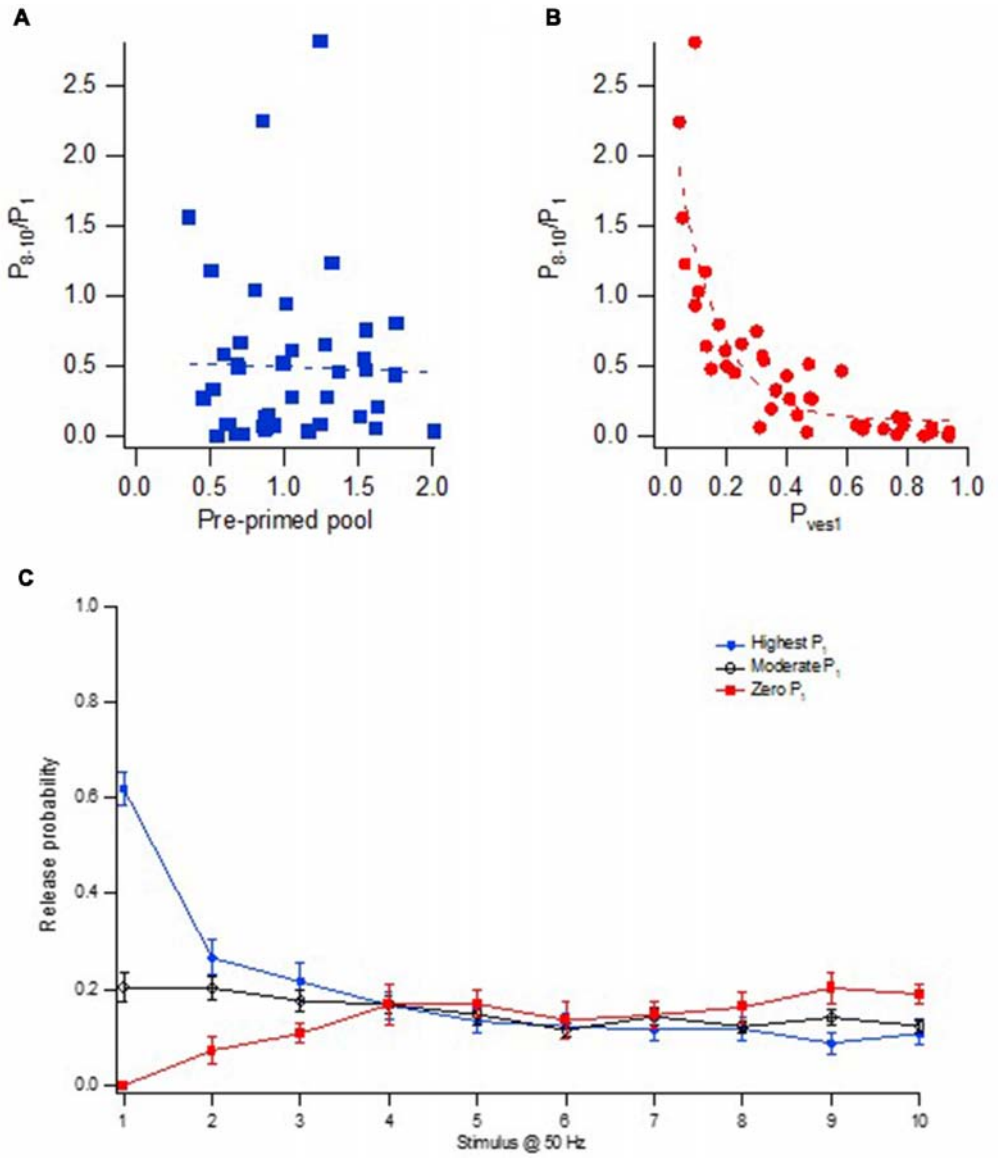

FIGURE 8 | Heterogeneity in frequency facilitation/depression among the synapses. **(A)** Relationship between facilitation/depression (P_{8-10}/P_1) and the size of the pre-primed pool for 43 synaptic inputs. **(B)** Relationship between facilitation/depression (P_{8-10}/P_1) and P_{ves1} for 43 synaptic inputs. **(C)** Release probability at each stimulus position in a 50 Hz train for three groups of synaptic inputs; High P_1 (n = 21, blue circles), moderate P_1 (n = 22, black open circles) and synaptic inputs with zero P_1 (n = 9, red squares). Adapted from Hanse and Gustafsson (2001a).

release locations thus produce the very initial ("phasic") release at the onset of activity.

When considering these vesicle pools to be in parallel, we do not suggest that vesicles in these two pools necessarily differ from each other. Instead, any given vesicle may enter either of these pools. It is not until it interacts with a release location that it enters into one of these pools. Thus, what may operate independently of (or parallel to) each other are the two sets of release locations, "phasic" and "tonic" ones, respectively. If such independence would be true, release from these locations would not only appear in isolation, as can be observed in some synapses, but also proceed in an additive manner when release from these locations may overlap temporally. That this may be the case is suggested by using the (average) release from synapses not displaying any initial release as a template for release from the "tonic" pool. Thus, subtraction of this template from the total release in synapses exhibiting initial release results in pre-primed pool values in good agreement with those obtained with the procedure described earlier (**Figure 5**; Hanse and Gustafsson, 2001d). On the other hand, as described earlier ("Determining the Pre-primed Pool" section), we observed that a 2nd release event that occurred within the first half of a 10-impulse train was associated with a P_1 value corresponding to that expected from two pre-primed vesicles. This result

would suggest that comparably few 2nd release events in the first half of the train came from the recruited pool, indicating a bias against the release of post-primed vesicles prior to the release from the pre-primed pool. However, we cannot exclude that this observation simply reflects the fact that the total release during a 10-impulse 50 Hz train is predominantly from the pre-primed pool (60%; Hanse and Gustafsson, 2001d), and that the 1st release from the recruited pool also for temporal reasons is more likely to be a 3rd than a 2nd release event.

Short-Term Synaptic Plasticity and Shift in Release Location

The short-term plasticity during brief train activation was in our studies quantified as the P_{8-10}/P_1 ratio, i.e., the ratio between the average release probability at stimulus position 8–10, and the release probability at the 1st stimulus position. This form of short-term plasticity (frequency facilitation/depression) was well correlated with P_{ves1} but not with pre-primed pool size (**Figure 8**). Important in shaping this short-term plasticity would be the form of correlations that exists between the factors that decide release from the "phasic" and "tonic" pools, respectively. Within a nanomodule there is a strong correlation between the number of docked vesicles and the nanomodule area, as judged from the data from more adult CA3–CA1 synapses (Schikorski and Stevens, 1997). If so, the variation in pre-primed pool size among the synapses is explained by variation in nanomodule area, and, likewise, also implies a correlated variation in the number of "tonic" release locations. Since both the "phasic" and "tonic" release then will co-vary with a variation in nanomodule size, this short-term plasticity will not depend on pre-primed pool size (**Figure 8A**) and thus not on nanomodule size. Instead, the variation in short-term plasticity among the synapses will be shaped by the correlation between P_{ves1} and recruitment per "tonic" release location. As a measure of recruitment per release location we used the P_{8-10} value divided by the pre-primed pool size (as an indicator of nanomodule area). Interestingly, these two parameters were found to be strongly negatively correlated among the synapses (Hanse and Gustafsson, 2001a), together producing the very large variation in facilitation/depression behavior among the synapses shown in **Figures 8A,B**.

In **Figure 8C** is plotted the release probability curves for three groups of synapses, those with high initial release probability (P_1), those with moderate initial release, and those without initial release, these groups of synapses exhibiting essentially the same absolute amount of late release. That is, on the average among the synapses, the late P_r is independent of the initial release. For the synapses exhibiting initial release, this independence from initial release is likely explained by the negative correlation between P_{ves1} and recruitment per "tonic" release location. Thus, the influence of a larger nanomodule area (and more release locations) on both P_1 and P_{8-10} will in itself result in both a higher late P_r and a higher P_1. However, synapses with high P_{ves1} will not only contribute to a high P_1 but also to a small late P_r (because of a low recruitment per release location), offsetting the effect of more "tonic" release locations in high P_1 synapses.

When it comes to the short-term synaptic plasticity that will be present when stimulation frequency is altered from the 50 Hz used in our study to lower frequencies such as 1 Hz and beyond, it becomes more difficult to delineate the manner in which the two sets of release locations will participate in release. This is because we still know too little about the kinetics of several of the involved processes, such as the reestablishment of P_{ves1} and of the pre-primed pool during inactivity. For example, if the P_{ves} heterogeneity should become re-established in parallel with the recovery of the pre-primed pool (>5 s), one might expect to see a quite prolonged paired-pulse depression as well as a frequency depression in the <1 Hz frequency range. Thus, with increased stimulation frequency and number of stimuli, release will increasingly shift from the "phasic" to the "tonic" pool. In fact, when studying synapses onto the distal dendritic tree in stratum lacunosum-moleculare (SLM) of the neonatal CA1 neurons (SLM—CA1 synapses), these synapses display such a depression (Ma et al., 2016), indicating that such a shift may occur. On the other hand, this form of plasticity was not observed for the synapses (neonatal CA3–CA1 synapses; Ma et al., 2016) from which our data are taken. A possible explanation could be that the manifestation of this plasticity depends upon the net effect on release of the P_{ves} normalization seen over a population of synapses. Thus, if the P_{ves} normalization results in a P_{ves2} that on average is greater than the average P_{ves1} for a synapse population, this will mask the depression. Further studies will obviously be needed to understand whether the depression observed in the SLM–CA1 synapses is actually explained by such a shift in release location and, if so, if the above explanation for its absence in the CA3–CA1 synapses holds true.

It can finally be noted that this concept of two separate sets of release locations for initial and later release is not a new one. In recent times, this concept has been suggested for neuromuscular synapses in zebra fish, although in this case a location within separate release sites rather than within a single release site was the preferred interpretation (Wen et al., 2016). Also, although discussed in terms of vesicles rather than of release locations, the parallel model with two populations involved in initial and later release, respectively, at the Calyx of Held synapses (Mahfooz et al., 2016; Taschenberger et al., 2016), quite resembles the release mechanism described here for the hippocampal synapses.

AUTHOR CONTRIBUTIONS

All authors took part in designing and writing the manuscript.

FUNDING

This project was supported by grants from the Swedish Medical Research Council (project numbers 05180 and 2016-00986), the Swedish Brain Foundation (F02017) and Alzheimerfonden (AF-640391).

ACKNOWLEDGMENTS

We thank My Forsberg, Henrik Seth and Mats Andersson for helpful comments on the manuscript.

REFERENCES

Andersson, M. S., and Hanse, E. (2011). Astrocyte-mediated short-term synaptic depression in the rat hippocampal CA1 area: two modes of decreasing release probability. *BMC Neurosci.* 12:87. doi: 10.1186/1471-2202-12-87

Biederer, T., Kaeser, P. S., and Blanpied, T. A. (2017). Transcellular nanoalignment of synaptic function. *Neuron* 96, 680–696. doi: 10.1016/j.neuron.2017.10.006

Calakos, N., Schoch, S., Südhof, T. C., and Malenka, R. C. (2004). Multiple roles for the active zone protein RIM1α in late stages of neurotransmitter release. *Neuron* 42, 889–896. doi: 10.1016/j.neuron.2004.05.014

Christie, J. M., and Jahr, C. E. (2006). Multivesicular release at Schaffer collateral-CA1 hippocampal synapses. *J. Neurosci.* 26, 210–216. doi: 10.1523/JNEUROSCI.4307-05.2006

Dobrunz, L. E., Huang, E. P., and Stevens, C. F. (1997). Very short-term plasticity in hippocampal synapses. *Proc. Natl. Acad. Sci. U S A* 94, 14843–14847. doi: 10.1073/pnas.94.26.14843

Dobrunz, L. E., and Stevens, C. F. (1997). Heterogeneity of release probability, facilitation, and depletion at central synapses. *Neuron* 18, 995–1008. doi: 10.1016/s0896-6273(00)80338-4

Éltes, T., Kirizs, T., Nusser, Z., and Holderith, N. (2017). Target cell type-dependent differences in Ca^{2+} channel function underlie distinct release probabilities at hippocampal glutamatergic terminals. *J. Neurosci.* 37, 1910–1924. doi: 10.1523/JNEUROSCI.2024-16.2017

Fiala, J. C., Feinberg, M., Popov, V., and Harris, K. M. (1998). Synaptogenesis via dendritic filopodia in developing hippocampal area CA1. *J. Neurosci.* 18, 8900–8911. doi: 10.1523/JNEUROSCI.18-21-08900.1998

Franks, K. M., Stevens, C. F., and Sejnowski, T. J. (2003). Independent sources of quantal variability at single glutamatergic synapses. *J. Neurosci.* 23, 3186–3195. doi: 10.1523/JNEUROSCI.23-08-03186.2003

Fukata, Y., Dimitrov, A., Boncompain, G., Vielemeyer, O., Perez, F., and Fukata, M. (2013). Local palmitoylation cycles define activity-regulated postsynaptic subdomains. *J. Cell Biol.* 202, 145–161. doi: 10.1083/jcb.201302071

Grabner, C. P., and Moser, T. (2018). Individual synaptic vesicles mediate stimulated exocytosis from cochlear inner hair cells. *Proc. Natl. Acad. Sci. U S A* 115, 12811–12816. doi: 10.1073/pnas.1811814115

Groc, L., Gustafsson, B., and Hanse, E. (2002). Spontaneous unitary synaptic activity in CA1 pyramidal neurons during early postnatal development: constant contribution of AMPA and NMDA receptors. *J. Neurosci.* 22, 5552–5562. doi: 10.1523/JNEUROSCI.22-13-05552.2002

Haas, K. T., Compans, B., Letellier, M., Bartol, T. M., Grillo-Bosch, D., Sejnowski, T. J., et al. (2018). Pre-post synaptic alignment through neuroligin-1 tunes synaptic transmission efficiency. *Elife* 7:e31755. doi: 10.7554/eLife.31755

Hanse, E., and Gustafsson, B. (2001a). Factors explaining heterogeneity in short-term synaptic dynamics of hippocampal glutamatergic synapses in the neonatal rat. *J. Physiol.* 537, 141–149. doi: 10.1111/j.1469-7793.2001.0141k.x

Hanse, E., and Gustafsson, B. (2001b). Paired-pulse plasticity at the single release site level: an experimental and computational study. *J. Neurosci.* 21, 8362–8369. doi: 10.1523/JNEUROSCI.21-21-08362.2001

Hanse, E., and Gustafsson, B. (2001c). Quantal variability at glutamatergic synapses in area CA1 of the rat neonatal hippocampus. *J. Physiol.* 531, 467–480. doi: 10.1111/j.1469-7793.2001.0467i.x

Hanse, E., and Gustafsson, B. (2001d). Vesicle release probability and pre-primed pool at glutamatergic synapses in area CA1 of the rat neonatal hippocampus. *J. Physiol.* 531, 481–493. doi: 10.1111/j.1469-7793.2001.0481i.x

Hanse, E., and Gustafsson, B. (2002). Release dependence to a paired stimulus at a synaptic release site with a small variable pool of immediately releasable vesicles. *J. Neurosci.* 22, 4381–4387. doi: 10.1523/JNEUROSCI.22-11-04381.2002

Hjelmstad, G. O., Nicoll, R. A., and Malenka, R. C. (1997). Synaptic refractory period provides a measure of probability of release in the hippocampus. *Neuron* 19, 1309–1318. doi: 10.1016/s0896-6273(00)80421-3

Hruska, M., Henderson, N., Le Marchand, S. J., Jafri, H., and Dalva, M. B. (2018). Synaptic nanomodules underlie the organization and plasticity of spine synapses. *Nat. Neurosci.* 21, 671–682. doi: 10.1038/s41593-018-0138-9

Hsia, A. Y., Malenka, R. C., and Nicoll, R. A. (1998). Development of excitatory circuitry in the hippocampus. *J. Neurophysiol.* 79, 2013–2024. doi: 10.1152/jn.1998.79.4.2013

Isaac, J. T., Hjelmstad, G. O., Nicoll, R. A., and Malenka, R. C. (1996). Long-term potentiation at single fiber inputs to hippocampal CA1 pyramidal cells. *Proc. Natl. Acad. Sci. U S A* 93, 8710–8715. doi: 10.1073/pnas.93.16.8710

Jackman, S. L., Turecek, J., Belinsky, J. E., and Regehr, W. G. (2016). The calcium sensor synaptotagmin 7 is required for synaptic facilitation. *Nature* 529, 88–91. doi: 10.1038/nature16507

Lai, Y., Choi, U. B., Leitz, J., Rhee, H. J., Lee, C., Altas, B., et al. (2017). Molecular mechanisms of synaptic vesicle priming by Munc13 and Munc18. *Neuron* 95, 591.e10–607.e10. doi: 10.1016/j.neuron.2017.07.004

Lisman, J., and Raghavachari, S. (2006). A unified model of the presynaptic and postsynaptic changes during LTP at CA1 synapses. *Sci. STKE* 2006:re11. doi: 10.1126/stke.3562006re11

Liu, G., Choi, S., and Tsien, R. W. (1999). Variability of neurotransmitter concentration and nonsaturation of postsynaptic AMPA receptors at synapses in hippocampal cultures and slices. *Neuron* 22, 395–409. doi: 10.1016/s0896-6273(00)81099-5

Ma, R., Xiao, M., and Gustafsson, B. (2016). Labile glutamate signaling onto CA1 pyramidal cells in the developing hippocampus depends mechanistically on input pathway. *Neuroscience* 337, 27–36. doi: 10.1016/j.neuroscience.2016.09.008

MacGillavry, H. D., Song, Y., Raghavachari, S., and Blanpied, T. A. (2013). Nanoscale scaffolding domains within the postsynaptic density concentrate synaptic AMPA receptors. *Neuron* 78, 615–622. doi: 10.1016/j.neuron.2013.03.009

Mahfooz, K., Singh, M., Renden, R., and Wesseling, J. F. (2016). A well-defined readily releasable pool with fixed capacity for storing vesicles at calyx of held. *PLoS Comput. Biol.* 12:e1004855. doi: 10.1371/journal.pcbi.1004855

Maschi, D., and Klyachko, V. A. (2017). Spatiotemporal regulation of synaptic vesicle fusion sites in central synapses. *Neuron* 94, 65.e3–73.e3. doi: 10.1016/j.neuron.2017.03.006

McAllister, A. K., and Stevens, C. F. (2000). Nonsaturation of AMPA and NMDA receptors at hippocampal synapses. *Proc. Natl. Acad. Sci. U S A* 97, 6173–6178. doi: 10.1073/pnas.100126497

Nadkarni, S., Bartol, T. M., Sejnowski, T. J., and Levine, H. (2010). Modelling vesicular release at hippocampal synapses. *PLoS Comput. Biol.* 6:e1000983. doi: 10.1371/journal.pcbi.1000983

Nakamura, Y., Harada, H., Kamasawa, N., Matsui, K., Rothman, J. S., Shigemoto, R., et al. (2015). Nanoscale distribution of presynaptic Ca^{2+} channels and its impact on vesicular release during development. *Neuron* 85, 145–158. doi: 10.1016/j.neuron.2014.11.019

Nakamura, Y., Reva, M., and Digregorio, D. A. (2018). Variations in Ca^{2+} influx can alter chelator-based estimates of Ca^{2+} channel-synaptic vesicle coupling distance. *J. Neurosci.* 38, 3971–3987. doi: 10.1523/JNEUROSCI.2061-17.2018

Neher, E. (2015). Merits and limitations of vesicle pool models in view of heterogeneous populations of synaptic vesicles. *Neuron* 87, 1131–1142. doi: 10.1016/j.neuron.2015.08.038

Oertner, T. G., Sabatini, B. L., Nimchinsky, E. A., and Svoboda, K. (2002). Facilitation at single synapses probed with optical quantal analysis. *Nat. Neurosci.* 5, 657–664. doi: 10.1038/nn867

Pulido, C., and Marty, A. (2017). Quantal fluctuations in central mammalian synapses: functional role of vesicular docking sites. *Physiol. Rev.* 97, 1403–1430. doi: 10.1152/physrev.00032.2016

Raastad, M., Storm, J. F., and Andersen, P. (1992). Putative single quantum and single fibre excitatory postsynaptic currents show similar amplitude range and variability in rat hippocampal slices. *Eur. J. Neurosci.* 4, 113–117. doi: 10.1111/j.1460-9568.1992.tb00114.x

Reddy-Alla, S., Bohme, M. A., Reynolds, E., Beis, C., Grasskamp, A. T., Mampell, M. M., et al. (2017). Stable positioning of Unc13 restricts synaptic vesicle fusion to defined release sites to promote synchronous neurotransmission. *Neuron* 95, 1350.e12–1364.e12. doi: 10.1016/j.neuron.2017.08.016

Ricci-Tersenghi, F., Minneci, F., Sola, E., Cherubini, E., and Maggi, L. (2006). Multivesicular release at developing Schaffer collateral-CA1 synapses: an analytic approach to describe experimental data. *J. Neurophysiol.* 96, 15–26. doi: 10.1152/jn.01202.2005

Rudolph, S., Tsai, M. C., von Gersdorff, H., and Wadiche, J. I. (2015). The ubiquitous nature of multivesicular release. *Trends Neurosci.* 38, 428–438. doi: 10.1016/j.tins.2015.05.008

Sakamoto, H., Ariyoshi, T., Kimpara, N., Sugao, K., Taiko, I., Takikawa, K., et al. (2018). Synaptic weight set by Munc13–1 supramolecular assemblies. *Nat. Neurosci.* 21, 41–49. doi: 10.1038/s41593-017-0041-9

Saviane, C., and Silver, R. A. (2007). Estimation of quantal parameters with multiple-probability fluctuation analysis. *Methods Mol. Biol.* 403, 303–317. doi: 10.1007/978-1-59745-529-9_19

Schikorski, T., and Stevens, C. F. (1997). Quantitative ultrastructural analysis of hippocampal excitatory synapses. *J. Neurosci.* 17, 5858–5867. doi: 10.1523/JNEUROSCI.17-15-05858.1997

Scimemi, A., and Diamond, J. S. (2012). The number and organization of Ca^{2+} channels in the active zone shapes neurotransmitter release from Schaffer collateral synapses. *J. Neurosci.* 32, 18157–18176. doi: 10.1523/JNEUROSCI.3827-12.2012

Stevens, C. F., and Wang, Y. (1994). Changes in reliability of synaptic function as a mechanism for plasticity. *Nature* 371, 704–707. doi: 10.1038/371704a0

Stevens, C. F., and Wang, Y. (1995). Facilitation and depression at single central synapses. *Neuron* 14, 795–802. doi: 10.1016/0896-6273(95)90223-6

Sulzer, D., and Edwards, R. (2000). Vesicles: equal in neurotransmitter concentration but not in volume. *Neuron* 28, 5–7. doi: 10.1016/S0896-6273(00)00077-5

Tang, A. H., Chen, H., Li, T. P., Metzbower, S. R., MacGillavry, H. D., and Blanpied, T. A. (2016). A trans-synaptic nanocolumn aligns neurotransmitter release to receptors. *Nature* 536, 210–214. doi: 10.1038/nature19058

Taschenberger, H., Woehler, A., and Neher, E. (2016). Superpriming of synaptic vesicles as a common basis for intersynapse variability and modulation of synaptic strength. *Proc. Natl. Acad. Sci. U S A* 113, E4548–E4557. doi: 10.1073/pnas.1606383113

Trigo, F. F., Sakaba, T., Ogden, D., and Marty, A. (2012). Readily releasable pool of synaptic vesicles measured at single synaptic contacts. *Proc. Natl. Acad. Sci. U S A* 109, 18138–18143. doi: 10.1073/pnas.1209798109

Wasling, P., Hanse, E., and Gustafsson, B. (2004). Developmental changes in release properties of the CA3-CA1 glutamate synapse in rat hippocampus. *J. Neurophysiol.* 92, 2714–2724. doi: 10.1152/jn.00464.2004

Wen, H., McGinley, M. J., Mandel, G., and Brehm, P. (2016). Nonequivalent release sites govern synaptic depression. *Proc. Natl. Acad. Sci. U S A* 113, E378–E386. doi: 10.1073/pnas.1523671113

Wu, X. S., Xue, L., Mohan, R., Paradiso, K., Gillis, K. D., and Wu, L. G. (2007). The origin of quantal size variation: vesicular glutamate concentration plays a significant role. *J. Neurosci.* 27, 3046–3056. doi: 10.1523/JNEUROSCI.4415-06.2007

Conflict of Interest Statement: The authors declare that the research was conducted in the absence of any commercial or financial relationships that could be construed as a potential conflict of interest.

frontiers in Synaptic Neuroscience

METHODS
published: 26 March 2019
doi: 10.3389/fnsyn.2019.00008

Optical Quantal Analysis

*Matthew J. MacDougall and Alan Fine**

Department of Physiology and Biophysics, Faculty of Medicine, Dalhousie University, Halifax, NS, Canada

Understanding the mechanisms by which long-term synaptic plasticity is expressed remains an important objective in neuroscience. From a physiological perspective, the strength of a synapse can be considered a consequence of several parameters including the probability that a presynaptic action potential (AP) evokes the release of neurotransmitter, the mean number of quanta of transmitter released when release is evoked, and the mean amplitude of a postsynaptic response to a single quantum. Various methods have been employed to estimate these quantal parameters from electrophysiological recordings; such "quantal analysis" has been used to support competing accounts of mechanisms of expression of long-term plasticity. Because electrophysiological recordings, even with minimal presynaptic stimulation, can reflect responses arising at multiple synaptic sites, these methods are open to alternative interpretations. By combining intracellular electrical recording with optical detection of transmission at individual synapses, however, it is possible to eliminate such ambiguity. Here, we describe methods for such combined optical and electrical monitoring of synaptic transmission in brain slice preparations and illustrate how quantal analyses thereby obtained permit more definitive conclusions about the physiological changes that underlie long-term synaptic plasticity.

Keywords: synaptic plasticity, synaptic potency, synaptic reliability, LTP (long-term potentiation), two photon microscopy

OPEN ACCESS

Edited by:
Dirk Feldmeyer, Forschungszentrum Jülich (HZ), Germany

Reviewed by:
Christian Wozny, University of Strathclyde, United Kingdom
Stefan Hallermann, Leipzig University, Germany
Dmitri A. Rusakov, University College London, United Kingdom

***Correspondence:**
Alan Fine
a.fine@dal.ca

Received: *16 November 2018*
Accepted: *05 March 2019*
Published: *26 March 2019*

Citation:
MacDougall MJ and Fine A (2019) Optical Quantal Analysis. Front. Synaptic Neurosci. 11:8. doi: 10.3389/fnsyn.2019.00008

INTRODUCTION

Physiological and anatomical characterization of synapses provides ongoing and central challenges to neuroscience. Paramount among these challenges is clarification of the mechanisms that govern activity-dependent changes in synaptic strength, such as long-term potentiation (LTP; Bliss and Lømo, 1973; Bliss and Gardner-Medwin, 1973) and long-term depression (LTD; Dudek and Bear, 1992), the purported cellular basis of learning and memory, continues to be an essential objective. While the *induction* of LTP at CA3-CA1 synapses is generally agreed to be chiefly a postsynaptic phenomenon, controversy remains with respect to the locus and nature of changes responsible for the *expression* of LTP at these synapses (Bliss and Collingridge, 2013; Granger and Nicoll, 2014; MacDougall and Fine, 2014; see Bear and Abraham, 1996; Collingridge et al., 2010 for reviews on LTD). Here, we present a brief summary of advances in the understanding of this issue, followed by a description of optical quantal analysis, a powerful method employed by our laboratory to investigate unitary synaptic function.

Classical Quantal Analysis

The pioneering work of Fatt and Katz (1952) and Del Castillo and Katz (1954) demonstrated that the release of transmitter substances occur in multi-molecular packets, now known

to be synaptic vesicles (Gray, 1959), at the frog neuromuscular junction. According to this model, the smallest electrical response at a synapse results from the release of a single vesicle or quantum of transmitter (Del Castillo and Katz, 1954; Boyd and Martin, 1956). Postsynaptic responses to evoked neurotransmitter release are therefore said to be quantal in nature; i.e., they reflect the summation of a number of discrete events due to the exocytosis of vesicular contents of neurotransmitter. Quantal analysis is a statistical procedure used to isolate the mechanistic components of synaptic transmission and their modifications (Del Castillo and Katz, 1954; Boyd and Martin, 1956). Attempts to assess the role of changes in these components in synaptic plasticity *via* quantal analysis of electrophysiological recordings of CA1 hippocampal synapses before and after induction of plasticity have been inconclusive (Voronin, 1994), with competing accounts supporting pre- (Voronin, 1983; Bekkers and Stevens, 1990; Larkman et al., 1991; Malinow, 1991; Tsien and Malinow, 1991; Voronin et al., 1992), post- (Foster and McNaughton, 1991; Isaac et al., 1996a,b), and in some instances a combination of pre- and postsynaptic components of plasticity expression (Kullmann and Nicoll, 1992; Larkman et al., 1992). All such attempts, however, have been susceptible to alternative interpretations and have been at the center of a continuing "locus debate" in LTP research (Nicoll, 2003; Kerchner and Nicoll, 2008; MacDougall and Fine, 2014). The sources of divergence may include differences in tissue preparation and times of analysis, but criticisms have largely focused on the heterogeneity of central synapses, the uncertain applicability of theoretical assumptions, and the fact that postsynaptic responses, even with minimal presynaptic stimulation, result from an unknown number of activated synapses, all of which complicate conclusions about unitary responses (Redman, 1990; Faber and Korn, 1991; Korn and Faber, 1991; Walmsley, 1995).

Fluorescence Microscopy and Dendritic Spines

The long-term visualization of individual dendritic spines using confocal fluorescence microscopy before and after LTP (Hosokawa et al., 1995) as well as the visualization of dendritic and spine Ca^{2+} signals (Connor et al., 1994; Malinow et al., 1994; Yuste and Denk, 1995; Emptage et al., 1999; Mainen et al., 1999; Yuste et al., 1999; Kovalchuk et al., 2000; Reid et al., 2001; Sabatini et al., 2002) during synaptic stimulation have greatly influenced the field of synaptic plasticity and have become indispensable techniques used to probe synaptic function. These technological and analytical developments, coupled with the statistical approach of classical quantal analysis, opened the possibility of optical quantal analysis of LTP at individual hippocampal synapses (Emptage et al., 2003).

Optical Quantal Analysis

Optical quantal analysis combines classical electrophysiological recording with optical monitoring of fluorescent Ca^{2+} indicators in dendritic spines. Optical detection of synaptically-evoked postsynaptic Ca^{2+} transients [EPSCaTs (pronounced epps'kats); Malinow et al., 1994; Yuste and Denk, 1995; Emptage et al., 1999] has given researchers a means to overcome many of the analytical and interpretational difficulties associated with classical quantal analysis. EPSCaTs in CA1 pyramidal cells are triggered by small synaptically-evoked Ca^{2+} influx through NMDA receptors, amplified by Ca^{2+}-induced Ca^{2+} release (CICR) from internal stores (Emptage et al., 1999) and display stochastic failures (Yuste and Denk, 1995; Emptage et al., 1999) corresponding to the statistical nature of transmitter release. Postsynaptic EPSCaT detection thus serves as a readout of presynaptic transmitter release from the directly apposed synaptic bouton. Here we review technical aspects of the procedure including simultaneous electrophysiological and optical recording, explain statistical aspects of their conjoint analysis, and illustrate some important conclusions thereby obtained.

MATERIALS AND METHODS

Hippocampal Slices

Transverse 350 μm slices of hippocampus, which retain much of the functional and structural integrity of the original tissue, are cut from 2 to 3-week-old male Wistar rats, according to standard protocols (e.g., Skrede and Westgaard, 1971; Geiger et al., 2002; Bischofberger et al., 2006; see Aitken et al., 1995 for discussion). We dissect hippocampal tissue in ice-cold sucrose-based cutting solution containing (in mM): 105 Sucrose, 50 NaCl, 1.25 NaH_2PO_4, 2.5 KCl, 26 $NaHCO_3$, 13 Glucose, 0.5 $CaCl_2$, 7 $MgCl_2$. Dissected hippocampi are then laid out in an agar block perpendicular to the cutting blade, and slices cut perpendicular to the longitudinal axis of the hippocampus using a vibrating tissue slicer (Leica VT1200, Leica Biosystems, Nussloch). Slices are then transferred to a custom interface chamber with supporting mesh and allowed to recover for 30–60 min at 32–33°C while oxygenated with 95% O_2/5% CO_2. Under these conditions, the slices remain viable for up 8 h. Alternatively, organotypic hippocampal slice cultures may be cut from 7 to 21 day-old male Wistar rat pups according to published methods (Yamamoto et al., 1989; Stoppini et al., 1991), placed on Millicell CM inserts (Millipore, Bedford, MA, USA) with media replaced every 2–3 days, and maintained for 1–3 weeks *in vitro* prior to recording. For recording, acute slices or organotypic slice cultures on their supporting membranes are transferred to a specially designed chamber where they are continually superfused (∼2 ml/min) with oxygenated (95% O_2/5% CO_2) artificial cerebrospinal fluid (ACSF) containing (in mM): 120 NaCl, 3 KCl, 1 $MgCl_2$, 2–3 $CaCl_2$, 1.2 NaH_2PO_4, 23 $NaHCO_3$, 11 glucose. ACSF should be maintained at near physiological temperatures (32–33°C) using a temperature control unit throughout the duration of experiments. Both methods of tissue preparation have been shown to yield similar physiological synaptic properties, with organotypic slices displaying greater connectivity (De Simoni et al., 2003), including aberrant recurrent connections.

Microscopy

Slices are viewed through an upright microscope (e.g., Olympus BX51W1) equipped with a high numerical aperture water immersion objective (e.g., Olympus 60×, N.A. 0.9)

via a confocal laser scan head (MRC1024MP, Bio-Rad Microsciences). Two-photon excitation is achieved using an ultrafast (100 fs pulses) Ti:Sapphire laser (Mai Tai, Spectra Physics: 3 W; 80 MHz). Emitted fluorescence is detected with a photomultiplier tube (PMT; H7422P-40 Hamamatsu) connected to a signal amplifier. If detection at an additional wavelength is required, a dichroic mirror is used to direct one waveband to a second PMT. Care should be taken when selecting fluorophores, to ensure that the emission spectra are non-overlapping. Two-photon excitation fluorescence images ("xy" and "xt" images) are acquired at 810 nm excitation and 15–20 mW average laser power in the focal plane, using LaserSharp software with 6× digital zoom. The microscope is also equipped with ordinary transmitted light and widefield fluorescence illuminators, digital camera, remotely controlled stage and micromanipulators, and temperature control units (**Figure 1**).

Electrophysiological and Optical Recording

For electrophysiological recording, sharp microelectrodes minimize undesirable diffusion of cytoplasmic constituents out of, and micropipette solution into, the target neuron (Malinow and Tsien, 1990; Enoki and Fine, 2005). A disadvantage of sharp microelectrode recordings is that a small but persistent non-selective leak conductance may occur around the site of impalement; if patch-clamp recordings are required, perforated patch configuration (Lindau and Fernandez, 1986; Horn and Marty, 1988) is preferable, to minimize perturbation of the intracellular milieu. Selected pyramidal cells in the CA1 region of the hippocampus are impaled with sharp glass microelectrodes (80–120 MΩ) under widefield illumination and visual control *via* a digital camera. Microelectrodes are filled with a fluorescent Ca^{2+} probe (e.g., 0.5–1 mM Oregon Green 488 BAPTA-1 in H_2O), optionally also with spectrally-distinct Ca^{2+}-insensitive fluorophore (e.g., Alexa 594; Goldberg and Yuste, 2005) to serve as a morphological marker, and backfilled with 3 M KCl. Ionophoretic loading of cells is achieved by delivering low frequency (2 Hz) hyperpolarizing current pulses (∼100–200 pA) *via* the intracellular amplifier (e.g., Multiclamp 700B, Molecular Devices, San Jose, CA, USA). After 5–20 min of loading, fluorescence in the soma and processes can be easily visualized (**Figure 2A**).

Dye loading of the target cell can be followed by two-photon excitation imaging using the lowest possible power. Once sufficient loading is achieved, hyperpolarizing pulses are discontinued; note that leakage from the pipette tip may contribute to additional loading over time. To assess the adequacy of loading, an action potential (AP) is evoked by depolarizing current injection, and corresponding fluorescent Ca^{2+} responses examined in the soma and proximal dendrites. As a useful guide, for adequate detection of EPSCaTs in dendritic spines, it should generally be the case that back-propagating APs cause a fractional change ($\%\Delta F/F$) >80% in Ca^{2+} probe fluorescence in the spines.

The extracellular stimulating electrode (SE), a sharpened, insulated, tungsten electrode (or theta-glass micropipette backfilled with 1 mM NaCl for minimal stimulation; Enoki et al., 2009), is placed in the stratum radiatum (sr) at distances not less than 50 μm (but <500 μm) from the soma, at a depth similar to the target dendrite and typically 50–200 μm from the border of the stratum pyramidale (**Figure 2A**). The extracellular stimulating pulses are increased to an intensity sufficient to elicit an AP-evoked Ca^{2+} transient in the soma and dendrites and then decreased by 50%–70% to a level at which subthreshold excitatory postsynaptic potentials (EPSPs) are reliably evoked.

Optically Searching for EPSCaTs

Pairs or triplets of extracellular stimuli (each 100–300 μs square pulses of intensity described above) separated by 70 ms are delivered to the tissue preparation and maintained at a constant level throughout the searching procedure. Multiple stimuli are used to increase the likelihood of finding low p_r synapses. The proximal region of the secondary and tertiary apical dendrites of the dye-filled CA1 pyramidal neuron is then systematically searched using fast raster scanning (e.g., 128 × 128 pixels), while simultaneously stimulating at a low frequency (∼0.05–0.1 Hz), until a spine exhibiting an EPSCaT is located (**Figure 2B**). Low stimulation frequencies are maintained during the searching procedure to prevent unintended plasticity induction. When optically searching the dendritic branches it is important to follow a consistent strategy to avoid unintentionally neglecting or re-searching branches. A strategy widely used in our lab is the "wall follower" (right or left-hand rule). Given the remote positioning of the SE relative to the apical branches, the location of responsive spines and the time needed to find them can be highly variable; spines positioned proximally, however, tend to be more easily found than those at more distal locations. With this in mind, searching for responsive spines should take no longer than 45 min per cell, and if no responsive spine can be found within that time the cell is abandoned; another cell, far enough away to minimize overlap of its dendritic arbor with that of the previous cell, is impaled and filled, and the search for a responsive spine is repeated.

Once a responsive spine has been identified, line scanning ("xt" images, **Figure 2C**) can be used to image with better temporal resolution in order to record EPSCaTs with greater fidelity. Line scans ranging from 100 to 200 successive sweeps at 2 ms intervals are obtained along a line passing through the center of the activated spine (**Figure 2B**) and subjacent parent dendrite. It is important to minimize the duration and intensity of target irradiation to reduce phototoxicity and indicator bleaching. A scan rotator (Scientific Systems Design, Mississauga, ON, Canada) can be used to orient the scan trajectory, and an LED near the photodetector can be used to insert into the xt image a precise optical marker of onset of electrical stimulation (**Figure 2C**). The stimulating intensity is continually decreased until the threshold for EPSCaT detection is established; once established, the stimulating intensity is then incrementally increased for the experiment to a level (approximately 20% above this threshold) that minimizes the likelihood of stimulation failures of the afferent fibers (see "Conclusions and Perspective" section).

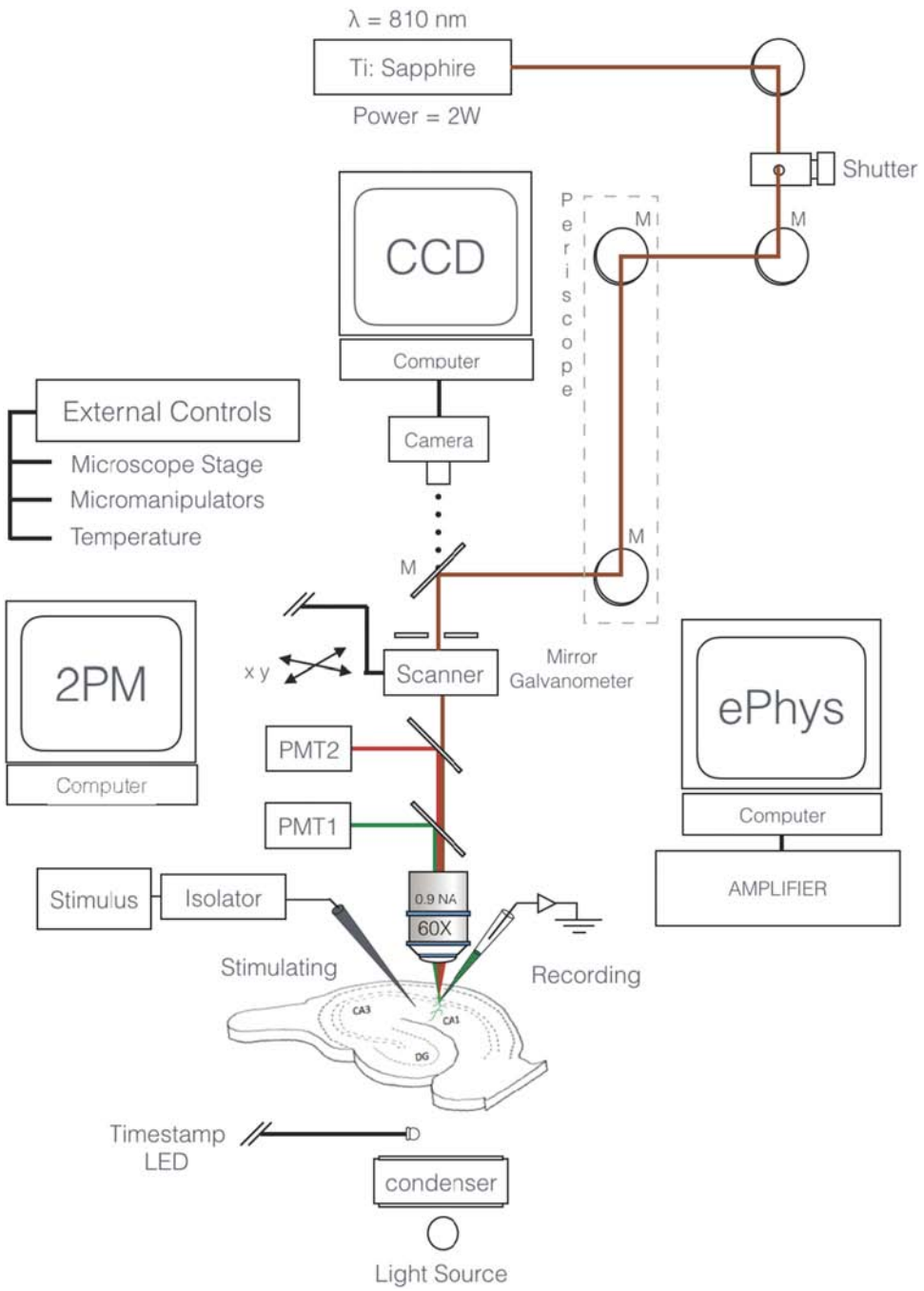

FIGURE 1 | Schematic of two-photon excitation microscopy imaging and recording configuration. Excitation beam (red) is focused by a 60×, NA 0.9 objective to a diffraction limited spot that excites the fluorescent intracellular calcium indicator (e.g., Oregon Green 488 BAPTA-1). The target neuron's membrane potential is constantly monitored through a somatic microelectrode. Excitation of inputs to the cell is achieved *via* a remote extracellular stimulating electrode (SE). Fluorescence is detected by a photomultiplier tube (PMT). A second fluorophore and secondary detector (PMT2 and dichroic) can be employed depending on the experiment. External control units for the micromanipulators, stage, and temperature are necessary components.

Estimating Release Probability

We (Emptage et al., 1999) and others (Yuste and Denk, 1995; Yuste et al., 1999) have provided evidence that the probability of a presynaptic stimulus evoking an EPSCaT in a postsynaptic spine (p_{Ca}) is equivalent to p_r, the probability that the stimulus evoked transmitter release from the unlabeled, and thus invisible, presynaptic bouton. A useful estimate of p_r (a measure of the "reliability" of the synapse) can therefore be achieved by delivering a sufficient number of stimuli (∼20–25 trials) to afferent fibers while recording EPSPs and EPSCaTs from the

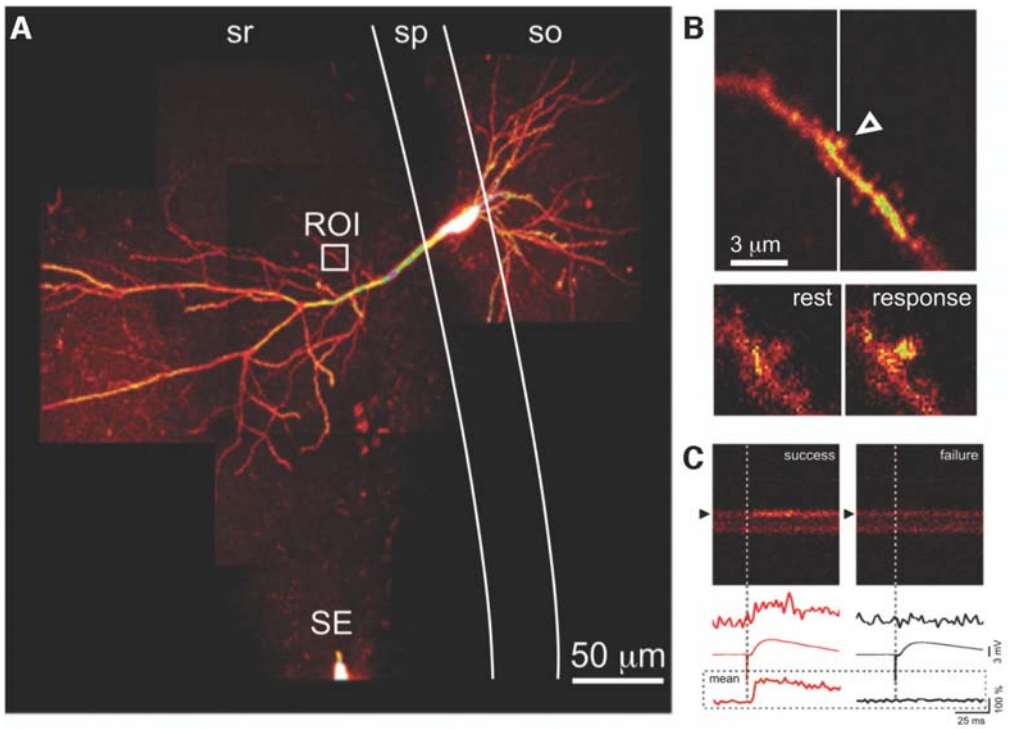

FIGURE 2 | Optical detection of synaptic transmission. **(A)** CA1 pyramidal neuron, filled with fluorescent Ca^{2+} indicator. Presynaptic axons are activated by a SE in stratum radiatum (sr); evoked excitatory postsynaptic potentials (EPSPs) are recorded *via* a somatic microelectrode (not visible). Fluorescence changes due to calcium transients evoked by the same stimulus in an apical dendritic segment (region of interest indicated by the white box) are seen at higher magnification in **(B)**. **(B)** Evoked postsynaptic calcium transients (EPSCaTs) are restricted to an individual dendritic spine (arrowhead), seen below at higher magnification in video frames at rest (bottom left) and immediately after synaptic activation (bottom right). **(C)** EPSCaTs monitored *via* line-scan (x-t) imaging across the spine (black arrowhead) and adjacent dendritic shaft. Successful synaptic transmission (left), visible as a fluorescence increase, can be clearly distinguished from transmission failure (right). EPSPs during transmission failure at this synapse are due to successful transmission at some of the other synapses activated by the same extracellular stimulus. Traces show (top to bottom) single-trial fluorescence from the spine, averaged EPSP, and averaged fluorescence from the spine, during success (red, left) and failure (black, right). sp, stratum pyramidale; so, stratum oriens. Figure adapted from Enoki et al. (2009).

postsynaptic neuron. A failure method can be used, whereby p_r is related to the number of successes within a sample of trials assessed over a given period of time:

$$p_r = N_{\text{success}}/N_{\text{trials}}$$

where N_{success} is the number of successful transmission events over N_{trials}, the total number of trials.

The Ca^{2+} transient amplitude is usefully expressed as

$$\%\Delta F/F = 100\left(F_{\text{transient}} - F_{\text{background}}\right) / \left(F_{\text{initial}} - F_{\text{background}}\right)$$

where F_{initial} is the mean fluorescence intensity of the imaged spine over a 20–40 ms time window prior to stimulation, $F_{\text{transient}}$ is the mean fluorescence intensity after stimulation, and $F_{\text{background}}$ is the mean intensity in regions devoid of labeled structures. To improve the signal-to-noise ratio, $F_{\text{transient}}$ is measured over a 10–30 ms window encompassing the peak of the Ca^{2+} transient (Enoki et al., 2009). Using this approach, an event may be counted as a success if the EPSCaT amplitude exceeds the unstimulated noise amplitude, a threshold that is typically $\%\Delta F/F > 20\%$. Once sufficient recordings of EPSCaTs and EPSPs have been obtained, yielding a stable ratio of successes to failures, long-term synaptic plasticity may be induced using any of several available protocols. Importantly, we select spines with baseline p_r neither too high (<0.7) nor too low (>0.3) to avoid ceiling or floor effects that could mask the outcome of the chosen plasticity protocol.

Modifications of Synaptic Efficacy

Various protocols can be used to induce long-term changes in synaptic efficacy. LTP may be induced using a spike-timing dependent plasticity (STDP; Song et al., 2000) protocol, wherein postsynaptic spiking is evoked shortly after a presynaptic stimulus (Markram et al., 1997; Bi and Poo, 1998; Nevian and Sakmann, 2006). Specifically, each EPSP is followed by (Δt = ~10–50 ms) the delivery of three pulses (at 100 Hz) of 2–10 ms postsynaptic depolarization (amplitude sufficient to evoke at least one AP), with 100 repetitions of this pairing at 0.33 Hz. LTD can also be induced with an STDP protocol, involving repetitive delivery of a postsynaptic AP preceding a single presynaptic stimulus (Feldman, 2012). Alternatively, a high-frequency stimulation (HFS) protocol may be used to induce LTP, where three bursts, at 1.5 s intervals, of 20 presynaptic pulses @ 100 Hz (with, if needed,

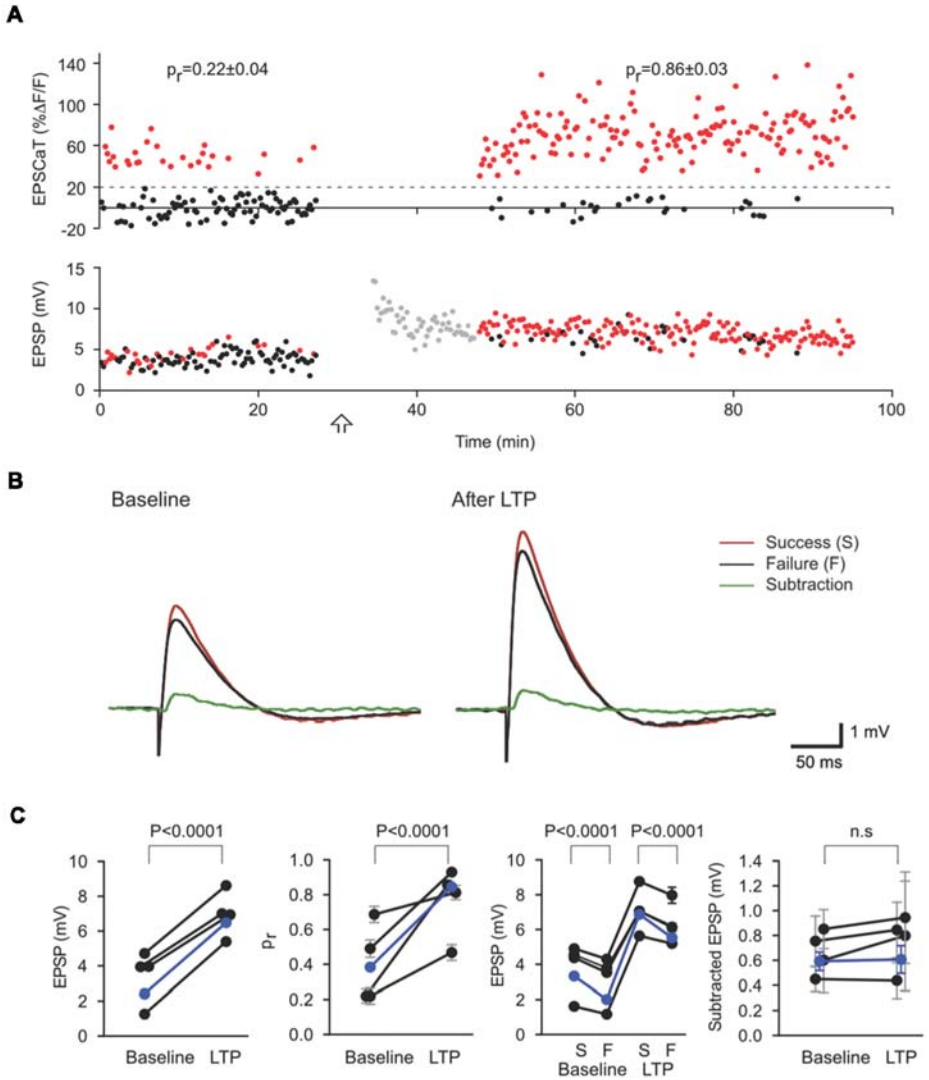

FIGURE 3 | Subtractive analysis of unitary EPSP as an estimate of quantal size. **(A)** EPSCaT amplitudes (above) and EPSP amplitudes (below) recorded before and after long-term potentiation (LTP) induction. Corresponding EPSP and EPSCaT amplitudes are color-coded on the basis of EPSCaTs, with successes in red and failures in black. **(B)** Mean EPSP traces corresponding to EPSCaT successes (red) and failures (black). The difference between these averages (Subtraction, green) represents the mean contribution to the EPSP (i.e., the unitary EPSP) from the imaged active synapse. Traces shown are means before (Baseline; left) and 20–60 min after (right) LTP induction. LTP results in large increases in the overall mean EPSP and *pr* at the imaged synapse. The unitary EPSP amplitude from this imaged synapse, however, does not significantly change. **(C)** Values of compound EPSP, *pr*, EPSPs grouped according to success (S) or failure (F), and unitary EPSP amplitude from the imaged synapse. As revealed by such subtractive analysis, LTP induction in these experiments led to significant and corresponding increases in *pr* at the imaged synapse and in the (multi-synaptic) EPSP, with no significant change in the unitary EPSP from the imaged synapse. Figure adapted from Enoki et al. (2009).

sufficient simultaneous postsynaptic depolarization such that at least some of the presynaptic stimuli evoke APs (Emptage et al., 2003; Enoki et al., 2009); conversely, a low-frequency stimulation (LFS; e.g., 1 Hz) protocol may be used to induce LTD. It should be borne in mind that distinct mechanistic processes may result from different patterns of neuronal activity (Padamsey and Emptage, 2014).

Re-evaluating Release Probability

Once the induction protocol is finished, p_r can be reassessed at desired time points using procedures outlined above (see "Estimating Release Probability" section). Statistical comparisons between initial p_r and post-plasticity p_r are made off-line using appropriate statistics. Using these experimental procedures, our results have consistently indicated that long-term synaptic plasticity in non-silent synapses involves changes in p_r. The precise molecular processes governing such changes and the contribution of altered modes of vesicular fusion (Choi et al., 2003) remain important unsettled questions even under these experimental circumstances. Furthermore, the presence of changes in p_r does not in itself establish the relative contribution of other possible mechanisms, such as

alterations in quantal amplitude q, to changes in the compound EPSP amplitude.

Estimating Synaptic Potency

Electrical recording by itself has proven inadequate to resolve unambiguously the magnitude of the evoked response from an individual synapse (sometimes called the "potency" of the synapse) that contributes to a compound EPSP. Conjoint EPSCaT recording, however, permits a subtractive analysis that can effectively address the ambiguity. On average, compound EPSP amplitudes are larger in trials where the imaged synapse releases transmitter than in those where the imaged synapse fails; indeed, subtracting the mean EPSP in failure trials from the mean EPSP in successes yields an estimate of the mean unitary EPSP from the EPSCaT-generating synapse (**Figures 3A,B**):

$$\overline{\mathrm{EPSP}}_{\mathrm{success}} - \overline{\mathrm{EPSP}}_{\mathrm{failure}} = \overline{\mathrm{EPSP}}_{\mathrm{unitary}}$$

With adequate sample sizes, this procedure can provide a reliable estimate of the mean unitary amplitude of the evoked response at the imaged synapse, and its potential modifications. Using this subtractive analysis, we have demonstrated that LTP at mature CA3-CA1 synapses is associated with increases in synaptic reliability (i.e., in p_r) while changes in potency (i.e., in $\overline{\mathrm{EPSP}}_{\mathrm{unitary}}$) are negligible (Enoki et al., 2009; **Figure 3C**).

Optically Confirmed Minimal Stimulation

The above conclusion is supported by other methods also enabled by conjoint optical and electrical recording. As noted previously, minimal presynaptic axon stimulation procedures (Raastad, 1995) suffer from ambiguity as to the actual number of synapses activated (Dobrunz and Stevens, 1997), as even single CA3 axons may make multiple contacts with a single CA1 neuron (Sorra and Harris, 1993). By combining optical quantal analysis with minimal presynaptic stimulation, however, such ambiguity can be eliminated, permitting a direct comparison of the contributions of p_r and unitary EPSP amplitude: in those cases where only the imaged synapse is being activated, there will be perfect correspondence between EPSCaTs and EPSPs for both successes and failures (**Figures 4A,B**). In all such cases, LTP-inducing stimuli increased p_r but had no effect on the amplitude of unitary EPSPs (**Figure 4C**; Enoki et al., 2009). These optical quantal analyses provide strong evidence that LTP at CA3-CA1 synapses is expressed chiefly through an increase in synaptic reliability, i.e., through an increase in p_r. We note, however, that these experiments have been mainly restricted to synapses on proximal dendrites, and to effects on transmission at low frequencies, so that the generality of these results, even for this class of synapse, remains to be established.

CONCLUSIONS AND PERSPECTIVE

Here we have outlined the procedures necessary to carry out optical quantal analyses at individual synapses within hippocampal slice preparations, and have summarized results on the mode of expression of LTP obtained by these methods.

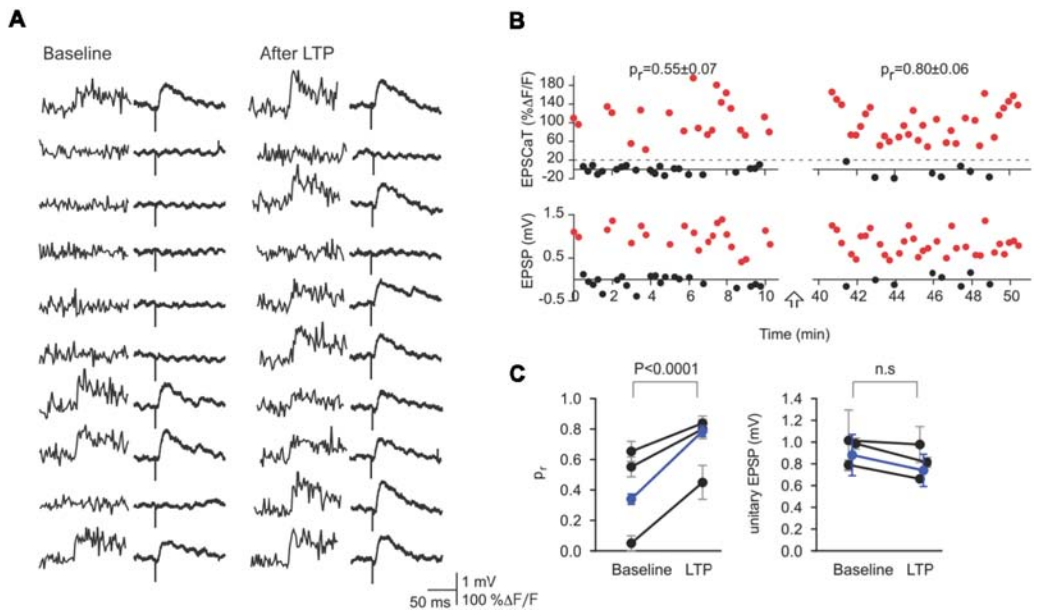

FIGURE 4 | Minimal stimulation and optical quantal analysis. **(A)** Representative sequential traces showing the perfect correspondence between success or failure of EPSCaTs (left) and EPSPs (right) before (Baseline) and After LTP. This constant correspondence provides strong evidence that the stimulus in this experiment activated only the imaged synapse and that EPSCaTs are reliable reporters of transmitter release. **(B)** EPSCaT (above) and EPSP amplitudes (below) recorded from this synapse before and after LTP induction. LTP induction increased *pr* but not the unitary EPSP amplitude. **(C)** Values of *pr* (left) and unitary EPSP (right) from the imaged synapse for this and two other experiments (black) are shown before and after LTP (weighted means shown in blue). Such optically confirmed minimal stimulation demonstrates that LTP induction leads to significant increases in *pr*, with no significant change in unitary EPSP amplitude. Figure adapted from Enoki et al. (2009).

Despite the distinct advantages of optical over traditional electrophysiological quantal analyses, several items must be kept in mind in interpreting such experiments. Buffering of intracellular Ca^{2+} by Ca^{2+} indicators could in principle interfere with calcium-dependent postsynaptic aspects of LTP expression, though this is unlikely given that the magnitude of LTP is unaltered by indicator loading (Enoki et al., 2009). Selection of spines for analysis may exclude small spines beyond the limit of optical resolution, or spines with small EPSCaTs (e.g., less mature spines lacking endoplasmic reticulum; Spacek and Harris, 1997). Observed spines, however, appear to account for the majority of the evoked response (Enoki et al., 2009). Additionally, although our extracellular stimulation protocols reliably induced APs, we have not excluded the possibility that some EPSCaT failures reflect factors other than p_r, e.g., failure of APs to reach the terminal, or stochasticity of Ca^{2+} store release, though this seems unlikely given that the probability of evoking EPSCaTs is influenced by the same factors that influence p_r. Thus, notwithstanding the experimental constraints that limit trial numbers and thus the precision of p_r determination, our estimates of p_r using the procedures described here have been reliably and predictably influenced by manipulations known to alter vesicular release (Emptage et al., 1999; Reid et al., 2001). Moreover, the fact that increasing stimulus intensity does not alter our estimate of p_r (Emptage et al., 1999) provides a compelling argument against the spurious effects of axon excitability.

Controversies remain regarding possible roles of changes in the number of transmitter release sites (Walmsley et al., 1987) and alteration in the amount of transmitter released per quantum (Choi et al., 2003; Midorikawa and Sakaba, 2017) in the expression of LTP and LTD (see MacDougall and Fine, 2014) for a unified model and more extensive discussion). Unfortunately, because CICR from internal stores contributes significantly and nonlinearly to the EPSCaT (Emptage et al., 1999), fluctuations in EPSCaT amplitude cannot resolve these controversies.

Although we have described this technique specifically in area CA1 of the hippocampus, optical quantal analysis can be carried out at other synapses (Reid et al., 2004; Chalifoux and Carter, 2010) and in other preparations (Sinnen et al., 2016) and model organisms (Newman et al., 2017). Importantly, this method can be adapted for *in vivo* investigations and functional mapping of cortical (Svoboda et al., 1997; Chen et al., 2011; Wilson et al., 2016; Scholl et al., 2017) and subcortical tissue, including the hippocampus (Mizrahi et al., 2004; Gu et al., 2014). Such applications have been facilitated by ongoing improvements in the useful depth of multiphoton excitation fluorescence microscopy (Theer et al., 2003; Kobat et al., 2009, 2011; Horton et al., 2013), adaptive micro-optics (Andermann et al., 2013; Velasco and Levene, 2014), genetically encoded voltage, Ca^{2+}, and other optogenetic sensors (Akerboom et al., 2013; Storace et al., 2016; Yang and St-Pierre, 2016) and two-photon microendoscopy (Jung and Schnitzer, 2003; Bocarsly et al., 2015; Sato et al., 2017; Ohayon et al., 2018). At the same time, rapidly advancing developments in optical sensors for the detection of neurotransmitters, including but not limited to glutamate (Marvin et al., 2013; Helassa et al., 2018) and GABA (Masharina et al., 2012), provide exciting complementary strategies for optical quantal analyses both in organized tissue preparations (Borghuis et al., 2013; Jensen et al., 2017) and *in vivo* applications (Helassa et al., 2018). We expect that the wide applicability and power of optical quantal analysis will lead to its increasing use to reveal the mechanisms of synaptic transmission and their modifications in learning and other phenomena.

AUTHOR CONTRIBUTIONS

Both authors wrote the manuscript together.

REFERENCES

Aitken, P. G., Breese, G. R., Dudek, F. F., Edwards, F., Espanol, M. T., Larkman, P. M., et al. (1995). Preparative methods for brain slices: a discussion. *J. Neurosci. Methods* 59, 139–149. doi: 10.1016/0165-0270(94)00204-t

Akerboom, J., Calderon Carreras, N., Tian, L., Wabnig, S., Prigge, M., Tolo, J., et al. (2013). Genetically encoded calcium indicators for multi-color neural activity imaging and combination with optogenetics. *Front. Mol. Neurosci.* 6:2. doi: 10.3389/fnmol.2013.00002

Andermann, M. L., Gilfoy, N. B., Goldey, G. J., Sachdev, R. N., Wolfel, M., McCormick, D. A., et al. (2013). Chronic cellular imaging of entire cortical columns in awake mice using microprisms. *Neuron* 80, 900–913. doi: 10.1016/j.neuron.2013.07.052

Bear, M. F., and Abraham, W. C. (1996). Long-term depression in hippocampus. *Annu. Rev. Neurosci.* 19, 437–462. doi: 10.1146/annurev.neuro.19.1.437

Bekkers, J. M., and Stevens, C. F. (1990). Presynaptic mechanism for long-term potentiation in the hippocampus. *Nature* 346, 724–729. doi: 10.1038/346724a0

Bi, G. Q., and Poo, M. M. (1998). Synaptic modifications in cultured hippocampal neurons: dependence on spike timing, synaptic strength, and postsynaptic cell type. *J. Neurosci.* 18, 10464–10472. doi: 10.1523/jneurosci.18-24-10464.1998

Bischofberger, J., Engel, D., Li, L., Geiger, J. R., and Jonas, P. (2006). Patch-clamp recording from mossy fiber terminals in hippocampal slices. *Nat. Protoc.* 1, 2075–2081. doi: 10.1038/nprot.2006.312

Bliss, T. V., and Collingridge, G. L. (2013). Expression of NMDA receptor-dependent LTP in the hippocampus: bridging the divide. *Mol. Brain* 6:5. doi: 10.1186/1756-6606-6-5

Bliss, T. V., and Gardner-Medwin, A. R. (1973). Long-lasting potentiation of synaptic transmission in the dentate area of the unanaesthetized rabbit following stimulation of the perforant path. *J. Physiol.* 232, 357–374. doi: 10.1113/jphysiol.1973.sp010274

Bliss, T. V., and Lømo, T. (1973). Long-lasting potentiation of synaptic transmission in the dentate area of the anaesthetized rabbit following stimulation of the perforant path. *J. Physiol.* 232, 331–356. doi: 10.1113/jphysiol.1973.sp010273

Bocarsly, M. E., Jiang, W. C., Wang, C., Dudman, J. T., Ji, N., and Aponte, Y. (2015). Minimally invasive microendoscopy system for *in vivo* functional imaging of deep nuclei in the mouse brain. *Biomed. Opt. Express* 6, 4546–4556. doi: 10.1364/boe.6.004546

Borghuis, B. G., Marvin, S. J., Looger, L. L., and Demb, J. B. (2013). Two-photon imaging of nonlinear gltamate release dynamics at bipolar cell synapses in the mouse retina. *J. Neurosci.* 33, 10972–10985. doi: 10.1523/jneurosci.1241-13.2013

Boyd, I. A., and Martin, A. R. (1956). The end-plate potential in mammalian muscle. *J. Physiol.* 132, 74–91. doi: 10.1113/jphysiol.1956.sp005503

Chalifoux, J. R., and Carter, A. G. (2010). $GABA_B$ receptors modulate NMDA receptor calcium signals in dendritic spines. *Neuron* 66, 101–113. doi: 10.1016/j.neuron.2010.03.012

Chen, X., Leischner, U., Rochefort, N. L., Nelken, I., and Konnerth, A. (2011). Functional mapping of single spines in cortical neurons *in vivo*. *Nature* 475, 501–505. doi: 10.1038/nature10193

Choi, S., Klingauf, J., and Tsien, R. W. (2003). Fusion pore modulation as a presynaptic mechanism contributing to expression of long-term potentiation. *Philos. Trans. R. Soc. Lond. B Biol. Sci.* 358, 695–705. doi: 10.1098/rstb.2002.1249

Collingridge, G. L., Peineau, S., Howland, J. G., and Wang, Y. T. (2010). Long-term depression in the CNS. *Nat. Rev. Neurosci.* 11, 459–473. doi: 10.1038/nrn2867

Connor, J. A., Miller, L. D., Petrozzino, J., and Muller, W. (1994). Calcium signaling in dendritic spines of hippocampal neurons. *J. Neurobiol.* 25, 234–242. doi: 10.1002/neu.480250304

De Simoni, A., Griesinger, C. B., and Edwards, F. A. (2003). Development of rat CA1 neurones in acute versus organotypic slices: role of experience in synaptic morphology and activity. *J. Physiol.* 550, 135–147. doi: 10.1113/jphysiol.2003.039099

Del Castillo, J., and Katz, B. (1954). Quantal components of the end-plate potential. *J. Physiol.* 124, 560–573. doi: 10.1113/jphysiol.1954.sp005129

Dobrunz, L. E., and Stevens, C. F. (1997). Heterogeneity of release probability, facilitation and depletion at central synapses. *Neuron* 18, 995–1008. doi: 10.1016/s0896-6273(00)80338-4

Dudek, S. M., and Bear, M. F. (1992). Homosynaptic long-term depression in area CA1 of hippocampus and effects of N-methyl-D-aspartate receptor blockade. *Proc. Natl. Acad. Sci. U S A* 89, 4363–4367. doi: 10.1073/pnas.89.10.4363

Emptage, N. J., Reid, C. A., Fine, A., and Bliss, T. V. P. (2003). Optical quantal analysis reveals a presynaptic component of LTP at hippocampal Schaffer-associational synapses. *Neuron* 38, 797–804. doi: 10.1016/s0896-6273(03)00325-8

Emptage, N., Bliss, T. V., and Fine, A. (1999). Single synaptic events evoke NMDA receptor-mediated release of calcium from internal stores in hippocampal dendritic spines. *Neuron* 22, 115–124. doi: 10.1016/s0896-6273(00)80683-2

Enoki, R., and Fine, A. (2005). *Ryanodine Receptors and Internal Stores Are the Source of Synaptic Calcium Transients in Dendritic Spines But are Inactivated by Patch Recording*. Washington, DC: Society for Neuroscience.

Enoki, R., Hu, Y. L., Hamilton, D., and Fine, A. (2009). Expression of long-term plasticity at individual synapses in hippocampus is graded, bidirectional, and mainly presynaptic: optical quantal analysis. *Neuron* 62, 242–253. doi: 10.1016/j.neuron.2009.02.026

Faber, D. S., and Korn, H. (1991). Applicability of the coefficient of variation method for analyzing synaptic plasticity. *Biophys. J.* 60, 1288–1294. doi: 10.1016/s0006-3495(91)82162-2

Fatt, P., and Katz, B. (1952). Spontaneous subthreshold activity at motor nerve endings. *J. Physiol.* 117, 109–128.

Feldman, D. E. (2012). The spike-timing dependence of plasticity. *Neuron* 75, 556–571. doi: 10.1016/j.neuron.2012.08.001

Foster, T. C., and McNaughton, B. L. (1991). Long-term enhancement of CA1 synaptic transmission is due to increased quantal size, not quantal content. *Hippocampus* 1, 79–91. doi: 10.1002/hipo.450010108

Geiger, J. R., Bischofberger, J., Vida, I., Frobe, U., Pfitzinger, S., Weber, H. J., et al. (2002). Patch-clamp recording in brain slices with improved slicer technology. *Pflugers Arch.* 443, 491–501. doi: 10.1007/s00424-001-0735-3

Granger, A. J., and Nicoll, R. A. (2014). Expression mechanisms underlying long-term potentiation: a postsynaptic view, 10 years on. *Philos. Trans. R. Soc. Lond. B Biol. Sci.* 369:20130136. doi: 10.1098/rstb.2013.0136

Gray, E. G. (1959). Electron microscopy of synaptic contacts on dendrite spines of the cerebral cortex. *Nature* 183, 1592–1593. doi: 10.1038/1831592a0

Gu, L., Kleiber, S., Schmid, L., Nebeling, F., Chamoun, M., Steffen, J., et al. (2014). Long-term *in vivo* imaging of dendritic spines in the hippocampus reveals structural plasticity. *J. Neurosci.* 34, 13948–13953. doi: 10.1523/jneurosci.1464-14.2014

Goldberg, J., and Yuste, R. (2005). "A practical guide: Two-photon calcium imaging of spines and dendrites," in *Imaging in Neuroscience and Development: a Laboratory Manual*, eds R. Yuste and A. Konnerth (Cold Spring Harbor, NY: Cold Spring Harbor Laboratory Press).

Helassa, N., Dürst, C. D., Coates, C., Kerruth, S., Arif, U., Schulze, C., et al. (2018). Ultrafast glutamate sensors resolve high-frequency release at Schaffer collateral synapses. *Proc. Natl. Acad. Sci. U S A* 115, 5594–5599. doi: 10.1073/pnas.1720648115

Horn, R., and Marty, A. (1988). Muscarinic activation of ionic currents measured by a new whole-cell recording method. *J. Gen. Physiol.* 92, 145–159. doi: 10.1085/jgp.92.2.145

Horton, N. G., Wang, K., Kobat, D., Clark, C. G., Wise, F. W., Schaffer, C. B., et al. (2013). *In vivo* three-photon microscopy of subcortical structures within an intact mouse brain. *Nat. Photonics* 7, 205–209. doi: 10.1038/nphoton.2012.336

Hosokawa, T., Rusakov, D. A., T. Bliss, V. P., and Fine, A. (1995). Repeated confocal imaging of individual dendritic spines in the living hippocampal slice: evidence for changes in length and orientation associated with chemically-induced LTP. *J. Neurosci.* 15, 5560–5573. doi: 10.1523/jneurosci.15-08-05560.1995

Isaac, J. T., Hjelmstad, O., Nicoll, R. A., and Malenka, R. C. (1996a). Long-term potentiation at single fiber inputs to hippocampal CA1 pyramidal cells. *Proc. Natl. Acad. Sci. U S A* 93, 8710–8715. doi: 10.1073/pnas.93.16.8710

Isaac, J. T., Oliet, S. H., Hjelmstad, G. O., Nicoll, R. A., and Malenka, R. C. (1996b). Expression mechanisms of long-term potentiation in the hippocampus. *J. Physiol.* 90, 299–303. doi: 10.1016/s0928-4257(97)87901-6

Jensen, T. P., Zheng, K., Tyurikova, O., Reynolds, J. P., and Rusakov, D. A. (2017). Monitoring single-synapse glutamate release and presynaptic calcium concentration in organized brain tissue. *Cell Calcium* 64, 102–108. doi: 10.1016/j.ceca.2017.03.007

Jung, J. C., and Schnitzer, M. J. (2003). Multiphoton endoscopy. *Opt. Lett.* 28, 902–904. doi: 10.1364/ol.28.000902

Kerchner, G. A., and Nicoll, R. A. (2008). Silent synapses and the emergence of a postsynaptic mechanism for LTP. *Nat. Rev. Neurosci.* 9, 813–825. doi: 10.1038/nrn2501

Kobat, D., Durst, M. E., Nishimura, N., Wong, A. W., Schaffer, C. B., and Xu, C. (2009). Deep tissue multiphoton microscopy using longer wavelength excitation. *Opt. Express* 17, 13354–13364. doi: 10.1364/oe.17.013354

Kobat, D., Horton, N. G., and Xu, C. (2011). *In vivo* two-photon microscopy to 1.6-mm depth in mouse cortex. *J. Biomed. Opt.* 16:106014. doi: 10.1117/1.3646209

Korn, H., and Faber, D. S. (1991). Quantal analysis and synaptic efficacy in the CNS. *Trends Neurosci.* 14, 439–445. doi: 10.1016/0166-2236(91)90042-s

Kovalchuk, Y., Eilers, J., Lisman, J., and Konnerth, A. (2000). NMDA receptor-mediated subthreshold Ca^{2+} signlas in spines of hippocampal neurons. *J. Neurosci.* 20, 1791–1799. doi: 10.1523/jneurosci.20-05-01791.2000

Kullmann, D. M., and Nicoll, R. A. (1992). Long-term potentiation is associated with increases in quantal content and quantal amplitude. *Nature* 357, 240–244. doi: 10.1038/357240a0

Larkman, A., Stratford, K., and Jack, J. (1991). Quantal analysis of excitatory synaptic action and depression in hippocampal slices. *Nature* 350, 344–347. doi: 10.1038/350344a0

Larkman, A., Hannay, T., Stratford, K., and Jack, J. (1992). Presynaptic release probability influences the locus of long-term potentiation. *Nature* 360, 70–73. doi: 10.1038/360070a0

Lindau, M., and Fernandez, J. M. (1986). IgE-mediated degranulation of mast cells does not require opening of ion channels. *Nature* 319, 150–153. doi: 10.1038/319150a0

MacDougall, M. J., and Fine, A. (2014). The expression of long-term potentiation: reconciling the preists and the postivists. *Philos. Trans. R. Soc. Lond. B Biol. Sci.* 369:20130135. doi: 10.1098/rstb.2013.0135

Mainen, Z. F., Malinow, R., and Svoboda, K. (1999). Synaptic calcium transients in single spines indicate that NMDA receptors are not saturated. *Nature* 399, 151–155. doi: 10.1038/20187

Malinow, R. (1991). Transmission between pairs of hippocampal slice neurons: quantal levels, oscillations, and LTP. *Science* 252, 722–724. doi: 10.1126/science.1850871

Malinow, R., Otmakhov, N., Blum, K. I., and Lisman, J. (1994). Visualizing hippocampal synaptic function by optical detection of Ca^{2+} entry through the N-methyl-D-aspartate channel. *Proc. Natl. Acad. Sci. U S A* 91, 8170–8174. doi: 10.1073/pnas.91.17.8170

Malinow, R., and Tsien, R. W. (1990). Presynaptic enhancement shown by whole-cell recordings of long-term potentiation in hippocampal slices. *Nature* 346, 177–180. doi: 10.1038/346177a0

Markram, H., Lubke, J., Frotscher, M., and Sakmann, B. (1997). Regulation of synaptic efficacy by coincidence of postsynaptic APs and EPSPs. *Science* 275, 213–215. doi: 10.1126/science.275.5297.213

Marvin, J. S., Borghuis, G. B., Tian, L., Chichon, J., Harnett, T. M., Akerboom, J., et al. (2013). An optimized fluorescent probe for visualizing glutamate transmission. *Nat. Methods* 10, 162–170. doi: 10.1038/nmeth.2333

Masharina, A., Reymond, L., Maurel, D., Umezawa, K., and Johnsson, K. (2012). A fluorescent sensor for GABA and $GABA_B$ receptor ligands. *J. Am. Chem. Soc.* 134, 19026–19034. doi: 10.1021/ja306320s

Midorikawa, M., and Sakaba, T. (2017). Kinetics of releasable synaptic vesicles and their plastic changes at hippocampal mossy fiber synapses. *Neuron* 96, 1033.e3–1040.e3. doi: 10.1016/j.neuron.2017.10.016

Mizrahi, A., Crowley, J. C., Shtoyerman, E., and Katz, L. C. (2004). High-resolution *in vivo* imaging of hippocampal dendrites and spines. *J. Neurosci.* 24, 3147–3151. doi: 10.1523/JNEUROSCI.5218-03.2004

Nevian, T., and Sakmann, B. (2006). Spine Ca^{2+} signaling in spike-timing-dependent plasticity. *J. Neurosci.* 26, 11001–11013. doi: 10.1523/JNEUROSCI.1749-06.2006

Newman, Z. L., Hoagland, A., Aghi, K., Worden, K., Levy, S. L., Son, J. H., et al. (2017). Input-specific plasticity and homeostasis at the drosophila larval neuromuscular junction. *Neuron* 93, 1388.e10–1404.e10. doi: 10.1016/j.neuron.2017.02.028

Nicoll, R. A. (2003). Expression mechanisms underlying long-term potentiation: a postsynaptic view. *Philos. Trans. R. Soc. Lond. B Biol. Sci.* 358, 721–726. doi: 10.1098/rstb.2002.1228

Ohayon, S., Caravaca-Aguirre, A., Piestun, R., and DiCarlo, J. J. (2018). Minimally invasive multimode optical fiber microendoscope for deep brain fluorescence imaging. *Biomed. Opt. Express* 9, 1492–1509. doi: 10.1364/boe.9.001492

Padamsey, Z., and Emptage, N. (2014). Two sides to long-term potentiation: a view towards reconciliation. *Philos. Trans. R. Soc. Lond. B Biol. Sci.* 369:20130154. doi: 10.1098/rstb.2013.0154

Raastad, M. (1995). Extracellular activation of unitary excitatory synapses between hippocampal CA3 and CA1 pyramidal cells. *Eur. J. Neurosci.* 7, 1882–1888. doi: 10.1111/j.1460-9568.1995.tb00709.x

Redman, S. (1990). Quantal analysis of synaptic potentials in neurons of the central nervous system. *Physiol. Rev.* 70, 165–198. doi: 10.1152/physrev.1990.70.1.165

Reid, C. A., Fabian-Fine, R., and Fine, A. (2001). Postsynaptic calcium transients evoked by activation of individual hippocampal mossy fiber synapses. *J. Neurosci.* 21, 2206–2214. doi: 10.1523/JNEUROSCI.21-07-02206.2001

Reid, C. A., Dixon, D. B., Takahashi, M., Bliss, T. V., and Fine, A. (2004). Optical quantal analysis indicates that long-term potentiation at single hippocampal mossy fiber synapses is expressed through increased release probability, recruitment of new release sites, and activation of silent synapses. *J. Neurosci.* 24, 3618–3626. doi: 10.1523/JNEUROSCI.3567-03.2004

Sabatini, B. L., Oertner, T. G., and Svoboda, K. (2002). The life cycle of Ca^{2+} ions in dendritic spines. *Neuron* 33, 439–452. doi: 10.1016/s0896-6273(02)00573-1

Sato, M., Motegi, Y., Yagi, S., Gengyo-Ando, K., Ohkura, M., and Nakai, J. (2017). Fast varifocal two-photon microendoscope for imaging neuronal activity in the deep brain. *Biomed. Opt. Express* 8, 4049–4060. doi: 10.1364/boe.8.004049

Scholl, B., Wilson, D. E., and Fitzpatrick, D. (2017). Local order within global disorder: synaptic architecture of visual space. *Neuron* 96, 1127–1138. doi: 10.1016/j.neuron.2017.10.017

Sinnen, B. L., Bowen, A. B., Gibson, E. S., and Kennedy, M. J. (2016). Local and use-dependent effects of β-Amyloid oligomers on NMDA receptor function revealed by optical quantal analysis. *J. Neurosci.* 36, 11532–11543. doi: 10.1523/JNEUROSCI.1603-16.2016

Skrede, K. K., and Westgaard, R. H. (1971). The transverse hippocampal slice: a well-defined cortical structure maintained *in vitro*. *Brain Res.* 35, 589–593. doi: 10.1016/0006-8993(71)90508-7

Song, S., Miller, K. D., and Abbott, L. F. (2000). Competitive Hebbian learning through spike-timing-dependent synaptic plasticity. *Nat. Neurosci.* 3, 919–926. doi: 10.1038/78829

Sorra, K. E., and Harris, K. M. (1993). Occurrence and three-dimensional structure of multiple synapses between individual radiatum axons and their target pyramidal cells in hippocampal area CA1. *J. Neurosci.* 13, 3736–3748. doi: 10.1523/JNEUROSCI.13-09-03736.1993

Spacek, J., and Harris, K. M. (1997). Three-dimensional organization of smooth endoplasmic reticulum in hippocampal CA1 dendrites and dendritic spines of the immature and mature rat. *J. Neurosci.* 17, 190–203. doi: 10.1523/JNEUROSCI.17-01-00190.1997

Stoppini, L., Buchs, P., and Muller, D. (1991). A simple method for organotypic culture of nervous tissue. *J. Neurosci. Methods* 37, 173–182. doi: 10.1016/0165-0270(91)90128-m

Storace, D., Sepehri Rad, M., Kang, B., Cohen, L. B., Hughes, T., and Baker, B. J. (2016). Toward better genetically encoded sensors of membrane potential. *Trends Neurosci.* 39, 277–289. doi: 10.1016/j.tins.2016.02.005

Svoboda, K., Denk, W., Kleinfeld, D., and Tank, D. W. (1997). *In vivo* dendritic calcium dynamics in neocortical pyramidal neurons. *Nature* 385, 161–165. doi: 10.1038/385161a0

Theer, P., Hasan, M. T., and Denk, W. (2003). Two-photon imaging to a depth of 1000 microns in living brains by use of a $Ti:Al_2O_3$ regenerative amplifier. *Opt. Lett.* 28, 1022–1024. doi: 10.1364/ol.28.001022

Tsien, R. W., and Malinow, R. (1991). Changes in presynaptic function during long-term potentiation. *Ann. N Y Acad. Sci.* 635, 208–220. doi: 10.1111/j.1749-6632.1991.tb36493.x

Velasco, M. G., and Levene, M. J. (2014). *In vivo* two-photon microscopy of the hippocampus using glass plugs. *Biomed. Opt. Express* 5, 1700–1708. doi: 10.1364/boe.5.001700

Voronin, L. L. (1983). Long-term potentiation in the hippocampus. *Neuroscience* 10, 1051–1069. doi: 10.1016/0306-4522(83)90099-4

Voronin, L. L. (1994). Quantal analysis of hippocampal long-term potentiation. *Rev. Neurosci.* 5, 141–170. doi: 10.1515/revneuro.1994.5.2.141

Voronin, L. L., Kuhnt, U., Gusev, A. G., and Hess, G. (1992). Quantal analysis of long-term potentiation of "minimal" excitatory postsynaptic potentials in guinea pig hippocampal slices: binomial approach. *Exp. Brain Res.* 89, 275–287. doi: 10.1007/bf00228244

Walmsley, B. (1995). Interpretation of 'quantal' peaks in distributions of evoked synaptic transmission at central synapses. *Proc. Biol. Sci.* 261, 245–250. doi: 10.1098/rspb.1995.0144

Walmsley, B., Edwards, F. R., and Tracey, D. J. (1987). The probabilistic nature of synaptic transmission at a mammalian excitatory central synapse. *J. Neurosci.* 7, 1037–1046. doi: 10.1523/JNEUROSCI.07-04-01037.1987

Wilson, D. E., Whitney, D. E., Scholl, B., and Fitzpatrick, D. (2016). Orientation selectivity and the functional clustering of synaptic inputs in primary visual cortex. *Nat. Neurosci.* 19, 1003–1009. doi: 10.1038/nn.4323

Yamamoto, N., Kurotani, T., and Toyama, K. (1989). Neural connections between the lateral geniculate nucleus and visual cortex *in vitro*. *Science* 245, 192–194. doi: 10.1126/science.2749258

Yang, H. H., and St-Pierre, F. (2016). Genetically encoded voltage indicators: opportunities and challenges. *J. Neurosci.* 36, 9977–9989. doi: 10.1523/JNEUROSCI.1095-16.2016

Yuste, R., and Denk, W. (1995). Dendritic spines as basic functional units of neural integration. *Nature* 375, 682–684. doi: 10.1038/375682a0

Yuste, R., Majewska, A., Cash, S. S., and Denk, W. (1999). Mechanisms of calcium influx into hippocampal spines: heterogeneity among spines, coincidence detection by NMDA receptors, and optical quantal analysis. *J. Neurosci.* 19, 1976–1987. doi: 10.1523/JNEUROSCI.19-06-01976.1999

Conflict of Interest Statement: The authors declare that the research was conducted in the absence of any commercial or financial relationships that could be construed as a potential conflict of interest.

frontiers in Synaptic Neuroscience

ORIGINAL RESEARCH
published: 16 April 2019
doi: 10.3389/fnsyn.2019.00012

Imaging and Analysis of Presynaptic Calcium Influx in Cultured Neurons Using synGCaMP6f

Johannes Brockhaus, Bianca Brüggen and Markus Missler*

Institute of Anatomy and Molecular Neurobiology, Westfälische Wilhelms-University, Münster, Germany

Presynaptic Ca^{2+} influx through voltage-gated calcium channels (VGCCs) is a key step in synaptic transmission that links action potential (AP)-derived depolarization to vesicle release. However, investigation of presynaptic Ca^{2+} influx by patch clamp recordings is difficult due to the small size of the majority of synaptic boutons along thin axons that hamper clamp control. Genetically encoded calcium indicators (GECIs) in combination with live cell imaging provide an alternative method to study Ca^{2+} transients in individual presynaptic terminals. The indicator GCaMP6f was developed for fast speed and high sensitivity in detecting Ca^{2+} transients even in subcellular compartments. We fused GCaMP6f to synaptophysin (synGCaMP6f) to enrich the calcium indicator in presynaptic boutons of transfected primary hippocampal neurons to study presynaptic Ca^{2+} changes in response to individual APs or short bursts. Changes in fluorescence intensity were evaluated by normalization to control level or, alternatively, by normalization to maximal fluorescence using the calcium ionophore ionomycin. Measurements revealed robust Ca^{2+} transients with amplitudes that depend on parameters like the number of APs, stimulation frequency or external calcium concentration. Our findings indicate an appropriate sensitivity of synGCaMP6f for studying total presynaptic Ca^{2+} transients induced by single APs or short bursts that showed little rundown of the response after repeated bursts. Moreover, these recordings are fast enough to even study short-term plasticity like paired pulse facilitation (PPF) and frequency dependence of Ca^{2+} transients. In addition, synGCaMP6f could be used to dissect the contribution of different subtypes of VGCCs to presynaptic Ca^{2+} influx. Our results demonstrate that synGCaMP6f allows the reliable analysis of changes in presynaptic calcium concentration at many individual synaptic boutons in parallel and provides the possibility to study the regulation of this important step in synaptic transmission.

Keywords: synapse, live imaging, paired pulse facilitation, high voltage activated calcium channels, synaptic transmission, genetically encoded calcium indicator

OPEN ACCESS

Edited by:
Dirk Feldmeyer, Julich Research Centre, Helmholtz Association of German Research Centers (HZ), Germany

Reviewed by:
Volker Haucke, Freie Universität Berlin, Germany
William Ross, New York Medical College, United States
James T. Porter, Ponce Health Sciences University, Puerto Rico
Marijn Kuijpers contributed to the review of Volker Haucke

****Correspondence:***
Johannes Brockhaus
jbrock@uni-muenster.de

Received: *18 December 2018*
Accepted: *26 March 2019*
Published: *16 April 2019*

Citation:
Brockhaus J, Brüggen B and Missler M (2019) Imaging and Analysis of Presynaptic Calcium Influx in Cultured Neurons Using synGCaMP6f. Front. Synaptic Neurosci. 11:12. doi: 10.3389/fnsyn.2019.00012

INTRODUCTION

In presynaptic terminals, action potentials (APs) induce calcium transients that are the key factor in the translation of electric activity to transmitter release (Neher, 1998). Calcium transients depend on voltage-gated calcium channels (VGCCs) and their regulation, for example, *via* metabotropic receptors by retrograde action of released transmitters. Also other factors like the subunit composition or splice variants of the VGCCs (Hoppa et al., 2012; Thalhammer et al., 2017),

the calcium storage within the endoplasmic reticulum (de Juan-Sanz et al., 2017), or other interacting molecules like neurexins (Brockhaus et al., 2018) shape the presynaptic calcium transient in response to invading APs and, by this, modulate the efficiency of the presynaptic release machinery. However, recording of presynaptic calcium currents is challenging due to the small size of normal presynaptic boutons. Direct recording with patch clamp pipettes is hardly possible due to size restrains and investigations of bigger presynapses like the squid giant axon (Augustine et al., 1991), the calyx of Held (Borst et al., 1995) or mossy fiber boutons (Li et al., 2007) are technically challenging and limited by concerns these specialized synapses allow generalized conclusions.

To study smaller, prototypical presynaptic boutons with respect to calcium dynamics, fluorescent indicators may provide a solution. Fluorescence recordings of changes in the concentration of free calcium ions were first performed with an organic fluorescent sensors like the widely used double-wavelength indicator Fura-2 (Tsien et al., 1985; Takahashi et al., 1999), or the single wavelength dyes Oregon-green-BAPTA (OGB), Fluo5F and others. These dyes were often applied as AM-esters (Tsien, 1981) or *via* the patch pipette solution for use in combination with electrophysiological recordings (Augustine, 1994). These dyes provided substantial insight into many intracellular processes and the central role of calcium.

However, the AM-ester loading does not differentiate between pre- and post-synaptic sites. Therefore sophisticated further labeling in combination with synaptic receptor blocking would be required to investigate pure presynaptic calcium transients (Kirischuk et al., 1999).

Also loading *via* a patch pipette is challenging (Ermolyuk et al., 2012; Liu et al., 2014) as labeling of presynaptic boutons by diffusion is slow along thin axons. Furthermore, diffusion is impeded by the small volume of boutons and low dye concentrations, which would restrain recordings to boutons near the soma.

More recently, the small-molecule synthetic indicators got competition from the growing class of genetically encoded calcium indicators (GECIs). GECIs usually combine a fluorescent protein, for example, a modified EGFP, with a calcium chelator protein like calmodulin that switches the fluorescence intensity after binding of Ca^{2+} ions. GECIs made it much easier to visualize intracellular calcium changes as they can be applied by transient transfection *in vitro* or *in vivo* several days before investigation (Lin and Schnitzer, 2016). Moreover, GECIs can be incorporated in the mouse genome, and allow targeting to specific cell types by use of adequate promotors. Currently, the arguably most popular GECI is GCaMP (Nakai et al., 2001; Tian et al., 2009) which combines a circular permutated green fluorescent protein (GFP) with calmodulin at the C-terminus and the calmodulin binding region of the chicken myosin light chain (M13) at the N-terminus. Calcium binding to the calmodulin initiates an interaction with the M13 leading to a conformation change that induces a substantial increase in the fluorescence of the GFP moiety. GCaMP underwent several improvements and version GCaMP6f is now available in three forms (slow, medium and fast), with slightly distinct properties (Chen et al., 2013; Horikawa, 2015). With GCaMP6f, the fast version of the GCaMP6 family, the dynamic range, i.e., the fluorescence increase factor from calcium-free to calcium-saturated, is now above 50 (Chen et al., 2013), and thus rivals the range of the small-molecule synthetic indicators. Originally intended to observe spontaneous activity in living animals, the GCaMP6 indicators may cause some problems when permanently expressed in transgenic models *in vivo*, inducing increased buffering in the targeted compartments (Singh et al., 2018) and aberrant electrical activity similar to interictal spikes (Steinmetz et al., 2017). Very recently, modifications of Cav1.3 calcium currents by GCaMP6f in transient transfection of HEK cells are described next to the *in vivo* problems and a GCaMP-X that claims to overcome these problems was introduced (Yang et al., 2018), but this is not tested here.

GCaMP was used in transient transfections of neurons for visualizing calcium dynamics in a wide range of experiments on subcellular compartments: in presynaptic compartments GCaMP3 elucidated the role of overexpressed α2δ subunits of VGCCs (Hoppa et al., 2012), GCaMP6f was used to study the role of presynaptic active zone plasticity (Glebov et al., 2017) and allowed to investigate the modulation of presynaptic calcium transients by neurexin (Brockhaus et al., 2018). Postsynaptically, it was used to investigate single synapse responses of NMDA receptors after coupling GCaMP6f to PSD95 (Reese and Kavalali, 2016). In addition, it was applied in an analysis of long-term plasticity of individual synapses in rat hippocampal brain slice culture (Wiegert et al., 2018).

Here, we show that GCaMP6f targeted to presynaptic terminals of primary hippocampal neurons can be used as a reliable indicator to elucidate important properties of the AP-induced presynaptic calcium transient such as dose dependence, short-term plasticity and contribution of the different subtypes of VGCCs.

MATERIALS AND METHODS

Animals

Mice of either sex were used for neuronal cultures derived from timed-pregnant females at E17. Animal experiments were performed at the University of Münster in accordance with government regulations for animal welfare and approved by the Landesamt für Natur, Umwelt und Verbraucherschutz (LANUV, NRW, Germany), license numbers 84-02.05.20.11.209 and 84-02.04.2015.A423.

Cell Culture

Dissociated primary neurons were prepared in Hank's Balanced Salt Solution (HBSS) from hippocampi as described (Neupert et al., 2015). Briefly, cell suspensions obtained after 0.25% trypsin and trituration were plated onto 18 mm glass coverslips (Menzel-Glaeser, Braunschweig, Germany) coated with poly-L-lysine (Sigma) at a density of 55,000 cells/coverslip. After 4 h at 37°C in plating medium (MEM, 10% horse serum, 0.6% glucose, 1 mM sodium pyruvate), coverslips were inverted onto a 70%–80% confluent monolayer of astrocytes grown in 12-well plates (Falcon), and incubated in Neurobasal medium

supplemented with B27, 0.5 mM glutamine and 12.5 μM glutamate. After 3 days, media were refreshed with Neurobasal medium supplemented with B27, 0.5 mM glutamine and 5 μM AraC. Cultures were maintained at 37°C in a humidified incubator with an atmosphere of 95% air and 5% CO_2. Neurons were transfected at day-*in vitro* (DIV) 14 using lipofectamine (Thermo Fisher Scientific, Waltham, MA, USA), and experiments performed between DIV17 and DIV21.

Expression Vectors

For Ca^{2+} imaging, we used GCaMP6f (Chen et al., 2013) or a version, that coupled GCaMP6f to synaptophysin and was driven by the synapsin promotor (synGCaMP6f) as described earlier (Brockhaus et al., 2018). For better identification of neuronal morphology, in some experiments, we used pMH4-SYN-tdimer2-RFP (RFP, T. Oertner, Hamburg, Germany).

Immunohistochemistry

Primary hippocampal neurons were transfected with RFP and synGCamP6f at DIV 14 using lipofectamin, following the supplier's protocol (Thermo Fischer Scientific). Three days after transfection, cells were washed in PBS containing 0.4% sucrose and fixed in 4% PFA containing 0.4% sucrose for 10 min. All the following washing steps were performed using PBS. After washing, cells were permeabilized using 0.3% PBS-Triton X-100 for 10 min and then blocked in PBS containing 5% normal goat serum (NGS) for 30 min. Primary antibodies [rabbit-anti-GFP, Abcam (ab290); rabbit-anti-GFP, Santa Cruz (sc8334); mouse-anti-synapsin 1, Synaptic Systems (106001)] were diluted 1:1,000 in PBS containing 5% NGS and cells were incubated overnight at 4°C. After several washing steps, secondary antibodies [goat-anti-rabbit IgG (H+L), Alexa Fluor 488, Thermo Fisher Scientific (A-11034); goat-anti-mouse IgG (H+L), Alexa Fluor 647, Thermo Fisher Scientific (A-21235)] were diluted 1:1,000 in the same way and applied for 1 h. After washing, cells were mounted with Dako Fluorescence Mounting Medium.

Alternatively, to analyze the localization of synGCaMP6f at active presynaptic terminals, we preincubated the neurons for 45 min with an oyster550-labeled antibody against the luminal domain of the vesicular GABA-transporter (VGAT, 1:200; Synaptic Systems, catalog #131103C3) as a marker for (inhibitory) presynaptic boutons (Neupert et al., 2015). The marker was visualized with an excitation wave length of 540 nm by use of a monochromator (Visitron Systems, Puchheim, Germany) and an emission filter of 562 nm. The labeling prior to the recording of calcium dynamics allowed to examine the co-localization of spots with stimulation-induced increase in the synGCaMP6f fluorescence.

Image Acquisition and Analysis

For antibody staining, confocal images were acquired with a spinning disc Axio Observer-Z1 (Visitron) with an EMCCD camera (ImagEM 512 CCD, Hamamatsu) using a 40× immersion objective and lasers at 488 nm, 568 nm and 647 nm wavelength. Z-stacks were acquired with 0.2 μm intersection.

Image processing was performed using FIJI/ImageJ (National Institute of Health, USA). Confocal stacks from five subsequent slices were background subtracted (rolling ball radius = 20 pixels) and collapsed to a projection of average intensity. All images were adjusted for brightness and contrast for presentational purposes.

Ca^{2+} Imaging

To determine presynaptic Ca^{2+} influx, primary neurons were transfected at DIV14 with synGCaMP6f (see above) and, as indicated, additional plasmids like RFP were co-transfected. Three to five days post transfection, neurons growing on glass coverslips were placed in a recording chamber mounted to an inverted microscope (Observer.A1, Zeiss, Oberkochen, Germany) and superfused at 1.0–1.5 ml/min with bath solution (temperature 32°C), containing (in mM): NaCl 145, KCl 3, $MgCl_2$ 1.5, $CaCl_2$ 1.5, glucose 11, HEPES 10; pH 7.3 adjusted with NaOH; to suppress postsynaptic signaling, 10 μM 6-cyano-7-nitroquinoxaline-2,3-dione (CNQX), 25 μM D, L-2-amino-5-phosphonovaleric acid (AP5), and 10 μM bicuculline were added. All chemicals were obtained from Sigma (St. Louis, MO, USA), except calcium channel blockers (Alomone Labs, Jerusalem, Israel). A stimulation electrode, built by two platinum wires of 10 mm length in 10 mm distance was positioned with a micromanipulator (MPC-200, Sutter Instrument, Novato, CA, USA) and neurons were stimulated with 50 Hz trains of 1, 3, 10 or 30 current pulses (1 ms, 55 mA). Ca^{2+} transients were visualized and recorded (10 or 20 ms exposure time, frame rate 100 or 50 Hz, binning 2: 0.46 μm per pixel) with a CMOS camera (Orca Flash4.0, Hamamatsu, Japan), a LED-light source (SpectraX, Lumencor, Beaverton, OR, USA) using the green channel (excitation at 470 ± 20 nm) or red channel (640 ± 20 nm) and controlled by VisiView software (Visitron Systems, Puchheim, Germany). As a standard, 20 frames were recorded before the stimulus train was triggered. For stimulation with one AP, four individual recordings with 10 s time interval were averaged frame by frame to improve the signal-to-noise ratio.

To normalize the change in fluorescence to the maximal fluorescence (F_{max}), in a subset of experiments the Ca^{2+} ionophore ionomycin (10 μM) was applied after halting the perfusion at the end of the recording to saturate the Ca^{2+} indicator. For each cell, the maximum of the stimulation-induced Ca transients was compared to the maximal fluorescence, obtained with ionomycin, to calculate the relative fluorescence increase.

In some experiments, Ca^{2+} channel antagonists were added by direct application into the recording chamber. During halted perfusion, 10 μl of stock solution (ω-conotoxin GVIA, 200 μM; ω-agatoxin IVa, 40 μM; nifedipine, 2 mM; SNX-482, 50 μM) was applied to the bath solution (volume ≈1 ml) above the recording area at least 1 min before recording, leading to calculated final antagonist concentrations of 2 μM (ω-conotoxin), 400 nM (ω-agatoxin), 20 μM (nifedipine) and 0.5 μM (SNX-482), respectively. The antagonist concentration was proven to be sufficient by a full blockade after subsequent application of all four blockers.

Data Analysis

Data analysis of imaging recordings of Ca^{2+} transients was done with FIJI/ImageJ (National Institute of Health, MA, USA) and

IgorPro (Wavemetrics, Lake Oswego, Oregon). Up to 50 regions of interest (ROIs) per measurement area were drawn around active boutons as indicated by stimulation with a train of three AP. Active boutons were identified in a picture isolating regions that showed an increase in fluorescence (ΔF; **Figure 1**) by subtracting the averaged picture of frame numbers 10–20 (control before stimulation) from the average of 11 consecutive frames around the maximal response. On this picture, ROIs were placed on active boutons by use of the plugin "Time Series Analyzer V3" with an AutoROI diameter of 10 pixels. To quantify fluorescence changes in individual boutons, we first applied the commonly used (Iwabuchi et al., 2014) "Subtract Background..." tool of ImageJ (employing a "rolling ball" algorithm with a radius of 20 pixels $\approx$ 10 μm), to remove the background signal deriving from faint autofluorescence and the dark current of the camera. For each ROI and each frame, the mean of the four highest fluorescence pixels was calculated by use of a self-made macro. The area of four pixels (0.85 μm^2) corresponds to the size of a normal bouton and the restriction to the four brightest pixels avoids the problem of the relevance of the ROI size in relation to the area of increased fluorescence. Further calculations used IgorPro to average for each ROI the value of frame 10–20 as a background control (F_0). Changes were calculated as the change of fluorescence intensity ($F–F_0 = \Delta F$) divided by the control ($\Delta F/F_0$) for each ROI. Single AP responses were analyzed after averaging four consecutive recordings already within ImageJ, and for analysis of the individual amplitudes the traces were binomial Gaussian smoothed (IgorPro) to improve the signal-to-noise ratio. In 100 Hz recordings (10 ms sampling) we used coefficient 5 (employing five passes of binomial smoothing), in 50 Hz recordings (20 ms sampling) coefficient 3.

Statistical Analysis

No statistical methods were engaged to predetermine sample size, instead, we based our experimental design on numbers reported in previous studies. The experiments were not randomized, and investigators were only partially blinded during experiments and analyses. Statistical tests were performed with Prism (GraphPad Software, La Jolla, CA, USA). If samples met the criteria for normality, we used a Student's *t*-test to compare two groups. Data are presented as means $\pm$ SEM. Significance levels were as indicated in figures: $^*P < 0.05$; $^{**}P < 0.01$ and $^{***}P < 0.001$.

RESULTS

The study of presynaptic calcium signaling using hippocampal neurons in culture has the advantage that almost all synapses are in a horizontal plane. This allows superior visibility and the observation of changes of fluorescence in many individual boutons in parallel. To measure Ca^{2+} transients in identified transfected neurons, we co-transfected the calcium-indicator protein GCaMP6f with RFP, allowing to search for positive neurons on the RFP channel (excitation at 640 $\pm$ 20 nm). Healthy transfected neurons showed strong fluorescence in the soma (not shown), several intensely labeled dendrites mostly with spines, and a fine arbor of thin axonal processes (**Figure 1A**). Almost all of these cells were also positive for the green fluorescence of GCaMP6f or synGCaMP6f, a variant fused to the synaptic vesicle protein synaptophysin, and visible on the green channel (excitation at 470 $\pm$ 20 nm). GCaMP6f-expressing neurons showed green fluorescence throughout the cytoplasm, leading to brighter labeling of soma and dendrites compared to axons (**Figure 1B**, left). SynGCaMP6f expression revealed a more punctate pattern of the fluorescence that was enriched at synaptic boutons, whereas labeling of dendrites and somata appeared more moderate (**Figure 1B**, right). To identify responsive regions of boutons, short bursts (3–10 stimuli) of APs were applied. Each stimulation increased the fluorescence intensity (**Figure 1C**). We visualized this by subtracting a control frame before stimulation (like **Figure 1B**) from a frame during stimulation (like **Figure 1C**) leading to a ΔF image (**Figure 1D**). Particularly axonal regions showed punctate-like putative presynaptic boutons (sample regions in blue circles, **Figures 1B,D**). In contrast, dendritic regions (samples in red or orange circles, **Figures 1B,D**) responded less frequently. Evaluation of the changes in fluorescence intensity indicated a clear increase of calcium in the axon-associated putative presynaptic boutons (**Figure 1F**, blue traces) but only in some dendritic areas (**Figure 1F**, orange traces). Other dendritic regions showed almost no Ca^{2+} transients (**Figure 1F**, red traces).

Co-localization of synGCaMP6f with presynaptic markers was examined by two different methods. On the one hand, we performed double staining of synapsin1 and synGCaMP6f (**Figures 2A–F**). Since stimulation was missing, we enhanced the synGCaMP6f signal by anti-GFP labeling (**Figures 2A,B**), which showed various varicosities similar to those obtained under stimulation (**Figure 2G**). Most of those tentative synapses were also immunoreactive for synapsin1 (**Figures 2C–F**, arrowheads), indicating that synGCaMP6f is indeed enriched in presynaptic boutons. In another set of experiments (**Figures 2G–I**) the neurons were incubated with an antibody against a VGAT prior to measurements of calcium dynamics to label presynaptic boutons of GABAergic neurons (**Figure 2H**). In synGCaMP6f-transfected inhibitory neurons the regions of stimulus-induced fluorescence increase that were isolated by subtraction (**Figure 2G**) clearly co-localized with VGAT (**Figure 2I**), indicating the presynaptic boutons as the locus of synGCaMP6f-measured calcium transients.

Due to the more focused fluorescence of synGCaMP6f enriched in presynaptic boutons, we selected this presynaptic GECI for further analysis of presynaptic Ca^{2+} transients.

synGCaMP6f Is a Fast and Reliable GECI

After choosing a recording area within the axonal region of a single transfected neuron we investigated the presynaptic calcium transients in response to single APs and small bursts. As shown in a representative recording in **Figure 3A**, the fluorescence changes of 38 individual synaptic boutons from a single neuron were recorded in parallel (gray traces) but varied strongly. The average synGCaMP6f fluorescence of 887 boutons from 34 hippocampal neurons increased more than four-fold compared to the resting fluorescence ($\Delta F/F_0$: 3.51 $\pm$ 0.06, n = 887/34) upon stimulation with a train of 10 stimuli (50 Hz).

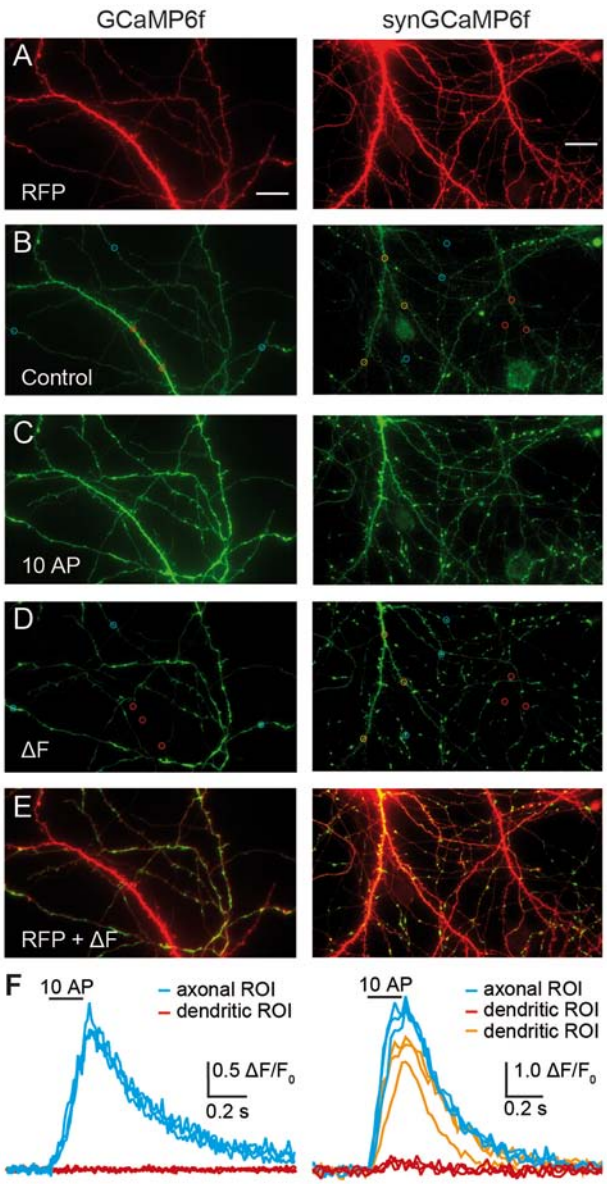

FIGURE 1 | Targeting of GCaMP6f to synaptic terminals improves signal intensity for presynaptic Ca^{2+} transients. Cultured hippocampal neurons were co-transfected with RFP and GCaMP6f (left panels) or RFP and synGCaMP6f (right panels). **(A)** The RFP-fluorescence (red) shows axons and dendrites of a transfected neuron, of which the soma is positioned outside of the shown area due to its intense fluorescence. **(B)** The green fluorescence of GCaMP6f (left) is more homogeneously distributed along all processes and is stronger in thicker dendrites. In contrast, synGCaMP6f emphasizes punctate, presumably synaptic areas and is less intense over axonal shafts and dendrites. Circles depict putative presynaptic boutons (blue) and dendritic sample regions of interest (ROIs; red or orange). **(C)** A train of 10 action potential (AP) at 50 Hz increased fluorescence levels. Images in **(B,C)** are documented with identical light and exposure conditions. **(D)** Subtraction (ΔF) of control fluorescence **(B)** from the signal during stimulation **(C)** isolates the cellular compartments with enhanced fluorescence by stimulation. Circles show same ROIs as in **(B)**. **(E)** Overlay of subtraction **(D)** and RFP **(A)** images identifies the preferential position of active compartments on thinner axonal branches. The intensely labeled left dendrite (identified by its numerous

(*Continued*)

FIGURE 1 | Continued
spines) in the synGCaMP6f-picture shows green fluorescence in its upper parts. **(F)** Quantitative evaluation of the fluorescence intensity changes of the axonal/presynaptic traces (blue) of the ROIs shown in **(B,D)** during stimulation. ROIs from dendritic compartments (red traces, red ROIs shown in **B,D**) show no change, as postsynaptic receptors are pharmacologically blocked or, in the ROIs of more distal branches (orange traces, orange ROIs shown in **B,D**) have enhanced fluorescence, possibly due to backpropagating APs. Scale bar in **(A)** for all panels: 20 μm.

This increase was fast and continued during the stimulation period (**Figure 3A**). Under stimulation with three AP, the same presynaptic boutons more than doubled their fluorescence ($\Delta F/F_0$: 1.22 ± 0.05; n = 887 boutons/34 neurons). Importantly, even stimulation with single APs induced detectable signals in individual boutons (**Figure 3B**) that averaged to 25.8 ± 0.1% fluorescence increase ($\Delta F/F_0$: 0.258 ± 0.001; n = 34/887; **Figures 3C,D**). Longer trains of 30 AP induced a calcium transient that increased the fluorescence almost six-fold ($\Delta F/F_0$: 5.36 ± 0.07; n = 877/34). The response to this 30 AP train showed a steep increase in the beginning but a weaker rise in the later phase of the stimulation period. However, only few boutons reached a constant maximum as would be expected for a full saturation of the recording dye. Since stimulation with longer stimulus trains (30 AP) showed varying grades of saturation (**Figure 3F**), we focused further experiments on single AP and shorter trains. Repeated stimulation with 10 AP bursts showed less than 5% run-down of the response after three stimulations (not shown). When the neurons were kept in bath solutions with different extracellular calcium concentrations [$(Ca^{2+})_e$], the response to 1 AP was reduced to 0.144 ± 0.005 in 0.5 mM $[Ca^{2+}]_e$ and enhanced to 0.365 ± 0.011 in 3 mM $[Ca^{2+}]_e$ (**Figure 3D**). Likewise, the response to three AP was smaller (0.686 ± 0.018) with 0.5 mM $[Ca^{2+}]_e$ and larger (1.51 ± 0.03) in 3 mM $[Ca^{2+}]_e$.

In a subset of experiments, we compared the fluorescence change between recordings using GCaMP6f or synGCaMP6f. We normalized it to the maximal value (F_{max}) after we equilibrated the intra- and extracellular Ca^{2+} concentration using ionomycin. In this recordings a single AP induced an increase of 2.7 ± 1.0% (GCaMP6f; n = 128/7) or 4.9 ± 1.3% (synGCaMP6f; n = 260/8) of the F_{max}. For GCaMP6f or synGCaMP6f three AP induced 10.9 ± 2.5% or 25.3 ± 4.2% and 10 AP increased the fluorescence by 35.3 ± 6.2% or 58.3 ± 5.6% of F_{max} (**Figure 3E**), respectively.

As expected from a GECI, there are also well-known limitations for the use of synGCaMP6f in assessing rise or decay times of the presynaptic Ca^{2+} signal. Averaging the mean response of all boutons of a neuron (black line in **Figure 3B**) for all neurons recorded with 100 Hz recording frequency reveals a time-to-peak in fluorescence change of 60–70 ms, and a 10%–90% rise time of less than 40 ms (**Figure 3C**). This value is clearly much slower than the time-to-peak in actual presynaptic Ca^{2+} current recordings (Borst et al., 1995), and slower than values recorded with other calcium indicators such as Fluo5F (Liu et al., 2014; Brockhaus et al., 2018). Similarly, the decay time of the fluorescence signal of synGCaMP6f in response to a single AP is slow with 279 ± 33 ms and increased only moderately when the amount of stimulation is enhanced

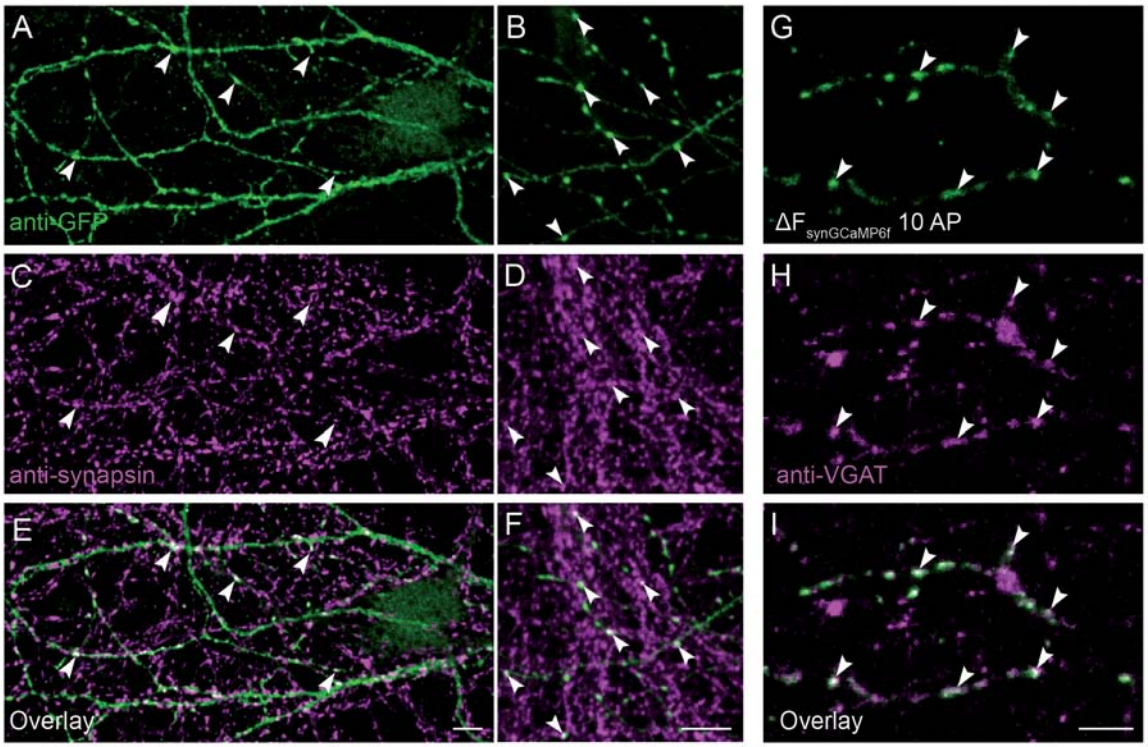

FIGURE 2 | Presynaptic localization of synGCaMP6f. **(A,B)** Anti-green fluorescent protein (GFP) antibodies were used to enhance the synGCaMP6f signal (green) and showed cell processes with various varicosities, presumably mostly at presynaptic boutons. **(C,D)** To verify this, we performed double labeling with anti-synapsin1 (magenta). **(E,F)** Synaptic GFP-positive varicosities were also immunopositive for synapsin1 (white, arrowheads), indicating the enrichment of synGCaMP6f in presynaptic boutons. **(G)** The subtraction figure (ΔF, like in **Figure 1D**) indicates regions with synGCaMP6f fluorescence increase during stimulation with 10 AP. **(H)** GABAergic presynaptic boutons are identified by incubation with an antibody against VGAT::oyster prior to calcium imaging. **(I)** The overlay (white) identifies the localization of the synGCaMP6f fluorescence transients (green) to the VGAT-positive GABAergic presynaptic compartments (magenta). Note that no all GABAergic presynapses in this area belong to the neuron that was transfected with synGCaMP6f, as numerous VGAT-positive boutons show no synGCaMP6f signal. Scale bars in **(E,F,I)**: 10 μm.

(**Figures 3F,G**). These data indicate that the kinetics of the calcium transients as recorded with synGCaMP6f are dominated by intrinsic properties of the indicator, for example, its buffering properties. On the other hand, the slow kinetics allows longer light sampling (20 ms) and a related recording frequency of 50 Hz without loss of the maximal response, which improves the signal-to-noise ratio.

Despite the limitations with respect to kinetics, the observation that individual presynaptic calcium transients respond reliably and robustly to single APs opens the possibility to test presynaptic short-term plasticity, at least for time intervals of 100 ms or more. Consistently, a second stimulation within 1 s or shorter elicited a larger amplitude in presynaptic calcium compared to the initial transient (**Figure 4**), indicating presynaptic paired-pulse facilitation (PPF). The observation of calcium transients in presynaptic boutons offered a focus on the first steps of synaptic transmission and a facilitation already prior to transmitter release. The paired-pulse ratio was 1.63 ± 0.04 (n = 29 cells) with a stimulus interval of 100 ms, decreased to 1.28 ± 0.02 (n = 29) with 1 s interval and was not detectable after 5 s (**Figure 4C**). For shorter stimulus intervals, the response to a single stimulus (red trace in **Figure 4B**) was subtracted prior to the evaluation to make sure that the second amplitude is not overestimated. Due to the slow increase of the response to single APs with more than 50 ms time-to-peak (**Figure 3C**) and a recording frequency of 50 Hz (20 ms exposure time), paired-pulse intervals shorter than 100 ms were not used. We measured the PPF in the dendritic compartment and found it significantly smaller than the PPF in the axonal boutons. This increases our confidence that the bouton signal was distinct.

Additionally, we tested the importance of the stimulation frequency and applied a 10 AP burst with different frequencies (2–50 Hz; **Figure 4D**). Faster stimulus series induced larger fluorescence changes but this may result mainly from the summation of responses to individual stimuli together with enhanced responses due to PPF (see above). Evaluation of the area under the curve, which corresponds to the amount of increasing calcium, was not strongly affected by frequencies of 5–50 Hz (**Figure 4D**, inset).

Analysis of Ca^{2+} Channel Subtypes With synGCaMP6f

Presynaptic calcium rise is dominated by N- and P/Q-type Ca^{2+} channels ($Ca_V2.1$ and $Ca_V2.2$, respectively; Li et al., 2007;

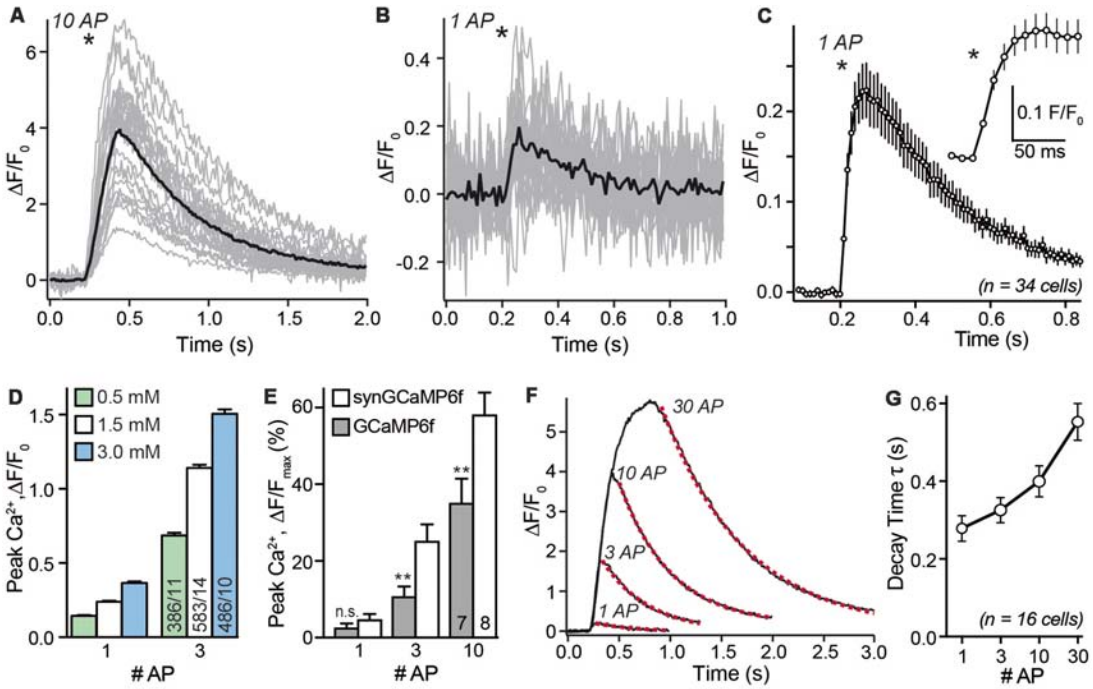

FIGURE 3 | Stimulus-response relationship of synGCaMP6f-measured Ca^{2+} transients. **(A)** Stimulation with a train of 10 AP (50 Hz) reliably induced a transient increase in synGCaMP6f fluorescence that varied in size. The sample recording evaluated 23 ROIs of presynaptic boutons from a single neuron (gray lines). Black line shows averaged response; asterisk indicates onset of the stimulation. Panel **(B)** in the same ROIs shown in **(A)** a single AP elicited smaller calcium transients. Black line, averaged response to one AP. **(C)** Combining the averaged responses of 34 neurons, representing 887 ROIs, reveals the kinetics of fluorescence changes in response to a single AP. The circles illustrate the fluorescence of a 10 ms exposure period (recording with 100 Hz) averaged from 34 separate recordings. The maximum of the synGCaMP6f fluorescence intensity is sampled 60–70 ms after the AP and it lasts more than 0.8 s to reach the baseline level again. Inset shows the initial response at higher resolution. Asterisks indicates onset of stimulation. **(D)** Recording of presynaptic calcium transients induced by one or three APs in different concentrations of extracellular calcium [$(Ca^{2+})_e$]. In normal recordings, 1.5 mM [$(Ca^{2+})_e$] was used. **(E)** Peak values of Ca^{2+} transients in response to increasing numbers of APs are compared between GCaMP6f and synGCaMP6f and normalized to F_{max} as revealed with ionomycin application at the end of each experiment. These measurements indicate stronger fluorescence changes with the synaptophysin-coupled GCaMP. **(F)** Averaged responses (compare black lines in **A,B**) from 32 presynaptic boutons of a single neuron to 1, 3, 10 and 30 APs that underwent a mono-exponential decay time fit (dotted red line). **(G)** Analysis of decay time in >500 presynaptic ROIs from 16 neurons reveals a moderate increase to longer AP trains. Data in **(C–E,G)** are mean ± SEM; in **(E)**, columns with equal stimulation are compared by student's *t*-test; n.s.: $p > 0.05$; $^{**}p < 0.01$.

Cao and Tsien, 2010). These channels can be blocked by the highly specific toxins ω-conotoxin GVIA (conotoxin; N-type blocker) and ω-agatoxin IVa (agatoxin, P/Q-type blocker). We, therefore, investigated if synGCaMP6f is suitable to determine the contribution of different Ca^{2+} channel subtypes to presynaptic calcium transients. We applied the blockers in concentrations that were successfully used by others to achieve full channel-specific blockade (Randall and Tsien, 1995; Li et al., 2007; Cao and Tsien, 2010). First, we stimulated with trains of 10 AP to get a robust signal-noise ratio even after reduced responses due to a partial blockade. Consecutive use of conotoxin, agatoxin and the L-type channel ($Ca_V1.x$) blocker nifedipine (n = 239/9; **Figures 5A,C**) revealed a predominant role of P/Q-type (47.4 ± 1.7%) and N-type (39.7 ± 1.3%) Ca^{2+} channels and a minor contribution from L-type (12.9 ± 1.3%). To overcome bias imposed by the order of blocker application (Cao and Tsien, 2010), we performed a second set of recordings with sequential application of nifedipine, agatoxin and conotoxin (**Figures 5B,D**). In addition, we applied the R-type antagonist SNX-482 (n = 235/11) to identify the source of the small transient sometimes left in the first set of recordings. Again, the majority of calcium influx results from P/Q-type (38.4 ± 1.5%) and N-type (36.9 ± 1.3%) channels. However, in this order 16.5 ± 1.1% of the calcium influx was due to L-type channels and an additional 8.2 ± 0.9% were shown to be sensitive to the R-type antagonist SNX-482.

By fluorescence measurements of many individual presynaptic boutons with Ca^{2+} channel blockers, synGCaMP6f allowed the analysis of the distribution of the different Ca^{2+} channel subtypes in individual boutons. This evaluation was done on the first set of recordings with 10 APs to focus on the comparison of N- and P/Q-type channels. We asked whether both subtypes were equally strong in all boutons or showed individual divergence. We calculated the relative contribution of N-, P/Q- and L-type channels for the calcium transient of each bouton. A frequency histogram shows the frequency of the relative contribution of each channel subtype (**Figure 5E**). For N- and P/Q-type channels, contribution ranges from almost equal to boutons that are dominated by either one of the two major subtypes. L-type channels contributed only little to the calcium

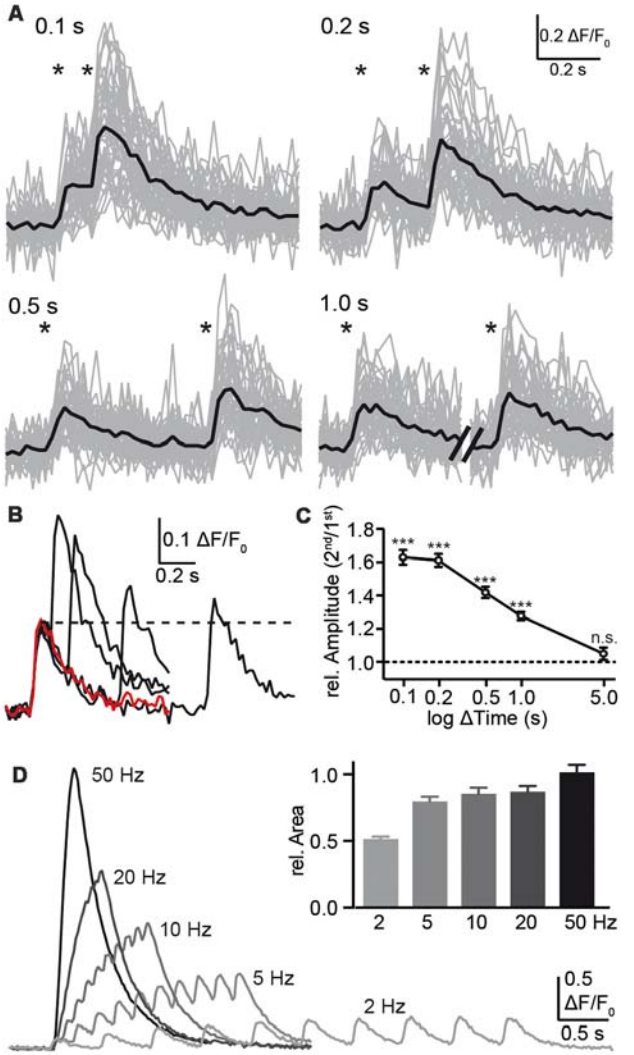

FIGURE 4 | Analysis of paired-pulse facilitation (PPF) using synGCaMP6f. **(A)** Pairs of single AP stimulations with intervals between 0.1 and 1.0 s as indicated by asterisks induced an enhancement amplitude in Ca^{2+} transients following the second AP. Sample recordings show the strongest enhancement with the shortest possible interval at 0.1 s. Black traces, averaged responses from 47 ROIs. **(B)** The overlay of the averaged responses (black traces from the recordings in **(A)** are compared to the response to a single AP (red trace) of the same neuron. The dotted line indicates the amplitude maximum of the first calcium transient for comparison. **(C)** Summary of presynaptic paired-pulse ratios determined from calcium transients of 29 neurons shows a long-lasting facilitation of the presynaptic calcium response with significant amplification even at 1 s interval. For the shorter intervals <1 s, the response to a single stimulus (red trace in **B**) was subtracted prior to the evaluation due to ongoing decay of the first transient. Data in **(C)** are mean ± SEM of 29 neurons. Significance was tested in **(C)** by a paired student's *t*-test comparing $\Delta F/F_0$ values of the first and second response; significance levels are indicated with $^{***}p < 0.001$, n.s.: $p > 0.05$. **(D)** Trains with 10 AP were applied with different frequencies as indicated and the area under the curves were normalized to the response to the standard frequency 50 Hz (inset; $n = 148/3$).

transients in most boutons (<20%; green line in **Figure 5E**) but dominated the response in few boutons with up to 70% of the total calcium. This diversity among individual presynaptic boutons indicates an independent distribution of Ca^{2+} channel subtypes. Together with the widespread amplitude distribution in response to single stimuli or short bursts, our results suggest that data from individual boutons can be treated as independent in the statistical evaluation of such experiments.

DISCUSSION

With the invention of GCaMP as a genetically encoded fluorescent calcium indicator (Nakai et al., 2001; Chen et al., 2013), a potent tool for the observation of calcium dynamics has become available. Originally intended as an indicator for active neurons (Chen et al., 2013), it also allows the investigation of changes in the internal calcium concentrations in subcellular compartments, including small regions such as individual presynaptic boutons (Reese and Kavalali, 2016; Brockhaus et al., 2018). We focussed on the presynaptic compartments of standard preparations like cultured hippocampal neurons that typically have diameters of 1 μm or smaller. To avoid a mixture with signals from adjacent postsynaptic areas we used three independent methods: (1) we coupled GCaMP6f to the presynaptic protein synaptophysin to localize the calcium indicator by intrinsic sorting mechanisms preferentially to presynaptic loci; (2) we pharmacologically blocked ionotropic glutamate and GABA receptors with CNQX, AP5 and bicuculline to prevent postsynaptic signaling and subsequent returning network activity; and (3) we sparsely transfected only a minority of neurons to exclude co-labeling of pre- and postsynaptic areas. Additionally, co-labeling with presynaptic markers, like the vesicular GABA-transporter VGAT or synapsin, provided support for the presynaptic localization of synGCaMP6f fluorescence transients.

Evaluation of putative dendritic areas of the transfected neurons without labeling in the presynaptic boutons (**Figure 1**) only rarely showed transients, even in cells transfected with the uncoupled GCaMP6f. SynGCaMP6f showed a more punctual fluorescence, often weak without stimulation. The low baseline fluorescence may in part be due to the small volume of presynaptic boutons but also reflects a low resting concentration of free calcium as typical for healthy physiological conditions of these neurons.

We used fluorescence changes of synCGaMP6f as a measure for changes in the internal concentration of free Ca^{2+}. The baseline fluorescence F_0, recorded during the resting state before stimulation, is the central reference point for the quantification of the relative changes $(F–F_0)/F_0$. In neurons, in which the intracellular Ca^{2+} concentration is important for many signaling cascades, the resting calcium concentration is strongly controlled. Still, the use of only this baseline fluorescence would be a disadvantageous aspect of the evaluation. To make the resting calcium concentration a relevant measure as a reference point, it is a prerequisite that the neuron was not spontaneous active in the seconds before the recording. Since we used blockade of fast glutamatergic transmission, we hardly saw spontaneous activity in the neuronal network in long lasting observation periods (data not shown) and can exclude

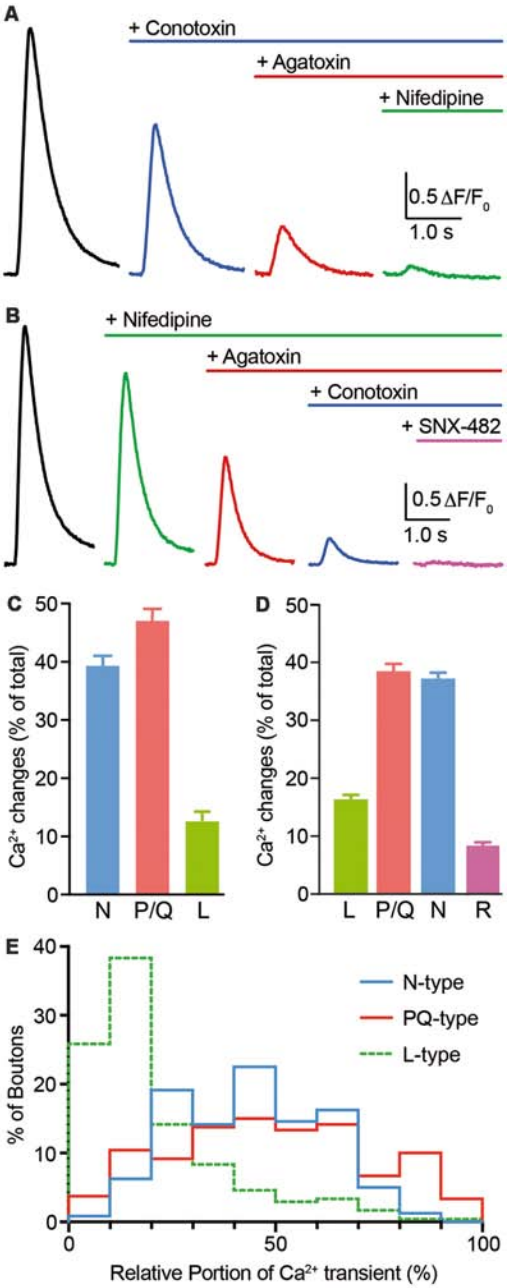

FIGURE 5 | Voltage-gated calcium channel (VGCC) subtype contribution to Ca^{2+} transients monitored by synGCaMP6f. **(A)** Consecutive application of ω-conotoxin GVIA (2 μM; N-type Ca^{2+} channel blocker), ω-agatoxin IVa (0.4 μM; P/Q-type Ca^{2+} channel blocker) and nifedipine (20 μM; L-type Ca^{2+} channel blocker) was employed to evaluate the contribution of different VGCC subtypes to fluorescence changes induced by trains of 10 APs (50 Hz). Color-coded traces show averaged responses from 239 ROIs in nine neurons before (black) and after sequential addition of blockers as indicated. **(B)** Independent set of experiments (n = 235/11) similar to **(A)** but with altered order of application and addition of SNX-482 (0.5 μM; R-type Ca^{2+} channel blocker). **(C,D)** Bar diagrams summarizing the relative contribution of Ca^{2+} channel subtypes from experiments in **(A,B)**. Both diagrams confirm that N- and P/Q-type VGCCs contribute mostly and almost equally to presynaptic calcium transient in hippocampal neurons. **(E)** Histogram presenting the wide

(*Continued*)

FIGURE 5 | Continued
variability of VGCC subtype contributions to Ca^{2+} transients at the level of individual presynaptic boutons (n = 239/9) as evaluated from the recordings in **(A,C)**. A few percent of the boutons even had more than 50% nifedipine-sensitive L-type Ca^{2+} current.

a disturbance of our evaluations. Additionally, spontaneous activity or recovery would be seen in the control period of the recording before stimulation (duration 0.2–0.4 s) and exclude this measurement from further use.

Opposing the baseline fluorescence, the maximal fluorescence can serve as a second reference point for the quantification. It can be seen during application of an ionophore (e.g., ionomycin, Hoppa et al., 2012) or long lasting stimulation (e.g., 100 AP, 100 Hz; Ermolyuk et al., 2012). Here, we used this method to compare the fluorescence changes measured with GCaMP6f and synGCaMP6f, a form targeted to the presynaptic vesicles by coupling to synaptophysin. Short bursts induced significantly stronger responses with synGCaMP6f. This may result from a position closer to the presynaptic calcium channels which would result in higher Ca^{2+} transients in its surrounding area as the calcium gradient is steep during APs near the presynaptic membrane (Stanley, 2016). One may speculate that the higher response of the targeted synGCaMP6f does not result from a change in the sensitivity but from its more relevant position around synaptic vesicles near to the presynaptic Ca^{2+} channels. Overall, the ionophore application makes recording much more sophisticated and time consuming and does not lead to more powerful results.

How much change in fluorescence can we see during neuronal activity? Inducing a short burst by a stimulation of three APs already doubled the fluorescence ($\Delta F/F_0 > 1$) and was immediately visible. Stronger bursts (10–30 AP) increased the fluorescence several fold. Even the presynaptic calcium transients during a single AP could be recorded. With reasonable signal-noise ratio after averaging four consecutive single AP stimulations with 10 s distance, fluorescence increased on average by 25.8% ($\Delta F/F_0$ = 0.258). This presynaptic response to single APs is slightly higher than the transients described in the original study inventing GCaMP6f (Chen et al., 2013; total cell 19%). This may be explained with different conditions when evaluating somatic fluorescence, e.g., the density of calcium channels in relation to the volume is lower.

Although hippocampal neurons are shown to have backpropagating APs, we only saw substantial Ca^{2+} transients in some dendritic compartments (Johnston et al., 1996; Waters et al., 2005). The efficacy of backpropagating APs to induce Ca^{2+} transients depends on different parameters like the rather low density of Ca^{2+} channels in relation to the higher volume of the dendrite. Also, the membrane potential affects the highly present A-type K^+ channels and results in a shunt of depolarization decreasing the amplitude to values ineffective in activating Ca^{2+} channels (Hoffman et al., 1997; Waters et al., 2005). The delicate regulation of AP backpropagation may even lead to a dichotomy within the same neuron (Golding et al., 2001; Sheffield and Dombeck, 2015). Thus, the increase in synGCaMP6f fluorescence may be below the threshold

for visibility in dendritic compartments when compared to presynaptic Ca^{2+} transients, where the synaptophysin-coupled indicator is enriched. This does not exclude a backpropagating component of the stimulation-induced AP.

The kinetic of the presynaptic response was rather slow, taking 60–70 ms to reach the peak. This is in line with the original description of GCaMP6f (80 ms; Chen et al., 2013) but slower than seen with other dyes like fura-2 or mag-fura-5 (Atluri and Regehr, 1996), Fluo5F (Liu et al., 2014; Brockhaus et al., 2018) or OGB (Kirischuk et al., 1999). Comparatively, electrophysiological recording of the Ca^{2+} current, that induces the rise in internal free Ca^{2+} concentration lasts about 1 ms (Augustine et al., 1991; Kawaguchi and Sakaba, 2015).

Thus, the rise time in GCaMP6f recording does not describe the kinetics of free presynaptic calcium changes but rather indicates binding constants of calcium ions to the calmodulin part of the indicator. Also, the decay time constant of almost 280 ms for single AP transients is substantially slower than seen with other methods, but in the ranges described earlier (Chen et al., 2013). In conclusion, recording of calcium transients with (syn-)GCaMP6f does not allow investigating the kinetics of fast changes in Ca^{2+} concentration. On the other hand, the slow kinetics allow exposure times (as long as 20 ms) and low recording frequency (resulting in 50 Hz), which improves the signal-noise ratio and helps with the evaluation of small regions like presynaptic boutons of hippocampal or cortical cells.

The amplitude of the calcium transient in response to an increasing number of APs showed a steep increase in relation to the AP number. However, the response to three AP strongly exceeded the three-fold increase of a single response ($1.22 > 3 \times 0.258$). This led to the question of whether synGCaMP6f enabled us to measure presynaptic short-term plasticity like PPF within closely timed APs in cultured hippocampal neurons. To further investigate this, stimulus pairs were applied with different time intervals between 0.1 and 5 s. Shorter time intervals were not possible as a clear maximal response to the first pulse has to be established before the second stimulation which was only reached after 60 ms or more, probably due to intrinsic features of the sensor protein (see above). The stimulus pairs of up to 1 s distance induced significant presynaptic PPF and reached more than a doubling with 0.1 s pairs. Presynaptic origin of the usually postsynaptically recorded PPF is a well-known phenomenon (Zucker and Regehr, 2002; Jackman and Regehr, 2017) with several possible causes. It may account from enhanced calcium entry, reduced buffering or increased probability of vesicle release due to the recruitment of additional synaptotagmin subtypes (SyT7, Jackman et al., 2016). Here we employ a method directly to observe modifications of presynaptic Ca^{2+} concentrations during paired-pulse stimulation. One possible mechanism for the observed presynaptic PPF of Ca^{2+} transients is buffer saturation and subsequently an enhanced transient of free Ca^{2+} in response to the second pulse. Also, a stronger calcium current itself induced by the second pulse due to binding of the calcium channels C-terminus (EF-hand-like motif of Cav2.1; Chaudhuri et al., 2004) to calcium-bound calmodulin and other intrinsic Ca^{2+} buffers is known. Both mechanisms may be enhanced by the transfected GECI, synGCaMP6f, as it uses a calmodulin domain for calcium binding (and sensing) and adds additional calcium buffer capacity to the neuron (McMahon and Jackson, 2018). This needs to be considered in direct comparison of results with and without GCaMP but is a problem of almost all fluorescent calcium indicators. In a study of different conditions that were all measured with GCaMP, the interference is equal and hardly perturbs the result. In a recent study on hippocampal PPF, Jackman et al. (2016) used bulk-loading of CA3 fibers with different calcium indicators in brain slices and stimulation in presence of NBQX and picrotoxin to suppress postsynaptic responses. They saw no presynaptic PPF in CA3-CA1 synapses in photodiode recordings. Observation of calcium dynamics in individual presynaptic boutons, as presented here, showed PPF. This discrepancy may result from the different recording techniques and a broader mixture of synapses in cell culture of hippocampal neurons, from different conditions in brain slices vs. cell culture or from different intracellular calcium buffering, as this is a crucial factor for presynaptic PPF (Jackman and Regehr, 2017).

Another set of experiments scrutinized the contribution of different calcium channel subtypes to the presynaptic calcium transients in response to a burst of APs in hippocampal neurons. We are aware that the quantification depends on the assumption of an almost linear relation of calcium concentration and fluorescence change. Two strategies were used to minimize related constraints: With 10 AP, a stimulus was chosen that induced a response of less than 60% of the saturated indicator (**Figure 3E**). Additionally, two different orders of blocker application avoided corruption by non-linear fluorescence-calcium relation, e.g., if higher fluorescence showed weaker changes with related changes in calcium concentration. As expected, the transients were dominated by P/Q- and N-type channels, which almost equally contributed to the response. Additionally, nifedipine-sensitive L-type channels had a share of more than 10% and also SNX-482-sensitive R-type channels were identified. Helton et al. (2005) found that nifedipine did not block L-type channels during stimulation with APs, but we found that nifedipine was effective. This difference may be due to the different conditions of the experiments. Cao and Tsien (2010) examined the contribution of the different subtypes in hippocampal synapses by evaluation of excitatory postsynaptic currents (EPSCs) with a comparable consecutive blocker application and also saw an almost equal share of N- and P/Q-type channels with a minor contribution of R-type channels. But with an observation of EPSCs there was no evidence for L-type channels since a block of N-, P/Q- and R-type channels completely suppressed the postsynaptic response (Li et al., 2007; Cao and Tsien, 2010). The different observation of the role of L-type channels may result from a different measure for the contribution to presynaptic calcium transients, namely the direct recording of changes in presynaptic free Ca^{2+} ions vs. recording of the final (and relevant) effect of presynaptic calcium rises, the postsynaptic current. Thus, an exclusive involvement of N- and P/Q-type channels (and a minor amount of R-type) to the release-inducing nano-domains (Eggermann et al., 2011) *via* direct coupling of calcium channels

to the release machinery (Kaeser et al., 2011; Südhof, 2013) may explain that L-type-depended calcium increase is seen in the presynaptic compartments, but does not contribute to postsynaptic currents.

A special feature of the synCGaMP6f-driven presynaptic recording is the possibility to investigate large numbers of synaptic boutons individually. When evaluating the channel subtype contribution this enabled us to compare many boutons. Interestingly, the contribution of N- or P/Q-type calcium channels was widely scattered with some boutons almost completely driven by P/Q-type channels and others showing less than 10% P/Q-type contribution. A few boutons even showed more than 50% L-type dependent transients whereas most boutons had 20% or less originating for L-type channels. This wide divergence of subtype contribution is in line with the findings of Miyazaki et al. (2005) and fits to the assumption that only very few calcium channels per presynaptic bouton contribute to vesicle release (Eggermann et al., 2011; Ermolyuk et al., 2012), because a statistical distribution can induce a large variability with small numbers.

Several studies identify problems with GCaMP-transfected neurons that reach beyond the problem of enhanced calcium buffering. Different mouse lines with stable transfection of GCaMP-expression, in which the entire development was affected by the presence of the indicator, show modified neuronal activity with interictal spikes up to epileptiform events (Steinmetz et al., 2017). In AAV-infected mice moderately reduced vesicle release was described in the calyx of Held synapse more than 18 days after transfection (Singh et al., 2018) and accumulation of GCaMP6 in the nucleus occurred in the third week of transfection (Yang et al., 2018). GCaMP6m modifies the gating of Cav1.3 channels, that show enhanced voltage gated activation and calcium-dependent inactivation, which in part resembles the effect of additional apo-calmodulin, but Cav2.2 (N-type) calcium channels were not significantly affected (Yang et al., 2018). These problems have to be considered when using longer transfection periods or studying Cav1.3-dependent calcium effects but are of minor relevance in investigations on fast presynaptic transients.

Despite such drawbacks that almost all fluorescent calcium indicators show, synGCaMP6f provides many advances for the investigation of presynaptic calcium transients. What stands out is the possibility to observe the response of individual presynaptic boutons to short bursts or even single APs. In particular, the response to single APs has the advantage of not being affected by short-term plasticity, retrograde signaling or other secondary processes. This supports the comparison of data from different laboratories. Combined with the superior visibility of cultured neurons, where many synapses are positioned in one optical plane, synGCaMP6f offers a powerful tool for studies on basic presynaptic processes within large numbers of synaptic boutons and without disturbance from postsynaptic activities.

ETHICS STATEMENT

Animal experiments were performed at the University of Münster in accordance with government regulations for animal welfare and approved by the Landesamt für Natur, Umwelt und Verbraucherschutz (LANUV, NRW, Germany), license numbers 84-02.05.20.11.209 and 84-02.04.2015.A423.

AUTHOR CONTRIBUTIONS

JB and MM designed the experiments. JB and BB recorded and evaluated data and prepared the figures. BB performed the immunohistochemistry. JB, BB and MM wrote and edited the manuscript.

FUNDING

This work was supported by grants from the Deutsche Forschungsgemeinschaft (SFB1348-TPA03) and the Interdisciplinary Center for Clinical Research Münster (IZKF Mi3/004/19) and CiM FF-2015-05 to MM.

ACKNOWLEDGMENTS

We are grateful to I. Wolff and K. Kerkhoff for technical assistance with cell culture and mouse genotyping.

REFERENCES

Atluri, P. P., and Regehr, W. G. (1996). Determinants of the time course of facilitation at the granule cell to Purkinje cell synapse. *J. Neurosci.* 16, 5661–5671. doi: 10.1523/jneurosci.16-18-05661.1996

Augustine, G. J. (1994). Combining patch-clamp and optical methods in brain slices. *J. Neurosci. Methods* 54, 163–169. doi: 10.1016/0165-0270(94)90190-2

Augustine, G. J., Adler, E. M., and Charlton, M. P. (1991). The calcium signal for transmitter secretion from presynaptic nerve terminals. *Ann. N. Y. Acad. Sci.* 635, 365–381. doi: 10.1111/j.1749-6632.1991.tb36505.x

Borst, J. G., Helmchen, F., and Sakmann, B. (1995). Pre- and postsynaptic whole-cell recordings in the medial nucleus of the trapezoid body of the rat. *J. Physiol.* 489, 825–840. doi: 10.1113/jphysiol.1995.sp021095

Brockhaus, J., Schreitmüller, M., Repetto, D., Klatt, O., Reissner, C., Elmslie, K., et al. (2018). α-Neurexins together with α2δ-1 auxiliary subunits regulate Ca^{2+} influx through $Ca_v2.1$ channels. *J. Neurosci.* 38, 8277–8294. doi: 10.1523/JNEUROSCI.0511-18.2018

Cao, Y. Q., and Tsien, R. W. (2010). Different relationship of N- and P/Q-type Ca^{2+} channels to channel-interacting slots in controlling neurotransmission at cultured hippocampal synapses. *J. Neurosci.* 30, 4536–4546. doi: 10.1523/jneurosci.5161-09.2010

Chaudhuri, D., Chang, S. Y., DeMaria, C. D., Alvania, R. S., Soong, T. W., and Yue, D. T. (2004). Alternative splicing as a molecular switch for Ca^{2+} /calmodulin-dependent facilitation of P/Q-type Ca^{2+} channels. *J. Neurosci.* 24, 6334–6342. doi: 10.1523/jneurosci.1712-04.2004

Chen, T. W., Wardill, T. J., Sun, Y., Pulver, S. R., Renninger, S. L., Baohan, A., et al. (2013). Ultrasensitive fluorescent proteins for imaging neuronal activity. *Nature* 499, 295–300. doi: 10.1038/nature12354

de Juan-Sanz, J., Holt, G. T., Schreiter, E. R., de Juan, F., Kim, D. S., and Ryan, T. A. (2017). Axonal endoplasmic reticulum Ca^{2+} content controls release probability in CNS nerve terminals. *Neuron* 93, 867–881. doi: 10.1016/j.neuron.2017.01.010

Eggermann, E., Bucurenciu, I., Goswami, S. P., and Jonas, P. (2011). Nanodomain coupling between Ca^{2+} channels and sensors of exocytosis

at fast mammalian synapses. *Nat. Rev. Neurosci.* 13, 7–21. doi: 10.1038/nrn3125

Ermolyuk, Y. S., Alder, F. G., Henneberger, C., Rusakov, D. A., Kullmann, D. M., and Volynski, K. E. (2012). Independent regulation of basal neurotransmitter release efficacy by variable Ca^{2+} influx and bouton size at small central synapses. *PLoS Biol.* 10:e1001396. doi: 10.1371/journal.pbio.1001396

Glebov, O. O., Jackson, R. E., Winterflood, C. M., Owen, D. M., Barker, E. A., Doherty, P., et al. (2017). Nanoscale structural plasticity of the active zone matrix modulates presynaptic function. *Cell Rep.* 18, 2715–2728. doi: 10.1016/j.celrep.2017.02.064

Golding, N. L., Kath, W. L., and Spruston, N. (2001). Dichotomy of action-potential backpropagation in CA1 pyramidal neuron dendrites. *J. Neurophysiol.* 86, 2998–3010. doi: 10.1152/jn.2001.86.6.2998

Helton, T. D., Xu, W., and Lipscombe, D. (2005). Neuronal L-type calcium channels open quickly and are inhibited slowly. *J. Neurosci.* 25, 10247–10251. doi: 10.1523/JNEUROSCI.1089-05.2005

Hoffman, D. A., Magee, J. C., Colbert, C. M., and Johnston, D. (1997). K^+ channel regulation of signal propagation in dendrites of hippocampal pyramidal neurons. *Nature* 387, 869–875. doi: 10.1038/43119

Hoppa, M. B., Lana, B., Margas, W., Dolphin, A. C., and Ryan, T. A. (2012). $\alpha 2\delta$ expression sets presynaptic calcium channel abundance and release probability. *Nature* 486, 122–125. doi: 10.1038/nature11033

Horikawa, K. (2015). Recent progress in the development of genetically encoded Ca^{2+} indicators. *J. Med. Invest.* 62, 24–28. doi: 10.2152/jmi.62.24

Iwabuchi, S., Kakazu, Y., Koh, J. Y., and Harata, N. C. (2014). Evaluation of the effectiveness of gaussian filtering in distinguishing punctate synaptic signals from background noise during image analysis. *J. Neurosci. Methods* 223, 92–113. doi: 10.1016/j.jneumeth.2013.12.003

Jackman, S. L., and Regehr, W. G. (2017). The mechanisms and functions of synaptic functionsacilitation. *Neuron* 94, 447–464. doi: 10.1016/j.neuron.2017.02.047

Jackman, S. L., Turecek, J., Belinsky, J. E., and Regehr, W. G. (2016). The calcium sensor synaptotagmin 7 is required for synaptic facilitation. *Nature* 529, 88–91. doi: 10.1038/nature16507

Johnston, D., Magee, J. C., Colbert, C. M., and Cristie, B. R. (1996). Active properties of neuronal dendrites. *Annu. Rev. Neurosci.* 19, 165–186. doi: 10.1146/annurev.ne.19.030196.001121

Kaeser, P. S., Deng, L., Wang, Y., Dulubova, I., Liu, X., Rizo, J., et al. (2011). RIM proteins tether Ca^{2+}-channels to presynaptic active zones via a direct PDZ-domain interaction. *Cell* 144, 282–295. doi: 10.1016/j.cell.2010.12.029

Kawaguchi, S. Y., and Sakaba, T. (2015). Control of inhibitory synaptic outputs by low excitability of axon terminals revealed by direct recording. *Neuron* 85, 1273–1288. doi: 10.1016/j.neuron.2015.02.013

Kirischuk, S., Veselovsky, N., and Grantyn, R. (1999). Relationship between presynaptic calcium transients and postsynaptic currents at single γ-aminobutyric acid (GABA)ergic boutons. *Proc. Natl. Acad. Sci. U S A* 96, 7520–7525. doi: 10.1073/pnas.96.13.7520

Li, L., Bischofberger, J., and Jonas, P. (2007). Differential gating and recruitment of P/Q-, N- and R-type Ca^{2+} channels in hippocampal mossy fiber boutons. *J. Neurosci.* 27, 13420–13429. doi: 10.1523/jneurosci.1709-07.2007

Lin, M. Z., and Schnitzer, M. J. (2016). Genetically encoded indicators of neuronal activity. *Nat. Neurosci.* 19, 1142–1153. doi: 10.1038/nn.4359

Liu, C., Bickford, L. S., Held, R. G., Nyitrai, H., Südhof, T. C., and Kaeser, P. S. (2014). The active zone protein family ELKS supports Ca^{2+} influx at nerve terminals of inhibitory hippocampal neurons. *J. Neurosci.* 34, 12289–12303. doi: 10.1523/jneurosci.0999-14.2014

McMahon, S. M., and Jackson, M. B. (2018). An inconvenient truth: calcium sensors are calcium buffers. *Trends Neurosci.* 41, 880–884. doi: 10.1016/j.tins.2018.09.005

Miyazaki, K., Ishizuka, T., and Yawo, H. (2005). Synapse-to-synapse variation of calcium channel subtype contributions in large mossy fiber terminals of mouse hippocampus. *Neuroscience* 136, 1003–1014. doi: 10.1016/j.neuroscience.2005.08.049

Nakai, J., Ohkura, M., and Imoto, K. (2001). A high signal-to-noise Ca^{2+} probe composed of a single green fluorescent protein. *Nat. Biotechnol.* 19, 137–141. doi: 10.1038/84397

Neher, E. (1998). Vesicle pools and Ca^{2+} microdomains: new tools for understanding their roles in neurotransmitter release. *Neuron* 20, 389–399. doi: 10.1016/s0896-6273(00)80983-6

Neupert, C., Schneider, R., Klatt, O., Reissner, C., Repetto, D., Biermann, B., et al. (2015). Regulated dynamic trafficking of neurexins inside and outside of synaptic terminals. *J. Neurosci.* 35, 13629–13647. doi: 10.1523/jneurosci.4041-14.2015

Randall, A., and Tsien, R. W. (1995). Pharmacological dissection of multiple types of Ca^{2+} channel currents in rat cerebellar granule neurons. *J. Neurosci.* 15, 2995–3012. doi: 10.1523/jneurosci.15-04-02995.1995

Reese, A. L., and Kavalali, E. T. (2016). Single synapse evaluation of the postsynaptic NMDA receptors targeted by evoked and spontaneous neurotransmission. *Elife* 5:e21170. doi: 10.7554/eLife.21170

Sheffield, M. E., and Dombeck, D. A. (2015). Calcium transient prevalence across the dendritic arbour predicts place field properties. *Nature* 517, 200–204. doi: 10.1038/nature13871

Singh, M., Lujan, B., and Renden, R. (2018). Presynaptic GCaMP expression decreases vesicle release probability at the calyx of held. *Synapse* 72:e22040. doi: 10.1002/syn.22040

Stanley, E. F. (2016). The nanophysiology of fast transmitter release. *Trends Neurosci.* 39, 183–197. doi: 10.1016/j.tins.2016.01.005

Steinmetz, N. A., Buetfering, C., Lecoq, J., Lee, C. R., Peters, A. J., Jacobs, E. A. K., et al. (2017). Aberrant cortical activity in multiple GCaMP6-expressing transgenic mouse lines. *eNeuro* 4:ENEURO.0207-17.2017. doi: 10.1523/ENEURO.0207-17.2017

Südhof, T. C. (2013). Neurotransmitter release: the last millisecond in the life of a synaptic vesicle. *Neuron* 80, 675–690. doi: 10.1016/j.neuron.2013.10.022

Takahashi, A., Camacho, P., Lechleiter, J. D., and Herman, B. (1999). Measurement of intracellular calcium. *Physiol. Rev.* 79, 1089–1125. doi: 10.1152/physrev.1999.79.4.1089

Thalhammer, A., Contestabile, A., Ermolyuk, Y. S., Ng, T., Volynski, K. E., Soong, T. W., et al. (2017). Alternative splicing of P/Q-type Ca^{2+} channels shapes presynaptic plasticity. *Cell Rep.* 20, 333–343. doi: 10.1016/j.celrep.2017.06.055

Tian, L., Hires, S. A., Mao, T., Huber, D., Chiappe, M. E., Chalasani, S. H., et al. (2009). Imaging neural activity in worms, flies and mice with improved GCaMP calcium indicators. *Nat. Methods* 6, 875–881. doi: 10.1038/nmeth.1398

Tsien, R. Y. (1981). A non-disruptive technique for loading calcium buffers and indicators into cells. *Nature* 290, 527–528. doi: 10.1038/290527a0

Tsien, R. Y., Rink, T. J., and Poenie, M. (1985). Measurement of cytosolic free Ca^{2+} in individual small cells using fluorescence microscopy with dual excitation wavelengths. *Cell Calcium* 6, 145–157. doi: 10.1016/0143-4160(85)90041-7

Waters, J., Schaefer, A., and Sakmann, B. (2005). Backpropagating action potentials in neurones: measurement, mechanisms and potential functions. *Prog. Biophys. Mol. Biol.* 87, 145–170. doi: 10.1016/j.pbiomolbio.2004.06.009

Wiegert, J. S., Pulin, M., Gee, C. E., and Oertner, T. G. (2018). The fate of hippocampal synapses depends on the sequence of plasticity-inducing events. *Elife* 7:e39151. doi: 10.7554/elife.39151

Yang, Y., Liu, N., He, Y., Liu, Y., Ge, L., Zou, L., et al. (2018). Improved calcium sensor GCaMP-X overcomes the calcium channel perturbations induced by the calmodulin in GCaMP. *Nat. Commun.* 9:1504. doi: 10.1038/s41467-018-03719-6

Zucker, R. S., and Regehr, W. G. (2002). Short-term synaptic plasticity. *Annu. Rev. Physiol.* 64, 355–405. doi: 10.1146/annurev.physiol.64.092501.114547

Conflict of Interest Statement: The authors declare that the research was conducted in the absence of any commercial or financial relationships that could be construed as a potential conflict of interest.

frontiers in Synaptic Neuroscience

METHODS
published: 16 May 2019
doi: 10.3389/fnsyn.2019.00015

Multiple Two-Photon Targeted Whole-Cell Patch-Clamp Recordings From Monosynaptically Connected Neurons *in vivo*

Jean-Sébastien Jouhanneau[1,2] *and James F. A. Poulet*[1,2]*

[1]*Department of Neuroscience, Max Delbrück Center for Molecular Medicine in the Helmholtz Association (MDC), Berlin, Germany,* [2]*Neuroscience Research Center, Charité-Universitätsmedizin, Berlin, Germany*

Although we know a great deal about monosynaptic connectivity, transmission and integration in the mammalian nervous system from *in vitro* studies, very little is known *in vivo*. This is partly because it is technically difficult to evoke action potentials and simultaneously record small amplitude subthreshold responses in closely (<150 μm) located pairs of neurons. To address this, we have developed *in vivo* two-photon targeted multiple (2–4) whole-cell patch clamp recordings of nearby neurons in superficial cortical layers 1–3. Here, we describe a step-by-step guide to this approach in the anesthetized mouse primary somatosensory cortex, including: the design of the setup, surgery, preparation of pipettes, targeting and acquisition of multiple whole-cell recordings, as well as *in vivo* and *post hoc* histology. The procedure takes ∼4 h from start of surgery to end of recording and allows examinations both into the electrophysiological features of unitary excitatory and inhibitory monosynaptic inputs during different brain states as well as the synaptic mechanisms of correlated neuronal activity.

Keywords: cortex, synapse, whole-cell, two-photon microscopy, *in vivo*

OPEN ACCESS

Edited by:
Dirk Feldmeyer,
Julich Research Centre, Germany

Reviewed by:
Paul Chadderton,
University of Bristol, United Kingdom
Dominique Debanne,
INSERM U1072 Neurobiologie des canaux Ioniques et de la Synapse, France
Szabolcs Oláh,
University of Szeged, Hungary

***Correspondence:**
James F. A. Poulet
james.poulet@mdc-berlin.de

Received: *20 December 2018*
Accepted: *23 April 2019*
Published: *16 May 2019*

Citation:
Jouhanneau J-S and Poulet JFA (2019) Multiple Two-Photon Targeted Whole-Cell Patch-Clamp Recordings From Monosynaptically Connected Neurons in vivo. Front. Synaptic Neurosci. 11:15. doi: 10.3389/fnsyn.2019.00015

INTRODUCTION

Monosynaptic transmission underpins action potential generation and the flow of information within neural circuits. Over the last decades, *in vitro* approaches have provided an enormous amount of data on the connectivity rates and the electrophysiological and anatomical properties of synaptic connections. More recently, a hybrid approach has been developed to link neuronal function, measured *in vivo*, with connectivity, measured *in vitro* (Ko et al., 2011; Cossell et al., 2015; Weiler et al., 2018). There is still, however, a large gap in our knowledge about monosynaptic transmission and the membrane potential (V_m) activity of connected neurons *in vivo*.

In vivo approaches to identify connected pairs of neurons in the mammalian nervous system have typically performed electrophysiological recordings of multiple single neurons and examined the average response of one neuron to spontaneously occurring action potentials in another neuron. "Spike triggered averaging" of cortical neurons has been performed both with multiple extracellular recordings (Reid and Alonso, 1995; Csicsvari et al., 1998; Swadlow and Gusev, 2002; Barthó et al., 2004; Fujisawa et al., 2008; English et al., 2017), a combination of extracellular and intracellular V_m recordings (Matsumura et al., 1996; Bruno and Sakmann, 2006; London et al., 2010; Yu and Ferster, 2013) and dual V_m recordings (Crochet et al., 2005). However, because it is

not yet possible to record the activity of all neurons presynaptic to the cells of interest and cortical neurons can fire simultaneously, it is difficult to confirm whether correlated activity is the result of a direct synaptic connection between the two recorded neurons or input from a third, unrecorded neuron with similar firing dynamics. One approach to get around this problem is to have experimental control of action potential timing using single cell stimulation while simultaneously recording the evoked V_m response from a second neuron. While care has to be taken in concluding that any synaptic response is the result of a monosynaptic rather than polysynaptic input (Berry and Pentreath, 1976; Parker, 2010), this approach has been used *in vivo* to characterize the wiring and functional properties of synaptic connections in a number of non-mammalian species (Burrows, 1996; Parker, 2003; Poulet and Hedwig, 2006; Roberts et al., 2010) as well as in a more limited number of studies in mammals (Crochet et al., 2005; Jouhanneau et al., 2015, 2018; Pala and Petersen, 2015, 2018).

Mapping the synaptic properties and monosynaptic connectivity rates in neocortex has been a central aim of *in vitro* slice studies, with visually guided multiple whole-cell patch clamp V_m recordings being the method of choice (Edwards et al., 1989; Mason et al., 1991; Deuchars and Thomson, 1995; Geiger et al., 1997; Markram et al., 1997b; Feldmeyer et al., 2006; Debanne et al., 2008; Lefort et al., 2009; Yassin et al., 2010; Wozny and Williams, 2011; Wang et al., 2015; Feldmeyer and Radnikow, 2016; Lalanne et al., 2016). The whole-cell recording technique has also been adapted for use *in vivo* (Margrie et al., 2002; Petersen, 2017; Lee and Brecht, 2018), with more recent studies using dual, blind, whole-cell recordings to assess correlations of sub- and supra-threshold V_m activity between pairs of cortical neurons in awake mice (Poulet and Petersen, 2008; Gentet et al., 2010; Zhao et al., 2016; Arroyo et al., 2018). Dual V_m recordings provide a technical basis for testing for monosynaptic connectivity, but the likelihood of two cortical neurons being connected is low, dependent on cell type and negatively correlated with inter-somatic distance (Holmgren et al., 2003; Perin et al., 2011). Therefore, to identify connected pairs of cortical neurons *in vivo*, it would help to be able to record from nearby, genetically labeled neurons using visual control.

Here, we describe in detail an approach using *in vivo* two-photon microscopy to target whole-cell recordings to neighboring, fluorescently labeled layer 2/3 cortical neurons. We show that this technique can be used to evoke action potentials and isolate unitary excitatory and inhibitory postsynaptic potentials in postsynaptic neurons (Jouhanneau et al., 2015, 2018; Ferrarese et al., 2018). A troubleshooting table is provided (**Table 1**) and we go on to discuss potential improvements and future applications of this technique in assessing the link between monosynaptic transmission and cortical function.

MATERIALS AND METHODS

The aim of this article is to provide a description of multiple, two-photon targeted whole-cell patch-clamp recordings to monitor monosynaptic connectivity *in vivo*. The procedure is described for an acute 1-day experiment in anesthetized mice. All experiments were performed according to protocols approved by the Berlin Animal Ethics committee (Landesamt für Gesundheit und Sociales, LAGeSo) and comply with the European animal welfare law.

Two-Photon Microscope

In vivo two-photon microscopy with galvanometric scanning (Femto2D, Femtonics) is used to visualize neurons and the whole-cell recording pipettes (**Figure 1**). The microscope is fixed to an air damped table (Tuned damping table RS 2000, Newport). While our microscope can only move in the vertical Z axis, the experimental equipment, including pipette manipulators and headstages and mouse holder, are mounted on a shifting table (V380FM-L, Luigs and Neumann) allowing horizontal movements in X and Y. Two, photomultiplier tubes (PMTs; GasAsP detectors, Hamamatsu) are used to detect light, one fitted with a 498–570 nm band pass filter and the second with a 598–700 nm band pass filter to enable detection of green and red fluorophores respectively. A CCD camera is coupled to the microscope and used at the start of the experiment to place the electrodes over the region of interest using a 4× objective (UPLFLN 4×, NA 0.13, W.D 17 mm, Olympus). Subsequently, a 40× water immersion objective with a long working distance (LUMPLFLN 40×W, NA 0.8, W.D 3.3 mm, Olympus) is used to target cell soma of interest in a field of view of 200 × 200 μm (0.84 μm per pixel). The tunable (680–1,080 nm), mode-locked Ti:Sapphire laser (Chameleon Ultra II, Coherent) is used to excite a wide range of fluorophores (e.g., GFP, Alexa 488, Alexa 594, tdTomato). The Pockel cell (E.O. Modulator, Conoptics) enables a fine control of the laser beam intensity. To avoid tissue damage during cellular two-photon imaging, we kept the laser power <20 mW under the objective as we observed that damage can occur while targeting neurons with a laser power >20 mW. The microscope is controlled by a Matlab (mathworks) based imaging data acquisition software (MES v4.0 software, Femtonics). Different combinations of pipette and cellular fluorophores can be used. For example, we used the red fluorophore Alexa 594 in the intracellular solution when using mice lines expressing GFP in neurons. Note that because of their different excitation spectra it is possible to use the red fluorophore Alexa 594 in the intracellular solution visible at 820 nm to target neurons expressing td-Tomato which are visible at 950 nm (Jouhanneau et al., 2018). For deeper recordings, soma-restricted expression of fluorescent proteins may help improve depth resolution by reducing neuropil fluorescence (Baker et al., 2016).

Mice

The technique works with both wild type mice and strains expressing fluorescent proteins in subsets of neurons. In this article, we used mice aged between P18 and P30 from C57bl6J, NEX-cre (Goebbels et al., 2006) × Ai9 (Madisen et al., 2010), fosGFP (Barth et al., 2004), GAD67-GFP (Tamamaki et al., 2003), PV-cre (Hippenmeyer et al., 2005) × Ai9, or SST-cre (Taniguchi et al., 2011) × Ai9. Mice were maintained on a 12 h light-dark cycle and had food and water *ad libitum*.

TABLE 1 | Troubleshooting during multiple whole cell patching.

Step	Problem	Possible reason	Solution
Surgery	Edema	Brain surface damaged	Take care when removing the dura as damaging the pia will result in tissue swelling.
		Craniotomy too large	Keep size ∼700 μm^2
		Anesthesia	Isoflurane increases plasma volume which can induce swelling (Hamada et al., 1993). Drill a smaller craniotomy and use 1.2% agarose in Ringer's solution on the craniotomy to damp the swelling. Try using urethane, which does not increase plasma volume as much.
2	Pipettes unable to enter the brain	Dura intact	Attempt to remove the dura.
		Blood vessel in the way	Make sure your brain entry point is clear. The use of green light will help to increase the contrast between blood vessels and brain tissue.
3	Dye not flowing out the pipette	Pipette clogged	Make sure the positive pressure is on before entering the ringer solution this will help maintaining a clean pipette tip. Use a fresh pipette.
		Debris accumulating outside the pipette tip	Precipitate accumulating outside of the pipette could result from a grounding issue. Make sure the Ringer's solution in the recording chamber is not touching the head post.
		Pipette clogged, visible debris inside the pipette	Debris inside the pipette can come from the intracellular solution itself. Use a fresh 0.45 μm syringe filter (Minisart SRP4, Sartorius) for each experiment. Debris can also come from the silver chloride electrode. Make sure the end of the pipettes are flame polished to avoid removing pieces of silver chloride coating. Try clearing the tip of the pipette by increasing briefly the pressure (+50 mbar). If unsuccessful use new pipettes. Do not use clogged pipettes even if the tip resistance is acceptable as it will most likely impair sealing.
		Faulty pressure system	Check air pressure system can maintain a stable pressure.
	No image	Laser off	Turn laser on.
		Shutter closed	Open shutter.
		PMT overload	Check external lights are switched off while the PMTs are on. Reset the PMT.
	Poor imaging quality	High background fluorescence	Decrease the internal pipette pressure to reduce efflux of intracellular solution.
		Leak of Ringer's solution out of the recording chamber	Check the contact between Ringer's solution and the objective. Try fixing the leak with Vaseline.
		Laser power is too high	Small spherical dark spots appearing in the image is a sign of tissue damage caused by high laser power. The quality of the preparation is compromised and experiment should be terminated.
4	Unable to seal	Pipette resistance not optimal	Although lower resistance pipette (<5 MΩ) will give you a better access to the cell it can also decrease sealing success. Aim for pipette resistance of 5–8 MΩ.
		Dirt on pipette tip	Although the resistance of the dirty pipette tip might be in the expected range, visible dirt dramatically reduce chances to seal successfully on neurons. Use a fresh pipette.
		High pressure in Steps 3/4	Decrease the pressure to <30 mBar while approaching the cell. Higher pressure will tend to "push" away the targeted neuron. In addition, in some cases, a slight negative pressure while sealing on the cell might be beneficial.
		Intracellular solution	Check the osmolarity of your internal solution which usually need to be lower than the one of the Ringer's solution.
		Holding potential not set to −70 mV	Make sure the holding potential is set up to −70 mV while sealing on the cell. In some cases, it will help to bring gradually the cell to −100 mV during the sealing procedure and then back to −70 mV before breaking in.
5	Unable to break in	Pipette resistance is too high	Pipette with a resistance higher than 8 MΩ will tend to be more difficult to break in. The optimum pipette tip resistance is between 5–8 MΩ.
		Patched a blood vessel	Blood vessels can look like cell bodies but a fast vertical scan will usually help identify cells from capillaries. Use a fresh pipette.
		Patched on buddle of fibres	In some cases, the pipette might catch on fibres on the way to the cells of interest and even though a giga-seal will be made breaking in will fail. Use a fresh pipette.
		Faulty pressure system	Make sure the pressure system is reactive to your suction. Suction must be brief. If something is damping the change of pressure breaking in will be impaired.

(Continued)

TABLE 1 | Continued

Step	Problem	Possible reason	Solution
Recording	Short duration recordings (<5 mins)	Brain movement	Breathing of the mouse might create movement. Check the position of the mouse head relative to the body. If movement persist use 1.2% agarose ringer solution to stabilize the brain movements, or stop the experiment. Multiple pipettes entering the brain can cause a pressure build up in the surrounding tissue and the tissue will eventually relax to its original position. This may create tension on the seal and sometimes cause the pipette to push through or away from the cell. Visual checking during the recording using two-photon scanning and small adjustments of the pipette position can help stabilize recordings. Isoflurane induces stronger pulsations of the brain than urethane.
		Craniotomy is too large	New experiment with smaller craniotomy. If attempting awake recordings reduce craniotomy size even further.
		Unstable head implant	The head implant may have become loosened due to tissue regrowth or poor gluing. Attempt adding extra glue or new experiment required.
		Location of the pipette relative to the cell of interest	Aim for the most dorsal third of the targeted neuron soma to increase success rate and stability.
	Unable to trigger action potentials	Patched on glial cell	Check firing pattern, glial cells do not spike and typically have a very hyperpolarized V_m with little or no spontaneous input. Change pipette and start over.
		Access resistance is too high	Transiently applying negative pressure to the pipette tip. Slightly increase positive pressure during the final targeting approach. Improve brain stabilization procedure to reduce movement which can increase the access resistance during the recording. Retract and use a lower resistance pipette.
	V_m depolarized	Recording solution	Use fresh Ringer's and intracellular solutions and check osmolarity.
	V_m drift	Reference electrodes	Change or re-chloridize the recording and reference electrodes.
		Metal head implant touching Ringer's solution	Isolate head implant from Ringer's solution in recording chamber.
	No spontaneous activity	Anesthesia level too high	Reduce isoflurane levels.
		Body temperature is too low	Adjust the temperature controller.

Surgery

To expose the brain for recordings, mice are first anesthetized with 1.5% isoflurane and show an absence of tail pinch reflex and whisker movements. Eye ointment (Bei trockenen Auge, Visidic) is used to protect the eyes and body temperature is maintained using a closed loop system with rectal probe and heating pad (DC Temperature controller, FHC). All tools are cleaned and dry heat sterilized using hot glass beads sterilizer (Steri 250, Keller, Fine Science Tools) prior to surgery. The head is shaved, skin removed and skull cleaned, if necessary, intrinsic optical imaging through the skull can be performed at this stage if functional localization of recording site is required. The connective tissue is carefully removed using forceps and micro-scissors (Fine science Tools) and the skull is cleaned using a microcurette (Fine science Tools) to remove any remaining tissue on the surface of the bone. A solution of 3% hydrogen peroxide (H_2O_2) can be applied for 30 s at this stage to help clean the exposed bone surface, however, the bone can also be cleaned by gently scraping the bone with a razor blade. Next, the skull is washed thoroughly with Ringer's solution (in mM: 135 NaCl, 5 KCl, 5 HEPES, 1.8 $CaCl_2$, and 1 $MgCl_2$135 NaCl, 5 KCl, 5 HEPES, 1.8 $CaCl_2$, and 1 $MgCl_2$) and thoroughly dried. Avoiding the recording site, the exposed skull is then lightly scratched with a 25G syringe needle to create grooves in the skull. It is important to remove any remaining hairs or dirt at this stage to avoid possible infection. Next, glue (Loctite 401) is applied first at the edges of the exposed skull, to glue the skin to the bone, and then to the entire exposed skull surface avoiding the recording site. A lightweight metal head implant is then placed on the hemisphere contralateral to the recording site and covered with glue. To secure the head implant, dental cement is applied on top of the entire layer of glue. As the dental cement viscosity increases, a recording chamber with access for the recording pipettes can be modeled around the area of interest using a spatula. It is important to completely cover the head implant with glue and dental cement to avoid any possible contact between the Ringer's solution and the metal of the head implant during the recording which can lead to electrical noise and voltage offsets.

Once hardened, the recording chamber is filled with Ringer's solution. After a few minutes, the skull will become translucent and the blood vessels visible. Then, the Ringer's solution should be removed to let the bone dry and a 500 μm diameter dental drill head (Komet, Brassler) operated by a dental drill (Success 40, Osada) is used to thin the skull over the recording site. The ideal craniotomy size is ∼700 μm^2 for anesthetized mice; note that a craniotomy exceeding 1 mm in diameter will impair recording stability (see **Table 1**). Drilling is stopped as soon as blood vessels become clearly visible through the bone. This corresponds to a bone thickness of ∼50 μm (Papadopoulos et al., 2017). Bone dust is removed with wet tissue paper and the chamber is refilled with Ringer's solution. A 30G syringe needle is used to pick away the final layer of bone with great care. Next, a durectomy is made using a smaller diameter needle (e.g., 29G), with a handmade small hook at the tip of the needle. Adjusting the angle of illumination of the craniotomy is key to visualizing the dura (∼30°). The handmade hooked-tip of the needle is used to gently lift the dura away from the future spot of pipette insertion.

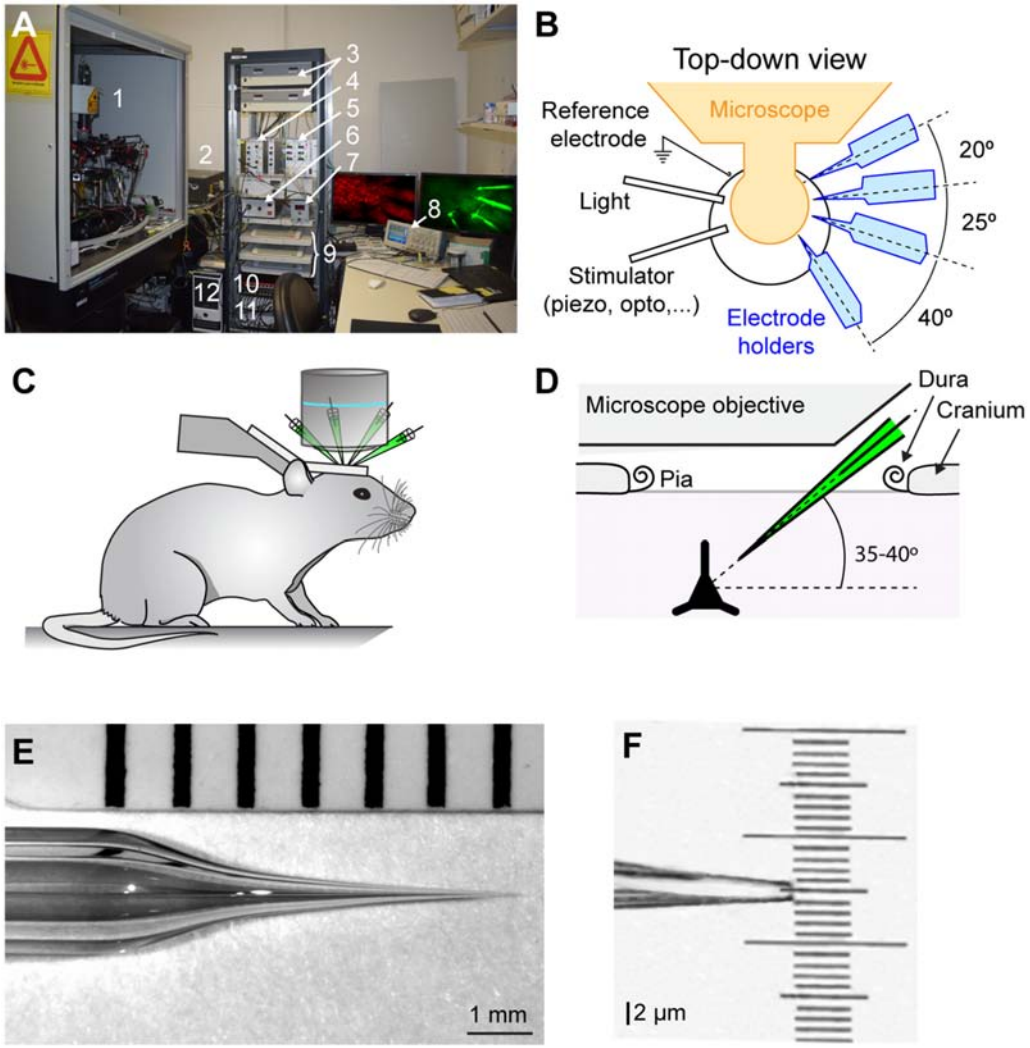

FIGURE 1 | *In vivo* two-photon targeted multiple whole-cell patch-clamp setup. **(A)** Photograph of the setup showing: (1) two-photon microscope, micromanipulators and pre-amplifier fixed on an air-damped table; (2) Chameleon Ultra II laser; (3) Luigs and Neumann micromanipulator control units; (4) Sigmann Electronik air pressure controller; (5) Sigmann Electronik dual piezo amplifier; (6) light source to illuminate the preparation; (7) FHC temperature controller for anesthetized experiments; (8) Tektronix Oscilloscope; (9) Luigs and Neumman micromanipulator and shifting table control pads; (10) ITC-18 Heka analog to digital converter board; (11) Multiclamp 700B amplifier; and (12) data acquisition computer. **(B)** Schematic top-down view of recording area showing arrangement of electrode holders, light, reference electrode and somatosensory/optogenetic stimulator. Note that all the recording electrodes are on the same side for ease of targeting and to allow space on the contralateral side for stimulation devices. **(C)** Cartoon showing mouse position and head support. **(D)** Schematic showing the angle of pipettes defined by the X-axis used to allow access under the objective. **(E)** Photograph of the glass recording pipette showing optimal taper for *in vivo* two-photon targeted patch-clamp recording. **(F)** Photograph showing a zoom of the pipette tip from **(E)**.

Whole-Cell Pipettes and Electrophysiological Equipment

We use a four-step pulling custom program on a Sutter puller (Model P-1000, Sutter instrument) with 2 mm diameter borosilicate capillaries (Hilgenberg) to pull 5–8 MΩ pipettes. The first two steps of the pulling program are identical and used to create a taper of ∼6 mm, the third step is short and design to decrease the diameter of the capillary, and finally, the fourth step is used to create a tip of ∼2 µm (**Figures 1E,F**). The taper is slightly longer than that typically used *in vitro* to avoid causing excess pressure on surrounding tissue and possible damage. Three to four pipettes are filled with intracellular solution containing, in mM: 135 potassium gluconate, 4 KCl, 10 HEPES, 10 phosphocreatine, 4 MgATP, 0.3 Na3GTP (adjusted to pH 7.3 with KOH), 25 µM Alexa-594 (Invitrogen) and 2 mg/ml biocytin. Pipettes are next fixed to a pipette holder (Molecular Devices) mounted on a LN Junior 3-axis (X, Y, and Z) micromanipulator with low drift and a long traverse path (up to 22 mm on the X-axis) where the X-axis is angled at 35–40° (**Figure 1D**; Luigs and Neumann). An Ag/AgCl ground electrode is next placed into the recording chamber filled with Ringer's solution and electrophysiological signals are amplified

using Axon Instruments amplifiers Multiclamp 700B (Molecular Devices). The analog signals recorded are filtered at 10 kHz and digitized at 20 kHz using the analog/digital converter ITC-18 board (Heka) and IgorPro (Wavemetrics) running on a Windows PC. For online visualization of the electrophysiological signal, we use an oscilloscope (Tektronix TDS2024C). To allow easier and faster access to the exposed brain and space for stimulators on the contralateral side, all pipettes are positioned on one side of the preparation (**Figure 1B**).

Multiple Two-Photon Targeted Whole-Cell Patch Clamp Recordings

As soon as the pipettes are inserted into the pipette holders, a 180–200 mbar positive pressure is applied *via* a syringe. A manual-seal-sucker (Sigmann Elektronik GmbH) manometer is used to monitor the pressure applied to all channels independently. All electrodes are moved into the Ringer's solution in the recording chamber in voltage-clamp seal-test mode to monitor the pipette tip resistance on the oscilloscope.

Step 1: Positioning Above Brain (Figure 2A)

Using the low magnification 4× objective with green light illumination and the CCD camera, the pipettes are placed under positive pressure (∼200 mbar) into the Ringer's solution and then the tips are moved to within ∼20–30 μm apart from each other and ∼300 μm above the craniotomy. At this time, the pipette resistance is checked (5–8 MΩ; see **Table 1**). Then, by switching to the higher magnification 40× objective, the Ringer's solution comes in contact with the objective and the pipettes tips are moved to the same focal plane. The coordinates of the pipette micromanipulator control pads are reset to zero. Next, we use the experimental stage micromanipulators (X and Y axis) and the objective focus (Z axis) to inspect the brain surface and find an entry point clear from large blood vessels, dirt or irregular surfaces. Clean entrance of the pipettes into the brain is critical for successful patching. The coordinates of the manipulator units controlling the stage are noted at the selected insertion point as a reference to help guide the movement of the pipette tips onto the brain surface. Next, the focus is moved back up to the pipette tips which are then carefully aligned. The focal plane is moved to the brain surface and the pipettes are lowered vertically one by one using a medium control sensitivity of the micromanipulator control pads (28 μm per handwheel rotation). As the pipettes are lowered, slight lateral movements are performed to help visualize the shadow of the tips. Because of the positive pressure applied to the pipette, as soon as the pipette gets into contact with the brain a clear depression can be seen on its surface which will coincide with a sudden increase in resistance of about ∼20% of the peak value (as observed by a decrease in the current step amplitude on the oscilloscope). At this point, the pipette micromanipulator control pad values are reset to zero.

Step 2: Entering the Brain (Figure 2B)

Using the highest sensitivity speed on the micromanipulator (3 μm per handwheel rotation), the pipettes are slowly moved through the pia one-by-one. During insertion into the brain, the pipette resistance will gradually increase and then suddenly return to their initial value as they break throughout the pial surface. Then the pressure is reduced to 70–90 mbar. Next, two-photon imaging is used to move the pipette tips to −50 μm depth using the X-axis focus. Because of the positive pressure, the dye (Alexa-594) contained in the intracellular solution will diffuse into the neuropil and highlight blood vessels, cell soma and dendrites as dark "shadows" allowing targeting cells of interest even in wild type mice (Kitamura et al., 2008). Care should be taken during this step not to use high laser power as it may cause tissue damage (see **Table 1**).

Step 3: Targeting Cells of Interest (Figure 2C)

Having lowered the pressure to 70–90 mbar, the pipettes are then moved one-by-one to a depth of −150 to −200 μm (border of cortical layers 1 and 2) using the highest sensitivity movement setting. During pipette travel through the brain, great care is taken to avoid cells bodies and capillaries using both visual control from the two-photon imaging and the seal test pulse on the oscilloscope. In wild-type mice, without expression of fluorescent proteins, the contrast between the dye in the neuropil and the dark unlabeled cells, the shadow patching technique (Kitamura et al., 2008), can be used to target neurons of interest. With experience, the dendritic shape of the cell can help identify excitatory from inhibitory neurons. Lateral movement should be kept to a minimum with a maximum of 100 μm per pipette. Then the pressure is decreased to 30 mbar and the pipette micromanipulator controls are switched to a stepping mode (2 μm per step).

Step 4: Sealing (Figure 2D)

The final approach and seal is performed sequentially, one pipette at a time. The pipette voltage offset is set to 0 mV and the first pipette tip is lowered using 2 μm steps onto the cell membrane using the X-axis while watching the oscilloscope closely to observe changes in tip resistance. The sign of a good contact between the pipette tip and the neuron membrane is when the seal test pulse rapidly reduces in amplitude and fluctuates with a wave-like pattern. In contrast, an abrupt and sustained reduction in pulse amplitude (i.e., resistance increase) without fluctuations is typical of a contact with a capillary. Good contact can sometimes be visualized during two-photon scanning as a small, expanding, fluorescent dimple in the cell membrane. As soon as a good first contact has been observed, one or two further steps are made and the positive pressure immediately released followed by a transient negative pressure to optimize the seal. V_m holding voltage is immediately placed at −70 mV to help improve seal. Typically, this leads to a large reduction in the amplitude of the test pulse and the formation of a giga-seal, however light manual suction is sometimes required to improve the quality of the seal and/or transiently hyperpolarizing the cell to −100 mV. This procedure is then repeated with the other pipettes one after the other.

Step 5: Whole-Cell Configuration (Figure 2E)

When all the pipettes are sealed onto the targeted neurons, a brief and gentle suction is used to break the membrane and enter whole-cell configuration. With the whole-cell configuration established, we next slowly retract each pipette away from the cell body ∼5 μm using the axis used for the final approach to the

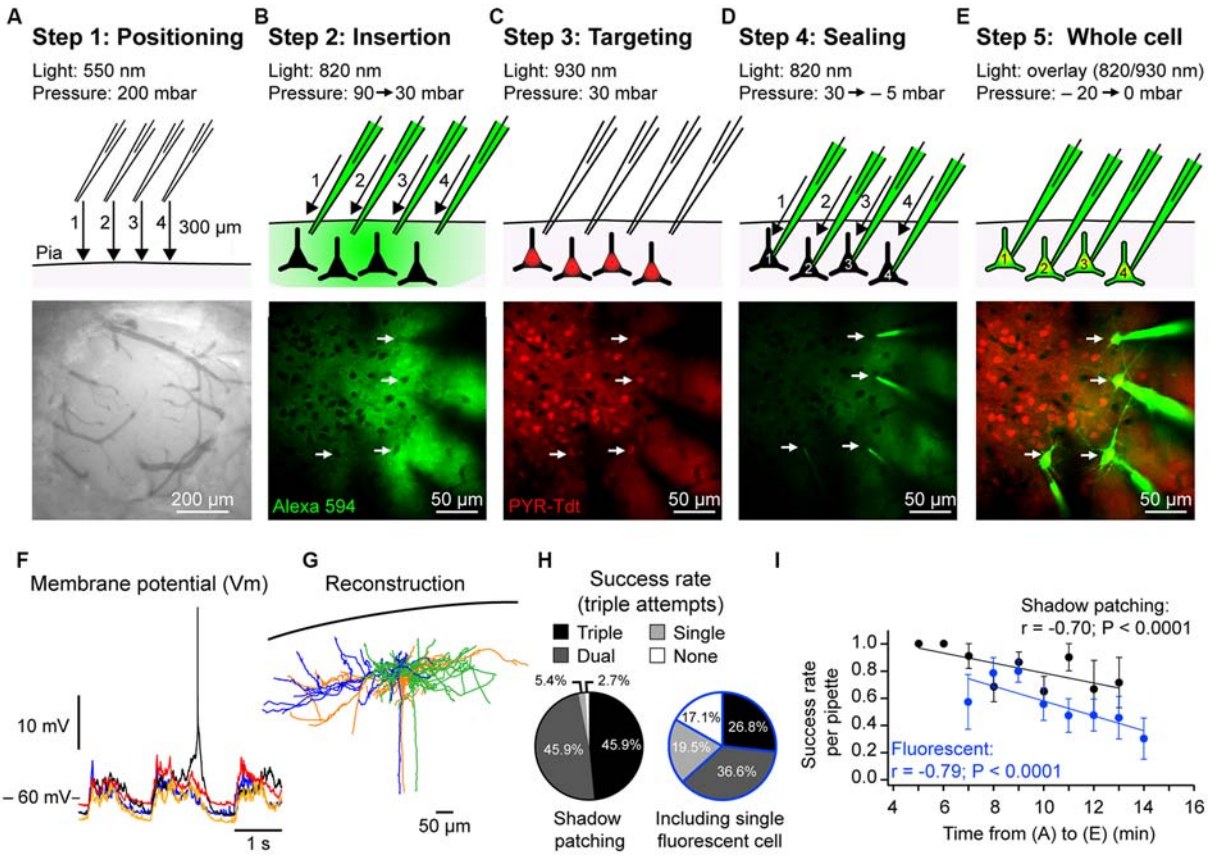

FIGURE 2 | Two-photon targeted whole-cell patch-clamp procedure. **(A)** Step 1. Top: schematic showing position, movement direction (arrow) and movement order (1–4) of dye-filled (Alexa 594) recording pipettes from ∼300 µm above the craniotomy to the brain surface, high positive pressure is maintained to avoid pipette tip clogging. Bottom: photograph taken using a CCD camera illuminated with green light showing example craniotomy used for anesthetized patching (∼500 µm diameter) in which the dura has been removed. **(B)** Step 2. As in **(A)**, but showing, top: the insertion of the pipettes through the pia under visual control (820 nm) using high positive pressure to ∼−100 µm from pial surface. As soon as the pipettes enter the brain the pressure is reduced to 100 mbar and then 30 mbar when closer to the cell body positions. Bottom: *in vivo* two-photon image showing the position of four pipettes in the same focal plane near the cell bodies of interest. Positioning is performed sequentially, one pipette at a time. Cell bodies are revealed as dark shadows contrasting with the fluorescent signal of the extracellular dye. **(C)** Step 3. Top: the targeting phase where the excitation light wavelength is altered to visualize the cells of interest; in this case, excitatory glutamatergic neurons expressing the red fluorophore tdT (white arrows). Bottom: *in vivo* fluorescent image of pyramidal neurons (PYR) expressing tdT corresponding to the photo in **(B)**. **(D)** Step 4. Top: the final sealing phase of the procedure. A recording pipette is pushed into the cell soma membrane and then, upon strong contact, the pressure is released to achieve a giga-seal. The cells are sealed sequentially under visual control. Bottom: *in vivo* image following sealing of all four pipettes. Note the reduction in background fluorescence during sealing because of the reduction in extracellular dye. **(E)** Step 5. Top: entering whole-cell configuration following seal-breaking by applying a transient negative pressure. As soon as the membrane patch is ruptured the dye within the pipettes will fill the neurons. Bottom: *in vivo* image of neurons filled with Alexa 594 (pseudo-colored) after the recording experiments. **(F)** Simultaneous example *in vivo* whole-cell V_m recordings of the four excitatory pyramidal neurons shown in **(E)** showing spontaneous activity with Up- and Down-states under urethane anesthesia. **(G)** *Post hoc* reconstruction of three biocytin-filled excitatory pyramidal neurons from a multiple whole-cell recording. **(H)** Proportion of triple, double, single and no recordings from trials using three pipettes in (left) wild type mice using the shadow patching method and (right) in mice expressing a cell type-specific fluorophore (PV-cre x Ai9 and SST-cre x Ai9). Data from fluorescent mice included at least one fluorescent neuron in the single/double/triple recordings. **(I)** Plots showing the negative correlation between the success rate of achieving a whole-cell patch clamp recording in wild type and fluorescent mice (same data as in **(H)**) and the time taken from phases **(A)** to **(E)** described above. Each dot represents the mean success rate for a 1 min time bin from 15 wild type mice (37 trials) and 18 mice expressing fluorescent proteins (SST-cre × Ai9 and PV-crex Ai9; 42 trials).

cell. All recordings are then switched to current clamp mode for V_m recordings.

Intracellular Current Injection

After allowing the cells to recover (∼2–3 min), we next use intracellular current stimulation protocol to characterize their intrinsic properties. In our experiments, each neuron receives 500 ms square current injections ranging in the amplitude of −200, −100 pA, and then 50, 100, 150, 200 pA. This helps define rheobase, intrinsic excitability, and firing pattern of the recorded neurons. Next, hyperpolarizing current pulses of −100 pA, 200 ms duration, 200 ms interval, are applied for 30 s to determine the input resistance followed by 30 s without stimulation to record spontaneous sub- and supra-threshold activity. The access resistance should be <50 MΩ, high access resistance can make it difficult to inject sufficient current to

evoke single spikes, filters action potential recordings and makes estimation of the V_m during current injection problematic. Next, we define the square current pulse amplitude necessary to drive the recorded neuron to fire a single action potential. We aim to use the smallest duration possible, usually between 10 and 15 ms of 100–400 pA amplitude, however higher amplitude and shorter duration pulses could be attempted. After establishing these parameters, we stimulated at 0.5 or 1 Hz (**Figure 3C**).

There was no tonic current injection applied during the recording to avoid misestimation of the V_m due to possible changes in the access resistance during the recording. Recordings are terminated when the most hyperpolarized sections of the Downstate V_m are more depolarized than −50 mV. Due to differences in ionic concentration, valency and mobility between the intracellular and extracellular solution, a Liquid Junction Potential (LJP) will be established when the pipette enters the recording chamber (Barry and Lynch, 1991). The LJP can be ∼10 mV and is complex to calculate accurately *in vivo*, therefore, to avoid miscalculation, we do not subtract the LJP from the recorded values.

Identifying a Connection

In anesthetized Downstates or during hyperpolarized phases of network activity in awake animals, even small amplitude (0.1–0.5 mV) monosynaptic connections can typically be observed by eye in single trials. However, online, running averages of the postsynaptic response to an evoked spike helps monitor the presence of a connection as well as the quality of the recording. To confirm the presence of a connection *post hoc*, we used a non-parametric two-tailed Wilcoxon signed rank test comparing trial-by-trial amplitude measurements of the connection with shuffled measurements. We also used a bootstrapping method in which we compared a randomly selected, with replacement, amplitude measurements from the individual trial responses with those from shuffled measurements of amplitude. Next, we calculated the mean response amplitude and the mean shuffled, noise amplitude from the bootstrapped distributions. To obtain the 95% confidence intervals, we then repeated this process 10,000 times (see Jouhanneau et al., 2015).

Anatomy: Live Fluorescent Two-Photon Imaging and *Post Hoc* Biocytin Staining

During a successful recording, the fluorophore Alexa 594 diffuses into the neurons and allows live visualization of the cell's anatomy (**Figures 2E**, **3A,E**). Stacks of scans at 820 nm wavelength separated by 2 μm can help identify the cell type using the somatic and dendritic anatomy as well as the presence of dendritic spines. However, for higher resolution, anatomical reconstruction mice are deeply anesthetized with an i.p. injection of urethane (2.5 g/kg, Sigma-Aldrich) before being transcardially perfused with cold Ringer's solution and then by 4% paraformaldehyde solution (PFA, Roti-Histofix 4%, Roth). After perfusion, the brain is removed and placed in 4% PFA overnight at 4°C and then in phosphate buffer (Roti-CELL 10× PBS, Roth) and stored at 4°C until further processing.

Tangential slices of 100 μm are cut using a Leica VT1000 S vibratome and stored in phosphate buffer. Intracellular staining with biocytin is then revealed using a standard ABC kit (Vectastain Elite ABC-Peroxidase kit, Biozol), with diaminobenzidine (DAB, Vector lab) enhancement. Treated slices are mounted on glass slides using a gel mounting agent (Moviol, Sigma-Aldrich), sealed with nail polish and stored at 4°C. Reconstructions of the recorded neurons are performed using the software NeuroLucida (MicroBrightField; **Figure 2G**).

Success Rates

We next calculated the success rates of our approach during patching of layer 2 neurons (depth: −182.0 ± 2.5 μm; distance: 39.0 ± 1.8 μm) in 37 trials, each trial corresponding to one insertion of three pipettes into the brain, in 15 anesthetized wild-type mice (males, 22.0 ± 0.3 days-old) using the shadow patch method performed by a trained researcher. We calculated the number of times we were unsuccessful or obtained a single, dual or triple whole-cell recording. In 17/37 trials we obtained a triple recording, in 17/37 trials a dual, in 2/37 single and in 1/37 no recordings (**Figure 2H**). Thus in 92% of shadow patching trials using three pipettes, we obtained at least a dual recoding that would allow a connectivity test. We then repeated this analysis for attempted triple recordings (three pipettes) in mice expressing a fluorescently labeled indicator in a subset of GABA-ergic interneurons (PV-tdT or SST-tdT), where a successful recording trial had to include a least one fluorescently labeled neuron. In 11/41 trials from 18 mice, we obtained a triple recording, in 15/41 trials double, 8/41 single (i.e., one tdT labeled neuron recorded) and were unsuccessful in 7/41 attempts (**Figure 2H**). Thus, in 63% of trials with fluorescently labeled mice, we obtained at least a dual recording including one fluorescent GABA-ergic neuron to allow for a connectivity test.

During these experiments, we noticed that for trials that took longer it seemed harder to perform a successful whole-cell recording. From our triple recording dataset in **Figure 2**, we therefore systematically recorded the time to go from Step 1 (positioning above brain) to Step 5 (whole-cell recording). Plotting the time taken against the success rates of successfully patching one neuron showed a significant negative correlation and confirmed that reducing the time taken to patch improves success rates for patching (**Figure 2I**). In a different set of experiments where the recordings were not terminated prematurely and the Downstate V_m was ≤50 mV, we calculated a mean recording time of 15 ± 6 min (n = 143 cells) with a minimum recording time of 5 min and a maximum of 32 min.

In vivo Glutamatergic Excitatory Monosynaptic Inputs to Excitatory Pyramidal Neurons and GABA-ergic Inhibitory Interneurons

During slow-wave sleep and under anesthesia, the V_m of cortical neurons fluctuates between hyperpolarized, synaptically quiescent, Downstates and depolarized, synaptically active, Upstates (Steriade et al., 1993). We first examined synaptic transmission between excitatory pyramidal neurons in

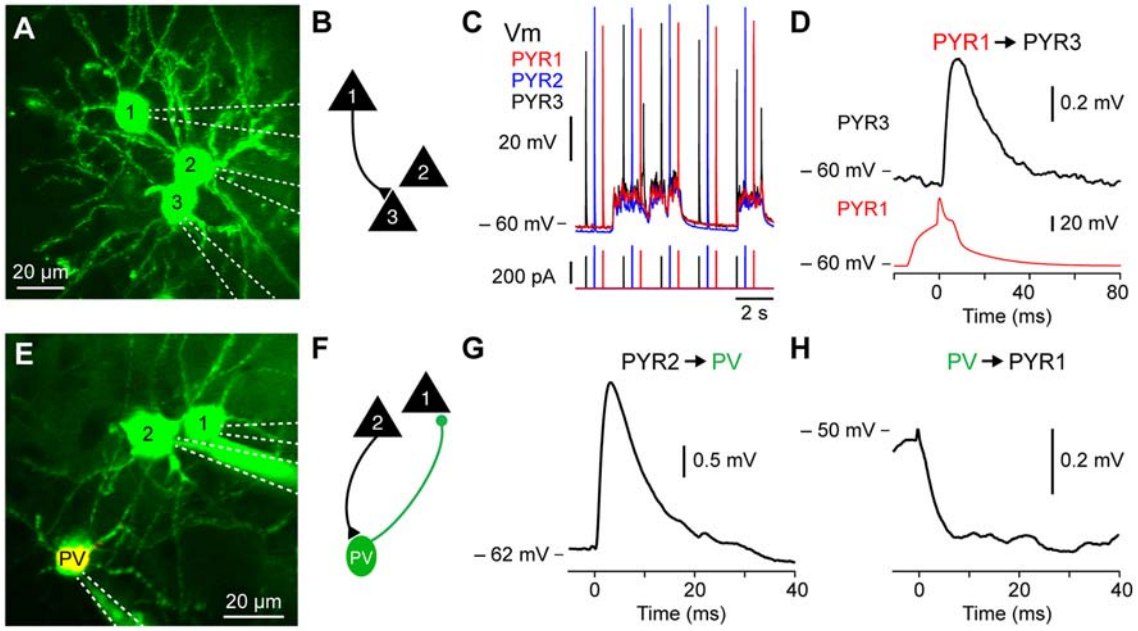

FIGURE 3 | Excitatory and inhibitory monosynaptic connections *in vivo*. **(A)** *In vivo* two-photon fluorescent imaging of three excitatory pyramidal neurons filled with Alexa 594 pseudo-colored. **(B)** Connectivity diagram of experiment shown in **(A)** where PYR1 is connected to PYR3. **(C)** V_m fluctuation of the pyramidal neurons recoded in **(A)** showing the stimulation protocol consisting of brief current injection to evoke single action potentials in each neuron every 2 s. **(D)** Example monosynaptic excitatory connection from PYR1 to PYR3 shown in **(A–C)**. **(E)** *In vivo* image of a triple recording including a PV-tdT expressing GABA-ergic inhibitory interneuron. **(F)** Connectivity diagram of experiment from the triple recording shown in **(E)** where an excitatory pyramidal neuron PYR2 is connected to PV-tdT expressing GABA-ergic inhibitory PV, while PV sends an inhibitory monosynaptic connection to the excitatory pyramidal neuron PYR1. **(G)** Excitatory monosynaptic connection from PYR2 to PV shown in **(E,F)**. **(H)** Inhibitory monosynaptic connection from PV to PYR1 shown in **(D)**.

Downstates. In wild type mice, pyramidal neurons were targeted using their pyramidal shaped soma and apical trunk visible as shadows against the fluorescent extracellular space and after each successful recording, confirmed using Z-stack images to visualize the somatic and dendritic morphology (e.g., spines). Moreover, we used transgenic mice expressing fluorophore in excitatory pyramidal neurons (PYR) using offspring of the NEX-cre line crossed with the Ai9 reporter mouse to study PYR to PYR monosynaptic connectivity. To trigger spikes and measure synaptic transmission we depolarized each neuron with injection of a short depolarizing current 100–400 pA of 20–50 ms duration at 0.5 or 1 Hz to evoked a single action potential and used spike-triggered averages to look at the corresponding unitary excitatory postsynaptic potential ($_u$EPSP) (**Figures 3A–D**). To study short term synaptic dynamics, multiple action potentials could be triggered by increasing the current duration number and time.

We went on to use the same approach to examine excitatory connections from PYRs to different subtypes of GABA-ergic inhibitory interneurons (INTs) including parvalbumin (PV), somatostatin (SST) and vasoactive intestinal polypeptide (VIP) expressing neurons (**Figures 3E–G**). The PV-cre, SST-cre and VIP-cre mice were crossed with the Ai9 reporter line to visualize the subpopulation of GABA-ergic neurons of interest. The approach to target recordings of interneurons is technically similar to that of excitatory neurons. However, in some cases, during the sealing step, the positive pressure was lower than usual (∼10 mbar) in order to target small diameter neurons like VIP interneurons. For further details on inputs to PV and SST interneurons *in vivo* see Jouhanneau et al. (2018).

Using this approach, we found that barrel cortex layer 2 excitatory pyramidal neurons had a connectivity rate of 6.7% (Jouhanneau et al., 2015), while connections from excitatory pyramidal neuron to PV neurons was 44.4% and to SST neurons was 43.6% (Jouhanneau et al., 2018). For further details see Jouhanneau et al. (2015, 2018).

Inhibitory Monosynaptic Connections to PYRs and INTs *in vivo*

We next used multiple two-photon targeted patch-clamp recordings to examine inhibitory monosynaptic neurotransmission from GABA-ergic INTs to PYRs (**Figures 3E,F,H**). The connectivity rate from layer 2 barrel PV neurons to excitatory neurons was 60.6% and from SST neurons to excitatory neurons 47.1% (see Jouhanneau et al., 2018). The recording procedure is similar to that described above, but because interneurons often have a higher input resistance, small amplitude and shorter duration current steps are used to trigger single action potentials. Moreover, because of their hyperpolarized reversal potential, $_u$IPSPs are more visible at more depolarized postsynaptic V_m values. This was evident in our recordings, where the amplitude of $_u$IPSPs was larger in Upstates compared to Downstates (see Jouhanneau et al., 2018).

DISCUSSION

Understanding the link between monosynaptic connectivity and the functional properties of cortical neurons is a key goal of neuroscience. Here, we have described an approach that allows V_m recordings of monosynaptically connected cortical neurons *in vivo*. The setup uses a standard *in vivo* two-photon microscope, whole-cell patch clamp amplifiers and motorized micromanipulators. With training, multiple whole-cell recordings of neurons in layer 2 can be performed with a success rate of forming a dual recording of ∼90% and recording duration (∼15 min) similar to single electrode, blind, *in vivo* patch clamp recordings. Perhaps the key indicator of patching success is an unhindered pipette entrance into the brain and rapid progress through the tissue (**Figure 2**). In **Table 1**, we have outlined a list of common problems with targeted patch-clamp recordings and possible solutions. Here, we discuss the key features, limitations and future perspectives for multiple, targeted *in vivo* whole-cell recordings.

Increasing the number of pipettes per trial helps test more possible connections with two pipettes allow the testing of two possible connections, three allowing six tests and four 12 tests. More pipettes provide an opportunity to not only to improve the changes of identifying a connection but also look at higher order connectivity motifs (Guzman et al., 2016; Peng et al., 2017). While we have successfully used four pipettes to obtain quadruple whole-cell recordings (**Figures 2A–E**), our data on success rates (**Figures 2H,I**) was taken from a series of experiments using three pipettes. In wildtype mice, during shadow patching, four pipettes or more could be a significant advantage to help increase the yield of recorded cells. However, for targeting fluorescently labeled subsets of neurons, the experimenter needs to weigh the advantage of using a fourth pipette against the extra time taken to insert four pipettes into the brain and target the labeled neurons.

A limitation of our approach is the use of anesthesia during the recording session. While multiple whole-cell recordings have been performed in awake animals (Poulet and Petersen, 2008; Gentet et al., 2010; Zhao et al., 2016; Arroyo et al., 2018), little data exists on monosynaptic transmission in awake animals (Jouhanneau et al., 2018; Pala and Petersen, 2018). The increased movement of the brain in awake animals not only limits the chances of forming a seal between the pipette and the cell membrane but also reduces the recording duration preventing longer-term plasticity protocols (e.g., spike timing dependent plasticity (Bell et al., 1997; Markram et al., 1997a). The use of agarose or glass cover slips on the brain surface helps reduce movement during imaging experiments and can be used for targeted whole-cell recordings. Moreover, having the mouse standing on a trackball or platform with suspension can help reduce the pressure exerted on the head during leg movements. Together, these approaches may help stabilize the brain for longer duration recordings both in anesthetized and awake mice.

The approach presented above focusses on recordings from superficial layer cortical neurons. Moreover, as with the vast majority of cortical slice work, the neurons targeted were closely positioned (<150 μm apart). It is important to examine synaptic transmission between deeper and more distant neurons, perhaps even in different cortical regions. Electrodes can easily be positioned to target different parts or depths of the brain, but both the depth and field of view are determined by the optical properties of the microscope. The combination of cell type-specific mouse lines (Gerfen et al., 2013; Harris et al., 2014; Daigle et al., 2018) with improved depth resolution two-photon microscopes (Papadopoulos et al., 2017) has provided optical access to granular and infragranular layers and may make multiple targeted recordings possible in deeper layers. Moreover, new two-photon microscope designs with larger fields of view could allow experimenters to examine neurons situated 1,000s of micrometers apart (Sofroniew et al., 2016; Stirman et al., 2016). Even with improved microscopes, however, the scattered fluorescence from the extracellular dye puffed out during patching remains a problem for accurate visualization of the pipette tip and targeted recordings. One possibility may be to use a coating material on the pipette tip to limit light scatter and improve contrast of the tips (Andrásfalvy et al., 2014).

Cortical excitatory neurons are sparsely connected and therefore a key limitation to the throughput of any connectivity study is to find and record from connected pairs. Both *in vitro* and *in vivo* studies are normally made blind to connectivity which can lead to many frustrating recordings from unconnected neurons. One way to address this is to increase the numbers of recording pipettes to allow the testing of more connections per recording session. This has been successfully implemented *in vitro* (Perin et al., 2011; Peng et al., 2017), but will require more challenging surgery and manipulation of the pipettes *in vivo*. Another approach could be to use transsynaptic tracing to visualize connected pairs prior to recording (Wickersham et al., 2007). So far, however, single cell initiated transsynaptic tracing has been used with sequential rather than simultaneous anatomical tracing (Vélez-Fort et al., 2018), or calcium imaging (Wertz et al., 2015) of presynaptic neurons. With the development of less toxic rabies viruses variants (Reardon et al., 2016; Ciabatti et al., 2017), however, this approach could now be attempted with simultaneous recordings from pre- and post-synaptic neurons.

Our approach allows a limited number of cells (2–4) to be tested for putative connections, but cortical neurons integrate synaptic inputs from thousands of presynaptic neurons. To investigate synaptic integration further, it will be important to be able to activate unitary monosynaptic inputs from more than one neuron with high temporal precision. The recent development of *in vivo* single cell optogenetic stimulation (Rickgauer et al., 2014; Packer et al., 2015), has provided a way to activate multiple single neurons with high resolution spatial and temporal patterns. A combination of this technique with *in vivo* whole-cell recordings to monitor small amplitude subthreshold synaptic inputs could provide an exciting method to investigate the integration of multiple unitary inputs *in vivo*.

An *in vivo* patch clamp recording session can be slow, especially when learning the technique or using multiple electrodes. In particular, the replacement of old pipettes with unused ones at each new recording attempt takes up valuable time. A recent study has circumvented this problem with the

use of a commercially available detergent and rinsing procedure (Kolb et al., 2016). This allowed the reuse of the same pipettes with no degradation in signal fidelity both *in vitro* and *in vivo*. Robotic assistance to move the pipettes also may help speed up this process and has recently been implemented for the entire visualized patching process (Annecchino et al., 2017; Suk et al., 2017).

The whole-cell technique allows intracellular access to the recorded neurons and future work could make a more detailed anatomical and genetic characterization of the recorded neurons. For example using single-cell RNA sequencing (Jiang et al., 2015; Cadwell et al., 2016; Fuzik et al., 2016; Muñoz et al., 2017; Boldog et al., 2018) or higher resolution bright field (Feldmeyer et al., 2006) or electron microscopic (Fernández et al., 1996) anatomical analysis of the recorded synaptic connections.

The craniotomy and glass recording pipette exposes the brain and requires the use of extracellular Ringer's solution as well as an intracellular solution. These solutions are made in the lab and therefore provide an access point for the application of extra- and intra-cellular (Palmer et al., 2014; Ferrarese et al., 2018), pharmacological agents *in vivo*. For example, we recently applied intracellular blockers of different ion channels *via* the intracellular solution to investigate their impact on synaptic integration during network activity (Ferrarese et al., 2018), and extracellular antagonist to monitor the impact of acetylcholine on monosynaptic excitatory transmission between PYR neurons and neighboring SST GABA-ergic neurons (Urban-Ciecko et al., 2018). Future work could, therefore, use specific pharmacological agents to help understand the ionic mechanisms of synaptic transmission in active, intact networks.

CONCLUSION

Two-photon targeted multiple-whole cell recordings provide a high resolution and cell-type specific way of identifying monosynaptically connected neurons *in vivo*. This approach will allow studies into the impact of network activity on synaptic transmission, the synaptic mechanisms underlying action potentials generation and link connectivity to functional responses at a millisecond time scale. Moreover, the possibility to record the V_m of both pre- and post-synaptic neurons provides a way to examine the synaptic basis of correlated spiking activity of cortical neurons.

ETHICS STATEMENT

All experiments were performed according to protocols approved by the Berlin Animal Ethics committee (Landesamt für Gesundheit und Sociales, LAGeSo) and comply with the European animal welfare law.

AUTHOR CONTRIBUTIONS

J-SJ performed the experiments and analyzed the data. J-SJ and JP designed the study and wrote the manuscript.

FUNDING

This work was funded by the European Research Council (ERC-2015-CoG-682422, JP), the European Union (3x3 Dimaging 323945), the Deutsche Forschungsgemeinschaft (DFG, FOR 2143, SFB 1315, JP), the American National Institute of Health (NIH R01NS088958, JP), the Thyssen Foundation (JP), and the Helmholtz Society (JP).

ACKNOWLEDGMENTS

We would like to thank Janett König, Charlene Memler and Femtonics for technical assistance, Mario Carta, Sylvain Crochet, Alison Barth and Evgeny Bobrov for comments on earlier version of the manuscript. We thank Poulet lab members for help and constructive comments.

REFERENCES

Andrásfalvy, B. K., Galiñanes, G. L., Huber, D., Barbic, M., Macklin, J. J., Susumu, K., et al. (2014). Quantum dot-based multiphoton fluorescent pipettes for targeted neuronal electrophysiology. *Nat. Methods* 11, 1237–1241. doi: 10.1038/nmeth.3146

Annecchino, L. A., Morris, A. R., Copeland, C. S., Agabi, O. E., Chadderton, P., and Schultz, S. R. (2017). Robotic automation of *in vivo* two-photon targeted whole-cell patch-clamp electrophysiology. *Neuron* 95, 1048.e3–1055.e3. doi: 10.1016/j.neuron.2017.08.018

Arroyo, S., Bennett, C., and Hestrin, S. (2018). Correlaon of synaptic inputs in the visual cortex of awake, behaving mice. *Neuron* 99, 1289.e2–1301.e2. doi: 10.1016/j.neuron.2018.08.008

Baker, C. A., Elyada, Y. M., Parra, A., and Bolton, M. M. L. (2016). Cellular resolution circuit mapping with temporal-focused excitation of soma-targeted channelrhodopsin. *Elife* 5:e14193. doi: 10.7554/elife.14193

Barry, P. H., and Lynch, J. W. (1991). Liquid junction potentials and small cell effects in patch-clamp analysis. *J. Membr. Biol.* 121, 101–117. doi: 10.1007/bf01870526

Barth, A. L., Gerkin, R. C., and Dean, K. L. (2004). Alteration of neuronal firing properties after *in vivo* experience in a FosGFP transgenic mouse. *J. Neurosci.* 24, 6466–6475. doi: 10.1523/JNEUROSCI.4737-03.2004

Barthó, P., Hirase, H., Monconduit, L., Zugaro, M., Harris, K. D., and Buzsáki, G. (2004). Characterization of neocortical principal cells and interneurons by network interactions and extracellular features. *J. Neurophysiol.* 92, 600–608. doi: 10.1152/jn.01170.2003

Bell, C. C., Han, V. Z., Sugawara, Y., and Grant, K. (1997). Synaptic plasticity in a cerebellum-like structure depends on temporal order. *Nature* 387, 278–281. doi: 10.1038/387278a0

Berry, M. S., and Pentreath, V. W. (1976). Criteria for distinguishing between monosynaptic and polysynaptic transmission. *Brain Res.* 105, 1–20. doi: 10.1016/0006-8993(76)90919-7

Boldog, E., Bakken, T. E., Hodge, R. D., Novotny, M., Aevermann, B. D., Baka, J., et al. (2018). Transcriptomic and morphophysiological evidence for a specialized human cortical GABAergic cell type. *Nat. Neurosci.* 21, 1185–1195. doi: 10.1038/s41593-018-0205-2

Bruno, R. M., and Sakmann, B. (2006). Cortex is driven by weak but synchronously active thalamocortical synapses. *Science* 312, 1622–1627. doi: 10.1126/science.1124593

Burrows, M. (1996). *The Neurobiology of an Insect Brain*. Oxford: Oxford University Press.

Cadwell, C. R., Palasantza, A., Jiang, X., Berens, P., Deng, Q., Yilmaz, M., et al. (2016). Electrophysiological, transcriptomic and morphologic profiling

of single neurons using Patch-seq. *Nat. Biotechnol.* 34, 199–203. doi: 10.1038/nbt.3445

Ciabatti, E., González-Rueda, A., Mariotti, L., Morgese, F., and Tripodi, M. (2017). Life-long genetic and functional access to neural circuits using self-inactivating rabies virus. *Cell* 170, 382.e14–392.e14. doi: 10.1016/j.cell.2017.06.014

Cossell, L., Iacaruso, M. F., Muir, D. R., Houlton, R., Sader, E. N., Ko, H., et al. (2015). Functional organization of excitatory synaptic strength in primary visual cortex. *Nature* 518, 399–403. doi: 10.1038/nature14182

Crochet, S., Chauvette, S., Boucetta, S., and Timofeev, I. (2005). Modulation of synaptic transmission in neocortex by network activities. *Eur. J. Neurosci.* 21, 1030–1044. doi: 10.1111/j.1460-9568.2005.03932.x

Csicsvari, J., Hirase, H., Czurko, A., and Buzsaki, G. (1998). Reliability and state dependence of pyramidal cell-interneuron synapses in the hippocampus: an ensemble approach in the behaving rat. *Neuron* 21, 179–189. doi: 10.1016/s0896-6273(00)80525-5

Daigle, T. L., Madisen, L., Hage, T. A., Valley, M. T., Knoblich, U., Larsen, R. S., et al. (2018). A suite of transgenic driver and reporter mouse lines with enhanced brain-cell-type targeting and functionality. *Cell* 174, 465.e22–480.e22. doi: 10.1016/j.cell.2018.06.035

Debanne, D., Boudkkazi, S., Campanac, E., Cudmore, R. H., Giraud, P., Fronzaroli-Molinieres, L., et al. (2008). Paired-recordings from synaptically coupled cortical and hippocampal neurons in acute and cultured brain slices. *Nat. Protoc.* 3, 1559–1568. doi: 10.1038/nprot.2008.147

Deuchars, J., and Thomson, A. M. (1995). Innervation of burst firing spiny interneurons by pyramidal cells in deep layers of rat somatomotor cortex: paired intracellular recordings with biocytin filling. *Neuroscience* 69, 739–755. doi: 10.1016/0306-4522(95)00288-t

Edwards, F. A., Konnerth, A., Sakmann, B., and Takahashi, T. (1989). A thin slice preparation for patch clamp recordings from neurones of the mammalian central nervous system. *Pflugers Arch.* 414, 600–612. doi: 10.1007/bf00580998

English, D. F., McKenzie, S., Evans, T., Kim, K., Yoon, E., and Buzsáki, G. (2017). Pyramidal cell-interneuron circuit architecture and dynamics in hippocampal networks. *Neuron* 96, 505.e7–520.e7. doi: 10.1016/j.neuron.2017.09.033

Feldmeyer, D., Lübke, J., and Sakmann, B. (2006). Efficacy and connectivity of intracolumnar pairs of layer 2/3 pyramidal cells in the barrel cortex of juvenile rats. *J. Physiol.* 575, 583–602. doi: 10.1113/jphysiol.2006.105106

Feldmeyer, D., and Radnikow, G. (2016). "Paired recordings from synaptically coupled neurones in acute neocortical slices," in *Advanced Patch-Clamp Analysis for Neuroscientists*, ed. A. Korngreen (New York, NY: Springer), 171–191.

Fernández, A., Radmilovich, M., Russo, R. E., Hounsgaard, J., and Trujillo-Cenóz, O. (1996). Monosynaptic connections between primary afferents and giant neurons in the turtle spinal dorsal horn. *Exp. Brain Res.* 108, 347–356. doi: 10.1007/bf00227258

Ferrarese, L., Jouhanneau, J.-S., Remme, M. W. H., Kremkow, J., Katona, G., Rózsa, B., et al. (2018). Dendrite-specific amplification of weak synaptic input during network activity *in vivo*. *Cell Rep.* 24, 3455.e5–3465.e5. doi: 10.1016/j.celrep.2018.08.088

Fujisawa, S., Amarasingham, A., Harrison, M. T., and Buzsáki, G. (2008). Behavior-dependent short-term assembly dynamics in the medial prefrontal cortex. *Nat. Neurosci.* 11, 823–833. doi: 10.1038/nn.2134

Fuzik, J., Zeisel, A., Máté, Z., Calvigioni, D., Yanagawa, Y., Szabó, G., et al. (2016). Integration of electrophysiological recordings with single-cell RNA-seq data identifies neuronal subtypes. *Nat. Biotechnol.* 34, 175–183. doi: 10.1038/nbt.3443

Geiger, J. R., Lübke, J., Roth, A., Frotscher, M., and Jonas, P. (1997). Submillisecond AMPA receptor-mediated signaling at a principal neuron-interneuron synapse. *Neuron* 18, 1009–1023. doi: 10.1016/s0896-6273(00)80339-6

Gentet, L. J., Avermann, M., Matyas, F., Staiger, J. F., and Petersen, C. C. H. (2010). Membrane potential dynamics of GABAergic neurons in the barrel cortex of behaving mice. *Neuron* 65, 422–435. doi: 10.1016/j.neuron.2010.01.006

Gerfen, C. R., Paletzki, R., and Heintz, N. (2013). GENSAT BAC cre-recombinase driver lines to study the functional organization of cerebral cortical and basal ganglia circuits. *Neuron* 80, 1368–1383. doi: 10.1016/j.neuron.2013.10.016

Goebbels, S., Bormuth, I., Bode, U., Hermanson, O., Schwab, M. H., and Nave, K.-A. (2006). Genetic targeting of principal neurons in neocortex and hippocampus of NEX-Cre mice. *Genesis* 44, 611–621. doi: 10.1002/dvg.20256

Guzman, S. J., Schlögl, A., Frotscher, M., and Jonas, P. (2016). Synaptic mechanisms of pattern completion in the hippocampal CA3 network. *Science* 353, 1117–1123. doi: 10.1126/science.aaf1836

Hamada, H., Takaori, M., Kimura, K., Fukui, A., and Fujita, Y. (1993). Changes in circulating blood volume following isoflurane or sevoflurane anesthesia. *Pharmacol. Rep.* 7, 316–324. doi: 10.1007/s0054030070316

Harris, J. A., Hirokawa, K. E., Sorensen, S. A., Gu, H., Mills, M., Ng, L. L., et al. (2014). Anatomical characterization of Cre driver mice for neural circuit mapping and manipulation. *Front. Neural Circuits* 8:76. doi: 10.3389/fncir.2014.00076

Hippenmeyer, S., Vrieseling, E., Sigrist, M., Portmann, T., Laengle, C., Ladle, D. R., et al. (2005). A developmental switch in the response of DRG neurons to ETS transcription factor signaling. *PLoS Biol.* 3:e159. doi: 10.1371/journal.pbio.0030159

Holmgren, C., Harkany, T., Svennenfors, B., and Zilberter, Y. (2003). Pyramidal cell communication within local networks in layer 2/3 of rat neocortex. *J. Physiol.* 551, 139–153. doi: 10.1113/jphysiol.2003.044784

Jiang, X., Shen, S., Cadwell, C. R., Berens, P., Sinz, F., Ecker, A. S., et al. (2015). Principles of connectivity among morphologically defined cell types in adult neocortex. *Science* 350:aac9462. doi: 10.1126/science.aac9462

Jouhanneau, J.-S., Kremkow, J., and Poulet, J. F. A. (2018). Single synaptic inputs drive high-precision action potentials in parvalbumin expressing GABA-ergic cortical neurons *in vivo*. *Nat. Commun.* 9:1540. doi: 10.1038/s41467-018-03995-2

Jouhanneau, J.-S., Kremkow, J., Dorrn, A. L., and Poulet, J. F. A. (2015). *In vivo* monosynaptic excitatory transmission between layer 2 cortical pyramidal neurons. *Cell Rep.* 13, 2098–2106. doi: 10.1016/j.celrep.2015.11.011

Kitamura, K., Judkewitz, B., Kano, M., Denk, W., and Häusser, M. (2008). Targeted patch-clamp recordings and single-cell electroporation of unlabeled neurons *in vivo*. *Nat. Methods* 5, 61–67. doi: 10.1038/nmeth1150

Ko, H., Hofer, S. B., Pichler, B., Buchanan, K. A., Sjöström, P. J., and Mrsic-Flogel, T. D. (2011). Functional specificity of local synaptic connections in neocortical networks. *Nature* 473, 87–91. doi: 10.1038/nature09880

Kolb, I., Stoy, W. A., Rousseau, E. B., Moody, O. A., Jenkins, A., and Forest, C. R. (2016). Cleaning patch-clamp pipettes for immediate reuse. *Sci. Rep.* 6:35001. doi: 10.1038/srep35001

Lalanne, T., Abrahamsson, T., and Sjöström, P. J. (2016). Using multiple whole-cell recordings to study spike-timing-dependent plasticity in acute neocortical slices. *Cold Spring Harb. Protoc.* 2016:pdb.prot091306. doi: 10.1101/pdb.prot091306

Lee, A. K., and Brecht, M. (2018). Elucidating neuronal mechanisms using intracellular recordings during behavior. *Trends Neurosci.* 41, 385–403. doi: 10.1016/j.tins.2018.03.014

Lefort, S., Tomm, C., Sarria, J. C. F., and Petersen, C. C. H. (2009). The excitatory neuronal networkof the C2 barrel columnin mouse primary somatosensory cortex. *Neuron* 61, 301–316. doi: 10.1016/j.neuron.2008.12.020

London, M., Roth, A., Beeren, L., Häusser, M., and Latham, P. E. (2010). Sensitivity to perturbations *in vivo* implies high noise and suggests rate coding in cortex. *Nature* 466, 123–127. doi: 10.1038/nature09086

Madisen, L., Zwingman, T. A., Sunkin, S. M., Oh, S. W., Zariwala, H. A., Gu, H., et al. (2010). A robust and high-throughput Cre reporting and characterization system for the whole mouse brain. *Nat. Neurosci.* 13, 133–140. doi: 10.1038/nn.2467

Margrie, T., Brecht, M., and Sakmann, B. (2002). *In vivo*, low-resistance, whole-cell recordings from neurons in the anaesthetized and awake mammalian brain. *Pflugers Arch.* 444, 491–498. doi: 10.1007/s00424-002-0831-z

Markram, H., Lübke, J., Frotscher, M., Roth, A., and Sakmann, B. (1997a). Physiology and anatomy of synaptic connections between thick tufted pyramidal neurones in the developing rat neocortex. *J. Physiol.* 500, 409–440. doi: 10.1113/jphysiol.1997.sp022031

Markram, H., Lübke, J., Frotscher, M., and Sakmann, B. (1997b). Regulation of synaptic efficacy by coincidence of postsynaptic APs and EPSPs. *Science* 275, 213–215. doi: 10.1126/science.275.5297.213

Mason, A., Nicoll, A., and Stratford, K. (1991). Synaptic transmission between individual pyramidal neurons of the rat visual cortex *in vitro*. *J. Neurosci.* 11, 72–84. doi: 10.1523/JNEUROSCI.11-01-00072.1991

Matsumura, M., Chen, D., Sawaguchi, T., Kubota, K., and Fetz, E. E. (1996). Synaptic interactions between primate precentral cortex neurons revealed by spike-triggered averaging of intracellular membrane potentials *in vivo*. *J. Neurosci.* 16, 7757–7767. doi: 10.1523/JNEUROSCI.16-23-07757.1996

Muñoz, W., Tremblay, R., Levenstein, D., and Rudy, B. (2017). Layer-specific modulation of neocortical dendritic inhibition during active wakefulness. *Science* 355, 954–959. doi: 10.1126/science.aag2599

Packer, A. M., Russell, L. E., Dalgleish, H. W. P., and Häusser, M. (2015). Simultaneous all-optical manipulation and recording of neural circuit activity with cellular resolution *in vivo*. *Nat. Methods* 12, 140–146. doi: 10.1038/nmeth.3217

Pala, A., and Petersen, C. C. H. (2015). *In vivo* measurement of cell-type-specific synaptic connectivity and synaptic transmission in layer 2/3 mouse barrel cortex. *Neuron* 85, 68–75. doi: 10.1016/j.neuron.2014.11.025

Pala, A., and Petersen, C. C. (2018). State-dependent cell-type-specific membrane potential dynamics and unitary synaptic inputs in awake mice. *eLife* 7:e35869. doi: 10.7554/elife.35869

Palmer, L. M., Shai, A. S., Reeve, J. E., Anderson, H. L., Paulsen, O., and Larkum, M. E. (2014). NMDA spikes enhance action potential generation during sensory input. *Nat. Neurosci.* 17, 383–390. doi: 10.1038/nn.3646

Papadopoulos, I. N., Jouhanneau, J.-S., Poulet, J. F. A., and Judkewitz, B. (2017). Scattering compensation by focus scanning holographic aberration probing (F-SHARP). *Nat. Photonics* 11, 116–123. doi: 10.1038/nphoton.2016.252

Parker, D. (2003). Variable properties in a single class of excitatory spinal synapse. *J. Neurosci.* 23, 3154–3163. doi: 10.1523/JNEUROSCI.23-08-03154.2003

Parker, D. (2010). Neuronal network analyses: premises, promises and uncertainties. *Philos. Trans. R. Soc. B Biol. Sci.* 365, 2315–2328. doi: 10.1098/rstb.2010.0043

Peng, Y., Barreda Tomás, F. J., Klisch, C., Vida, I., and Geiger, J. R. P. (2017). Layer-specific organization of local excitatory and inhibitory synaptic connectivity in the rat presubiculum. *Cereb. Cortex* 27, 2435–2452. doi: 10.1093/cercor/bhx049

Perin, R., Berger, T. K., and Markram, H. (2011). A synaptic organizing principle for cortical neuronal groups. *Proc. Natl. Acad. Sci. U S A* 108, 5419–5424. doi: 10.1073/pnas.1016051108

Petersen, C. C. H. (2017). Whole-cell recording of neuronal membrane potential during behavior. *Neuron* 95, 1266–1281. doi: 10.1016/j.neuron.2017.06.049

Poulet, J. F. A., and Hedwig, B. (2006). The cellular basis of a corollary discharge. *Science* 311, 518–522. doi: 10.1126/science.1120847

Poulet, J. F. A., and Petersen, C. C. H. (2008). Internal brain state regulates membrane potential synchrony in barrel cortex of behaving mice. *Nature* 454, 881–885. doi: 10.1038/nature07150

Reardon, T. R., Murray, A. J., Turi, G. F., Wirblich, C., Croce, K. R., Schnell, M. J., et al. (2016). Rabies virus CVS-N2c(ΔG) strain enhances retrograde synaptic transfer and neuronal viability. *Neuron* 89, 711–724. doi: 10.1016/j.neuron.2016.01.004

Reid, R. C., and Alonso, J. M. (1995). Specificity of monosynaptic connections from thalamus to visual cortex. *Nature* 378, 281–284. doi: 10.1038/378281a0

Rickgauer, J. P., Deisseroth, K., and Tank, D. W. (2014). Simultaneous cellular-resolution optical perturbation and imaging of place cell firing fields. *Nat. Neurosci.* 17, 1816–1824. doi: 10.1038/nn.3866

Roberts, A., Li, W.-C., and Soffe, S. R. (2010). How neurons generate behavior in a hatchling amphibian tadpole: an outline. *Front. Behav. Neurosci.* 4:16. doi: 10.3389/fnbeh.2010.00016

Sofroniew, N. J., Flickinger, D., King, J., and Svoboda, K. (2016). A large field of view two-photon mesoscope with subcellular resolution for *in vivo* imaging. *eLife* 5:e14472. doi: 10.7554/elife.14472

Steriade, M., Nuñez, A., and Amzica, F. (1993). A novel slow (<1 Hz) oscillation of neocortical neurons *in vivo*: depolarizing and hyperpolarizing components. *J. Neurosci. Methods* 13, 3252–3265. doi: 10.1523/JNEUROSCI.13-08-03252.1993

Stirman, J. N., Smith, I. T., Kudenov, M. W., and Smith, S. L. (2016). Wide field-of-view, multi-region, two-photon imaging of neuronal activity in the mammalian brain. *Nat. Biotechnol.* 34, 857–862. doi: 10.1038/nbt.3594

Suk, H.-J., van Welie, I., Kodandaramaiah, S. B., Allen, B., Forest, C. R., and Boyden, E. S. (2017). Closed-loop real-time imaging enables fully automated cell-targeted patch-clamp neural recording *in vivo*. *Neuron* 96, 244–245. doi: 10.1016/j.neuron.2017.09.012

Swadlow, H. A., and Gusev, A. G. (2002). Receptive-field construction in cortical inhibitory interneurons. *Nat. Neurosci.* 5, 403–404. doi: 10.1038/nn847

Tamamaki, N., Yanagawa, Y., Tomioka, R., Miyazaki, J.-I., Obata, K., and Kaneko, T. (2003). Green fluorescent protein expression and colocalization with calretinin, parvalbumin, and somatostatin in the GAD67-GFP knock-in mouse. *J. Comp. Neurol.* 467, 60–79. doi: 10.1002/cne.10905

Taniguchi, H., He, M., Wu, P., Kim, S., Paik, R., Sugino, K., et al. (2011). A resource of Cre driver lines for genetic targeting of GABAergic neurons in cerebral cortex. *Neuron* 71, 995–1013. doi: 10.1016/j.neuron.2011.07.026

Urban-Ciecko, J., Jouhanneau, J.-S., Myal, S. E., Poulet, J. F. A., and Barth, A. L. (2018). Precisely timed nicotinic activation drives SST inhibition in neocortical circuits. *Neuron* 97, 611.e5–625.e5. doi: 10.1016/j.neuron.2018.01.037

Vélez-Fort, M., Bracey, E. F., Keshavarzi, S., Rousseau, C. V., Cossell, L., Lenzi, S. C., et al. (2018). A circuit for integration of head- and visual-motion signals in layer 6 of mouse primary visual cortex. *Neuron* 98, 179.e6–191.e6. doi: 10.1016/j.neuron.2018.02.023

Wang, G., Wyskiel, D. R., Yang, W., Wang, Y., Milbern, L. C., Lalanne, T., et al. (2015). An optogenetics- and imaging-assisted simultaneous multiple patch-clamp recording system for decoding complex neural circuits. *Nat. Protoc.* 10, 397–412. doi: 10.1038/nprot.2015.019

Weiler, S., Bauer, J., Hübener, M., Bonhoeffer, T., Rose, T., and Scheuss, V. (2018). High-yield *in vitro* recordings from neurons functionally characterized *in vivo*. *Nat. Protoc.* 13, 1275–1293. doi: 10.1038/nprot.2018.026

Wertz, A., Trenholm, S., Yonehara, K., Hillier, D., Raics, Z., Leinweber, M., et al. (2015). Presynaptic Networks. Single-cell-initiated monosynaptic tracing reveals layer-specific cortical network modules. *Science* 349, 70–74. doi: 10.1126/science.aab1687

Wickersham, I. R., Lyon, D. C., Barnard, R. J. O., Mori, T., Finke, S., Conzelmann, K.-K., et al. (2007). Monosynaptic restriction of transsynaptic tracing from single, genetically targeted neurons. *Neuron* 53, 639–647. doi: 10.1016/j.neuron.2007.01.033

Wozny, C., and Williams, S. R. (2011). Specificity of synaptic connectivity between layer 1 inhibitory interneurons and layer 2/3 pyramidal neurons in the rat neocortex. *Cereb. Cortex* 21, 1818–1826. doi: 10.1093/cercor/bhq257

Yassin, L., Benedetti, B. L., Jouhanneau, J.-S., Wen, J. A., Poulet, J. F. A., and Barth, A. L. (2010). An embedded subnetwork of highly active neurons in the neocortex. *Neuron* 68, 1043–1050. doi: 10.1016/j.neuron.2010.11.029

Yu, J., and Ferster, D. (2013). Functional coupling from simple to complex cells in the visually driven cortical circuit. *J. Neurosci.* 33, 18855–18866. doi: 10.1523/JNEUROSCI.2665-13.2013

Zhao, W.-J., Kremkow, J., and Poulet, J. F. A. (2016). Translaminar cortical membrane potential synchrony in behaving mice. *Cell Rep.* 15, 2387–2399. doi: 10.1016/j.celrep.2016.05.026

Conflict of Interest Statement: The authors declare that the research was conducted in the absence of any commercial or financial relationships that could be construed as a potential conflict of interest.

frontiers in Synaptic Neuroscience

PROTOCOLS
published: 24 May 2019
doi: 10.3389/fnsyn.2019.00016

Optically Induced Calcium-Dependent Gene Activation and Labeling of Active Neurons Using CaMPARI and Cal-Light

Christian Ebner[1,2], Julia Ledderose[3], Timothy A. Zolnik[2], Sina E. Dominiak[2], Paul Turko[1,4], Athanasia Papoutsi[5], Panayiota Poirazi[5], Britta J. Eickholt[3], Imre Vida[1,4], Matthew E. Larkum[1,2] and Robert N. S. Sachdev[2]**

[1] NeuroCure Cluster of Excellence, Charité—Universitätsmedizin Berlin, Berlin, Germany, [2] Institute for Biology, Humboldt-Universität zu Berlin, Berlin, Germany, [3] Institute for Biochemistry, Charité—Universitätsmedizin Berlin, Berlin, Germany, [4] Institute for Integrative Neuroanatomy, Charité—Universitätsmedizin Berlin, Berlin, Germany, [5] Institute of Molecular Biology and Biotechnology, Foundation for Research and Technology—Hellas, Heraklion, Greece

The advent of optogenetic methods has made it possible to use endogeneously produced molecules to image and manipulate cellular, subcellular, and synaptic activity. It has also led to the development of photoactivatable calcium-dependent indicators that mark active synapses, neurons, and circuits. Furthermore, calcium-dependent photoactivation can be used to trigger gene expression in active neurons. Here we describe two sets of protocols, one using CaMPARI and a second one using Cal-Light. CaMPARI, a calcium-modulated photoactivatable ratiometric integrator, enables rapid network-wide, tunable, all-optical functional circuit mapping. Cal-Light, a photoactivatable calcium sensor, while slower to respond than CaMPARI, has the capacity to trigger the expression of genes, including effectors, activators, indicators, or other constructs. Here we describe the rationale and provide procedures for using these two calcium-dependent constructs (1) *in vitro* in dissociated primary neuronal cell cultures (CaMPARI & Cal-Light); (2) *in vitro* in acute brain slices for circuit mapping (CaMPARI); (3) *in vivo* for triggering photoconversion or gene expression (CaMPARI & Cal-Light); and finally, (4) for recovering photoconverted neurons post-fixation with immunocytochemistry (CaMPARI). The approaches and protocols we describe are examples of the potential uses of both CaMPARI & Cal-Light. The ability to mark and manipulate neurons that are active during specific epochs of behavior has a vast unexplored experimental potential.

Keywords: CaMPARI, Cal-Light, photoconversion, photoactivation, calcium, optogenetics, gene expression

OPEN ACCESS

Edited by:
Dirk Feldmeyer, Julich Research Centre, Germany

Reviewed by:
Serena M. Dudek, National Institute of Environmental Health Sciences (NIEHS), United States
Michele H. Jacob, Tufts University, United States

***Correspondence:**
Matthew E. Larkum
Matthew.Larkum@charite.de
Robert N. S. Sachdev
Robert.Sachdev@charite.de

Received: *22 February 2019*
Accepted: *03 May 2019*
Published: *24 May 2019*

Citation:
Ebner C, Ledderose J, Zolnik TA, Dominiak SE, Turko P, Papoutsi A, Poirazi P, Eickholt BJ, Vida I, Larkum ME and Sachdev RNS (2019) Optically Induced Calcium-Dependent Gene Activation and Labeling of Active Neurons Using CaMPARI and Cal-Light. Front. Synaptic Neurosci. 11:16. doi: 10.3389/fnsyn.2019.00016

INTRODUCTION

A fundamental goal of neuroscience research is to understand what the activity of neurons represents: is the activity correlated with a particular sensory input or to a particular behavior? Do the neurons involved in learning, memory or behavior express specific markers or genetic programs that are activated during the learning or consolidation phase? To study why some neurons are

active while neighboring neurons are inactive, or why some neurons show genetic changes during learning or consolidation or memory formation, requires a detailed understanding of their input and their genetic and physiological properties. To begin such analysis, we first need to identify a population of active neurons *in vivo* that can then be targeted with additional methods (DeNardo and Luo, 2017) to further interrogate their biophysical and genetic properties *in vitro*. To achieve this level of understanding, the ability to mark and track active neurons and recover them for additional experiments and analysis is essential.

Immediate early gene (IEG) expression has provided means to recover active neurons in experimental paradigms for decades. IEGs show low expression when cells are quiescent but stimulation can elicit transient high expression within minutes (Greenberg et al., 1986; Morgan and Curran, 1986; Kawashima et al., 2014; Yap and Greenberg, 2018). IEG expressing cells can be tracked online with fluorescence indicators or *post-hoc* by immunocytochemistry in fixed tissue. While IEG expression has proven useful, it has become clear that triggers for transcription of IEGs include metabolic activity, stress, growth factors, and the release of neurotransmitters (Sheng and Greenberg, 1990). Thus, the expression of those genes is not necessarily uniformly or tightly linked to activity, such as spiking or synaptic input. There have also been multiple forays into chemically induced gene expression (Mansuy et al., 1998; Dogbevia et al., 2015; Cazzulino et al., 2016). While these methods have been successfully applied to a variety of experimental paradigms, other recent approaches are both more versatile and temporally more precise. These new approaches can track active neurons *in vivo* and recover them for *ex vivo* experiments (Barth, 2007; Wang et al., 2019). They rely on optical measurements or photoconversion of calcium indicator dyes to tag activity of neurons with two-photon imaging, followed by *in vitro* recording from the same neurons (Ko et al., 2011), photoactivatable GFP for targeting neurons *in vivo* and *in vitro* (Lien and Scanziani, 2011; Peter et al., 2013) and chronic imaging with virally expressed GCaMP and fluorescent beads that make it possible to identify the set of neurons for *ex vivo* slice work (Weiler et al., 2018). These developments all point toward the need for developing simple methods to track active neurons over longer periods (over days) or from one experimental condition to another (e.g., from *in vivo* to *in vitro* experiments). Here, we describe procedures to make use of two calcium-dependent tools: CaMPARI and Cal-Light. Both can be used for marking active neurons, circuit mapping or optogenetic manipulations.

CaMPARI (calcium-modulated photoactivatable ratiometric integrator) is a calcium indicator that can be rapidly photoconverted in active neurons to perform circuit mapping (Fosque et al., 2015; Zolnik et al., 2017; Moeyaert et al., 2018). CaMPARI works well with channelrhodopsin (ChR2)-based circuit mapping because 405 nm light triggers both photoconversion of CaMPARI and activation of ChR2-positive neurons and axon terminals.

Cal-Light is another photoactivatable calcium-sensitive indicator that is able to trigger the expression of a variety of genes in active neurons (Lee et al., 2017). This property of Cal-Light allows for the selective expression of genes in active neurons and therefore can be used to interrogate whether the activity of these neurons is necessary and/or sufficient for a given behavior when driving the expression of constructs such as optogenetic silencers or enhancers.

Both CaMPARI and Cal-Light require illumination, coincident to the cytosolic calcium increase, to trigger conversion or activation, respectively. However, CaMPARI and Cal-Light operate on different time scales: CaMPARI converts rapidly within seconds (Fosque et al., 2015; Zolnik et al., 2017), whereas Cal-Light-dependent expression takes about 2–5 days (Lee et al., 2017). CaMPARI conversion and in principle Cal-Light activation can be used with ChR2 activation, since CaMPARI uses 405 nm light and Cal-Light 470 nm light, both of which can activate ChR2. Cal-Light offers the possibility to then trigger the expression of other constructs such as fluorescent proteins or optogenetic activators/inhibitors (e.g., GFP, ARChT, iChloC, etc.) in active neurons.

Mechanisms of CaMPARI Action

CaMPARI is a bright green fluorescent protein that—via allosteric modulation of the chromophore—converts to a bright red fluorescent species upon illumination with violet light during high calcium availability (Fosque et al., 2015; Zolnik et al., 2017; **Figure 1**). The main advantage of CaMPARI over other genetically encoded calcium indicators (GECIs, Pologruto et al., 2004) is that photoconverted CaMPARI neurons are labeled irreversibly, allowing for imaging of an active network long after the photoconversion snapshot of activity has been obtained. Not only are active neurons marked but because CaMPARI is a ratiometric integrator, its red/green ratio indicates the level of their activity or, more precisely, the level of calcium influx. It is also a negative fluorescent indicator, meaning that it reports momentary calcium influx by a reduction in fluorescence intensity in both the unconverted green state and in the converted red state (see **Supplementary Video Files 1, 2**). A drawback with CaMPARI is that its expression is sensitive to tissue fixation using formaldehyde-based solutions. So while it is possible to track neurons in an *in vivo* experiment and follow them *in vitro*, it is not possible to make high quality images of the same neurons post-fixation (Zolnik et al., 2017). To overcome this problem, antibodies against a second generation of CaMPARI, CaMPARI2, have been designed to allow usage of immunocytochemistry to recover neurons that were marked *in vivo* (Moeyaert et al., 2018). In this study, except where explicitly stated otherwise, we used CaMPARI2.

Mechanisms of Cal-Light Action

Cal-Light is light-sensitive and calcium-dependent (Lee et al., 2017). Activity-driven calcium increase in the cytosol is linked to gene transcription in the nucleus (**Figure 1**). To make this work, a tetracycline-controlled transcriptional activator (tTA) is tethered to the cell-membrane and the transcriptional activator is linked to a protease (Tobacco Etch Virus Protease, TEVp) cleavage sequence (TEVseq). Cleavage depends on blue light and calcium concentration. An increase in cytosolic calcium levels under presence of blue light leads to the release of tTA which then initiates gene transcription in the nucleus.

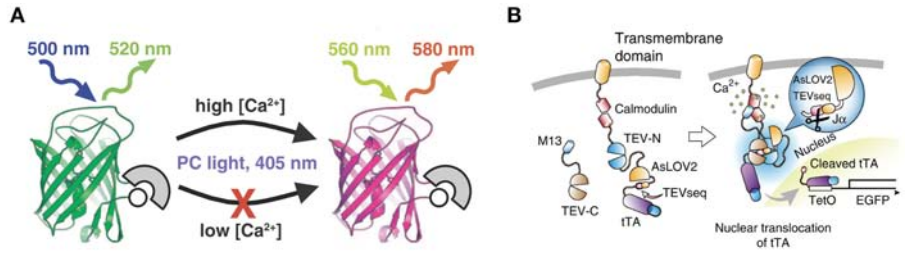

FIGURE 1 | Schematic drawings of CaMPARI and Cal-Light. **(A)** CaMPARI, a calcium-modulated photoactivatable ratiometric integrator, is a circularly permuted fluorescent protein with calcium sensor domains that undergoes green-to-red photoconversion when exposed to ∼400 nm light in the presence of high Ca^{2+}. Adapted with permission from Fosque et al. (2015). **(B)** Cal-Light activation. When Ca^{2+} increases in the cytosol it triggers M13 and calmodulin to bind each other, allowing TEV-C and TEV-N to regain proteolytic functions. However, TEV protease cannot recognize TEVseq in a dark condition, because TEVseq is inserted at the C terminus of AsLOV2 Jα-helix. Blue light causes a conformational change in the Jα-helix, unmasking TEVseq. Cleaved tTA translocates to the nucleus and initiates gene expression. Adapted with permission from Lee et al. (2017).

General Rationale

The protocols presented here describe how we use these tools, and some of our modifications. The labs that developed these constructs have published papers demonstrating that they work *in vivo* in mice, and *in vitro* in tissue culture (Fosque et al., 2015; Lee et al., 2017) as well as in other model species including Drosophila and C. elegans (Fosque et al., 2015). Here, we describe the following procedures (**Figure 2**): (1) wide-field imaging for photoconversion and photoactivation in neuronal cell culture, (2) using CaMPARI and ChR2 *ex vivo* in acute brain slices for circuit mapping (Zolnik et al., 2017), (3) using both CaMPARI and Cal-Light *in vivo* in quietly sitting head-fixed mice as proof of concept experiments for monitoring large scale photoconversion and photoactivation with epifluorescence microscopy and *ex vivo* imaging, and (4) immunohistochemistry to recover CAMPARI2 expression in formaldehyde-fixed tissue.

Rationale for Expressing CaMPARI and Cal-Light Constructs in Neuronal Cell Culture

The key requirement of photoconversion and photactivation is that calcium entry is coupled to exposure to light. However, the minimum duration of light exposure and the optimal timing of illumination and calcium entry are still not completely known. To measure the effectiveness of different light parameters, preparations such as dissociated neuronal culture combined with wide-field stimulation and live-cell imaging prove to be useful (**Figures 3A**, **4**). Dissociated neurons can be routinely cultured from the cortex and hippocampus of postnatal day (P) 0–3 rat or mouse pups and can be maintained in culture for weeks to months. Although the network architecture is not conserved, dissociated neurons develop morphologically identifiable axons and dendrites, establish synaptic connections and fire repetitive trains of action potentials (Turko et al., 2019). Dissociated neurons are cultured in a monolayer, which makes them readily accessible to both optical and experimental manipulation. This accessibility is a distinct advantage over *ex vivo* and *in vivo* procedures, particularly when investigating the efficiency of viral transfection, gene expression and effectiveness of the light parameters. Dissociated cell cultures are therefore particularly well-suited for characterizing the expression and function of virus-mediated genetic manipulations.

Rationale for Using Brain Slices

A fundamental problem of all calcium sensors is to identify the cause and source of calcium entry. Cytosolic calcium levels rise when neurons fire action potentials, when synaptic activity depolarizes neurons, or when calcium is released from internal stores (Sabatini et al., 2002). Consequently, it is difficult to interpret calcium signals in experiments performed *in vivo*. In contrast, neurons are quiescent in brain slices and synaptic activity can be easily and specifically controlled. For the purpose of investigating the effectiveness of activity-tracking methods, we used *in vitro* experiments to establish that CaMPARI photoconversion was sensitive to changes in internal calcium caused by synaptic input, i.e., photoconversion did not depend on action potentials. Thus, in order to evaluate the CaMPARI signal, it was necessary to determine whether CaMPARI photoconversion occurred even when action potentials were blocked. For these kinds of experiments and for circuit mapping (**Figure 5**), brain slices are ideal due to the controlled conditions they offer: action potentials, synaptic transmission, and even intra- and extracellular conditions can be easily regulated using ionic composition and pharmacology.

Rationale for *in vivo* Photostimulation and Epifluorescence Imaging Through a Cranial Window

The main purpose of these methods is to mark active neurons *in vivo* and to recover the neurons that were active for further analysis. Individual neurons can be tracked *in vivo* with two-photon imaging, while photoconverted regions of cortex can be tracked with epifluorescence. The principal advantage of epifluorescence is that measurements are simple, they take little time and the costs of wide-field epifluoresence microscopes are low compared to the costs of two-photon imaging setups (Andermann et al., 2013). The principal disadvantage is that the images are not at cellular resolution, nevertheless both Cal-Light-induced gene expression and CaMPARI photoconversion can be tracked using epifluorescence imaging through a cranial

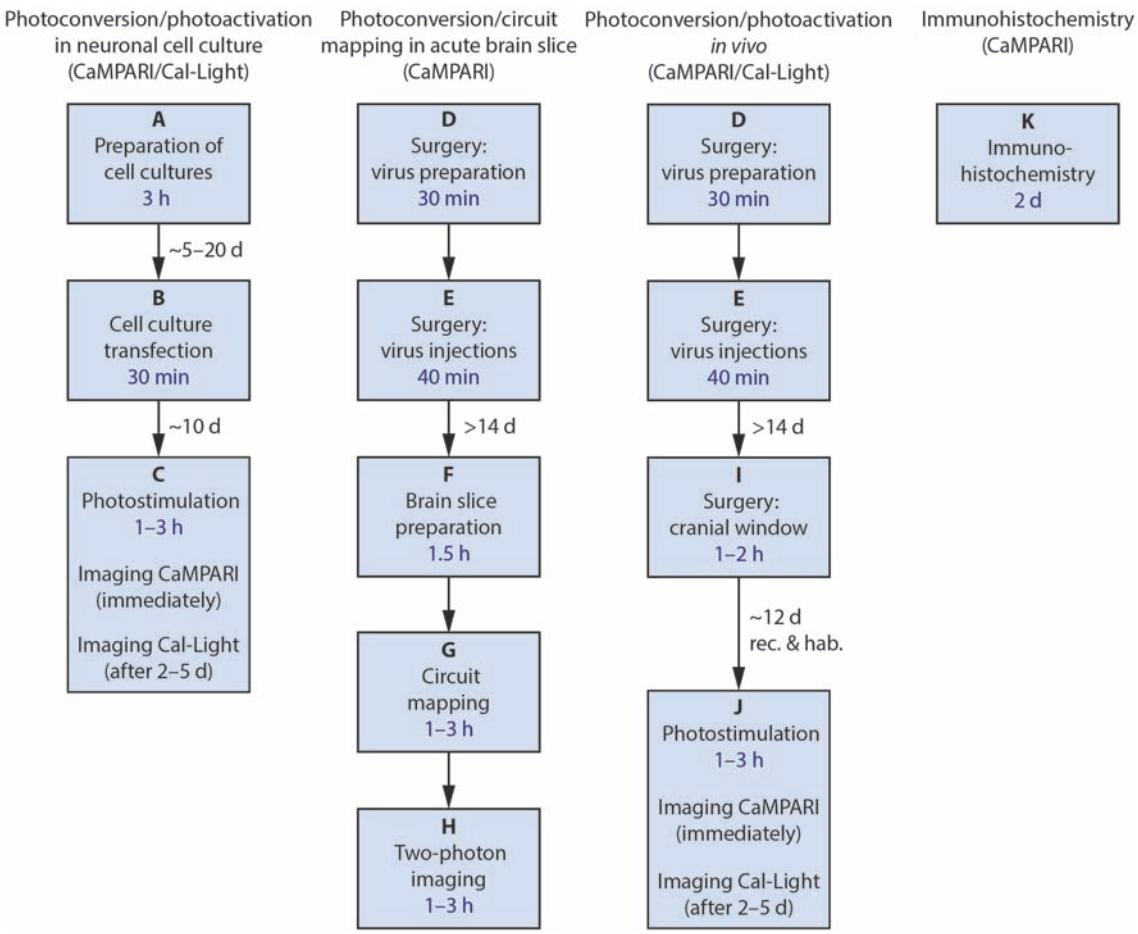

FIGURE 2 | Flowchart of the four main procedures described. After each final process, confocal imaging and data analysis may be performed. Estimated amount of time needed for the main steps is included in the boxes in blue; necessary delays between major steps are given near the arrows. rec., recovery; hab., habituation.

window (**Figure 3B**). Finally, neurons that were active *in vivo* can be imaged *ex vivo* (**Figure 6**) and characterized with respect to their physiology, anatomy, laminar distribution of their axon and dendrites as well as their expression of neurochemical markers. This offline approach means that the quantification of activity *in vivo* can be done more accurately without the need to keep the animal alive for extended periods.

Rationale for Immunohistochemistry

This method allows for recovery of CaMPARI-expressing neurons (including the photoconversion snapshot) in fixed tissue, opening up the possibility to mount sections and use them for confocal imaging at a later stage (**Figure 7**). In principle, this can then be used to identify and further characterize labeled neurons in terms of morphology and anatomical connectivity.

Overview of the Procedures

We split procedures into several modules (**Figure 2**). For every experimental preparation, from tissue culture to *in vivo* work, the first step with both Cal-Light and CaMPARI is to obtain expression of the viral construct. Expression is then monitored through wide-field epifluorescence microscopy. Photoconversion or gene expression is triggered when light is applied to the cell culture, to the brain slice or through a cranial window onto the brain. In the case of *in vivo* procedures, neurons expressing the constructs can be recovered *ex vivo* for recording or circuit mapping. Finally, CaMPARI-expressing neurons that have been photoconverted and fixed in formaldehyde-based solution (and thus have lost their native fluorescence) can be recovered with immunohistochemistry.

MATERIALS AND EQUIPMENT

Animals

Rats. For neuronal cell cultures, we use wild type rat pups (Wistar, P0–2).

Mice. For circuit mapping, we use young (P21–30) wild type mice (C57/BL6J) of either sex. For *in vivo* photoactivation and photoconversion, we use adult (P40–90) mice of either sex.

Chemicals

Neural Basal A media (ThermoFisher Scientific, 10888022)
B27 (ThermoFisher Scientific, 17504001)
Glutamax (ThermoFisher Scientific, 35050-038)

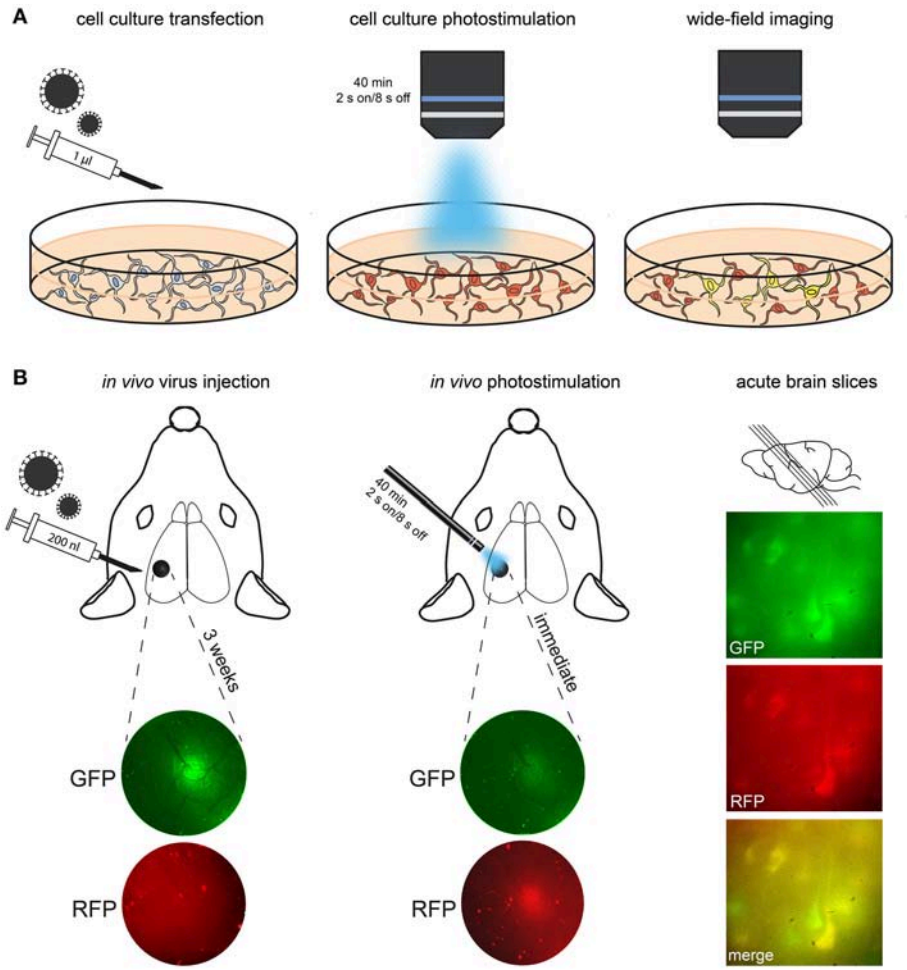

FIGURE 3 | Procedure for transfection, conversion and imaging. **(A)** In this schematic, cultured neurons are treated with Cal-Light virus. After expression of the construct (indicated via red fluorescence), photostimulation is applied. Imaging then reveals neurons that were active while receiving the light stimulus (i.e., they co-express GFP and thus appear yellow in merged channels). **(B)** In this example, CaMPARI virus was injected into S1 cortex; expression of the construct is imaged using an epifluorescence microscope. A large number of neurons express CaMPARI 3 weeks after virus injection. Left, injection site imaged through the cranial window before and after 405 nm photoconversion. Note the reduction of green/red ratio immediately after photoconversion. Right, demonstration of photoconverted neurons in acute brain slices of S1 (parasagittal, 300 µm).

Penicillin-Streptomycin (10,000 U/ml, ThermoFisher Scientific, 15140-122)
Poly-L-Lysine (Sigma, P1399 Coverslip coating)
Papain (Sigma, P4762)
Bovine Serum Albumin (Sigma, A3294)
Hibernate A low fluorescence media (Brain Bits Ltd, HALF)
NaCl (Carl Roth, HN00.2)
KCl (Carl Roth, HN02.2)
NaH_2PO_4 (monohydrate, Carl Roth, K300.1)
$NaHCO_3$ (Carl Roth, HN01.2)
$CaCl_2$ (dihydrate, Carl Roth, HN04.2)
$MgCl_2$ (hexahydrate, Carl Roth, HN03.1)
D-glucose (Carl Roth, HN06.3)
Choline chloride (Sigma, C7527)
Na-L-ascorbate (Sigma, A4034)
Na-pyruvate (Sigma, P2256)
KH_2PO_4 (Carl Roth, 3904.1)
NaOH (Carl Roth, 9356.1)
HCl (37%, Carl Roth, 9277.2)
Paraformaldehyde (Merck, 1.04005)
Gabazine (SR-95531 hydrobromide, Tocris, 1262)
Carbachol (carbamoylcholine chloride, Tocris, 2810)
Ethanol (96%, Carl Roth, T171.4)
Normal goat serum (Gibco, 16210-072)
Triton X-100 (Sigma, T8787)
Glycerol (Sigma, G5516)
DAPCO (Carl Roth, 0718.1).

Drugs for Animal Use

Ketamine (10%, Medistart)
Xylazine (Xylavet, 20 mg/ml, CP-Pharma)
Isoflurane (Forene, Abbvie)

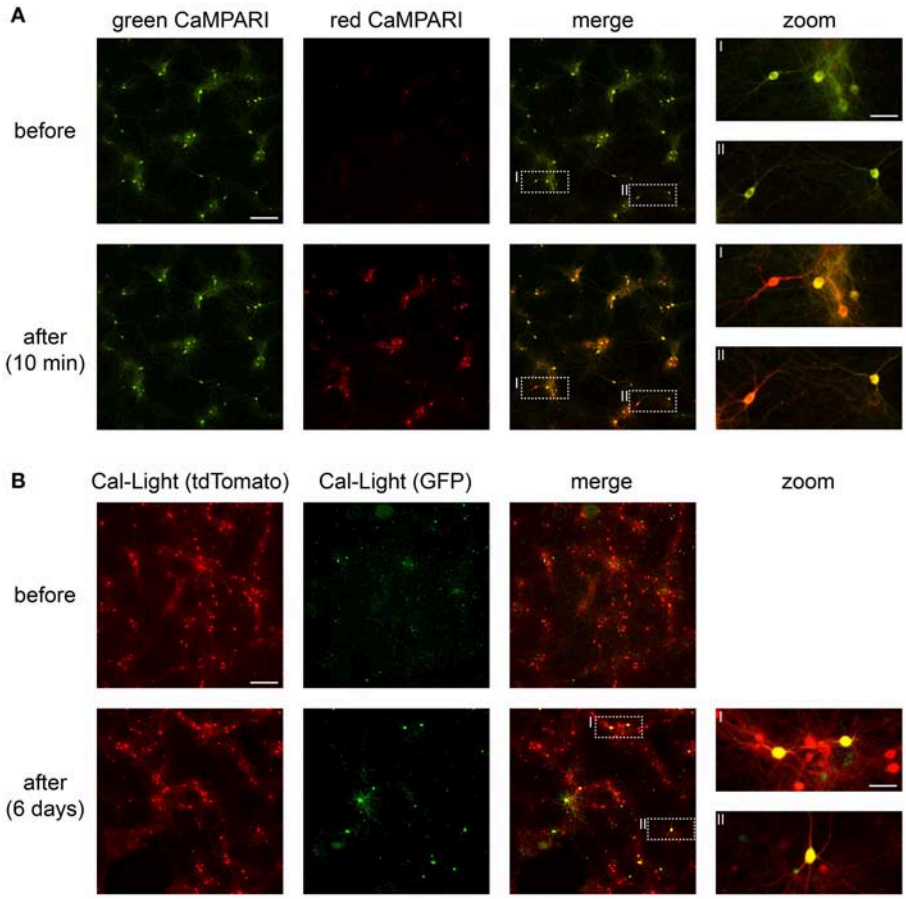

FIGURE 4 | CaMPARI and Cal-Light expression and functionality in neuronal cell culture. **(A)** Wide-field epifluorescence images of neuronal cell culture expressing CaMPARI. Top row, pre-photoconversion images showing fluorescence exclusively in the green channel. Bottom row, post-photoconversion images showing mixed green and red fluorescence after ∼5 min of total illumination with 395 nm light. **(B)** Wide-field epifluorescence images of neuronal cell culture expressing Cal-Light. Top row, pre-photoactivation images showing fluorescence in the red (tdTomato) channel. Bottom row, post-photoactivation images showing mixed red and green (GFP) fluorescence after ∼8–10 min of total illumination with 470 nm light and after 6 days of expression time. Scale bars, 200 μm and 50 μm in insets. Images were taken on a wide-field epifluorescence microscope (Nikon Ti2) using a 10x air objective (Plan Apo, 0.8 NA, 1,000 μm WD) and a Lumencor Spectra X LED. Fluorescence was imaged through 519/26 nm (GFP) and 642/80 nm (tdTomato) bandpass emission filters.

Buprenorphine (Temgesic, Reckitt Benckiser)
Carprofen (Rimadyl, Zoetis)
Lidocaine (Sigma, L7757).

Solutions

Neural Basal A (NBA) complete medium. NBA medium, supplemented with B27 (at 1× concentration), GlutaMAX (at 1× concentration) and Penicillin-Streptomycin (100 U/ml).

Hibernate a Complete Medium. Hibernate A medium, supplemented with B27 (at 1× concentration), GlutaMAX (at 1× concentration) and Penicillin-Streptomycin (100 U/ml).

ACSF. (in mM): 125 NaCl, 2.5 KCl, 1.25 NaH_2PO_4, 25 $NaHCO_3$, 2 $CaCl_2$, 1 $MgCl_2$, and 25 D-glucose in distilled water, pH ∼7.4.

Choline-ACSF. (in mM): 110 choline chloride, 2.5 KCl, 1.25 NaH_2PO_4, 26 $NaHCO_3$, 11.6 Na-L-ascorbate, 3.1 Na-pyruvate, 7 $MgCl_2$, 0.5 $CaCl_2$, and 10 D-glucose in distilled water, pH ∼7.4.

Sterile PBS. (in mM): 137 NaCl, 2.7 KCl, 10 Na_2HPO_4, 1.8 KH_2PO_4 in distilled water. Adjust the pH to 7.4 using NaOH.

Sterile Paraformaldehyde (4%). Dissolve 40 g of paraformaldehyde (PFA) in 800 ml of distilled water at 60°C. Add some drops of 1 M NaOH until the solution clears, and 100 ml of 10× PBS. Adjust the pH to 7.4 with 1 M HCl. Adjust to 1,000 ml with distilled water and filter sterilize.

Caution! The formaldehyde is toxic and a known carcinogenic. Do not inhale, or come into contact with skin and eyes.

Antibody and Blocking Solution. Brain sections are treated with blocking solution (5% Normal goat serum (NGS), 1% Triton X-100 in 1× PBS). Antibodies are incubated in the same solution.

Mounting Solution. 80% Glycerol + 2.5% DAPCO in PBS.

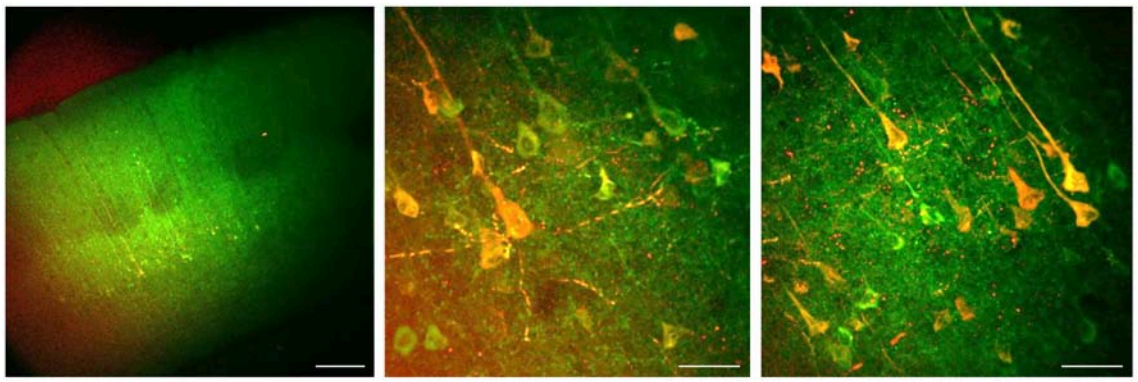

FIGURE 5 | CaMPARI for all-optical functional connectivity mapping. CaMPARI was expressed in S1 and ChR2-EYFP was expressed in M1 cortex. In acute *ex vivo* brain slices, violet light (405 nm, 120 mW cm^{-2}) was applied to S1 cortex that activates ChR2 and simultaneously drives conversion of post-synaptic CaMPARI-expressing neurons in layer 2/3 and 5. Here, conversion and stimulation light pulses were delivered at 10 Hz for a second, with a step of light for 5 s after the stimulus. There was a 12 s interval between each train, and this was repeated 10 times. Left, one-photon image of CaMPARI green/ChR2-EYFP under 4× magnification. After violet light illumination, red CaMPARI fluorescence is evident in layers 2/3 and 5. Scale bar, 200 μm. Middle and right panels, post-stimulation/conversion 60× magnification two-photon images of CaMPARI red/green in layers 2/3 and 5, from the corresponding slices. Scale bar, 50 μm. Exclusively in this Figure, CaMPARI (not CaMPARI2) was expressed.

Viruses/Antibodies

Viruses

All viruses were made in house by the Charité Viral Core Facility and were aliquoted and stored at −80°C. Aliquots of viruses in use (5 μl aliquots are typical) can be stored in a standard refrigerator at 4°C for several months. Viruses we used are:

- pAAV-TM-CaM-NES-TEV-N-AsLOV2-TEVseq-tTA
- pAAV-M13-TEV-C-P2A-TdTomato
- pAAV-TetO-GFP
- pAAV-Syn-CaMPARI2
- pAAV-ChR2-H134R-EYFP

Antibodies

- 1st antibody, CaMPARI 4F6, made at Janelia Farm Research Campus, Schreiter Lab, 1:1000
- 2nd antibody, Alexa 633, goat anti-mouse, Invitrogen A21050, 1:500

Microscopes

Wide-field epifluorescence (used for cell cultures; Nikon Ti2)
Epifluorescence (used to check *in vivo* expression; Nikon Stereo SMZ1270i)
Confocal laser scanning (Nikon A1Rsi+)
Two-photon (Femto 2D two-photon laser scanning system, Femtonics Ltd, Budapest, Hungary).

Surgical and Brain Slice Equipment

Dumont no. 5/45 cover slip forceps (Fine Science Tools, 11251-33)
Dumont no. 3, 4, 5, 7 forceps, assorted styles, straight (Fine Science Tools, 11231-30, 11254-20, 11241-30, 11251-10, 11271-30)
Standard-pattern forceps (Fine Science Tools, 11000-12, various lengths & diameters)
Spatula
Fine scissors (Fine Science Tools, 14060-09, 14058-09, 14090-09).
Dental drill (Osada Success 40 or Foredom Micromotor, HPA917).
Drill bits (Fine Science Tools, 19007-05, 19007-07, 19007-09)
Sterile single-use syringe, 0.4 ml (Omnican, B. Braun, 9161627)
Sugi absorbant swabs (Kettenbach Medical, 31602)
Parafilm (Sigma, P7793)
PCR Micropipettes, 1–5 μl (Drummond, 5-000-1001-X)
Eye care cream (Bepanthen, Bayer)
Mineral oil (Sigma, M3516)
Heating pad (Temperature Regulation System, FHC)
Self-adhesive resin cement (RelyX Unicem, 3M, Applicaps, 56815)
Contemporary Ortho-jet powder (black, Lang Dental, 1520BLK)
Kwik-Cast sealant (World Precision Instruments)
Pressure injector for low rate and small volume (Stoelting Quintessential Pressure injector, 53311)
Micropipette puller for virus-injection pipettes (Sutter Instrument, P-97)
Stereotaxic apparatus for small animals (KOPF, 940)
Vibratome (Leica, VT1200S)

Illumination Equipment

Ti:sapphire laser (MaiTai HP DeepSee; Spectra-Physics/Newport)
455 nm LED (for *in vivo* stimulation; Prizmatix, UHP LED Head 455)
405 nm LED (for *in vivo* stimulation; ThorLabs, 405FP1e)

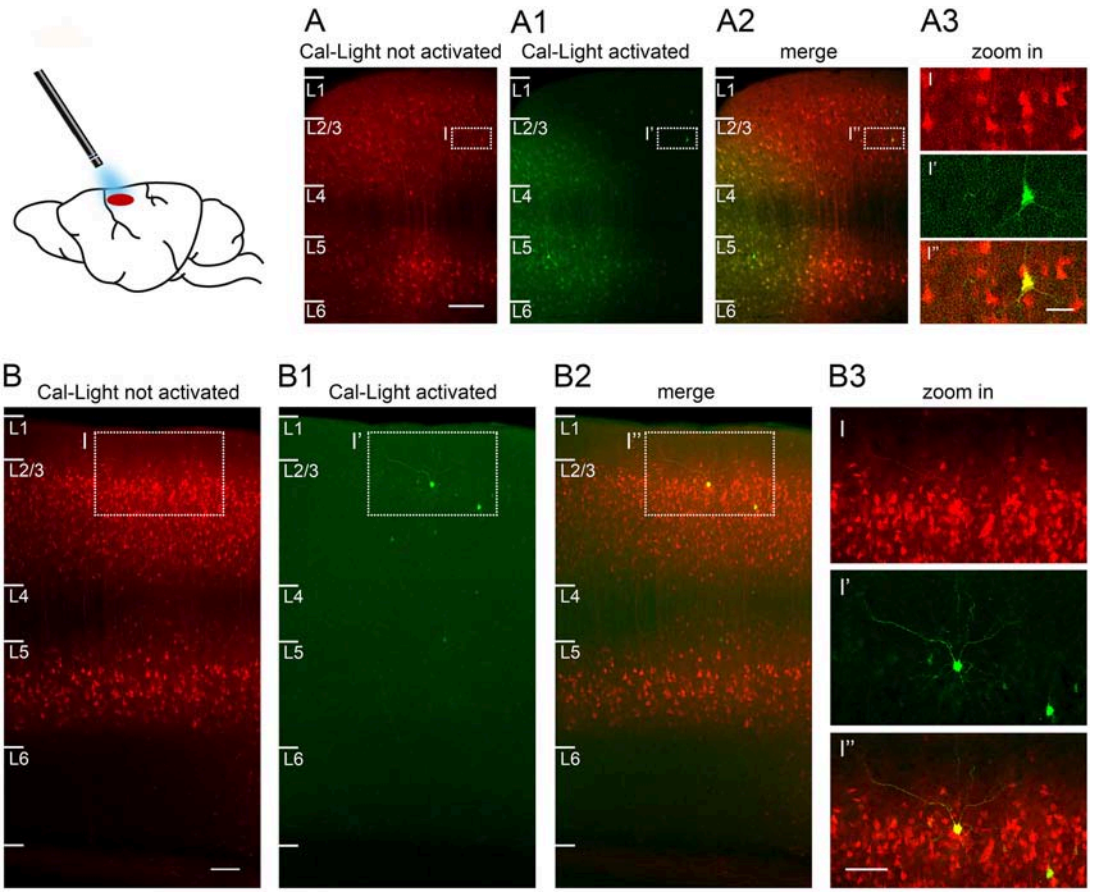

FIGURE 6 | Sparse Cal-Light expression triggered through a cranial window in an awake quietly sitting head-fixed mouse. **(A)** A large number of neurons express Cal-Light three weeks after virus injection. **(A1)** Neurons from layer 1 to layer 4 express GFP six days after exposure to 470 nm light while the mouse was head-fixed and awake. A halo of GFP expression marks the extent of spread of the 470 nm light *in vivo*. **(A2)** Merged image showing photoactivated, double-labeled neurons (yellow) in layers 2–5. **(A3)** Magnified view of one strongly photoactivated neuron in layer 3. **(B)** Example of S1 cortex neurons expressing Cal-Light three weeks after virus injection. **(B1,B2)** Images are taken slightly off the center of injection to highlight the few intensely GFP expressing neurons in layers 1–4, 6 days after exposure to 470 nm light while the mouse was head-fixed and awake. **(B3)** Magnified view of one strongly photoactivated neuron (bright yellow) and one less strongly photoactivated neuron (pale yellow) in layer 2. Sections are parasagittal, 300 μm. Scale bar in A 100 μm, in B 200 μm, in insets 50 μm. Slices were imaged on a confocal laser scanning microscope (Nikon A1Rsi+) using a 20x air objective (Plan Apo, 0.8 NA, 1.000 WD) and a 647 nm laser. Fluorescence was imaged through a 700/50 bandpass emission filter.

Optic fiber (for *in vivo* stimulation; Prizmatix, Optogenetics Fiber-500 *in-vitro*)
Mercury lamp (X-cite 200 W, Excelitas Technologies)
Optical power meter (ThorLabs, PM200 & S120VC)

Software

For two-photon image acquisition: Matlab-based MES software package (Femtonics)
Image-processing software (ImageJ, https://imagej.nih.gov/ij/)

Other

Eppendorf tubes, 0.5 ml (Sigma, T891)
Falcon tubes, 50 ml (Corning, 430921)
Glass coverslips (12 mm round; Roth, P231.1)
Glass coverslips (3–5 mm round; Warner Instruments, CS-3R-0, CS-4R, CS-5R-1)
Glass-bottom dishes (Eppendorf, 0030740017)
0.2 μm filters (Carl Roth, P668.1)
Haemocytometer (A. Hartenstein, ZK06)
24-well cell culture plates (Corning, 353047)

PROCEDURES

(A) Preparation of dissociated primary neuronal cell cultures (duration: 3 h)

Note: The production of dissociated primary neuronal cell cultures has been described previously (Turko et al., 2019). All procedures should be performed under sterile conditions. All solutions should be filter sterilized using a 0.2 μm filter. Glass coverslips and dissection tools should be heat sterilized for 3 h at 185°C.

(1) Dissociate wild type cortico-hippocampal tissue from Wistar rat pups (post-natal days 0–2).

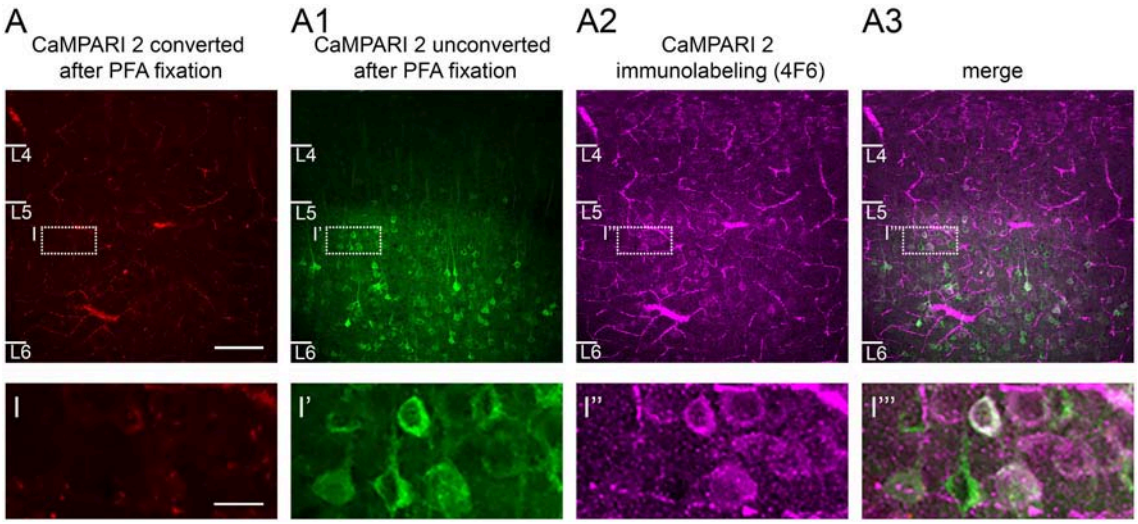

FIGURE 7 | CaMPARI expression: Effects of fixation and use of immunostaining to recover converted neurons. **(A)** After fixation in 4% PFA, only a few neurons in S1 cortex show some weak red fluorescence signal reflecting the photoconversion of CaMPARI carried out *in vivo*. **(A1)** A large number of unconverted green neurons are still visible. **(A2)** When the CaMPARI 4F6 antibody targeting the converted form of CaMPARI is used, it reveals converted neurons, and **(A3)**, distinguishes them from neighboring unconverted neurons as seen in the merged image. Bottom row, magnified views of inset regions showing converted vs. non-converted cells. Sections are coronal, 300 μm and were taken directly from an *in vitro* experiment and placed in PFA overnight. Blood vessels are prominent because the brain was not perfused prior to fixation. Scale bar in A 100 μm, in inset 50 μm.

(2) Estimate cell densities using a haemocytometer or automated cell counter.
(3) Grow cells on 12 mm round-glass coverslips coated with Poly-L-Lysine (1 h coating; 20 μg/ml concentration).
(4) Plate cells in 24-well cell culture plates, at a density of 400 cells per μl in a 500 μl droplet (total cells per well: 2×10^5).
(5) Culture cells in Neural Basal A medium, supplemented with B27 (at 1× concentration), GlutaMAX (at 1× concentration) and Penicillin-Streptomycin (100 U/ml). The incubator temperature should be 37°C.
(6) Feed cells weekly by removing 100 μl of conditioned cell culture medium and adding 200 μl of freshly made cell culture medium.

(B) Cell culture transfection (duration: 20 min)
Prepare virus solutions in sterile aliquots. The total volume should be 1 μl per coverslip to be transfected.

(1) Wait 5–20 days for cultures to grow before infecting.
(2) Virus solutions:

- For CaMPARI, prepare pAAV-Syn-CaMPARI2 with a titer of ∼10^{11}-10^{12} GC/ml.
- For Cal-Light, mix three components:
  - pAAV-TM-CaM-NES-TEV-N-AsLOV2-TEVseq-tTA
  - pAAV-M13-TEV-C-P2A-TdTomato
  - pAAV-TetO-GFP

The pAAV-TetO-GFP can be replaced by viruses linking other genetic constructs, e.g., ChR2, iChloC, or ArCHT to TetO. GFP is expressed when pAAV-TetO-GFP is used. The ratio of the TetO construct to the two other viruses can be varied, depending on the experimental requirements (see Lee et al., 2017). Here, we use a mixture of 1:1:2 for the three viruses. The titers for each construct we used were ∼10^{12}-10^{13} GC/ml.
(3) Dilute the virus solution in 20 μl sterile PBS per 1 μl of virus. Vortex thoroughly.
(4) Take the well plate(s) out of the incubator and rapidly add 20 μl of the solution to each well in the plate containing coverslips to be transfected and then put them back into the incubator.

(C) Photostimulation and imaging (duration: 1–3 h, Figure 4, Supplementary Video Files 1, 2)
To test CaMPARI photoconversion and Cal-Light photoactivation, cells have to be active and cytosolic calcium increases have to be coupled to light exposure. To promote network activity in cell cultures, cells were incubated with the $GABA_A$ receptor antagonist gabazine blocking fast GABA-mediated synaptic inhibition. To further promote network activity, some cultures were also treated with the muscarinic receptor agonist carbachol.
Critical step: After transfection, wait ∼10 days for sufficient expression levels. If possible, check for expression of the constructs using an epifluorescence microscope. Optimally, cultures should be >21 days old at the time of photostimulation, leaving enough time for network maturation.

(1) Thaw frozen stock solutions of gabazine and carbachol at room temperature for 15 min. Incubate a conical tube containing 8 ml of hibernate A complete media in a water bath (37°C) for 15 min.

(2) Following incubation, pipette 2 ml of hibernate A complete media to a glass-bottom plate. Transfer a 24-well plate from the incubator to a laminar flow hood. Use sharp forceps to transfer a coverslip containing cells from the 24-well plate to the glass-bottom plate. Use a platinum ring (or suitable alternative) to hold the coverslip in place. Quickly transfer the 24-well cell culture plate back to the incubator.
Critical step: We recommend using glass bottom dishes for imaging, as they offer improved optical quality.
Caution! As hibernate A complete media is buffered for ambient CO_2 levels, it is not compatible with incubators that are gassed with 5% CO_2.

(3) Place the glass-bottom dish inside the microscope sample holder and focus on the cell layer. Depending on the experiment, drugs may be carefully pipetted into the hibernate solution to increase network activity. To reduce inhibition and to generate repetitive bursts of action potentials and increased network activity, apply 10 μM gabazine (final concentration) to cell cultures. If after 10 min gabazine does not increase network activity (activity can be monitored if cells express CaMPARI, see below), apply 10 μM carbachol (final concentration) to promote a further increase in activity. Take pre-stimulation images in any fluorescence channels that are of interest (see next step).
Note: We use a Nikon Ti2 wide-field microscope designed for live-cell imaging.

(4) Image acquisition:

- In cultures expressing CaMPARI, network activity can be monitored before photoconversion. This is possible because CaMPARI is also a calcium indicator related to GCaMP3, which dims rapidly and reversibly upon calcium influx (Fosque et al., 2015). Thus, changes in luminosity of CaMPARI-expressing neurons indicate that cells and circuits are active, with the dimming in fluorescence indicating an increase in intracellular Ca^{2+} concentration. A time series of 60 images at 1 Hz can be used to detect activity. Prior to photoconversion, there should be little to no fluorescent signal in the 555 nm channel.
- In cultures expressing Cal-Light, images are acquired at 555 nm (to check tdTomato expression) and at 470 nm (to check GFP expression). In the pre-stimulation period, when 470 nm light has not been applied, there should be no fluorescent neurons in the green (470 nm) channel.

Note: We used the following filters: 395/25 nm, 470/24 nm and 550/15 nm for excitation and 519/26 nm (GFP) and 642/80 nm (tdTomato) for emission.

Critical step: If drugs are applied to the cultures, we recommend that light for photoconversion or photoactivation be delivered to the culture ∼10 min after drug application. This ensures that there is sufficient time for diffusion of the drugs in the medium and develop their action on the neurons.

(5) Macros:

- For CaMPARI, set up an automated macro script to acquire images in both 470 and 550 nm light channels, interspersed with 395 nm light stimulus (**Supplementary Video Files 1, 2**). We suggest acquiring a series of 60 images per channel, each followed by a 5 s pulse of 395 nm light, leading to 5 min of total light delivery. Carefully observe conversion and stop the procedure earlier if desired conversion levels are reached. The light power of the stimulus should be ∼4–10 $mW{\cdot}cm^{-2}$.
- For Cal-Light, set up an automated macro script that repetitively triggers a light stimulus at 470 nm (ON), followed by an interval of darkness (OFF). We suggest applying either 2 s ON/8 s OFF or 1 s ON/4 s OFF for 40–60 min, leading to 8–12 min of total light delivery. The light power of the stimulus should be ∼4–10 $mW{\cdot}cm^{-2}$.

Critical step: Due to its susceptibility to photobleaching, we recommend testing CaMPARI photoconversion at low light power first.
Note: While CaMPARI photoconversion can be imaged immediately, photoactivation of Cal-Light takes ∼2–5 days.

(6) Once photoconversion occurs or light for photoactivation of Cal-Light expression has been delivered, transfer the coverslip from the hibernate solution to a well-filled with cell culture medium in a laminar flow hood. Return the cell culture plate to the incubator.

(7) Further handling:

- CaMPARI remains in its converted form for 2–3 days but will be progressively removed by protein turnover. In other words, the most reliable CaMPARI signal is detected right after conversion. Cells expressing CaMPARI can be used for additional experiments once protein turnover has removed the conversion, i.e., red CaMPARI has been fully replaced by newly produced green CaMPARI.
- Cells expressing Cal-Light require at least 2–5 days to show reliable expression of the photoactivated construct. Make sure that incubator conditions (atmosphere and temperature) are optimal during that time and feed as required.

(D) Surgical preparation for *in vivo* and *in vitro* expression of Cal-Light and CaMPARI: virus dilution, mixing, and loading (duration: 30 min)

(1) Virus solutions:

- Cal-Light: Prepare Cal-Light as described above [in section **(B)**(2)]. Mix three components:
  pAAV-TM-CaM-NES-TEV-N-AsLOV2-TEVseq-tTA,
  pAAV-M13-TEV-C-P2A-TdTomato and
  pAAV-TetO-GFP at a ratio of 1:1:2 (titers $\sim 10^{12}$-10^{13} GC/ml)
- CaMPARI: Prepare pAAV-Syn-CaMPARI2 with a final titer of $\sim 10^{11}$-10^{12} GC/ml in a sterile 0.5 ml Eppendorf tube (total volume should be $\sim 5\ \mu l$).

Critical step: The optimal expression parameters of each virus should be determined in an initial step, where various virus dilutions series are tested.
Note: Manual injections with pipettes or Hamilton syringes can be effective for injecting viruses, but here we use a motorized Quintessential injector (Stoelting). This injector is effective for controlled delivery of small volumes of virus. The flow rate and volumes (down to picoliters) can be adjusted. The injector is attached to a stereotaxic frame and pulled pipettes designed to deliver 5–10 μl, are positioned in the injector. 50–200 nl of virus are injected at 2–3 different depths at each injection site. Note that there are many methods for filling pipettes. It is possible to back-fill injection pipettes with mineral oil and then withdraw virus into the pipette tip, or to invert the process and fill the pipette tip with virus and back-fill with mineral oil.

(2) Pull glass pipettes for injections (5 or 10 μl) on a Sutter puller. Carefully cut the pulled pipettes back to ∼10–20 μm with sharp scissors under a stereo-microscope. Before loading the virus, place a drop of mineral oil on a piece of sterile Parafilm.

(3) To load the virus, insert a pulled glass-micropipette tip-first into a plastic-pipetting tip attached to an insulin syringe. Make sure that there is no air leaking when negative pressure is applied on the syringe. Carefully back-load 300–500 nl of virus from an Eppendorf tube into the open end of the micropipette. After loading the virus, release the pressure on the insulin syringe. Position the plastic pipette opening over the prepared oil drop on the piece of Parafilm. Apply negative pressure on the syringe and load ∼500 nl of mineral oil. The boundary between virus solution and mineral oil should be visible as a clear contrast of phases. Carefully remove the filled glass micropipette from the plastic syringe and place it into the injector attached to a stereotaxic arm. Dispose the Parafilm in a biohazard waste bin and keep the remaining virus solution in the refrigerator at 4°C.

Critical step: Ensure that the tip of the micropipette is not damaged and that it has the correct size (diameter ∼10 μm). This precaution should be taken to avoid damaging of dura and brain tissue.

(E) Surgical preparation for *in vivo* and *in vitro* expression of Cal-Light and CaMPARI: stereotaxic injections (duration: 40 min)

Critical step: Clean the surgery area and the surgical instruments with 70% ethanol and let dry. If possible, to prevent any infections, surgical instruments can be autoclaved and sterile packs can be prepared for use in surgery.

(1) Before surgery, anesthetize mice deeply with an intraperitoneal injection of ketamine/xylazine (100/10 mg kg^{-1}) solution. Once mice no longer react to tail or toe pinches, trim the fur on the head with sharp scissors or with an electric trimmer. Place mice into the stereotaxic apparatus (Kopf Instruments Inc., California, USA). Make sure that ear bars and the mouth piece are positioned correctly to hold mice in place for the duration of the surgery.

Caution! All experiments with animals must have an animal license number and be approved by institutional and/or governmental agencies. The experiments described in this protocol were conducted after approval by the Landesamt for Gesundheit und Soziales (LAGeSo), Berlin, Germany.
Critical step: It is absolutely crucial that the mice are well-anesthetized and receive the correct doses of analgesics.

(2) Provide local analgesia by injecting lidocaine (1–2%, 0.1–0.2 ml) locally under the scalp where the craniotomy is to be made.

Caution! Apply eye care cream (Bepanthen) to prevent the eyes from drying out.

(3) When mice are fully sedated and positioned properly in the stereotaxic frame, ensure that the head is leveled and aligned. For injections deep into the brain it is necessary to ascertain that the *Z*-plane, the anterior and posterior parts of the skull are flat, positioned completely horizontally. Flat plane skull can be ascertained by positioning the micropipette tip at bregma, measuring the *z*-position, and repeating this measurement at lambda. Head fixation can be adjusted until the readings at the two points on the skull are identical.

(4) Once the fur is trimmed, disinfect the scalp using 70% ethanol. Carefully cut the scalp with a sterile scalpel and the splay the skin out with a forceps (Dumont, no 5). If needed, irrigate the wound edge with saline. Remove any excess liquid using absorbent swabs (Sugi, Kettenbach).

(5) Define the stereotaxic coordinates by setting the reference point "0" at bregma. Mark the cortical area of interest (in our case, barrel cortex, medial-lateral 2.5 mm, anterior-posterior −2.0 mm) with a pen or carefully with a scalpel blade. Drill a circular craniotomy of 1 mm radius around the mark. Apply careful and slow drilling without fully perforating the bone. By constantly applying sterile PBS to the bone, heating, and damaging of the dura can be avoided. After thinning

the bone by continuous drilling, it should be possible to remove the perforated piece of bone.

Critical step: While drilling, carefully check the thickness of the remaining bone. Avoid damaging the dura or the brain by applying too much pressure or by overheating the drill bit by persistent drilling. Regular irrigating with saline solution or air cooling is essential!

(6) Apply sterile PBS onto the craniotomy and carefully clean the injection site using absorbent swabs. Keep the brain moist with PBS.
(7) Put the virus-filled injection micropipette into the stereotaxic holder and place the pipette over the injection site in a 90° angle to the brain. Use the micro-injection controller to apply positive pressure and to generate a small drop of virus, visible at the tip of the pipette. This is to assure that the pipette is not clogged and virus solution can be injected smoothly.
(8) Lower the injection micropipette and penetrate the dura to reach the desired depth (in our experiments, we injected at 0.6, 0.4, 0.2, and 0.1 mm) below the pial surface. Once the pipette is at its correct position, the virus can be injected with positive pressure (100–200 nl at 15–20 nl min^{-1}).

Critical step: Ensure that the micropipette is not clogged and that the dura is moist so that the brain is not damaged when penetrating the pia with the injection pipette.

(9) After injection, wait for 5 min before removing the micropipette slowly from the cortex. Remove the pipette from the stereotaxic holder and dispose in a biohazard waste bin. Carefully clean the brain again with sterile PBS.

Note: If CaMPARI circuit mapping [procedure **(G)**] is planned, perform another virus injection using ChR2 in the presynaptic area of interest.

(10) Inject the analgesics carprofen (5 mg/kg) and buprenorphine (0.05–0.1 mg/kg) intraperitoneally to ensure a pain-free recovery of the animal.
(11) Remove the mouse from the stereotaxic frame by loosening the ear bars and the nose piece.
(12) Suture the scalp with sterile suture sewing thread. Carefully put the mouse back into its home cage, which is put on a warming device. Monitor the mouse until it has woken up.

Critical step: Ensure that the mouse is waking up under smooth conditions. Avoid placing an anesthetized mouse together with awake mates in one cage.
Caution! After surgery, care has to be applied to each mouse individually and according to the regulations and guidelines. The mice of our experiments were monitored daily for 3 days after the surgery for pain, divergent behavior in food uptake, and abnormal social behavior.

(F) Acute brain slice preparation (duration: 1.5 h)

(1) Allow CaMPARI to express for >14 days following viral injection(s) *in vivo*.
(2) Deeply anesthetize the mouse (postnatal age >P21) with isoflurane (1.5–3% in O_2). Remove and section the brain into coronal, 300 μm thick slices with a vibratome under cold (∼0°C) choline-based artificial cerebrospinal fluid (ACSF).

Note: For brain slicing and initial incubation (≤5 min), the use of choline-ACSF may help to improve slice viability. For photoconversion and recording, use normal ACSF.

(3) Transfer each slice after sectioning to an incubation chamber at 32°C for 5 min in a solution containing choline ACSF saturated with 95% O_2/5% CO_2.
(4) Transfer the slices into an incubation chamber containing normal ACSF at 32°C for 25 min and then at room temperature for an additional 30 min before use in experiments.

Note: Brain sections stored in ACSF saturated with 95% O_2/5% CO_2 at room temperature remain viable for up to ∼6–8 h.

(G) Circuit mapping *in vitro* with CaMPARI (duration: 1–3 h, Figure 5)

CaMPARI can be used to map cortical circuit activity driven by optogenetically defined inputs in brain slices (Zolnik et al., 2017). After slicing, axon terminals remain functional and excitable by light when expressing ChR2 (Petreanu et al., 2007; Cruikshank et al., 2010), enabling an *in vivo*-like assessment of specific input pathways. Additionally, neurons in acute brain slices are normally hyperpolarized and minimally active, which provides a low background for more reliable signal. As a planar section, the brain slice can be uniformly illuminated, eliminating confounds from uneven illumination intensity. The resulting post-synaptic activation pattern in an acute brain slice reflects functional connectivity from the target pathway. Control experiments with the same stimulation and light conditions can be performed to measure background conversion from green to red in the absence of ChR2 expression (see **Figure 4** in Zolnik et al., 2017).
Note: A range of filters and stimulation parameters can work for circuit mapping with ChR2 and CaMPARI. For example, a Cy3 emission filter (∼580/50 nm) includes the peak fluorescent emission of CaMPARI red (Fosque et al., 2015). However, even a 650/50 nm filter works for imaging CaMPARI red, despite its very red shifted emission band (Zolnik et al., 2017). For imaging CaMPARI green, a FITC filter (∼475/35 nm), appropriate for GFP or GCaMP imaging is ideal.

(1) Deliver violet light for optogenetic stimulation and CaMPARI photoconversion using an X-cite 200 W mercury lamp (Excelitas Technologies, Mississauga, Ontario, Canada) and light guided through a 405/10 nm bandpass filter (Semrock, FF01-405/10-25). In one-photon imaging experiments, photoconversion/stimulation light is delivered by a UPlanFL 4×/NA 0.13 objective.

Measure the light stimulus intensity with a Thor Labs optical power meter (PM 200) and a photodiode sensor that works in the UV range (S120VC). For the experiments in **Figure 5**, the light power was 120 mW cm^{-2} at 405 nm. This light intensity is sufficient for inducing conversion and activating ChR2. The stimulation/conversion and initial fluorescence imaging was performed under a one-photon microscope through a 4× objective.

Critical step: Before applying the stimulation protocol, it is necessary to acquire baseline images in both red and green wavelengths.

Critical step: In case slices are to be used for immunocytochemistry [procedure **(K)**], live imaged brain sections should be marked prior to fixation—this is essential for aligning the *post-hoc* image to the anti-CaMPARI immunostained section.

Note: ChR2 is not efficiently activated at 405 nm (peak activation ∼470 nm), and therefore higher light intensities may be necessary or additional light must be delivered at 470 nm to boost the ChR2 excitation. If using stronger 405 nm light to activate ChR2, this will increase the CaMPARI conversion rate (Zolnik et al., 2017) and thus the duration of illumination may need to be adjusted.

(2) Photoconvert neurons with 10 pulses, 15 ms in duration, delivered at 10 Hz, followed by a 5 s-long light pulse. This protocol—especially the 5 s light pulse at the end of the stimulus train—ensures that the photoconversion light is delivered when calcium is elevated in the post-synaptic target neurons.
(3) For quantification of the red/green ratios of each neuron, two-photon imaging is necessary. A standard brain slice immersion chamber is needed to maintain slice viability during live imaging for these experiments.

Note: Optimally, the photoconversion and imaging steps can be combined by delivering 405 nm light through the objective used on a two-photon imaging setup. However, it is also possible to deliver light obliquely to the sample by using the light guide, filter, and a collimator (Cairn Research, Faversham, UK) and lens (Thorlabs, Newton, NJ, USA; AC254-030-A-ML, $F = 30$ mm).

(H) Two-photon imaging (duration: 1–3 h, Figure 5)

(1) Use a two-photon laser scanning system equipped with a femtosecond pulsed Chameleon Ti:Sapphire laser controlled by the MES software package.
(2) Tune the laser to $\lambda = 820$ nm for excitation of CaMPARI red and green fluorescence.

Note: If you have access to a two-photon system with a widely tunable laser, we would recommend imaging CaMPARI green at $\lambda = 980$ nm and CaMPARI red at $\lambda = 1{,}040$ nm.

(3) Detect fluorescence in epifluorescence mode with a water immersion objective (LUMPLFL 60×/1.0 NA, Olympus, Hamburg, Germany), and trans-fluorescence and transmitted infrared light with an oil immersion condenser (Olympus; 1.4 NA). Emission light can be divided with a dichroic mirror at ∼590–600 nm, and green and red signals filtered using 525/50 and 650/50 bandpass filters, respectively.

Note: The emission of CaMPARI red peaks at ∼580 nm, and thus a filter that contains this fluorescence band is ideal, but be careful to check that there is no bleed through from the excitation of the CaMPARI green.

Critical step: Carefully handle the slices when placing them in the recording chamber to maintain cell viability during photoconversion.

Caution! Ensure that the slice remains in a stable position before starting z-stack image collection. Slice movement can distort your images.

(I) Surgical preparation for *in vivo* expression of Cal-Light and CaMPARI: cranial window and head post-implant (duration: 1–2 h)

(1) Allow >14 days for expression of constructs after surgery.
(2) Follow steps (1)–(4) of module **(E)**.
(3) Incise the scalp and scrape the skull. Carefully remove the fascia and let the skull air dry. When dry, place a metal head post (ours are custom-made, the shape varies) on the clean and dry skull. Next, use self-adhesive resin cement (RelyX Unicem, 3M ESPE) to glue the head post in place.
(4) Once the cement has hardened, drill a circular craniotomy of 3 mm radius around the spot where virus had been injected previously. Apply careful and slow drilling without fully perforating the bone. By constantly applying sterile PBS to the bone, heating and damaging of the dura can be avoided. After thinning the bone by continuous drilling, it should be possible to remove the perforated piece of bone.

Critical step: While drilling, carefully monitor the thickness of the underlying bone. Avoid damaging the dura or the brain by applying too much pressure or by drilling continuously and overheating the drill bit and brain. Irrigate using sterile saline/PBS if needed and remove excess liquid with absorbent swabs.

(5) Prepare a 3 mm glass coverslip by cleaning in 70% ethanol. Carefully place the coverslip on the part of the mouse brain that is uncovered by the craniotomy. Use the arm on the stereotaxic apparatus to position a wooden tipped applicator or toothpick over the coverslip and apply slight pressure to push the coverslip into the craniotomy and hold in place.
(6) Apply superglue at the edges of the coverslip and bone to fix the coverslip into the craniotomy, then wait for the glue to dry and carefully release the wooden tip off the window.

Critical step: Be careful not to drop glue on top of the glass window as this will reduce the imaging quality.

(7) Cover the head post using Ortho-jet powder (Lang Dental, Black) to fill any gaps and to increase stability.
(8) Cover the glass and well-around the craniotomy with Kwik-Cast Sealant silicone (WPI, World Precision Instruments).
(9) Once the sealant firmed up, apply analgesics [see procedure **(F)**], take the mouse out of the stereotaxic apparatus and monitor. Once the mouse wakes up, place it back in its home cage.

(J) *In vivo* photostimulation (duration: 1–3 h; Figures 3B, 6)

Critical step: Allow >7 days for mice to recover from head post and cranial window surgery. Habituate mice by handling and head-fixing them for increasing durations in several sessions. Reward (e.g., sweet milk) may be given to mice to make them more comfortable during the habituation process. In head-fixed mice, check for expression of the construct and take an image using an epifluorescence microscope.
Critical step: Re-apply Kwik-Cast silicone whenever the sealant is lost or removed for microscopy to avoid possible unwanted photostimulation via ambient light sources.

(1) For the main photostimulation session, head-fix the mouse in the stimulation setup and remove the sealant. Place the tip of an optic fiber connected to the LED light source directly on top of the glass window at a 90° angle. Make sure that the light spot overlaps with the area of expression.

Caution! If the mouse appears to be in pain or severe discomfort during the session, stop the experiment and extend the habituation period.

(2) Photostimulation.

- For Cal-Light-expressing animals, set up an automated macro script that repetitively triggers a light stimulus at 470 nm (ON), followed by an interval of darkness (OFF). We suggest applying either 2 s ON/8 s OFF or 1 s ON/4 s OFF for 40–60 min, leading to 8–12 min of total light delivery. The light power of the stimulus should be ∼20–30 mW (measured at the tip of the optic fiber).
- For CaMPARI, set up an automated macro that repetitively triggers a light stimulus at ∼395–405 nm (ON), followed by an interval of darkness (OFF). We suggest applying either 2 s ON/8 s OFF or 1 s ON/4 s OFF for 40–60 min, leading to 8–12 min of total light delivery. The light power of the stimulus should be ∼20–30 mW (measured at the tip of the optic fiber).

Caution! Measure light intensity at the fiber tip and use light intensity at surface of <30 mW and carefully monitor light application, as high light power may cause damage on the brain!
Note: Cal-Light-triggered gene expression takes 2–5 days. CaMPARI photoconversion occurs within seconds.

(K) CaMPARI immunohistochemistry (duration: 2 days; Figure 7)

(1) After imaging of the live brain slices, fix them in formaldehyde-based (4%) fixative at 4°C overnight.

Critical step: After formaldehyde fixation, an image can be taken for control that no endogenous expression is left.
Critical step: Be careful not to confound sides of brain slice (upper, converted vs. lower, non-converted side). This is important for later analysis at the confocal microscope.

(2) Wash slices in phosphate buffered saline solution (PBS) and block in blocking solution for 2 h at room temperature.

Critical step: Rinse slices in PBS thoroughly to ensure that compounds are washed out.

(3) Incubate brain slices in primary antibody containing solution (CaMPARI 4F6, at a dilution of 1:1,000 in blocking solution) at 4°C overnight.
(4) Dispose the primary antibody, rinse slices in PBS before incubation in the secondary antibody solution (Alexa 633, goat anti mouse, Invitrogen A21050, at a dilution of 1:500 in blocking solution) for 2 h at room temperature.
(5) Dispose the secondary antibody, rinse slices in PBS.
(6) Mount slices in mounting solution (80% glycerol + 2.5% DAPCO in PBS) on a regular slide and coverslip.

Note: An immunostaining for endogenous CaMPARI in blue (405 nm excitation wavelength) can be added with the Flag antibody (Sigma F425), which works nicely in cultured neurons.

ANTICIPATED RESULTS

Photostimulation in Neuronal Cell Culture

After transfection, cultured neurons begin to express CaMPARI within ∼10 days, this appears as a green fluorescent signal. Calcium transients in these neurons are noticeable as dimming in fluorescence and occur when network activity increases (e.g., via blocking inhibition and/or by application of carbachol; see **Supplementary Video Files 1, 2**). Active neurons expressing CaMPARI photoconvert from green to red when 395 nm light is applied during active states (**Supplementary Video Files 1, 2** and **Figure 4**).

Cultured neurons express Cal-Light within ∼10 days, indicated by a red fluorescent signal via tdTomato expression. When network activity increases (e.g., by blocking inhibition and/or by application of carbachol), active neurons expressing Cal-Light are photoactivated and express GFP within 2–5 days after exposure to 470 nm light (**Figure 4**).

Circuit Mapping in Acute Brain Slices

Two to three weeks after virus injection, neurons begin to express CaMPARI. At this point, *ex vivo* brain slices can be prepared in which CaMPARI green-expressing neurons

should be visible in both single-photon and two-photon excitation. Circuit mapping experiments, by applying 405 nm light, then reveal post-synaptic targets of axon fibers expressing ChR2 via photoconversion of CaMPARI from green to red (**Figure 5**).

Photostimulation *in vivo*

Two to three weeks after virus injection, neurons begin to express Cal-light or CaMPARI. This expression (green CaMPARI or red Cal-Light) is visible through the cranial window using epifluorescence microscopy (**Figure 3B**). At this point, photostimulation is applied *in vivo* in head-fixed, habituated quietly sitting mice. After photostimulation, a shift from green to red fluorescence should appear within seconds in the case of CaMPARI (**Figure 3B**) or additional green fluorescence should appear after 2–5 days in the case of Cal-Light. Preparation and imaging of brain slices or sections will then reveal individual neurons that were labeled (**Figures 3B**, **6**).

Immunohistochemistry

Immunostaining recovers the CaMPARI red signal in photoconverted neurons that is quenched after fixation (**Figure 7**). Following the immunostaining steps, single converted and non-converted neurons are distinguishable based on their expression, conversion, laminar localization and other anatomical features.

DATA AVAILABILITY

All datasets generated for this study are included in the manuscript and/or the **Supplementary Files**.

ETHICS STATEMENT

We performed all procedures in accordance with protocols approved by the Charité—Universitätsmedizin Berlin and the Berlin Landesamt für Gesundheit und Soziales (LAGeSo) for the care and use of laboratory animals.

AUTHOR CONTRIBUTIONS

CE, SD, PT, PP, BE, IV, ML, and RS designed the study. CE, JL, TZ, SD, and AP did the experiments. CE, JL, PT, and RS wrote the paper. All authors read and edited text, contributed to manuscript revision and approved the submitted version.

FUNDING

The following funding sources have supported this project: (1) Deutsche Forschungsgemeinschaft (Exc 257 NeuroCure Ph.D. Fellowship to CE; Exc 257 NeuroCure International Visiting Fellowship to PP; Grant No. 2112280105 to ML; Grant No. LA 3442/3-1 & Grant No. LA 3442/5-1 to ML), (2) European Research Council (ERC StG 311435 to PP; European Union's Horizon 2020 research and innovation program and Euratom research and training program 2014–2018, under grant agreement No. 670118 to ML), (3) Human Brain Project (EU Grant 720270, HBP SGA1 & SGA2, Context-sensitive Multisensory Object Recognition: A Deep Network Model Constrained by Multi-Level, Multi-Species Data to ML), (4) Einstein Stiftung Berlin.

ACKNOWLEDGMENTS

We would like to thank Alexander Schill, Jan-Erik Ode, and Daniel Deblitz of the Charité Workshop for technical assistance; Thorsten Trimbuch, Anke Schönherr, and Bettina Brokowski of Viral Core Facility of the Charité (vcf.charite.de) for the production of viruses; Friedrich Johenning and the Schmitz lab for the use of a Femtonics two-photon system; Jan Schmoranzer and the Charité AMBIO facility for the training and use of the wide field imaging setup and Marti Ritter for assistance during cell culture photostimulation experiments. We would also like to thank Eric Schreiter and Hyung-Bae Kwon for commenting on an earlier version of this manuscript.

SUPPLEMENTARY MATERIAL

The Supplementary Material for this article can be found online at: https://www.frontiersin.org/articles/10.3389/fnsyn.2019.00016/full#supplementary-material

Supplementary Video Files 1 and 2 | Photoconversion of CaMPARI-expressing cells in neuronal cell culture using wide-field epifluorescence imaging. Momentary dimming of fluorescence indicates calcium-intensive events. Videos contain 60 frames, each taken prior to a 5-s long pulse of 395 nm light. Green and red imaging channels are merged. Video 1, using 10× objective and Video 2, using 20× objective.

REFERENCES

Andermann, M. L., Gilfoy, N. B., Goldey, G. J., Sachdev, R. N., Wölfel, M., McCormick, D. A., et al. (2013). Chronic cellular imaging of entire cortical columns in awake mice using microprisms. *Neuron* 80, 900–913. doi: 10.1016/j.neuron.2013.07.052

Barth, A. L. (2007). Visualizing circuits and systems using transgenic reporters of neural activity. *Curr. Opin. Neurobiol.* 17, 567–571. doi: 10.1016/j.conb.2007.10.003

Cazzulino, A. S., Martinez, R., Tomm, M. K., and Denny, C. A. (2016). Improved specificity of hippocampal memory trace labeling. *Hippocampus* 26, 752–762. doi: 10.1002/hipo.22556

Cruikshank, S. J., Urabe, H., Nurmikko, A. V., and Connors, B. W. (2010). Pathway-specific feedforward circuits between thalamus and neocortex revealed by selective optical stimulation of axons. *Neuron* 65, 230–245. doi: 10.1016/j.neuron.2009.12.025

DeNardo, L., and Luo, L. (2017). Genetic strategies to access activated neurons. *Curr. Opin. Neurobiol.* 45, 121–128. doi: 10.1016/j.conb.2017.05.014

Dogbevia, G. K., Marticorena-Alvarez, R., Bausen, M., Sprengel, R., and Hasan, M. T. (2015). Inducible and combinatorial gene manipulation in mouse brain. *Front. Cell. Neurosci.* 9:142. doi: 10.3389/fncel.2015.00142

Fosque, B. F., Sun, Y., Dana, H., Yang, C. T., Ohyama, T., Tadross, M. R., et al. (2015). Labeling of active neural circuits *in vivo* with designed calcium integrators. *Science* 347, 755–760. doi: 10.1126/science.1260922

Greenberg, M. E., Ziff, E. B., and Greene, L. A. (1986). Stimulation of neuronal acetylcholine receptors induces rapid gene transcription. *Science* 234, 80–83. doi: 10.1126/science.3749894

Kawashima, T., Okuno, H., and Bito, H. (2014). A new era for functional labeling of neurons: activity-dependent promoters have come of age. *Front. Neural. Circuits* 8:37. doi: 10.3389/fncir.2014.00037

Ko, H., Hofer, S. B., Pichler, B., Buchanan, K. A., Sjöström , P. J., and Mrsic-Flogel, T. D. (2011). Functional specificity of local synaptic connections in neocortical networks. *Nature* 473, 87–91. doi: 10.1038/nature09880

Lee, D., Hyun, J. H., Jung, K., Hannan, P., and Kwon, H. B. (2017). A calcium- and light-gated switch to induce gene expression in activated neurons. *Nat. Biotechnol.* 35, 858–863. doi: 10.1038/nbt.3902

Lien, A. D., and Scanziani, M. (2011). *In vivo* labeling of constellations of functionally identified neurons for targeted *in vitro* recordings. *Front. Neural. Circuits* 5:16. doi: 10.3389/fncir.2011.00016

Mansuy, I. M., Winder, D. G., Moallem, T. M., Osman, M., Mayford, M., Hawkins, R. D., et al. (1998). Inducible and reversible gene expression with the rtTA system for the study of memory. *Neuron* 21, 257–265. doi: 10.1016/S0896-6273(00)80533-4

Moeyaert, B., Holt, G., Madangopal, R., Perez-Alvarez, A., Fearey, B. C., Trojanowski, N. F., et al. (2018). Improved methods for marking active neuron populations. *Nat. Commun.* 9:4440. doi: 10.1038/s41467-018-06935-2

Morgan, J. I., and Curran, T. (1986). Role of ion flux in the control of c-fos expression. *Nature* 322, 552–555. doi: 10.1038/322552a0

Peter, M., Bathellier, B., Fontinha, B., Pliota, P., Haubensak, W., and Rumpel, S. (2013). Transgenic mouse models enabling photolabeling of individual neurons *in vivo*. *PLoS ONE* 8:e62132. doi: 10.1371/journal.pone.0062132

Petreanu, L., Huber, D., Sobczyk, A., and Svoboda, K. (2007). Channelrhodopsin-2-assisted circuit mapping of long-range callosal projections. *Nat. Neurosci.* 10, 663–668. doi: 10.1038/nn1891

Pologruto, T. A., Yasuda, R., and Svoboda, K. (2004). Monitoring neural activity and [Ca2+] with genetically encoded Ca2+ indicators. *J. Neurosci.* 24, 9572–9579. doi: 10.1523/JNEUROSCI.2854-04.2004

Sabatini, B. L., Oertner, T. G., and Svoboda, K. (2002). The life cycle of Ca(2+) ions in dendritic spines. *Neuron* 33, 439–452. doi: 10.1016/S0896-6273(02)00573-1

Sheng, M., and Greenberg, M. E. (1990). The regulation and function of c-fos and other immediate early genes in the nervous system. *Neuron* 4, 477–485. doi: 10.1016/0896-6273(90)90106-P

Turko, P., Groberman, K., Browa, F., Cobb, S., and Vida, I. (2019). Differential dependence of GABAergic and glutamatergic neurons on glia for the establishment of synaptic transmission. *Cereb. Cortex* 29, 1230–1243. doi: 10.1093/cercor/bhy029

Wang, W., Kim, C. K., and Ting, A. Y. (2019). Molecular tools for imaging and recording neuronal activity. *Nat. Chem. Biol.* 15, 101–110. doi: 10.1038/s41589-018-0207-0

Weiler, S., Bauer, J., Hübener, M., Bonhoeffer, T., Rose, T., and Scheuss, V. (2018). High-yield *in vitro* recordings from neurons functionally characterized *in vivo*. *Nat. Protoc.* 13, 1275–1293. doi: 10.1038/nprot.2018.026

Yap, E. L., and Greenberg, M. E. (2018). Activity-related transcription: bridging the gap between neural activity and behavior. *Neuron* 100, 330–348. doi: 10.1016/j.neuron.2018.10.013

Zolnik, T. A., Sha, F., Johenning, F. W., Schreiter, E. R., Looger, L. L., Larkum, M. E., et al. (2017). All-optical functional synaptic connectivity mapping in acute brain slices using the calcium integrator CaMPARI. *J. Physiol.* 595, 1465–1477. doi: 10.1113/JP273116

Conflict of Interest Statement: The authors declare that the research was conducted in the absence of any commercial or financial relationships that could be construed as a potential conflict of interest.

frontiers in Synaptic Neuroscience

METHODS
published: 12 July 2019
doi: 10.3389/fnsyn.2019.00019

Probing Single Synapses *via* the Photolytic Release of Neurotransmitters

Diana E. Mitchell[1,2], *Éric Martineau*[1,2], *Sabrina Tazerart*[1,2] *and Roberto Araya*[1,2]*

[1]*Department of Neurosciences, Faculty of Medicine, University of Montreal, Montreal, QC, Canada,* [2]*The CHU Sainte-Justine Research Center, Montreal, QC, Canada*

The development of two-photon microscopy has revolutionized our understanding of how synapses are formed and how they transform synaptic inputs in dendritic spines—tiny protrusions that cover the dendrites of pyramidal neurons that receive most excitatory synaptic information in the brain. These discoveries have led us to better comprehend the neuronal computations that take place at the level of dendritic spines as well as within neuronal circuits with unprecedented resolution. Here, we describe a method that uses a two-photon (2P) microscope and 2P uncaging of caged neurotransmitters for the activation of single and multiple spines in the dendrites of cortical pyramidal neurons. In addition, we propose a cost-effective description of the components necessary for the construction of a one laser source-2P microscope capable of nearly simultaneous 2P uncaging of neurotransmitters and 2P calcium imaging of the activated spines and nearby dendrites. We provide a brief overview on how the use of these techniques have helped researchers in the last 15 years unravel the function of spines in: (a) information processing; (b) storage; and (c) integration of excitatory synaptic inputs.

Keywords: dendritic spines, pyramidal neuron, non-linear microscopy, synaptic transmission, neocortex, two-photon (2P) uncaging

OPEN ACCESS

Edited by:
P. Jesper Sjöström, McGill University, Canada

Reviewed by:
Hyungbae Kwon, Max Planck Florida Institute for Neuroscience (MPFI), United States
Won Chan Oh, University of Colorado Denver, United States

***Correspondence:**
Roberto Araya
roberto.araya@umontreal.ca

Received: *30 April 2019*
Accepted: *24 June 2019*
Published: *12 July 2019*

Citation:
Mitchell DE, Martineau É, Tazerart S and Araya R (2019) Probing Single Synapses via the Photolytic Release of Neurotransmitters. Front. Synaptic Neurosci. 11:19. doi: 10.3389/fnsyn.2019.00019

INTRODUCTION

A major goal in neuroscience is to understand how neurons integrate and store information they receive from their synaptic inputs and, in turn, transmit signals to their postsynaptic targets. The pyramidal neuron, the most abundant in the cerebral cortex, is marked by a single axon (emanating from the soma in a straight fashion for the first 50–100 μm after it extensively ramifies), a long apical dendrite, several basal dendrites, and a pyramidal shaped soma (Spruston, 2008; Araya, 2016). Cortical pyramidal neurons are characterized by dendrites covered with dendritic spines—tiny protrusions along the dendritic tree which receive the majority (∼95%) of excitatory inputs (Gray, 1959; Colonnier, 1968; Arellano et al., 2007). Dendritic spines have a very small head (∼1 μm in diameter and <1 fL volume) and are separated from the dendrite by a slender neck (Arellano et al., 2007; Araya, 2014). Although these structures are incredibly small, the development of two-photon (2P) microscopy—which provides depth penetration in live tissue and 2P absorption only in the focal plane (Denk et al., 1990; Denk and Svoboda, 1997;

Zipfel et al., 2003; Helmchen and Denk, 2005), and of 2P uncaging microscopy (Matsuzaki et al., 2001; Araya et al., 2006a)—where caged-neurotransmitters can be released from its cage only in the focal plane to mimic presynaptic release at single synapses—have allowed us to image and directly probe dendritic spine function in excitatory and inhibitory synaptic input transformations in pyramidal neurons (Matsuzaki et al., 2001; Araya et al., 2006a,b, 2007, 2014; Bloodgood and Sabatini, 2007; Tanaka et al., 2008; Harnett et al., 2012; Chiu et al., 2013; Oh et al., 2016). Importantly, probing the function of individual spines was not previously possible using standard electrophysiological techniques.

The uncaging of caged-compounds relies on converting an inert compound into its active form using light, by shattering the covalent bond connecting the aromatic cage and the neurotransmitter (Shoham et al., 2005). Two-photon uncaging of caged-compounds has become a widely used technique to optically manipulate single synapses (Matsuzaki et al., 2001; Araya et al., 2006a; Araya, 2014) and neuronal circuits (Nikolenko et al., 2007; Kim et al., 2016). Several caged neurotransmitters with relatively high two-photon absorption cross section have been developed (Ellis-Davies, 2007, 2019; Fino et al., 2009; Araya et al., 2013). Among those, nitrophenyl-, nitrobenzyl- and ruthenium-based caged neurotransmitters are the most successfully used in neuroscience to probe synapses and neuronal networks. In particular the development of caged-glutamate, with the use of either functionalized nitrobenzyl derivatives, such as 4-methoxy-7-nitroindolinyl-caged (MNI) glutamate (Canepari et al., 2001; Matsuzaki et al., 2001), or the use of a ruthenium polypyridine cage complex, such as Ruthenium-bipyridine-trimethylphosphine caged (RuBi) glutamate (Zayat et al., 2003, 2006; Fino et al., 2009), has proven to be a very powerful and effective way to photorelease glutamate in single dendritic spines (Matsuzaki et al., 2001; Fino et al., 2009; Araya, 2014; Tazerart et al., 2019). This technique has allowed us to study glutamatergic synaptic input transformations by dendritic spines in the dendrites of pyramidal neurons (Matsuzaki et al., 2001, 2004; Araya et al., 2006a,b, 2007, 2014; Nikolenko et al., 2008; Fino et al., 2009; Harnett et al., 2012; Tazerart et al., 2019).

Combining 2P uncaging of caged glutamate in single spines with 2P imaging of spine calcium (Bloodgood and Sabatini, 2005, 2007; Araya et al., 2006b; Chalifoux and Carter, 2010; Harnett et al., 2012; Beaulieu-Laroche and Harnett, 2018; Tazerart et al., 2019), voltage (Kwon et al., 2017), or the use of FRET-based sensors (Colgan and Yasuda, 2014; Nishiyama and Yasuda, 2015) is a powerful technique to probe the electrical (Araya et al., 2006b, 2014; Harnett et al., 2012; Tønnesen et al., 2014; Beaulieu-Laroche and Harnett, 2018) and biochemical processes at the level of a single synapse during synaptic transmission and plasticity (Araya, 2014; Colgan and Yasuda, 2014). Notably, calcium is an important signal for cellular processes, such as synaptic plasticity (Lynch et al., 1983; Malenka et al., 1988; Artola and Singer, 1993; Cummings et al., 1996; Fino et al., 2010). It has been shown that local concentration differences in dendrites and spines are associated with the induction of long-term plasticity (LTP, high calcium concentration) or long-term depression (LTD, low calcium concentration; Lisman, 1989; Ismailov et al., 2004; Nevian and Sakmann, 2006). A widespread approach for combining 2P uncaging of caged neurotransmitters with 2P imaging (e.g., calcium) in the activated spines and nearby dendrites has been to use two pulsed-lasers (Matsuzaki et al., 2004; Bloodgood and Sabatini, 2005): one laser for 2P uncaging of caged neurotransmitters (i.e., MNI-glutamate using 720 nm excitation light), and a second laser for 2P excitation of calcium indicators in the activated spine (s) (i.e., Fluo-4 using 800–850 nm excitation light). This configuration allows for the simultaneous uncaging of caged neurotransmitters and calcium imaging of events in single spines (and/or imaging the short- or long-term changes in the morphology of spines loaded with other fluorophores) during development and during the induction of synaptic plasticity (Matsuzaki et al., 2004; Harvey and Svoboda, 2007; Lee et al., 2016). In addition, the two 2P laser configuration has been widely used to simultaneously uncage in single spines and image FRET-based sensors (Colgan and Yasuda, 2014; Nishiyama and Yasuda, 2015; Tang and Yasuda, 2017). This approach, however, is costly and not a possibility for all laboratories, especially those just starting up.

Here, we describe a cost-effective description of the components necessary for the construction of a one laser source-2P microscope capable of nearly simultaneous 2P uncaging of neurotransmitters and 2P calcium imaging of the activated spines and nearby dendrites using a single wavelength with low-laser power for calcium imaging (power not sufficient to result in any partial uncaging of the caged glutamate) and short high-laser power pulses to uncage caged glutamate. In addition, we describe the anticipated results that can be obtained with this microscope configuration as well as an overview on how the 2P uncaging of caged glutamate to activate single dendritic spines has helped in understanding spine function in: (a) information processing; (b) storage; and (c) integration of excitatory synaptic inputs.

MATERIALS AND EQUIPMENTS

Two Photon Set-up

- *Laser*: a femtosecond-pulsed Ti:Sapphire laser from Coherent Inc., Santa Clara, CA, USA was used for imaging and uncaging (see "Procedures" section for details). More specifically, we used the Chameleon ULTRA II ultrafast tunable Ti:Sapphire laser, which provides 140 femtosecond pulses of near infrared light (NIR) from 680 nm to 1,080 nm, that scatters less in tissue and induces less photodamage than shorter wavelengths, with a peak power of ∼3.5 W at 800 nm. In particular, our laser has a Ti:Sapphire oscillator with a 80 MHz repetition rate. In addition, the tunable capabilities of the Ti:sapphire laser allow us to perform experiments in which different excitation wavelengths are needed (e.g., ∼810 nm excitation light for fluorescent calcium indicators and 2P uncaging of RuBi-glutamate or ∼720 nm for 2P uncaging of MNI-glutamate, see below) and have the freedom to excite a wide range of fluorophores.
- *Optical table*: laser light is delivered to the scan head and microscope (see below) through a series of optical elements that include a Pockels Cell (see below), mirrors, retardation

wave plate (lambda/2), beam expander (set of lenses to act as a telescope to expand the laser beam) to change the beam size and overfill the back aperture of either a 60× and of a 40× microscope objective. The retardation wave plate is placed in the optical path for experiments where the polarization of the laser beam needs to be directed.

- *Pockels Cell*: for the experiments presented here, where fast and dynamic control of light intensity from pulsed femtosecond lasers with great contrast is needed, we used an electro-optical laser modulator (model 350–80 Pockels Cell), and driver (model 302RM driver, DC-to-250 KHz bandwidth, 1-microsec rise/fall time, 750 V. max. output) from ConOptics Inc., Danbury, CT USA. These devices allow us to control at high speed the intensity of light—e.g., fast change from high-laser-power-neurotransmitter-uncaging mode to a low-laser-power-spine-imaging mode. This laser modulator and its driver are extremely reliable devices that we have extensively used in the past (Araya et al., 2006a,b, 2007, 2013; Fino et al., 2009; Tazerart et al., 2019).
- *Scanning system*: a Bruker Inc., Billerica, MA, USA (formerly Prairie Technologies Inc.) scan head with a single pair of 6 mm galvanometer mirrors was mounted on an Olympus upright BX51WI microscope connected to a PC workstation unit with *PrairieView* software for frame scanning, line scanning, region of interest (ROI) selection, scan rotation and optical zoom modes. The scan box is optically linked to the Olympus microscope (**Figure 1A**). Importantly, this scanning system uses the same pair of galvanometer mirrors for both imaging and uncaging.
- *Objectives*: the light is focused using a high numerical aperture (NA) objective that confines the light spatially, while the pulsed-laser provides a concentration of photons in time. Specifically, we used a 60× 0.9 NA water immersion objectives from Olympus. In addition, a 10× (0.3 NA) objective to easily locate the neurons from different cortical layers and the patch pipettes for patch-clamp recordings was used.
- *Fluorescence detection*: high NA objectives (see "Objectives" section) are used to collect as many emission photons as possible from the sample—where two-photon (2P) absorption and excitation of fluorescence from the excited region of the sample irradiates fluorescence in all directions. A set of two top mounted external photomultiplier tube (PMT) detectors, controlled by a high voltage power supply, and designed to optimize collection efficiency when used with 40× and 60× microscope objective lenses were used. In particular, we used two Hamamatsu multi-alkali PMTs with low dark current (10 nA) and high sensitivity (8,500A/lumen) each with a specific emission filter (525/70 nm and 607/45 nm) and 575 nm dichroic beam splitter, allowing for the simultaneous viewing and acquisition from both detectors. The signal obtained from the PMTs is then directed to a pre-amplifier, which is then directed to the Prairie view acquisition board. *TriggerSync* software integrates the collection of PMT based fluorescence data with electrophysiology (see below). Multiple inputs and outputs are independently programmable for customized experimental protocols designed by the user. All data (PMT and electrical) are recorded by a single computer for accurate time synchrony. To block any reflected laser light into the PMT during each uncaging pulse we placed an IR filter before the PMT dichroic. Alternatively, fast shutters can be employed.
- *High-speed electronics module ("Switch box")*: a customized high-speed electronics module by Bruker (formerly Prairie Technologies) that allows us to switch between imaging and photoactivation (uncaging) mode in less than 2 ms. The module is fully integrated with the *PrairieView* software and allows synchronized photoactivation (uncaging) and electrophysiology. The module consists of a number of 2 × 1 multiplexers to integrate and route imaging and uncaging commands to the galvanometer and Pockels Cell controllers as directed by the user at very precise time points. This gives us the ability to set up sophisticated experimental protocols in a user-friendly manner using a single laser two-photon scanning/uncaging system. This module receives: (1) the software-driven imaging and uncaging Galvanometer mirror (X-Y scanning) commands; (2) the imaging and uncaging laser power command (the voltage to the Pockels cells); and (3) the software-controlled TTL pulse, the "Switch" command (**Figure 1A**). In the absence of a TTL pulse, this module outputs the imaging scanning and laser power commands to the Galvanometer mirrors and Pockels cell control boxes, respectively. Upon reception of a TTL pulse (5V), the module rapidly switches to uncaging mode output (∼2 ms delay) and sends the uncaging scanning and laser power commands to the same control boxes, effectively overriding the imaging commands for the duration of the TTL pulse. In essence, this module "switches" a single pair of Galvanometer mirrors and laser power source between an "imaging mode" and an "uncaging mode" by alternating which set of commands is output to the control boxes.

Electrophysiology

MultiClamp 700 B amplifiers (Molecular Devices) were used for electrophysiological recordings in layer 5 (L5) pyramidal neurons with a patch electrode filled with internal solution (see "Solutions" section). *Patchstar* micromanipulators and software from Scientifica Inc., Coral Gables, FL, USA were used. A motorized movable X-Y base plate from Scientifica Inc., Coral Gables, FL, USA was used to place the micromanipulators and the brain slice chamber to move them independently of the microscope and light path. DIC optics were used to clearly visualize and patch the soma of pyramidal neurons. A camera and monitor were used to visualize the patch pipette and neurons for somatic patching.

Mice

C57B/6 mice, obtained from Jackson Laboratory.

Tissue

Coronal visual cortex brain slices.

Caged Neurotransmitters

4-methoxy-7-nitroindolinyl (MNI)-caged L-glutamate (2.5 mM; Tocris) or Ruthenium-bipyridine-trimethylphosphine (RuBi)-caged glutamate (800 μM; Tocris) were used.

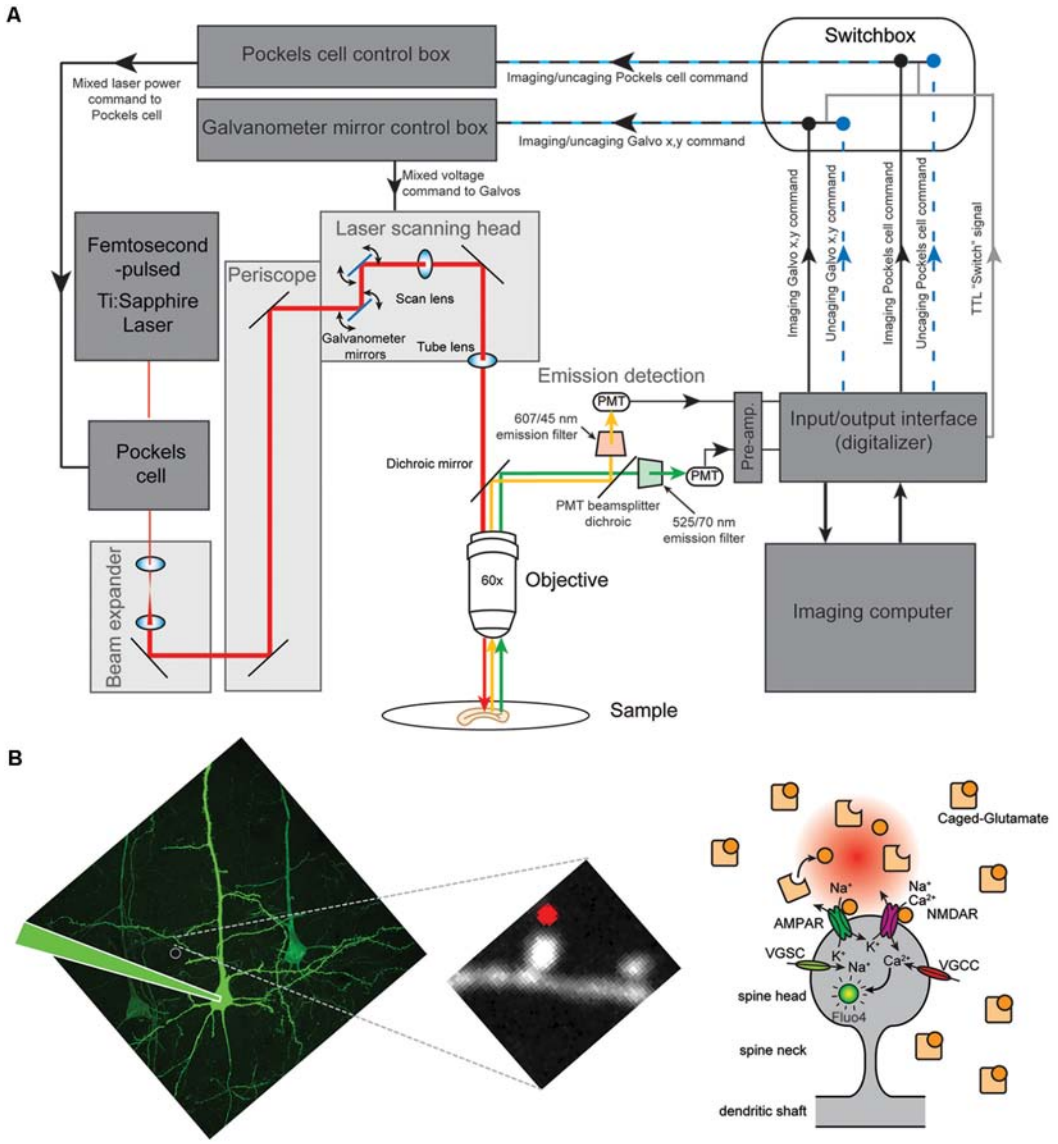

FIGURE 1 | Two photon uncaging of caged glutamate at single spines of layer 5 (L5) pyramidal neurons. **(A)** Schematic illustration of the custom imaging system. A customized high-speed electronics module by Bruker (formerly Prairie Technologies) is integrated between the input/output interface and the laser scanning control boxes to rapidly switch (in less than 2 ms) between the command strings (imaging or photoactivation mode) being routed to the control boxes. The module is fully integrated with the imaging software and allows synchronized photoactivation (uncaging), imaging and electrophysiology. This gives the ability to set-up sophisticated experimental protocols in a user-friendly manner using a single laser source and scanning system. (**B**; *Left*) Two-photon (2P) image of a L5 pyramidal neuron from V1 cortex and a zoomed in image of a piece of dendrite showing the spines. (*Right*) Cartoon drawing of a dendritic spine. AMPAR, AMPA receptor; NMDAR, NMDA receptor; VGSC, voltage-gated sodium channel; VGCC, voltage-gated calcium channel.

Solutions

Artificial cerebrospinal fluid (ACSF), containing (in mM) 126 NaCl, 26 $NaHCO_3$, 10 Dextrose, 1.15 NaH_2PO_4, 3 KCl, 2 $CaCl_2$, 2$MgSO_4$, Internal solution containing (in mM) 0.3 Fluo-4, 0.1 Alexa-568 (to use with MNI-caged glutamate) or Alexa-594 (to use with RuBi-caged glutamate), 130 Potassium D-Gluconic Acid (Potassium Gluconate), 2 $MgCl_2$, 5 KCl, 10 HEPES, 2 MgATP, 0.3 NaGTP, pH 7.4, and 0.4% Biocytin; Sucrose cutting solution, containing (in mM) 27 $NaHCO_3$, 1.5 NaH_2PO_4, 222 Sucrose, 2.6 KCl, 1 $CaCl_2$, and 3 $MgSO_4$.

Note on the Selection of Caged-Compounds and Fluorophores

Since a single 2P laser source is used, one must select a caged neurotransmitter, that can be uncaged with short high-laser power pulses, and a fluorophore that is excited at the same wavelength but with a laser power that is not sufficient to uncage the caged neurotransmitter (Araya et al., 2006b; Tazerart et al., 2019). For instance, in the experiments presented here, where glutamate uncaging is performed to activate a single spine (with high laser power

on sample) nearly simultaneously with imaging fluorescence in dye-loaded dendritic spines (with low laser power on sample) to uncover their morphology, MNI-glutamate and Alexa-568 or RuBi-glutamate and Alexa-594 were used at 720 or 810 nm, respectively. In experiments where 2P uncaging of caged glutamate onto single spines was paired with nearly simultaneous calcium imaging in the activated spines, we chose RuBi-glutamate uncaging in Alexa-594 and Fluo-4 loaded L5 pyramidal neurons using a wavelength of 810 nm. Another important consideration in choosing a calcium sensor for these experiments is its affinity for calcium, signal-to-noise ratio, dynamic range and response kinetics. We chose Fluo-4 to measure spine calcium signals due to its high dynamic range, its brightness (low power to excite), low Kd (345 nM), and high signal-to-noise ratio. Furthermore, it is a widely used indicator to measure spine calcium signals (Harnett et al., 2012; Araya et al., 2014; Beaulieu-Laroche and Harnett, 2018). In addition, Fluo-4 is one of the lowest Kd green indicators with a peak 2P excitation absorption in the 800 nm range (Svoboda and Yasuda, 2006). Other alternatives include Calcium Green-1 (Kd = 190 nM) or Fluo-8 (Kd = 389 nM).

PROCEDURE

Brain Slices Preparation and Electrophysiology

Brain slices were made from C57B/6 mice, aged postnatal day 14–21 as described previously (Araya et al., 2006a,b, 2007, 2014). Brains were removed and submerged in cold (4°C) sucrose cutting solution saturated with 95% O_2, 5% CO_2. In these experiments, we prepared coronal slices of the visual cortex that were 300 μm thick. Slices were incubated in ACSF saturated with 95% O_2, 5% CO_2, at 32°C for 30 min and then at room temperature until ready for use (∼40 min). Recordings were made from the soma of layer 5 (L5) pyramidal cells in the current-clamp configuration with MultiClamp 700B amplifiers (Molecular Devices) using a pipette (pulled from borosilicate glass tubes) filled with the internal solution described above (see "Materials and Equipments" section). The membrane potential of cells was held at −65 mV in current-clamp configuration throughout the recordings. We only used cells for which the injected current to hold the cell at −65 mV was <100 pA.

Near-Simultaneous 2P Imaging and Uncaging of Dendritic Spines in Layer 5 (L5) Pyramidal Cells

Once a successful patch was obtained, cells were allowed to dye fill for ∼25 min for visualization of spines located on the basal dendrites for high magnification imaging and uncaging. Then, we used the above-described 2P laser scanning microscope to acquire morphological images of dendritic spines of L5 pyramidal neurons. Excitation light of ∼5–8 mW on sample was used (i.e., after the objective) at a wavelength of 720 nm in neurons filled with Alexa-568 or 810 nm in neurons loaded with Fluo-4 and Alexa-594. These images allowed us to identify dendritic spines of interest.

Once the neuron was allowed to dye-fill and morphological images were taken, MNI- or RuBi-caged glutamate (named from here on MNI-glutamate and RuBi-glutamate for simplicity) was added to the bath solution at a final concentration of 2.5 mM or 800 μM, respectively. Morphological images of selected spines were used to position the uncaging spot ∼0.3 μm away from the edge of the spine head as previously described (Araya et al., 2006a,b, 2007, 2014). Uncaging of MNI- or RuBi-glutamate was performed using a wavelength of 720 nm or 810 nm, respectively, and a laser power of ∼25–30 mW on sample for 4 ms. Uncaging-evoked excitatory postsynaptic potentials (uEPSPs) were recorded at the soma through the patch pipette. We have previously published control experiments showing the stability of uEPSP amplitude or spine morphology over time (∼30 min; see Figure S2 from Tazerart et al., 2019). Importantly, 2P uncaging of glutamate in single spines with this uncaging protocol not only induces uEPSPs of similar amplitude to spontaneous (s) EPSPs, but also recapitulates the correlations observed between spine morphology (head size and neck length) and EPSP amplitude when single spines are activated with minimal electrical stimulation (see "Results" section and Araya et al., 2014).

Alternatively, high concentrations of caged-glutamate compounds (∼10 mM MNI-glutamate) can be applied locally with a pipette positioned close to the selected spine and parent dendrite and uncaged using shorter laser pulses (<1 ms; Matsuzaki et al., 2001, 2004; Losonczy and Magee, 2006; Harnett et al., 2013; Beaulieu-Laroche and Harnett, 2018). Although this approach was not used in this study, it has the advantage of using shorter pulses, shortening the delay between sites for multi-site (spine) uncaging, and of producing uEPSPs with kinetics almost identical to spontaneous EPSPs (sEPSPs; see below). However, it cannot ensure that the added caged-compound concentration is stable and uniform across all uncaging sites. Altogether, uncaging parameters (laser power, pulse length and caged-compound concentration) can be adjusted according to the experimental needs of the user.

To uncage glutamate at a single spine while near-simultaneously imaging calcium signals (e.g., Fluo-4 loaded cells) and/or morphological changes (Alexa-568 or -594 loaded cells), imaging was performed for 500 ms before uncaging and almost immediately after 2P uncaging for at least 600 ms. This was achieved by sending a 7 ms TTL-pulse to the switchbox, starting 2 ms before the start of the 4 ms uncaging command. The duration of the TTL-pulse is determined based on the switchbox delay (<2 ms) and the duration of the uncaging pulse in order to ensure that the system will be in "uncaging mode" for the entire duration of the uncaging command (in our case, 2 ms before plus 1 ms after). Switching from imaging mode to uncaging mode effectively interrupts the imaging for ∼7 ms, allowing 2P uncaging of caged-glutamate in the selected spine.

Two different imaging strategies were used based on our experimental needs, "linescan imaging" and "ROI imaging."

For experiments where a high temporal resolution is required, such as those designed to report and analyze fast spine calcium signals, a single line across the middle of the spine head was scanned at high speed (1.6 μs dwell time; ∼1 ms/line). For experiments where more spatial information is required, such as those where the calcium signal of not only the activated spine head but also of the parent dendritic shaft and neighboring spines is required, as well as the activated spine morphological changes, the imaging acquisition was set to a small portion, or ROI, of the entire field of view (∼150 × 150 pixels). Images were acquired at ∼30 Hz, averaged eight times, with 8 μs dwell time (image period ∼300 ms). For ROI imaging, the uncaging command and TTL "switch" pulse were set to occur in the lag period between two images to ensure that no image is interrupted while being scanned (no pixels are skipped) by the 2P uncaging pulse. In both cases, Alexa-594 fluorescence was acquired simultaneously with Fluo-4 fluorescence, serving both as a normalization signal for the analysis of calcium signals (see below).

Analysis of Calcium Linescan Signals

Analysis of calcium linescans obtained during uncaging was performed using custom algorithms (MATLAB; MathWorks). We restricted this analysis to the portion of the linescan that overlapped with the spine head. The fluorescence of each line was calculated as the mean of all pixels. The relative change in calcium levels ($\frac{\Delta G}{R}$) over time was calculated using the following formula:

$$\frac{\Delta G}{R} = \frac{G - G_{\text{baseline}}}{R} \quad (1)$$

where G is the fluorescence from the Fluo-4 dye and R is the fluorescence from the Alexa-594 dye. G_{baseline} is the mean Fluo-4 fluorescence of the first image of the sequence.

Analysis of Calcium ROI Signals

Analysis of calcium images obtained during uncaging was performed using custom algorithms (MATLAB; MathWorks). We confined the quantification of the change in Fluo-4 fluorescence to either the spine head or the dendrite. We manually drew ROIs in the shape of a circle for spine heads and of a polygon for dendrites. The fluorescence of each image was calculated as the mean of all pixels within each ROI. The relative change in calcium levels ($\frac{\Delta G}{R}$) over time was calculated using equation 1. To show the change in calcium signal in the activated spine and parent dendrite, we calculated the change in Fluo-4 fluorescence (ΔF) on the ROI images obtained, from the first image in the sequence.

Ethics

This study was performed in compliance with experimental protocols (13-185, 15-002, 16-011, 17-012, 18-011 and 19-018) approved by the *Comité de déontologie de l'expérimentation sur les animaux* (CDEA) of the University of Montreal.

RESULTS

Activation of Single Dendritic Spines Using Two-Photon (2P) Uncaging of Caged Glutamate

Two photon (2P) glutamate uncaging is an effective tool to locally release caged glutamate and activate glutamate receptors at a precise dendritic location to evoke a depolarization (**Figure 1B**) that can mimic the physiological stimulation of a single synapse (Matsuzaki et al., 2001, 2004; Araya et al., 2006a,b, 2007, 2013, 2014; Fino et al., 2009; Tazerart et al., 2019). Here, we performed 2P uncaging of bath applied MNI-glutamate (2.5 mM; **Figure 2A**) or RuBi-glutamate (800 μM; **Figures 2B,C**)—two commercially available caged glutamate compounds with relatively high two-photon absorption cross section (Canepari et al., 2001; Matsuzaki et al., 2001; Zayat et al., 2003, 2006; Fino et al., 2009)—at a single spine on basal dendrites of L5 pyramidal neurons from mouse V1 cortical slices. Short laser pulses (4 ms, ∼25–30 mW on sample) just above the spine head (**Figures 2A,B**) were delivered while recording the uncaging-evoked excitatory postsynaptic potentials [uncaging(u)EPSP] at the soma using whole-cell recordings in current-clamp mode. Two-photon uncaging MNI-glutamate or RuBi-glutamate induced a sharp depolarization that is similar in amplitude (MNI-glutamate: 0.65 ± 0.06 mV; RuBi-glutamate: 0.74 ± 0.011 mV) and that has a slightly slower rise time and slightly longer duration (10/90 rate of rise: 0.063 ± 0.01 and 0.056 ± 0.02 mV/ms; duration: 124.6 ± 17.1 and 108.14 ± 13.25 ms, for uncaging MNI-glutamate and RuBi-glutamate, respectively) than sEPSPs (**Figures 2A,B**; Fino et al., 2009; Araya et al., 2014; sEPSP amplitude: 0.86 ± 0.07 mV; sEPSP 10/90 rate of rise: 0.25 ± 0.03 mV/ms; sEPSP duration: 50.4 ± 4 ms; Araya et al., 2006b).

A main feature of 2P glutamate uncaging is that it allows for the precise activation of a single synapse (Matsuzaki et al., 2001; Araya et al., 2006a,b; Fino et al., 2009). To test the 2P uncaging spatial resolution of our approach, we targeted the laser at six different locations that were located at a range of distances from the head of the spine (the first three locations are shown in **Figure 2C**). Importantly, uncaging at locations further from the spine head generated smaller uEPSPs (**Figure 2C**). To quantify the spatial resolution of uncaging, we plotted the uEPSP amplitude as a function of distance of the uncaging spot from the spine head. We fit these data with an exponential curve, which revealed a distance constant (λ) of ∼0.5 μm (**Figure 2C**). Hence, with this experimental configuration, we have single-spine uncaging spatial resolution, which allowed us to rapidly and precisely mimic synaptic activation of single spines while synchronously recording the uEPSP at the soma, as we have shown before (Araya et al., 2006a,b).

Another important technical control is to ensure that the imaging laser power is not sufficient for the photolytic release caged-glutamate. We previously showed that 5–8 mW at 720 nm is insufficient to uncage MNI-glutamate (for detailed control

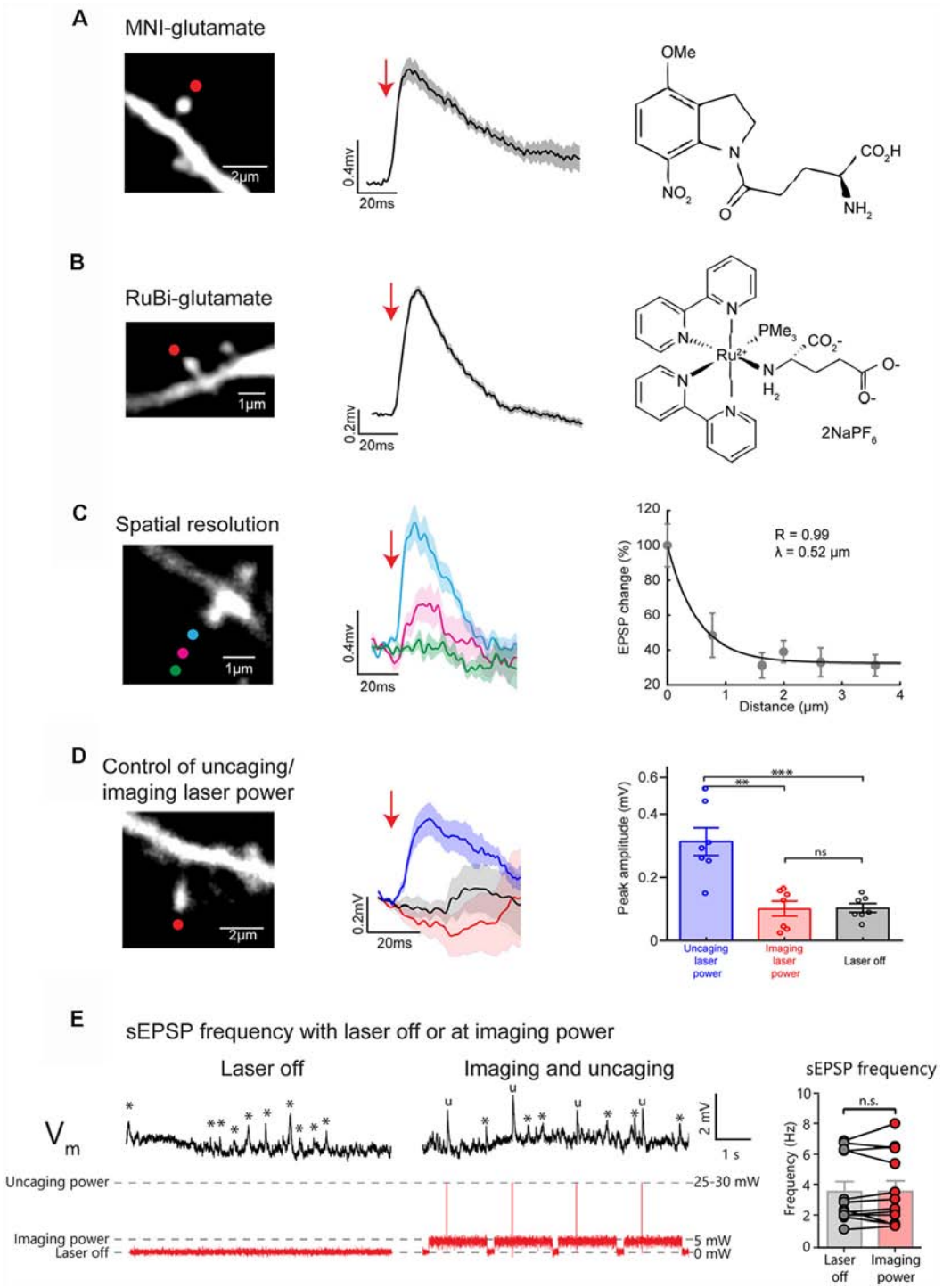

FIGURE 2 | Uncaging caged glutamate at single spines evokes uncaging (u)EPSPs detected at the soma of layer 5 (L5) pyramidal neurons with high spatial precision. **(A)** Representative 2P uncaging of MNI-glutamate experiment in a single spine. (*Left*) Two-photon (2P) image of a single spine in the basal dendrites of a L5 pyramidal neuron (red dot indicate site of uncaging). (*Center*), 2P uncaging of caged MNI-glutamate near the selected spine induces a uncaging-evoked excitatory postsynaptic potential (uEPSP) measured at the soma in current-clamp configuration. The tick line and the shaded area represent the mean ± standard error of the mean (SEM) of 10 uEPSP generated at this spine. (*Right)* Chemical formula for MNI-glutamate. **(B)** Representative 2P uncaging of RuBi-glutamate experiment in a single spine. (*Left*), 2P image of a single spine on the basal dendrites of a L5 pyramidal neuron (red dot indicate site of uncaging). (*Center*) 2P uncaging of caged RuBi-glutamate near the selected spine induces a uEPSP measured at the soma in current-clamp configuration. The tick line and the shaded area represent the mean ± SEM of 10 uEPSPs generated at this spine. (*Right*) Chemical formula for RuBi-Glutamate. **(C)** Representative 2P uncaging of MNI-glutamate in a

(*Continued*)

FIGURE 2 | Continued
single spine spatial resolution experiment. (*Left*) 2P image of a single spine in the basal dendrites of a L5 pyramidal neuron with colored circles showing the location of different MNI-glutamate uncaging spots. (*Center*) 2P uncaging in the selected spine at different locations and their corresponding uEPSPs measured at the soma. The tick line and the shaded area represent the mean ± SEM of 10 uEPSPs generated at this spine. (*Right*) Relationship between the distance of the uncaging spot from the spine and the evoked uEPSP. Each dot corresponds to the mean ± SEM of 10 uEPSPs generated a given distance from a single spine. **(D)** Representative experiment to explore the effect of 2P uncaging pulses in a single spine with imaging or uncaging power. (*Left*) 2P image of a single spine on the basal dendrites of a L5 pyramidal neuron showing the uncaging spot (red dot). (*Center*) 2P uncaging of RuBi-glutamate right next to the selected spine using uncaging (blue trace) or imaging laser power (red trace) while uEPSP are recorded at the soma. Note the absence of induction of a uEPSPs when short pulses at imaging laser power were given. Black traces represent the averaged membrane potential recorded (10 trials) while the laser was off, 100 ms before the onset of uncaging laser pulses. Thicker traces are an average of 10 uEPSPs, and shaded areas illustrate ± SEM. (*Right*) Plot showing the peak amplitude (mV) of the responses measured in seven independent experiments, from $n = 7$ independent spines, where the average triggerd 2P uEPSP (10 trials per spine) was recorded at either uncaging (blue bar and points) imaging laser power (red bar and dots), or when the laser was off (black bar and dots). $^{**}p < 0.01$; $^{***}p < 0.001$; *ns*, not significant. **(E)** Example traces of membrane voltage recorded at the soma of a L5 pyramidal neuron while the laser was off (*Left*) or at imaging laser power during an uncaging/imaging protocol (*Center*). Asterisks indicate the presence of a spontaneous EPSPs (sEPSPs) while "u" marks uEPSPs. Note the similar frequency of sEPSPs (*) when the laser is off or at imaging laser power. (*Right*) Plot represents the frequency of events measured over a 30–60 s period before and during the uncaging/imaging protocol for each spine ($n = 12$ cells). *ns*, not significant. The first 50 ms following uncaging pulses were not included in this analysis.

experiments see Figure S9 from Tazerart et al., 2019). We now show that short laser pulses of 5–8 mW at 810 nm are not sufficient to uncage RuBi-glutamate or to induce any postsynaptic response, while short pulses of 25–30 mW on sample reliably induced uEPSPs at the same dendritic spines (**Figure 2D**; 0.31 ± 0.043 mV vs. 0.101 ± 0.023 mV, $n = 7$ spines, Paired t-test, $p = 0.004$). To further validate that imaging laser power does not inadvertently uncage RuBi-glutamate, we performed experiments where we looked at the frequency of sEPSPs during periods where the laser was off or on at imaging power while scanning a dendritic spine (**Figure 2E**). These results showed that the frequency of sEPSP in each cell was similar during periods where the laser was off vs. at imaging laser power (**Figure 2E**; Laser Off: 3.63 ± 0.64 Hz, Imaging laser power: 3.65 ± 0.67 Hz; $n = 12$ spines; Paired t-test, $p = 0.936$).

Nearly Simultaneous 2P Calcium Imaging and 2P Uncaging of Caged Neurotransmitters With One Pulsed-Laser Source

Calcium is an important signal for cellular processes, such as the induction of LTP or LTD (Lynch et al., 1983; Malenka et al., 1988; Lisman, 1989; Artola and Singer, 1993; Cummings et al., 1996; Ismailov et al., 2004; Nevian and Sakmann, 2006; Fino et al., 2010). Since 2P uncaging of MNI-glutamate or RuBi-glutamate has excellent spatiotemporal resolution (**Figure 2C**, and see Araya et al., 2006b, 2007; Fino et al., 2009), combining 2P calcium imaging with 2P uncaging of neurotransmitters is a powerful approach to probe the mechanism of cellular processes (e.g., LTP or LTD) at the level of a single synapse. To demonstrate that a single laser configuration is suitable to perform such an approach, we performed near-simultaneously 2P glutamate uncaging and calcium-imaging at the activated spines in the basal dendrites of L5 pyramidal neurons.

First, we used a "linescan" approach to track calcium signals in the activated spine head with high spatiotemporal precision (**Figures 3A–D**). Briefly, a line through the middle of the spine located in the basal dendrites of L5 pyramidal neurons is scanned before and after 2P uncaging of caged glutamate at a spot positioned ∼0.3 μm from the spine head (**Figure 3C**, line and red spot, respectively). As shown in **Figure 3B**, 2P glutamate uncaging reliably induced somatic uEPSPs (average of 10 depolarizations, amplitude: 0.99 ± 0.03 mV; duration: 185.2 ± 23.8 ms; ranging from ∼0.81 to 1.14 mV in amplitude, and from 100.6 to 292.4 ms in duration), and an increase in spine calcium signals in the activated spine head of Fluo-4 loaded neurons. Importantly, the fluorescence from the Alexa-594 dye remained constant before and after the 2P uncaging of glutamate (**Figure 3D**), showing that the application of a short, high power, laser pulse next to the spine does not damage the spine head, which otherwise would trigger fluctuations in Alexa-594 fluorescence after the uncaging pulse. We quantified these calcium dynamics using a custom algorithm in MATLAB by calculating the ratiometric measurement $\frac{\Delta G}{R}$ (see "Procedures" section). This method of quantification allows us to measure calcium signals that are insensitive to small fluctuations in basal calcium levels and independent of the spine head volume (Sabatini et al., 2002; Bloodgood and Sabatini, 2007). The trace in the lower panel of **Figure 3D** shows the average change in fluorescence from baseline following 10 uncaging events at this dendritic spine. Initially, calcium levels are quite stable with a rapid increase immediately following 2P uncaging of glutamate right next to the activated spine head. We observed a peak calcium single of 12.0% ± 0.54% $\frac{\Delta G}{R}$ (**Figure 3D**). Using this approach, we observed a range of calcium signals in the activated spine heads between 3% and 20% $\frac{\Delta G}{R}$, which is consistent with previous published results obtained using a similar analytical method (Sabatini et al., 2002; Yasuda et al., 2003; Bloodgood and Sabatini, 2007).

Next, we used an "ROI-scan" approach to monitor the spatial dynamics of calcium signaling in the activated spines, parent dendrite and neighboring spines (**Figures 3E–H**). In the example presented in **Figures 3E–H**, a small portion of the entire field of view of the ROI containing the spine of interest and its parent dendrite are imaged before and after 2P uncaging of caged glutamate at a spot positioned ∼0.3 μm away from the spine head (**Figure 3G**, red spot) is performed. The activation of a single spine by 2P uncaging of glutamate (RuBi-glutamate) reliably induced somatic uEPSPs (**Figure 3F**, average of 20 depolarizations), and clear calcium signals in the activated spine head, which remains elevated for ∼300 ms (**Figure 3H**, image 2) before decreasing back to

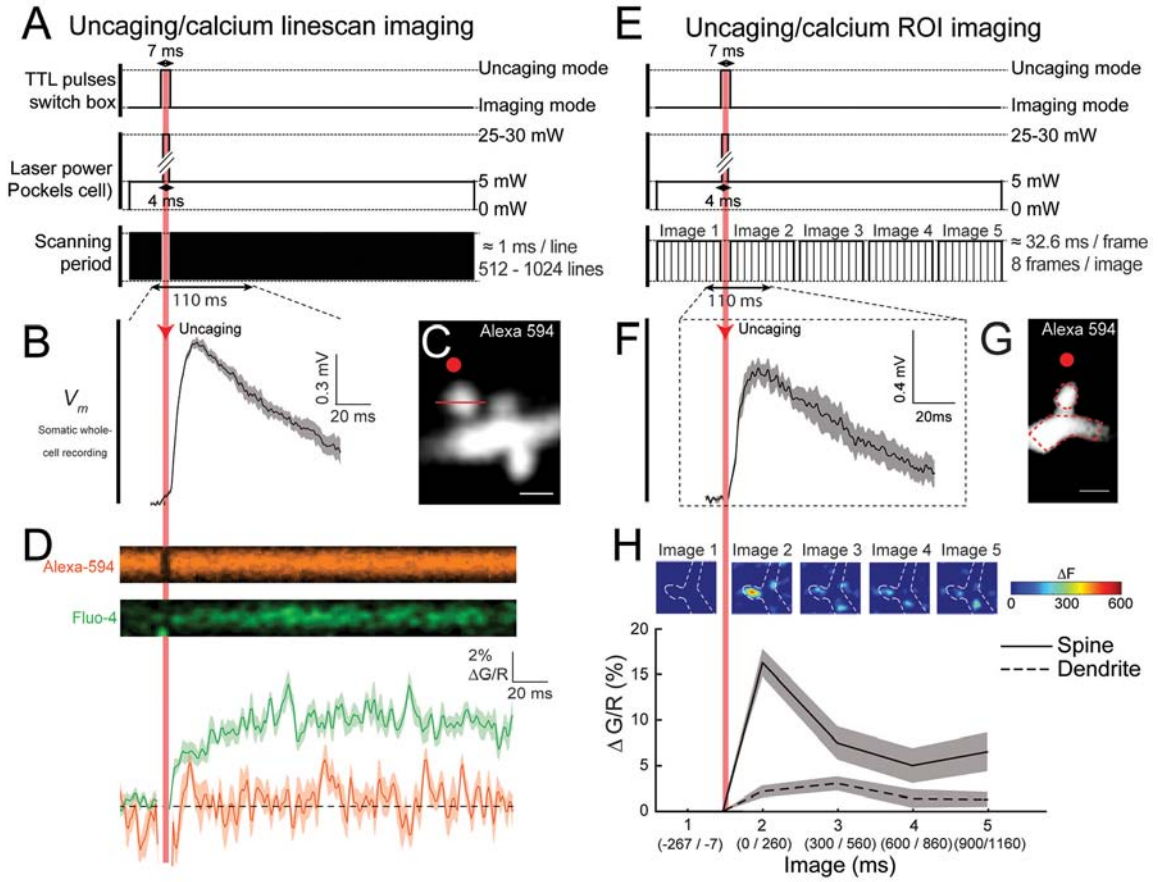

FIGURE 3 | Near simultaneously imaging of calcium dynamics in the spines of layer 5 (L5) pyramidal neurons following glutamate uncaging. **(A)** Schematic representation of the TTL pulses being sent to the switchbox, the change in laser power over time and the imaging scanning period during a single trial, where each black line represents the beginning of a new linescan. Note the very brief interruption in the imaging during the uncaging. **(B)** Averaged uEPSP, recorded at the soma, evoked by 2P glutamate uncaging targeted 0.3 μm away from the head of the selected spine (20 trials). **(C)** 2P image of the selected spine of a L5 pyramidal neuron. Red dot: the uncaging spot; Red line: position of the linescan during calcium signal acquisition. **(D)** Top panel: linescan images illustrating the change in Alexa-594 and Fluo-4 fluorescence over time during a single trial. Bottom panel: quantification of the average change in the calcium and Alexa-594 signal ($\frac{\Delta G}{R}$) in the spine head following 2P glutamate uncaging for 10 trials. **(E)** Schematic representation of the TTL pulses being sent to the switchbox, the change in laser power over time and the scanning period during a single trial, where each thin black line represents the beginning of a new framescan and each black box represents a single averaged image being generated. **(F)** Averaged uEPSP, recorded at the soma, evoked by glutamate uncaging targeted 0.3 μm away from the head of the selected spine (20 trials). **(G)** 2P image of the selected spine of a L5 pyramidal neuron. The red dot represents the uncaging spot. **(H)** Top: color-coded images of the changes in fluorescence across the region of interest (ROI) during a single trial (ΔF). Quantification of the average change in the calcium signal ($\frac{\Delta G}{R}$) in the spine head and parent dendrites following glutamate uncaging at the spine head for 20 trials.

baseline levels (**Figure 3H**, insets). Interestingly, the images depicted in **Figure 3H** show that calcium increases (ΔF) remained mostly located in the spine head following its activation and a much smaller response occurred in the parent dendrite (**Figure 3H**, insets). Using custom algorithms in MATLAB, which measures the change in fluorescence ($\frac{\Delta G}{R}$) over time within a selected area (i.e., spine head or dendrite), these calcium dynamics can be further quantified (see "Procedures" section). Calculation of $\frac{\Delta G}{R}$ clearly shows that calcium signals were initially minimal in the spine head (image 1 in **Figure 3H** insets), whereas following uncaging they reach levels 16.2% ± 1.6% $\frac{\Delta G}{R}$ (image 2 in **Figure 3H**, insets). Interestingly, calcium signals were considerably smaller in the parent dendrite, only reaching values of ∼5% $\frac{\Delta G}{R}$ (**Figure 3H**), revealing that dendritic spines favor calcium level rises following synaptic activation (**Figure 3H**)—acting as biochemical compartments that can effectively confine calcium in the spine head without affecting neighboring spines, a pretty well established function of spines (Araya, 2014). Hence, depending on experimental requirements (high spatial vs. high temporal resolution), either a "linescan" or an "ROI-scan" approach can be used to track calcium dynamics in spines after fast 2P uncaging of caged glutamate.

DISCUSSION

In this article, we have outlined a cost-effective description of the components necessary for the construction of a one

laser source-2P microscope capable of nearly simultaneous 2P uncaging of caged-neurotransmitters and 2P calcium imaging of the activated spines and nearby dendrites. Below we briefly discuss the function of spines that have been elucidated using 2P microscopy, as well as the potential applications of a one-laser system and its limitations.

Function of Spines

Spines, first described by Cajal (1888) are the main recipient of a neuron's excitatory input (Gray, 1959; Spacek and Harris, 1998; Arellano et al., 2007). In addition, spines can act as recipients of some GABAergic inputs (Somogyi and Cowey, 1981; Freund et al., 1986; DeFelipe et al., 1989; Chen et al., 2012), and their electrical and biochemical properties are believed to provide them with the capacity to shape how excitatory and inhibitory synaptic inputs are processed and stored (Araya, 2014).

With the development of 2P microscopy (Denk et al., 1990) in combination with 2P uncaging of caged neurotransmitters it has been possible to probe live dendritic spines deep in tissue and with high spatial resolution (Denk et al., 1990; Matsuzaki et al., 2001; Araya et al., 2006b, 2014; Bloodgood and Sabatini, 2007; Harvey and Svoboda, 2007). Using this technology it is well established that dendritic spines are the minimal functional unit for the induction of long-term potentiation (LTP; Lang et al., 2004; Matsuzaki et al., 2004; Harvey and Svoboda, 2007; Tanaka et al., 2008; Araya et al., 2014; Tazerart et al., 2019) and LTD (Holbro et al., 2009; Oh et al., 2013). Furthermore, the development of calcium indicators (Tsien, 1988) in combination with 2P microscopy has allowed researchers to study the spatiotemporal calcium dynamics in dendritic spines during synaptic transmission, LTP and LTD, and synaptic integration (Araya, 2014). In addition, local calcium imaging in activated dendritic spines have allowed us to estimate the effect of spine geometry (i.e., spine head volume and neck length) on the local amplitude and compartmentalization of calcium signals (Noguchi et al., 2005; Sobczyk et al., 2005; Araya et al., 2006b; Grunditz et al., 2008; Takasaki and Sabatini, 2014). These results suggest that spine morphology—spine head volume and/or neck length and diameter—are likely important determinants in controlling the amplitude and diffusion of calcium from the spine head to the dendrite (Araya, 2014). However, the understanding of how spine geometry can affect calcium amplitude and compartmentalization in the spine head has to be understood together with other variables, such as the spine calcium buffering capabilities (Raghuram et al., 2012), extrusion mechanisms (Yuste et al., 2000; Higley and Sabatini, 2012), and the activation of voltage-gated calcium conductances in the spine (Bloodgood and Sabatini, 2007).

Using two-photon (2P) microscopy to image and photo-activate dendritic spines (Denk et al., 1990), we and others have demonstrated experimentally that: (a) spines are electrical compartments (Araya et al., 2006b; Grunditz et al., 2008; Bloodgood et al., 2009; Beaulieu-Laroche and Harnett, 2018) that can attenuate synaptic potentials through the spine neck; and (b) spines are active devices which, upon synaptic activity, can engage voltage-gated Na^+ (Araya et al., 2007; Bloodgood and Sabatini, 2007; Carter et al., 2012), Ca^{2+} (Bloodgood and Sabatini, 2007), and K^+ channels (Ngo-Anh et al., 2005; Allen et al., 2011).

The electrical compartmentalization of spines not only affects synaptic transmission but also how inputs are integrated. In fact, it has been shown that nearly simultaneous sub-threshold excitatory inputs onto two or three neighboring spines in basal dendrites of L5 pyramidal neurons summate linearly, whereas neighboring inputs onto the dendritic shaft shunt each other (Araya et al., 2006a). The linear integration of inputs onto spines—before the generation of a dendritic spike—have also been observed when 2P uncaging of caged glutamate was performed in >10 neighboring spines (Gasparini and Magee, 2006; Losonczy and Magee, 2006). Modeling studies have predicted that in order for this linear integration of sub-threshold inputs onto clustered spines to be reproduced, spines with neck resistances of 600 MΩ are required (Grunditz et al., 2008)—similar to the calculated neck resistances in CA1 pyramidal neuron spines (Harnett et al., 2012).

In conclusion, the use of 2P microscopy, together with 2P uncaging of caged glutamate and calcium imaging in the activated spines has allowed us to understand a great deal of the function of spines during synaptic transmission, plasticity and integration of excitatory inputs. We refer the reader to the following review for further information on the function of spines and how this technology has helped uncover the role of spines in input transformations in pyramidal neurons (Araya, 2014).

A One Laser Source 2P Imaging and Uncaging Microscope

Here, we provide the detailed components required for the construction of a one laser source-2P microscope capable of nearly simultaneous 2P uncaging of neurotransmitters and 2P calcium imaging of the activated spines and nearby dendrites. In particular, we explain the use of an ultrafast tunable Ti:Sapphire pulsed-laser where a single wavelength can be used: (1) at low-laser power on sample, which is not sufficient to result in any uncaging of the caged glutamate compounds, for calcium imaging; and (2) with short high-laser power pulses to 2P uncage caged glutamate. In addition, we describe two types of 2P calcium imaging experiments: linescan (**Figures 3A–D**) and ROI imaging mode (**Figures 3E–H**). Linescan imaging mode can be used to obtain a high temporal resolution of calcium imaging within a line crossing the spine head, and ROI imaging mode for experiments where more spatial information (i.e., the calcium signals in the activated spine and its parent dendrite) is required. For details see "Procedure" section.

Although this set-up does allow for the design of sophisticated experiments, it does have some restrictions. First, we are limited in terms of the excitation wavelength of the laser used. Since there is only one laser and the wavelength cannot be rapidly changed from one to another during the experiment, this variable must be set such that it is in the proper range for 2P fluorophore excitation for imaging and for 2P uncaging of caged neurotransmitters and care must

be taken to select compatible compounds (see "Materials and Equipments" section). Second, there are also limitations in terms of temporal accuracy. Again, since there is only one laser, uncaging and imaging cannot be performed exactly simultaneously. Specifically, the switch from linescan or ROI calcium imaging to uncaging mode can take ∼2 ms. This delay, although not very relevant for the measurement of calcium signals (hundreds of ms), could be detrimental when fast voltage response signals using voltage sensitive dyes (VSD) or genetically encoded voltage indicators (GEVI) are measured in spines (Peterka et al., 2011). A third limitation is the necessity to validate that the imaging laser power is not sufficient to photorelease glutamate, or any other caged neurotransmitter selected, from its cage as demonstrated in **Figures 2D,E**, and by Tazerart et al. (2019). Finally, another limitation is when multiple spines (>2 or 3 spines) are nearly simultaneously activated while calcium imaging is performed. Under these conditions, the imaging-to-uncaging switch delay is added to the small unavoidable delay between different stimulations, since the pair of galvanometer mirrors directing the laser spot to each spine will have to move from one location to another. To avoid the issue of temporal accuracy, one can combine a conventional galvanometer-based 2P scanning system with a spatially multiplexed imaging/uncaging technique (Nikolenko et al., 2008, 2013). The technique is based on the use of a spatial light modulator (SLM) to generate any desired laser pattern at the sample (Nikolenko et al., 2008, 2013). With the SLM one can split the excitation beam into multiple beamlets and can thus create nearly any spatiotemporal pattern of light, allowing for imaging or photoactivation (uncaging) of multiple regions of interest at once. Hence, with this technology it is possible to simultaneously uncage glutamate (with single spine resolution) at several spines (up to 30 in a 2P regime; Nikolenko et al., 2008, 2013), to study their role in spatial summation. This is a powerful approach, which can be used for true simultaneous activation of a large group of spines.

Caged Compounds

In recent years, multiple caged compounds have been designed and can be used in conjunction with the techniques described in this article to probe and dissect a variety of brain circuits and function. To be effective, such compounds need to be resistant to spontaneous hydrolysis and to have a rapid photorelease time. For instance, caged glutamate has been one of the most widely used caged neurotransmitters, MNI-glutamate is uncaged in a 2P regime at a wavelength of 720 nm with photorelease half time of ≤0.26 ms (Canepari et al., 2001). In addition to caged glutamate, there is also caged γ-aminobutyric acid (GABA; RuBi-GABA; Rial Verde et al., 2008); 7-(dicarboxymethyl)-aminocoumarin (N-DCAC)—caged GABA; Kantevari et al., 2010), which has been a powerful tool to study for example the role that GABAergic inhibition has on spine function (Chiu et al., 2013).

Furthermore, the development of a novel 2P active caged dopamine compound—RuBi-Dopamine—that can be released with 2P precision in single dendritic spines has been recently described (Araya et al., 2013). Since dysfunction of dopaminergic neurotransmission in the central nervous system (CNS) underlies a variety of neuropsychiatric disorders, caged dopamine allows for the examination of dopaminergic transmission in the brain in both wild-type animals as well as animal models of mental disorders. This compound can further our understanding of neurotransmission at the subcellular level that could potentially be the root of neuropsychiatric disorders. In addition, caged acetylcholine (Passlick et al., 2018), caged glycine (Ellis-Davies, 2007), caged serotonin (Cabrera et al., 2017), caged nicotine (Filevich et al., 2010), and other caged compounds have been developed. We refer the reader to the following reviews for further information on this topic (Ellis-Davies, 2007, 2019).

The single 2P laser approach described here, where a single wavelength is used for 2P imaging spines and 2P uncaging of neurotransmitters, could benefit from the design and development of new caged compounds that could be paired with calcium or voltage indicators. However, one limitation in the design of these novel caged compounds is that, although the absorption and fluorescence spectra can be very well predicted for a one photon (1P) regime using time-dependent density functional theory (TD-DFT; Petroni et al., 2008), the absorption spectra is not accurately predicted for a 2P regime using a similar computational algorithm. This limitation usually makes this endeavor almost purely empirical. Nevertheless, the approach described here could easily be implemented to a battery of existing nitrophenyl-, nitrobenzyl- and ruthenium-based caged neurotransmitters, shown to be successful in probing synapses and neuronal networks in a 2P-regime.

In addition, the experimental approach described here could be used with genetically-encoded calcium indicators (GECIs). Indeed, GECIs provide many advantages over organic calcium indicators, notably avoiding the potential dialysis of intracellular signaling molecules through the whole-cell patch pipette for *in vitro* studies and being more readily usable for *in vivo* studies. However, while the peak 2P absorption of RuBi-caged compounds is compatible with many organic calcium indicators (i.e., Fluo-4, Calcium-green-1, etc.), it is not compatible with currently-available GECI, which have a peak 2P excitation around 880–940 nm (Podor et al., 2015). DEAC450-glutamate is a caged-glutamate compound with peak 2P absorption in the 900 nm range (Olson et al., 2013; Ellis-Davies, 2019). However, this compound emits fluorescence in the 500–540 nm range, making its use with the most commonly-used GECI (GCaMPs) challenging (Ellis-Davies, 2019). Red-shifted GECI could possibly be used with DEAC450-Glu, but they currently suffer from overall poor performance compared with GCaMPs (Podor et al., 2015). Hence, future development of caged-compounds sensitive to wavelengths around 900 nm could extend the applicability of a single-laser source 2P imaging and uncaging system to studies using GECIs *in vitro* or *in vivo*.

CONCLUSION

Here, we provide a brief overview on how the use of 2P calcium imaging and 2P glutamate uncaging have helped

researchers in the last 15 years unravel the function of spines in: (a) information processing; (b) storage; and (c) integration of excitatory synaptic inputs.

DATA AVAILABILITY

The raw data supporting the conclusions of this manuscript will be made available by the authors, without undue reservation, to any qualified researcher.

ETHICS STATEMENT

This study was performed in compliance with experimental protocols (13-185, 15-002, 16-011, 17-012, 18-011 and 19-018) approved by the Comité De déontologie de l'Expérimentation sur les Animaux (CDEA) of the University of Montreal, Montreal, QC, Canada.

AUTHOR CONTRIBUTIONS

RA conceived the project and supervised the project. DM and ST performed the experiments. DM, ST, and ÉM performed data analyses. RA, ST, and DM designed the experiments. RA, ÉM, and DM wrote the manuscript. All authors read and approved the contents of the manuscript.

FUNDING

This work was funded by the Canadian Institutes of Health Research (CIHR) grant MOP-133711 to RA, a Canada Foundation for Innovation (CFI) equipment grant Fonds des leaders 29970 to RA, and a Natural Sciences and Engineering Research Council of Canada (NSERC Discovery Grant) grant application No. 418113-2012 (NSERC PIN 392027) to RA. DM was supported in part by a postdoctoral fellowship from the Fonds de recherche du Québec—Santé (FRQS). ST was supported in part by a postdoctoral fellowship from the Groupe de Recherche sur le Système Nerveux Central (GRSNC) at University of Montreal.

ACKNOWLEDGMENTS

We thank Soledad Miranda-Rottmann for help in the discussions that led to the conception of the work, and are grateful to Pierre Drapeau and all other members of Roberto Araya's laboratory for the kind support.

REFERENCES

Allen, D., Bond, C. T., Lujan, R., Ballesteros-Merino, C., Lin, M. T., Wang, K., et al. (2011). The SK2-long isoform directs synaptic localization and function of SK2-containing channels. *Nat. Neurosci.* 14, 744–749. doi: 10.1038/nn.2832

Araya, R. (2014). Input transformation by dendritic spines of pyramidal neurons. *Front. Neuroanat.* 8:141. doi: 10.3389/fnana.2014.00141

Araya, R. (2016). "Dendritic morphology and function," in *Neuroscience in the 21st Century*, eds D. W. Pfaff and N. D. Volkow (New York, NY: Springer New York), 1–35.

Araya, R., Andino-Pavlovsky, V., Yuste, R., and Etchenique, R. (2013). Two-photon optical interrogation of individual dendritic spines with caged dopamine. *ACS Chem. Neurosci.* 4, 1163–1167. doi: 10.1021/cn4000692

Araya, R., Eisenthal, K. B., and Yuste, R. (2006a). Dendritic spines linearize the summation of excitatory potentials. *Proc. Natl. Acad. Sci. U S A* 103, 18799–18804. doi: 10.1073/pnas.0609225103

Araya, R., Jiang, J., Eisenthal, K. B., and Yuste, R. (2006b). The spine neck filters membrane potentials. *Proc. Natl. Acad. Sci. U S A* 103, 17961–17966. doi: 10.1073/pnas.0608755103

Araya, R., Nikolenko, V., Eisenthal, K. B., and Yuste, R. (2007). Sodium channels amplify spine potentials. *Proc. Natl. Acad. Sci. U S A* 104, 12347–12352. doi: 10.1073/pnas.0705282104

Araya, R., Vogels, T. P., and Yuste, R. (2014). Activity-dependent dendritic spine neck changes are correlated with synaptic strength. *Proc. Natl. Acad. Sci. U S A* 111, E2895–E2904. doi: 10.1073/pnas.1321869111

Arellano, J. I., Espinosa, A., Fairén, A., Yuste, R., and DeFelipe, J. (2007). Non-synaptic dendritic spines in neocortex. *Neuroscience* 145, 464–469. doi: 10.1016/j.neuroscience.2006.12.015

Artola, A., and Singer, W. (1993). Long-term depression of excitatory synaptic transmission and its relationship to long-term potentiation. *Trends Neurosci.* 16, 480–487. doi: 10.1016/0166-2236(93)90081-v

Beaulieu-Laroche, L., and Harnett, M. T. (2018). Dendritic spines prevent synaptic voltage clamp. *Neuron* 97, 75.e3–82.e3. doi: 10.1016/j.neuron.2017.11.016

Bloodgood, B. L., and Sabatini, B. L. (2005). Neuronal activity regulates diffusion across the neck of dendritic spines. *Science* 310, 866–869. doi: 10.1126/science.1114816

Bloodgood, B. L., and Sabatini, B. L. (2007). Nonlinear regulation of unitary synaptic signals by $CaV_{2.3}$ voltage-sensitive calcium channels located in dendritic spines. *Neuron* 53, 249–260. doi: 10.1016/j.neuron.2006.12.017

Bloodgood, B. L., Giessel, A. J., and Sabatini, B. L. (2009). Biphasic synaptic Ca influx arising from compartmentalized electrical signals in dendritic spines. *PLoS Biol* 7:e1000190. doi: 10.1371/journal.pbio.1000190

Cabrera, R., Filevich, O., Garcia-Acosta, B., Athilingam, J., Bender, K. J., Poskanzer, K. E., et al. (2017). A visible-light-sensitive caged serotonin. *ACS Chem. Neurosci.* 8, 1036–1042. doi: 10.1021/acschemneuro.7b00083

Cajal, S. R. (1888). Estructura de los centros nerviosos de las aves. *Rev. Trim. Histol. Norm. Patol.* 1, 1–10.

Canepari, M., Nelson, L., Papageorgiou, G., Corrie, J. E., and Ogden, D. (2001). Photochemical and pharmacological evaluation of 7-nitroindolinyl-and 4-methoxy-7-nitroindolinyl-amino acids as novel, fast caged neurotransmitters. *J. Neurosci. Methods* 112, 29–42. doi: 10.1016/s0165-0270(01)00451-4

Carter, B. C., Giessel, A. J., Sabatini, B. L., and Bean, B. P. (2012). Transient sodium current at subthreshold voltages: activation by EPSP waveforms. *Neuron* 75, 1081–1093. doi: 10.1016/j.neuron.2012.08.033

Chalifoux, J. R., and Carter, A. G. (2010). GABAB receptors modulate NMDA receptor calcium signals in dendritic spines. *Neuron* 66, 101–113. doi: 10.1016/j.neuron.2010.03.012

Chen, J. L., Villa, K. L., Cha, J. W., So, P. T., Kubota, Y., and Nedivi, E. (2012). Clustered dynamics of inhibitory synapses and dendritic spines in the adult neocortex. *Neuron* 74, 361–373. doi: 10.1016/j.neuron.2012.02.030

Chiu, C. Q., Lur, G., Morse, T. M., Carnevale, N. T., Ellis-Davies, G. C., and Higley, M. J. (2013). Compartmentalization of GABAergic inhibition by dendritic spines. *Science* 340, 759–762. doi: 10.1126/science.1234274

Colgan, L. A., and Yasuda, R. (2014). Plasticity of dendritic spines: subcompartmentalization of signaling. *Annu. Rev. Physiol.* 76, 365–385. doi: 10.1146/annurev-physiol-021113-170400

Colonnier, M. (1968). Synaptic patterns on different cell types in the different laminae of the cat visual cortex. An electron microscope study. *Brain Res.* 9, 268–287. doi: 10.1016/0006-8993(68)90234-5

Cummings, J. A., Mulkey, R. M., Nicoll, R. A., and Malenka, R. C. (1996). Ca^{2+} signaling requirements for long-term depression in the hippocampus. *Neuron* 16, 825–833. doi: 10.1016/s0896-6273(00)80102-6

DeFelipe, J., Hendry, S. H., and Jones, E. G. (1989). Synapses of double bouquet cells in monkey cerebral cortex visualized by calbindin immunoreactivity. *Brain Res.* 503, 49–54. doi: 10.1016/0006-8993(89)91702-2

Denk, W., Strickler, J. H., and Webb, W. W. (1990). Two-photon laser scanning fluorescence microscopy. *Science* 248, 73–76. doi: 10.1126/science.2321027

Denk, W., and Svoboda, K. (1997). Photon upmanship: why multiphoton imaging is more than a gimmick. *Neuron* 18, 351–357. doi: 10.1016/s0896-6273(00)81237-4

Ellis-Davies, G. C. R. (2007). Caged compounds: photorelease technology for control of cellular chemistry and physiology. *Nat. Methods* 4, 619–628. doi: 10.1038/nmeth1072

Ellis-Davies, G. C. R. (2019). Two-photon uncaging of glutamate. *Front. Synaptic Neurosci.* 10:48. doi: 10.3389/fnsyn.2018.00048

Filevich, O., Salierno, M., and Etchenique, R. (2010). A caged nicotine with nanosecond range kinetics and visible light sensitivity. *J. Inorg. Biochem.* 104, 1248–1251. doi: 10.1016/j.jinorgbio.2010.08.003

Fino, E., Araya, R., Peterka, D. S., Salierno, M., Etchenique, R., and Yuste, R. (2009). RuBi-glutamate: two-photon and visible-light photoactivation of neurons and dendritic spines. *Front. Neural Circuits* 3:2. doi: 10.3389/neuro.04.002.2009

Fino, E., Paille, V., Cui, Y., Morera-Herreras, T., Deniau, J. M., and Venance, L. (2010). Distinct coincidence detectors govern the corticostriatal spike timing-dependent plasticity. *J. Physiol.* 588, 3045–3062. doi: 10.1113/jphysiol.2010.188466

Freund, T. F., Maglóczky, Z., Soltész, I., and Somogyi, P. (1986). Synaptic connections, axonal and dendritic patterns of neurons immunoreactive for cholecystokinin in the visual cortex of the cat. *Neuroscience* 19, 1133–1159. doi: 10.1016/0306-4522(86)90129-6

Gasparini, S., and Magee, J. C. (2006). State-dependent dendritic computation in hippocampal CA1 pyramidal neurons. *J. Neurosci.* 26, 2088–2100. doi: 10.1523/jneurosci.4428-05.2006

Gray, E. G. (1959). Electron microscopy of synaptic contacts on dendrite spines of the cerebral cortex. *Nature* 183, 1592–1593. doi: 10.1038/1831592a0

Grunditz, A., Holbro, N., Tian, L., Zuo, Y., and Oertner, T. G. (2008). Spine neck plasticity controls postsynaptic calcium signals through electrical compartmentalization. *J. Neurosci.* 28, 13457–13466. doi: 10.1523/jneurosci.2702-08.2008

Harnett, M. T., Makara, J. K., Spruston, N., Kath, W. L., and Magee, J. C. (2012). Synaptic amplification by dendritic spines enhances input cooperativity. *Nature* 491, 599–602. doi: 10.1038/nature11554

Harnett, M. T., Xu, N. L., Magee, J. C., and Williams, S. R. (2013). Potassium channels control the interaction between active dendritic integration compartments in layer 5 cortical pyramidal neurons. *Neuron* 79, 516–529. doi: 10.1016/j.neuron.2013.06.005

Harvey, C. D., and Svoboda, K. (2007). Locally dynamic synaptic learning rules in pyramidal neuron dendrites. *Nature* 450, 1195–1200. doi: 10.1038/nature06416

Helmchen, F., and Denk, W. (2005). Deep tissue two-photon microscopy. *Nat. Methods* 2, 932–940. doi: 10.1038/nmeth818

Higley, M. J., and Sabatini, B. L. (2012). Calcium signaling in dendritic spines. *Cold Spring Harb. Perspect. Biol.* 4:a005686. doi: 10.1101/cshperspect.a005686

Holbro, N., Grunditz, A., and Oertner, T. G. (2009). Differential distribution of endoplasmic reticulum controls metabotropic signaling and plasticity at hippocampal synapses. *Proc. Natl. Acad. Sci. U S A* 106, 15055–15060. doi: 10.1073/pnas.0905110106

Ismailov, I., Kalikulov, D., Inoue, T., and Friedlander, M. J. (2004). The kinetic profile of intracellular calcium predicts long-term potentiation and long-term depression. *J. Neurosci.* 24, 9847–9861. doi: 10.1523/jneurosci.0738-04.2004

Kantevari, S., Matsuzaki, M., Kanemoto, Y., Kasai, H., and Ellis-Davies, G. C. R. (2010). Two-color, two-photon uncaging of glutamate and GABA. *Nat. Methods* 7, 123–125. doi: 10.1038/nmeth.1413

Kim, T., Oh, W. C., Choi, J. H., and Kwon, H. B. (2016). Emergence of functional subnetworks in layer 2/3 cortex induced by sequential spikes *in vivo*. *Proc. Natl. Acad. Sci. U S A* 113, E1372–E1381. doi: 10.1073/pnas.1513410113

Kwon, T., Sakamoto, M., Peterka, D. S., and Yuste, R. (2017). Attenuation of synaptic potentials in dendritic spines. *Cell Rep.* 20, 1100–1110. doi: 10.1016/j.celrep.2017.07.012

Lang, C., Barco, A., Zablow, L., Kandel, E. R., Siegelbaum, S. A., and Zakharenko, S. S. (2004). Transient expansion of synaptically connected dendritic spines upon induction of hippocampal long-term potentiation. *Proc. Natl. Acad. Sci. U S A* 101, 16665–16670. doi: 10.1073/pnas.0407581101

Lee, K. F., Soares, C., Thivierge, J. P., and Beique, J. C. (2016). Correlated synaptic inputs drive dendritic calcium amplification and cooperative plasticity during clustered synapse development. *Neuron* 89, 784–799. doi: 10.1016/j.neuron.2016.01.012

Lisman, J. (1989). A mechanism for the Hebb and the anti-Hebb processes underlying learning and memory. *Proc. Natl. Acad. Sci. U S A* 86, 9574–9578. doi: 10.1073/pnas.86.23.9574

Losonczy, A., and Magee, J. C. (2006). Integrative properties of radial oblique dendrites in hippocampal CA1 pyramidal neurons. *Neuron* 50, 291–307. doi: 10.1016/j.neuron.2006.03.016

Lynch, G., Larson, J., Kelso, S., Barrionuevo, G., and Schottler, F. (1983). Intracellular injections of EGTA block induction of hippocampal long-term potentiation. *Nature* 305, 719–721. doi: 10.1038/305719a0

Malenka, R. C., Kauer, J. A., Zucker, R. S., and Nicoll, R. A. (1988). Postsynaptic calcium is sufficient for potentiation of hippocampal synaptic transmission. *Science* 242, 81–84. doi: 10.1126/science.2845577

Matsuzaki, M., Ellis-Davies, G. C. R., Nemoto, T., Miyashita, Y., Iino, M., and Kasai, H. (2001). Dendritic spine geometry is critical for AMPA receptor expression in hippocampal CA1 pyramidal neurons. *Nat. Neurosci.* 4, 1086–1092. doi: 10.1038/nn736

Matsuzaki, M., Honkura, N., Ellis-Davies, G. C. R., and Kasai, H. (2004). Structural basis of long-term potentiation in single dendritic spines. *Nature* 429, 761–766. doi: 10.1038/nature02617

Nevian, T., and Sakmann, B. (2006). Spine Ca^{2+} signaling in spike-timing-dependent plasticity. *J. Neurosci.* 26, 11001–11013. doi: 10.1523/jneurosci.1749-06.2006

Ngo-Anh, T. J., Bloodgood, B. L., Lin, M., Sabatini, B. L., Maylie, J., and Adelman, J. P. (2005). SK channels and NMDA receptors form a Ca^{2+}-mediated feedback loop in dendritic spines. *Nat. Neurosci.* 8, 642–649. doi: 10.1038/nn1449

Nikolenko, V., Peterka, D. S., Araya, R., Woodruff, A., and Yuste, R. (2013). Spatial light modulator microscopy. *Cold Spring Harb. Protoc.* 2013:pdb.top079517. doi: 10.1101/pdb.top079517

Nikolenko, V., Poskanzer, K. E., and Yuste, R. (2007). Two-photon photostimulation and imaging of neural circuits. *Nat. Methods* 4, 943–950. doi: 10.1038/nmeth1105

Nikolenko, V., Watson, B. O., Araya, R., Woodruff, A., Peterka, D. S., and Yuste, R. (2008). SLM microscopy: scanless two-photon imaging and photostimulation with spatial light modulators. *Front. Neural Circuits* 2:5. doi: 10.3389/neuro.04.005.2008

Nishiyama, J., and Yasuda, R. (2015). Biochemical computation for spine structural plasticity. *Neuron* 87, 63–75. doi: 10.1016/j.neuron.2015.05.043

Noguchi, J., Matsuzaki, M., Ellis-Davies, G. C. R., and Kasai, H. (2005). Spine-neck geometry determines NMDA receptor-dependent Ca^{2+} signaling in dendrites. *Neuron* 46, 609–622. doi: 10.1016/j.neuron.2005.03.015

Oh, W. C., Hill, T. C., and Zito, K. (2013). Synapse-specific and size-dependent mechanisms of spine structural plasticity accompanying synaptic weakening. *Proc. Natl. Acad. Sci. U S A* 110, E305–E312. doi: 10.1073/pnas.1214705110

Oh, W. C., Lutzu, S., Castillo, P. E., and Kwon, H. B. (2016). *De novo* synaptogenesis induced by GABA in the developing mouse cortex. *Science* 353, 1037–1040. doi: 10.1126/science.aaf5206

Olson, J. P., Kwon, H. B., Takasaki, K. T., Chiu, C. Q., Higley, M. J., Sabatini, B. L., et al. (2013). Optically selective two-photon uncaging of glutamate at 900 nm. *J. Am. Chem. Soc.* 135, 5954–5957. doi: 10.1021/ja4019379

Passlick, S., Thapaliya, E. R., Chen, Z., Richers, M. T., and Ellis-Davies, G. C. R. (2018). Optical probing of acetylcholine receptors on neurons in the medial habenula with a novel caged nicotine drug analogue. *J. Physiol.* 596, 5307–5318. doi: 10.1113/jp276615

Peterka, D. S., Takahashi, H., and Yuste, R. (2011). Imaging voltage in neurons. *Neuron* 69, 9–21. doi: 10.1016/j.neuron.2010.12.010

Petroni, A., Slep, L. D., and Etchenique, R. (2008). Ruthenium(II) 2,2′-Bipyridyl tetrakis acetonitrile undergoes selective axial photocleavage. *Inorg. Chem.* 47, 951–956. doi: 10.1021/ic7018204

Podor, B., Hu, Y. L., Ohkura, M., Nakai, J., Croll, R., and Fine, A. (2015). Comparison of genetically encoded calcium indicators for monitoring action potentials in mammalian brain by two-photon excitation fluorescence microscopy. *Neurophotonics* 2:021014. doi: 10.1117/1.nph.2.2.021014

Raghuram, V., Sharma, Y., and Kreutz, M. R. (2012). Ca^{2+} sensor proteins in dendritic spines: a race for Ca^{2+}. *Front. Mol. Neurosci.* 5:61. doi: 10.3389/fnmol.2012.00061

Rial Verde, E. M., Zayat, L., Etchenique, R., and Yuste, R. (2008). Photorelease of GABA with visible light using an inorganic caging group. *Front. Neural Circuits* 2:2. doi: 10.3389/neuro.04.002.2008

Sabatini, B. L., Oertner, T. G., and Svoboda, K. (2002). The life cycle of Ca^{2+} ions in dendritic spines. *Neuron* 33, 439–452. doi: 10.1016/s0896-6273(02)00573-1

Shoham, S., O'Connor, D. H., Sarkisov, D. V., and Wang, S. S.-H. (2005). Rapid neurotransmitter uncaging in spatially defined patterns. *Nat. Methods* 2, 837–843. doi: 10.1038/nmeth793

Sobczyk, A., Scheuss, V., and Svoboda, K. (2005). NMDA receptor subunit-dependent $[Ca^{2+}]$ signaling in individual hippocampal dendritic spines. *J. Neurosci.* 25, 6037–6046. doi: 10.1523/JNEUROSCI.1221-05.2005

Somogyi, P., and Cowey, A. (1981). Combined Golgi and electron microscopic study on the synapses formed by double bouquet cells in the visual cortex of the cat and monkey. *J. Comp. Neurol.* 195, 547–566. doi: 10.1002/cne.901950402

Spacek, J., and Harris, K. M. (1998). Three-dimensional organization of cell adhesion junctions at synapses and dendritic spines in area CA1 of the rat hippocampus. *J. Comp. Neurol.* 393, 58–68. doi: 10.1002/(sici)1096-9861(19980330)393:1<58::aid-cne6>3.0.co;2-p

Spruston, N. (2008). Pyramidal neurons: dendritic structure and synaptic integration. *Nat. Rev. Neurosci.* 9, 206–221. doi: 10.1038/nrn2286

Svoboda, K., and Yasuda, R. (2006). Principles of two-photon excitation microscopy and its applications to neuroscience. *Neuron* 50, 823–839. doi: 10.1016/j.neuron.2006.05.019

Takasaki, K., and Sabatini, B. L. (2014). Super-resolution 2-photon microscopy reveals that the morphology of each dendritic spine correlates with diffusive but not synaptic properties. *Front. Neuroanat.* 8:29. doi: 10.3389/fnana.2014.00029

Tanaka, J. I., Horiike, Y., Matsuzaki, M., Miyazaki, T., Ellis-Davies, G. C. R., and Kasai, H. (2008). Protein synthesis and neurotrophin-dependent structural plasticity of single dendritic spines. *Science* 319, 1683–1687. doi: 10.1126/science.1152864

Tang, S., and Yasuda, R. (2017). Imaging ERK and PKA activation in single dendritic spines during structural plasticity. *Neuron* 93, 1315.e3–1324.e3. doi: 10.1016/j.neuron.2017.02.032

Tazerart, S., Mitchell, D. E., Miranda-Rottmann, S., and Araya, R. (2019). A spike-timing-dependent plasticity rule for single, clustered and distributed dendritic spines. *bioRxiv* [Preprint] 397323.

Tønnesen, J., Katona, G., Rózsa, B., and Nägerl, U. V. (2014). Spine neck plasticity regulates compartmentalization of synapses. *Nat. Neurosci.* 17, 678–685. doi: 10.1038/nn.3682

Tsien, R. Y. (1988). Fluorescence measurement and photochemical manipulation of cytosolic free calcium. *Trends Neurosci.* 11, 419–424. doi: 10.1016/0166-2236(88)90192-0

Yasuda, R., Sabatini, B. L., and Svoboda, K. (2003). Plasticity of calcium channels in dendritic spines. *Nat. Neurosci.* 6, 948–955. doi: 10.1038/nn1112

Yuste, R., Majewska, A., and Holthoff, K. (2000). From form to function: calcium compartmentalization in dendritic spines. *Nat. Neurosci.* 3, 653–659. doi: 10.1038/76609

Zayat, L., Calero, C., Albores, P., Baraldo, L., and Etchenique, R. (2003). A new strategy for neurochemical photodelivery: metal-ligand heterolytic cleavage. *J. Am. Chem. Soc.* 125, 882–883. doi: 10.1021/ja0278943

Zayat, L., Salierno, M., and Etchenique, R. (2006). Ruthenium(II) bipyridyl complexes as photolabile caging groups for amines. *Inorg. Chem.* 45, 1728–1731. doi: 10.1021/ic0512983

Zipfel, W. R., Williams, R. M., and Webb, W. W. (2003). Nonlinear magic: multiphoton microscopy in the biosciences. *Nat. Biotechnol.* 21, 1369–1377. doi: 10.1038/nbt899

Conflict of Interest Statement: The authors declare that the research was conducted in the absence of any commercial or financial relationships that could be construed as a potential conflict of interest.

frontiers in Synaptic Neuroscience

REVIEW
published: 24 July 2019
doi: 10.3389/fnsyn.2019.00020

Approaches and Limitations in the Investigation of Synaptic Transmission and Plasticity

*Stephen D. Glasgow, Ryan McPhedrain, Jeanne F. Madranges, Timothy E. Kennedy and Edward S. Ruthazer**

Department of Neurology & Neurosurgery, Montreal Neurological Institute-Hospital, McGill University, Montreal, QC, Canada

The numbers and strengths of synapses in the brain change throughout development, and even into adulthood, as synaptic inputs are added, eliminated, and refined in response to ongoing neural activity. A number of experimental techniques can assess these changes, including single-cell electrophysiological recording which offers measurements of synaptic inputs with high temporal resolution. Coupled with electrical stimulation, photoactivatable opsins, and caged compounds, to facilitate fine spatiotemporal control over release of neurotransmitters, electrophysiological recordings allow for precise dissection of presynaptic and postsynaptic mechanisms of action. Here, we discuss the strengths and pitfalls of various techniques commonly used to analyze synapses, including miniature excitatory/inhibitory (E/I) postsynaptic currents, evoked release, and optogenetic stimulation. Together, these techniques can provide multiple lines of convergent evidence to generate meaningful insight into the emergence of circuit connectivity and maturation. A full understanding of potential caveats and alternative explanations for findings is essential to avoid data misinterpretation.

Keywords: synapse, electrophysiology, analysis, mEPSCs, evoked potential, LTP (long term potentiation), spontaneous release

OPEN ACCESS

Edited by:
Dirk Feldmeyer, Julich Research Centre, Germany

Reviewed by:
Dominique Debanne, INSERM U1072 Neurobiologie des Canaux Ioniques et de la Synapse, France
Joanna Urban Ciecko, Nencki Institute of Experimental Biology (PAS), Poland

***Correspondence:**
Edward S. Ruthazer
edward.ruthazer@mcgill.ca

Received: *30 April 2019*
Accepted: *04 July 2019*
Published: *24 July 2019*

Citation:
Glasgow SD, McPhedrain R, Madranges JF, Kennedy TE and Ruthazer ES (2019) Approaches and Limitations in the Investigation of Synaptic Transmission and Plasticity. Front. Synaptic Neurosci. 11:20. doi: 10.3389/fnsyn.2019.00020

INTRODUCTION

A fundamental basis of information transfer in the nervous system is the release of neurotransmitter from the presynaptic terminal into the synaptic cleft to activate receptors on the postsynaptic neuron. These receptors can activate downstream signaling processes and initiate ionic flux through receptor pores. This in turn can alter the transmembrane electrical potential, which propagates to the cell body and axon hillock to evoke an action potential (AP) in the postsynaptic neuron. Temporal and spatial summation play pivotal roles in regulating neuronal output, through the filtering and integration of synaptic events with a range of amplitudes and durations (Magee and Johnston, 2005; Spruston, 2008). Indeed, coincident pre- and post-synaptic firing can lead to forms of synaptic strengthening of connections between two or more neurons, which can last for seconds, minutes, hours, days, and even a lifetime (Bliss and Gardner-Medwin, 1973; Abraham et al., 2002). Through dynamic recruitment of postsynaptic receptor complexes and modulation of presynaptic vesicular release, these changes contribute to the cellular basis of learning and memory in the brain.

Synaptic transmission and plasticity have been studied using various approaches, including molecular biology, behavior, electrophysiology, and imaging, however no single method is without drawbacks. Electrophysiology provides high temporal resolution, on the order of fractions of milliseconds, while enabling the pharmacological investigation of synaptic physiology. However, extracellular electrophysiological techniques, such as field potential recording and spike sorting, suffer from relatively poor spatial resolution. Whole-cell electrophysiology provides high temporal and spatial localization, but is typically configured for single or simultaneous double neuronal recordings (though some labs have successfully recorded from up to 12 neurons in parallel), limiting its utility for understanding complex network-level interactions (Miles and Poncer, 1996; Markram et al., 1997; Gal et al., 2019). In contrast, biochemical techniques such as immunohistochemistry, *in situ* hybridization and single cell transcriptomics provide high neuroanatomical specificity, and can allow for quantitative comparisons, but exhibit relatively low temporal acuity. More recently, the development of optogenetics, genetically-encoded calcium indicators (GECIs) and voltage probes have provided methods for cell-type specific cellular, and even synaptic, interrogation (Fenno et al., 2011; Lin and Schnitzer, 2016). In this review, we discuss common electrophysiological techniques as well as integration of novel optical methods used to investigate synaptic transmission and plasticity in the developing and mature brain. We further discuss the interpretation and caveats associated with the use of these methods to investigate synaptic properties.

From Networks to Synapses: Insights Into Synaptic Transmission

Synaptic transmission between neurons consists of highly conserved electrical and chemical elements. Indeed, many of the key players in mammalian synaptic function and modulation were first identified through screens in invertebrates like fruit flies and nematodes (Gerschenfeld, 1973; Sweeney et al., 1995). Excitatory dendritic and somatic inputs result in the influx of positively-charged cations, which in turn leads to plasma membrane depolarization. At the axon hillock, this triggers the activation of voltage-dependent Na^+ channels which propagates the ionic flux down the axon while simultaneously driving back-propagating voltage deflections in non-axonal compartments of the cell. Arriving at the presynaptic terminal, the membrane depolarization activates voltage-dependent Ca^{2+} channels, which allow Ca^{2+} to enter the terminal (**Figure 1a**). Increased intracellular Ca^{2+} mobilizes neurotransmitter-containing vesicles to fuse at active zone release sites on the presynaptic membrane, which are localized in direct apposition to postsynaptic specializations across the narrow synaptic cleft (∼20 nm; Savtchenko and Rusakov, 2007; Südhof, 2012). Concentrations of transmitter in the synaptic cleft vary, but at a typical excitatory synapse, glutamate released from the presynaptic terminal quickly reaches concentrations >1 mM before dissipating with a decay time constant of ∼1.2 ms (Clements et al., 1992). Neurotransmitter ligand-binding to postsynaptic receptor proteins evokes direct (ionotropic) ion flux or indirect (metabotropic) intracellular signaling cascades, which can lead to second-messenger signaling, structural growth, and protein synthesis. A number of human diseases are characterized by altered synaptic function, the development of therapeutic approaches and treatments for which depend on improving our understanding of the mechanisms that underlie synaptic transmission and its modulation.

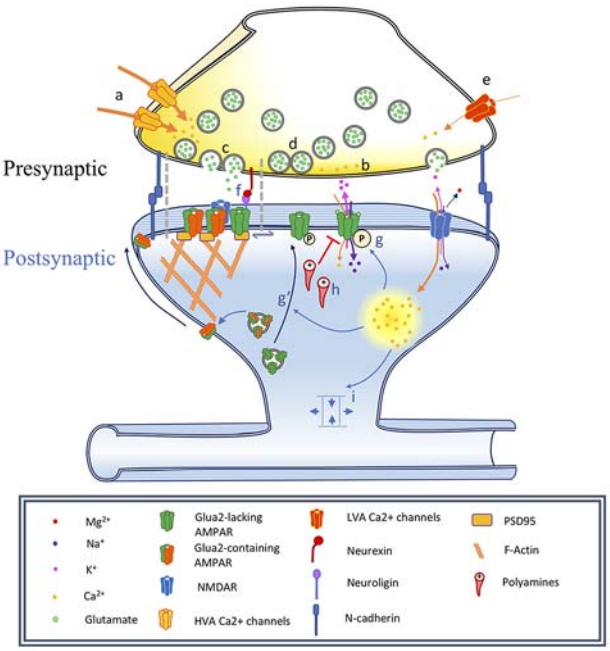

FIGURE 1 | Changes associated with long-term potentiation and synaptic maturation. Under basal conditions synapses are adhesive junctions between a presynaptic terminal containing neurotransmitter vesicles and Ca^{2+}-dependent release machinery, in close proximity to a postsynaptic site where various neurotransmitter receptors are present, often on electrotonically and biochemically isolated structures called dendritic spines. Long-term potentiation can be induced by specific stimulation paradigms resulting in the activation of specific biochemical signaling cascades. This has consequences on the spine structure, as well as on the trafficking and localization of neurotransmitter receptors, especially AMPA receptors. In this figure, we illustrate a number of events associated with synaptic plasticity. In the phenomenon of developmental synapse maturation many similar events are observed. Presynaptic changes: **(a)** Changes in high voltage-activated (HVA) voltage-dependent calcium channels (VDCCs) single-channel conductance affect Pr, changing the PPR and miniature postsynaptic current recordings (mPSCs) frequencies. **(b)** Changes in residual Ca^{2+} clearance affect Pr and therefore PPR, mPSCs frequencies. **(c)** Modulation of the vesicle fusion machinery would affect Pr and therefore PPR, mPSCs frequencies. **(d)** Depletion of the pool of readily releasable vesicles might reduce mPSC frequency and impact PPR. Due to synapses variability, could influence recorded mPSCs amplitude. **(e)** Changes in T-type low voltage-activated (LVA) VDCC properties would impact mEPSC frequency. Postsynaptic changes: **(f)** Nanodomains align active zones for vesicular release with postsynaptic receptors, constituting potential sites for the rapid exchange of receptors. **(g)** α-amino-3-hydroxy-5-methyl-4-isoxazolepropionic acid receptors (AMPAR) phosphorylation modulates single-channel conductance and **(g′)** membrane translocation. **(h)** Polyamine blockade: mediates rectification of Ca^{2+}-permeable AMPARs, can produce changes in PPR. **(i)** Alteration of synapse geometry such as spine neck shortening can decrease resistance and facilitate cooperativity of synaptic responses.

Development of Methodologies for Electrophysiological Investigation of Synaptic Events

The discovery by Katz and colleagues that spontaneous miniature end-plate potentials (MEPPs) recorded from the frog neuromuscular junction were similar in shape and amplitude to minimally evoked end-plate potentials in the presence of high Mg^{2+} or low Ca^{2+} led to the proposal that neurotransmission at synapses relies on the release of quantized packets of neurotransmitters in an all-or-none fashion (Del Castillo and Katz, 1954). This observation provided the basis for the quantal hypothesis, which posited that the measurement of a postsynaptic response (I) depends on the release probability (Pr) from a pool of releasable quanta (N) of defined quantal amplitude (Q). Therefore, the strength of an evoked postsynaptic response was modeled as:

$$I = QPrN$$

Although the precise definitions for these parameters may somewhat differ, this model provides a basis for understanding how changes in synaptic strength are measured. Indeed, these canonical electrophysiological approaches are still applied today and continue to provide insights into quantal parameters at the resolution of an individual synapse.

However, synapses in the central nervous system (CNS) are fundamentally distinct from peripheral neuromuscular junction synapses. The frog neuromuscular junction characteristically exhibits a low probability of release from defined inputs and high signal-to-noise ratio of quantal events that summate in a linear fashion (Mallart and Martin, 1967). In contrast, measurements of synaptic parameters in the CNS are confounded by a low signal-to-noise ratio that renders small-amplitude quantal events difficult to detect. Peripheral synaptic targets are innervated by individual or a relatively low number of inputs, whereas neurons in the CNS receive numerous synaptic connections, which impedes attribution of spontaneous quantal events to any single synapse (Megías et al., 2001; Gibbins and Morris, 2006). Further, in the CNS, excitatory and inhibitory inputs can terminate onto different neuronal compartments that, based on various geometric and resistive properties, modulate the amplitude of a measured response (Araya et al., 2006). Not only do different synaptic sites exhibit differences in quantal amplitude, but the probability of vesicular release can be non-uniform, with some presynaptic terminals disproportionately contributing to postsynaptic responses (Walmsley et al., 1988; Rosenmund et al., 1993). Together, these issues indicate that the foundational models based on the study of peripheral synapses are insufficient to fully interpret the function of central synapses.

Techniques to Understand Synaptic Function in the Brain

Brain slice electrophysiology has been used experimentally for over 60 years, allowing for functional dissection of synaptic transmission at molecular, cellular, and network levels. First developed by Henry McIlwain in the late 1950s, these preparations allow for measurement of electrical potentials in maintained mammalian synaptic networks and have been an invaluable tool for virtually every field of neuroscience (Li and McIlwain, 1957; Yamamoto and McIlwain, 1966). Briefly, brain tissue is quickly extracted and cut into thick slices (250–400 μm). These slices are kept viable in oxygenated media containing appropriate ionic species, including Na^+, K^+, Mg^{2+}, and Ca^{2+}, mimicking the extracellular cerebrospinal fluid, termed artificial cerebrospinal fluid (ASCF). While various recipes have been used, ASCF generally contains high levels of Na^+ and lower levels of other monovalent and divalent cations and anions. By replacing the endogenous constituents of the extracellular cerebrospinal fluid with known quantities, while using the internal ionic concentrations in the recording electrode to approximate transmembrane ionic gradients, the specific ion species that pass through synaptic receptor channels can be readily identified. Levels of extracellular Ca^{2+} are critical regulators of synaptic responses, and therefore altering Ca^{2+} concentrations can have a major impact on the release probability and degree of presynaptic vesicular mobilization, with higher concentrations resulting in increased presynaptic glutamate release and recorded postsynaptic current amplitude (Katz and Miledi, 1967; Malinow and Tsien, 1990; Llinás et al., 1992). Isolating currents and varying ionic concentrations to systematically shift the equilibrium potentials of specific ions allows extensive biophysical characterization of various channels and provides detailed insights into how chemical neurotransmission is converted to electrical impulses in the brain.

This basic approach has been modified in numerous ways to address questions that might otherwise be unfeasible in a traditional brain slice. For example, organotypic slice cultures, which result in an optically accessible monolayer that preserves much of the general organization and connection specificity of the brain, are particularly well suited for experiments in which repeated imaging is combined with recording, as well as for coculturing brain areas whose normal connectivity is severed by slicing (Gähwiler, 1981; Gähwiler et al., 1997). Some of these approaches can also be applied in intact or acutely isolated brain from amphibian and reptilian preparations that exhibit greater tolerance for hypoxia and temperature change (Wu et al., 1996; Bickler and Buck, 2007). Finally, with the advent to two-photon microscopy, the technique of "shadow-patching," in which imaging and targeting of recording pipettes are performed through a cranial window, following the injection of fluorescent dye into the extracellular space to provide a three-dimensional inverted image of neuron locations, has improved the feasibility of whole-cell recording in the intact mammalian brain (Svoboda et al., 1997; Schmidt-Hieber and Häusser, 2013; Jayant et al., 2019). Such techniques preserve full network connectivity, but at the cost of reduced control over extracellular cerebrospinal fluid composition for drug application. Below, we discuss electrophysiology techniques used to record from brain tissue and address strengths and weaknesses associated with each method.

Spontaneous and Miniature Synaptic Transmission: Interpretations and Implications for Network, Cellular, and Molecular Signaling

Spontaneous Post-synaptic Currents

Spontaneous postsynaptic currents (sPSCs) can be recorded while leaving network activity intact. Therefore, sPSCs provide information about the overall synaptic drive and activity of an intact neural circuit in the absence of exogenous artificial stimulation. Used in conjunction with miniature postsynaptic current recordings (mPSCs) in which AP generation is pharmacologically blocked, sPSCs allow for the dissection of overall network activity compared to stochastic spontaneous release and can inform whether alterations following an experimental condition result in changes in network properties or individual synaptic probabilities.

Recording sPSCs allows for measurement of the relative excitatory and inhibitory synaptic drive within a network, which have important functional implications for the overall output of a given neuron. Spontaneous current recordings can also be applied to probe the identity of the postsynaptic receptors when used in conjunction with pharmacological interrogation, or by varying the membrane potential of the recorded neuron to isolate the currents associated with a specific receptor. Ionotropic glutamate receptors pass cations, including Na^+ and K^+, with roughly equal permeability, producing a depolarizing current that reverses near 0 mV membrane potential. In contrast, activation of ionotropic inhibitory $GABA_A$ receptors passes Cl^-, and results in a current that reverses at the equilibrium potential for Cl^-, usually near −65 mV. Consequently, by clamping the voltage of a cell at −65 mV, the driving force for the inhibitory component is effectively eliminated leaving only excitatory currents while depolarizing the cell to 0 mV can mute glutamatergic currents to reveal outward GABA responses. Comparison of the respective currents at each of these potentials allows for the calculation of the excitatory/inhibitory (E/I) ratio, which reflects the interplay of network activity that converges on an individual neuron. The balance of excitation vs. inhibition reflects the relative number of excitatory and inhibitory synapses and in healthy neurons, these levels of transmission are assumed to covary proportionally (Shu et al., 2003).

Changes in this balance can result in abnormal neural processing and computation. Synapse maturation during development leads to strengthening of cortical connectivity, reflected by increases in coherent neuronal network activity. In some neurodevelopmental disorders such as autism spectrum disorder (ASD), attention deficit hyperactivity disorder (ADHD), and schizophrenia, this balance is not maintained during synaptic pruning or the removal of aberrant synapses, for example, leading to a state of hyperexcitability that is characteristic of patients diagnosed with autism (Kehrer et al., 2008; Yizhar et al., 2011b; Nelson and Valakh, 2015). Consistent with an alteration in E/I balance, many neurodevelopmental disorders, including autism and schizophrenia, show co-morbidity with seizure-related pathologies, suggesting possible circuit dysregulation (Tuchman and Rapin, 2002; Friedman et al., 2008). However, a recent study systematically compared E/I balance in four different autism mouse models, and found that shifts in E/I balance, rather than being causative, may in fact reflect corrective homeostatic mechanisms designed to maintain stable overall synaptic drive to compensate for circuit dysfunction (Antoine et al., 2019).

Changes in the frequency of sPSCs are difficult to interpret since they may be affected by both pre- and postsynaptic mechanisms as well as alteration of overall network activity. Consequently, knowledge of the intrinsic and extrinsic network properties of the tissue preparation are important when considering the mechanisms that underlie changes in sPSCs. Further, in contrast to mPSCs, sPSCs show an increased probability of multivesicular release, which in turn can influence measured current amplitude. However, sPSC analysis is based on underlying assumptions of commonality between synchronous and spontaneous release mechanisms, presuming that these mechanisms exist in overlapping populations of synapses. Conversely, studies have demonstrated that ∼40% of synapses in *Drosphila* exhibit dual-mode active zones, with ∼36% of active zones showing preference for evoked release and 22% for spontaneous release alone (Melom et al., 2013). Indeed, highly-active synapses tend to show a preference for one mode of transmission over the other, indicating a specialization of synapses for different forms of synaptic communication (Peled et al., 2014). Consequently, localization of synaptic changes using sPSCs and mPSCs is problematic, due to differential expression of stochastic and synchronous evoked release mechanisms. Further, gross increases in levels of network activation can generate reverberatory activity, which can then mask alterations in synaptic frequency.

Miniature Post-synaptic Currents

Quantal release of neurotransmitter from the presynaptic terminal is stochastic when APs are eliminated using tetrodotoxin (TTX), a selective and potent blocker of voltage-gated Na^+ currents. Under these conditions, spontaneous vesicular fusion events can be recorded from the postsynaptic neuron as mPSCs, resulting in either miniature excitatory post-synaptic currents (mEPSCs) or miniature inhibitory post-synaptic currents (mIPSCs). While AP-generated presynaptic responses strongly activate high-threshold P/Q- (Cav2.2) and N-type (Cav2.1) voltage-gated Ca^{2+} channels, stochastic Ca^{2+} influx for mPSC release is primarily mediated by low-threshold T-type Ca^{2+} channels including Cav3.1 and Cav3.2 (Catterall, 2011; **Figure 1e**). It should be noted, however, that mPSCs appear to consist of both Ca^{2+}-dependent and independent events (Südhof, 2012). The frequency and amplitude of mPSCs have been used as proxies for the number of synapses and relative strength of synapses, respectively, made onto the postsynaptic cell (Segal, 2010). Stochastic spontaneous release suggests that a single mPSC event is likely the result of the release of a single vesicle. Consequently, recorded mPSC amplitude is a direct measure of ionic flux through postsynaptic receptors, with the underlying assumption that amount of neurotransmitter within a synaptic vesicle remains constant. However, variability between synapses that could also contribute

to changes in average quantal amplitudes, as well as increases in either *Pr* or in the number of releasable quanta at a subset of synaptic inputs, will skew the distribution of mPSCs towards these inputs, meaning that changes in mPSC amplitude may not unequivocally reflect changes in postsynaptic receptors. Further, plasticity-induced changes in the geometry of a dendritic spine, such as changes that alter the resistance of a spine neck (Matsuzaki et al., 2001; Richards et al., 2005; Araya et al., 2014), may influence estimated measurements of *Q* independent of changes in postsynaptic receptor sensitivity (**Figure 1i**; Beaulieu-Laroche and Harnett, 2018; Cartailler et al., 2018).

Changes in the frequency of mPSCs have traditionally been associated with alterations in presynaptic function, arising from interactions between *Pr* and the pool of releasable quanta. To delineate the contribution of these presynaptic parameters, use-dependent pharmacological blockers may be employed to estimate the rate of spontaneous release that relies solely on *Pr* by measuring the decay of recorded currents (Atasoy et al., 2008; Sara et al., 2011). The recording of mPSCs in conjunction with the use of fluorescent molecule dyes (FM dyes) may also provide insights into changes in the synaptic vesicle pool (Gaffield and Betz, 2006). Therefore, a combination of techniques is required to ascribe a unitary underlying mechanism to a change in presynaptic function.

Postsynaptic mechanisms can also contribute to observed changes in mPSC frequency following pharmacological manipulation or induction of plasticity. N-methyl-D-aspartate receptors (NMDAR) and α-amino-3-hydroxy-5-methyl-4-isoxazolepropionic acid receptors (AMPAR) are two types of ionotropic glutamatergic neurotransmitter receptors. The conductance pore of the NMDAR can be blocked by extracellular Mg^{2+} ions when the cell sits at a hyperpolarized potential, rendering it functionally silent. The discovery that as excitatory synapses mature they can pass through a "silent synapse" stage in which they exclusively contain NMDARs with no AMPARs, provides a dramatic example of how an increase in the number and composition of postsynaptic receptors can result in an increase in mPSC frequency that is independent of *Pr* (Isaac et al., 1995; Liao et al., 1995). Indeed, insertion of postsynaptic AMPARs can increase the frequency of mPSC events by rendering the postsynaptic neuron more sensitive to presynaptic release at previously-silent synapses. While this phenomenon is quite well accepted in the developing nervous system, it has also been observed at hippocampal synapses in the adult brain (Sametsky et al., 2010; Glasgow et al., 2018).

Initial studies suggested that spontaneous events resulted from stochastic release of synaptic vesicles due to random Ca^{2+} fluctuations that engaged presynaptic mechanisms of vesicular release similar to evoked release (Fatt and Katz, 1950). Based on this assumption, miniature postsynaptic responses have been used as a proxy for evoked release mechanisms that define synaptic strength. However, more recent evidence suggests that spontaneous and evoked release may be distinct phenomena with different regulatory mechanisms and functional roles (Kaeser and Regehr, 2014; Kavalali, 2015). Evidence for this difference between spontaneous and evoked release has been demonstrated in multiple ways, including investigating vesicular release machinery (Schneggenburger and Rosenmund, 2015; Abrahamsson et al., 2017), the specific pool of vesicles released (Sara et al., 2005; Fredj and Burrone, 2009), postsynaptic targets (Atasoy et al., 2008; Sara et al., 2011), regulatory mechanisms (Nakamura et al., 2015; Maschi and Klyachko, 2017), and subcellular localization (Kneussel and Hausrat, 2016). Given such differences, it is highly likely that spontaneous and evoked release are mechanistically distinct, but the reasons for this apparent dissociation remain unclear.

Does spontaneous release contribute to ongoing activity? Spontaneous release of neurotransmitter is necessary for the maintenance of synaptic connections but is not required for initial synaptogenesis (Verhage et al., 2000; Varoqueaux et al., 2002). Consistent with a role in synaptic maintenance, CA1 hippocampal neurons require spontaneous postsynaptic receptor activation to maintain dendritic spines (McKinney et al., 1999; Segal, 2010). A number of excellent reviews have been published on the mechanisms underlying this form of synaptic plasticity (Turrigiano, 2008; Lisman, 2017; Diering and Huganir, 2018).

Synaptic Analysis Using Evoked Vesicular Release

Due to the independent mechanisms underlying spontaneous and evoked vesicular release, understanding the synaptic properties of a cell by measuring mEPSCs in TTX will not provide completely accurate insights into synaptic activation evoked by AP firing. Additionally, evoked stimulation typically excites multiple presynaptic axons, rendering postsynaptic recording as an integrated response to all vesicular exocytotic events. Minimal stimulation, in which the intensity of current delivered through a stimulating electrode is reduced to a level just above where complete failure of evoked release occurs, can be used to characterize individual synaptic properties in an identified pathway. However, the analytical strength of minimal stimulation experiments can be limited by many basic properties of fiber inputs, such as the heterogeneity of synapses formed by axons of different diameters, and the frequency of axonal conduction failures at branch points (Debanne, 2004; Kerchner and Nicoll, 2008).

Another powerful way to assess quantal synaptic characteristics in evoked stimulation studies is to induce asynchronous release, in which evoked synaptic release takes place over a much longer time period, allowing the discrimination of multiple individual quantal events (Otsu et al., 2004; Kaeser and Regehr, 2014). Substitution of Ca^{2+} with Sr^{2+} has been commonly used to transform synchronous release to asynchronous release, resulting in substantial reduction in the peak amplitude of evoked synaptic events while increasing the occurrence of asynchronous events that can be attributed to release from single synaptic sites (Goda and Stevens, 1994). Sr^{2+} enters the presynaptic terminal through voltage-dependent calcium channels (VDCCs) and activates the fast Ca^{2+} sensor, synaptotagmin-1, albeit with lower efficacy than Ca^{2+}. Further, Sr^{2+} is extruded from presynaptic terminals less efficiently, resulting in a slowing of vesicular mobilization machinery (Xu-Friedman and Regehr, 2000). The quantal events induced by Sr^{2+}-mediated asynchronous release can serve as a proxy

for evoked EPSC strength since they appear to rely on the same release machinery and mechanisms as evoked release in the presence of Ca^{2+} (Kaeser and Regehr, 2014).

Use-dependent pharmacological blockers, such as MK-801 which stably occupies and occludes NMDAR channels in the open state, have also been applied to estimate the probability of release by measuring the decay of the curve as it relates to the reduced charge transfer of the evoked currents (Atasoy et al., 2008; Sara et al., 2011). However, typical pharmacological inhibition using bath application can result in changes in both presynaptic and postsynaptic neurons, confounding the spatial localization of function. To address the lack of spatial specificity of pharmacological blockers when used *in vitro* or *in vivo*, specific blockers can alternatively be included in the internal patch solution, circumventing network-wide alteration of function.

Quantal content at a given synapse is partially dependent on presynaptic factors, such as vesicular loading and exocytosis (Kaeser and Regehr, 2014). Estimations of multivesicular release can also confound the interpretation of single quantal events (Malagon et al., 2016). The rate of neurotransmitter reuptake by presynaptic terminals or astrocytes may also alter *Q* (Takamori, 2016). To isolate the postsynaptic contribution of *Q* it is possible to use optical uncaging, fast local perfusion, or microiontophoresis of pharmacological agents to control the concentration of neurotransmitter at a given synapse. Moreover, recent developments in fluorescent probes have facilitated estimation of quantal content using glutamate reporters such as igluSNfR (Marvin et al., 2013; Soares et al., 2017).

Measuring Changes in Evoked Synaptic Strength

Changes in the relative strength of synapses are typically measured as alterations in postsynaptic current evoked in response to electrical, chemical, or optogenetic stimulation. Evoked stimulation using *in vitro* models provides robust and controlled levels of synaptic activation. Electrical stimulation has been used for several decades, however, it suffers from low cellular specificity, often requiring constant pharmacological antagonism of different receptor subtypes to record isolated excitatory or inhibitory synaptic currents. Further, stimulation of defined pathways results in simultaneous, synchronized release of presynaptic transmitter from multiple inputs, unlike physiologically-relevant conditions where synaptic release is far more desynchronized. Stimulation using novel chemogenetic and optogenetic actuators have helped to overcome some of the issues associated with low cell-type specificity characteristic of electrical stimulation but still presents important limitations. This section will address the various measures of evoked responses that have been used previously to spatially localize changes in function across a synapse and discuss some recent technical improvements for circuit dissection.

Synaptic plasticity involves the possibility of changes in both pre- and post-synaptic components. Coordinated changes in both compartments are often observed, which can make differentiating the specific roles of pre- vs. post-synaptic components in functional changes difficult to interpret accurately. While a few labs have been able to successfully record responses from axon terminals using patch clamp recordings (Alle and Geiger, 2006; Shu et al., 2006; Oltedal et al., 2007; Sasaki et al., 2012; Novak et al., 2013; Kawaguchi and Sakaba, 2015), the small size of presynaptic terminals (∼1–2 μm) renders direct electrophysiological measurement difficult, and therefore the majority of research has relied on recordings from postsynaptic neurons to infer changes in presynaptic function. Such inference of presynaptic change relies on the protocols used to dissect out relative contribution of synaptic transmission. Below, we discuss the main techniques that have been used to identify the site and effectors of synaptic plasticity.

Paired-Pulse Ratio

APs travel down the axon to innervate the presynaptic terminal, resulting in the activation of voltage-dependent Ca^{2+} channels to trigger the mobilization and secretion of neurotransmitters. When two pulses are paired in quick succession (typically 20–100 ms), it is thought that residual Ca^{2+} left over from the first stimulus will transiently increase the release probability upon the second stimulus, termed short-term plasticity (Katz and Miledi, 1968; Zucker and Regehr, 2002). The relative peak amplitude of the first and second pulse, known as the paired-pulse ratio (PPR), therefore directly relates to presynaptic Pr. If the presynaptic terminal shows a high Pr, vesicular pools will be depleted following the first pulse, resulting in attenuated synaptic responses following the second stimuli and associated paired-pulse depression (PPD). In contrast, synapses showing low *Pr* can demonstrate facilitation following the second stimuli due to slow clearing of presynaptic intracellular Ca^{2+}, a phenomenon termed paired-pulse facilitation (PPF). Consequently, changes in PPR have been interpreted to reflect presynaptic changes in *Pr*, although there are a variety of alternative mechanisms that may contribute to alterations in PPR (**Figures 1b–d**).

While PPR may be correlated with the relative *Pr* of a synapse, it is now clear that a diversity of other cellular mechanisms can influence the synaptic response to trains of input. The rapid reuptake of neurotransmitters from the synaptic cleft by transporters on astrocytes and synaptic terminals has been postulated to modulate PPF. Indeed, astrocytic coverage has been shown to reduce synaptic efficacy due to increased efficiency of glutamate clearance (Oliet et al., 2001). At the hippocampal Schaffer collateral synapse, the activation of glutamate uptake transporters by local CA1 astrocytes alters available glutamate levels (Bergles and Jahr, 1997), contributing to short-term changes in synaptic strength that include changes in PPR.

Rapid modification of postsynaptic receptors can also result in changes in PPR. Approximately 50% of all AMPA receptors are stably clustered within ∼80 nm of the postsynaptic density at excitatory synapses, with the other fraction freely and quickly diffusing between them (Nair et al., 2013). Consistent with rapid exchange of AMPA receptors underlying short-term plasticity at individual synapses, experimentally crosslinking common AMPA receptor subtypes can modify forms of PPD, likely by blocking the swapping and postsynaptic removal of receptors (Heine et al., 2008). Rapid diffusion of AMPA receptors appears to increase the rate of recovery from PPD, which has been postulated to be due to endocytosis of desensitized

receptors and replacement with naïve receptors (Constals et al., 2015). Additionally, it is possible that desensitized receptors may be exchanged for receptors with modified single-channel conductance (**Figure 1g**), which in turn can facilitate the postsynaptic response to pairs of presynaptic inputs that are differentially active across very brief intervals.

Synaptic strengthening has been linked to increased single-channel AMPA receptor conductance, resulting in enhanced ionic flow through an individual ionophore (Benke et al., 1998). Short term plasticity can elicit changes in the relative permeability of AMPA receptors to ionic flux. Calcium-permeable AMPA receptors (CP-AMPARs), which typically consist of GluA2-lacking AMPARs, are known to mediate fast excitatory synaptic transmission but are typically blocked by intracellular polyamines (PA; Burnashev et al., 1992; Anggono and Huganir, 2012). Endogenous cytoplasmic PA can tonically block CP-AMPARs to reduce the amplitude of evoked excitatory synaptic responses (**Figure 1h**). However, repetitive stimulation can relieve this PA block, resulting in a postsynaptic form of short-term plasticity (Toth et al., 2000). Neural activity can dynamically regulate PA synthesis to account for changes in PPR (Aizenman et al., 2003). Removal of the polyamine block through depolarization can result in attenuation of PPD and enhancement of PPF in cortical circuits (Rozov and Burnashev, 1999). Consistent with this, earlier work had demonstrated that PPR exhibits a strong voltage-dependence, and may rely on NMDA receptor activation (Clark et al., 1994). Further, PPR is decreased following postsynaptic activation of the Ca^{2+}/calmodulin protein kinase 2 (CaMKII) signaling pathway in CA1 pyramidal neurons in response to Schaffer collateral stimulation, while simultaneously resulting in significant potentiation of synaptic responses (Wang and Kelly, 1996, 1997). CaMKII/calmodulin signaling can facilitate the function of CP-AMPARs, which in turn can mediate synaptic enhancement during protocols using PPR. Taken together, these findings suggest that changes in paired-pulse ratios can be expressed exclusively by the postsynaptic neuron through voltage-dependent removal of PA, independent of *Pr*.

AMPAR-to-NMDAR Ratio

Fast excitatory neurotransmission at central synapses is mediated by presynaptic release of glutamate, which in turn binds to specialized receptors on the postsynaptic neuron. Three major categories of glutamate-sensitive receptors, including AMPA, NMDA, and kainate receptors, have distinct kinetics that facilitate electrophysiological dissection of synaptic responses (Dingledine et al., 1999). AMPA receptors show large inward currents when recorded at relatively hyperpolarized membrane potentials, which are primarily mediated by Na^+ influx with fast rise (2–7 ms) and decay kinetics (20–30 ms). In contrast, NMDA receptors, which are typically quiescent at resting potential and activate only upon depolarization-mediated removal of Mg^{2+} ionophore blockade, exhibit a slow rise (∼20 ms) to maximal current, exhibiting a permeability for Ca^{2+}, and a slow bi-exponential decay kinetic of 40–200 ms. Kainate receptors, which are active near rest potentials, show rapid rise-time accompanied by a slow decay constant that is sensitive to interactions with Neto1 auxiliary proteins (Straub et al., 2011); these have been reviewed in detail elsewhere (Huettner, 2003; Contractor et al., 2011). For the purpose of this review, we will focus on AMPA and NMDA receptor subtypes. Both receptor families are typically present at excitatory synapses in the CNS, and therefore the relative density of each receptor subtype is likely to play a key role in the function and plasticity of synaptic inputs.

Interrogation of postsynaptic receptor contribution to synaptic responses can co-opt voltage-dependence and decay kinetics to dissociate the relative contributions of receptor subtypes. Glutamate binds to both AMPA and NMDA receptors, with low and high affinity, respectively (Patneau and Mayer, 1990; Lester and Jahr, 1992). However, NMDARs do not flux ionic current when the membrane is near typical resting potential due to strong affinity for Mg^{2+} within the receptor ionophore, effectively blocking cationic movement upon glutamate receptor binding. In contrast, neuronal depolarization reveals an outward mixed synaptic current, consisting of both AMPAR-mediated and NMDAR-mediated components. Given the different time constants of NMDAR and AMPAR currents, the relative contribution of each receptor subtype can be readily dissected (Watt et al., 2000). While the initial component of the evoked EPSC shows a fast rise-time, including both NMDAR and AMPAR components, the rapid decay of AMPAR responses reveals a pure NMDAR-mediated current by >50 ms post-stimulus. This method of measuring AMPAR currents at hyperpolarized membrane potentials (typically −60 to −70 mV) and NMDAR currents around 50 ms post-stimulation at depolarized postsynaptic membrane potentials (typically +40 mV) allows for electrophysiological delineation of the glutamate receptor subtypes in the absence of pharmacological antagonists and is a fast and efficient measure of plastic changes in the composition of synaptic receptors.

Paired-Recordings of Synaptically-Coupled Neurons

The majority of studies focusing on synaptic transmission use bulk electrical stimulation of axonal fibers. Problematically, this can result in diffuse excitation of axons from multiple origins, confounding studies that routinely attribute stimulation to a single synaptic pathway. To overcome this issue, intracellular recording from pairs of monosynaptically-connected neurons provides an elegant technique to precisely measure circuit connectivity, presynaptic release mechanisms, and synaptic plasticity between defined neuron pairs. First developed in ganglionic recordings from *Aplysia*, paired recordings can effectively and robustly determine changes in both pre- and post-synaptic machinery at a small number of synaptic contacts, and allows for validation of presynaptic APs (Hughes and Tauc, 1968; Debanne et al., 2008). The benefits of this approach are 2-fold: APs of a single neuron can be measured as synaptic responses in a coupled neuron, and activity and relative timing of activation in two neurons can be correlated to facilitate investigation of activity-dependent forms of plasticity.

Coupled recordings can also be further validated using morphological reconstruction through inclusion of biocytin

or another marker in the intracellular patch solution, allowing for elucidation of synaptic connectivity at both anatomical and physiological levels of investigation. Interestingly, dual patch recordings from coupled CA3 and CA1 neurons revealed that CA3 neurons form at a single CA1 contact *via* the Schaffer collateral, and show relatively low probability of transmitter release (Bolshakov and Siegelbaum, 1995). In contrast, pairs of excitatory cortical neurons are typically connected by 2–8 synaptic sites (Deuchars et al., 1994; Feldmeyer et al., 2005). Moreover, quadruple whole-cell recordings from layer V pyramidal neurons have demonstrated that clusters of bidirectional synaptic connections are more common than anticipated, and that neurons that share common presynaptic inputs are more likely to show correlated activity, providing a physiological basis for correlation-mediated activity-dependent synaptic plasticity (Song et al., 2005).

Study of presynaptic release mechanisms has been hugely impacted by the development of paired neuronal recordings. Transmitter release from the presynaptic axon terminal was traditionally believed to be mediated in an "all-or-none" manner due to initiation of APs, effectively functioning as a "binary" signal onto synaptically-connected postsynaptic neurons. However, through use of paired presynaptic axon terminal and postsynaptic somatic recordings, two groups were able to show that fluctuations in axon terminal membrane potential can potently enhance transmitter release, resulting in increased EPSC amplitude (Alle and Geiger, 2006; Shu et al., 2006). These findings suggest that presynaptic alteration of membrane potential can result in an "analog-like" modulation of synaptic transmission, and provide evidence that transmitter release from presynaptic terminals can be regulated at individual synapses through changes in both pre- and post-synaptic cellular excitability.

Are all synapses equally susceptible to plasticity? Excitatory synaptic responses elicited by electrical stimulation are typically used in studies of synaptic plasticity of defined pathways, yet activate multiple convergent inputs. Consequently, changes in synaptic strength cannot be attributable to any individual synapse. However, paired recordings of monosynaptically connected CA3 and CA1 neurons have demonstrated that a large subset of Schaffer collateral synapses fail to show potentiation following long-term potentiation (LTP) induction, highlighting a functional heterogeneity of LTP expression at different synaptic connections (Debanne et al., 1999). Therefore, observed changes in synaptic strength following LTP induction using electrical stimulation is likely to reflect large changes in a small number of individual synapses rather than a global facilitation of postsynaptic responses.

Paired recordings from synaptically-coupled neurons are a potent technique that can reveal a number of important mechanistic insights into synaptic transmission in acute brain slices. Indeed, it is a useful tool to study anatomical and physiological connectivity, presynaptic release function, and synaptic plasticity, and can be used to dissect relative contributions of individual synapses that would not be feasible using traditional bulk electrical stimulation.

Methods for Detecting Nascent or Silent Synapses

Changes in synaptic strength following the induction of LTP in the CA1 field of the hippocampus are primarily mediated by alteration of postsynaptic receptors (**Figure 1g**). While much work has focused on the recruitment of AMPARs to existing synapses, LTP may also reflect the addition of new AMPAR-containing synapses (Kerchner and Nicoll, 2008; Araki et al., 2015). However, the investigation of these previously-silent or nascent synapses is particularly difficult. Previous literature has demonstrated the existence of silent synapses or maturation of nascent synapses by exploiting a variety of methods, including coefficient of variation analysis, minimal stimulation, paired recordings, and glutamate photo-uncaging (Kerchner and Nicoll, 2008).

Excitatory glutamatergic synapses containing NMDARs but lacking AMPARs in acute adult hippocampal brain slices were initially described through analysis of trial-to-trial variability of EPSC amplitude (Kullmann, 1994). The overall variability of AMPAR-mediated and NMDAR-mediated EPSC responses can be expressed as a function of the coefficient of variability ($1/CV^2$; the ratio of standard deviation of amplitude response to the mean amplitude of all events). Assuming that AMPARs and NMDARs are localized to all synapses, $1/CV^2$ should be equal for both receptor subtypes due to trial-by-trial variability of *Q* released from the presynaptic terminal. However, following LTP induction, $1/CV^2$ for AMPAR-mediated events is consistently decreased compared to NMDAR-mediated components (Kullmann, 1994). Synaptic responses exhibit a binomial probability distribution, which is a reflection of both the number of synapses and the *Pr* at each synaptic terminal. Consequently, in experiments when changes in synaptic strength following LTP induction were found to lead to a reduction in the overall variability of evoked AMPAR responses, this was initially erroneously attributed to increased *Pr*. Subsequent evidence revealed that the decreased variability was, in fact, attributable to AMPAR insertion into nascent synapses, effectively increasing the number (*N*) of synapses capable of responding (Lu et al., 2001). While silent synapses show no AMPA-mediated currents, they do contain NMDAR-mediated currents, measurable upon depolarization, that are unchanged following LTP induction (Kauer et al., 1988). Therefore, the NMDAR synaptic distribution does not appear to be altered by LTP induction, and is therefore useful as a stable electrophysiological measure for synapse function, even in the absence of AMPAR-mediated current.

Minimal stimulation to activate a few or even a single axonal fiber presumably elicits synaptic responses at a small number of postsynaptic sites. Following synaptic strengthening, the relative number of failures under minimal stimulation decreases despite using the same stimulus intensity, again suggesting that nascent synapses have been generated or that previously silent synapses have been unsilenced through insertion of AMPARs (Isaac et al., 1995). Similarly, intracellular recording from pairs of connected neurons has also been used to investigate synaptic unsilencing. Using paired recordings of CA3 neurons in organotypic hippocampal slices, Montgomery et al. (2001) showed that LTP can unsilence synapses (Montgomery

et al., 2001). Paired whole-cell patch clamp recordings from two connected CA3 neurons resulted in NMDAR-mediated synaptic transmission at depolarized voltages, but no AMPAR-mediated synaptic responses at hyperpolarized potentials. Further, manipulations to increase the release probability of presynaptic terminals failed to elicit any postsynaptic response, suggesting a lack of AMPAR-containing postsynaptic sites. However, following a pairing protocol that facilitated NMDAR function coupled with presynaptic stimulation, AMPAR-mediated currents were readily observed with no detectable change in the NMDAR-mediated EPSC. Consistent with the unmasking of silent synapses, the failure rate of AMPAR-mediated EPSCs was significantly decreased by ∼50% following LTP. These studies provide examples of methods to detect changes in silent synaptic connections and support the conclusion that activity can regulate synapse maturation through AMPAR insertion.

Isolated synaptic events can be simulated using photostimulation of caged compounds, such as MNI-glutamate, with diffraction-limited two-photon laser illumination. Caged compounds are biologically-active molecules that are rendered inert through a covalent attachment, which can be photolyzed with strong laser activation (Kaplan et al., 1978). A number of excellent reviews have been published on photo-uncaging in organotypic and acute hippocampal slices (Judkewitz et al., 2006; Reiner et al., 2015; Ellis-Davies, 2019). These findings show that changes in synaptic transmission can be due to a number of alterations in the postsynaptic neuron, including *de novo* spine formation and synaptogenesis.

Rapid Subunit Switching Without Receptor Exocytosis

Our focus thus far has compared pre-synaptic and post-synaptic mechanisms, however, recent studies have further parsed synaptic function, providing evidence that excitatory neurotransmission is mediated in the postsynaptic density at the nanometer scale (Eggermann et al., 2012). While previous models had primarily focused on the synapse as a whole, it is becoming exceedingly likely that excitatory synaptic transmission is organized as columnar nanodomains within the synapse. These "nanodomains" provide tight spatial constraints for postsynaptic activation, creating conditions in which presynaptic vesicular fusion occurs in extremely close proximity to the receptor site (**Figure 1f**; Choquet and Triller, 2013; Compans et al., 2016). What is the purpose of these nanodomains? While the answer remains elusive, it appears that certain types of neurotransmitter receptors, such as AMPARs, which exhibit relatively low affinity for glutamate, may be able to sit in reserve immediately adjacent to these nanodomains at the synaptic cleft, where they would contribute little or nothing to synaptic transmission. However, when mobilized during synaptic plasticity, they may be rapidly incorporated into the nanodomain. Consistent with this, various adhesion molecules that can mediate transsynaptic interactions and are well-known to have potent actions on the actin cytoskeleton, such as cadherin/β-catenin (Arikkath and Reichardt, 2008; Mills et al., 2017), neuroligin/neurexin (Chih et al., 2005; Haas et al., 2018), EphB/ephrin (Sheffler-Collins and Dalva, 2012), Slitrk/receptor protein tyrosine phosphatases (RPTPs; Yim et al., 2013), netrins (Goldman et al., 2013), integrins (Park and Goda, 2016), and others (Jang et al., 2017), have been found to be delivered to the synapse in response to activity and can affect rapid local structural reorganization (Benson et al., 2000).

Such local regulatory mechanisms are able to govern the density and spatial location of postsynaptic receptors at the synapse (Choquet, 2018). In contrast to previous models, which focused on a paradigm of receptor insertion at synapses, more recent work has begun to emphasize the importance of molecular-scale localization of excitatory glutamate receptors at postsynaptic slots, associated presynaptically with vesicular release sites and postsynaptically with intracellular scaffolding molecules like PSD-95. In turn, organization of the synapse can help to bring downstream signaling components into close proximity to excitatory ionic flux in the postsynaptic cell. Interestingly, other receptors such as NMDARs have higher affinity for their ligand and may therefore be less dependent on their sub-synaptic localization for signaling, allowing for extra-synaptic activation, potentially by different co-agonists (Rao and Craig, 1997; Dingledine et al., 1999; Papouin et al., 2012).

A nanodomain mechanism further raises the possibility of a role for the local trafficking of factors that can concomitantly regulate structural plasticity (Yamagata et al., 2003). Activity-dependent insertion or release of adhesion molecules such as protocadherins, cadherins, neuroligins, EphB, cerebellin, draxins, and others can promote specialization of postsynaptic and presynaptic densities (de Wit and Ghosh, 2016). These transsynaptic adhesion molecules span the synaptic cleft, and can rapidly modify the shape of synapses through intracellular interactions with the actin cytoskeleton (Murase et al., 2002; Okamura et al., 2004). Moreover, recent work has demonstrated that many adhesion molecules can interact with the N-terminal of glutamate receptors as well as synaptobrevin, suggesting that they may influence the local organization of nanodomains. Indeed, these findings indicate that synaptic structure is far more complex than originally proposed and that changes in synaptic strength may be mediated by rapid alteration of synaptic nanocolumns.

Extracellular Recordings

Extracellular field potential recordings *in vitro* offer access to identified neural circuitry for prolonged periods and facilitate pharmacological investigation, without dialyzing the intracellular contents of neurons. Measurements are typically made with glass electrodes filled with a highly-conductive solution such as 3M KCl, Na^+, or ASCF and positioned in the dendritic field of neurons of interest to record alterations in local field potential, which results from the sum of electric current flow stemming from nearby sources. Local field potentials correspond to the concerted behavior, mainly synaptic, of multiple neurons and their processes proximal to the tip of the recording electrode.

This approach facilitates investigation of the "group average" as opposed to individual neurons, which may express various ionic channels, receptors, and other proteins differentially to neighboring neurons. As such, extracellular electrophysiological

recordings can provide valuable insights to global changes in network properties following experimental manipulation. Moreover, because of their comparatively low level of invasiveness, field recording sessions can last for many hours, revealing so-called late-phase forms of LTP that persist for many hours and require protein synthesis (Nguyen et al., 1994).

In vivo field potential recordings permit repeated measurements of synaptic and network properties in the intact brain. Indeed, long-term recordings of neuronal activity have been maintained for up to several months. Recently, wireless electrophysiological recording systems have been developed and paired with video-based behavioral tracking for 24 h continuous observation over the course of 3 months (Grand et al., 2013), allowing for changes in neuronal excitability to be studied across long durations and under different behavioral contexts. Although these new techniques have tremendous potential, due to movement artifacts and other technical hurdles, it remains a significant technical challenge to perform robust long-term time-course recordings using *in vivo* recording electrodes.

Optical Techniques for Investigating Synaptic Function

Recent advances in neuroscientific tools have allowed for the functional dissection of brain wiring with previously unparalleled specificity, temporal precision, and cell-type selectivity. In addition to an ever-growing number of cell-type-specific actuators and inhibitors, optical readouts have also greatly evolved in the past decade. The availability of optical recording techniques has presented the field with novel methods to record synaptic activity without the perturbations typical of more invasive techniques like intracellular patch clamp recording. Optical "read-outs" provide real-time information of cellular activity, and allow for precise, spatially constrained measurements of ongoing network function. Combining these technologies allows for new experimental approaches that can stimulate with light and measure functional changes optically. However, critical validation with electrophysiology is sorely lacking in many studies. The following section will briefly describe new readouts for cellular and synaptic activity, followed by descriptions of light-activated actuators and inhibitors of cellular function.

Calcium Indicators

Live imaging of intracellular Ca^{2+} dynamics owes much of its success to the efforts of Roger Tsien's group starting in the early 1980s (Tsien, 1983; Grynkiewicz et al., 1985). A wide array of fluorometric and ratiometric dyes were developed with a range of affinities for Ca^{2+} binding that allowed for continuous monitoring of intracellular Ca^{2+} levels to investigate intrinsic and synaptic excitability in cultured cells and *in vivo*. Traditionally these dyes were loaded into neurons through a patch pipette, but a particularly powerful innovation involved the coupling of an acetoxymethyl (AM) ester to the dye, making it membrane permeant. AM-coupled dye could be injected directly into brain tissue to load hundreds of cells simultaneously. The AM ester would then be cleaved off the dye by intracellular esterases, trapping the activated fluorescent dye inside the cells (Garaschuk et al., 2006). However, toxicity and a lack of cell-type specificity associated with these dyes limited their applications in living tissue. Recent developments in both microscopy and GECIs, reviewed in detail elsewhere (Lin and Schnitzer, 2016), have allowed long-term analysis and investigation of synaptic strength. The most successful recent generation of GECIs, the GCaMP family, based on a circularly permutated green fluorescent protein fused with calmodulin and the M13 peptide from myosin light chain kinase, is now more sensitive than the original synthetic dyes, capable of detecting individual synaptic events and APs (Nakai et al., 2001; Tian et al., 2009; Dana et al., 2018). However, due to their slow kinetics of Ca^{2+} chelation, beneficial for relatively slow, laser-scanning microscopy approaches, many of these indicators offer relatively low temporal resolution of cellular excitation compared to more traditional electrophysiological methods. Multiple variants, with specifications for fluorescence change, spatial resolution, and response kinetics are constantly being developed. Recently, a set of four-color, spectrally-resolved Ca^{2+} indicators, XCaMPs that exhibit a large fluorescence signal change with more rapid kinetics has been reported (Inoue et al., 2019). Importantly, the spectral and kinetic properties of these new variants allow for better AP discrimination during trains and permit independent targeting of multiple genetically-defined cell types with different colors. The combination of whole-cell patch electrophysiology and new powerful GECIs variants with diverse characteristics substantially enables the subcellular localization of synaptic transmission and plasticity events within cells.

Optical Actuators

Optical stimulation employing light-activated actuators or inhibitors can elicit synaptic release or block synaptic input with precise spatial and temporal control. Early versions were based on neuronal ion channels modified to use light to gate conductances and depolarize neurons, but achievable time constants were slow and lacked specificity (Zemelman et al., 2003). The development of channelrhodopsin-2 (ChR2), a variant of an algal rhodopsin, shows millisecond precision and allows rapid, reversible control of neuronal or other cell type-specific activity. First described in 2005, ChR2 is a non-specific cationic channel that activates upon illumination with 473 nm light (Boyden et al., 2005). By combining viral delivery of ChR2 with Cre-LoxP mouse lines, optogenetic stimulation provides the ability to stimulate specific populations of genetically-defined neurons using light (Tsien et al., 1996; Yizhar et al., 2011a). This powerful technique has been used to dissect how different classes and ensembles of neurons regulate postsynaptic excitation, and more broadly how these neurons contribute to behavior (Glasgow et al., 2017). Further, recent work has used these optogenetic constructs delivered in retrograde viruses to facilitate pathway-specific excitation or inhibition (Schwarz et al., 2015), as well as ChR2-assisted circuit mapping (CRACM) of long-range projections (Petreanu et al., 2007).

Although extremely powerful, the use of optogenetics in measuring synaptic transmission, both *in vivo* and *in vitro*, faces

most of the same issues that concern electrical stimulation, as well as additional concerns that include toxic light exposure and perturbation of normal cellular function. Variability in the level of ChR2 expression can reduce the utility of optogenetics as a tool to study synaptic transmission. Excitation of ChR2 in high-expressing neurons induces a large Ca^{2+} transient that travels throughout to the neuron to trigger APs with relatively short delays and high reliability, whereas low-expressing neurons routinely require extended blue light activation to elicit neuronal firing, that can result in phototoxicity and deleterious effects on cell health (Wade et al., 1988). Due to the relatively slow kinetics of ChR2, the resultant depolarization and firing is often delayed relative to the onset of light stimulation, obfuscating any link between the pulse of light stimulation and firing of the presynaptic neuron. Such findings suggest that high expression levels are required for studies investigating synaptic transmission; however, high levels of ChR2 expression have also been linked to neuronal defects and toxicity (Yizhar et al., 2011a; Miyashita et al., 2013). Further, compared to APs elicited by somatic current injection, light-evoked APs result in significantly higher levels of intracellular Ca^{2+}, likely due to temporally-extended depolarization-mediated activation of voltage-gated Ca^{2+} channels (Zhang and Oertner, 2007). The reliance of presynaptic release machinery on the level of intracellular Ca^{2+} suggests that their saturation could alter *Pr* from the presynaptic terminal. These important characteristics of ChR2 require particular attention when using optogenetic tools to study synaptic transmission.

Optical stimulation can also impose artificial parameters on network activity. Due to light-mediated saturation of ChR2 currents in presynaptic inputs, a large number of presynaptic axons may be activated simultaneously by diffuse illumination. This mass excitation can impose non-physiological synchronous input on the postsynaptic neuron (Yizhar et al., 2011a). To mitigate the effects of simultaneous stimulation of presynaptic terminals, stable step-function opsins (SSFOs) can be used to generate a network-level depolarization or "up-state" (Berndt et al., 2009). Derived from the original ChR2, SSFOs exhibit temporally-extended decay kinetics (>20–30 min) and can be activated using a single pulse of blue light. This allows a single brief pulse (∼5 ms) of blue light to depolarize neurons for extended periods of time and promote a network-level state of increased excitation. The decay kinetic of SSFOs can be enhanced through illumination with a brief pulse of red or orange light, effectively returning the neuron to its normal rest potential. Using these opsins with long decay kinetics offers a number of advantages for modulating network-level excitation, including promoting the generation of asynchronous APs for more physiological-like stimulation.

Conversely, neuronal silencing using inhibitory opsins has been used to reduce firing in a defined population of neurons. Effective optogenetic silencing is possible using the chloride pump red-light sensitive halorhodopsin derived from *Natronomas pharaonis* (NpHR; Zhang and Oertner, 2007). However, NpHR and its variants can alter some synaptic and cellular properties. Extended use of NpHR will shift the Cl^- homeostasis and reversal potential, as the neuron is unable to clear the anionic charge through Cl^- transporters. Consequently, at the offset of a light stimulus, neurons expressing NpHR will show a period of rebound excitation, releasing previously-silenced transmitter onto the postsynaptic neuron (Raimondo et al., 2012). In contrast, no rebound excitation was observed following inhibition with an alternate optogenetic inhibitor, archaerhodopsin from *Halorubrum sodomense* strain TP009, termed ArchT (Chow et al., 2010; Han et al., 2011). ArchT is a light-activated transporter that extrudes protons from the cytoplasm of neurons, which elevates pH when activated over long time-courses. Vesicular mobilization at presynaptic terminals is sensitive to changes in pH, suggesting that manipulating pH can alter vesicular dynamics and release of neurotransmitter.

In summary, these new neuroscientific tools to investigate synaptic transmission in the developing and mature nervous system will undoubtedly play critical roles in further understanding network connectivity and synaptic transmission; however, it is critical to understand the utility and limitations of any new tool. A carefully-planned combination of these optical tools alongside electrophysiological validation and calibration is best to ascertain how genetically-defined groups of neurons interact at the synaptic level.

DISCUSSION

Multiple electrophysiological techniques can be used to interrogate synaptic function in the developing and mature brain, and the emergence of new optical tools for both manipulation and measurement has allowed for unparalleled resolution of cellular processes underlying synaptic transmission. It is clear that understanding the contribution of pre- and postsynaptic mechanisms to synaptic plasticity must involve a number of diverse approaches to decipher how the brain changes individual synapses. Traditional interpretations of miniature EPSCs and paired-pulse protocols suggest that changes in these measures can reveal changes at presynaptic terminals. While alteration in AMPAR-to-NMDAR ratio and photo-uncaging have been understood to reflect postsynaptic changes, multiple studies in recent years have provided evidence that it is naïve to conclude that a phenomenon identified using a limited number of traditional approaches is purely pre- or postsynaptic.

Implementation of multiple electrophysiological methods, coupled with imaging techniques, is enormously beneficial for dissecting pre- and post-synaptic contributions to synaptic transmission and plasticity. As an illustrative example, we have recently demonstrated that the chemotropic guidance cue, netrin-1, is released from dendrites following NMDAR activation, and contributes to synaptic plasticity in the adult hippocampus (Glasgow et al., 2018). Netrin-1 increases mEPSC frequency with no accompanying change in mEPSC amplitude, which would traditionally be interpreted as an alteration in presynaptic function. However, we did not observe changes in PPR. In contrast, netrin-1 induced a significant increase in the AMPAR-to-NMDAR ratio, indicating a postsynaptic locus of action. Together, these findings suggested that netrin-1, which

was been previously shown to direct cell and axon migration by regulating cytoskeletal reorganization in the developing nervous system, may promote the maturation of nascent synapses in the adult hippocampus, accounting for the increase in mEPSC frequency and the altered AMPAR-to-NMDAR ratio. Testing this idea, and consistent with a postsynaptic locus of action, failure rates using a minimal stimulation protocol were significantly decreased following the application of netrin-1, again supporting the conclusion that netrin-1 promotes the maturation and recruitment of nascent synapses. Through the combination of multiple different electrophysiological assays, the cellular and molecular mechanisms underlying netrin-1 mediated potentiation of synaptic transmission illustrate how the addition of new active synaptic connections can resemble alteration of presynaptic function, ultimately resulting in a facilitation of excitatory neurotransmission.

Recent technological developments have provided neuroscientists with an unprecedented tool-set to investigate synaptic transmission. The use of optical tools, in conjunction with classic electrophysiological methods, has provided new insights to traditional interpretation of synaptic function. By combining multiple approaches as described in this review article, convergent lines of evidence can be used to attribute changes in synaptic transmission to the pre- or postsynaptic compartment.

Conclusions

Recent data confirms that synaptic transmission is an exceedingly complex phenomenon, subject to modifications in signaling at both pre- and post-synaptic sites. The development and refinement of whole-cell patch clamp electrophysiological techniques have greatly improved our understanding of how changes in the relative strength of synapses can contribute to various important functions mediated by the nervous system. Genetically encoded optical reporters and actuators have added powerful cell-type specificity to this analysis. However, interpretation of electrophysiological data requires careful attention to a number of parameters, including voltage-dependence, ionic flux, and experimental conditions. When possible, multiple experimental techniques should be employed to evaluate all possible loci of action. Together, convergent lines of evidence can reveal novel effector sites, and lead to re-evaluation of traditional interpretations and conclusions.

AUTHOR CONTRIBUTIONS

All authors contributed to the writing of this review article. The initial draft was written by SG, RM and JM in consultation with ER and TK. It was edited for accuracy and clarity by TK and ER. The summary figure was created by JM with feedback from the other authors.

FUNDING

SG was supported by postdoctoral fellowships from Fonds de la Recherche Québec—Santé (FRQS) and the Canadian Institutes of Health Research (CIHR). RM was supported by graduate scholarships from Natural Sciences and Engineering Research Council of Canada (NSERC) and the "Healthy Brains for Healthy Lives" Canada First Research Excellence Fund (CFREF). This review article was supported by grants from CIHR to TK and ER. ER also holds a FRQS Research Chair (FRQS-31036).

REFERENCES

Abraham, W. C., Logan, B., Greenwood, J. M., and Dragunow, M. (2002). Induction and experience-dependent consolidation of stable long-term potentiation lasting months in the hippocampus. *J. Neurosci.* 22, 9626–9634. doi: 10.1523/jneurosci.22-21-09626.2002

Abrahamsson, T., Chou, C. Y. C., Li, S. Y., Mancino, A., Costa, R. P., Brock, J. A., et al. (2017). Differential regulation of evoked and spontaneous release by presynaptic NMDA receptors. *Neuron* 96, 839–855.e5. doi: 10.1016/j.neuron.2017.09.030

Aizenman, C. D., Akerman, C. J., Jensen, K. R., and Cline, H. T. (2003). Visually driven regulation of intrinsic neuronal excitability improves stimulus detection *in vivo*. *Neuron* 39, 831–842. doi: 10.1016/s0896-6273(03)00527-0

Alle, H., and Geiger, J. R. (2006). Combined analog and action potential coding in hippocampal mossy fibers. *Science* 311, 1290–1293. doi: 10.1126/science.1119055

Anggono, V., and Huganir, R. L. (2012). Regulation of AMPA receptor trafficking and synaptic plasticity. *Curr. Opin. Neurobiol.* 22, 461–469. doi: 10.1016/j.conb.2011.12.006

Antoine, M. W., Langberg, T., Schnepel, P., and Feldman, D. E. (2019). Increased excitation-inhibition ratio stabilizes synapse and circuit excitability in four autism mouse models. *Neuron* 101, 648–661.e4. doi: 10.1016/j.neuron.2018.12.026

Araki, Y., Zeng, M., Zhang, M., and Huganir, R. L. (2015). Rapid dispersion of SynGAP from synaptic spines triggers AMPA receptor insertion and spine enlargement during LTP. *Neuron* 85, 173–189. doi: 10.1016/j.neuron.2014.12.023

Araya, R., Jiang, J., Eisenthal, K. B., and Yuste, R. (2006). The spine neck filters membrane potentials. *Proc. Natl. Acad. Sci. U S A* 103, 17961–17966. doi: 10.1073/pnas.0608755103

Araya, R., Vogels, T. P., and Yuste, R. (2014). Activity-dependent dendritic spine neck changes are correlated with synaptic strength. *Proc. Natl. Acad. Sci. U S A* 111, E2895–E2904. doi: 10.1073/pnas.1321869111

Arikkath, J., and Reichardt, L. F. (2008). Cadherins and catenins at synapses: roles in synaptogenesis and synaptic plasticity. *Trends Neurosci.* 31, 487–494. doi: 10.1016/j.tins.2008.07.001

Atasoy, D., Ertunc, M., Moulder, K. L., Blackwell, J., Chung, C., Su, J., et al. (2008). Spontaneous and evoked glutamate release activates two populations of NMDA receptors with limited overlap. *J. Neurosci.* 28, 10151–10166. doi: 10.1523/jneurosci.2432-08.2008

Beaulieu-Laroche, L., and Harnett, M. T. (2018). Dendritic spines prevent synaptic voltage clamp. *Neuron* 97, 75.e3–82.e3. doi: 10.1016/j.neuron.2017.11.016

Benke, T. A., Lüthi, A., Isaac, J. T., and Collingridge, G. L. (1998). Modulation of AMPA receptor unitary conductance by synaptic activity. *Nature* 393, 793–797. doi: 10.1038/31709

Benson, D. L., Schnapp, L. M., Shapiro, L., and Huntley, G. W. (2000). Making memories stick: cell-adhesion molecules in synaptic plasticity. *Trends Cell Biol.* 10, 473–482. doi: 10.1016/s0962-8924(00)01838-9

Bergles, D. E., and Jahr, C. E. (1997). Synaptic activation of glutamate transporters in hippocampal astrocytes. *Neuron* 19, 1297–1308. doi: 10.1016/s0896-6273(00)80420-1

Berndt, A., Yizhar, O., Gunaydin, L. A., Hegemann, P., and Deisseroth, K. (2009). Bi-stable neural state switches. *Nat. Neurosci.* 12, 229–234. doi: 10.1038/nn.2247

Bickler, P. E., and Buck, L. T. (2007). Hypoxia tolerance in reptiles, amphibians, and fishes: life with variable oxygen availability. *Annu. Rev. Physiol.* 69, 145–170. doi: 10.1146/annurev.physiol.69.031905.162529

Bliss, T. V., and Gardner-Medwin, A. R. (1973). Long-lasting potentiation of synaptic transmission in the dentate area of the unanaestetized rabbit following stimulation of the perforant path. *J. Physiol.* 232, 357–374. doi: 10.1113/jphysiol.1973.sp010274

Bolshakov, V. Y., and Siegelbaum, S. A. (1995). Regulation of hippocampal transmitter release during development and long-term potentiation. *Science* 269, 1730–1734. doi: 10.1126/science.7569903

Boyden, E. S., Zhang, F., Bamberg, E., Nagel, G., and Deisseroth, K. (2005). Millisecond-timescale, genetically targeted optical control of neural activity. *Nat. Neurosci.* 8, 1263–1268. doi: 10.1038/nn1525

Burnashev, N., Monyer, H., Seeburg, P. H., and Sakmann, B. (1992). Divalent ion permeability of AMPA receptor channels is dominated by the edited form of a single subunit. *Neuron* 8, 189–198. doi: 10.1016/0896-6273(92)90120-3

Cartailler, J., Kwon, T., Yuste, R., and Holcman, D. (2018). Deconvolution of voltage sensor time series and electro-diffusion modeling reveal the role of spine geometry in controlling synaptic strength. *Neuron* 97, 1126.e10–1136.e10. doi: 10.1016/j.neuron.2018.01.034

Catterall, W. A. (2011). Voltage-gated calcium channels. *Cold Spring Harb. Perspect. Biol.* 3:a003947. doi: 10.1101/cshperspect.a003947

Chih, B., Engelman, H., and Scheiffele, P. (2005). Control of excitatory and inhibitory synapse formation by neuroligins. *Science* 307, 1324–1328. doi: 10.1126/science.1107470

Choquet, D. (2018). Linking nanoscale dynamics of AMPA receptor organization to plasticity of excitatory synapses and learning. *J. Neurosci.* 38, 9318–9329. doi: 10.1523/jneurosci.2119-18.2018

Choquet, D., and Triller, A. (2013). The dynamic synapse. *Neuron* 80, 691–703. doi: 10.1016/j.neuron.2013.10.013

Chow, B. Y., Han, X., Dobry, A. S., Qian, X., Chuong, A. S., Li, M., et al. (2010). High-performance genetically targetable optical neural silencing by light-driven proton pumps. *Nature* 463, 98–102. doi: 10.1038/nature08652

Clark, K. A., Randall, A. D., and Collingridge, G. L. (1994). A comparison of paired-pulsed facilitation of AMPA and NMDA receptor-mediated excitatory postsynaptic currents in the hippocampus. *Exp. Brain Res.* 101, 272–278. doi: 10.1007/bf00228747

Clements, J. D., Lester, R. A., Tong, G., Jahr, C. E., and Westbrook, G. L. (1992). The time course of glutamate in the synaptic cleft. *Science* 258, 1498–1501. doi: 10.1126/science.1359647

Compans, B., Choquet, D., and Hosy, E. (2016). Review on the role of AMPA receptor nano-organization and dynamic in the properties of synaptic transmission. *Neurophotonics* 3:041811. doi: 10.1117/1.nph.3.4.041811

Constals, A., Penn, A. C., Compans, B., Toulme, E., Phillipat, A., Marais, S., et al. (2015). Glutamate-induced AMPA receptor desensitization increases their mobility and modulates short-term plasticity through unbinding from Stargazin. *Neuron* 85, 787–803. doi: 10.1016/j.neuron.2015.01.012

Contractor, A., Mulle, C., and Swanson, G. T. (2011). Kainate receptors coming of age: milestones of two decades of research. *Trends Neurosci.* 34, 154–163. doi: 10.1016/j.tins.2010.12.002

Dana, H., Sun, Y., Mohar, B., Hulse, B., Hasseman, J. P., Tsegaye, G., et al. (2018). High-performance GFP-based calcium indicators for imaging activity in neuronal populations and microcompartments. *bioRxiv* [Preprint]. doi: 10.1101/434589

de Wit, J., and Ghosh, A. (2016). Specification of synaptic connectivity by cell surface interactions. *Nat. Rev. Neurosci.* 17, 22–35. doi: 10.1038/nrn.2015.3

Debanne, D. (2004). Information processing in the axon. *Nat. Rev. Neurosci.* 5, 304–316. doi: 10.1038/nrn1397

Debanne, D., Boudkkazi, S., Campanac, E., Cudmore, R. H., Giraud, P., Fronzaroli-Molinieres, L., et al. (2008). Paired-recordings from synaptically coupled cortical and hippocampal neurons in acute and cultured brain slices. *Nat. Protoc.* 3, 1559–1568. doi: 10.1038/nprot.2008.147

Debanne, D., Gähwiler, B. H., and Thompson, S. M. (1999). Heterogeneity of synaptic plasticity at unitary CA3-CA1 and CA3-CA3 connections in rat hippocampal slice cultures. *J. Neurosci.* 19, 10664–10671. doi: 10.1523/jneurosci.19-24-10664.1999

Del Castillo, J., and Katz, B. (1954). Quantal components of the end-plate potential. *J. Physiol.* 124, 560–573. doi: 10.1113/jphysiol.1954.sp005129

Deuchars, J., West, D. C., and Thomson, A. M. (1994). Relationships between morphology and physiology of pyramid-pyramid single axon connections in rat neocortex *in vitro*. *J. Physiol.* 478, 423–435. doi: 10.1113/jphysiol.1994.sp020262

Diering, G. H., and Huganir, R. L. (2018). The AMPA receptor code of synaptic plasticity. *Neuron* 100, 314–329. doi: 10.1016/j.neuron.2018.10.018

Dingledine, R., Borges, K., Bowie, D., and Traynelis, S. F. (1999). The glutamate receptor ion channels. *Pharmacol. Rev.* 51, 7–61.

Eggermann, E., Bucurenciu, I., Goswami, S. P., and Jonas, P. (2012). Nanodomain coupling between Ca^{2+} channels and sensors of exocytosis at fast mammalian synapses. *Nat. Rev. Neurosci.* 13, 7–21. doi: 10.1038/nrn3125

Ellis-Davies, G. C. R. (2019). Two-photon uncaging of glutamate. *Front. Synaptic Neurosci.* 10:48. doi: 10.3389/fnsyn.2018.00048

Fatt, P., and Katz, B. (1950). Some observations on biological noise. *Nature* 166, 597–598. doi: 10.1038/166597a0

Feldmeyer, D., Roth, A., and Sakmann, B. (2005). Monosynaptic connections between pairs of spiny stellate cells in layer 4 and pyramidal cells in layer 5A indicate that lemniscal and paralemniscal afferent pathways converge in the infragranular somatosensory cortex. *J. Neurosci.* 25, 3423–3431. doi: 10.1523/jneurosci.5227-04.2005

Fenno, L., Yizhar, O., and Deisseroth, K. (2011). The development and application of optogenetics. *Annu. Rev. Neurosci.* 34, 389–412. doi: 10.1146/annurev-neuro-061010-113817

Fredj, N. B., and Burrone, J. (2009). A resting pool of vesicles is responsible for spontaneous vesicle fusion at the synapse. *Nat. Neurosci.* 12, 751–758. doi: 10.1038/nn.2317

Friedman, J. I., Vrijenhoek, T., Markx, S., Janssen, I. M., Van Der Vliet, W. A., Faas, B. H., et al. (2008). CNTNAP2 gene dosage variation is associated with schizophrenia and epilepsy. *Mol. Psychiatry* 13, 261–266. doi: 10.1038/sj.mp.4002049

Gaffield, M. A., and Betz, W. J. (2006). Imaging synaptic vesicle exocytosis and endocytosis with FM dyes. *Nat. Protoc.* 1, 2916–2921. doi: 10.1038/nprot.2006.476

Gähwiler, B. H. (1981). Organotypic monolayer cultures of nervous tissue. *J. Neurosci. Methods* 4, 329–342. doi: 10.1016/0165-0270(81)90003-0

Gähwiler, B. H., Capogna, M., Debanne, D., Mckinney, R. A., and Thompson, S. M. (1997). Organotypic slice cultures: a technique has come of age. *Trends Neurosci.* 20, 471–477. doi: 10.1016/s0166-2236(97)01122-3

Gal, E., Perin, R., Markram, H., London, M., and Segev, I. (2019). Neuron geometry underlies a universal local architecture in neuronal networks. *bioRxiv* [Preprint]. doi: 10.1101/656058

Garaschuk, O., Milos, R. I., and Konnerth, A. (2006). Targeted bulk-loading of fluorescent indicators for two-photon brain imaging *in vivo*. *Nat. Protoc.* 1, 380–386. doi: 10.1038/nprot.2006.58

Gerschenfeld, H. M. (1973). Chemical transmission in invertebrate central nervous systems and neuromuscular junctions. *Physiol. Rev.* 53, 1–119. doi: 10.1152/physrev.1973.53.1.1

Gibbins, I. L., and Morris, J. L. (2006). Structure of peripheral synapses: autonomic ganglia. *Cell Tissue Res.* 326, 205–220. doi: 10.1007/s00441-006-0233-1

Glasgow, S. D., Herrera, C. G., and Adamantidis, A. R. (2017). "Behavioral phenotyping using optogenetic technology," in *Handbook of Neurobehavioral Genetics and Phenotyping*, ed. V. Tucci (Hoboken, NJ: Wiley), 469–488A.

Glasgow, S. D., Labrecque, S., Beamish, I. V., Aufmkolk, S., Gibon, J., Han, D., et al. (2018). Activity-dependent netrin-1 secretion drives synaptic insertion of GluA1-containing AMPA receptors in the hippocampus. *Cell Rep.* 25, 168.e6–182.e6. doi: 10.1016/j.celrep.2018.09.028

Goda, Y., and Stevens, C. F. (1994). Two components of transmitter release at a central synapse. *Proc. Natl. Acad. Sci. U S A* 91, 12942–12946. doi: 10.1073/pnas.91.26.12942

Goldman, J. S., Ashour, M. A., Magdesian, M. H., Tritsch, N. X., Harris, S. N., Christofi, N., et al. (2013). Netrin-1 promotes excitatory synaptogenesis between cortical neurons by initiating synapse assembly. *J. Neurosci.* 33, 17278–17289. doi: 10.1523/jneurosci.1085-13.2013

Grand, L., Ftomov, S., and Timofeev, I. (2013). Long-term synchronized electrophysiological and behavioral wireless monitoring of freely moving animals. *J. Neurosci. Methods* 212, 237–241. doi: 10.1016/j.jneumeth.2012.10.008

Grynkiewicz, G., Poenie, M., and Tsien, R. Y. (1985). A new generation of Ca^{2+} indicators with greatly improved fluorescence properties. *J. Biol. Chem.* 260, 3440–3450.

Haas, K. T., Compans, B., Letellier, M., Bartol, T. M., Grillo-Bosch, D., Sejnowski, T. J., et al. (2018). Pre-post synaptic alignment through neuroligin-1 tunes synaptic transmission efficiency. *Elife* 7:e31755. doi: 10.7554/elife.31755

Han, X., Chow, B. Y., Zhou, H., Klapoetke, N. C., Chuong, A., Rajimehr, R., et al. (2011). A high-light sensitivity optical neural silencer: development and application to optogenetic control of non-human primate cortex. *Front. Syst. Neurosci.* 5:18. doi: 10.3389/fnsys.2011.00018

Heine, M., Groc, L., Frischknecht, R., Beique, J. C., Lounis, B., Rumbaugh, G., et al. (2008). Surface mobility of postsynaptic AMPARs tunes synaptic transmission. *Science* 320, 201–205. doi: 10.1126/science.1152089

Huettner, J. E. (2003). Kainate receptors and synaptic transmission. *Prog. Neurobiol.* 70, 387–407. doi: 10.1016/s0301-0082(03)00122-9

Hughes, G. M., and Tauc, L. (1968). A direct synaptic connexion between left and right giant cells in aplysia. *J. Physiol.* 197, 511–527. doi: 10.1113/jphysiol.1968.sp008572

Inoue, M., Takeuchi, A., Manita, S., Horigane, S. I., Sakamoto, M., Kawakami, R., et al. (2019). Rational engineering of XCaMPs, a multicolor GECI suite for *in vivo* imaging of complex brain circuit dynamics. *Cell* 177, 1346.e24–1360.e24. doi: 10.1016/j.cell.2019.04.007

Isaac, J. T., Nicoll, R. A., and Malenka, R. C. (1995). Evidence for silent synapses: implications for the expression of LTP. *Neuron* 15, 427–434. doi: 10.1016/0896-6273(95)90046-2

Jang, S., Lee, H., and Kim, E. (2017). Synaptic adhesion molecules and excitatory synaptic transmission. *Curr. Opin. Neurobiol.* 45, 45–50. doi: 10.1016/j.conb.2017.03.005

Jayant, K., Wenzel, M., Bando, Y., Hamm, J. P., Mandriota, N., Rabinowitz, J. H., et al. (2019). Flexible nanopipettes for minimally invasive intracellular electrophysiology *in vivo*. *Cell Rep.* 26, 266.e5–278.e5. doi: 10.1016/j.celrep.2018.12.019

Judkewitz, B., Roth, A., and Häusser, M. (2006). Dendritic enlightenment: using patterned two-photon uncaging to reveal the secrets of the brain's smallest dendrites. *Neuron* 50, 180–183. doi: 10.1016/j.neuron.2006.04.011

Kaeser, P. S., and Regehr, W. G. (2014). Molecular mechanisms for synchronous, asynchronous, and spontaneous neurotransmitter release. *Annu. Rev. Physiol.* 76, 333–363. doi: 10.1146/annurev-physiol-021113-170338

Kaplan, J. H., Forbush, B. III., and Hoffman, J. F. (1978). Rapid photolytic release of adenosine 5′-triphosphate from a protected analogue: utilization by the Na:K pump of human red blood cell ghosts. *Biochemistry* 17, 1929–1935. doi: 10.1021/bi00603a020

Katz, B., and Miledi, R. (1967). The timing of calcium action during neuromuscular transmission. *J. Physiol.* 189, 535–544. doi: 10.1113/jphysiol.1967.sp008183

Katz, B., and Miledi, R. (1968). The role of calcium in neuromuscular facilitation. *J. Physiol.* 195, 481–492. doi: 10.1113/jphysiol.1968.sp008469

Kauer, J. A., Malenka, R. C., and Nicoll, R. A. (1988). A persistent postsynaptic modification mediates long-term potentiation in the hippocampus. *Neuron* 1, 911–917. doi: 10.1016/0896-6273(88)90148-1

Kavalali, E. T. (2015). The mechanisms and functions of spontaneous neurotransmitter release. *Nat. Rev. Neurosci.* 16, 5–16. doi: 10.1038/nrn3875

Kawaguchi, S. Y., and Sakaba, T. (2015). Control of inhibitory synaptic outputs by low excitability of axon terminals revealed by direct recording. *Neuron* 85, 1273–1288. doi: 10.1016/j.neuron.2015.02.013

Kehrer, C., Maziashvili, N., Dugladze, T., and Gloveli, T. (2008). Altered excitatory-inhibitory balance in the NMDA-hypofunction model of schizophrenia. *Front. Mol. Neurosci.* 1:6. doi: 10.3389/neuro.02.006.2008

Kerchner, G. A., and Nicoll, R. A. (2008). Silent synapses and the emergence of a postsynaptic mechanism for LTP. *Nat. Rev. Neurosci.* 9, 813–825. doi: 10.1038/nrn2501

Kneussel, M., and Hausrat, T. J. (2016). Postsynaptic neurotransmitter receptor reserve pools for synaptic potentiation. *Trends Neurosci.* 39, 170–182. doi: 10.1016/j.tins.2016.01.002

Kullmann, D. M. (1994). Amplitude fluctuations of dual-component EPSCs in hippocampal pyramidal cells: implications for long-term potentiation. *Neuron* 12, 1111–1120. doi: 10.1016/0896-6273(94)90318-2

Lester, R. A., and Jahr, C. E. (1992). NMDA channel behavior depends on agonist affinity. *J. Neurosci.* 12, 635–643. doi: 10.1523/jneurosci.12-02-00635.1992

Li, C. L., and McIlwain, H. (1957). Maintenance of resting membrane potentials in slices of mammalian cerebral cortex and other tissues *in vitro*. *J. Physiol.* 139, 178–190. doi: 10.1113/jphysiol.1957.sp005885

Liao, D., Hessler, N. A., and Malinow, R. (1995). Activation of postsynaptically silent synapses during pairing-induced LTP in CA1 region of hippocampal slice. *Nature* 375, 400–404. doi: 10.1038/375400a0

Lin, M. Z., and Schnitzer, M. J. (2016). Genetically encoded indicators of neuronal activity. *Nat. Neurosci.* 19, 1142–1153. doi: 10.1038/nn.4359

Lisman, J. (2017). Glutamatergic synapses are structurally and biochemically complex because of multiple plasticity processes: long-term potentiation, long-term depression, short-term potentiation and scaling. *Philos. Trans. R. Soc. Lond. B Biol. Sci.* 372:20160260. doi: 10.1098/rstb.2016.0260

Llinás, R., Sugimori, M., and Silver, R. B. (1992). Microdomains of high calcium concentration in a presynaptic terminal. *Science* 256, 677–679. doi: 10.1126/science.1350109

Lu, W., Man, H., Ju, W., Trimble, W. S., MacDonald, J. F., and Wang, Y. T. (2001). Activation of synaptic NMDA receptors induces membrane insertion of new AMPA receptors and LTP in cultured hippocampal neurons. *Neuron* 29, 243–254. doi: 10.1016/s0896-6273(01)00194-5

Magee, J. C., and Johnston, D. (2005). Plasticity of dendritic function. *Curr. Opin. Neurobiol.* 15, 334–342. doi: 10.1016/j.conb.2005.05.013

Malagon, G., Miki, T., Llano, I., Neher, E., and Marty, A. (2016). Counting vesicular release events reveals binomial release statistics at single glutamatergic synapses. *J. Neurosci.* 36, 4010–4025. doi: 10.1523/jneurosci.4352-15.2016

Malinow, R., and Tsien, R. W. (1990). Presynaptic enhancement shown by whole-cell recordings of long-term potentiation in hippocampal slices. *Nature* 346, 177–180. doi: 10.1038/346177a0

Mallart, A., and Martin, A. R. (1967). An analysis of facilitation of transmitter release at the neuromuscular junction of the frog. *J. Physiol.* 193, 679–694. doi: 10.1113/jphysiol.1967.sp008388

Markram, H., Lübke, J., Frotscher, M., and Sakmann, B. (1997). Regulation of synaptic efficacy by coincidence of postsynaptic APs and EPSPs. *Science* 275, 213–215. doi: 10.1126/science.275.5297.213

Marvin, J. S., Borghuis, B. G., Tian, L., Cichon, J., Harnett, M. T., Akerboom, J., et al. (2013). An optimized fluorescent probe for visualizing glutamate neurotransmission. *Nat. Methods* 10, 162–170. doi: 10.1038/nmeth.2333

Maschi, D., and Klyachko, V. A. (2017). Spatiotemporal regulation of synaptic vesicle fusion sites in central synapses. *Neuron* 94, 65.e3–73.e3. doi: 10.1016/j.neuron.2017.03.006

Matsuzaki, M., Ellis-Davies, G. C., Nemoto, T., Miyashita, Y., Iino, M., and Kasai, H. (2001). Dendritic spine geometry is critical for AMPA receptor expression in hippocampal CA1 pyramidal neurons. *Nat. Neurosci.* 4, 1086–1092. doi: 10.1038/nn736

McKinney, R. A., Capogna, M., Durr, R., Gahwiler, B. H., and Thompson, S. M. (1999). Miniature synaptic events maintain dendritic spines *via* AMPA receptor activation. *Nat. Neurosci.* 2, 44–49. doi: 10.1038/4548

Megías, M., Emri, Z., Freund, T. F., and Gulyás, A. I. (2001). Total number and distribution of inhibitory and excitatory synapses on hippocampal CA1 pyramidal cells. *Neuroscience* 102, 527–540. doi: 10.1016/s0306-4522(00)00496-6

Melom, J. E., Akbergenova, Y., Gavornik, J. P., and Littleton, J. T. (2013). Spontaneous and evoked release are independently regulated at individual active zones. *J. Neurosci.* 33, 17253–17263. doi: 10.1523/JNEUROSCI.3334-13.2013

Miles, R., and Poncer, J. C. (1996). Paired recordings from neurones. *Curr. Opin. Neurobiol.* 6, 387–394. doi: 10.1016/s0959-4388(96)80124-3

Mills, F., Globa, A. K., Liu, S., Cowan, C. M., Mobasser, M., Phillips, A. G., et al. (2017). Cadherins mediate cocaine-induced synaptic plasticity and behavioral conditioning. *Nat. Neurosci.* 20, 540–549. doi: 10.1038/nn.4503

Miyashita, T., Shao, Y. R., Chung, J., Pourzia, O., and Feldman, D. E. (2013). Long-term channelrhodopsin-2 (ChR2) expression can induce abnormal axonal morphology and targeting in cerebral cortex. *Front. Neural Circuits* 7:8. doi: 10.3389/fncir.2013.00008

Montgomery, J. M., Pavlidis, P., and Madison, D. V. (2001). Pair recordings reveal all-silent synaptic connections and the postsynaptic expression of long-term potentiation. *Neuron* 29, 691–701. doi: 10.1016/s0896-6273(01)00244-6

Murase, S., Mosser, E., and Schuman, E. M. (2002). Depolarization drives β-Catenin into neuronal spines promoting changes in synaptic structure and function. *Neuron* 35, 91–105. doi: 10.1016/s0896-6273(02)00764-x

Nair, D., Hosy, E., Petersen, J. D., Constals, A., Giannone, G., Choquet, D., et al. (2013). Super-resolution imaging reveals that AMPA receptors inside synapses are dynamically organized in nanodomains regulated by PSD95. *J. Neurosci.* 33, 13204–13224. doi: 10.1523/JNEUROSCI.2381-12.2013

Nakai, J., Ohkura, M., and Imoto, K. (2001). A high signal-to-noise Ca^{2+} probe composed of a single green fluorescent protein. *Nat. Biotechnol.* 19, 137–141. doi: 10.1038/84397

Nakamura, Y., Harada, H., Kamasawa, N., Matsui, K., Rothman, J. S., Shigemoto, R., et al. (2015). Nanoscale distribution of presynaptic Ca^{2+} channels and its impact on vesicular release during development. *Neuron* 85, 145–158. doi: 10.1016/j.neuron.2014.11.019

Nelson, S. B., and Valakh, V. (2015). Excitatory/inhibitory balance and circuit homeostasis in autism spectrum disorders. *Neuron* 87, 684–698. doi: 10.1016/j.neuron.2015.07.033

Nguyen, P. V., Abel, T., and Kandel, E. R. (1994). Requirement of a critical period of transcription for induction of a late phase of LTP. *Science* 265, 1104–1107. doi: 10.1126/science.8066450

Novak, P., Gorelik, J., Vivekananda, U., Shevchuk, A. I., Ermolyuk, Y. S., Bailey, R. J., et al. (2013). Nanoscale-targeted patch-clamp recordings of functional presynaptic ion channels. *Neuron* 79, 1067–1077. doi: 10.1016/j.neuron.2013.07.012

Okamura, K., Tanaka, H., Yagita, Y., Saeki, Y., Taguchi, A., Hiraoka, Y., et al. (2004). Cadherin activity is required for activity-induced spine remodeling. *J. Cell Biol.* 167, 961–972. doi: 10.1083/jcb.200406030

Oliet, S. H., Piet, R., and Poulain, D. A. (2001). Control of glutamate clearance and synaptic efficacy by glial coverage of neurons. *Science* 292, 923–926. doi: 10.1126/science.1059162

Oltedal, L., Mørkve, S. H., Veruki, M. L., and Hartveit, E. (2007). Patch-clamp investigations and compartmental modeling of rod bipolar axon terminals in an *in vitro* thin-slice preparation of the mammalian retina. *J. Neurophysiol.* 97, 1171–1187. doi: 10.1152/jn.01010.2006

Otsu, Y., Shahrezaei, V., Li, B., Raymond, L. A., Delaney, K. R., and Murphy, T. H. (2004). Competition between phasic and asynchronous release for recovered synaptic vesicles at developing hippocampal autaptic synapses. *J. Neurosci.* 24, 420–433. doi: 10.1523/jneurosci.4452-03.2004

Papouin, T., Ladépêche, L., Ruel, J., Sacchi, S., Labasque, M., Hanini, M., et al. (2012). Synaptic and extrasynaptic NMDA receptors are gated by different endogenous coagonists. *Cell* 150, 633–646. doi: 10.1016/j.cell.2012.06.029

Park, Y. K., and Goda, Y. (2016). Integrins in synapse regulation. *Nat. Rev. Neurosci.* 17, 745–756. doi: 10.1038/nrn.2016.138

Patneau, D. K., and Mayer, M. L. (1990). Structure-activity relationships for amino acid transmitter candidates acting at N-methyl-D-aspartate and quisqualate receptors. *J. Neurosci.* 10, 2385–2399. doi: 10.1523/jneurosci.10-07-02385.1990

Peled, E. S., Newman, Z. L., and Isacoff, E. Y. (2014). Evoked and spontaneous transmission favored by distinct sets of synapses. *Curr. Biol.* 24, 484–493. doi: 10.1016/j.cub.2014.01.022

Petreanu, L., Huber, D., Sobczyk, A., and Svoboda, K. (2007). Channelrhodopsin-2-assisted circuit mapping of long-range callosal projections. *Nat. Neurosci.* 10, 663–668. doi: 10.1038/nn1891

Raimondo, J. V., Kay, L., Ellender, T. J., and Akerman, C. J. (2012). Optogenetic silencing strategies differ in their effects on inhibitory synaptic transmission. *Nat. Neurosci.* 15, 1102–1104. doi: 10.1038/nn.3143

Rao, A., and Craig, A. M. (1997). Activity regulates the synaptic localization of the NMDA receptor in hippocampal neurons. *Neuron* 19, 801–812. doi: 10.1016/s0896-6273(00)80962-9

Reiner, A., Levitz, J., and Isacoff, E. Y. (2015). Controlling ionotropic and metabotropic glutamate receptors with light: principles and potential. *Curr. Opin. Pharmacol.* 20, 135–143. doi: 10.1016/j.coph.2014.12.008

Richards, D. A., Mateos, J. M., Hugel, S., De Paola, V., Caroni, P., Gahwiler, B. H., et al. (2005). Glutamate induces the rapid formation of spine head protrusions in hippocampal slice cultures. *Proc. Natl. Acad. Sci. U S A* 102, 6166–6171. doi: 10.1073/pnas.0501881102

Rosenmund, C., Clements, J. D., and Westbrook, G. L. (1993). Nonuniform probability of glutamate release at a hippocampal synapse. *Science* 262, 754–757. doi: 10.1126/science.7901909

Rozov, A., and Burnashev, N. (1999). Polyamine-dependent facilitation of postsynaptic AMPA receptors counteracts paired-pulse depression. *Nature* 401, 594–598. doi: 10.1038/44151

Sametsky, E. A., Disterhoft, J. F., Geinisman, Y., and Nicholson, D. A. (2010). Synaptic strength and postsynaptically silent synapses through advanced aging in rat hippocampal CA1 pyramidal neurons. *Neurobiol. Aging* 31, 813–825. doi: 10.1016/j.neurobiolaging.2008.05.029

Sara, Y., Bal, M., Adachi, M., Monteggia, L. M., and Kavalali, E. T. (2011). Use-dependent AMPA receptor block reveals segregation of spontaneous and evoked glutamatergic neurotransmission. *J. Neurosci.* 31, 5378–5382. doi: 10.1523/jneurosci.5234-10.2011

Sara, Y., Virmani, T., Deák, F., Liu, X., and Kavalali, E. T. (2005). An isolated pool of vesicles recycles at rest and drives spontaneous neurotransmission. *Neuron* 45, 563–573. doi: 10.1016/j.neuron.2004.12.056

Sasaki, T., Matsuki, N., and Ikegaya, Y. (2012). Targeted axon-attached recording with fluorescent patch-clamp pipettes in brain slices. *Nat. Protoc.* 7, 1228–1234. doi: 10.1038/nprot.2012.061

Savtchenko, L. P., and Rusakov, D. A. (2007). The optimal height of the synaptic cleft. *Proc. Natl. Acad. Sci. U S A* 104, 1823–1828. doi: 10.1073/pnas.0606636104

Schmidt-Hieber, C., and Häusser, M. (2013). Cellular mechanisms of spatial navigation in the medial entorhinal cortex. *Nat. Neurosci.* 16, 325–331. doi: 10.1038/nn.3340

Schneggenburger, R., and Rosenmund, C. (2015). Molecular mechanisms governing Ca^{2+} regulation of evoked and spontaneous release. *Nat. Neurosci.* 18, 935–941. doi: 10.1038/nn.4044

Schwarz, L. A., Miyamichi, K., Gao, X. J., Beier, K. T., Weissbourd, B., Deloach, K. E., et al. (2015). Viral-genetic tracing of the input-output organization of a central noradrenaline circuit. *Nature* 524, 88–92. doi: 10.1038/nature14600

Segal, M. (2010). Dendritic spines, synaptic plasticity and neuronal survival: activity shapes dendritic spines to enhance neuronal viability. *Eur. J. Neurosci.* 31, 2178–2184. doi: 10.1111/j.1460-9568.2010.07270.x

Sheffler-Collins, S. I., and Dalva, M. B. (2012). EphBs: an integral link between synaptic function and synaptopathies. *Trends Neurosci.* 35, 293–304. doi: 10.1016/j.tins.2012.03.003

Shu, Y., Hasenstaub, A., Duque, A., Yu, Y., and McCormick, D. A. (2006). Modulation of intracortical synaptic potentials by presynaptic somatic membrane potential. *Nature* 441, 761–765. doi: 10.1038/nature04720

Shu, Y., Hasenstaub, A., and McCormick, D. A. (2003). Turning on and off recurrent balanced cortical activity. *Nature* 423, 288–293. doi: 10.1038/nature01616

Soares, C., Lee, K. F. H., and Beique, J. C. (2017). Metaplasticity at CA1 synapses by homeostatic control of presynaptic release dynamics. *Cell Rep.* 21, 1293–1303. doi: 10.1016/j.celrep.2017.10.025

Song, S., Sjostrom, P. J., Reigl, M., Nelson, S., and Chklovskii, D. B. (2005). Highly nonrandom features of synaptic connectivity in local cortical circuits. *PLoS Biol.* 3:e68. doi: 10.1371/journal.pbio.0030068

Spruston, N. (2008). Pyramidal neurons: dendritic structure and synaptic integration. *Nat. Rev. Neurosci.* 9, 206–221. doi: 10.1038/nrn2286

Straub, C., Hunt, D. L., Yamasaki, M., Kim, K. S., Watanabe, M., Castillo, P. E., et al. (2011). Distinct functions of kainate receptors in the brain are determined by the auxiliary subunit Neto1. *Nat. Neurosci.* 14, 866–873. doi: 10.1038/nn.2837

Südhof, T. C. (2012). Calcium control of neurotransmitter release. *Cold Spring Harb. Perspect. Biol.* 4:a011353. doi: 10.1101/cshperspect.a011353

Svoboda, K., Denk, W., Kleinfeld, D., and Tank, D. W. (1997). *In vivo* dendritic calcium dynamics in neocortical pyramidal neurons. *Nature* 385, 161–165. doi: 10.1038/385161a0

Sweeney, S. T., Broadie, K., Keane, J., Niemann, H., and O'Kane, C. J. (1995). Targeted expression of tetanus toxin light chain in Drosophila specifically eliminates synaptic transmission and causes behavioral defects. *Neuron* 14, 341–351. doi: 10.1016/0896-6273(95)90290-2

Takamori, S. (2016). Presynaptic molecular determinants of quantal size. *Front. Synaptic Neurosci.* 8:2. doi: 10.3389/fnsyn.2016.00002

Tian, L., Hires, S. A., Mao, T., Huber, D., Chiappe, M. E., Chalasani, S. H., et al. (2009). Imaging neural activity in worms, flies and mice with improved GCaMP calcium indicators. *Nat. Methods* 6, 875–881. doi: 10.1038/nmeth.1398

Toth, K., Suares, G., Lawrence, J. J., Philips-Tansey, E., and McBain, C. J. (2000). Differential mechanisms of transmission at three types of mossy fiber synapse. *J. Neurosci.* 20, 8279–8289. doi: 10.1523/JNEUROSCI.20-22-08279.2000

Tsien, R. W. (1983). Calcium channels in excitable cell membranes. *Annu. Rev. Physiol.* 45, 341–358. doi: 10.1146/annurev.ph.45.030183.002013

Tsien, J. Z., Chen, D. F., Gerber, D., Tom, C., Mercer, E. H., Anderson, D. J., et al. (1996). Subregion- and cell type-restricted gene knockout in mouse brain. *Cell* 87, 1317–1326. doi: 10.1016/s0092-8674(00)81826-7

Tuchman, R., and Rapin, I. (2002). Epilepsy in autism. *Lancet Neurol.* 1, 352–358. doi: 10.1016/S1474-4422(02)00160-6

Turrigiano, G. G. (2008). The self-tuning neuron: synaptic scaling of excitatory synapses. *Cell* 135, 422–435. doi: 10.1016/j.cell.2008.10.008

Varoqueaux, F., Sigler, A., Rhee, J. S., Brose, N., Enk, C., Reim, K., et al. (2002). Total arrest of spontaneous and evoked synaptic transmission but normal synaptogenesis in the absence of Munc13-mediated vesicle priming. *Proc. Natl. Acad. Sci. U S A* 99, 9037–9042. doi: 10.1073/pnas.122623799

Verhage, M., Maia, A. S., Plomp, J. J., Brussaard, A. B., Heeroma, J. H., Vermeer, H., et al. (2000). Synaptic assembly of the brain in the absence of neurotransmitter secretion. *Science* 287, 864–869. doi: 10.1126/science.287.5454.864

Wade, P. D., Taylor, J., and Siekevitz, P. (1988). Mammalian cerebral cortical tissue responds to low-intensity visible light. *Proc. Natl. Acad. Sci. U S A* 85, 9322–9326. doi: 10.1073/pnas.85.23.9322

Walmsley, B., Edwards, F. R., and Tracey, D. J. (1988). Nonuniform release probabilities underlie quantal synaptic transmission at a mammalian excitatory central synapse. *J. Neurophysiol.* 60, 889–908. doi: 10.1152/jn.1988.60.3.889

Wang, J. H., and Kelly, P. T. (1996). Regulation of synaptic facilitation by postsynaptic Ca2+/CaM pathways in hippocampal CA1 neurons. *J. Neurophysiol.* 76, 276–286. doi: 10.1152/jn.1996.76.1.276

Wang, J. H., and Kelly, P. T. (1997). Attenuation of paired-pulse facilitation associated with synaptic potentiation mediated by postsynaptic mechanisms. *J. Neurophysiol.* 78, 2707–2716. doi: 10.1152/jn.1997.78.5.2707

Watt, A. J., van Rossum, M. C., MacLeod, K. M., Nelson, S. B., and Turrigiano, G. G. (2000). Activity coregulates quantal AMPA and NMDA currents at neocortical synapses. *Neuron* 26, 659–670. doi: 10.1016/s0896-6273(00)81202-7

Wu, G., Malinow, R., and Cline, H. T. (1996). Maturation of a central glutamatergic synapse. *Science* 274, 972–976. doi: 10.1126/science.274.5289.972

Xu-Friedman, M. A., and Regehr, W. G. (2000). Probing fundamental aspects of synaptic transmission with strontium. *J. Neurosci.* 20, 4414–4422. doi: 10.1523/JNEUROSCI.20-12-04414.2000

Yamagata, M., Sanes, J. R., and Weiner, J. A. (2003). Synaptic adhesion molecules. *Curr. Opin. Cell Biol.* 15, 621–632. doi: 10.1016/S0955-0674(03)00107-8

Yamamoto, C., and McIlwain, H. (1966). Potentials evoked *in vitro* in preparations from the mammalian brain. *Nature* 210, 1055–1056. doi: 10.1038/2101055a0

Yim, Y. S., Kwon, Y., Nam, J., Yoon, H. I., Lee, K., Kim, D. G., et al. (2013). Slitrks control excitatory and inhibitory synapse formation with LAR receptor protein tyrosine phosphatases. *Proc. Natl. Acad. Sci. U S A* 110, 4057–4062. doi: 10.1073/pnas.1209881110

Yizhar, O., Fenno, L. E., Davidson, T. J., Mogri, M., and Deisseroth, K. (2011a). Optogenetics in neural systems. *Neuron* 71, 9–34. doi: 10.1016/j.neuron.2011.06.004

Yizhar, O., Fenno, L. E., Prigge, M., Schneider, F., Davidson, T. J., O'Shea, D. J., et al. (2011b). Neocortical excitation/inhibition balance in information processing and social dysfunction. *Nature* 477, 171–178. doi: 10.1038/nature10360

Zemelman, B. V., Nesnas, N., Lee, G. A., and Miesenbock, G. (2003). Photochemical gating of heterologous ion channels: remote control over genetically designated populations of neurons. *Proc. Natl. Acad. Sci. U S A* 100, 1352–1357. doi: 10.1073/pnas.242738899

Zhang, Y. P., and Oertner, T. G. (2007). Optical induction of synaptic plasticity using a light-sensitive channel. *Nat. Methods* 4, 139–141. doi: 10.1038/nmeth988

Zucker, R. S., and Regehr, W. G. (2002). Short-term synaptic plasticity. *Annu. Rev. Physiol.* 64, 355–405. doi: 10.1146/annurev.physiol.64.092501.114547

Conflict of Interest Statement: The authors declare that the research was conducted in the absence of any commercial or financial relationships that could be construed as a potential conflict of interest.

frontiers in Synaptic Neuroscience

METHODS
published: 14 August 2019
doi: 10.3389/fnsyn.2019.00022

Parsing Out the Variability of Transmission at Central Synapses Using Optical Quantal Analysis

Cary Soares[1], *Daniel Trotter*[2], *André Longtin*[1,2], *Jean-Claude Béïque*[1]* and *Richard Naud*[1,2]*

[1] Department of Cellular and Molecular Medicine, uOttawa Brain and Mind Research Institute, Center for Neural Dynamics, University of Ottawa, Ottawa, ON, Canada, [2] Department of Physics, University of Ottawa, Ottawa, ON, Canada

Properties of synaptic release dictates the core of information transfer in neural circuits. Despite decades of technical and theoretical advances, distinguishing bona fide information content from the multiple sources of synaptic variability remains a challenging problem. Here, we employed a combination of computational approaches with cellular electrophysiology, two-photon uncaging of MNI-Glutamate and imaging at single synapses. We describe and calibrate the use of the fluorescent glutamate sensor iGluSnFR and found that its kinetic profile is close to that of AMPA receptors, therefore providing several distinct advantages over slower methods relying on NMDA receptor activation (i.e., chemical or genetically encoded calcium indicators). Using an array of statistical methods, we further developed, and validated on surrogate data, an expectation-maximization algorithm that, by biophysically constraining release variability, extracts the quantal parameters n (maximum number of released vesicles) and p (unitary probability of release) from single-synapse iGluSnFR-mediated transients. Together, we present a generalizable mathematical formalism which, when applied to optical recordings, paves the way to an increasingly precise investigation of information transfer at central synapses.

Keywords: optical physiology, synaptic vesicle release, neural coding, synaptic transmission, computational neuroscience, variational inference

OPEN ACCESS

Edited by:
P. Jesper Sjöström, McGill University, Canada

Reviewed by:
Mark C. W. Van Rossum, University of Nottingham, United Kingdom
Eric Hanse, University of Gothenburg, Sweden

***Correspondence:**
Jean-Claude Béïque
jbeique@uottawa.ca
Richard Naud
rnaud@uottawa.ca

Received: *01 May 2019*
Accepted: *31 July 2019*
Published: *14 August 2019*

Citation:
Soares C, Trotter D, Longtin A, Béïque J-C and Naud R (2019) Parsing Out the Variability of Transmission at Central Synapses Using Optical Quantal Analysis. Front. Synaptic Neurosci. 11:22. doi: 10.3389/fnsyn.2019.00022

1. INTRODUCTION

Our understanding of the factors that contribute to the stochastic and variable process of synaptic transmission has improved steadily over the last few decades (Branco and Staras, 2009; Ribrault et al., 2011; Llera-Montero et al., 2019). It is now generally agreed that, at most glutamatergic synapses, quantal release does not saturate postsynaptic receptors (Liu et al., 1999, 2003; Umemiya et al., 1999; McAllister and Stevens, 2000; Nimchinsky et al., 2004) and that variability in trial-to-trial neurotransmission arises primarily from differences in the profile of glutamate released into the synaptic cleft (Ribrault et al., 2011). Several presynaptic mechanisms have been proposed to account for such amplitude fluctuations – uneven packaging of glutamate into synaptic vesicles, differences in release location within a synaptic terminal, diffusion process in the synaptic cleft and mode of exocytosis (Choi et al., 2003; Franks et al., 2003; Wu et al., 2007; Richards, 2009). As an additional factor, multiquantal release has been observed at many central synapses (Auger et al., 1998; Wadiche and Jahr, 2001; Oertner et al., 2002; Conti and Lisman, 2003; Christie and Jahr, 2006; Higley et al., 2009; Rudolph et al., 2015), where two or more vesicles are released quasi

simultaneously at single synapses in response to the same electrical stimulus. Since each of these sources of variability impact the transmission of information differently, it is therefore important to parse out the relative proportion of different sources of variability at central synapses.

Several experimental methodologies have been developed to monitor transmission at single synapses (Malinow and Tsien, 1990; Dobrunz and Stevens, 1997, 1999; Oertner et al., 2002; Rudolph et al., 2015). Here we describe an optical-based technique and provide a number of validation and calibration experiments for the intensity-based optical glutamate sensor, iGluSnFR (Marvin et al., 2013), for optical quantal analysis at central synapses. We further provide a detailed theoretical and quantitative analysis for estimating fundamental features of quantal glutamate release. Leveraging experimental and statistical techniques, combined with a theoretically sound model, we present a formalism that is well poised to parse out the structure of variability and information content at central synapses.

2. RESULTS

To study quantal features of glutamate release at central synapses, we turned to a genetically encoded intensity-based glutamate sensing florescent reporter (iGluSnFR). The versatility and usefulness of iGluSnFR – a diffuse, plasma membrane-bound optical reporter of glutamate release – has been demonstrated in both microscopic and macroscopic brain compartments (Borghuis et al., 2013; Marvin et al., 2013; Park et al., 2014; Parsons et al., 2016; Xie et al., 2016), although it has relatively seldom been used to study features of glutamate release at single spines (Soares et al., 2017; Jensen et al., 2019). To this end, we introduced iGluSnFR along with the morphological marker mCherry to CA1 neurons in hippocampal organotypic slices using biolistic transfection several days prior the experiments (**Figure 1A**; Soares et al., 2014, 2017). A detailed description of these procedures is available in Soares et al. (2014). This overall approach was favored since it allows for sparse transfection thereby allowing us to resolve optical signals from single spines with high contrast. Transfected neurons were imaged by two-photon microscopy using an excitation wavelength of 950 nm (**Figure 1B**) which we found to allow detection of both the iGluSnFR and mCherry fluorescent signal simultaneously. Dendritic spines in the apical dendritic arbor of transfected CA1 neurons were targeted for optical quantal analysis experiments. These contacts are likely the postsynaptic targets of Schaffer's collateral axons.

2.1. iGluSnFR-Mediated Monitoring of Endogenous Glutamate Release

Pyramidal neurons were identified by their localization in the slice and morphology. Namely imaging targeted to the CA1 region and we sought the clear presence of basal and apical spinous dendritic arborisation. The morphological identification was typically carried out by solely monitoring mCherry fluorescence. However, the baseline iGluSnFR fluorescence was typically fairly high, homogenously distributed across neuronal compartments and spines were readily observable, thereby readily allowing for broad cell-type identification. A typical experiment began by randomly surveying the apical arbor of an iGluSnFR-expressing cell for dendritic spines that exhibit a time-locked fluorescent responses to electrical stimuli delivered via a glass pipette positioned in stratum radiatum. In a few experiments, Alexa 594 was included in the internal solution of the stimulating electrode for direct visualization (**Figure 1B**), however, in the majority of experiments this dye was omitted and the stimulating electrode was maneuvered in the slice under visual guidance solely using differential interference contrast microscopy.

The optical detection of synaptic events that are eminently short-lived, spatially distributed and scarce is inherently challenging and deserves attention. In principle, imaging in frame scanning mode would be ideal to monitor synaptic fluorescent events from large dendritic regions, but it is hindered by limited signal to noise ratio and temporal resolution (**Figure 1C**). We thus carried out line scan experiments wherein multiple neighboring spines were monitored simultaneously (**Figure 1D**). This approach offered the ability to survey multiple spines at once with a scanning frequency (>500 Hz) sufficient to visually identify rapid glutamate transients. To circumvent the relative paucity of synaptic events due to the probabilistic nature of release, paired-pulse electrical stimulation (50-100 ms inter-stimulus interval) were delivered to increase the likelihood of release during this initial probing phase. Lastly, realistic range of stimulus intensities was determined by parallel and historical whole-cell electrophysiological recordings by the same experimenter. Once a responsive spine was identified, a short line scan was redrawn through the spine and its parent dendritic compartment to capture the spatial profile of glutamate release. The electrical stimulation was then gradually reduced to the minimal intensity that still evoked time-locked responsiveness. This last step was taken in order to reduce the potential of signal contamination by glutamate spillover from neighboring synapses. The identified spines routinely stayed responsive to electrical stimulation for long durations (> 1 hour), opening the door to the repetitive low frequency sampling methodology required for building a dataset sufficient for optical quantal analysis.

2.2. Extraction of Regions of Interest

Spatial discrimination of iGluSnFR signals emanating from either spine or dendritic compartments was achieved by analyzing the intensity profile across the line scan, which was drawn orthogonal to the parent dendrite. The trough between spine and dendrite peaks was used to split the signal of the line scan into the two compartments (**Figure 1E**) to isolate spine- and dendrite-specific iGluSnFR transients (**Figure 1D**, right). Larger amplitude iGluSnFR transients were generally observed in the spine compartment, indicating that the density of glutamate release was mostly concentrated at the spine. When present, the dendritic fluorescence transients were of smaller amplitudes and co-varied with that recorded from the spine compartment, suggesting that dendritic signals were likely the result of

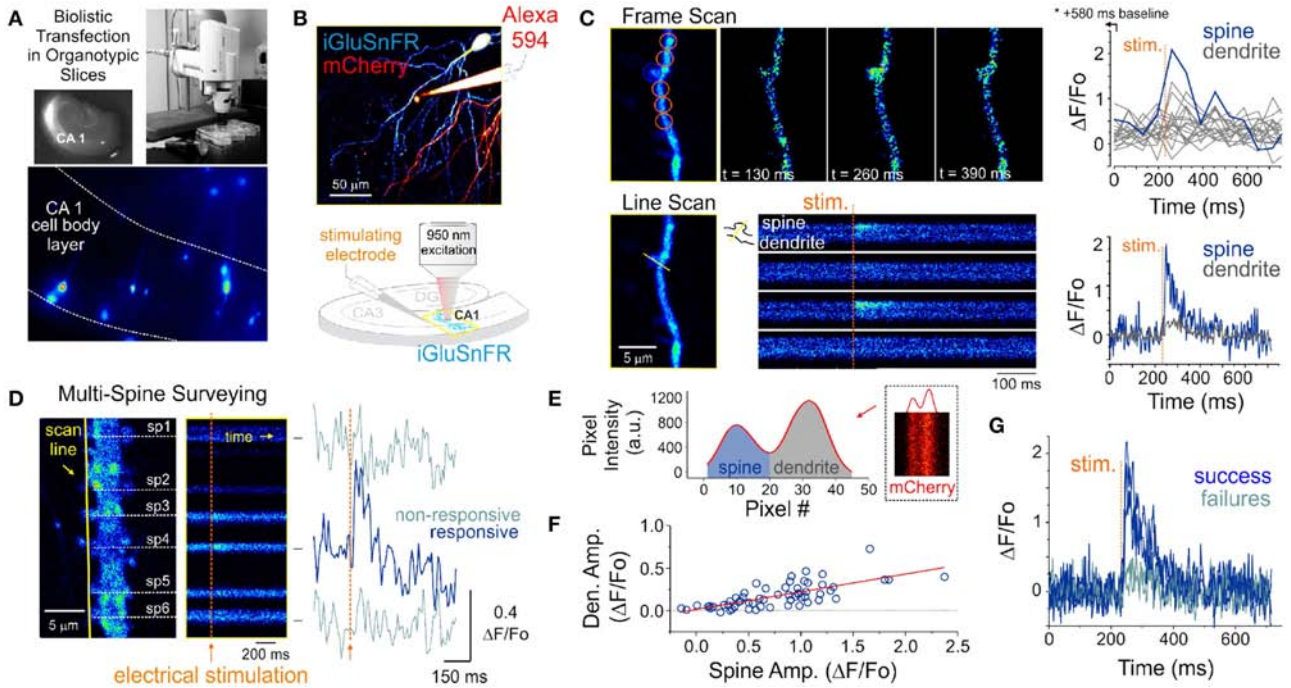

FIGURE 1 | Optical detection of glutamate release at single synapse using an genetically encoded glutamate sensor. **(A)** Biolistic transfection of CA1 hippocampal neurons with the intensity based glutamate sensor, iGluSnFR. **(B)** Experimental setup. A glass electrode filled with a fluorescent dye (Alexa 594) was positioned in the stratum radiatum adjacent to an iGluSnFR-expressing cell and was used to deliver electrical stimuli to the slice to evoke endogenous glutamate release. Neurons were typically transfected with both iGluSnFR and mCherry and expressed variable amount of the fluorescent proteins. **(C)** A comparison of iGluSnFR transients recorded at the same spine using either a frame-scan (spatial resolution > time resolution) or a line-scan (time resolution > spatial resolution) configuration. The fastest frame scan sampling rate of our optical system is 65 ms per frame, whereas rates of ≈ 1.4 ms perline were typically obtained in line-scan mode. **(D)** A line scan experiment is shown where multiple adjacent spines are surveyed simultaneously for evoked iGluSnFR transients. Shown at right is the time series resulting from a continuous line scan before and after an electrical stimulation. Spines 3 and 4 showed responsiveness to the electrical stimulus in this trial. **(E)** Isolation of spine and dendrite specific signals from a line scan is achieved by averaging pixels in their respective compartments, which was inferred by the presence of a dip in the mCherry signal. **(F)** The amplitude of spine iGluSnFR signals [same spine as in **(D)**] plotted against the corresponding amplitude of dendritic signals. A linear regression results in a significant positive correlation (slope 0.21, adjusted *R-squared* = 0.496). **(G)** Clearly distinguishable spine successes and failures demonstrate the probabilistic nature of vesicular release at these synapses.

spillover from the parent spine rather than from release from a distinct, neighboring synapse (**Figure 1F**). As such, we used only the spine compartment signal for all subsequent analyses. Finally, and consistent with the probabilistic release of glutamate vesicles at these synapses, release failures were readily observed (**Figure 1G**). These results demonstrate that iGluSnFR is a useful optical reporter for single-spine quantal analysis.

2.3. Glutamate vs. Post-synaptic Calcium Sensors for Opto-Quantal Analysis

The difficulty in unambiguously and routinely study neurotransmitter release from a single synapse due to the lack of spatial resolution afforded by electrophysiological recordings has been a longstanding shortcoming. By providing spatial information, optically-based approaches for quantal analysis offers promise of a solution to this problem, yet are limited by temporal resolution generally poorer than that afforded by cellular electrophysiology. By using two-photon uncaging of MNI-glutamate to precisely control the amount and timing of glutamate released onto single spines, we next sought to examine the kinetic performances of iGluSnFR by a side-by-side comparison with other commonly used reporters of glutamate release for quantal analysis. Specifically, we sought to compare with electrophysiological monitoring of synaptic AMPAR activation and optical recordings of quantal analysis using NMDAR-mediated calcium influx by calcium indicators. Since optical recordings of calcium influx using the GCaMP family of genetically encoded calcium-indicators are becoming increasingly popular, we turned our attention to GCaMP6f, a fast variant of the GCaMP family.

We obtained whole-cell recordings from CA1 neurons transfected with either iGluSnFR of GCaMP6f (**Figure 2A**) and voltage-clamped the cell at -70 mV. While continuously imaging the spine of interest (at ≈ 715 Hz), a second laser line tuned to 720 nm delivered a 1 ms light pulse to the tip of the spine in the presence of MNI-Glutamate (2.5mM), to induce uncaging-evoked optical transients recorded simultaneously with EPSCs (**Figures 2B,C**). In response to repetitive presentation of nominally constant concentration of glutamate by 2P uncaging at single synapses (**Figure 2D**), we

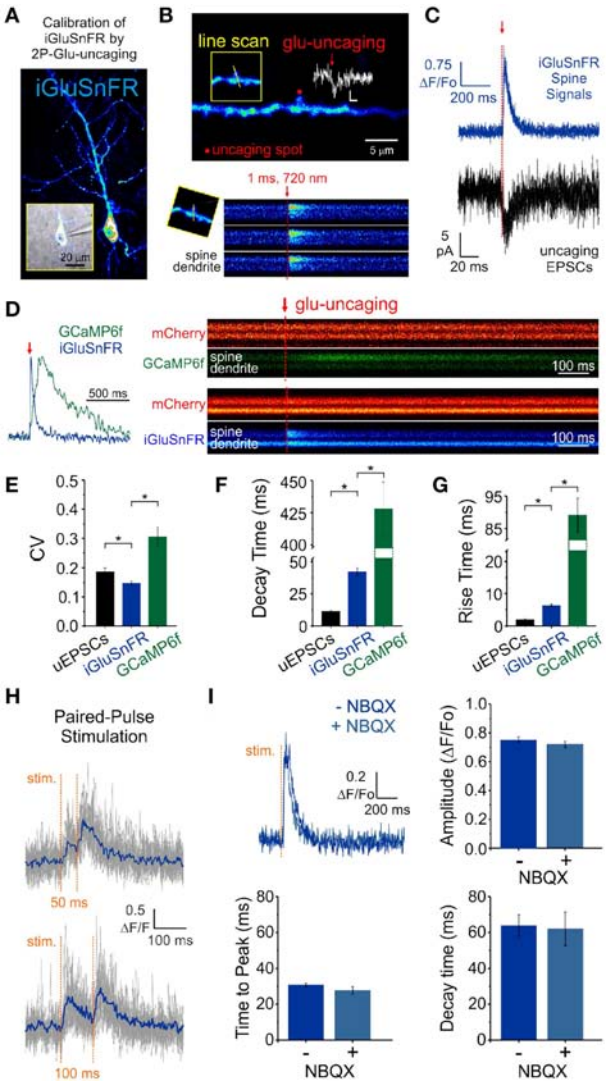

FIGURE 2 | Features of iGluSnFR-mediated responses. **(A)** Whole-cell recording of an iGluSnFR-expressing CA1 neuron. **(B)** Optically-evoked iGluSnFR transients were generated at a single spines by two-photon uncaging of MNI-glutamate. A continuous line scan was imaged at 950 nm while a second laser line tuned at 720 nm was used to deliver the uncaging events (1 ms; red arrow). **(C)** Spine iGluSnFR fluorescence transients from 10 consecutive uncaging stimuli (single trials) are displayed in the top panel along with the corresponding uncaging evoked EPSCs recorded at the soma (below). **(D)** A kinetic comparison of iGluSnFR and GCaMP6f. **(E)** Coefficient of variation (CV) of response peak amplitudes to a constant glutamate uncaging stimulus. The uEPSCs and iGluSnFR signals were recorded simultaneously in one set of experiments and the GCaMP6f signals were recorded using the exact same stimulus and experimental conditions in interleaved experiments. In response to an identical 1 ms light pulse used to uncage MNI-glutamate at a single spines, the decay **(F)** and rise **(G)** kinetics of iGluSnFR transients were much faster than calcium transients recorded from GCaMP6f-transfected neurons, but still slower than corresponding uncaging-evoked excitatory postsynaptic currents. *indicates $p < 0.05$. **(H)** The rapid kinetics of iGluSnFR enables peak-detection at stimulation frequencies that are suitable for studying synaptic facilitation and depression. **(I)** NBQX, an antagonist of AMPA-type glutamate receptors, has no effect on the amplitude or kinetics of evoked iGluSnFR transients ($n = 50$ stimuli in each condition; $p > 0.05$ in all

(Continued)

FIGURE 2 | cases, paired students *t*-test). Time to peak (after stimulus) was used to quantify rise times in this scenario rather than the 20–80% rise time method used previously on uncaging-evoked iGluSnFR transients **(G)** since a subset of evoked transients with small amplitudes were significantly impacted by optical noise leading to misleading measurements using the 20–80% rise time method.

compared the performance of 3 distinct reporters of glutamate transients at single synapses: (i) iGluSnFR transients; (ii) GCaMP6f transients (i.e., NMDAR-dependent calcium influx) and, (iii) AMPAR activation (uncaging-evoked EPSCs; uEPSCs). We found that the trial-to-trial variability of the iGluSnFR responses was remarkably low, even lower than that of uEPSCs (**Figure 2E**). In keeping with the more complex and convolved nature of NMDAR- and calcium-mediated optical detection of glutamate release, GCaMP6f-mediated signal displayed the largest variability of the 3 approaches (**Figure 2E**). iGluSnFR transients also displayed much faster decay kinetics (**Figure 2F**) and rise time (**Figure 2G**) compared to GCaMP6f, and were remarkably close but still slower than the kinetics of uEPSCs ($p < 0.001$ for both comparisons, unpaired student's *t*-test). The kinetic properties of iGluSnFR in response to glutamate uncaging therefore favorably compares to those of the calcium-sensitive organic dyes Alexa 4FF (Lee et al., 2016) and Oregon Green BAPTA-1 (unpublished observations) that are significantly slower. The fast kinetics of iGluSnFR enable discrimination of successive stimulus peaks at higher stimulus frequencies (50-100 ms inter-stimulus interval; **Figure 2H**) without the need of signal deconvolution. Moreover, neither the amplitude nor the kinetics of the iGluSnFR responses were affected by the competitive AMPA receptor antagonist NBQX ($n = 4$, **Figure 2I**), which may offer some flexibility to avoid specific experimental complications, such as minimizing excitability for experiments in highly recurrent networks or minimizing plasticity induction by repetitive and prolonged stimulation paradigms. Altogether, the iGluSnFR method for quantal analysis offers more experimental flexibility and faster kinetics than that afforded by NMDAR-mediated calcium influx detected by GCaMP6f.

2.4. Biophysics of Glutamate Release Variability

The goal of quantal analysis is to infer release properties of glutamate release from a distribution of recorded release magnitudes. Quantal analysis of synaptic release has been performed for decades and the formalism has evolved and adapted as new and improved recording technologies were developed. For didactic purposes, we revisited here some of the basic assumptions commonly held for performing quantal analysis of glutamate release events at single synapses.

We started by exploring the most appropriate continuous distribution to describe the inherent variability expected of a glutamate quantum. Our aim was to derive from the biophysical features of synaptic vesicles a mathematical description of the expected distribution of glutamate release amplitudes, along

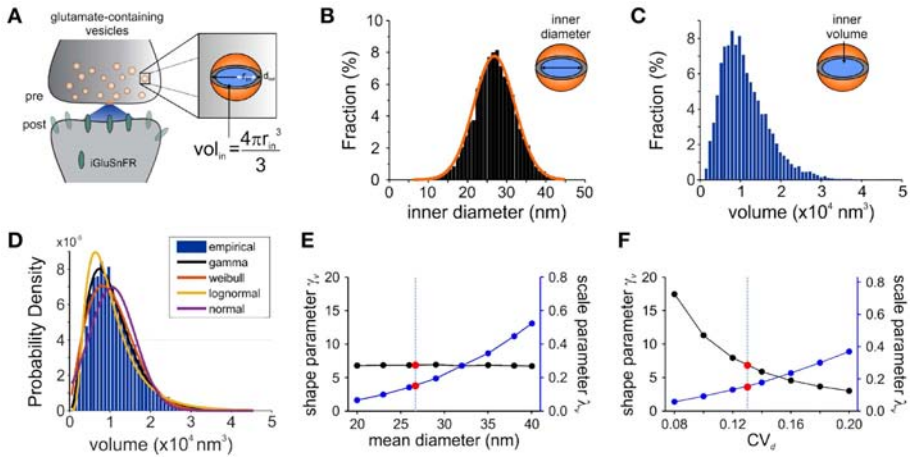

FIGURE 3 | Modeling Synaptic Glutamate Transients Following Vesicle Release. **(A)** A schematic description of the measurements and calculation used to infer synaptic vesicle volumes. This analysis was based on the assumptions that: (i) the distribution of synaptic vesicle diameters is uniform and; (ii) the shape of a synaptic vesicle is roughly spherical. **(B)** A simulated distribution of inner synaptic vesicle diameters using electron microscopy measurements described in Qu et al. (2009) [outer vesicle diameter = 38.7 nm; CV = 0.13; n = 10,000 vesicles, (Qu et al., 2009)]. The inner diameter of synaptic vesicles was calculated by subtracting the thickness of the vesicular membrane (2 × 6 nm). **(C)** A simulated distribution of inner volume of synaptic vesicle volumes derived from the simulated distribution of diameters presented in panel B, assuming that each vesicle volume can be approximated by the volume of a sphere. Assuming equal vesicular glutamate concentration, it is expected that the distribution of total vesicular glutamate content mirrors the distribution of vesicle volume. **(D)** Fitting of various continuous distributions to the modeled volume distribution, ordered in the legend based on the Bayesian Information Criteria (BIC). **(E,F)** Theoretical relationship between the parameters of a gamma distribution and the properties of the vesicle dimensions. Shape (black line) and scale parameter values (blue line) are shown against the mean vesicle diameter for $CV_d = 0.13$. **(E)** Electron microscopy observations of mean vesicle diameters are shown with red dots and vertical dashed line. Shape and scale parameter values as a function of CV_d for mean vesicle diameter of 38.7 nm. **(F)** Electron microscopy observations of $CV_d = 0.13$ is shown with red dots and vertical dashed line.

with their expected variability. Based on previous theoretical studies, we expect that the variability of inner vesicular volumes (**Figure 3A**) will be a potent determinant of the variability in the amount of glutamate molecules per quantum (Bekkers et al., 1990). What variability of glutamate release do we expect from fluctuations in vesicle diameters only? In order to find this, we first constrain the concentration of glutamate within synaptic vesicles to be constant across the many synaptic vesicles of a given neuron. In addition, we assume faithful release of a single vesicle (in this case release probability $p = 1$) and that the relative location and loading of vesicles does not introduce a significant amount of variability in the activation of post-synaptic receptors. We will revisit each of these assumptions sequentially as we assemble the mathematical synapse model.

Electron microscopy studies have shown that the variability in vesicle diameters at hippocampal synapses is normally distributed. Using the measurements obtained from one such study (mean vesicle diameter 38.7 nm, $CV_d = 0.13$ Qu et al., 2009) we generated a simulated distribution of 10,000 inner vesicle diameters (**Figure 3B**) and a corresponding distribution of the inner vesicle volumes (**Figure 3C**), assuming the shape of synaptic vesicles is approximated by a sphere. Inner vesicle diameters and volumes were calculated by first subtracting the thickness of the plasma membrane (12 nm Qu et al., 2009). This volume distribution can be readily calculated by a change in variable of the diameter distribution (Bekkers et al., 1990; Barri et al., 2016). In line with the cubic relationship between volume and diameter, the resulting distribution (**Figure 3C**) is non-Gaussian as it displays an important rightward skew.

To compare the possible distributions of volumes emanating from a range of experimentally derived vesicular diameter, we explored a set of continuous distributions (normal, gamma, Weibull, lognormal) that could accurately describe the skewed distribution of inner vesicle volumes simulated. Using the Bayesian Information Criteria (BIC) as a scoring metric, we ranked the distributions with the degree with which they fit the simulated distribution (**Figure 3D**). We found that the gamma distribution provided the best approximation of the empirical distribution of vesicle volumes, followed by the Weibull, lognormal, and finally the normal distribution. By assuming equal loading of vesicular glutamate concentration into vesicle, we would therefore expect that the distribution of glutamate content per vesicle would be dictated by that of vesicle volumes (that is, a gamma distribution). These findings are intriguing when we consider that many previous studies of quantal analysis have reported using a Gaussian mixture model of release events (Larkman et al., 1997; Hardingham et al., 2010; Malagon et al., 2016; Jensen et al., 2019), although some have used skewed distributions (Lavoie et al., 2011; Barri et al., 2016) and at least one study a gamma distribution (Bhumbra and Beato, 2013).

The gamma distribution is described by two parameters: a shape parameter γ and a scale parameter λ and it is expressed in

terms of the gamma function $\Gamma(\cdot)$. When used to approximate the distribution of vesicle volumes, v arising from normally distributed diameters, we write

$$p(v) \approx g(v|\gamma_v, \lambda_v) = \frac{v^{\gamma_v - 1} e^{-v/\lambda_v}}{\lambda_v^{\gamma_v} \Gamma(\gamma_v)} \quad (1)$$

where λ_v and γ_v are the parameters for the volume distribution. These paremeter values can be found by matching the first two moments of simulated (**Figure 3**) and theoretical (Equation 1) distributions. Equation 1 has a right-skew controlled by the parameter γ_v. Conveniently, its mean ($E[v] = \gamma_v \lambda_v$), its variance ($\mathrm{Var}[v] = \gamma_v \lambda_v^2$), its skewness ($\mathrm{skewness} = 2/\sqrt{\gamma_v}$) and its coefficient of variation ($\mathrm{CV}_v = 1/\sqrt{\gamma_v}$) are simple expressions of these parameters. Also of considerable practicality, the addition of two independent gamma-distributed variables results in a random variable that is itself gamma-distributed with shape parameter equal to the sum of the shape parameters. As pointed out by Bhumbra and Beato (2013), these properties allow for a clearer treatment glutatmate release variability without explicitly compromising the validity of the gamma-release model.

To relate the parameters of the gamma distribution with vesicle dimensions, we calculated the expected range of γ_v and λ_v as a function of the mean vesicle diameter (μ_d, **Figure 3E**) and diameter coefficient of variation (CV_d; **Figure 3F**) for simulated vesicle volume distributions. The shape parameter is unaffected by changes in mean diameter, but the scale parameter increases nonlinearly with increasing diameters. In addition, the shape parameter decreases and the scale parameter increases when the CV of vesicle diameter increases. It is therefore possible to interpret an increase of the scale parameter as an increase in the mean vesicle diameter, but only if the shape parameter shows no concomitant changes.

What are the theoretical predictions of vesicle volume variability for optical measurements of cleft glutamate? Using the mean diameter μ_d and the variability of diameters CV_d from electron microscopy recordings, we predict $\lambda_v = 0.15$ and $\gamma_v = 6.8$. Importantly, these parameters give rise to a variability of volumes CV_v of 0.38. In theory, unequal loading of vesicular glutamate content, neurotransmitter diffusion and observational noise should increase the coefficient of variation once we consider the glutamate reported on the post-synaptic membrane instead of vesicle volumes. Since these factors are likely to be captured by another skewed distribution (Franks et al., 2003; Bhumbra and Beato, 2013; Bird et al., 2016), it is appropriate to use a gamma distribution to capture the total variability of univesicular releases. To consider a possible discrepancy between the variability of univesicular releases and that of vesicle volumes, we use γ and λ to parameterize the distribution of univesicular releases, not to be confused with the parameters of the theoretical volume distribution γ_v and λ_v. In fact, since additional sources of variability can only increase the CV, our γ_v should be considered an upper bound on γ. To summarize, we derived biophysical constraints for the parameters of a gamma-distributed set of univesicular glutamate release events (UVR) using an experimentally-derived distribution of inner vesicular volumes and the assumption of equal glutamate loading across vesicles of different sizes.

2.5. Observational Error and iGluSnFR Transduction

In principle, the experimental readout expected from the non-uniform distribution of cleft glutamate will arise in part from the cubic transform outlined above but it can be corrupted by loading, diffusion and by non-optimality of the iGluSnFR signal transform. In order to begin addressing the issue of iGluSnFR transform, we sought to experimentally interrogate as directly as possible the relationship between the quantity of glutamate release at single spines and the amplitude of iGluSnFR-mediated transients. By varying the amount of glutamate released onto dendritic spines through step-wise increments in uncaging laser power during simultaneous optical and electrophysiological recordings (**Figure 4A**), we found that the relationship between uncaging laser power and iGluSnFR amplitude was linear (**Figure 4B**) within the expected physiological range of glutamate release, as determined by the average amplitude of uEPSCs (Béïque et al., 2006; Soares et al., 2014, 2017; Lee et al., 2016). Furthermore, we found an inverse relationship between the uncaging stimulus intensity and the CV of IGluSnFR responses (**Figure 4B**). Taken together, iGluSnFR can linearly report changes in glutamate concentration at dendritic spines with high precision.

We then estimated a convolved metric of observational error CV_{opt} to be 0.15, by measuring the variability of the iGluSnFR transients upon presentation of nominally fixed amounts of glutamate concentrations by repetitive uncaging at a fixed laser intensity (around 30 mW; **Figure 2E**); while uEPSC amplitudes were within an expected physiological range (**Figure 4E**). At most, adding this measurement noise brings the combination of diameter and optical variability to the upper bound $\sqrt{CV_v^2 + CV_{\mathrm{opt}}^2} = 0.40$. The formalism outlined above therefore predicts the distribution of optical signals when glutamate is released from a presynaptic terminal. We next considered the variability imposed by the stochastic nature of vesicle releases.

2.6. Release Failures

Large amount of variability is attributed to the stochastic failure of vesicle release (Calvin and Stevens, 1968) upon action potential arrival. To formally include this process in our predicted distribution of optical signals, we considered a mixture model wherein we stochastically sampled from one of many independent sub-distributions, which are called components. Since in certain conditions, multiple vesicle release (MVR) occur at central synapses (Wadiche and Jahr, 2001; Oertner et al., 2002; Conti and Lisman, 2003; Christie and Jahr, 2006), we consider a MVR model for which univesicular release (UVR) is a special case. When n vesicles are docked and ready to be released and when each of these vesicles are released independently with probability p, the number of vesicles released will follow the binomial distribution. It is important here to clarify that the parameter p is not to be confused with the synapse's overall

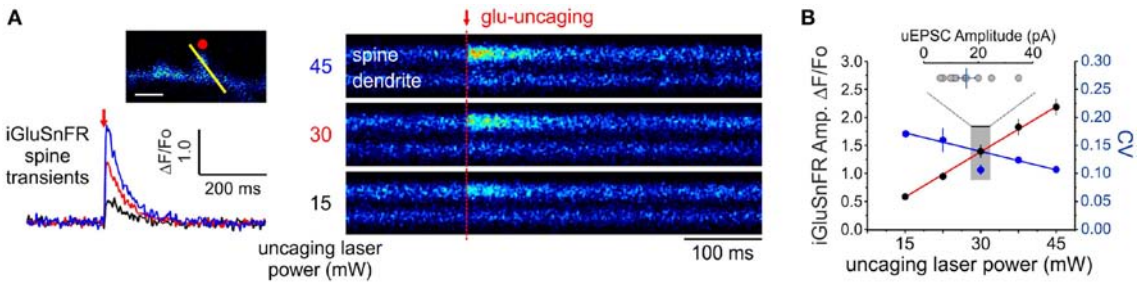

FIGURE 4 | Linearity and variability of optical reporter. **(A)** iGluSnFR transients generated at a single spine by two-photon glutamate uncaging at different uncaging laser powers (mW = milliwatts of power after the objective). **(B)** A positive linear relationship between uncaging laser power and the amplitude of iGluSnFR transients at a single spines (Adjusted $r^2 = 0.997$) indicates that the transduction is linear within this range. The relationship between the CV of single-trial iGluSnFR amplitudes and uncaging laser power is included as a second axis.

release probability (P_r) – the probability that any of the n docked vesicles will release. It is also important to note that the formalism does not specify whether or how multivesicular release is distributed in nanodomains. Irrespective of their sub-micron localization, we will expect that at times all vesicles have failed to release, in which case we will sample from the failure distribution. Assuming a Gaussian measurement noise – here called optical – for the failure distribution, we obtain the gamma-Gaussian mixture for observations of fluorescence amplitude F

$$p(F) = (1-p)^n G(F|0,\sigma^2_{opt}) + \sum_{k=1}^{n} \binom{n}{k} p^k (1-p)^{n-k} g(F|k\gamma,\lambda) \tag{2}$$

where σ^2_{opt} is the variance of the optical noise (derived in Section 2.5) and $G(F|\mu,\sigma^2)$ is a Gaussian distribution of mean μ and variance σ^2. In Equation 2, k ranges from 1 to n and refers to the possible number of vesicles released. The binomial coefficient $p^k(1-p)^{n-k}$ establishes the probability of observing k vesicles, while each time that k vesicles are released, we sample from a gamma distribution $g(F|k\gamma,\lambda)$ with a shape parameter corresponding to k times the univesicular shape parameter γ.

We make three observation on this gamma-Gaussian mixture model of glutamate release at single synaptic contacts. Firstly, we distinguish the vesicular release probability p from the probability of any vesicle being released $P_r = 1-(1-p)^n$. Secondly, the mean and the variance of this distribution now depend on the maximum number of vesicles released n, namely $\mu = np\gamma\lambda$ and $\sigma^2 = \sigma^2_{opt}(1-p)^n + \lambda^2\gamma np\left(1+\gamma(1-p)\right)$. Lastly, it can be useful to analyze the measured variability, CV, in terms of the variability of univesicular releases $CV_{\mathrm{UVR}} = 1/\sqrt{\gamma}$, the variability due to observational error σ_{opt} and the variability of a binomial process $CV^2_{\mathrm{bin}} = (1-p)/np$. In this way we can parse the variability in three terms (see Methods for derivation)

$$CV^2 = \frac{\sigma^2_{opt}(1-p)^n}{(np\gamma\lambda)^2} + \frac{1}{np}CV^2_{\mathrm{UVR}} + CV^2_{\mathrm{bin}}. \tag{3}$$

This expression allows us to parse out the variability in terms of distinct sources.

Overall, for the experiments described in **Figure 1**, the gamma-Gaussian mixture should capture the variability of glutamate-dependent optical events originating from: Optical (various optical measurement noise), Binomial (the stochastic behavior of releasing n vesicles independently), and Unitary (release variability of associated with each vesicle release). The latter comprises variability from vesicle sizes, loading and diffusion. It has a total of five parameters: σ^2_{opt} the variance of the optical noise, n the number of vesicles, p the probability of each vesicle being released, λ the scale and γ the shape parameters of the gamma distribution.

2.7. Inferring Release Parameters From Quantal Peaks

An intuitive approach to discriminate release events from failures lies in classifying a trial as a failure of release if the observed peak fluorescence is less than twice the standard deviation of the optical noise, and success otherwise (**Figure 5A**). From the distribution of success amplitudes, one then extracts the mean and coefficient of variation, called potency and CV_{suc}, respectively. It is not immediately clear, however, how false positives and false negatives arising from a thresholded detection method influences the estimates of potency and CV_{suc}. In this section, we use computer simulations to determine the bias introduced by optical noise on these measures.

To quantify the bias arising from classification errors, we generated surrogate amplitudes and calculated the potency and CV_{suc} using a threshold corresponding to two standard deviations of the optical noise (**Figures 5A,B**). We compared these estimates to potency and CV_{suc} calculated without classification errors. We found that for $\gamma = 2$ and $\lambda = 0.15$, classification errors leads to an over-estimation of the potency for all release probabilities (**Figure 5C**). This overestimate was restricted to the lower range of shape-parameter (**Figure 5D**) and scale parameter values (**Figure 5E**). These biases are overall relatively small, but the effects of optical noise are more dramatic on the calculation of CV_{suc}. Given $\gamma = 2$ and $\lambda = 0.15$, we found that CV_{suc} is drastically underestimated for all p (**Figure 5F**). This underestimate arises in a range of shape and scale parameters with low values (**Figures 5G,H**). In the case of

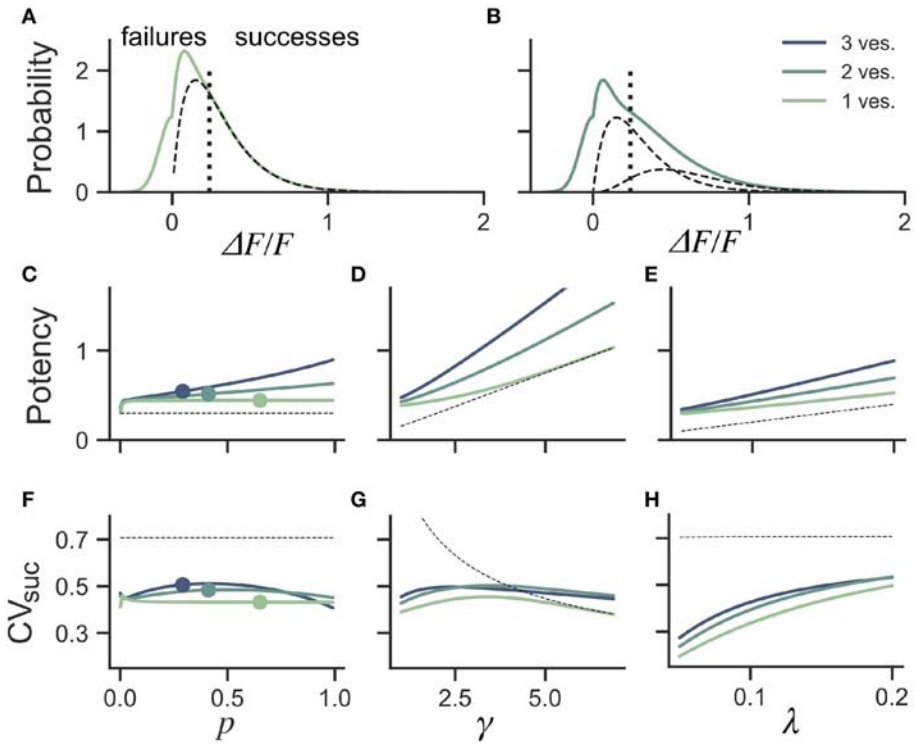

FIGURE 5 | Dependence of success distribution on synaptic release properties. **(A)** Peak amplitude probability in the univesicular release model. All peak amplitudes occurring below the detection threshold (vertical dotted line) are classified as failures. The underlying distribution of successes (dashed black curve) shows a small portion of false negatives. **(B)** Peak amplitude probability in the multivesicular release model with $n = 2$ vesicles. The distribution underlying one- and two-vesicle released are shown as dashed black curves. In **(A,B)** the probability distributions are drawn as histograms with bin size of 0.01. The mean amplitude of successes (potency) is shown as a function of the **(C)** the release probability for fixed shape ($\gamma = 2$) and scale ($\lambda = 0.15$) **(D)** as a function of the shape parameter γ for fixed release probability ($p = 0.65$) and scale ($\lambda = 0.15$) and **(E)** as a function of the scale parameter λ for fixed release probability ($p = 0.65$) and shape ($\gamma = 2$). The CV of successes is shown as a function of **(F)** the probability of release, **(G)** the shape parameter, and **(H)** the scale parameter. In **(C–H)**, three curves are shown for $n = 1$, 2, 3 vesicles. The dashed curve (black) shows the potency under the univesicular model in the absence of optical noise and with a detection threshold at zero.

threshold classificiation of successes and failures, we conclude that CV_{suc} will be heavily underestimated when the skewness is noticeable and the quantal size ($\gamma\lambda$) is small.

Next we investigated the the consequence of skewed distribution on the identification of quantal parameters n and p. Common approaches to estimate quantal parameters are based on the identification of quantal peaks (Larkman et al., 1991, 1997; Hardingham et al., 2010; Malagon et al., 2016). These approaches assume that the observation of a peak in the release-amplitude histogram can be read off as a quantal mode, an assumption that is often difficult to justify (Clements, 1991; Walmsley , 1995; Ninio, 2007). Peak identification can be even more problematic when the release components show an important skew. Indeed, we noted that mixtures of skewed distributions rarely show quantal peaks (**Figure 6**). For instance, a gamma-Gaussian mixture with $n = 2$ will transition from the absence of quantal peaks (**Figure 6A**) to the presence of quantal peaks (**Figure 6B**) only if the skewness of the components is reduced beyond the range predicted from biophysics (**Figure 6C**). These observations extend the limitations previously raised (Clements, 1991; Walmsley , 1995; Ninio, 2007) and show that analysis of quantal peaks is problematic especially when the distribution of univesicular release is skewed or only for a very narrow range of release probability. Since we expect a significant skew from known vesicle diameters (**Figure 3**), we sought a different method for extracting release properties.

2.8. Inferring Release Properties Using Likelihood Maximization

Maximizing the likelihood function provides an appealing alternative to feature-based approaches such as Bayesian quantal analysis (Bhumbra and Beato, 2013), non-stationary fluctuation analysis (Silver, 2003; Evstratova and Tóth, 2014), or to quantal-peaks approaches (Larkman et al., 1991). This approach does not rely on a trial per trial classification of successes and failures. Instead, the task is to find the set of parameters (n, p, γ, λ, σ_{opt}) that maximizes the probability of observing all recorded amplitudes given our gamma-Gaussian model. In the case of the likelihood written in Equation 2, there is no guarantee that only one such maximum exists, which means that it can be difficult to find the global maximum. Likelihood maximization algorithms can greatly help in solving this type of task.

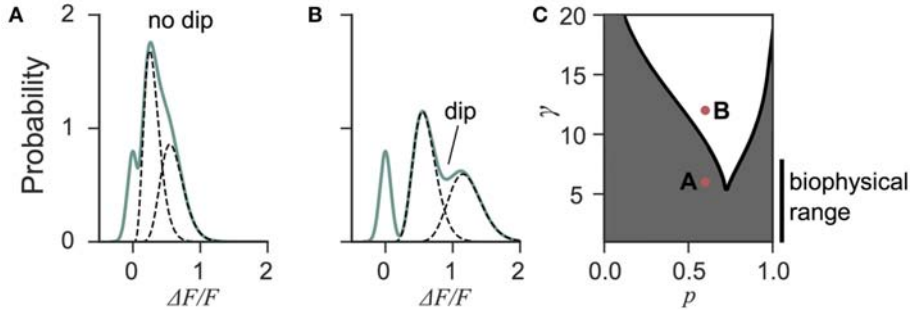

FIGURE 6 | Quantal peaks are rarely apparent in mixtures of skewed distributions. **(A)** Peak amplitude probability density function (green curve) of the gamma-mixture with $n = 2$ vesicles, a biophysical skewness $\gamma = 6$ and release probability $p = 0.6$. No dip is apparent between the individual components (dashed curves). **(B)** Peak amplitude distribution (green curve) of the gamma-mixture model with reduced skewness, $\gamma = 10$. A dip (indicated) can be observed between the quantal peaks (dashed curve). **(C)** Phase portrait of the presence, or absence, of a dip for a model with two vesicles ($n = 2$). The presence of a dip is restricted to small skewness (i.e., large γ) and a narrow range of release probability (white region). The shaded region represents parameter value combinations not associated with a dip in the probability density function. The parameter values used in A and B are indicated with red dots.

For our problem, the Expectation-Maximization (EM) algorithm appears a natural choice since it was developed to improve parameter inference in mixture models (Dempster et al., 1977). The EM algorithm has been used previously to infer synaptic properties, but using different experimental and computational methodologies (Barri et al., 2016). For efficient use of this algorithm, it is critical to derive estimation formulas specific to a given problem. Since we are not aware of any such estimation formulas for the gamma-Gaussian mixture (Equation 2), we next describe our adaptation of the EM algorithm.

The likelihood maximization in the EM algorithm is associated with the principle of gradient ascent (Xu and Jordan, 1996). Accordingly, it begins with an initial guess, and then iteratively updates these estimates to gradually maximize the likelihood $L(\mathbf{F}|\theta, n, \sigma^2_{\text{opt}})$ of observing the N observations of fluorescence amplitude denoted by the vector $\mathbf{F}$ given the parameters $\theta = (p, \gamma, \lambda)$. Using an initial guesses $\theta_0 = (p_0, \gamma_0, \lambda_0)$, the algorithm will have found the optimal value of each parameter $\hat{\theta} = (\hat{p}, \hat{\gamma}, \hat{\lambda})$. The parameter n will be treated as a meta-parameter to the EM algorithm, whose optimum is obtained by finding the $\hat{n}$ with its own optimal $\hat{\theta}$ that maximizes the likelihood $L(\mathbf{F}|\hat{\theta}, n, \sigma_0^2)$, or equivalently, minimizes the negative log-likelihood. The variance of the optical noise, σ_0^2, can be estimated independently by calculating the variance of the null distribution (see Methods).

Typically, a good initial estimate of the parameters can greatly speed the inference process. In the present case, we have argued that a good prior on the shape parameter can be obtained from the biophysics of vesicle release with known, Gaussian distributed, vesicle diameters (Qu et al., 2009). We initialize the shape parameter to a value of $\gamma_0 = 4$. To initialize the probability of release, we observe that only optical noise can capture fluorescence amplitudes smaller than zero. Therefore, we compute the fraction, c, of the total number of observations falling below zero and equate this to half the failure probability. This suggests the initialization $p_0 = 1 - (2c)^{1/n}$. There remains the initial value of the scale parameter. Given that the mean of fluorescence amplitude of the model is $np\gamma\lambda$, we use the mean of the observed fluorescence amplitudes μ_F to initialize $\lambda_0 = \mu_F / np_0\gamma_0$.

The EM algorithm is iterative and variational. That is, it first approximates the likelihood by an auxiliary function, which we will call Q. It then iterates between a maximization of this auxiliary function (the maximization step) and an improvement to the approximation by generating a new auxiliary function (the expectation step). Using $b(k|n, p)$ to denote the binomial distribution, the likelihood over N observations

$$L(\mathbf{F}|\theta) = \prod_{i=1}^{N} b(0|n,p)G(F_i|0,\sigma^2_{\text{opt}}) + \sum_{k=1}^{n} b(k|n,p)g(F_i|k\gamma,\lambda) \tag{4}$$

is replaced by

$$Q(\theta,\theta^{(t)}) = \sum_{i=1}^{N} \mu_{i,0}^{(t)} \log\left(b(0|n,p)G(F_i|0,\sigma^2_{\text{opt}})\right) + \sum_{k=1}^{n} \mu_{i,k}^{(t)} \log\left(b(k|n,p)g(F_i|k\gamma,\lambda)\right) \tag{5}$$

This auxiliary function relies on $N(n+1)$ variables $\mu_{i,k}^{(t)}$. These are the posterior probabilities of sampling from the kth component given a guess of the parameters $\theta^{(t)}$.

In the expectation step, we compute the posterior probabilities for $k > 0$

$$\mu_{i,k}^{(t)} \equiv p(k_i = k|F_i,\theta^{(t)}) = \frac{b(k|n,p^{(t)})g(F_i|k\gamma^{(t)},\lambda^{(t)})}{L(F_i|\theta^{(t)})}. \tag{6}$$

The posterior probabilities for $k = 0$, $\mu_{i,0}^{(t)}$, would need to be considered only if we were to use the EM algorithm to determine σ_{opt}. Importantly, these posterior probabilities are computed using the previous guess $\theta^{(t)} = (\gamma^{(t)}, \lambda^{(t)}, p^{(t)})$.

In the maximization step, we compute the new parameter set, which maximizes the auxiliary function

$\theta^{(t+1)} = \text{argmax}_\theta Q(\theta, \theta^{(t)})$. This is done via three re-evaluation formulas, obtained by setting the gradient of Q to zero. In what follows, we will use $\mathcal{H}(\cdot)$ to denote the Heaviside function. The first formula gives an update of p

$$p^{(t+1)} = \frac{1}{nN} \sum_{i=1}^{N} \sum_{k=1}^{n} k\mu_{i,k}^{(t)}. \quad (7)$$

To compute the second, we first calculate the model mean

$$m^{(t)} = \frac{1}{nN} \sum_{i=1}^{N} \sum_{k=1}^{n} \mu_{i,k}^{(t)} F_i \mathcal{H}(F_i) \quad (8)$$

and then maximize the terms of Q that depend on $\gamma^{(t+1)}$

$$\gamma^{(t+1)} = \arg\max_{\gamma} \sum_{i=1}^{N} \sum_{k=1}^{n} \mu_{i,k}^{(t)} \log\left(g\left(F_i | k\gamma, \frac{m^{(t)}}{\gamma p^{(t+1)}}\right)\right), \quad (9)$$

The third formula updates the scale factor

$$\lambda^{(t+1)} = \frac{m^{(t)}}{\gamma^{(t+1)} p^{(t+1)}}. \quad (10)$$

The expectation and maximization step are then repeated in alternation until convergence, which is defined by a tolerance value on the likelihood update.

We use these parameter estimates to compute the log-likelihood using Equation 4. Repeating the EM-method for n within a physiological range of 1-10 allows us to find the number of vesicles $\hat{n}$ which maximizes the log-likelihood

$$\hat{n} = \text{argmax}_n \log L(\mathbf{F} | \hat{\theta}, n). \quad (11)$$

Since the results may depend on the initialization point, we repeat the procedure with ten different initialization points. The parameter values associated with the highest likelihood become our parameter estimates.

2.9. Statistical Inference on Surrogate Data

To determine the precision and the validity of the EM method for extracting release properties, we apply the method on simulated data. We assume that the fluorescence amplitude are sampled from the gamma-Gaussian distribution. Once a sample is drawn, we will use the EM method to extract the release properties, namely the parameters γ, λ, n and p. Knowing the true parameters allows us to calculate the average difference between estimated and true parameters (bias) and the size of random fluctuations in the estimated parameters (variance). Since these estimator bias and variance will depend on the specific set of parameter values used to generate surrogate data, we must explore different types of parameter values. For the sake of illustration, we consider three cases: i) Univesicular release (**Figure 7A**), ii) multivesicular release with a low value of the shape parameter corresponding to the absence of dip in the probability distribution (**Figure 7B**) and; iii) multivesicular release with a high value of the shape parameter leading to well resolved quantal peaks but inconsistent with the biophysical constraints (**Figure 7C**).

We computed the bias and standard deviation of the estimates using 500 surrogate experiments and the expectation-maximization algorithm of the gamma-Gaussian mixture (see Methods Sect. 4.6). Since both the bias and the standard deviation are expected to depend on the number of samples per dataset, N, we report the bias and standard deviation as a function sample size. The correlation coefficients shown in **Figure 7D** reveal two interactions. Firstly, release probability as well as the shape and scale parameter estimates are strongly correlated. Secondly, these three parameter estimates are anti-correlated with the estimate of the number of vesicles. These compensations are also reflected in the sample-size dependent biases, where an underestimate (overestimate) in n is accompanied by an overestimate (underestimate) in the other parameters (**Figures 7E–H**). This reflects the fact that n is determined in a separate step from the other parameters and that for a larger n the other parameters must decrease to keep the same mean amplitude. We have verified with simulated sample sizes of 50 000 that these biases are restricted to small sample sizes, at very large sample sizes the biases reach zero.

Next, we consider the bias and variance of estimators for a sample size of 50, which represents a realistic sample size for our experimental conditions. At those sample sizes, we find that our method underestimates release probability, shape parameter and scale parameter (**Figures 7E–G**, red lines). These biases reflect the fact that, given the small number of vesicles considered, the number of vesicles can only be overestimated (**Figure 7H**). Considering sample size of 50 but for surrogate data with two vesicles, there remains a small underestimation of the shape parameter (**Figures 7E–G**, green lines) but the bias in the number of vesicles is much reduced (<0.25), and so is the bias in release probability and scale parameter. These biases are further reduced and become negligible in the less realistic situation where quantal peaks can be identified (**Figures 7E–H**, blue lines). Lastly, we note that the estimator standard deviations at $N = 50$ are sufficiently substantial to require averaging over multiple synapses in order to make precise parameter estimates.

2.10. Statistical Inference on Experimental Data

We next apply this EM algorithm on experimental data from iGluSnFR-mediated optical recordings of glutamate release. We used recordings of iGluSnFR-mediated signal induced by trains of ten axonal electrical stimulation at low frequencies (1,2,4, and 8Hz), from which we extracted a distribution of fitted release amplitudes (see Methods). Amplitude distribution from an exemplar spine is shown in **Figure 8A**. This distribution is captured very well by the gamma-Gaussian mixture model (Equation 2). The best fit for this recording was achieved for shape parameter $\gamma = 1.4$, scale parameter $\lambda = 0.2$, release probability $p = 0.42$ and 2 vesicles. **Figure 8A** shows that the theoretical distribution fits the empirical histogram well. This fit arises from individual components having an important skew.

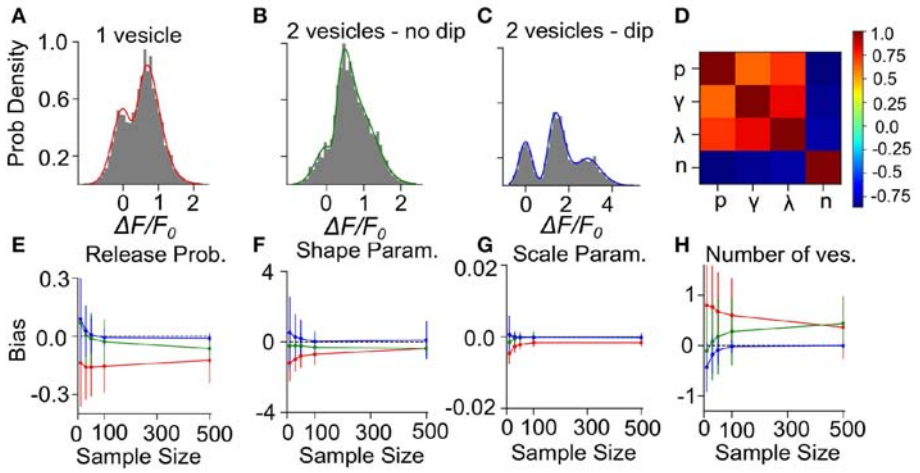

FIGURE 7 | Validation of the Expectation-Maximization method on simulated gamma-mixtures. Count histograms for simulated data (gray bars) and best fit probability density function (full line) for a gamma mixture with **(A)** $n = 1$ vesicles, a skew $\gamma = 7$, scale $\lambda = 0.12$ and release probability $p = 0.6$, **(B)** $n = 2$ vesicles, skew $\gamma = 6$, scale $\lambda = 0.1$ and release probability $p = 0.55$, **(C)** $n = 2$ vesicles, skew $\gamma = 15$, scale $\lambda = 0.1$ and release probability $p = 0.51$. **(D)** Correlation coefficient between parameter estimates of simulated data B with sample size = 100. The bias of estimates for **(E)** release probability (p), **(F)** shape parameter (γ), **(G)** scale parameter (λ), and **(H)** number of vesicles (n) is shown as a function of number of samples. Error bars show parameter estimates s.d.

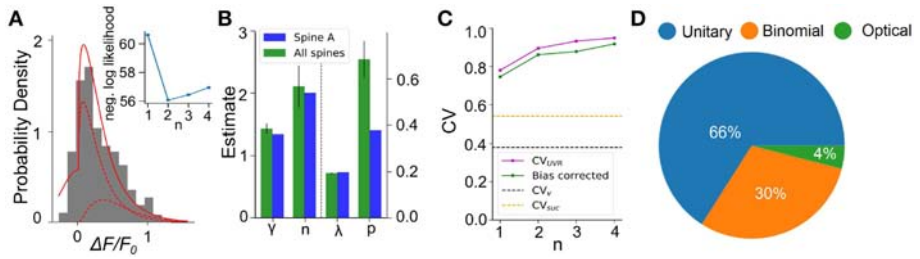

FIGURE 8 | Inferring quantal parameters from iGluSnFR recordings. **(A)** Evoked fluorescence amplitude histogram for one exemplar spine (gray bars) and probability distribution of the gamma-Gaussian model with properties inferred using the EM algorithm (full red line). A total of 400 electrical stimuli (40 trials of 10 stimuli) were delivered at varying frequencies (1–8 Hz) while recording the same spine and the peak amplitudes of iGluSnFR events were pooled. Individual release components for $k = 1$ and $k = 2$ are also shown (dashed red lines). Inset shows the negative log likelihood calculated by the EM algorithm versus number of vesicles released, n, for the spine shown. **(B)** Mean release properties obtained from the spine shown in A and a set of 18 spines. Bars left of dashed line use left axis scale, bars right of dashed line use right axis scale. Error bars represent s.e.m. The averages are 0.194 ± 0.003 for λ, 0.69 ± 0.08 for p, 2.1 ± 0.3 for n and 1.42 ± 0.08 for γ (mean $\pm$ SEM). Error bars show SEM. **(C)** Univesicular CV when n is the chosen vesicular release by the EM algorithm (blue), and averaging over all estimates at that n (green). The black dashed line shows the theoretical univesicular CV. **(D)** Factors explaining the variance in synaptic transmission. Based on average parameters obtained in panel **(B)** and Equation 3, we can parse out the variability in terms of optical noise (optical; green), the stochastic release of 0, 1, or 2 vesicles (binomial; orange) and the unequal potency of each vesicle (UVR; blue).

The inset of **Figure 8A** shows the negative log-likelihood as a function of the number of vesicles. Although there is a clear minimum at $n = 2$ vesicles, the curvature is fairly large, as is predicted by the small estimator variance (**Figure 7H**) under Cramer-Rao inequality. Importantly, the likelihood is considerably worse for the $n = 1$ model compared to any $n > 1$ models. Altogether, parameter inference using this EM algorithm on iGluSnFR-based analysis of glutamate release on single synapse argues that an action potential stochastically triggers the fusion of a few vesicles releasing a variable and highly skewed amount of glutamate.

We repeated this analysis on a set of experiments from 18 different spines (**Figure 8B**). Here, the average number of vesicles fitted by the algorithm was 2.10 ± 0.3, while individual spines were best fit by n ranging between 1 and 3 vesicles. The average shape parameter value was 1.42 ± 0.08. This parameter regulates the univesicular releases, the univesicular CV_{UVR}, described in the biophysical predictions. In principle, the average shape parameter fitted by the EM algorithm should correspond to a univesicular CV_{UVR} of 0.84, but we recall that our estimates of the shape parameter were shown to bear a small-sample bias, which we estimated to negative 0.2 (**Figure 7F**). As a consequence, our bias-corrected estimate of univesicular CV is 0.77. In comparison, we predicted that a $CV_v = 0.38$ (**Figure 3**) would arise from known vesicle dimensions, thus a difference of 0.39. To see how our estimate of univesicular CV depends on the

number of vesicles in the model, we fixed n and inferred CV_{UVR} for each spine (**Figure 8C**). We find that increasing n increases the CV_{UVR} inferred. This CV_{UVR} remained high and above both the variability expected from volumes (CV_v) and the variability of thresholded successes (CV_{suc}). This is consistent with the view that CV_v is a lower bound (Lavoie et al., 2011) and CV_{suc} is underestimated (**Figure 5**). In sum, statistical inference of our gamma-Gaussian model suggests CA3-CA1 stochastically release 1-3 vesicles with variable quantum.

The formalism outlined above allows to begin parsing out the variability of synaptic transmission at single synapses. Using the average parameters extracted using the expectation-maximization algorithm, Equation 3 can be used to separate the variability of observed evoked amplitudes in three terms. The first term captures the variability due to the glutamate sensor itself and to concurrent optical measurements The second term captures the fluctuations in release amplitude attributable to a single vesicle release and scaled by the average number of vesicle released (i.e., diffusion, loading and vesicle volume). The last term captures the variability of releasing sometimes two, one or zero vesicles (with zero unitary variability). We named these sources of variability optical, unitary and binomial, respectively. As shown in **Figure 8D**, we estimate that that 4% of the variability was optical, 30% binomial and 66% was unitary. Thus the results suggests that, despite the fluctuating number of vesicles being released, the variability of synaptic transmission arises mostly from the variability in unitary vesicle content released.

3. DISCUSSION

The use of the glutamate fluorescent reporter iGluSnFR provides a valuable proxy of glutamate release at single central synapses. To interpret the variability of glutamate release observed in our recordings, we built a gamma-Gaussian mixture model based on stochastic release of vesicles, each with a variable diameter size and additional sources of variability. We highlighted important biases in the traditional measures of the variability of successes and provided an alternative method based on the expectation-maximization algorithm. Our statistical method showed small biases on surrogate data and allows inference of estimates of quantal parameters. Together, these experimental and analytical tools allow to resolve the dynamic structure of synaptic transmission.

Optical quantal analysis confers several distinct advantages over classical electrophysiological methods, but also some limitations. One of the main advantages of optical methods is that the experiment is localized at an unambiguous source spine, thereby removing classical uncertainties such as the unknown location of synaptic inputs, the impact of dendritic filtering, and the determination that a single synaptic input is being monitored. While strong criteria have been developed in the past to classify electrophysiological data as arising from a single synaptic contact (i.e., minimal stimulation criteria; Malinow and Tsien, 1990; Raastad et al. , 1992; Stevens and Wang, 1995; Dobrunz and Stevens, 1997, 1999), some of these criteria may actually introduce false rejections and selection biases in population sampling, favoring against synapses that display multi-quantal, highly-variable, and/or a high probability of release. Optical methods are not without their disadvantages, chief amongst them being their still poorer temporal resolution as compared to traditional electrophysiological methods. Nevertheless, advances in molecular engineering have enabled faster and more specific optical reporters of synaptic transmission, including iGluSnFR which offers a significant temporal improvement over some of the fastest genetically-encoded optical calcium reporters (**Figure 2E**). Interestingly, the iGluSnFR family of reporters is still growing to include faster variants and variants with different emission spectra (Marvin et al., 2018; Wu et al., 2018).

One feature of the iGluSnFR relies on its non-reliance on postsynaptic glutamate receptor activation. Interpretation of calcium-based and electrophysiological-based measurements of synaptic release that rely on glutamate receptor activation are confounded by issues such as the non-linear relationship between glutamate concentration, glutamate receptor conductance and calcium-mediated fluorescence (Smith and Howe, 2000), the non-uniform distribution of glutamate receptors in the postsynaptic membrane (Biederer et al., 2017), and the distance between the presynaptic site of release and postsynaptic receptors (Franks et al., 2003), all of which are difficult to measure and contribute to convolving the end-result signal. iGluSnFR, being plasma membrane localized but lacking postsynaptic anchoring domains, is presumably evenly distributed on the cell surface and reports glutamate release largely independently of the precise location of vesicle release. Additionally, iGluSnFR reports glutamate release events in the presence of glutamate receptor antagonists (**Figure 2I**) which offers experimental flexibility. Finally, as demonstrated in **Figure 3F**, iGluSnFR provides a linear report of physiologically-relevant glutamate release, which allows for a more direct quantitative interpretation of the glutamate signal. Altogether, the experimental method we describe addresses a number of historical limitations and provides a welcome complement to existing methodologies to study basic features of synaptic transmission and plasticity.

Synaptic transmission is variable. Obtaining an accurate estimate of the size of this variability is an obligatory step in order to parse information content from noise during neural communication. By applying a traditional threshold-based classification of successes and failures on iGluSnFR transients, we obtained a fairly low average variability $CV_{suc} \approx 0.5$ (**Figure 8C**). Some of our recordings showed CV_{suc} in the 0.2-0.4 range, which closely matches the values reported for putative single-synapse electrophysiological recordings using either manual or threshold-based classification of failures and successes (Bekkers and Stevens, 1995; Dobrunz and Stevens, 1997; Hanse and Gustafsson, 2001). We however readily observed synapses that showed a higher CV_{suc} (up to 0.8) when optically probed. It is likely that these synapses would have been ignored when applying selection criteria commonly used for minimal stimulation experiments. Moreover, threshold-based classification inherently introduces classification errors, which can dramatically alter estimates of CV_{suc}. The statistical methodology presented here should circumvent this issue.

Consistent with our estimates on surrogate data (**Figure 5**), we observed that the variability of individual synaptic release can be much higher than threshold-based CV_{suc} and reach $CV_{UVR} = 0.8$. Further consistent with the effect of classification errors, our estimate of the average release probability of individual release is higher using the expectation algorithm ($p = 0.69$; **Figure 8B**) than using a threshold-based approaches (previous estimates were <0.61 Hanse and Gustafsson, 2001, 0.4 Bekkers and Stevens, 1995 and 0.2–0.4 Dobrunz and Stevens, 1997). Our assumption that glutamate is packaged at equal concentration in vesicles may be factually incorrect, implying that neurons have evolved a means to normalize glutamate content across vesicles that differ in volume. Such a result imply a redistribution of the relative breakdown of factors that contribute to quantal variability **Figure 8D**. Irrespective of this interpretation, our results further suggest that vesicle fusion can release very small but non-zero glutamate transients and that glutamate release variability is considerably higher than previously thought.

The usefulness of the experimental methodology and analytical formalism described herein extends beyond our preliminary efforts to identify the source of quantal variability. The iGluSnFR family of optical reporters are well suited to study the dynamical mechanisms that regulates synapse-specificity such as those controlling glutamate spillover (Asztely et al., 1997; Chalifoux and Carter, 2011; Lee, 2012) and its downstream impacts on neuronal function. Furthermore, by providing a direct proxy of release, it is well suited to interrogate several features of synaptic plasticity mechanisms across a wide range of central synapses and experimental preparations, including *in vivo*. In principle, optical fluorescent reporters may also be amenable to use in combination with complementary imaging modalities: for instance, one can envision using super-resolution imaging to estimate how strongly the modeled parameter n – the maximum number of vesicles released simultaneously – relates to optical estimates of the total number of active release sites (i.e., transsynaptic nanocolumns). Such investigations could provide a deeper understanding of the precise nature of quantal variability and its impact on the plasticity of information transfer at central synapses.

4. METHODS

The essential elements of optical quantal analysis are described in the main text. In this section, we give additional precisions on experimental, analytical and computational methods.

4.1. Organotypic Slices and Biolistic Transfection

A detailed description of our methodology for hippocamal organotypic slice preparation and biolistic transfection is described in (Soares et al., 2014). Briefly, organotypic slices were prepared from both male and female postnatal day 7 Sprague Daley rats (Charles River Laboratories, MA, USA) using the interface method originally described in Stoppini et al. (1991). In accordance with protocols approved by the University of Ottawa's Animal Care Committee, animals were anesthetized in an isofluorane infused chamber, decapitated, and hippocampi were removed in ice cold cutting solution containing (in mM): 119 choline chloride, 2.5 KCl, 4.3 $MgSO_4$, 1.0 $CaCl_2$, 1.0 NaH_2PO_4–H_2O, 1.3 Na-ascorbate, 11 glucose, 1 kynurenic acid, 26.2 $NaHCO_3$, saturated with 95% O_2 and 5% CO_2 (pH = 7.3; 295-310 mOsm/L). Transverse slices were cut at 400 μm thickness using a MX-TS tissue slicer (Siskiyou, Grants Pass, OR) and cultured on 0.4 mm millicell culture inserts (EMD Millipore, Etobicoke, Canada) at a temperature of 37^{o}C.

Hippocampal slices were transfected at 6-7 DIV using a hand held gene gun (Biorad, Hercules, CA). Cartridges for the gene gun were prepared in advance by precipitating 50 μg of cDNA plasmid onto 8-10 mg of gold microparticles (1.0 μm diameter; Biorad) at a ratio of 80/20 by weight of either iGluSnFR or GCaMP6f and mCherry cDNA plasmid, respectively. The precipitation step was performed in a 0.1 M KH_2PO_4 buffer solution containing 0.05 mM protamine sulfate (rather than spermine, as per previous protocols). The DNA-gold precipitate was washed and suspended (3 times) in 100% ethanol before loading in the tubing station. Once the cartridges were dried and cut, they were placed in a sealed container with desiccant pellets at 4 ^{o}C until used. The DNA-coated gold particles were delivered to the slice using ∼180 psi of helium air pressure. A modified gene gun barrel was used to protect slices from helium blast (Soares et al., 2014). Imaging experiments were performed 3-5 days after biolistic transfection.

4.2. Optical Recording of IGluSnFR Transients

Slices were removed from culture and placed in a custom recording chamber under a BX61WU upright microscope (60X, 1.0 NA objective; Olympus, Melville, NY). Slices were continuously perfused with a Ringer's solution containing (in mM): 119 NaCl, 2.5 KCl, 4 $MgSO_4$-$7H_20$, 4 $CaCl_2$, 1.0 NaH_2PO_4, 11 glucose, 26.2 $NaHCO_3$ and 1 Na-Ascorbate, saturated with 95% O_2 and 5% CO_2 (295-310 mOsm/L). For evoked stimulation experiments, a glass monopolar electrode filled with Ringer's solution was positioned adjacent to transfected cells in the direction of CA3. Simultaneous two-photon imaging of iGluSnFR and mCherry was performed using a Ti:Sapphire pulsed laser (MaiTai-DeepSee; Spectra Physics, Santa Clara, CA) tuned to 950 nm. Emission photons were spectrally separated using a dichroic mirror (570 nm) and the emitted light was additionally filtered using two separate bandpass filters (iGluSnFR: 495-540; mCherry: 575-630). The sampling frequency of our line-scan experiments depended on length of the imaged line segment (drawn over a spine and its parent dendrite), but was typically in the range of 1.2 - 1.5 ms / line for all optical quantal analysis experiments. This sampling rate was more than sufficient to fully capture and quantify the rise and falling phases of iGluSnFR transients. In our hands, an optimal trade-off between signal-to-noise, sampling frequency, and reduced bleaching, was obtained by using a 4 μs pixel dwell time. In the frame scan configuration, the sampling limit of our optical system was 65 ms/frame (2 μs pixel dwell time; 256 x 256 pixel frame) when

scanning bidirectionally, which was sub-optimal for optical quantal analysis.

Surveying methodology was designed to increase the probability of finding dendritic spines that were responsive to the electrical stimulus. While our frame scan configuration offered the spatial resolution to monitor several spines at once, we found it difficult in practice to identify rapid iGluSnFR-mediated transients due to a low signal to noise ratio and low sampling rate. As a result, line scans were exclusively used to survey the dendritic arbor for responsive spines. Short duration (0.1 ms) low intensity (5-25 mA) stimuli were delivered to the slice at low-frequency (0.1 Hz) while randomly surveying dendritic spines in the apical arbor of transfected cells. To facilitate the process of finding a responsive spine, line scans were performed simultaneously through multiple nearby dendritic spines and, generally, a paired-pulse stimulus (50-100 ms inter stimulus interval) was delivered to increase the probability of detecting glutamate release. Dendritic spines that were unresponsive to an initial probing phase consisting of 5-10 paired pulse stimuli, were not considered for further analysis, while spines demonstrating responsiveness to these initial probing stimuli were selected for quantal analysis experiments. Fluorescent transients were resolvable by eye and on-line analysis was not necessary. Prior to starting an optical quantal analysis experiment at a responsive spine, the stimulus intensity was gradually reduced up to a minimum where time-locked responsiveness was still observed. The process of identifying a responsive spine was generally not trivial and often necessitated several re-positioning of the stimulating electrode. Once a responsive spine was found, however, it was extremely rare to lose fluorescent responsiveness in response to electrical stimulation during an experiment.

4.3. Whole-Cell Electrophysiology and Two-Photon Glutamate Uncaging

Whole-cell recordings were carried out using an Axon Multiclamp 700B amplifier. Electrical signals were sampled at 10 kHz, filtered at 2 kHz, and digitized using an Axon Digidata 1440A digitizer (Molecular Devices, Sunnyvale, CA). Transfected CA1 pyramidal neurons were targeted and patched using borosilicate glass recording electrodes (World Precision Instruments, Sarasota, FL) with resistances ranging from 3-5 MΩ. All uncaging evoked currents were recorded at a holding potential of −70 mV. The intracellular recording solution contained (in mM): 115 cesium methane-sulfonate, 0.4 EGTA, 5 tetraethylammonium-chloride, 6.67 NaCl, 20 HEPES, 4 ATP-Mg, 0.5 GTP, 10 Na-phosphocreatine (all purchased from Life Technologies, Carlsbad, CA) and 5 QX-314 purchased from Abcam (pH = 7.2-7.3; 280-290 mOsm/L). The extracellular solution was similar to the one described above but also contained 2 mM MNI-glutamate-trifluoroacetate (Femtonics, Budapest, Hungary) and a reduced concentration of $MgSO_4$-$7H_20$ (1.3 mM) and $CaCl_2$ (2.5 mM). For glutamate uncaging experiments, a second laser line tuned to 720 nm was used to deliver 1 ms light pulses to the tips of dendritic spines while the other laser was tuned to 950 nm to image the uncaging-evoked iGluSnFR transients.

4.4. Analytical Derivation for Three Terms of Variability

We consider the gamma-Gaussian model described by Equation 2 of main article. To determine CV^2 we note that the mean of Equation 2 is $\mu_x = np\gamma\lambda$, the mean of the number of vesicles is $\sum_{k=0}^{n} kb(k|n,p) = np$ and the mean amplitude per vesicle is $\int xg(x|\gamma,\lambda)dx = \gamma\lambda$. The variance of x is

$$\sigma_x^2 = (1-p)^n \int (x-\mu_x)^2 G(x|0,\sigma_{opt}^2)dx + \sum_{k=1}^{n} b(k|n,p) \int_0^\infty (x-\mu_x)^2 g(x|k\gamma,\lambda)dx. \quad (12)$$

The first term of this equation becomes

$$(1-p)^n \left(\sigma_{opt}^2 + \mu_x^2\right) \quad (13)$$

and the second term is evaluated by centering the quadratic part of the integrand around the mean of a component, $k\gamma\lambda$. This gives for the second term of Equation 12

$$\sum_{k=1}^{n} b(k|n,p) \int_0^\infty \left[(x-k\gamma\lambda)^2 + \gamma^2\lambda^2(k-np)^2 + 2(x-k\gamma\lambda)(k-np)\gamma\lambda\right] g(x|k\gamma,\lambda)dx. \quad (14)$$

To evaluate this expression, one can isolate the variance of the number of vesicles: $\sum_{k=0}^{n}(k-np)^2 b(k|n,p) = np(1-p)$, as well as the variance of amplitude from k vesicles $\int (x-k\gamma\lambda)^2 g(x|k\gamma,\lambda)dx = \gamma\lambda^2$. Since the last term vanishes in Equation 14, we obtain

$$\sigma_x^2 = (1-p)^n\sigma_{opt}^2 + np\gamma\lambda^2 + \gamma^2\lambda^2 np(1-p). \quad (15)$$

Using $\mathrm{CV}_{UVR}^2 = 1/\gamma$ and $\mathrm{CV}_{bin}^2 = (1-p)/np$, taking the ratio $\mathrm{CV}^2 = \sigma_x^2/\mu_x^2$ we obtain Equation 3.

4.5. Regression for Amplitude Extraction

We describe the use of a template to extract the amplitude of the evoked responses. The method involves two steps. First we extract a template time-course $\mathbf{k}$ by computing the trial-averaged fluorescence response that is triggered by the electrical stimulation. This template is discretized, starts at the stimulation time and ends at a pre-defined time T after it. Trial averaging is performed on responses sufficiently isolated in time to be exempt from other synaptic events. For each trial i the template is scaled by β chosen so as to minimize the mean-squared error with the observed fluorescence $\mathbf{F}_{0:T}^{(i)}$ in the corresponding time window indicated by the subscript $0:T$. The solution of this least-square problem is well known and follows

$$\beta_i = (\mathbf{k}^T\mathbf{k})^{-1}\mathbf{k}^T\mathbf{F}_{0:T}^{(i)} \quad (16)$$

In order to report the maximum of the evoked waveform, we scale the β_i by the maximum value of the template. This is the value reported in **Figure 8**. We calculated the null distribution by fitting the template on fluorescence measurements without electric stimulation. The variance of the null distribution serves as our estimate of measurement noise $\sigma^2_{opt} = 0.07$.

4.6. Surrogate Data Analysis

To generate surrogate data, we simulate n surrogate fluorescence amplitudes and estimate the parameter values. Each surrogate experiment is repeated M times in order to have M sets of parameter estimates $\hat{\theta}_j$. Using this set of surrogate experiments, we can compute the bias, the variance and the correlation coefficients of the estimates. The bias is calculated by averaging the difference between the estimated parameter and the simulated parameters

$$\text{Estimator bias} = \frac{1}{M}\sum_{j=1}^{M}(\hat{\theta}_j - \theta).$$

In this way, a bias greater than zero means that the parameter tends to be overestimated, and a bias smaller than zero means that the inferred parameters are erroneously small.

To estimate the precision of the estimates, we calculate the variance:

$$\text{Estimator variance} = \frac{1}{M}\sum_{j=1}^{M}\left(\hat{\theta}_j - \frac{1}{M}\sum_{i=1}^{M}\hat{\theta}_i\right)^2.$$

A small variance means that the estimate is precise, although it may or may not be valid.

In addition, we compute the correlation coefficient between different parameter estimates. The correlation coefficient between a parameter $\theta^{(r)}$ and $\theta^{(q)}$ is simply

$$\text{Correlation coefficient} = \frac{\frac{1}{M}\sum_{j=1}^{M}\left(\hat{\theta}_j^{(r)} - \sum_{i=1}^{M}\hat{\theta}_i^{(r)}\right)\left(\hat{\theta}_j^{(q)} - \sum_{i=1}^{M}\hat{\theta}_i^{(q)}\right)}{\sigma_r\sigma_q}$$

where σ_r and σ_q are the square root of the estimator variances for $\theta^{(r)}$ and $\theta^{(q)}$, respectively. When the correlation coefficient is positive, it means that estimation errors tend to covary with the same sign, and when the correlation coefficient is negative, it means that an estimation error in parameter r is associated with an estimation error of opposite sign in parameter q.

5. ADDITIONAL REQUIREMENTS

For additional requirements for specific article types and further information please refer to Author Guidelines.

DATA AVAILABILITY

The datasets generated for this study are available on request to the corresponding author.

AUTHOR CONTRIBUTIONS

CS, J-CB, AL, and RN conceived the study. CS performed the experiments. CS, DT, and RN analyzed the data and performed the simulations.

FUNDING

This work was supported by CIHR grant 14242 (J-CB) and NSERC Discovery grant 06872 (RN) and 05830 (J-CB) and Brain Canada Support (AL and J-CB).

REFERENCES

Asztely, F., Erdemli, G., and Kullmann, D. M. (1997). Extrasynaptic glutamate spillover in the hippocampus: dependence on temperature and the role of active glutamate uptake. *Neuron* 18, 281–293. doi: 10.1016/S0896-6273(00)80268-8

Auger, C., Kondo, S., and Marty, A. (1998). Multivesicular release at single functional synaptic sites in cerebellar stellate and basket cells. *J. Neurosci.* 18, 4532–4547.

Barri, A., Wang, Y., Hansel, D., and Mongillo, G. (2016). Quantifying repetitive transmission at chemical synapses: a generative-model approach. *eNeuro* 3, ENEURO–0113. doi: 10.1523/ENEURO.0113-15.2016

Béïque, J.-C., Lin, D.-T., Kang, M.-G., Aizawa, H., Takamiya, K., and Huganir, R. L. (2006). Synapse-specific regulation of AMPA receptor function by PSD-95. *Proc. Natl. Acad. Sci. U.S.A.* 103, 19535–19540. doi: 10.1073/pnas.0608492103

Bekkers, J. M., Richerson, G. B., and Stevens, C. F. (1990). Origin of variability in quantal size in cultured hippocampal neurons and hippocampal slices. *Proc. Natl. Acad. Sci. U.S.A.* 87, 5359–5362.

Bekkers, J. M., and Stevens, C. F. (1995). Quantal analysis of EPSCs recorded from small numbers of synapses in hippocampal cultures. *J. Neurophysiol.* 73, 1145–1156.

Bhumbra, G. S., and Beato, M. (2013). Reliable evaluation of the quantal determinants of synaptic efficacy using bayesian analysis. *J. Neurophysiol.* 109, 603–620. doi: 10.1152/jn.00528.2012

Biederer, T., Kaeser, P. S., and Blanpied, T. A. (2017). Transcellular nanoalignment of synaptic function. *Neuron* 96, 680–696. doi: 10.1016/j.neuron.2017.10.006

Bird, A. D., Wall, M. J., and Richardson, M. J. (2016). Bayesian inference of synaptic quantal parameters from correlated vesicle release. *Front. Comput. Neurosci.* 10:116. doi: 10.3389/fncom.2016.00116

Borghuis, B. G., Marvin, J. S., Looger, L. L., and Demb, J. B. (2013). Two-photon imaging of nonlinear glutamate release dynamics at bipolar cell synapses in the mouse retina. *J. Neurosci.* 33, 10972–10985. doi: 10.1523/JNEUROSCI.1241-13.2013

Branco, T., and Staras, K. (2009). The probability of neurotransmitter release: variability and feedback control at single synapses. *Nat. Rev. Neurosci.* 10:373. doi: 10.1038/nrn2634

Calvin, W. H., and Stevens, C. F. (1968). Synaptic noise and other sources of randomness in motoneuron interspike intervals. *J. Neurophysiol.* 31, 574–587.

Chalifoux, J. R., and Carter, A. G. (2011). Glutamate spillover promotes the generation of NMDA spikes. *J. Neurosci.* 31, 16435–16446. doi: 10.1523/JNEUROSCI.2777-11.2011

Choi, S., Klingauf, J., and Tsien, R. W. (2003). Fusion pore modulation as a presynaptic mechanism contributing to expression of long-term potentiation. *Philos. Trans. R. Soc. Lond. B Biol. Sci.* 358, 695–705. doi: 10.1098/rstb.2002.1249

Christie, J. M., and Jahr, C. E. (2006). Multivesicular release at schaffer collateral–CA1 hippocampal synapses. *J. Neurosci.* 26, 210–216. doi: 10.1523/JNEUROSCI.4307-05.2006

Clements, J. (1991). Quantal synaptic transmission? *Nature* 353, 396–396.

Conti, R., and Lisman, J. (2003). The high variance of AMPA receptor-and NMDA receptor-mediated responses at single hippocampal synapses: evidence for multiquantal release. *Proc. Natl. Acad. Sci. U.S.A.* 100, 4885–4890. doi: 10.1073/pnas.0630290100

Dempster, A. P., Laird, N. M., and Rubin, D. B. (1977). Maximum likelihood from incomplete data via the em algorithm. *J. R. Statist. Soc. Ser. B (methodological)* 39, 1–38.

Dobrunz, L. E., and Stevens, C. F. (1997). Heterogeneity of release probability, facilitation, and depletion at central synapses. *Neuron* 18, 995–1008.

Dobrunz, L. E., and Stevens, C. F. (1999). Response of hippocampal synapses to natural stimulation patterns. *Neuron* 22, 157–166.

Evstratova, A., and Tóth, K. (2014). Information processing and synaptic plasticity at hippocampal mossy fiber terminals. *Front. Cell. Neurosci.* 8:28. doi: 10.3389/fncel.2014.00028

Franks, K. M., Stevens, C. F., and Sejnowski, T. J. (2003). Independent sources of quantal variability at single glutamatergic synapses. *J. Neurosci.* 23, 3186–3195. doi: 10.1523/JNEUROSCI.23-08-03186.2003

Hanse, E., and Gustafsson, B. (2001). Quantal variability at glutamatergic synapses in area CA1 of the rat neonatal hippocampus. *J. Physiol.* 531, 467–480. doi: 10.1111/j.1469-7793.2001.0467i.x

Hardingham, N. R., Read, J. C., Trevelyan, A. J., Nelson, J. C., Jack, J. J., and Bannister, N. J. (2010). Quantal analysis reveals a functional correlation between presynaptic and postsynaptic efficacy in excitatory connections from rat neocortex. *J. Neurosci.* 30, 1441–1451. doi: 10.1523/JNEUROSCI.3244-09.2010

Higley, M. J., Soler-Llavina, G. J., and Sabatini, B. L. (2009). Cholinergic modulation of multivesicular release regulates striatal synaptic potency and integration. *Nat. Neurosci.* 12, 1121–1128. doi: 10.1038/nn.2368

Jensen, T. P., Zheng, K., Cole, N., Marvin, J. S., Looger, L. L., and Rusakov, D. A. (2019). Multiplex imaging relates quantal glutamate release to presynaptic Ca^{2+} homeostasis at multiple synapses *in situ*. *Nat. Commun.* 10:1414. doi: 10.1038/s41467-019-09216-8

Larkman, A., Stratford, K., and Jack, J. (1991). Quantal analysis of excitatory synaptic action and depression in hippocampal slices. *Nature* 350:344.

Larkman, A. U., Jack, J. J., and Stratford, K. J. (1997). Quantal analysis of excitatory synapses in rat hippocampal CA1 *in vitro* during low-frequency depression. *J. Physiol.* 505, 457–471.

Lavoie, N., Jeyaraju, D. V., Peralta, M. R., Seress, L., Pellegrini, L., and Tóth, K. (2011). Vesicular zinc regulates the Ca^{2+} sensitivity of a subpopulation of presynaptic vesicles at hippocampal mossy fiber terminals. *J. Neurosci.* 31, 18251–18265. doi: 10.1523/JNEUROSCI.4164-11.2011

Lee, K. F. (2012). A unique mechanism of NMDA spike initiation supports a distinct role in synaptic input integration. *J. Neurosci.* 32, 2913–2914. doi: 10.1523/JNEUROSCI.6318-11.2012

Lee, K. F., Soares, C., Thivierge, J.-P., and Béïque, J.-C. (2016). Correlated synaptic inputs drive dendritic calcium amplification and cooperative plasticity during clustered synapse development. *Neuron* 89, 784–799. doi: 10.1016/j.neuron.2016.01.012

Liu, G., Choi, S., and Tsien, R. W. (1999). Variability of neurotransmitter concentration and nonsaturation of postsynaptic AMPA receptors at synapses in hippocampal cultures and slices. *Neuron* 22, 395–409.

Liu, K., Hu, J.-Y., Wang, D., and Schacher, S. (2003). Protein synthesis at synapse versus cell body: enhanced but transient expression of long-term facilitation at isolated synapses. *J. Neurobiol.* 56, 275–286. doi: 10.1002/neu.10242

Llera-Montero, M., Sacramento, J., and Costa, R. P. (2019). Computational roles of plastic probabilistic synapses. *Curr. Opin. Neurobiol.* 54, 90–97. doi: 10.1016/j.conb.2018.09.002

Malagon, G., Miki, T., Llano, I., Neher, E., and Marty, A. (2016). Counting vesicular release events reveals binomial release statistics at single glutamatergic synapses. *J. Neurosci.* 36, 4010–4025. doi: 10.1523/JNEUROSCI.4352-15.2016

Malinow, R., and Tsien, R. W. (1990). Presynaptic enhancement shown by whole-cell recordings of long-term potentiation in hippocampal slices. *Nature* 346, 177–180.

Marvin, J. S., Borghuis, B. G., Tian, L., Cichon, J., Harnett, M. T., Akerboom, J., et al. (2013). An optimized fluorescent probe for visualizing glutamate neurotransmission. *Nat. Methods* 10, 162–170. doi: 10.1038/nmeth.2333

Marvin, J. S., Scholl, B., Wilson, D. E., Podgorski, K., Kazemipour, A., Müller, J. A., et al. (2018). Stability, affinity, and chromatic variants of the glutamate sensor iGluSnFR. *Nat. Methods* 15, 936–939. doi: 10.1038/s41592-018-0171-3

McAllister, A. K., and Stevens, C. F. (2000). Nonsaturation of AMPA and NMDA receptors at hippocampal synapses. *Proc. Natl. Acad. Sci. U.S.A.* 97, 6173–6178. doi: 10.1073/pnas.100126497

Nimchinsky, E. A., Yasuda, R., Oertner, T. G., and Svoboda, K. (2004). The number of glutamate receptors opened by synaptic stimulation in single hippocampal spines. *J. Neurosci.* 24, 2054–2064. doi: 10.1523/JNEUROSCI.5066-03.2004

Ninio, J. (2007). Doubts about quantal analysis. *J. Neurophysiol.* 98, 1827–1835. doi: 10.1152/jn.01254.2006

Oertner, T. G., Sabatini, B. L., Nimchinsky, E. A., and Svoboda, K. (2002). Facilitation at single synapses probed with optical quantal analysis. *Nat. Neurosci.* 5, 657–664. doi: 10.1038/nn867

Park, S. J., Kim, I.-J., Looger, L. L., Demb, J. B., and Borghuis, B. G. (2014). Excitatory synaptic inputs to mouse on-off direction-selective retinal ganglion cells lack direction tuning. *J. Neurosci.* 34, 3976–3981. doi: 10.1523/JNEUROSCI.5017-13.2014

Parsons, M. P., Vanni, M. P., Woodard, C. L., Kang, R., Murphy, T. H., and Raymond, L. A. (2016). Real-time imaging of glutamate clearance reveals normal striatal uptake in huntington disease mouse models. *Nat. Commun.* 7:11251. doi: 10.1038/ncomms11251

Qu, L., Akbergenova, Y., Hu, Y., and Schikorski, T. (2009). Synapse-to-synapse variation in mean synaptic vesicle size and its relationship with synaptic morphology and function. *J. Comparat. Neurol.* 514, 343–352. doi: 10.1002/cne.22007

Raastad, M., Storm, J. F., and Andersen, P. (1992). Putative single quantum and single fibre excitatory postsynaptic currents show similar amplitude range and variability in rat hippocampal slices. *Eur. J. Neurosci.* 4, 113–117.

Ribrault, C., Sekimoto, K., and Triller, A. (2011). From the stochasticity of molecular processes to the variability of synaptic transmission. *Nat. Rev. Neurosci.* 12:375. doi: 10.1038/nrn3025

Richards, D. A. (2009). Vesicular release mode shapes the postsynaptic response at hippocampal synapses. *J. Physiol.* 587, 5073–5080. doi: 10.1113/jphysiol.2009.175315

Rudolph, S., Tsai, M.-C., Von Gersdorff, H., and Wadiche, J. I. (2015). The ubiquitous nature of multivesicular release. *Trends Neurosci.* 38, 428–438. doi: 10.1016/j.tins.2015.05.008

Silver, R. A. (2003). Estimation of nonuniform quantal parameters with multiple-probability fluctuation analysis: theory, application and limitations. *J. Neurosci. Methods* 130, 127–141. doi: 10.1016/j.jneumeth.2003.09.030

Smith, T. C., and Howe, J. R. (2000). Concentration-dependent substate behavior of native AMPA receptors. *Nat. Neurosci.* 3:992. doi: 10.1038/79931

Soares, C., Lee, K. F., and Béïque, J.-C. (2017). Metaplasticity at CA1 synapses by homeostatic control of presynaptic release dynamics. *Cell Rep.* 21, 1293–1303. doi: 10.1016/j.celrep.2017.10.025

Soares, C., Lee, K. F., Cook, D., and Béïque, J.-C. (2014). "A cost-effective method for preparing, maintaining, and transfecting neurons in organotypic slices," in *Patch-Clamp Methods and Protocols* (New York, NY: Humana Press), 205–219.

Stevens, C. F., and Wang, Y. (1995). Facilitation and depression at single central synapses. *Neuron* 14, 795–802.

Stoppini, L., Buchs, P.-A., and Muller, D. (1991). A simple method for organotypic cultures of nervous tissue. *J. Neurosci. Methods* 37, 173–182.

Umemiya, M., Senda, M., and Murphy, T. H. (1999). Behaviour of NMDA and AMPA receptor-mediated miniature epscs at rat cortical neuron synapses identified by calcium imaging. *J. Physiol.* 521, 113–122.

Wadiche, J. I., and Jahr, C. E. (2001). Multivesicular release at climbing fiber-purkinje cell synapses. *Neuron* 32, 301–313. doi: 10.1016/S0896-6273(01)00488-3

Walmsley, B. (1995). Interpretation of 'quantal' peaks in distributions of evoked synaptic transmission at central synapses. *Proc. R. Soc. Lond. B* 261, 245–250.

Wu, J., Abdelfattah, A. S., Zhou, H., Ruangkittisakul, A., Qian, Y., Ballanyi, K., et al. (2018). Genetically encoded glutamate indicators with altered color and topology. *ACS Chem Biol.* 13, 1832–1837. doi: 10.1021/acschembio.7b01085

Wu, L.-G., Ryan, T. A., and Lagnado, L. (2007). Modes of vesicle retrieval at ribbon synapses, calyx-type synapses, and small central synapses. *J. Neurosci.* 27, 11793–11802. doi: 10.1523/JNEUROSCI.3471-07.2007

Xie, Y., Chan, A. W., McGirr, A., Xue, S., Xiao, D., Zeng, H., et al. (2016). Resolution of high-frequency mesoscale intracortical maps using the genetically encoded glutamate sensor iGluSnFR. *J. Neurosci.* 36, 1261–1272. doi: 10.1523/JNEUROSCI.2744-15.2016

Xu, L., and Jordan, M. I. (1996). On convergence properties of the em algorithm for Gaussian mixtures. *Neural Comput.* 8, 129–151.

Conflict of Interest Statement: The authors declare that the research was conducted in the absence of any commercial or financial relationships that could be construed as a potential conflict of interest.

frontiers in Synaptic Neuroscience

MINI REVIEW
published: 20 August 2019
doi: 10.3389/fnsyn.2019.00021

Model-Based Inference of Synaptic Transmission

*Ola Bykowska[1], Camille Gontier[2], Anne-Lene Sax[1], David W. Jia[3], Milton Llera Montero[1,4], Alex D. Bird[5,6], Conor Houghton[1], Jean-Pascal Pfister[2,7] and Rui Ponte Costa[1,2]**

[1] Computational Neuroscience Unit, Department of Computer Science, SCEEM, Faculty of Engineering, University of Bristol, Bristol, United Kingdom, [2] Department of Physiology, University of Bern, Bern, Switzerland, [3] Department of Physiology, Anatomy and Genetics, Centre for Neural Circuits and Behaviour, University of Oxford, Oxford, United Kingdom, [4] School of Psychological Science, Faculty of Life Sciences, University of Bristol, Bristol, United Kingdom, [5] Ernst Strungmann Institute for Neuroscience in Cooperation With Max Planck Society, Frankfurt, Germany, [6] Frankfurt Institute for Advanced Studies, Frankfurt, Germany, [7] Institute of Neuroinformatics and Neuroscience Center Zurich, University of Zurich/ETH Zurich, Zurich, Switzerland

Synaptic computation is believed to underlie many forms of animal behavior. A correct identification of synaptic transmission properties is thus crucial for a better understanding of how the brain processes information, stores memories and learns. Recently, a number of new statistical methods for inferring synaptic transmission parameters have been introduced. Here we review and contrast these developments, with a focus on methods aimed at inferring both synaptic release statistics and synaptic dynamics. Furthermore, based on recent proposals we discuss how such methods can be applied to data across different levels of investigation: from intracellular paired experiments to *in vivo* network-wide recordings. Overall, these developments open the window to reliably estimating synaptic parameters in behaving animals.

Keywords: synaptic transmission, short-term synaptic plasticity, model inference, probabilistic inference, quantal analysis

OPEN ACCESS

Edited by:
P. Jesper Sjöström, McGill University, Canada

Reviewed by:
Ian Stevenson, University of Connecticut, United States
Matthias H. Hennig, University of Edinburgh, United Kingdom
Christian Stricker, Australian National University, Australia

***Correspondence:**
Rui Ponte Costa
rui.costa@bristol.ac.uk

Received: *06 June 2019*
Accepted: *29 July 2019*
Published: *20 August 2019*

Citation:
Bykowska O, Gontier C, Sax A-L, Jia DW, Montero ML, Bird AD, Houghton C, Pfister J-P and Costa RP (2019) Model-Based Inference of Synaptic Transmission. Front. Synaptic Neurosci. 11:21. doi: 10.3389/fnsyn.2019.00021

1. INTRODUCTION

Modifications of synaptic transmission properties are believed to underlie learning, memory and, more generally, neural dynamics (Nabavi et al., 2014; Costa et al., 2017; Roelfsema and Holtmaat, 2018; Williams and Holtmaat, 2018; Llera-Montero et al., 2019). It is therefore of great importance to accurately infer synaptic transmission properties. Two key features that define synaptic communication are: stochastic transmission (Malagon et al., 2016) and (relatively fast) temporal dynamics (Markram et al., 1998; Zucker and Regehr, 2002). The former is reflected as trial to trial variability of synaptic transmission as the combined result of pre- and postsynaptic sources of noise, such as probabilistic vesicle release (presynaptic) or binding of quantal neurotransmitter packets to (postsynaptic) receptors (Faber and Korn, 1991; Traynelis et al., 1993). Whereas temporal dynamics is reflected in the temporal modulation of synaptic responses, which is mediated by the multiple time constants of the synaptic transmission machinery. Such dynamics give rise to the commonly observed phenomenon of short-term plasticity (STP) (Tsodyks and Markram, 1997; Zucker and Regehr, 2002). In this review we summarize, discuss and contrast recent developments in inference methods that capture either of these two elements (i.e., stochastic release and STP), or both. In particular our review focus on relatively simple phenomenological and statistical models, which abstract out the underlying biophysics and do not capture some aspects of synaptic transmission.

We also highlight recent advances toward inferring synaptic properties *in vivo*. Studying synaptic transmission parameters under naturalistic conditions is not only likely to give more precise parameters estimates, but also insights into what synaptic transmission properties are relevant in behaving animals (Dobrunz and Stevens, 1999; Isaac et al., 2009).

2. INFERENCE OF STOCHASTIC TRANSMISSION

Synaptic transmission is inherently stochastic (see **Figure 1** for a schematic). In the quantal view of synaptic transmission neurotransmitter-containing vesicles (quanta) are released into the synaptic cleft from N release sites with probability P_{rel} (Del Castillo and Katz, 1954; Korn and Faber, 1991; Larkman et al., 1991; Lanore and Silver, 2016) (**Figure 1A**). Once released, neurotransmitters bind to postsynaptic receptors triggering a postsynaptic response with mean quantal amplitude q. A *binomial model* is often used to describe these three aspects (i.e., number of release sites N, release probability P_{rel} and the mean quantal amplitude q). In this model the mean peak of postsynaptic responses is given by $\mu = qNP_{\text{rel}}$ and their variance by $\sigma^2 = q^2NP_{\text{rel}}(1 - P_{\text{rel}})$ (**Figure 1B**)[1]. Several methods based on the binomial release model have been proposed to infer synaptic transmission parameters. A simple method relies solely on using the mean and variance to get estimates of both q and P_{rel} by rearranging the terms as $\hat{q} = \frac{\sigma^2}{\mu} + \frac{\mu}{N}$ and $\hat{P}_{\text{rel}} = \frac{\mu}{N\hat{q}}$ given a number of release sites N (Markram et al., 1997; Costa et al., 2015). The variance-mean analysis (also known as multiple-probability fluctuation analysis) is a slightly more advanced technique that relies on recording postsynaptic responses under different release probability conditions, which are typical set experimentally by varying the concentration of extracellular calcium. The relationship between the variance and the mean (i.e., μ and σ^2 as above) under different release probabilities is then fitted to the parabolic function given by the binomial model (**Figure 3A**). This method estimates all three parameters (N, P_{rel}, and q; see Lanore and Silver, 2016 for a detailed review on the topic). Because this method depends on having an accurate estimation of mean and variance of the postsynaptic responses, it requires relatively long and stable electrophysiological recordings under different conditions.

The binomial model described above may suffer from identifiability issues. For example, in the presence of a high level of noise it may not be possible to reliably separate the multiple peaks of the postsynaptic responses. In this case a simple Gaussian description of the synaptic responses may be preferable (**Figure 2A**). In addition, the methods described above also rely on point estimates which may lead to inaccurate conclusions due to correlations in the parameters (see **Figure 2A** for an example of such a case). A more principled approach to the problem that explicitly represents the uncertainty in the parameters should offer a better understanding of how well a particular model explains a given dataset (see section 3 for examples of this).

Building on earlier work (Turner and West, 1993), Bhumbra and Beato (2013) introduced a more principled quantal analysis method—Bayesian Quantal Analysis (BQA). This method applies Bayesian statistics which allows model inference to combine prior knowledge $P(\theta)$ over model parameters θ (e.g, $\theta = (P_{rel}, N, q)$) with the data likelihood $P(D|\theta)$ following Bayes' theorem as $P(\theta|D) \propto P(\theta)P(D|\theta)$. In contrast to standard optimization methods, Bayesian inference explicitly models uncertainty over parameters given prior knowledge. Choosing the appropriate prior is an important step when developing Bayesian frameworks as it shapes the posterior distribution over parameters given by the likelihood. In BQA, the prior is used to integrate *a priori* knowledge about the synaptic release statistics (e.g., expected bounds), which simultaneously models the distributions of postsynaptic responses recorded under multiple release probabilities (independent of each other). This is in contrast with standard mean-variance analysis described above, which simply models the mean responses across different release probabilities. By incorporating prior information, this method improves the accuracy of parameter inference and, importantly, reduces the number of samples needed compared to the mean-variance analysis (from about 100 samples to about 60 samples). Therefore, this new method may be preferable in experimental conditions where long recordings are particularly challenging (see a more detailed comparison in **Table 1**).

[1]The binomial release model makes a few assumptions, namely that each site releases vesicles independently and that P_{rel} is the same across different release sites.

3. INFERENCE OF SHORT-TERM PLASTICITY

Postsynaptic responses are dynamic—the peak response amplitude depends not only on the quantal parameters, but also on previous activity. If the presynaptic neuron fires in quick succession, the released vesicles are not given enough time to be recycled, which leads to less vesicles available for release. As a consequence synaptic responses become weaker, also known as *short-term depression* (**Figure 1A**) and such recovery rates are often modeled with an exponential with timeconstant τ_D. At the same time the presynaptic calcium levels can increase with every consecutive spike, which may lead to an increase in the postsynaptic response rather than a decrease—this is known as *short-term facilitation*.

3.1. Deterministic Models of Short-Term Plasticity

A number of deterministic short-term plasticity models have been proposed that characterize the dynamic properties of synaptic transmission (for a review on STP models see Hennig, 2013). These models capture STP data relatively well, and thus may enable us to uncover how STP may be regulated under different conditions.

The parameters of these models are commonly fit using least-squares optimization to obtain a single set of parameters (point estimates) where the goal is to find the best (or at least a good) set of parameters that captures a given experimental dataset (Markram et al., 1998; Le Bé and Markram, 2006; Markram, 2006; Wang et al., 2006; Rinaldi et al., 2008; Ramaswamy et al., 2012; Testa-Silva et al., 2012; Romani et al., 2013) (**Figure 3B**).

However, estimating parameters of STP models poses a challenge. Similar to the issues highlighted above for binomial models, in most STP models different parameter sets produce model outputs that follow the observed data equally well

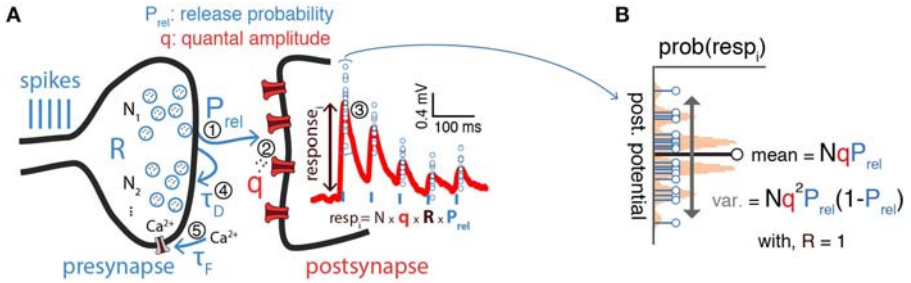

FIGURE 1 | Inference of synaptic transmission parameters. **(A)** Schematic of synaptic transmission parameters. On the left the different elements of the synaptic transmission process are represented: first (1), presynaptic spikes (blue vertical bars) lead to release of vesicles containing neurotransmitter (*R*, for presynaptic resources) from one of *N* possible release sites with probability P_{rel}; second (2), released neurotransmitters (quanta) bind to postsynaptic receptors triggering a response with amplitude *q*; third (3), this process triggers a postsynaptic response with average amplitude $NqRP_{rel}$, which takes into account both binomial and short-term synaptic plasticity; fourth (4), presynaptic vesicles are recovered with a time constant τ_D which may lead to *short-term depression* of consecutive postsynaptic responses (red trace on the postsynapse) before the presynaptic resources, *R*, fully recover; fifth (5), at the same time presynaptic voltage-dependent calcium (Ca^{2+}) channels can lead to calcium build-up on the presynapse (modeled by a time constant τ_F), which may increase release probability (P_{rel}) and in turn lead to an increase of consecutive postsynaptic responses, also known as *short-term facilitation* (not shown). **(B)** Postsynaptic responses exhibit variability [blue circles from **(A)** overlaid on top of the mean postsynaptic response in red]. Such variability is often described as a simple binomial process, with *N* release sites and variance given by $Nq^2P_{rel}(1 - P_{rel})$. Plot represents a binomial release model with $N = 5$, $P_{rel} = 0.5$ and some arbitrary *q*.

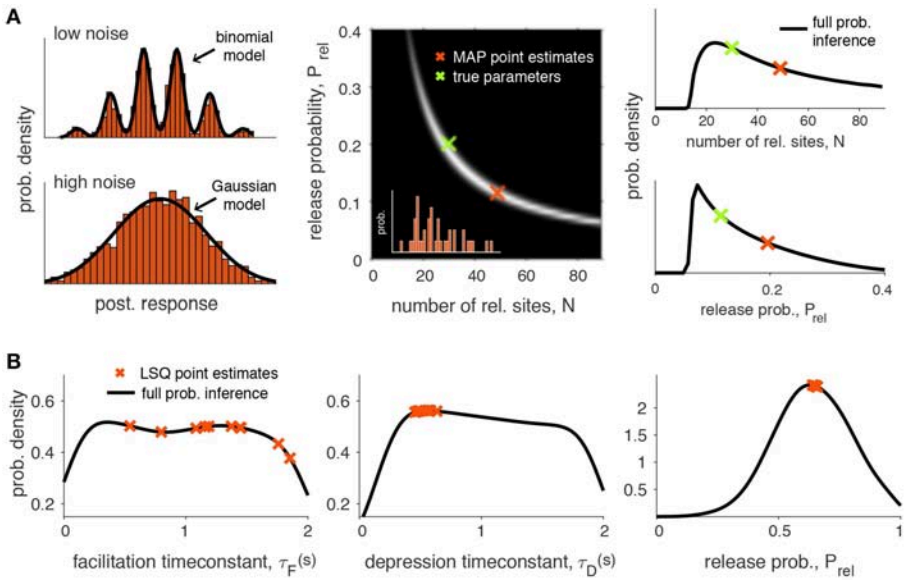

FIGURE 2 | Identifiability of synaptic transmission parameters. **(A)** Identifiability issues of quantal release models. Left upper figure: Histogram of 2000 simulated postsynaptic responses with $N = 5$, $P_{rel} = 0.5$, $q = 1$, $\sigma = 0.3$. In this case it is possible to fit a binomial model. Left lower figure: same simulation, but for high noise ($\sigma = 0.7$). The quantal peaks (i.e., the parameter N) are not identifiable anymore if the recording noise is too high, and in this case a Gaussian model provides a better description of the synaptic responses. Middle panel: Pairwise posterior marginal for *N* and P_{rel} for a typical experimental case with 40 observations (simulated postsynaptic responses shown in inset) where the true parameters were $N = 30$, $P_{rel} = 0.2$ and $q = 1$ (green cross). The maximum a posterior (MAP) estimates is obtained for $N = 49$ and $P_{rel} = 0.11$ (red cross): as *N* and *p* are anticorrelated, the posterior is roughly the same over a long band were *N* and *p* can be substituted, leading to inference error for a small number of observations. Right panel: Marginal posterior for *N* and P_{rel} from the previous panel. **(B)** Identifiability issues of short-term synaptic plasticity models. Given experimental data it is often of interest to infer the synaptic parameters. Two main types of inference have been applied: point estimations where a single scalar is estimated for one or more parameters (red crosses) or full probabilistic inference, where the full probability density over the parameters is obtained (black line). This particular example was obtained by inferring the Tsodyks-Markram model with four parameters given short-term plasticity recordings between pyramidal cells in layer-5 visual cortex (see Costa et al., 2013 for more details, only three parameters are shown here for simplicity: τ_F, τ_D and P_{rel}). Point estimates were obtained using a standard least-square (LSQ) fitting method (simulated annealing). Full probabilistic inference was done using MCMC sampling following Costa et al. (2013) (see main text for more details). As demonstrated by Costa et al. (2013) the uncertainty over the parameters can be greatly reduced by using more informative protocols that cover a wider frequency range.

TABLE 1 | Comparison of different model-based approaches.

Approach	Binomial	STP	Inference quality[h]	Experimental ease[h]	Algorithm complexity
Mean-variance analysis[a]	✓	×	**	* (PSR)	$\mathcal{O}(M)$
Bayesian quantal analysis[b]	✓	×	***	** (PSR)	$\mathcal{O}(MN)$
Least-square STP fitting[c]	×	✓	**	*** (PSR)	$\mathcal{O}(M)$
Bayesian Gaussian-STP[d]	×	✓	****	*** (PSR)	$\mathcal{O}(MS)$
Binomial-STP[e]	✓	✓	***	*** (PSR)	$\mathcal{O}(MN^4)$
Bayesian binomial-STP[f]	✓	✓	*****	*** (PSR)	$\mathcal{O}(MN^4)$
Spike-based GLM[g]	×	✓	*	**** (spikes)	$\mathcal{O}(M)$

Note that the approaches that consider parameter uncertainty can be readily extended to Bayesian. In the $\mathcal{O}$ algorithm complexity analysis M refers to the number of data points, N to the number of release sites and S to the number of samples needed. Point estimate methods that obtain some measures of uncertainty of the parameters rely on getting multiple point estimates, whereas this comes naturally in full probabilistic methods (this is here reflected in the inference quality). The list of methods presented here is grouped into quantal methods (first two rows) and into STP models (last 5 rows) and then sorted by their publication date (earlier first). PSR: Postsynaptic responses. We use star-based ranking system for both inference quality and experimental ease, where one star means worse/harder.

[a] *see Korn and Faber (1991), Lanore and Silver (2016), and* ***Figure 3A****.*

[b] *see Bhumbra and Beato (2013) and* ***Figure 3A****.*

[c] *see for example Markram et al. (1998), Le Bé and Markram (2006), Markram (2006), Wang et al. (2006), Rinaldi et al. (2008), Ramaswamy et al. (2012), Testa-Silva et al. (2012), Romani et al. (2013) and* ***Figure 3B****.*

[d] *see Costa et al. (2013) and* ***Figure 3C****.*

[e] *see Loebel et al. (2009), Barri et al. (2016), and* ***Figure 3C****.*

[f] *see Bird et al. (2016) and* ***Figure 3C****.*

[g] *see Ghanbari et al. (2017) and* ***Figure 3D****.*

[h] *Note that this ranking is subjective and based purely on our experience with these methods.*

(**Figure 2B**; Costa et al., 2013). The existence of these multiple plausible solutions opens problems when relying on point estimates to draw conclusions about the underlying biological mechanisms. Therefore, it is important to also consider the uncertainty of the parameter estimation. Unlike single point estimate approaches, full probabilistic inference naturally captures parameter uncertainty, which enables a more comprehensive model comparison (e.g., Akaike Information Criterion, Bayesian Information Criterion or Bayes factor). Note that this can also be in principle obtained using sensitivity or cross-validation analysis when using standard fitting methods (Varela et al., 1997; Tennøe et al., 2018), but as highlighted in **Figure 2B** these methods may not provide a complete picture of the parameter landscape. One form of probabilistic inference is full Bayesian inference where, similar to the BQA approach, we aim to obtain the posterior distribution of STP parameters given experimentally observed data.

Costa et al. (2013) introduced the first Bayesian inference framework of STP models (Bayesian Gaussian-STP; **Figure 3C**; **Table 1**). In this work the authors modeled the mean postsynaptic peak responses using the Tsodyks-Markram STP model to account for the dynamic properties of the synapse (Tsodyks and Markram, 1997; Markram et al., 1998). The Tsodyks-Markram STP model is a commonly used model built around the synaptic dynamics discussed above. In order to capture the variability of synaptic responses, Costa et al. (2013) used a Gaussian approximation as the likelihood and a flat (uninformative) prior with reasonable bounds over the parameters. Calculating the posterior exactly is often intractable due to complex likelihoods and intractable normalizing constants. Instead, Costa et al. (2013) obtained the posterior distribution $P(\theta|D)$ via sampling using a Markov Chain Monte Carlo (MCMC) algorithm. MCMC methods rely on constructing a Markov chain[2] that should converge to the desired probability distribution in the equilibrium (i.e., after long enough observations).

This method was used to study the parameter uncertainty given datasets obtained with common experimental protocols, which are typically based on regular spike trains. The posterior distributions revealed that some of the parameters from the Tsodyks-Markram STP models were poorly constrained by such experimental protocols (**Figure 2B**). This observation led to the proposal of new and irregular experimental protocols that span a broader stimulation frequency range and result in substantially reduced uncertainty over the parameter values. Such protocols not only lead to reduced uncertainty, but can also be more easily applied in realistic and natural conditions (Dobrunz and Stevens, 1999).

Furthermore, obtaining the posterior distribution helps to understand the dependencies between parameters, which is not straightforward using traditional fitting methods. For example, in Stone et al. (2014), the authors used an MCMC method to obtain the posterior distribution over the parameters (similar to Costa et al., 2013) allowing the authors to highlight two strongly correlated parameters. Importantly, the identification of this correlation led to a reparameterization of the model which improved parameter inference. Therefore, obtaining the posterior distribution over the parameters makes it possible to characterize their uncertainty and explore possible dependencies between parameters. Such MCMC methods are relatively efficient as long as the model can be computed efficiently (up to a few seconds) and the number of STP parameters remains relatively low (less than a few dozens).

[2] A Markov chain represents a probabilistic transition between states, in which a given transition depends only on the previous state.

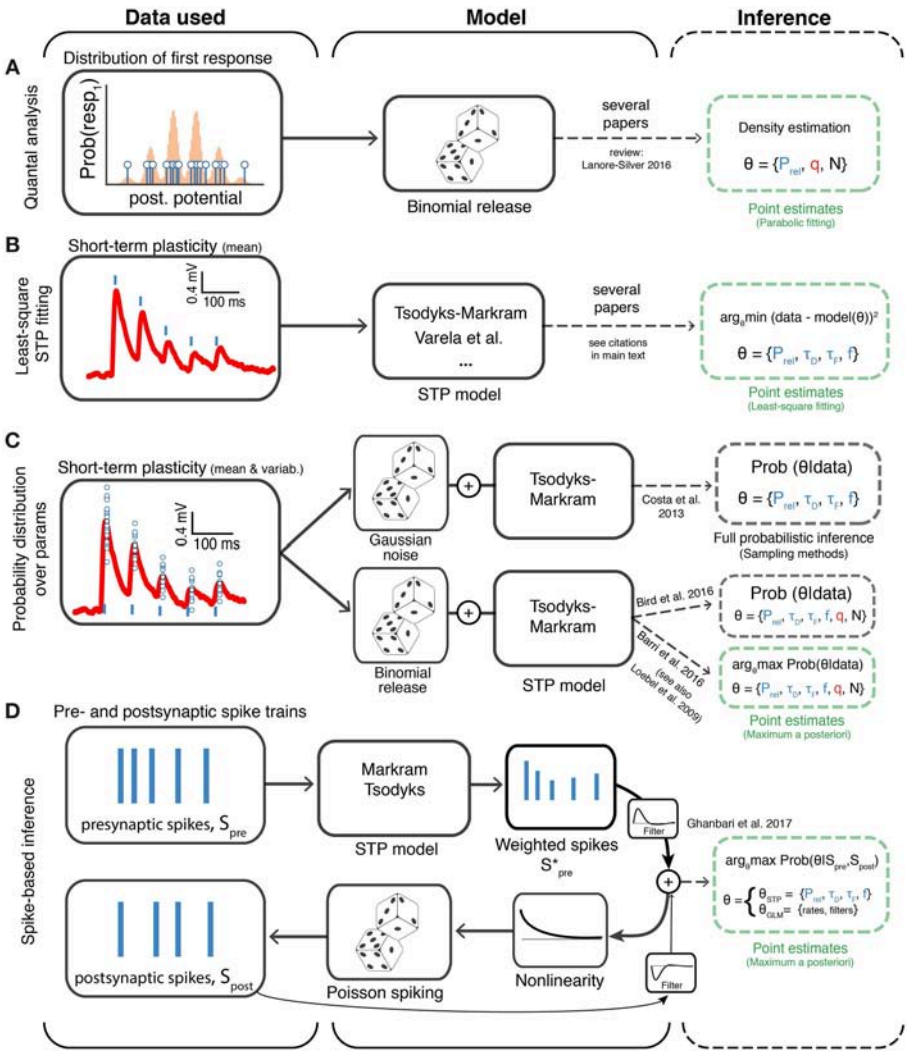

FIGURE 3 | Different approaches to model-based inference of synaptic transmission. The different methods are organized based on the type of experimental data to which they are applied (first column), the model being assumed (second column) and the method of parameter inference (third column; dashed green and gray boxes indicate point estimate and full probabilistic inference, respectively). **(A)** Methods that use the variability of the first postsynaptic responses to infer binomial release statistics. **(B)** Methods that rely on multiple averaged responses to fit short-term plasticity (STP) models, which typically discard binomial release statistics. **(C)** Methods that directly consider both variability and multiple synaptic responses using probability theory to infer the synaptic transmission parameters. Here two variants have been explored: (i) a Bayesian framework where Gaussian noise is used to model the synaptic response variability (Costa et al., 2013) and (ii) a framework in which binomial release statistics are explicitly considered (Barri et al., 2016; Bird et al., 2016). The later has been explored using two variants: full inference (using sampling, Bird et al., 2016) and optimization methods (Barri et al., 2016). **(D)** Methods that work directly at the level of spike trains and try to infer short-term plasticity parameters. Ghanbari et al. (2017) introduced a new method based on generalized linear models (GLMs) to obtain point estimates of short-term plasticity models. P_{rel}: Release probability; q: mean quantal amplitude; N: number of release sites; τ_D: depression time constant; τ_F: facilitation time constant; f: facilitation rate. Similarly to previous figures the mean postsynaptic responses are shown in red, spikes in blue (vertical lines) and small blue circles represent individual samples of postsynaptic responses.

3.2. Stochastic Short-Term Plasticity Models

There are two important limitations of relying on deterministic STP models. First, the optimization depends on an accurate estimation of the mean synaptic responses. As mentioned above, this requires a high number of trials, which is experimentally challenging (see **Table 1**). Second, by only considering averages these methods ignore the correlations between postsynaptic peaks, yet these correlations may provide valuable information to accurately infer the synaptic properties.

A couple of recent studies introduced methods that incorporate correlations between postsynaptic responses in the inference of STP parameters. These methods allow the extraction of both quantal and dynamic parameters of synaptic transmission from trains of postsynaptic responses without the requirement of averaging over multiple sweeps (Loebel

et al., 2009; Barri et al., 2016; Bird et al., 2016). These studies implemented stochastic models of synaptic transmission by combining phenomenological Tsodyks-Markram STP models with binomial models of vesicular release and replenishment. The probability of vesicle release is derived from a Tsodyks-Markram model and the vesicle replenishment probability is modeled with a Poisson process controlled by a depression time constant parameter τ_D. The quantal size of the postsynaptic response evoked by each vesicle can be approximated by either a gamma distribution in Bird et al. (2016), or an inverse Gaussian distribution in Barri et al. (2016), and the total amplitude is modeled as a linear combination of these distributions. The choice of these distributions is motivated by the fact that the quantal amplitude distribution is positively skewed, a feature that can not be captured by a Gaussian distribution.

The full formulation of the stochastic STP model can be used to define the likelihood of the observed data given the model, $P(D|\theta)$. The stochasticity of the model introduces correlations between peaks in the train and these correlations pose the main difficulty in the likelihood calculation. In particular, because the amplitude of the postsynaptic response is dependent on the number of released vesicles. As discussed in Barri et al. (2016), if the likelihood is to be formulated using the probability distribution of released vesicles, the number of terms in the calculation would grow exponentially. This becomes a permutation with repetition problem, in order to account for correlations of released vesicles the number of terms in the calculation would grow as $(N+1)^K$ with N being the number of release sites and K corresponding to the number of spikes in the train. To make the calculation more efficient, in both studies the likelihood function is formulated in terms of the probability distributions of the release sites before and after a spike (rather than continuously), which fully captures the state of the system.

These two studies apply different strategies to obtain point estimates from the likelihood. Barri et al. (2016) uses an expectation-maximization algorithm (referred to as Binomial-STP in **Table 1**; see also Loebel et al., 2009), while Bird et al. (2016) uses MCMC sampling and flat priors (referred to as Bayesian binomial-STP in **Table 1**). While both methods return a point estimate of the parameter set that maximizes the likelihood function, only the sampling approach approximates the joint likelihood distribution of the parameters. As discussed above, by obtaining the full likelihood, not just a point estimate, Bird et al. (2016) explicitly quantifies the uncertainty over the parameters, and the full likelihood density (or posterior) can be analyzed. Moreover, it also allows for correlations between the distributions over the parameters to be studied.

The main features of these approaches are (i) accounting for correlations between subsequent postsynaptic responses and (ii) using individual postsynaptic traces for fitting the models, which offers theoretical and practical advantages. Interestingly, both Barri et al. (2016) and Bird et al. (2016) report that considering correlations during inference yields estimates of synaptic parameters that are more accurate and require less sweeps when compared to ignoring correlations. This means that the experimental protocols can be shorter, hence making these inference methods particularly attractive for experiments *in vivo*.

4. TOWARD INFERENCE OF SYNAPTIC TRANSMISSION *IN VIVO*

Recent developments have started to raise the possibility of accurately inferring synaptic transmission properties *in vivo*. One way to tackle this problem is to perform whole-cell recordings *in vivo* while stimulating the presynaptic neurons (or presenting a stimuli) (Costa et al., 2015; Pala and Petersen, 2015; Sedigh-Sarvestani et al., 2019). This is a valuable approach that is enabling the community to confirm previous *in vitro* results *in vivo*. For example, Costa et al. (2015) applied binomial-based estimation methods typically used in slices to *in vivo* data, and obtained results consistent with both modeling predictions and slice data. Puggioni et al. (2017) and Latimer et al. (2018) introduced new statistical methods with some success in inferring synaptic conductances from *in vivo* intracellular recordings and spike trains, respectively. However, these methods were not developed to estimate quantal or synaptic dynamics properties. In order to test how such synaptic features are shaped in more natural conditions across different brain regions new methods are required that can operate on the growing imaging-based or spike-based datasets.

Detecting synaptic connections from spikes alone is challenging. Even in the case of simple monosynaptic connections this is not straightforward (Fetz et al., 1991), but there have been recent successful attempts (English et al., 2017). One of the key difficulties in inferring synaptic parameters from spikes is that several non-synaptic variables can have an impact on the spiking statistics (Stevenson et al., 2008). For example, when a presynaptic neuron fires at high frequencies one would expect a reduction in the firing rate of the postsynaptic neuron due to short-term depression at their synaptic connections, but a similar effect can also be mediated by postsynaptic neuron-wide adaptation mechanisms (Brette and Gerstner, 2005).

A first attempt at tackling this problem has recently been put forward (Ghanbari et al., 2017). In this framework, the authors extended a generalized linear model to infer both neuronal and STP parameters directly from spike-trains (**Figure 3D**, referred to as spike-based GLM in **Table 1**). Interestingly, using their framework Ghanbari et al. (2017) showed that in a reduced system—a single postsynaptic neuron in slices with simulated inputs—postsynaptic adaptation can be distinguished from short-term depression as they are predominantly correlated with pre- and postsynaptic firing rates, respectively. More recently the same authors (Ghanbari et al., 2018) went further and used their framework to show that functional connectivity with STP may explain the diversity of activity patterns observed *in vivo* between different brain areas. However, for these approaches to provide accurate estimates of synaptic transmission properties (**Table 1**) *in vivo* many other factors need to be considered in future work, such as network dynamics, cell-type specificity and dendritic integration.

As highlighted above (section 3), inferring synaptic parameters using naturalistic conditions (e.g., spike patterns) not only is likely to give more precise estimates of synaptic parameters, but also insights into which synaptic transmission

properties are relevant in behaving animals (Dobrunz and Stevens, 1999; Isaac et al., 2009).

5. DISCUSSION

In this review we have provided an overview of standard methods and recent developments of model-based inference of synaptic transmission. We started out by reviewing methods that rely on the binomial statistics of the first postsynaptic response alone and moved on to methods that consider the dynamics of consecutive synaptic responses (short-term plasticity) and their statistical properties. Historically, inference methods have mostly focused on point estimations, which give a biased interpretation of synaptic data (Costa et al., 2013). More recent developments have focused on full probabilistic inference, thus providing a more comprehensive picture on the most likely synaptic transmission parameters (Bhumbra and Beato, 2013; Costa et al., 2013; Bird et al., 2016).

One research direction that should improve the inference quality of the short-term plasticity parameters is to optimize the experimental protocol, namely the timings of the presynaptic action potentials. The stimulation protocol needs to be within some acceptable range (a too high stimulation frequency would induce long-term plasticity and thereby violate the stationarity assumption). However, within such a range, there is a lot of freedom that can be exploited to improve the quality of the parameter estimates. For example, Costa et al. (2013) explored a few different protocols (regular spike trains, regular spike train + recovery spike(s) or Poisson spike trains). It would be important to systematically study the space of protocols and determine which ones are the most informative. Pushing this idea even further, it would be interesting to design a closed-loop inference scheme such that after each spike and its subsequent postsynaptic response, the algorithm determines the best interval for the next spike that is maximally informative about the synaptic parameters.

In this review, we have not covered some other properties that are of interest. One that has received attention recently is the inference of the size of the presynaptic readily-releasable vesicle pool (Abrahamsson et al., 2017; Barros-Zulaica et al., 2019). Additionally, we have focused on the binomial release model, but many synapses require different release probabilities and quantal amplitudes across release sites, which is better captured by multinomial statistics (Walmsley et al., 1988; Lanore and Silver, 2016). There are several other important aspects of synaptic transmissoin not considered here, such as constrains on trial-to-trial quantal variability (Kullmann, 1993), STP models that also account for changes in quantal amplitude (Scheuss et al., 2002), frequency-dependent recovery rates in STP (Fuhrmann et al., 2004), and release-independent short-term depression (Bellingham and Walmsley, 1999; Fuhrmann et al., 2004). In future work, it would be important to understand how the developments reviewed here can also consider and be used to better understand these finer aspects of synaptic transmission.

There have been remarkable developments in measuring synaptic properties with high temporal and spatial resolution (Rey et al., 2015; Tang et al., 2016). Of particular interest are recent advances in ultrafast optical glutamate sensors, which are enabling measurements of synaptic release with high accuracy (Helassa et al., 2018). These developments, when coupled with the statistical inference frameworks reviewed here (Costa et al., 2013; Bird et al., 2016; Ghanbari et al., 2017, but see also Soares et al., 2019), raise the possibility of accurate optical estimation of synaptic transmission properties in awake behaving animals.

Finally, there has been a recent surge in new and exciting large-scale recordings, such as voltage and calcium imaging (Piatkevich et al., 2019), multi-patch recordings (Peng et al., 2019) and multi-electrode spike recordings (Jun et al., 2017). With such methods at hand now is the right time to start asking questions that bridge systems neuroscience and synaptic transmission properties. By building on initial studies on how synapses are shaped by naturalistic spike-trains (Dobrunz and Stevens, 1999; Isaac et al., 2009), this body of work opens the possibility of inferring quantal and dynamic properties of synapses over multiple brain areas as animals learn a particular task.

Taken together these novel inference and experimental methods open the possibility of testing different theories put forward for the role of synaptic transmission in learning and memory (Pfister et al., 2010; Costa et al., 2015, 2017; Llera-Montero et al., 2019), but also their impact in pathological states (Jackson et al., 2017).

AUTHOR CONTRIBUTIONS

OB, CG, and RC generated the figures. OB, CG, A-LS, DJ, MM, AB, CH, J-PP, and RC wrote the manuscript.

ACKNOWLEDGMENTS

We would like to thank Mark van Rossum and Magnus Richardson for useful feedback on this review. OB and A-LS work was supported by the Wellcome Trust Doctoral Training Programme in Neural Dynamics, Grant no. 105207/Z/14/Z and 215303/Z/19/Z, respectively. MM was supported by the European Research Council, grant no. 741134 to Jeff Bowers.

REFERENCES

Abrahamsson, T., Chou, C. Y. C., Li, S. Y., Mancino, A., Costa, R. P., Brock, J. A., et al. (2017). Differential regulation of evoked and spontaneous release by presynaptic NMDA receptors. *Neuron* 96, 839–855. doi: 10.1016/j.neuron.2017.09.030

Barri, A., Wang, Y., Hansel, D., and Mongillo, G. (2016). Quantifying repetitive transmission at chemical synapses: a generative-model approach. *eNeuro* 3:ENEURO.0113-15.2016. 113–115. doi: 10.1523/ENEURO.0113-15.2016

Barros-Zulaica, N., Rahmon, J., Chindemi, G., Perin, R., Markram, H., Ramaswamy, S., et al. (2019). Estimating the readily-releasable vesicle pool

size at synaptic connections in a neocortical microcircuit. *bioRxiv* 646497. doi: 10.1101/646497

Bellingham, M. C., and Walmsley, B. (1999). A novel presynaptic inhibitory mechanism underlies paired pulse depression at a fast central synapse. *Neuron* 23, 159–170. doi: 10.1016/S0896-6273(00)80762-X

Bhumbra, G. S., and Beato, M. (2013). Reliable evaluation of the quantal determinants of synaptic efficacy using Bayesian analysis. *J. Neurophysiol.* 109, 603–620. doi: 10.1152/jn.00528.2012

Bird, A. D., Wall, M. J., and Richardson, M. J. (2016). Bayesian inference of synaptic quantal parameters from correlated vesicle release. *Front. Comput. Neurosci.* 10:116. doi: 10.3389/fncom.2016.00116

Brette, R., and Gerstner, W. (2005). Adaptive exponential integrate-and-fire model as an effective description of neuronal activity. *J. Neurophysiol.* 94:3637. doi: 10.1152/jn.00686.2005

Costa, R. P., Froemke, R. C., Sjostrom, P. J., and van Rossum, M. C. W. (2015). Unified pre- and postsynaptic long-term plasticity enables reliable and flexible learning. *eLife* 4:e09457. doi: 10.7554/eLife.11988

Costa, R. P., Padamsey, Z., D'amour, J. A., Emptage, N. J., Froemke, R. C., and Vogels, T. P. (2017). Synaptic transmission optimization predicts expression loci of long-term plasticity. *Neuron* 96, 177–189.e7. doi: 10.1016/j.neuron.2017.09.021

Costa, R. P., Sjöström, P. J., and van Rossum, M. C. W. (2013). Probabilistic inference of short-term synaptic plasticity in neocortical microcircuits. *Front. Comput. Neurosci.* 7:75. doi: 10.3389/fncom.2013.00075

Del Castillo, J., and Katz, B. (1954). Quantal components of the end-plate potential. *J. Physiol.* 124, 560–573. doi: 10.1113/jphysiol.1954.sp005129

Dobrunz, L. E., and Stevens, C. F. (1999). Response of hippocampal synapses to natural stimulation patterns. *Neuron* 22, 157–166. doi: 10.1016/S0896-6273(00)80687-X

English, D. F., McKenzie, S., Evans, T., Kim, K., Yoon, E., and Buzsáki, G. (2017). Pyramidal cell-interneuron circuit architecture and dynamics in hippocampal networks. *Neuron* 96, 505–520.e7. doi: 10.1016/j.neuron.2017.09.033

Faber, D. S., and Korn, H. (1991). Applicability of the coefficient of variation method for analyzing synaptic plasticity. *Biophys. J.* 60, 1288–1294. doi: 10.1016/S0006-3495(91)82162-2

Fetz, E., Toyama, K., and Smith, W. (1991). "Synaptic interactions between cortical neurons," in *Normal and Altered States of Function*, eds A. Peters and E. J. Jones (Boston, MA: Springer), 1–47.

Fuhrmann, G., Cowan, A., Segev, I., Tsodyks, M., and Stricker, C. (2004). Multiple mechanisms govern the dynamics of depression at neocortical synapses of young rats. *J. Physiol.* 557(Pt 2):415–438. doi: 10.1113/jphysiol.2003.058107

Ghanbari, A., Malyshev, A., Volgushev, M., and Stevenson, I. H. (2017). Estimating short-term synaptic plasticity from pre- and postsynaptic spiking. *PLoS Comput. Biol.* 13:e1005738. doi: 10.1371/journal.pcbi.1005738

Ghanbari, A., Ren, N., Keine, C., Stoelzel, C., and Stevenson, I. H. (2018). Functional connectivity with short-term dynamics explains diverse patterns of excitatory spike transmission *in vivo*. *bioRxiv*. doi: 10.1101/475178

Helassa, N., Dürst, C. D., Coates, C., Kerruth, S., Arif, U., Schulze, C., et al. (2018). Ultrafast glutamate sensors resolve high-frequency release at Schaffer collateral synapses. *Proc. Natl. Acad. Sci. U.S.A.* 115, 5594–5599. doi: 10.1073/pnas.1720648115

Hennig, M. H. (2013). Theoretical models of synaptic short term plasticity. *Front. Comput. Neurosci.* 7:45. doi: 10.3389/fncom.2013.00045

Isaac, J. T., Buchanan, K. A., Muller, R. U., and Mellor, J. R. (2009). Hippocampal place cell firing patterns can induce long-term synaptic plasticity *in vitro*. *J. Neurosci.* 29, 6840–6850. doi: 10.1523/JNEUROSCI.0731-09.2009

Jackson, J. S., Witton, J., Johnson, J. D., Ahmed, Z., Ward, M., Randall, A. D., et al. (2017). Altered synapse stability in the early stages of tauopathy. *Cell Rep.* 18, 3063–3068. doi: 10.1016/j.celrep.2017.03.013

Jun, J. J., Steinmetz, N. A., Siegle, J. H., Denman, D. J., Bauza, M., Barbarits, B., et al. (2017). Fully integrated silicon probes for high-density recording of neural activity. *Nature* 551, 232–236. doi: 10.1038/nature24636

Korn, H., and Faber, D. S. (1991). Quantal analysis and synaptic efficacy in the CNS. *Trends Neurosci.* 14, 439–445. doi: 10.1016/0166-2236(91)90042-S

Kullmann, D. M. (1993). Quantal variability of excitatory transmission in the hippocampus: implications for the opening probability of fast glutamate-gated channels. *Proc. Biol. Sci.* 253, 107–116. doi: 10.1098/rspb.1993.0088

Lanore, F., and Silver, R. A. (2016). "Extracting quantal properties of transmission at central synapses," in *Advanced Patch-Clamp Analysis for Neuroscientists*, ed A. Korngreen (New York, NY: Springer), 193–211.

Larkman, A., Stratford, K., and Jack, J. (1991). Quantal analysis of excitatory synaptic action and depression in hippocampal slices. *Nature* 350, 344–347. doi: 10.1038/350344a0

Latimer, K., Rieke, F., and Pillow, J. W. (2018). Inferring synaptic inputs from spikes with a conductance-based neural encoding model. *bioRxiv* 281089. doi: 10.1101/281089

Le Bé, J., and Markram, H. (2006). Spontaneous and evoked synaptic rewiring in the neonatal neocortex. *Proc. Natl. Acad. Sci. U.S.A.* 103:13214. doi: 10.1073/pnas.0604691103

Llera-Montero, M., Sacramento, J., and Costa, R. P. (2019). Computational roles of plastic probabilistic synapses. *Curr. Opin. Neurobiol.* 54, 90–97. doi: 10.1016/j.conb.2018.09.002

Loebel, A., Silberberg, G., Helbig, D., Markram, H., Tsodyks, M., and Richardson, M. J. E. (2009). Multiquantal release underlies the distribution of synaptic efficacies in the neocortex. *Front. Comput. Neurosci.* 3:27. doi: 10.3389/neuro.10.027.2009

Malagon, G., Miki, T., Llano, I., Neher, E., and Marty, A. (2016). Counting vesicular release events reveals binomial release statistics at single glutamatergic synapses. *J. Neurosci.* 36, 4010–4025. doi: 10.1523/JNEUROSCI.4352-15.2016

Markram, H. (2006). The blue brain project. *Nat. Rev. Neurosci.* 7, 153–160. doi: 10.1038/nrn1848

Markram, H., Lübke, J., Frotscher, M., Roth, A., and Sakmann, B. (1997). Physiology and anatomy of synaptic connections between thick tufted pyramidal neurones in the developing rat neocortex. *J. Physiol.* 500(Pt 2):409–440. doi: 10.1113/jphysiol.1997.sp022031

Markram, H., Wang, Y., and Tsodyks, M. (1998). Differential signaling via the same axon of neocortical pyramidal neurons. *Proc. Natl. Acad. Sci. U.S.A.* 95, 5323–5328. doi: 10.1073/pnas.95.9.5323

Nabavi, S., Fox, R., Proulx, C. D., Lin, J. Y., and Tsien, R. Y. (2014). Engineering a memory with LTD and LTP. *Nature*. 511:348. doi: 10.1038/nature13294

Pala, A., and Petersen, C. C. H. (2015). *In vivo* measurement of cell-type-specific synaptic connectivity and Synaptic transmission in layer 2/3 mouse barrel cortex. *Neuron* 85, 68–75. doi: 10.1016/j.neuron.2014.11.025

Peng, Y., Mittermaier, F. X., Planert, H., Schneider, U. C., Alle, H., and Geiger, J. R. P. (2019). High-throughput microcircuit analysis of individual human brains through next-generation multineuron patch-clamp. *bioRxiv* 284:639328. doi: 10.1101/639328

Pfister, J. P., Dayan, P., and Lengyel, M. (2010). Synapses with short-term plasticity are optimal estimators of presynaptic membrane potentials. *Nat. Neurosci.* 13, 1271–1275. doi: 10.1038/nn.2640

Piatkevich, K. D., Bensussen, S., Tseng, H.-A., Shroff, S. N., Lopez-Huerta, V. G., Park, D., et al. (2019). Population imaging of neural activity in awake behaving mice in multiple brain regions. *bioRxiv* 350:616094. doi: 10.1101/616094

Puggioni, P., Jelitai, M., Duguid, I., and van Rossum, M. C. W. (2017). Extraction of synaptic input properties *in vivo*. *Neural Comput.* 29, 1745–1768. doi: 10.1162/NECO_a_00975

Ramaswamy, S., Hill, S. L., King, J. G., Schürmann, F., Wang, Y., and Markram, H. (2012). Intrinsic morphological diversity of thick-tufted layer 5 pyramidal neurons ensures robust and invariant properties of *in silico* synaptic connections. *J. Physiol.* 590, 737–752. doi: 10.1113/jphysiol.2011.219576

Rey, S. A., Smith, C. A., Fowler, M. W., Crawford, F., Burden, J. J., and Staras, K. (2015). Ultrastructural and functional fate of recycled vesicles in hippocampal synapses. *Nat. Commun.* 6:8043. doi: 10.1038/ncomms9043

Rinaldi, T., Silberberg, G., and Markram, H. (2008). Hyperconnectivity of local neocortical microcircuitry induced by prenatal exposure to valproic acid. *Cereb. Cortex* 18, 763–770. doi: 10.1093/cercor/bhm117

Roelfsema, P. R., and Holtmaat, A. (2018). Control of synaptic plasticity in deep cortical networks. *Nat. Rev. Neurosci.* 19, 166–180. doi: 10.1038/nrn.2018.6

Romani, A., Marchetti, C., Bianchi, D., Leinekugel, X., Poirazi, P., Migliore, M., et al. (2013). Computational modeling of the effects of amyloid-beta on release probability at hippocampal synapses. *Front. Comput. Neurosci.* 7:1. doi: 10.3389/fncom.2013.00001

Scheuss, V., Schneggenburger, R., and Neher, E. (2002). Separation of presynaptic and postsynaptic contributions to depression by covariance analysis of successive EPSCs at the calyx of held synapse. *J. Neurosci.* 22, 728–739. doi: 10.1523/JNEUROSCI.22-03-00728.2002

Sedigh-Sarvestani, M., Palmer, L. A., and Contreras, D. (2019). Thalamocortical synapses in the cat visual system *in vivo* are weak and unreliable. *eLife* 8:e41925. doi: 10.7554/eLife.41925

Soares,1 C., Trotter, D., Longtin, A., Béïque, J.-C., and Naud, R. (2019). Parsing out the variability of transmission at central synapses using optical quantal analysis. *bioRxiv* 10:624692. doi: 10.1101/624692

Stevenson, I. H., Rebesco, J. M., Miller, L. E., and Kording, K. P. (2008). Inferring functional connections between neurons. *Curr. Opin. Neurobiol.* 18, 582–588. doi: 10.1016/j.conb.2008.11.005

Stone, E., Haario, H., and Lawrence, J. J. (2014). A kinetic model for the frequency dependence of cholinergic modulation at hippocampal GABAergic synapses. *Math. Biosci.* 258, 162–175. doi: 10.1016/j.mbs.2014.09.013

Tang, A. H., Chen, H., Li, T. P., Metzbower, S. R., MacGillavry, H. D., and Blanpied, T. A. (2016). A trans-synaptic nanocolumn aligns neurotransmitter release to receptors. *Nature* 536, 210–214. doi: 10.1038/nature19058

Tennøe, S., Halnes, G., and Einevoll, G. T. (2018). Uncertainpy: a python toolbox for uncertainty quantification and sensitivity analysis in computational neuroscience. *Front. Neuroinformat.* 12:e94. doi: 10.3389/fninf.2018.00049

Testa-Silva, G., Loebel, A., Giugliano, M., de Kock, C. P. J., Mansvelder, H. D., and Meredith, R. M. (2012). Hyperconnectivity and slow synapses during early development of medial prefrontal cortex in a mouse model for mental retardation and autism. *Cereb. Cortex* 22, 1333–1342. doi: 10.1093/cercor/bhr224

Traynelis, S. F., Silver, R. A., and Cull-Candy, S. G. (1993). Estimated conductance of glutamate receptor channels activated during EPSCs at the cerebellar mossy fiber-granule cell synapse. *Neuron* 11, 279–289. doi: 10.1016/0896-6273(93)90184-S

Tsodyks, M. V., and Markram, H. (1997). The neural code between neocortical pyramidal neurons depends on neurotransmitter release probability. *Proc. Natl. Acad. Sci. U.S.A.* 94, 719–723. doi: 10.1073/pnas.94.2.719

Turner, D. A., and West, M. (1993). Bayesian analysis of mixtures applied to post-synaptic potential fluctuations. *J. Neurosci. Methods* 47, 1–21. doi: 10.1016/0165-0270(93)90017-L

Varela, J. A., Sen, K., Gibson, J., Fost, J., Abbott, L. F., and Nelson, S. (1997). A quantitative description of short-term plasticity at excitatory synapses in layer 2/3 of rat primary visual cortex. *J. Neurosci.* 17:7926. doi: 10.1523/JNEUROSCI.17-20-07926.1997

Walmsley, B., Edwards, F. R., and Tracey, D. J. (1988). Nonuniform release probabilities underlie quantal synaptic transmission at a mammalian excitatory central synapse. *J. Neurophysiol.* 60, 889–908. doi: 10.1152/jn.1988.60.3.889

Wang, Y., Markram, H., Goodman, P. H., Berger, T. K., Ma, J., and Goldman-Rakic, P. S. (2006). Heterogeneity in the pyramidal network of the medial prefrontal cortex. *Nat. Publ. Group* 9, 534–542. doi: 10.1038/nn1670

Williams, L. E., and Holtmaat, A. (2018). Higher-order thalamocortical inputs gate synaptic long-term potentiation via disinhibition. *Neuron* 101, 1–17. doi: 10.1101/281477

Zucker, R. S., and Regehr, W. G. (2002). Short-term synaptic plasticity. *Annu. Rev. Physiol.* 64, 355–405. doi: 10.1146/annurev.physiol.64.092501.114547

Conflict of Interest Statement: The authors declare that the research was conducted in the absence of any commercial or financial relationships that could be construed as a potential conflict of interest.

frontiers in Synaptic Neuroscience

REVIEW
published: 23 August 2019
doi: 10.3389/fnsyn.2019.00023

Interrogating Synaptic Architecture: Approaches for Labeling Organelles and Cytoskeleton Components

Sofiia Reshetniak[1,2]* *and Silvio O. Rizzoli*[1]

[1] *Institute for Neuro- and Sensory Physiology, Center for Biostructural Imaging of Neurodegeneration (BIN), University Medical Center Göttingen, Göttingen, Germany,* [2] *International Max Planck Research School for Molecular Biology, Göttingen, Germany*

Synaptic transmission has been studied for decades, as a fundamental step in brain function. The structure of the synapse, and its changes during activity, turned out to be key aspects not only in the transfer of information between neurons, but also in cognitive processes such as learning and memory. The overall synaptic morphology has traditionally been studied by electron microscopy, which enables the visualization of synaptic structure in great detail. The changes in the organization of easily identified structures, such as the presynaptic active zone, or the postsynaptic density, are optimally studied via electron microscopy. However, few reliable methods are available for labeling individual organelles or protein complexes in electron microscopy. For such targets one typically relies either on combination of electron and fluorescence microscopy, or on super-resolution fluorescence microscopy. This review focuses on approaches and techniques used to specifically reveal synaptic organelles and protein complexes, such as cytoskeletal assemblies. We place the strongest emphasis on methods detecting the targets of interest by affinity binding, and we discuss the advantages and limitations of each method.

Keywords: synapse, vesicles, cytoskeleton, actin, nanoscopy, super-resolution

OPEN ACCESS

Edited by:
John F. Wesseling, Institute of Neurosciences of Alicante (IN), Spain

Reviewed by:
Thomas A. Blanpied, University of Maryland, Baltimore, United States
Natali Lujan Chanaday Ricagni, Vanderbilt University, United States

***Correspondence:**
Sofiia Reshetniak
sofiia.reshetniak@med.uni-goettingen.de

Received: *06 June 2019*
Accepted: *02 August 2019*
Published: *23 August 2019*

Citation:
Reshetniak S and Rizzoli SO (2019) Interrogating Synaptic Architecture: Approaches for Labeling Organelles and Cytoskeleton Components. Front. Synaptic Neurosci. 11:23. doi: 10.3389/fnsyn.2019.00023

INTRODUCTION

Chemical synapses support neurotransmission by releasing neurotransmitter from the presynaptic side, and responding to it on the postsynaptic side. The presynaptic bouton, or terminal, has here a highly dynamic role, since it responds to activation via plasma membrane depolarization by forcing the fusion of synaptic vesicles to the membrane, which is followed by the diffusion of the neurotransmitter molecules to postsynaptic receptors. The synaptic vesicles, defined as small organelles with an outer diameter of approximately 40 nm which contain neurotransmitters and fuse to the plasma membrane upon stimulation (Schikorski and Stevens, 1997), are highly enriched in synaptic boutons, and are, in principle, not functional elsewhere. Along with vesicles, the boutons also contain several other organelles that are not necessarily specific for synapses, such as endosome-like structures (with which synaptic vesicles as well as other endocytic vesicles fuse and where, presumably, their cargo undergoes sorting) (Heuser and Reese, 1973), ribosomes (Crispino et al., 1997), smooth endoplasmic reticulum (ER), and mitochondria (Lysakowski et al., 1999; **Figure 1A**). While the constant presence of endosomes and components of the protein-synthesizing and -sorting machineries (endoplasmic reticulum, ribosomes) in pre-synaptic terminals throughout synaptic development is still heavily debated (Akins et al., 2009), the presence of mitochondria here has been well-established since the first electron microscopy observations of

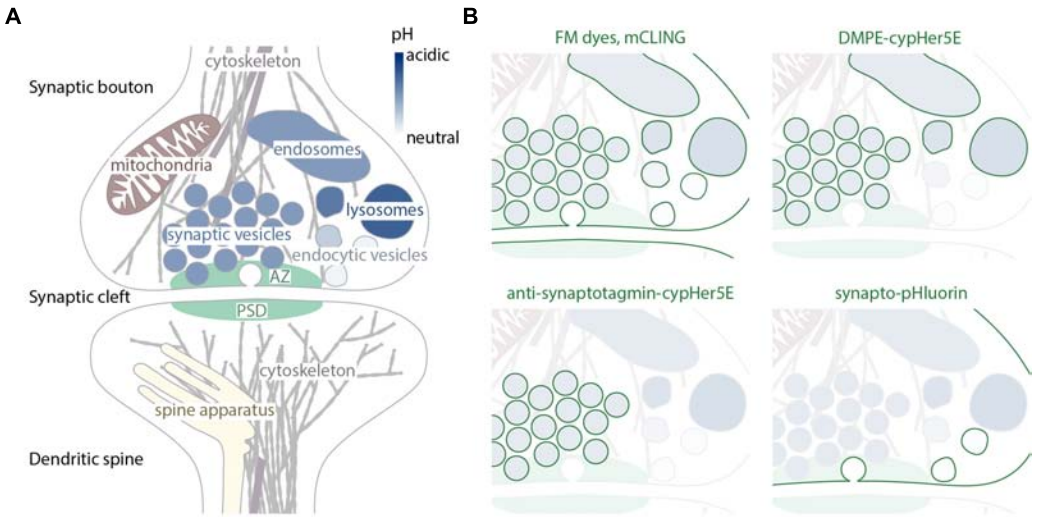

FIGURE 1 | Synaptic organelles and specificity of probes directed toward recycling membranes. **(A)** Schematic representation of main organelles present at the synapses. The pH level of endosomal components is visualized with different shades of blue. The different pHs aid in differential labeling by membrane probes, as shown in **(B)**. **(B)** Membranes that are labeled by different membrane-labeling tools highlighted in green, the identity of the organelles preserved from **(A)**.

synapses (Palay, 1956). Large mushroom spines tend to contain a specialized compartment, composed of multiple membrane stacks, known as the spine apparatus (Spacek and Harris, 1997; **Figure 1A**).

Apart from synaptic vesicles, two non-membrane bound structures can be considered synapse-specific organelles: the active zone and the post-synaptic density (**Figure 1A**). The active zone (AZ) of presynaptic terminals contains multiple proteins, including molecules involved in cellular adhesion, voltage-gated calcium channels, scaffold proteins, and multiple exocytosis co-factors. The AZ proteins regulate the docking, priming and fusion of synaptic vesicles (Südhof, 2012). AZs are apposed to post-synaptic densities (PSDs), which are protein-rich structures containing adhesion molecules, neurotransmitter receptors, adaptors (such as the PSD95 family proteins), and signaling proteins (Kaizuka and Takumi, 2018).

Cytoskeletal proteins found in the synapses include tubulin, actin, and septin (Wilhelm et al., 2014). Microtubules are known to form bundles along axons and bind presynaptic mitochondria (Chan and Bunt, 1978; Perkins et al., 2010; Graffe et al., 2015), synaptic vesicles (Bird, 1976), and to be positioned close to the plasma membrane and the active zone in the synaptic boutons (Gordon-Weeks et al., 1982). Actin is the most predominant component of the cytoskeleton and in presynaptic terminals two distinct populations of actin filaments are described. First, F-actin was shown to be a component of the active zone cytomatrix (Bloom et al., 2003), where it may form a barrier for vesicle release (Morales et al., 2000). Second, it has been also shown to surround synaptic vesicle clusters (Sankaranarayanan et al., 2003; Richards et al., 2004), where it is thought to contribute to vesicle recycling. In post-synapses actin forms a network of long linear and short branched filaments (Korobova and Svitkina, 2009) that reach the PSD where they may stabilize postsynaptic proteins (Allison et al., 1998; Kuriu et al., 2006).

Many synaptic components were discovered and studied using electron microscopy. The main advantage of this technique is its high resolving power that allows examining fine structures with nanometer precision. A crucial drawback, however, is its inability to reveal the identity of the structures. This has been addressed by labeling structures of interest using gold-conjugated antibodies raised against target proteins (immunoelectron microscopy) but such stainings often result in relatively low labeling densities.

A widely used approach to specifically visualize cellular components is to use genetically encoded fluorescent tags [such as green fluorescent protein (GFP) and its derivatives] fused to proteins of interest with consequent imaging with fluorescent microscopy. This requires protein overexpression or genome editing but results in a high labeling density, and enables live cell imaging of tagged molecules. The common problem associated with such an approach is impaired targeting or trafficking of tagged proteins, which can lead to a different behavior, and different subcellular localization, for the chimeric proteins when compared to native ones.

Nevertheless, the properties of most fluorescent proteins, in terms of intensity or stability during imaging, are sub-optimal, when compared to chemical dyes. This has raised substantially the interest in fluorescent probes that specifically bind to molecules of interest, and that can be conjugated to specific chemical dyes. Such elements are commonly used to visualize endogenous cellular components at their native locations, and enable investigators to exploit recent advances in super-resolution microscopy, thereby combining the two main advantages of the methods described above: labeling of cellular components with high specificity and efficiency, and nanometer resolution (Hell and Wichmann, 1994; Hofmann et al., 2005; Rust et al., 2006; Sharonov and Hochstrasser, 2006). Fluorescently labeled antibodies are the most commonly used tool in this approach, but many other probes have been developed for

labeling of different cellular organelles and components. In the following section we will discuss the most prominent ones, their mechanisms of action, main advantages, and disadvantages.

MATERIALS AND METHODS

Super-Resolution Microscopy Techniques

The probes we will discuss here were developed to be used in combination with light microscopy to specifically visualize certain organelles and structures. However, conventional imaging techniques have a significant disadvantage of not being able to resolve objects that are positioned closer than ∼200 nm to each other, due to the diffraction limit. Two types of approaches have been developed to overcome the diffraction barrier. First, the coordinate-targeted approach, which uses a patterned light beam to determine the coordinates from which fluorophores are permitted to emit. This approach is used by the stimulated emission depletion microscopy family (STED; Hell and Wichmann, 1994), and the saturated structured illumination microscopy family (SIM; Gustafsson, 2005). SIM currently reaches resolutions of ∼60–100 nm, while most STED applications in biology reach ∼40–50 nm. Second, the single-molecule based approach, which is based on the determination of the positions of single fluorophores that are allowed to emit randomly. This approach is typical of concepts such as photo-activated localization microscopy (PALM; Betzig et al., 2006), stochastic optical reconstruction microscopy (STORM and dSTORM; Rust et al., 2006; van de Linde et al., 2011), or ground state depletion microscopy followed by individual molecule return (GSDIM; Testa et al., 2010). This approach can reach a higher spatial resolution, typically of ∼20–30 nm in biological samples. Even higher resolution has been obtained with the MINFLUX concept (maximally informative luminescence excitation; Balzarotti et al., 2017). This technique combines a coordinate-targeted approach, such as used in STED microscopy, with single-molecule localization, as in PALM or STORM, and enables resolutions of ∼1–4 nm. Finally, super-resolution can also be achieved through physically expanding the specimen after embedding into a swellable gel (Chen et al., 2015). Resolutions of ∼20–70 nm have been attained with this approach (Chen et al., 2015; Chang et al., 2017; Truckenbrodt et al., 2018a).

Visualizing Synaptic Organelles Using Non-specific Membrane-Labeling Tools

With synaptic vesicles and endosomes being the most prominent and important organelles of the pre-synapse, many tools exists for their visualization (**Figure 1B**). These labels are often hydrophobic molecules capable to incorporate into or permeate the plasma membrane. One classical example is styryl dyes such as FM 1–43. They are molecules that are highly fluorescent in a hydrophobic environment of cellular membranes and have significantly lower quantum yield in aqueous solutions such as extracellular medium (Betz et al., 1992). Their ability to reversibly incorporate into outer leaflet of the plasma membrane but not to penetrate it makes them a perfect tool to study endo- and exocytosis in live cells. Upon addition to cells, FM dye molecules incorporate into the plasma membrane and some of them get internalized via endocytosis. When cells are washed and all FM dye molecules that remained in the outer leaflet of the plasma membrane are gone, the only source of fluorescence is the internalized vesicles whose recycling can be now followed by fluorescence microscopy. When these vesicles undergo exocytosis following stimulation, the fluorescence is lost again due to FM dye leaving the membrane for the aqueous extracellular solution (**Figure 2A**).

An interesting application of FM dyes has exploited the different molecular structures of these probes. Both FM 1-43 and FM 2-10 are green dyes, but the former is a larger molecule, and inserts more strongly into membranes. This renders it more difficult to wash from synaptic membranes (Pyle et al., 2000; Richards et al., 2000). A comparison between the wash-off (destaining) kinetics of the dyes can reveal endocytosis intermediates, such as infoldings, that remain open on the plasma membrane after stimulation. Such intermediates lose FM 2–10, as this dyes is easily washed off, but not FM 1–43 (Richards et al., 2000). The FM 1–43 retained in vesicles or in endocytosis intermediates can be quenched by adding to the buffers small molecules such as bromphenol blue (Harata et al., 2006), thereby providing further information on the different vesicle recycling modalities.

In addition to fluorescent properties, FM dyes can be used in electron microscopy due to their ability to undergo photoconvertion (or photo-oxydation). Upon strong illumination in the presence of diaminobenzidine, a dark precipitate is formed where FM dye is located making it visible in electron microscopy. This allows even higher resolution for imaging of structures labeled with FM dye (Denker et al., 2009, 2011; Hoopmann et al., 2012).

The chemical structure of FM dyes does not allow them to be fixed by aldehyde-based fixatives, which renders it problematic to use them in combination with immunostainings (**Figure 2B**). They are often lost from trafficking organelles, and can even be trapped in other cellular compartments after fixation (Revelo et al., 2014). Fixable variants of FM dyes containing single amine functional groups were developed to overcome this difficulty (e.g., FM 1–43FX), but they are still poorly fixed by common fixatives, and are also not optimized for use in super-resolution microscopy. These problems have beed solved with development of the membrane-binding fluorophorecysteine-lysine-palmitoyl group (mCLING). mCLING consists of a fluorophore bridged to a palmitoyl tail by an octapeptide. Six lysines of the peptide allow the probe to be fixed by aldehydes thus preventing its loss from the membrane or mislocalization post-fixation (Revelo et al., 2014).

Both styryl dyes and mCLING have a common disadvantage: they are not specific for any particular organelle and stain all vesicles that undergo recycling of membranes, as well as the plasma membrane (**Figure 1B**). This issue can be partially solved by usage of lipid-based pH-sensitive labels. Dyes such as cypHer5E are highly fluorescent in acidic environments and are quenched at a neutral pH. If conjugated to phospholipids

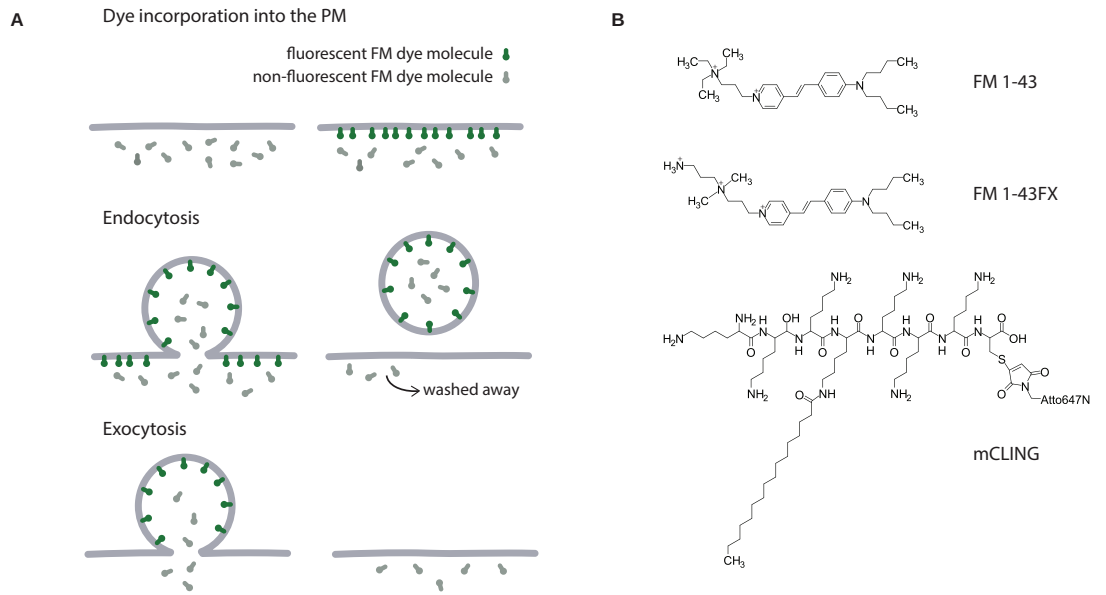

FIGURE 2 | Tools for visualizing recycling vesicles. **(A)** The mechanism of styryl dyes action. Colored and gray shapes represent fluorescent and non-fluorescent FM molecules, respectively. Upon addition to cellular medium, FM dye incorporates into the outer leaflet of the PM and becomes fluorescent. Following endocytosis, these fluorescent molecules are trapped in recycling vesicles, while unspecific signal from the PM can be eliminated by washing the cells. Since FM dye incorporation into the membrane is reversible, after the vesicle is fused with the PM during exocytosis, the fluorescent signal is lost again. **(B)** Chemical structures of FM 1–43, FM 1–43FX, and mCLING.

they can get incorporated into the plasma membrane just like FM dyes, but remain non-fluorescent there. Only after the dye is internalized and reaches a lumen of an acidic organelle such as a late endosome or a synaptic vesicle, it becomes fluorescent allowing visualization of the organelle (Kahms and Klingauf, 2018). As soon as the vesicle undergoes exocytosis exposing the pH-sensitive dye to a neutral environment of the extracellular fluid, the fluorescence disappears again. While allowing the investigator to differentiate between the plasma membrane, coated vesicles, and endo-lysosomal system or synaptic vesicles, this approach is unable to distinguish different organelles that have the same luminal pH (**Figure 1B**).

One note of caution in using lipid dyes that insert in the plasma membrane, as the ones presented here, is that they could, in principle, affect membrane tension, and may therefore influence synaptic vesicle fusion. One study suggested this for FM 4–64 (Zhu and Stevens, 2008), by comparing synaptic release in presence and in absence of the dye. However, the effects noted were mild, and could also be attributed to a Förster Resonance Energy Transfer (FRET) effect taking place between the green reporter used here to measure exocytosis and the red FM 4–64. Overall, this suggests that such dyes are relatively "safe" tools to use for synaptic investigations, albeit one should aim to use low concentrations. Low concentrations are also useful in reducing phototoxicity. The FM dyes have a low photostability, which renders them excellent tools for photo-oxydation, as mentioned above, but reduces their applicability to long-term live imaging. Complex live imaging experiments, such as measurements of single-vesicle dynamics, can be performed (Zenisek et al., 2000, 2002), but long imaging periods should be avoided, especially as photodamage to the cells takes place several minutes before significant photobleaching can be observed, in our experience.

Increasing Specificity by Using Antibodies Directed to Epitopes Exposed on the Cell Surface

To specifically visualize particular organelles one can turn to affinity tools. A classical approach of labeling synaptic vesicles is use of fluorescently labeled antibodies against luminal domain of synaptotagmin (Matteoli et al., 1992). High specificity and affinity of antibodies to the target proteins ensure specific labeling of desired organelles even after they undergo membrane recycling. Usage of antibodies against a luminal domain of the protein allows tracking vesicle trafficking in live cells, as the antibodies can be added to the cellular medium and internalized via endocytosis. The antibodies can be coupled to various fluorophores to fit requirements for specific experiment and microscopy method used. For example, the pH-sensitive dye cypHer5E, which we described above, can be used to follow synaptic vesicle when coupled to a luminal domain of a synaptic vesicle protein synaptotagmin (**Figures 1B**, **3**). Since cypHer5E is only fluorescent in the acidic environment of synaptic vesicles and is quenched at the neutral pH of extracellular medium, it can specifically reveal the exocytosis of synaptic vesicles when bound to a synaptic vesicle protein (Martens et al., 2008; Hua et al., 2011). It is important to note, however, that some antibodies might affect protein distribution and trafficking in live cells. Thus, rabbit polyclonal antibodies against the luminal domain of

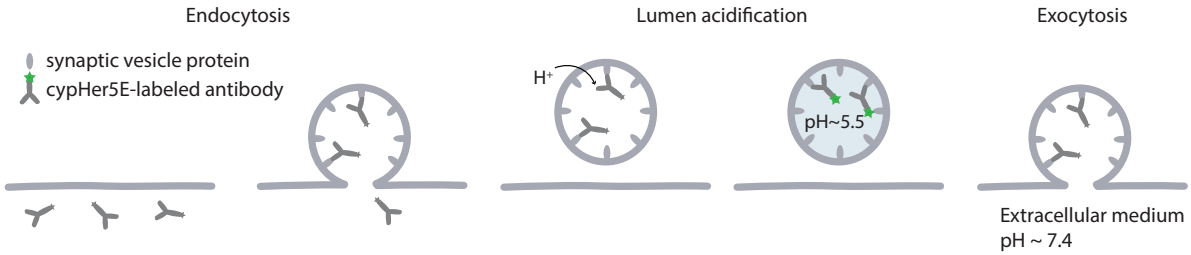

FIGURE 3 | CypHer5E as a tool to visualize the synaptic vesicle cycle. CypHer5E is a pH-sensitive fluorophore that can be coupled to antibodies against the luminal domain of synaptic vesicle proteins. Following exocytosis, the luminal domains of the antibodies are exposed to the extracellular medium and the antibodies can bind them. At the neutral pH of the extracellular medium, the fluorophore is quenched. When the luminal pH is lowered after endocytosis, the fluorophores bound to the synaptic vesicle proteins through respective antibodies become fluorescent and allow visualization of internalized vesicles. When such a vesicle fuses with the plasma membrane during synaptic activity, the fluorescence is lost again.

synaptotagmin 1 have been suggested to alter synaptic function (Afuwape et al., 2017). At the same time, mouse antibodies against the same target, which are usually used for vesicle tracking experiments (Matteoli et al., 1992; Kraszewski et al., 1995; Sara et al., 2005; Fernández-Alfonso et al., 2006; Wienisch and Klingauf, 2006; Hua et al., 2010), have not been reported to have such an effect, and do not perturb vesicle trafficking even when used for several days (Truckenbrodt et al., 2018b).

Strong and selective binding of antibodies to the target proteins makes them also a useful tool for long-term imaging. When labeled with a bright and photo-stable reporter such as a quantum dot, they can be used for prolonged observation of organelles (Park et al., 2012) or even single molecules such as postsynaptic receptors (Dahan et al., 2003; Groc et al., 2004). To visualize the organelles, quantum dots must be coupled to the antibodies against the luminal domains of the synaptic vesicle proteins, as in the case of cypHer5E-labeled antibodies. This is often achieved through usage of biotinylated secondary antibodies and streptavidin-coated quantum dots. Alternatively, quantum dots can be directly coated with secondary antibodies. When the luminal domain of the synaptic vesicle protein faces the extracellular medium after exocytosis, the antibodies and the quantum dots can label the inside of the vesicle. They are then internalized together with the target protein, resulting in the newly formed synaptic vesicle being loaded with the quantum dot. This has been used to visualize endocytosis (Hoopmann et al., 2010) as well as single exocytic events (Zhang et al., 2009; Park et al., 2012). To track plasma membrane proteins, quantum dots are coupled to antibodies against extracellular domains of the target proteins. This allows following diffusion of single post-synaptic receptors in the plasma membrane of a live neuron (Tardin et al., 2003; Howarth et al., 2005; Bannai et al., 2006; Chang et al., 2012; Wang et al., 2016; Taylor et al., 2018). Physical and optical properties of quantum dots allow the observation of the labeled structures for minutes without considerable photobleaching, what is usually difficult to achieve with the use of most organic dyes and especially genetically encoded fluorophores such as GFP. Additionally, since quantum dots are electron-dense, they can, in principle, be used for the visualization of the structure of interest in the electron microscopy. By their nature, quantum dots are hydrophobic and also toxic to the cell, so have to be coated with shells of polar substances to make them water-soluble and compatible with biological specimens (Dubertret et al., 2002). In addition to these shells, quantum dots have to be covered with streptavidin and antibodies layers, increasing their size substantially. While the fluorescent core might be as small as 2 nm, the total size of the label can reach 20–40 nm (Michalet et al., 2005), which is comparable with the width of the synaptic cleft and the synaptic vesicle diameter (**Figure 4**). This limits quantum dots' ability to penetrate synaptic cleft, resulting in labeling of mainly extrasynaptic population of membrane proteins, and can affect diffusion of the labeled proteins (Lee et al., 2017; Delgado and Selvin, 2018). Hence, special care must be taken when designing an experiment with the use of quantum dot labeling, to ensure that the quantum dots are of a suitable size to effectively label proteins in the desired compartment, and to avoid causing significant changes to the location and trafficking of the proteins.

Identifying Organelles by Specific Cell-Permeable Labels

All probes discussed above bind at the outer surface of the plasma membrane and must be endocytosed to label organelles of interest, where they remain attached to the luminal surface of the membrane. This approach cannot be used to visualize organelles that are not involved in direct membrane exchange with the plasma membrane, such as lysosomes or mitochondria. Cell-permeable labels that accumulate in the organelles of interest were developed to label these.

To label lysosomes, acidotropic dyes such as neutral red, acridine orange, DAMP (N-(3-[2,4-dinitrophenyl amino] propyl)-N-(3-aminopropyl)methylamine), and LysoTracker can be used. They are able to penetrate cellular membranes, but after getting protonated at acidic pH of lysosomes they lose this ability and are unable to escape the organelle (Wiederschain, 2011). Similarly to pH-sensitive dyes, most acidotropic molecules cannot discriminate between different organelles and accumulate in any organelle that has low pH. Additionally, DAMP is not fluorescent, and therefore has to be visualized by fluorophore-coupled antibodies, thus making it unsuitable for live cell studies. LysoTracker® (Thermo Fisher Scientific) is the most commonly

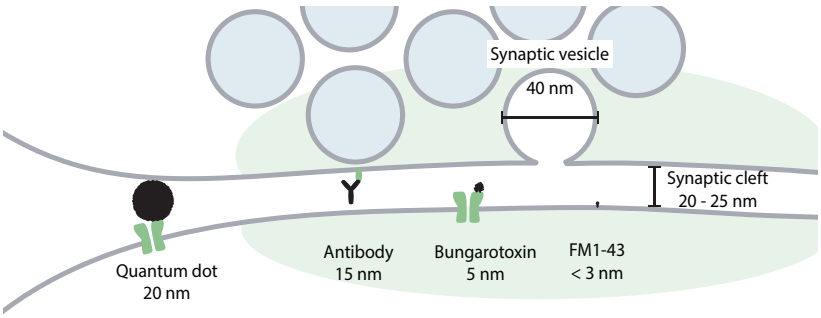

FIGURE 4 | Comparison of the size of quantum dots with synaptic structures and other probes used to label the plasma membrane, recycling membranes, or membrane receptors in the synapse. Realistic sizes are presented for all labels. For quantum dots we assume that their core is covered by a streptavidin layer, to which antibodies are then attached.

used tool for labeling lysosomes and is commercially available in various colors, making it suitable for multi-color imaging. While LysoTracker can be used for live imaging, it induces lysosomes' alkylation following longer incubation periods and thus can only be used for shorter periods of time. Similar to LysoTracker, LysoSensor™ probes (Thermo Fisher Scientific) also accumulate in acidic organelles, but, additionally, they also exhibit changes in fluorescence intensity in reaction to changes in pH, making it possible to observe lysosomes dynamic and biogenesis (Diwu et al., 1999).

For labeling of mitochondria, membrane-potential-dependent dyes such as rhodamine 123, tetramethylrhodamine methyl ester (TMRM), and tetramethylrhodamine ethyl ester (TMRE) can be used. They are cell-permeable dyes that accumulate in mitochondria in response to mitochondrial transmembrane potential. These dyes are highly fluorescent in the inner mitochondrial membrane but are self-quenched in mitochondrial lumen. Since their retention in mitochondria depends on the membrane potential, they can only be sequestered by active mitochondria and are washed away from dead and fixed cells (Scaduto and Grotyohann, 1999). MitoTracker® (Thermo Fisher Scientific) is a similar label that has an additional chloromethyl moiety, which reacts with thiols in mitochondria keeping MitoTracker associated with mitochondria even after fixation (Poot et al., 1996).

Similar membrane-permeable probes for labeling of endoplasmic reticulum have also been developed. Commercially available ER-Tracker™ Green and Red (Thermo Fisher Scientific) contain glibenclamide moieties that bind to the sulfonylurea receptors of ATP-sensitive K^+ channels (Hambrock et al., 2002), commonly found in ER (Smith et al., 2007), while ER-Tracker Blue-White DPX selectively labels ER through an unexplained mechanism. All of these labels penetrate cellular membranes and have been used to image ER in live neurons (Bannai et al., 2004; Choi et al., 2006; Gallego-Sandín et al., 2009; Tucker et al., 2016). Another probe, called ER Thermo Yellow enables ER staining in live and fixed cells and, in addition, enables monitoring temperature changes inside ER (Arai et al., 2014). Fluorescent flavonoids have been also shown to be a potential tool for ER visualization with minimal toxicity (McDonald et al., 2016), but have gained little popularity so far. Finally, NH_2-BODIPY is a new probe that can be used for labeling of ER in both live and fixed cells and imaged with STED microscopes (Sekhar et al., 2019), providing a valuable option for super-resolution studies of ER in fixed cells, without the need to express ER markers fused to fluorescent proteins or immunostainings.

Visualisation of Other Synapse-Specific Structures

All discussed above probes for the visualization of membranous compartments rely on binding to epitopes as they are exposed during the fusion of the compartments to the plasma membrane, or become trapped in the respective compartments due to their specific transmembrane potentials or luminal pH values. Synapse-specific structures from the cytosol, such as the AZ and PSD, cannot be labeled by a similar approach, and their visualization remains limited to the use of antibodies or GFP chimeras. AZs are often visualized by labeling scaffold proteins RIM1, Piccolo and Bassoon (Dani et al., 2010; Nishimune et al., 2016; Schoen et al., 2016; Truckenbrodt et al., 2018a; Heller et al., 2019). In the case of PSD, the most commonly targeted soluble proteins are scaffolds PSD-95, Shank and Homer proteins. By employing super-resolution imaging and antibody stainings or fluorescent protein fusions, they can be visualized in fixed or live cells to report the localization and organization of the PSD (Dani et al., 2010; MacGillavry et al., 2013; Tao-Cheng et al., 2014; Broadhead et al., 2016). Other commonly labeled epitopes include the cytosol-exposed or extracellular domains of neuroligins and of postsynaptic AMPA, NMDA, GABA, and Glycin receptors. They can be labeled by antibodies, or monomeric streptavidin [when tagged with a biotinylation substrate peptide (Liu et al., 2013; Chamma et al., 2016a; Lee et al., 2017)]. Many can be also targeted in live cells (Schapitz et al., 2010; Ladepeche et al., 2013; Liu et al., 2013; Nair et al., 2013; Specht et al., 2013; Bannai et al., 2015; Chamma et al., 2016a; Jézéquel et al., 2017; Lee et al., 2017; Mikasova et al., 2017; Patrizio et al., 2017; Choquet, 2018; Haas et al., 2018). ER in dendritic spines can be revealed if actin binding protein synaptopodin, which is also known to be associated with the spine apparatus,

is targeted by fluorescent protein fusion or immunostaining (Mundel et al., 1997; Deller et al., 2000; Orth et al., 2005; Vlachos et al., 2009). In addition to antibodies, an increasing selection of smaller probes, including nanobodies (Vincke and Muyldermans, 2012), becomes available for improved imaging of synaptic proteins with super-resolution microscopy. Nanobodies against SNAP25, syntaxin 1, Homer 1, gephyrin, alpha-synuclein, vGLUT and several other proteins have been developed (Lynch et al., 2008; Schenck et al., 2017; Dong et al., 2019; Maidorn et al., 2019), enabling labeling of these proteins in cells without the need to overexpress them.

Probing Synaptic Structure by Using Natural or Chemically Derived Toxins

An alternative to antibodies that allows very specific recognition and hence makes effective labeling of target proteins in the synapse possible is neurotoxins. Naturally used by venomous predators to paralyze or kill their prey as quick as possible, neurotoxins evolved to bind strongly and highly selectively to their targets, making them a useful tool for visualization of these proteins. Some neurotoxins and their chemical analogs have been used for investigation of postsynaptic receptors for decades (Adams and Olivera, 1994). One such an example is bungarotoxin – a short protein toxin found in the venom of snakes from the genus *Bungarus*. Kappa-bungarotoxin is a variant specific to nicotinic acetylcholine receptors in neurons, which, when appropriately labeled, can reveal localization of the acetylcholine receptors in the post synaptic terminals (Chiappinelli, 1983). Fluorescently labeled alpha-bungarotoxin is commonly used for imaging of the alpha-subunit of the nicotinic acetylcholine receptor in neuromuscular junctions (Anderson and Cohen, 1977; Borodinsky and Spitzer, 2007; Fricker et al., 2013) and is commercially available in variety of colors from different manufacturers. It has also been shown to bind the acetylcholine receptor in post-synapses of neurons (Colquhoun and Patrick, 1997) and used for imaging of the receptors *in vivo* (McCann and Lichtman, 2008). Besides acetylcholine receptors, alpha-bungarotoxin was also used for studying AMPA receptor and GABA receptors localization and trafficking in neurons (Sekine-Aizawa and Huganir, 2004; Wilkins et al., 2008; Brady et al., 2014). In the latter studies, the alpha-bungarotoxin-binding site was fused to the proteins of interest, to enable the toxin to recognize receptors it usually does not bind to. This makes the bungarotoxin-binding site an affinity tag which, in principle, can be used for specific visualization of any membrane protein as long as adding this tag does not change the receptor targeting and trafficking.

Another group of neurotoxins that started to be used for postsynaptic receptor visualization more recently is conotoxins – small peptides of 10–30 amino acids found in the venom of the *Conum* snails. Various types of conotoxins were identified, each having a high affinity to a different target protein, including nicotinic acetylcholine receptors (Nicke et al., 2004), voltage-gated sodium channels (Leipold et al., 2005), potassium channels (Shon et al., 1998), and calcium channels (Nielsen et al., 2000). These small peptides can be conjugated chemically to fluorescent dyes and used as small probes to label respective proteins (Vishwanath and McIntosh, 2006). Very similar in structure, a component of deathstalker scorpion venom chlorotoxin has high affinity for chloride channels (DeBin et al., 1993). Many other scorpion venom components are used to study channels and receptors and can also be produced as recombinant fluorescent proteins to be used in microscopy (Kuzmenkov et al., 2016). While these toxins provide very high affinity and specificity, working in nano- and picomolar concentrations and being able to distinguish between very similar classes of receptors, their small size often makes it difficult and expensive to label them with fluorescent reporters, thus limiting their use.

Labeling Proteins With Small Affinity Tags

When no specific binder exists for a target protein, and fusion with a fluorescent protein has to be avoided, small peptide tags can be used to specifically visualize such proteins. They are short sequences of several amino acids that can be fused to any protein of interest and then targeted by a strong specific binder. The FLAG-, HA-, and myc-tags (Evan et al., 1985; Hopp et al., 1988; Wilson et al., 2005) are ones of the most commonly used affinity tags in imaging. Due to their small size (∼1.1 kDa) they are not expected to drastically affect the proteins' traffic or function, and can be visualized by any imaging method following a staining with antibodies labeled with a suitable fluorophore. To increase the brightness of labeling, several copies of one tag can be fused to a protein, resulting in several antibodies binding to one target. When expressed on the extracellular domains of the plasma membrane proteins, these tags can be used for live cell imaging and tracking, as in the case of discussed above bungarotoxin-binding sites. However, the bivalency of the antibodies might introduce artifacts caused by protein clusters formation. The large size of the antibodies also restricts their ability to penetrate into confined and crowded environments, and can affect protein trafficking when applied to live cells. To solve these issues, smaller monovalent binders can be used. One possible alternative is monomeric streptavidin (Chamma et al., 2016a). To be recognized by streptavidin, the target protein must be fused to a 15 amino acid biotinylation substrate peptide (AP-tag). When biotin and biotin ligase are added to the cellular medium, the AP-tag is biotinylated and can be specifically bound by streptavidin. In addition to having an advantage of not cross-linking the target proteins, monomeric streptavidin is also substantially smaller in size compared to antibodies or monovalent streptavidin, decreasing the influence of large label on protein trafficking. This approach has been used to visualize several synaptic proteins including neuroligin, neurexin, stargazin, and LRRTM2 (Liu et al., 2013; Chamma et al., 2016a,b). Small tags that are detected by nanobodies directly, without the use of biotin, have also been developed recently (for example Virant et al., 2018).

Visualizing Synapse Volume and Activity

Most labels described above allow to specifically reveal distinct organelles or proteins. To visualize the overall synapse

morphology and volume, probes with lower specificity can be used. Calcium imaging is a classical approach, since it does not specifically label any of the synaptic components, but allows visualizing both the synaptic volume and synaptic activity. Synaptic physiology relies heavily on the calcium concentration: in the presynapse it triggers synaptic vesicle exocytosis, while in the post-synapse it regulates synaptic plasticity. Calcium imaging allows monitoring intracellular changes in the calcium concentration by the use of calcium indicators – molecules whose fluorescence changes upon binding to calcium (reviewed in Grienberger and Konnerth, 2012). Calcium indicators can be a useful tool to visualize synapse volume since due to not being specific to any organelles, they fill the whole synapse, effectively illuminating the total synaptic volume. Many calcium indicators with different modes of action exist and can be divided into two groups: genetically encoded and synthetic indicators. The first indicator to be used was the bioluminescent protein aequorin, which emits blue light upon binding to calcium without the need of excitation by light (Shimomura et al., 1962). Multiple different genetically encoded calcium sensors exist (Lin and Schnitzer, 2016). Some, such as Yellow Cameleon, rely on Förster resonance energy transfer (FRET) to function. Yellow Cameleon is a chimeric protein consisting of a calcium-bindng protein calmodulin, a calmodulin-binding peptide and to two fluorescent proteins: ECFP and Venus. Upon binding to calcium, calmodulin undergoes conformational changes that bring ECFP and Venus close enough to enable FRET, effectively shifting emitted light from blue to green (Nagai et al., 2004). The second group of genetically encoded calcium indicators includes proteins with a single fluorophore. One example is GCaMP family of proteins. These proteins consist of EGFP flanked on different sides by calmodulin and a calmodulin-binding peptide. Conformational changes in presence of calcium lead to an increase of the fluorescence intensity (Nakai et al., 2001). Newer genetically encoded calcium sensors have been developed to provide wider color selection and smaller size. Most genetically encoded calcium dyes emit green light, but a few variants with other wavelengths also exist, such as blue B-GECO (Zhao et al., 2011), red R-CaMP2 (Inoue et al., 2015), R-GECO (Zhao et al., 2011), jRCaMP1 and jRGECO1 (Dana et al., 2016), and near-infrared NIR-GECO1 (Qian et al., 2019) and GAF-CaMP2 (Subach et al., 2019). NTnC is a recently developed small and bright calcium indicator that combines the sensing part of FRET sensors with reporting domain of single fluorophore sensors (Barykina et al., 2016). Genetically encoded calcium sensors can be used for calcium imaging in cultured cells following transfection, or in transgenic animals where their expression can be specifically targeted to neural cells and can be maintained over long time periods. However, creating and maintaining such transgenic lines can be time-consuming and expensive. Synthetic indicators are small chemicals that consist of a chelating site which is binding calcium ions, and fluorescent chromophore part which emits light. Examples of such indicators include Quin, Fura, Oregon Green and Fluo calcium dyes. Upon binding to calcium these indicators display changes in fluorescence intensity and/or shift in peak excitation or emission wavelength (Paredes et al., 2008). Ratiometric indicators such as Fura-2 show a change in the excitation wavelength upon calcium binding and allow quantitatively measurements of intracellular calcium concentration that are not affected by the probe concentration. Synthetic calcium dyes are available in a large variety of spectral characteristics and different affinities to calcium (Takahashi et al., 1999), do not require transfection to be delivered in the cells and thus allow for faster experimental procedures, however, are usually expelled from the cells during long experiments and hence are difficult to use for long-term imaging, as well as cannot be targeted to a specific cell type (Paredes et al., 2008). An important point of consideration when using both genetically encoded and synthetic calcium dyes is their possible cytotoxicity. Due to their binding to calcium, calcium sensors act as calcium buffers, effectively decreasing the free calcium concentration in the cells, which can lead to significant changes in the cellular physiology, especially in the context of synaptic activity where calcium plays crucial role (McMahon and Jackson, 2018).

Apart from calcium imaging, multiple approaches were developed to visualize synaptic activity (Lin and Schnitzer, 2016; Deo and Lavis, 2018). These include voltage, neurotransmitter and vesicle fusion sensors. To monitor changes in the membrane potential, both small organic molecules such as cyanine dyes (Miller, 2016) or VoltageFluor (Woodford et al., 2015), and genetically encoded sensors (for example based on a voltage-sensitive phosphatase, St-Pierre et al., 2015) can be used. Molecules that display an increase in the fluorescence intensity upon binding to a neurotransmitter (e.g., ExoSensor, Klockow et al., 2013) or genetically encoded sensors containing a neurotransmitter-binding domains of natural proteins (e.g., FLIPE, Okumoto et al., 2005) are employed to directly detect neurotransmitters. Alternatively, synaptic vesicle exocytosis can be visualized as a measure of synaptic activity. This is achieved through usage of FM dyes or of fluorescent neurotransmitters. The latter mimic natural neurotransmitters, are loaded into the synaptic vesicles, and are released during synaptic activity. By following the fluorescence of these false neurotransmitters one can visualize synaptic vesicle release, just as for the FM dyes (Gubernator et al., 2009).

The most commonly used tools for measuring synaptic release are currently pH-sensitive variants of GFP (pHluorins). Synapto-pHluorin is a pHluorin sensor based on synaptic vesicle protein VAMP2, and is ∼10-fold more fluorescent at neutral pH than in the acidic environment of the synaptic vesicles. Synapto-pHluorin localizes to the synaptic vesicles and emits light only after the vesicle is exocytosed, when the fluorescent protein is exposed to the neutral pH of the extracellular medium (Sankaranarayanan et al., 2000; **Figure 1B**).

Visualizing the Synaptic Cytoskeleton: Affinity Tools

Widely used for other cellular components, GFP fusions and antibody stainings have been less effective for visualization of cytoskeletal filaments. The common major problem is that both approaches result in labeling of both monomers and cytoskeletal filaments (**Figures 5A,C**), decreasing the apparent signal to noise ratio. This problem is relatively easily solved

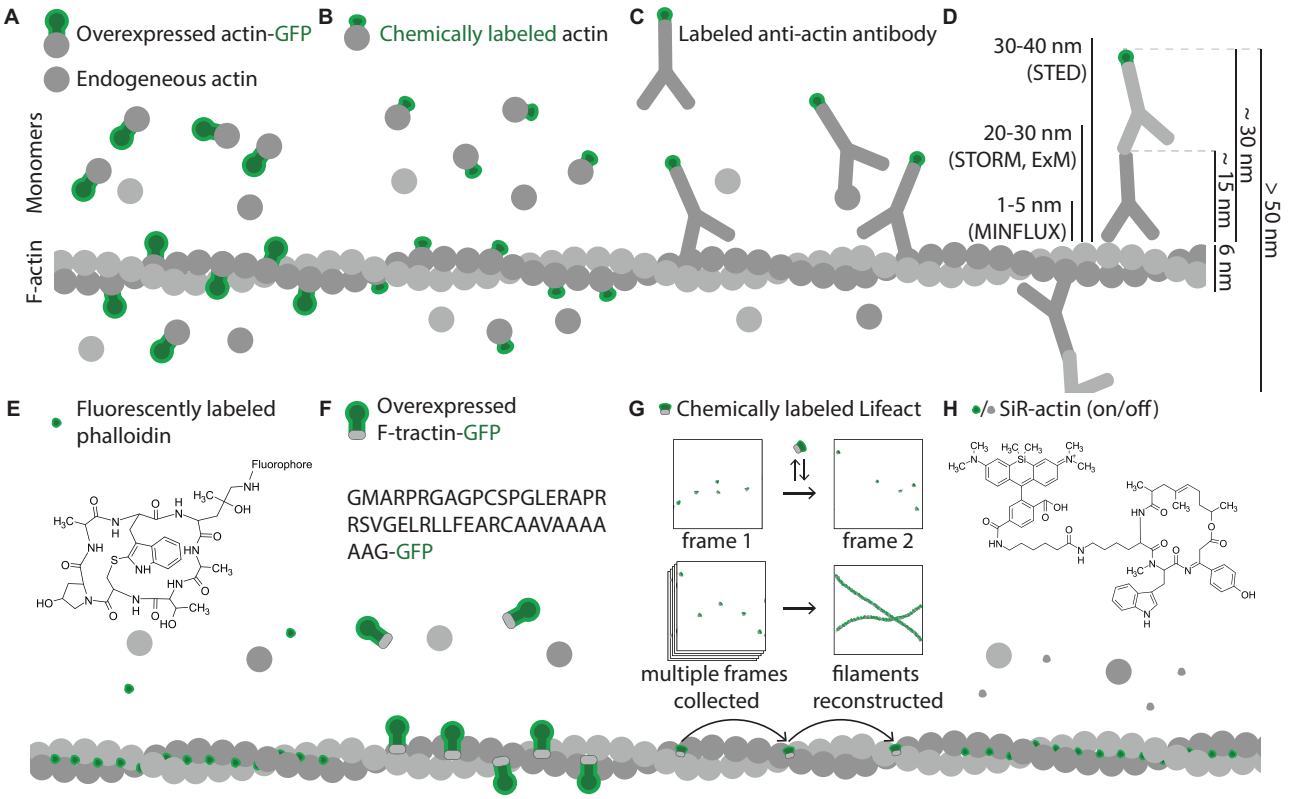

FIGURE 5 | Commonly used actin probes. Green shapes represent fluorescent moieties; all molecules shown in different shades of gray are non-fluorescent and hence are invisible under fluorescent microscope. Size differences of the shapes approximately represent size differences of the molecules. **(A)** Ectopically expressed actin-GFP partially incorporates into actin filaments but also contributes to background fluorescence from monomeric actin-GFP molecules and increases the concentration of the monomers. **(B)** Due to small size of dyes, chemically labeled actin has higher polymerization ability, however, still displays significant background fluorescence from monomers and also increases the concentration of actin monomers. **(C)** Density of antibody labeling depends on epitope accessibility and is significantly restricted by large size of antibody molecules, which also introduces large linkage errors; background fluorescence observed from antibodies bound to actin monomers in solution. **(D)** Comparison of fluorophore displacement from targeted epitope caused by common immunostaining procedures with resolution abilities of modern super resolution methods. When a combination of primary and secondary antibodies is used to image an actin filament, fluorophores of antibodies that recognize neighboring actin subunits might be located more than 50 nm apart (10 times larger distance then a thickness of an actin filament). Modern microscopy techniques can resolve objects that are as close as few nanometers apart, so usage of such large probes leads to significant loss of advantages super-resolution methods can offer. **(E)** Phalloidin is a small chemical that binds exclusively F-actin with high specificity and affinity, shows high density of labeling and low background signal. **(F)** Genetically encoded actin binders (F-tractin illustrated as an example) fused to GFP bind F-actin *in vivo*. Unbound molecules contribute to background fluorescence, but the concentration of actin monomers is not changed. **(G)** Low affinity of Lifeact binding to F-actin can be used for certain types of super resolution microscopy. Here Lifeact coupled to a dye acts as an exchangeable probe. Multiple frames are collected with Lifeact molecules having different locations in different frames. Post-imaging processing allows reconstructing F-actin architecture from all individual Lifeact locations. **(H)** SiR-actin is cell membrane-permeable, specifically labels F-actin and additionally has low fluorescence when not bound to F-actin (off state) but cannot be fixed by aldehydes.

for antibody stainings in fixed samples by detergent treatments that remove most soluble proteins, but is prominent when overexpression of monomers fused to fluorescent proteins is used, since chimeric proteins are less likely to get incorporated in the filaments (Westphal et al., 1997). As a result, significant fraction of the fluorescence comes from the free monomers, while cytoskeletal filaments are only partially labeled as they mainly consist of native proteins that are not labeled by the fluorescent protein (**Figure 5A**). To increase polymerization ability and decrease effects of bulky GFP, the monomers can be coupled to small chemical fluorophores instead of overexpression as GFP fusion (Kellogg et al., 1988). This approach requires technically challenging microinjections to be performed to deliver labeled monomers into the cells and does not result in high density of labeling since fluorophore-coupled monomers just like the ones labeled with fluorescent proteins are less likely to polymerize than native endogenous proteins (**Figure 5B**; Kovar et al., 2006). In addition, both approaches change the native concentration of actin monomers in the cell, while most physiological processes requiring actin polymerization still rely on buffering by endogenous unmodified actin. Multiple effects of GFP fusions on actin dynamics have been reported (Aizawa et al., 1997; Feng et al., 2005; Deibler et al., 2011), rendering live-cell measurements of actin dynamics based on labeled actin monomers to some extent unrepresentative of the physiological situation. Nonetheless, it remained to be one of the most popular approaches to visualize actin in live cells for years since it's easy to perform, and many insights in cytoskeleton dynamics were

obtained by utilizing fusions with fluorescent proteins (Doyle and Botstein, 1996; Westphal et al., 1997; Lorenz et al., 2004; Dovas et al., 2009, 2011; Flynn et al., 2009; Oser et al., 2009; Francis et al., 2011; Koskinen and Hotulainen, 2014; Lei et al., 2017).

To make GFP-based labeling more specific to cytoskeletal structures, filament-binding proteins can be targeted instead of cytoskeletal proteins themselves. This is a common approach to label F-actin and GFP-fusions of actin-binding domains are often used to reveal actin cytoskeleton. Examples of such domains will be discussed in detail later. Similarly, to track microtubule dynamics, it is common to label plus-end-tracking proteins with GFP instead of tubulin itself (Stepanova et al., 2003; Yau et al., 2016). Also, targeting with antibodies native proteins that bind cytoskeletal elements, but do not form filaments, can be useful for the visualization of some features of cytoskeleton. Thus, anti-spectrin antibodies are commonly used for visualization of the neural membrane-associated periodic skeleton (Xu et al., 2013; D'Este et al., 2015, 2016; He et al., 2016; Vassilopoulos et al., 2019), and expression of spectrin-GFP allowed to visualize this structure in live cells (Zhong et al., 2014).

While immunostained microtubules can be imaged well with diffraction limited imaging techniques, many observations of microtubules with super resolution microscopy revealed that antibodies are not able to provide sufficiently high quality of staining. The density of labeling achieved by antibodies is low enough for modern imaging techniques to resolve single fluorophores along the microtubules. This results in a single microtubule appearing as a row of separate aligned objects instead of one continuous filament or creates an impression of microtubules being interrupted (Bossi et al., 2008; Huang et al., 2008; Heilemann et al., 2009; Wildanger et al., 2009a; Gould et al., 2011). The same is also observed in the case of neurofilaments (Hell, 2007; Wildanger et al., 2009b) which are in some cases cannot even be seen as rows of aligned objects but rather a set of randomly placed dots, making it impossible to make any conclusions about neurofilament cytoskeleton architecture (Donnert et al., 2006; Rankin et al., 2008). Even conventional imaging can show that most neurofilament antibodies do not provide a high quality of staining. In contrast, many anti-tubulin antibodies are known to have high affinity and specificity for tubulin. Their low labeling density can be attributed to the large size of the antibodies, which does not allow them to bind many of the epitopes, due to steric hindrance.

Another crucial drawback of the antibodies caused by their large size is the fact that they introduce a substantial linkage error what makes them unsuitable for super-resolution studies of such fine structures as cytoskeletal filaments. Actin filaments, for example, have a diameter of ∼5 nm, while conventional antibodies have a size of ∼15 nm, placing the fluorophore at a several-fold larger than the thickness of the filament itself distance from the filament. With recent super resolution microscopy methods offering nanometer resolution (Balzarotti et al., 2017), the usage of such large labels might lead to erroneous conclusions about protein locations and the shapes and sizes of the structures under investigation (**Figure 5D**). For example, based on electron microscopy observations, microtubules are known to have a diameter of 25 nm (Theg, 1964). After a conventional immunostaining procedure, the perceived thickness of the microtubules is increased approximately 2.5-fold due to the size of primary and secondary antibodies now decorating the microtubules. While this increase is not noticeable in diffraction limited microscopy since the resulting thickness is still less than 200 nm, it can be observed using super resolution technics and can be substantially reduced if smaller labels are used (Ries et al., 2012; Pleiner et al., 2018). Also, co-localization of proteins can be underestimated at high resolutions (Xu et al., 2016), an effect that would be increased when additional linkage error is introduced by antibodies, as has been shown for SNAP25 and syntaxin 1 clusters (Maidorn et al., 2019). Additionally, antibodies cannot be used for live imaging of cytoskeleton unless delivered through microinjections.

As an alternative to classical antibodies, derivatives of single chain camelid antibodies – nanobodies – can be used. Their considerably smaller size (<5 nm) makes nanobodies a better probe to be used with super resolution microscopy as they allow to overcome many of the problems discussed above. Since nanobodies consist of only one protein chain, they can also be fused to fluorescent proteins and expressed in cells, allowing live cell imaging. A commercially available Actin-Chromobody® (Chromotek, Germany) have been used to track actin dynamics in plants, zebrafish, and nuclei of mammalian cells (Rocchetti et al., 2014; Panza et al., 2015; Plessner et al., 2015) as well as for super resolution live imaging of actin in neurons (Wegner et al., 2017) and for correlative light electron microscopy, where chromobodies were labeled with anti-GFP and gold-conjugated secondary antibodies (Abdellatif et al., 2019). A stable cell line expressing Actin-Chromobody has been generated, allowing tracking actin dynamics without the need of transfections (Keller et al., 2019). While ectopic expression of fluorescent protein leads to relatively high background coming from the unbound molecules, Actin-Chromobodies offer an advantage over direct actin-GFP fusion since they do not increase the total amount of actin molecules in the cell and report localization and dynamics of endogenous actin. Nevertheless, some studies report that at high expression levels Actin-Chromobodies can affect actin morphology in neurons (Wegner et al., 2017), presumably due to the chromobodies modifying either the dynamics of monomeric actin, by increasing the mass and size of the molecule, or the polymerization process, through steric hindrance. Synthetic anti-actin nanobodies have been also developed for use in staining of fixed cells (Moutel et al., 2016), however, their performance in super resolution imaging was not tested, and they are only compatible with methanol fixation – a fixation method that is usually avoided when actin cytoskeleton is targeted, and often destroys epitopes for classical antibodies, making co-immunostaining with other proteins challenging.

Anti-tubulin nanobodies have also been developed, allowing to visualize some structures that cannot be resolved using conventional antibodies at all. The spacing between microtubules in densely packed bundles, which are found in axons, is ∼20–70 nm (Chen et al., 1992). When microtubules are labeled with antibodies each having size of 15 nm, signals from

fluorescent labels on antibodies merge together. This does not allow resolving individual microtubules in such bundles despite high resolution power of modern microscopes – a problem that has been solved with application of anti-tubulin nanobodies (Mikhaylova et al., 2015). Chemically labeled anti-tubulin nanobodies allow nanometer resolution in fixed cells (Mikhaylova et al., 2015; Fabricius et al., 2018), but have not been tested in live cells as fusions to fluorescent proteins so far.

As an alternative to nanobodies, affimers, which are similar in size, can be also used. Affirmers binding both actin and tubulin were recently developed, allowing visualization of these cytoskeletal elements in fixed cells and *in vivo* (Tiede et al., 2017; Lopata et al., 2018).

Visualizing the Synaptic Actin Cytoskeleton: Actin- and Tubulin-Specific Toxins and Other Small Labels

While immunostainings and GFP fusions remain to be the main approaches to visualize some of the cytoskeletal components such as neurofilaments and septin filaments, multiple small probes were developed to overcome above-described difficulties associated with direct actin coupling to fluorophore or immunostainings to make both live and super resolution imaging of actin cytoskeleton possible.

A classical tool for actin labeling is phalloidin – a toxin from *Amanita phalloides* that binds F-actin and prevents actin depolymerization (Wulf et al., 1979). Phalloidin is a small cyclopeptide with a size of ∼6 Å, it has high affinity and specificity to actin filaments, shows no binding to actin monomers, and provides high labeling density and signal to noise ratio in fluorescence microscopy (**Figure 5E**). It has been used for actin visualization for decades and majority of information on actin distribution in neurons was obtained from phalloidin stainings (Drenckhahn et al., 1984; Bernstein and Bamburg, 1992; Morales et al., 2000; Shupliakov et al., 2002; Bleckert et al., 2012; Blunk et al., 2014). It is a great choice for super resolution light microscopy when labeled with suitable fluorophore as been shown by multiple groups in recent years that used it in STED (Mace and Orange, 2012; D'Este et al., 2015; Neupane et al., 2015; Bär et al., 2016; Sidenstein et al., 2016), single molecule localization microscopy including STORM and dSTORM (van den Dries et al., 2013; Xu et al., 2013; Ganguly et al., 2015; Leyton-Puig et al., 2016; Hauser et al., 2018; Pan et al., 2018), and structured illumination microscopy (Guizetti et al., 2011; Zobel and Bogdan, 2013). It cannot, however, be used for live cell experiments as it does not readily penetrate the plasma membrane, is toxic if delivered intracellularly, and alters actin polymerization even at small concentrations, making studies of actin dynamics impossible (Wehland et al., 1977; Coluccio and Tilney, 1984; Cooper, 1987; Visegrády et al., 2004).

Toxin-based labels are also used for microtubules visualization. Paclitaxel (also known as taxol), a drug that induces tubulin assembly (Caplow et al., 1994), is one such example. It can be used as a constantly fluorescent derivative (Abal et al., 2001; Lillo et al., 2002; Barasoain et al., 2010) or as a modified reagent that only attains fluorescence inside the cell – known as Tubulin Tracker™ (Thermo Fisher Scientific), available with green and deep-red fluorophores (Grau et al., 2013; Zarrouk et al., 2015; Gao et al., 2018; Wang et al., 2018). These derivatives are membrane-permeable and can label microtubules in live cells when simply added to the cellular medium, but cannot be used in fixed samples or for long-term imaging as they are not retained well inside the cells. A similar taxol-based probe ViaFluor (Biotum) allows imaging for up to 72 h, and is available with SIM and STED-compatible fluorescent label.

Newer actin labels make live imaging possible precluding mentioned above problems associated with use of direct actin labeling. One common approach is usage of genetically encoded actin labels based on actin-binding proteins. These labels typically consist of an actin-binding domain of a naturally occurring protein fused to a fluorescent protein and can be expressed in the cell allowing tracking of actin filaments in live. GFP-labeled actin-binding domains have a number of advantages over direct actin-GFP fusions or GFP-nanobodies: they predominantly bind to actin filaments and not actin monomers, allowing to visualize the filaments with less background; do not impair actin polymerization as toxins targeting actin do, better preserving native cytoskeleton architecture and allowing to study its dynamics; and do not change the total concentration of actin monomers in the cell, what could otherwise affect cellular physiology through sequestering of actin-binding proteins, initiation of polymerization or other mechanisms (**Figure 5F**). Three such labels became popular in recent years: UtrCH, F-tractin, and Lifeact (Schell et al., 2001; Burkel et al., 2007; Riedl et al., 2008). UtrCH, a label consisting of the first 261 amino acids of human actin-binding protein Utrophin and a fluorescent protein, does not stabilize F-actin *in vitro* (Burkel et al., 2007) and have been used for live imaging of actin in neurons (Ganguly et al., 2015; Balasanyan et al., 2017). F-tractin, a 43 amino acids long fragment of rat inositol 1,4,5-trisphosphate 3-kinase A (Johnson and Schell, 2009), has also been used for live imaging in neurons (Johnson and Schell, 2009; Merriam et al., 2013; Winans et al., 2016) as well as other cell types (Yi et al., 2012).

Lifeact, derived from yeast F-actin-binding protein Abp140, is the most commonly used genetically encoded actin label. Unlike other actin-binding domains, Lifeact does not have homologs in higher eukaryotes, and is also the smallest of the available genetically encoded labels, consisting of only 17 amino acids (Riedl et al., 2008), which contributed to the growing popularity of this label. Lifeact has been extensively used for live imaging in various cell types including neurons (Li et al., 2008; Vidali et al., 2009; Jang et al., 2010; Römer et al., 2010; Deinhardt et al., 2011; Dupin et al., 2011; Huang et al., 2012; Kerr and Blanpied, 2012; Taylor et al., 2012; Merriam et al., 2013; Torregrosa-Hetland et al., 2013; Kronlage et al., 2015; Lu et al., 2015), as well as for super resolution, including live-PALM (Fuchs et al., 2010; Izeddin et al., 2011), live-RESOLFT and STED of living brain slices (Urban et al., 2011; Testa et al., 2012), and structured illumination microscopy (Rego et al., 2012; Li et al., 2015). Transgenic mice expressing Lifeact fused to mRFPruby2

or EGFP were also generated, allowing live studies of actin dynamics without the need of transfections (Riedl et al., 2010). Lifeact can be used for super-resolution microscopy in both live and fixed cells. For live imaging it is usually fused to a far-red fluorescent protein (e.g., mNeptune2) and expressed in neurons for subsequent visualization with live super resolution techniques (Urban et al., 2011; Testa et al., 2012; Wegner et al., 2017). To achieve even higher resolution, instead of ectopic expression with a fluorescent protein, purified Lifeact can be labeled with a chemical dye and used for staining of fixed and permeabilized cells. Since Lifeact has low affinity to F-actin (Riedl et al., 2008), its transient association with actin filaments can be visualized with single molecule localization techniques based on probe exchange such as IRIS (Kiuchi et al., 2015; **Figure 5G**). Low affinity of purified Lifeact binding to F-actin makes it unsuitable for usage in stainings of fixed cells in combination with many other super resolution techniques, since most of them do not rely on probe exchange, but require strong binding to the structure of interest.

Although the small labels discussed here are not expected to have such drastic effects on F-actin morphology and dynamics as actin overexpression or phalloidin, their potential influence on cytoskeletal dynamics must be considered, as growing evidence suggests that they do affect some of the aspects of actin physiology. UtrCH, for example, has been shown to perturb actin assembly dynamics *in vitro* (Belin et al., 2013), increase dendritic branching in cultured neurons (Patel et al., 2017), cause cortical actin breakdown and female sterility during *Drosophila* oogenesis (Spracklen et al., 2014), and stabilize vesicle-actin network in oocytes if expressed at high levels (Holubcová et al., 2013). Its short variant (Utr230) can induce the formation of various actin aggregates in both cell nuclei and cytoplasm (Du et al., 2015). The latter work has reported that Lifeact can also induce actin polymerization, albeit this effect was restricted to cell nuclei and resulted only in filamentous arrangements (Du et al., 2015). Other studies showed that Lifeact has concentration-depended effects on actin nucleation, elongation and cofilin-induced severing, as well as on the length of neurites, dendritic spine morphology and overall morphology of mesenchymal stem cells (Courtemanche et al., 2016; Patel et al., 2017; Wegner et al., 2017; Flores et al., 2019). These effects differ depending on position and identity of the fused fluorescent reporter, the promoter used, and the resulting protein abundance (Courtemanche et al., 2016; Patel et al., 2017; Flores et al., 2019). F-tractin has been reported to induce formation of long filopodia and to perturb the overall morphology of *Xenopus* XTC cells (Belin et al., 2014) and cause abnormal spine elongation (Johnson and Schell, 2009), but did not alter actin dynamics during *Drosophila* oogenesis (Spracklen et al., 2014). Both Lifeact-mEGFP and F-tractin-EGFP, expressed under control of the CMV promoter, have only minor effects on neuronal morphology in primary hippocampal neurons (Patel et al., 2017). Transgenic mice expressing Lifeact were viable and had a normal phenotype, with the primary neurons derived from these mice also demonstrating normal development and morphology (Riedl et al., 2010).

To avoid problems caused by fluorescent protein fusions and protein overexpression, membrane-permeable cytoskeleton labels can be used, such as SiR-actin and SiR-tubulin. SiR-actin is one of the newest probes developed that can be used for live imaging of actin without the need of transfection. It is a silicon-rhodamine based derivative of an actin filament-stabilizing toxin jasplakinolide. It has minimal cytotoxicity, permeates the plasma membrane, and shows an ∼100-fold increase in fluorescence intensity upon binding to F-actin (**Figure 5H**; Lukinavičius et al., 2014). SiR-actin has been used in a number of studies focused on super resolution imaging of actin cytoskeleton in neurons (D'Este et al., 2015, 2016; Gokhin et al., 2015; Qu et al., 2016; Hoyle et al., 2017) and appears to be the easiest tool to label actin so far: its usage does not require transfection, cell membrane permeabilization or other manipulations to deliver the probe in the cell. A conjugate of silicon-rhodamine and microtubule-stabilizing drug docetaxel, named SiR-tubulin (Lukinavičius et al., 2014), can be used for visualization of microtubules (Robison et al., 2016; Dmitrieff et al., 2017; Magliocca et al., 2017; Larsson et al., 2018; Paknikar et al., 2019). Other similar fluorogenic probes based on STED-compatible dyes (such as 510R, 580CP, GeR) and tubulin-binding drugs cabazitaxel and larotaxel have been also developed recently (Lukinavičius et al., 2018). Fluorogenic character of these labels allows using them without any washing steps, and their spectral characteristics and high photostability make them suitable for super resolution imaging such as STED. While originally described to have low cytotoxicity, SiR-actin and SiR-tubulin are derivatives of F-actin- and microtubule-stabilizing compounds, hence their potential effects on cytoskeleton dynamics and morphology should be thoroughly investigated before they can be considered safe to use for studying actin and tubulin dynamics *in vivo*. Additionally, since SiR-actin and SiR-tubulin have no primary amines it their structures, it is not possible to fix them with commonly used aldehyde-based fixatives, what makes their use in co-immunostainings with other proteins problematic.

In addition to all the individual disadvantages of described probes, they are usually not able to stain all cytoskeletal structures. For example the actin "gold standard" phalloidin as well as Lifeact are not able to bind actin polymers decorated with actin-binding protein cofilin such as for example stress-induced fibers (McGough et al., 1997; Munsie et al., 2009; Sanders et al., 2013). Both Lifeact and actin-GFP label actin cytoskeleton in lamellipodia, but not in filopodia or lamella (Belin et al., 2014). Interestingly, in mesenchyme cells Lifeact only labels proximal regions of the cytoplasmic protrusions, but not the distal tips (Sanders et al., 2013). UtrCH, on the contrary, binds to filaments in lamella and much less in lamellipodia (Belin et al., 2014). While UtrCH is excluded from Arp2/3-induced structures, GFP-tagged actin is often excluded from formin-generated filaments (Chen et al., 2012; Belin et al., 2014). Utr230, a short variant of UtrCH, predominantly binds to the most stable actin structures such as stress-induced fibers and cortical networks, and also stains structures that cannot be visualized with phalloidin such as Golgi-associated filaments (Belin et al., 2014). Anti-actin affimers demonstrate differences in their affinity to stable or dynamic actin filaments (Lopata et al., 2018). Importantly, fluorescent reporters and their positions can also affect the structures that probes can bind (Lemieux et al., 2014), Thus, mEGFP-Lifeact visualized

TABLE 1 | Probes to specifically label synaptic structures and their potential uses.

Label	Specificity	Chemical nature	MW/size	Live imaging	Super resolution	EM	Compatible with aldehyde fixation	Membrane-permeable
Antibodies	Almost any protein	Multi-chain proteins	∼150 kDa	Only for proteins exposed on the PM surface	Yes, but reduce performance of techniques capable of resolution <40 nm	Yes	Yes	No
FM1–43	PM, recycling membranes	Styryl dye	0.61 kDa	Yes	No	Yes	No	No
FM1-43FX	PM, recycling membranes	Styryl dye	0.56 kDa	Yes	No	Yes	Yes	No
mCLING	PM, recycling membranes	Palmitoylated octapeptide	1.2 kDa	Yes	Yes	No	Yes	No
DMPE-cypHer5E	Membranes of acidic organelles	Phospholipid conjugated to pH-sensitive organic dye	1.4 kDa	Yes	No	No	No	No
Quantum dots	Depends on antibody/ streptavidin coating, can be directed to PM proteins or luminal domains of vesicular proteins	Inorganic semiconductor nanocrystals, have to be covered with layers of organic molecules	10–40 nm	Yes	Yes	Yes	Yes	No
Acridine orange	Lysosomes	Fluorescent cationic dye	0.3 kDa	Yes	No	No	No	Yes
DAMP	Lysosomes	Non-fluorescent weakly basic amine	0.4 kDa	No	Yes, when labeled by antibodies	No**	Yes	Yes
LysoTracker	Lysosomes	Fluorophore linked to a weak base	0.4 kDa	Yes	Difficult	Yes	No	Yes
Rhodamine 123	Mitochondria	Membrane-potential-sensitive organic dye	0.4 kDa	Yes	Difficult	No	No	Yes
TMRM	Mitochondria	Membrane-potential-sensitive dye	0.5 kDa	Yes	Yes	No	No	Yes
TMRE	Mitochondria	Membrane-potential-sensitive dye	0.5 kDa	Yes	Difficult	No	No	Yes
MitoTracker	Mitochondria	Membrane-potential-sensitive dye with a thiol-reactive moiety	0.5 kDa	Yes	Yes (for red-shifted variants)	No	Yes	Yes
ER-Tracker	ER	Small fluorescently labeled organic molecule	∼1 kDa	Yes	Yes (for red-shifted variants)	No	Partially	Yes
ER thermo yellow	ER	Small fluorescently labeled organic molecule	0.6 kDa	Yes	No	No	Yes	Yes
NH_2-BODIPY	ER	Small fluorescently labeled organic molecule	0.5 kDa	Yes	Yes	No	Yes	Yes
Certain neurotoxins	Various post-synaptic receptors	Peptides and short proteins	1.3–10 kDa	Yes	Yes	No	Yes	No
Actin-Chromobody	Actin	Anti-actin nanobody fused to a fluorescent protein	42 kDa	Yes	Yes	No**	Yes	No, but can be expressed in the cells
hs2dAb anti-actin	Actin	Synthetic single domain antibody	14 kDa	No	Yes	No	No	No
Anti-tubulin nanobody	Tubulin	Camelid single domain antibody	∼14 kDa	Potentially yes*	Yes	No	Yes	No
Phalloidin	F-actin	F-actin-stabilizing toxin	0.8 kDa	No	Yes	No**	Yes	No
Tubulin Tracker	Microtubules	Fluorescently labeled mictotubule-stabilizing toxin	∼1.3 kDa	Yes	No	No	No	Yes

(Continued)

TABLE 1 | Continued

Label	Specificity	Chemical nature	MW/size	Live imaging	Super resolution	EM	Compatible with aldehyde fixation	Membrane-permeable
ViaFluor	Microtubules	Fluorescently labeled mictotubule-stabilizing toxin	~1.3 kDa	Yes	Yes	No	No	Yes
UtrCH	F-actin	Actin-binding domain of Utrophin	261 aa	Yes	Potentially yes*	No	Yes	No, but can be expressed in the cells
F-tractin	F-actin	Actin-binding domain of inositol 1,4,5-trisphosphate 3-kinase A	43 aa	Yes	Potentially yes*	No	Yes	No, but can be expressed in the cells
Lifeact	F-actin	Actin-binding domain of Abp140	17 aa	Yes	Yes	No	Yes	No, but can be expressed in the cells
SiR-actin	F-actin	Fluorogenic derivative of an actin filament-stabilizing toxin	~1.3 kDa	Yes	Yes	No	No	Yes
SiR-tubulin	Microtubules	Fluorogenic derivative of a microtubule-stabilizing toxin	~1.3 kDa	Yes	Yes	No	No	Yes

**The nature of the label is compatible with the corresponding method, but its performance has not been tested yet; **the label itself is not visible in EM, but can be visualized with gold-coupled antibodies against the fluorophore (either organic dye or fluorescent protein).*

lamellipodia well, while TagRFP-Lifeact is excluded from the same structures (DesMarais et al., 2019). Even small dyes attached to the classical phalloidin can change the quality of staining. For example, staining with Phalloidin-Alexa Fluor® 488 results in more detailed labeling than with Phalloidin-iFluor™ 405, Phalloidin – Alexa Fluor® 488, Phalloidin – Alexa Fluor® 555 or Phalloidin – Alexa Fluor® 647 (DesMarais et al., 2019). Similarly, different clones of commonly used antibodies recognize different populations of actin cytoskeleton (DesMarais et al., 2019). Taken together, this illustrates a strong influence of multiple factors on labels ability to recognize cytoskeletal structures. Consequently, differences in the preferences of the labels for actin structures decorated with certain actin binding proteins should be considered in relation to actin-binding proteins distribution. For example, it is known that in dendritic spines the actin cytoskeleton forms a stable core in the center of the spine, and a more dynamic shell at the periphery. The dynamics of the latter shell is maintained by the actin-depolymerizing factor cofilin, while actin branching Abp2/3 complex is localized closer to the stable core (Rácz and Weinberg, 2013). This differential distribution of actin binding proteins would result in significantly different staining patterns produced by UtrCH and Lifeact, which are excluded from Arp2/3- or cofilin-bound structures, respectively. It is highly likely that less commonly used actin probes, such as F-tractin and SiR-actin, also reveal only a subpopulation of the actin cytoskeleton, and therefore the choice of a label would often depend on specific actin cytoskeleton components one wants to investigate.

Problems and Solutions in Visualizing the Cytoskeleton in Fixed Cells

Apart from a choice of label, another crucial issue in cytoskeleton visualization is preservation of its structure in fixed cells. While thick stress fibers are preserved well by most fixatives, many fine components of actin cytoskeleton are sensitive to physical and chemical perturbations and are damaged, destroyed or not completely preserved by commonly used fixation procedures. Paraformaldehyde has been shown not to be able to preserve thin actin bundles and structures (Whelan and Bell, 2015; Bachmann et al., 2016) and 0.5–3% glutaraldehyde is commonly used as fixative to preserve actin cytoskeleton, as it provides more effective cross-linking. Nonetheless, even after fixation with glutaraldehyde, actin cytoskeleton can still be severely damaged by following procedures routinely used for visualization of other structures such as osmium tetroxide staining for transmission electron microscopy (Maupin-Szamier and Pollard, 1978), highlighting the need for careful choice of treatment procedures when imaging actin cytoskeleton. To stabilize actin cytoskeleton, specific buffers containing $MgCl_2$and EGTA are used during fixation (Small, 1988). Additionally, most cytoskeleton fixation procedures involve extraction of all other cellular components before strong fixation of the filaments. This is usually done by adding relatively high amounts on detergents and leads to loss of all cellular membranes and most soluble proteins (Rinnerthaler et al., 1988; Xu et al., 2013). This results in better actin staining and reduced background signal,

however, makes in very difficult to image actin cytoskeleton at the same time with other proteins as (a) most proteins are washed away after the extraction and (b) many conventional antibody epitopes get destroyed by glutaraldehyde fixation significantly reducing the effectiveness of immunostainings. Paraformaldehyde fixation in actin-stabilizing buffer with no extraction can be used when actin co-staining with other proteins is required. This results in less effective preservation of actin ultrastructure, but might still be sufficient to visualize certain structures (Xu et al., 2013). In addition to actin-stabilizing buffers, paraformaldehyde fixation can be further improved if performed at 37°C, illustrating that temperature can also affect the quality of fixation (Leyton-Puig et al., 2016; Pereira et al., 2019). In general, the choice of fixation procedure, just like the choice of a label to use, still largely depends on structures one aims to image and other specific requirements of the experiments and no universal method have been developed yet (Richter et al., 2017).

Combining Genetic Encoding With Chemical Labeling: Enzymatic Tagging and Click Chemistry

As described above, usage of both genetically encoded labels and chemically labeled probes have some disadvantages. The most prominent ones are low fluorescence intensity of fluorescent proteins and often high background/non-specific binding of affine probes. To solve these problems, techniques combining genetic encoding and chemical labeling have been developed. These techniques usually involve genetic manipulation of the protein of interest, resulting in attachment of a tag sequence to it. This tag is then specifically recognized and covalently bound to chemical fluorophores of choice. This results in highly specific labeling of only proteins containing the tag with highly fluorescent chemical fluorophores. Two examples where such an approach is used are SNAP and Halo tags. The SNAP tag is a 182 amino acids long polypeptide that can be fused to a protein of interest, generating a chimeric protein that is not fluorescent. The SNAP tag is derived from O^6-alkylguanine-DNA alkyltransferase, whose natural function is to transfer the alkyl group of O^6-alkylated guanine in DNA to a cysteine residue in the alkyltransferase active center after which the alkyltransferase is permanently inactivated. Mutations introduced to generate SNAP tag changed its specificity to benzylguanine derivatives of type 1 (Keppler et al., 2003), which can be generated from many common fluorophores. When such fluorescent derivatives are added to cells expressing SNAP tag, the latter catalyzes self-labeling with the fluorophore by covalently attaching the fluorophore with the benzyl group to a cysteine residue in SNAP tag sequence. The reaction is highly specific and can be highly effective, resulting in nearly all present SNAP tags labeling, but recent studies report much lower efficiency (Thevathasan et al., 2019). The labeling reaction can be triggered in live cells when membrane permeable dyes such as tetramethyl-rhodamine-Star or 647-SiR are used. The HaloTag is a similar self-labeling polypeptide generated from bacterial haloalkane dehalogenase (Los et al., 2008). Similar to SNAP tag, HaloTag it is a non-fluorescent tag that catalyzes transfer of reactive compounds (species modified to be recognizable by the HaloTag – HaloTag ligands) to itself (Los et al., 2008). Available HaloTag ligands include cell-permeable dyes tetramethylrhodamine, diacetyl derivative of fluorescein, rhodamine 110 and Oregon Green, as well as cell-impermeable ones Alexa Fluor® 488 and Alexa Fluor® 660.

While these tags provide fast, specific and efficient protein labeling in cells, an obvious disadvantage is rather large size of the tags (19.4 and 33 kDa for SNAP and Halo tags, respectively). Similar to labeling with fluorescent proteins, in some cases attachment of such a tag might impede the natural targeting and trafficking of the protein. This problem can be solved by substituting a large polypeptide tag with a small moiety, which can interact quickly and specifically with another small compound, effectively conjugating them. Such process is referred to as click chemistry and in general is represented by multiple reactions with different mechanisms. One example of such a reaction is copper-mediated azide–alkyne cycloaddition. It can be used to specifically label proteins with chemical dyes without the need to introduce a large tag. Instead, a single amino acid containing an alkyne group has to be incorporated in the protein of interest. A dye with an azide moiety can be added to the specimen and bound covalently to the alkyne, labeling the protein with the fluorophore (Milles et al., 2012). While offering an advantage of a small tag that should not interfere with protein's localization and functioning, this is a rather challenging and labor-demanding approach. Since it requires the presence of unnatural amino acids in the protein of interest, a relatively complicated genetic setup has to be used to provide machinery for inclusion of the unnatural amino acid in the normal protein translation.

CONCLUSION

Over the years multiple methods and approaches were developed to label synaptic organelles and structures (**Table 1**). Many of these rely on naturally evolved compounds such as intrinsically fluorescent proteins or natural toxins, while others employ rational design and chemical synthesis or modifications. Respectively, they all have their own advantages and preferred uses, and none of the available labels suits every experiment. The first point of consideration should always be whether selected label can introduce biological artifacts that would lead to erroneous conclusions. For example, while the use of GFP-actin chimeras might not result in high signal to noise ratio when imaging actin dynamics, it would still be a preferred method compared to use of toxins altering actin dynamics, such as phalloidin. This would not be a problem when fixed cells are imaged. At the same time, the optical characteristics of GFP might not be suitable for some super resolution techniques, and chemically labeled phalloidin would be preferred there. Similarly, while quantum dot-conjugated antibodies provide high specificity and photostability, the size of the quantum dots might limit the structures that can be effectively visualized.

Although specificity of labeling is the main concern when imaging synaptic organelles, the compatibility of the labels with specimen preparation should be also carefully considered. This is an especially important point when imaging cytoskeletal elements, as those are not preserved by many commonly used procedures. With the wide selection of different labels for synaptic organelles, the perfect use still depends on specific experimental requirements and novel imaging techniques often require novel probes to be developed.

AUTHOR CONTRIBUTIONS

Both authors took part in designing and writing the manuscript.

FUNDING

In this work, SOR was supported by grants from the German Research Foundation, SFB1190/P09 and SFB1286/B2.

REFERENCES

Abal, M., Souto, A. A., Amat-Guerri, F., Acuña, A. U., Andreu, J. M., and Barasoain, I. (2001). Centrosome and spindle pole microtubules are main targets of a fluorescent taxoid inducing cell death. *Cell Motil. Cytoskeleton* 49, 1–15. doi: 10.1002/cm.1016

Abdellatif, M. E. A., Hipp, L., Plessner, M., Walther, P., and Knöll, B. (2019). Indirect visualization of endogenous nuclear actin by correlative light and electron microscopy (CLEM) using an actin-directed chromobody. *Histochem. Cell Biol.* 152, 133–143. doi: 10.1007/s00418-019-01795-3

Adams, M. E., and Olivera, B. M. (1994). Neurotoxins: overview of an emerging research technology. *Trends Neurosci.* 17, 151–155. doi: 10.1016/0166-2236(94)90092-2

Afuwape, O. A. T., Wasser, C. R., Schikorski, T., and Kavalali, E. T. (2017). Synaptic vesicle pool-specific modification of neurotransmitter release by intravesicular free radical generation. *J. Physiol.* 595, 1223–1238. doi: 10.1113/JP273115

Aizawa, H., Sameshima, M., and Yahara, I. (1997). A green fluorescent protein-actin fusion protein dominantly inhibits cytokinesis, cell spreading, and locomotion in Dictyostelium. *Cell Struct. Funct.* 22, 335–345. doi: 10.1247/csf.22.335

Akins, M. R., Berk-Rauch, H. E., and Fallon, J. (2009). Presynaptic translation: stepping out of the postsynaptic shadow. *Front. Neural Circuits* 3:17. doi: 10.3389/neuro.04.017.2009

Allison, D. W., Gelfand, V. I., Spector, I., and Craig, A. M. (1998). Role of actin in anchoring postsynaptic receptors in cultured hippocampal neurons: differential attachment of NMDA versus AMPA receptors. *J. Neurosci.* 18, 2423–2436. doi: 10.1523/JNEUROSCI.18-07-02423.1998

Anderson, M. J., and Cohen, M. W. (1977). Nerve-induced and spontaneous redistribution of acetylcholine receptors on cultured muscle cells. *J. Physiol.* 268, 757–773. doi: 10.1113/jphysiol.1977.sp011880

Arai, S., Lee, S.-C., Zhai, D., Suzuki, M., and Chang, Y. T. (2014). A Molecular fluorescent probe for targeted visualization of temperature at the endoplasmic reticulum. *Sci. Rep.* 4:6701. doi: 10.1038/srep06701

Bachmann, M., Fiederling, F., and Bastmeyer, M. (2016). Practical limitations of superresolution imaging due to conventional sample preparation revealed by a direct comparison of CLSM, SIM and dSTORM. *J. Microsc.* 262, 306–315. doi: 10.1111/jmi.12365

Balasanyan, V., Watanabe, K., Dempsey, W. P., Lewis, T. L., Trinh, L. A., and Arnold, D. B. (2017). Structure and function of an actin-based filter in the proximal axon. *Cell Rep.* 21, 2696–2705. doi: 10.1016/j.celrep.2017.11.046

Balzarotti, F., Eilers, Y., Gwosch, K. C., Gynnå, A. H., Westphal, V., Stefani, F. D., et al. (2017). Nanometer resolution imaging and tracking of fluorescent molecules with minimal photon fluxes. *Science* 355, 606–612. doi: 10.1126/science.aak9913

Bannai, H., Inoue, T., Nakayama, T., Hattori, M., and Mikoshiba, K. (2004). Kinesin dependent, rapid, bi-directional transport of ER sub-compartment in dendrites of hippocampal neurons. *J. Cell Sci.* 117, 163–175. doi: 10.1242/jcs.00854

Bannai, H., Lévi, S., Schweizer, C., Dahan, M., and Triller, A. (2006). Imaging the lateral diffusion of membrane molecules with quantum dots. *Nat. Protoc.* 1, 2628–2634. doi: 10.1038/nprot.2006.429

Bannai, H., Niwa, F., Sherwood, M. W., Shrivastava, A. N., Arizono, M., Miyamoto, A., et al. (2015). Bidirectional control of synaptic GABAAR clustering by glutamate and calcium. *Cell Rep.* 13, 2768–2780. doi: 10.1016/j.celrep.2015.12.002

Bär, J., Kobler, O., van Bommel, B., and Mikhaylova, M. (2016). Periodic F-actin structures shape the neck of dendritic spines. *Sci. Rep.* 6:37136. doi: 10.1038/srep37136

Barasoain, I., Díaz, J. F., and Andreu, J. M. (2010). Fluorescent taxoid probes for microtubule research. *Methods Cell Biol.* 95, 353–372. doi: 10.1016/S0091-679X(10)95019-X

Barykina, N. V., Subach, O. M., Doronin, D. A., Sotskov, V. P., Roshchina, M. A., Kunitsyna, T. A., et al. (2016). A new design for a green calcium indicator with a smaller size and a reduced number of calcium-binding sites. *Sci. Rep.* 6:34447. doi: 10.1038/srep34447

Belin, B. J., Cimini, B. A., Blackburn, E. H., and Mullins, R. D. (2013). Visualization of actin filaments and monomers in somatic cell nuclei. *Mol. Biol. Cell* 24, 982–994. doi: 10.1091/mbc.E12-09-0685

Belin, B. J., Goins, L. M., and Mullins, R. D. (2014). Comparative analysis of tools for live cell imaging of actin network architecture. *Bioarchitecture* 4, 189–202. doi: 10.1080/19490992.2014.1047714

Bernstein, B. W., and Bamburg, J. R. (1992). Actin in emerging neurites is recruited from a monomer pool. *Mol. Neurobiol.* 6, 95–106. doi: 10.1007/BF02780546

Betz, W. J., Mao, F., and Bewick, G. S. (1992). Activity-dependent fluorescent staining and destaining of living vertebrate motor nerve terminals. *J. Neurosci.* 12, 363–375. doi: 10.1523/jneurosci.12-02-00363.1992

Betzig, E., Patterson, G. H., Sougrat, R., Lindwasser, O. W., Olenych, S., Bonifacino, J. S., et al. (2006). Imaging intracellular fluorescent proteins at nanometer resolution. *Science* 313, 1642–1645. doi: 10.1126/science.1127344

Bird, M. M. (1976). Microtubule–synaptic vesicle associations in cultured rat spinal cord neurons. *Cell Tissue Res.* 168, 101–115.

Bleckert, A., Photowala, H., and Alford, S. (2012). Dual pools of actin at presynaptic terminals. *J. Neurophysiol.* 107, 3479–3492. doi: 10.1152/jn.00789.2011

Bloom, O., Evergren, E., Tomilin, N., Kjaerulff, O., Löw, P., Brodin, L., et al. (2003). Colocalization of synapsin and actin during synaptic vesicle recycling. *J. Cell Biol.* 161, 737–747. doi: 10.1083/jcb.200212140

Blunk, A. D., Akbergenova, Y., Cho, R. W., Lee, J., Walldorf, U., Xu, K., et al. (2014). Postsynaptic actin regulates active zone spacing and glutamate receptor apposition at the *Drosophila neuromuscular* junction. *Mol. Cell. Neurosci.* 0, 241–254. doi: 10.1016/j.mcn.2014.07.005

Borodinsky, L. N., and Spitzer, N. C. (2007). Activity-dependent neurotransmitter-receptor matching at the neuromuscular junction. *Proc. Natl. Acad. Sci. U.S.A.* 104, 335–340. doi: 10.1073/pnas.0607450104

Bossi, M., Fölling, J., Belov, V. N., Boyarskiy, V. P., Medda, R., Egner, A., et al. (2008). Multicolor far-field fluorescence nanoscopy through isolated detection of distinct molecular species. *NANO Lett.* 8, 2463–2468. doi: 10.1021/nl801471d

Brady, M. L., Moon, C. E., and Jacob, T. C. (2014). Using an α-bungarotoxin binding site tag to study GABA A receptor membrane localization and trafficking. *J. Vis. Exp.* 2014:51365. doi: 10.3791/51365

Broadhead, M. J., Horrocks, M. H., Zhu, F., Muresan, L., Benavides-Piccione, R., DeFelipe, J., et al. (2016). PSD95 nanoclusters are postsynaptic building blocks in hippocampus circuits. *Sci. Rep.* 6:24626. doi: 10.1038/srep24626

Burkel, B. M., von Dassow, G., and Bement, W. M. (2007). Versatile fluorescent probes for actin filaments based on the actin-binding domain of utrophin. *Cell Motil.* 64, 822–832. doi: 10.1002/cm.20226

Caplow, M., Shanks, J., and Ruhlen, R. (1994). How taxol modulates microtubule disassembly. *J. Biol. Chem.* 269, 23399–23402.

Chamma, I., Letellier, M., Butler, C., Tessier, B., Lim, K.-H., Gauthereau, I., et al. (2016a). Mapping the dynamics and nanoscale organization of synaptic adhesion proteins using monomeric streptavidin. *Nat. Commun.* 7:10773. doi: 10.1038/ncomms10773

Chamma, I., Levet, F., Sibarita, J.-B., Sainlos, M., and Thoumine, O. (2016b). Nanoscale organization of synaptic adhesion proteins revealed by single-molecule localization microscopy. *Neurophotonics* 3:041810. doi: 10.1117/1.NPh.3.4.041810

Chan, K. Y., and Bunt, A. H. (1978). An association between mitochondria and microtubules in synaptosomes and axon terminals of cerebral cortex. *J. Neurocytol.* 7, 137–143. doi: 10.1007/bf01217913

Chang, J.-B., Chen, F., Yoon, Y.-G., Jung, E. E., Babcock, H., Kang, J. S., et al. (2017). Iterative expansion microscopy. *Nat. Methods* 14, 593–599. doi: 10.1038/nmeth.4261

Chang, J. C., Kovtun, O., Blakely, R. D., and Rosenthal, S. J. (2012). Labeling of neuronal receptors and transporters with quantum dots. *Wiley Interdiscip. Rev. Nanomed. Nanobiotechnol.* 4, 605–619. doi: 10.1002/wnan.1186

Chen, F., Tillberg, P. W., and Boyden, E. S. (2015). Expansion microscopy. *Science* 347, 543–548. doi: 10.1126/science.1260088

Chen, J., Kanai, Y., Cowan, N. J., and Hirokawa, N. (1992). Projection domains of MAP2 and tau determine spacings between microtubules in dendrites and axons. *Nature* 360, 674–677. doi: 10.1038/360674a0

Chen, Q., Nag, S., and Pollard, T. D. (2012). Formins filter modified actin subunits during processive elongation. *J. Struct. Biol.* 177, 32–39. doi: 10.1016/j.jsb.2011.10.005

Chiappinelli, V. A. (1983). Kappa-bungarotoxin: a probe for the neuronal nicotinic receptor in the avian ciliary ganglion. *Brain Res.* 277, 9–22. doi: 10.1016/0006-8993(83)90902

Choi, Y. M., Kim, S. H., Chung, S., Uhm, D. Y., and Park, M. K. (2006). Regional interaction of endoplasmic reticulum Ca2+ signals between soma and dendrites through rapid luminal Ca2+ diffusion. *J. Neurosci.* 26, 12127–12136. doi: 10.1523/JNEUROSCI.3158-06.2006

Choquet, D. (2018). Linking nanoscale dynamics of AMPA receptor organization to plasticity of excitatory synapses and learning. *J. Neurosci.* 38, 9318–9329. doi: 10.1523/JNEUROSCI.2119-18.2018

Colquhoun, L. M., and Patrick, J. W. (1997). Pharmacology of neuronal nicotinic acetylcholine receptor subtypes. *Adv. Pharmacol. San Diego Calif* 39, 191–220. doi: 10.1016/s1054-3589(08)60072-1

Coluccio, L. M., and Tilney, L. G. (1984). Phalloidin enhances actin assembly by preventing monomer dissociation. *J. Cell Biol.* 99, 529–535. doi: 10.1083/jcb.99.2.529

Cooper, J. A. (1987). Effects of cytochalasin and phalloidin on actin. *J. Cell Biol.* 105, 1473–1478. doi: 10.1083/jcb.105.4.1473

Courtemanche, N., Pollard, T. D., and Chen, Q. (2016). Avoiding artefacts when counting polymerized actin in live cells with lifeact fused to fluorescent proteins. *Nat. Cell Biol.* 18, 676–683. doi: 10.1038/ncb3351

Crispino, M., Kaplan, B. B., Martin, R., Alvarez, J., Chun, J. T., Benech, J. C., et al. (1997). Active polysomes are present in the large presynaptic endings of the synaptosomal fraction from squid brain. *J. Neurosci. Off. J. Soc. Neurosci.* 17, 7694–7702. doi: 10.1523/jneurosci.17-20-07694.1997

Dahan, M., Lévi, S., Luccardini, C., Rostaing, P., Riveau, B., and Triller, A. (2003). Diffusion dynamics of glycine receptors revealed by single-quantum dot tracking. *Science* 302, 442–445. doi: 10.1126/science.1088525

Dana, H., Mohar, B., Sun, Y., Narayan, S., Gordus, A., Hasseman, J. P., et al. (2016). Sensitive red protein calcium indicators for imaging neural activity. *ELIFE* 5:e12727. doi: 10.7554/eLife.12727

Dani, A., Huang, B., Bergan, J., Dulac, C., and Zhuang, X. (2010). Superresolution imaging of chemical synapses in the brain. *Neuron* 68, 843–856. doi: 10.1016/j.neuron.2010.11.021

DeBin, J. A., Maggio, J. E., and Strichartz, G. R. (1993). Purification and characterization of chlorotoxin, a chloride channel ligand from the venom of the scorpion. *Am. J. Physiol. Cell Physiol.* 264, C361–C369. doi: 10.1152/ajpcell.1993.264.2.C361

Deibler, M., Spatz, J. P., and Kemkemer, R. (2011). Actin fusion proteins alter the dynamics of mechanically induced cytoskeleton rearrangement. *PLoS One* 6:e22941. doi: 10.1371/journal.pone.0022941

Deinhardt, K., Kim, T., Spellman, D. S., Mains, R. E., Eipper, B. A., Neubert, T. A., et al. (2011). Neuronal growth cone retraction relies on proneurotrophin receptor signaling through rac. *Sci. Signal.* 4, ra82–ra82. doi: 10.1126/scisignal.2002060

Delgado, J. Y., and Selvin, P. R. (2018). A revised view on the role of surface AMPAR mobility in tuning synaptic transmission: limitations, tools, and alternative views. *Front. Synaptic Neurosci.* 10:21. doi: 10.3389/fnsyn.2018.00021

Deller, T., Merten, T., Roth, S. U., Mundel, P., and Frotscher, M. (2000). Actin-associated protein synaptopodin in the rat hippocampal formation: localization in the spine neck and close association with the spine apparatus of principal neurons. *J. Comp. Neurol.* 418, 164–181. doi: 10.1002/(sici)1096-9861(20000306)418:2<164::aid-cne4>3.0.co;2-0

Denker, A., Bethani, I., Kröhnert, K., Körber, C., Horstmann, H., Wilhelm, B. G., et al. (2011). A small pool of vesicles maintains synaptic activity in vivo. *Proc. Natl. Acad. Sci. U.S.A.* 108, 17177–17182. doi: 10.1073/pnas.1112688108

Denker, A., Kröhnert, K., and Rizzoli, S. O. (2009). Revisiting synaptic vesicle pool localization in the *Drosophila neuromuscular* junction. *J. Physiol.* 587, 2919–2926. doi: 10.1113/jphysiol.2009.170985

Deo, C., and Lavis, L. D. (2018). Synthetic and genetically encoded fluorescent neural activity indicators. *Curr. Opin. Neurobiol.* 50, 101–108. doi: 10.1016/j.conb.2018.01.003

DesMarais, V., Eddy, R. J., Sharma, V. P., Stone, O., and Condeelis, J. S. (2019). Optimizing leading edge F-actin labeling using multiple actin probes, fixation methods and imaging modalities. *BioTechniques* 66, 113–119. doi: 10.2144/btn-2018-0112

D'Este, E., Kamin, D., Göttfert, F., El-Hady, A., and Hell, S. W. (2015). STED nanoscopy reveals the ubiquity of subcortical cytoskeleton periodicity in living neurons. *Cell Rep.* 10, 1246–1251. doi: 10.1016/j.celrep.2015.02.007

D'Este, E., Kamin, D., Velte, C., Göttfert, F., Simons, M., and Hell, S. W. (2016). Subcortical cytoskeleton periodicity throughout the nervous system. *Sci. Rep.* 6:22741. doi: 10.1038/srep22741

Diwu, Z., Chen, C. S., Zhang, C., Klaubert, D. H., and Haugland, R. P. (1999). A novel acidotropic pH indicator and its potential application in labeling acidic organelles of live cells. *Chem. Biol.* 6, 411–418. doi: 10.1016/s1074-5521(99)80059-3

Dmitrieff, S., Alsina, A., Mathur, A., and Nédélec, F. J. (2017). Balance of microtubule stiffness and cortical tension determines the size of blood cells with marginal band across species. *Proc. Natl. Acad. Sci. U.S.A.* 114, 4418–4423. doi: 10.1073/pnas.1618041114

Dong, J. X., Lee, Y., Kirmiz, M., Palacio, S., Dumitras, C., Moreno, C. M., et al. (2019). A toolbox of nanobodies developed and validated for diverse neuroscience research applications. *bioRxiv* 631762. doi: 10.1101/631762

Donnert, G., Keller, J., Medda, R., Andrei, M. A., Rizzoli, S. O., Lührmann, R., et al. (2006). Macromolecular-scale resolution in biological fluorescence microscopy. *Proc. Natl. Acad. Sci. U.S.A.* 103, 11440–11445. doi: 10.1073/pnas.0604965103

Dovas, A., Gevrey, J.-C., Grossi, A., Park, H., Abou-Kheir, W., and Cox, D. (2009). Regulation of podosome dynamics by WASp phosphorylation: implication in matrix degradation and chemotaxis in macrophages. *J. Cell Sci.* 122, 3873–3882. doi: 10.1242/jcs.051755

Dovas, A., Gligorijevic, B., Chen, X., Entenberg, D., Condeelis, J., and Cox, D. (2011). Visualization of actin polymerization in invasive structures of macrophages and carcinoma cells using photoconvertible β-actin – dendra2 fusion proteins. *PLoS One* 6:e16485. doi: 10.1371/journal.pone.0016485

Doyle, T., and Botstein, D. (1996). Movement of yeast cortical actin cytoskeleton visualized in vivo. *Proc. Natl. Acad. Sci. U.S.A.* 93, 3886–3891. doi: 10.1073/pnas.93.9.3886

Drenckhahn, D., Frotscher, M., and Kaiser, H. W. (1984). Concentration of F-actin in synaptic formations of the hippocampus as visualized by staining with fluorescent phalloidin. *Brain Res.* 300, 381–384. doi: 10.1016/0006-8993(84)90851-5

Du, J., Fan, Y.-L., Chen, T.-L., and Feng, X.-Q. (2015). Lifeact and Utr230 induce distinct actin assemblies in cell nuclei. *Cytoskelet.* 72, 570–575. doi: 10.1002/cm.21262

Dubertret, B., Skourides, P., Norris, D. J., Noireaux, V., Brivanlou, A. H., and Libchaber, A. (2002). In vivo imaging of quantum dots encapsulated in phospholipid micelles. *Science* 298, 1759–1762. doi: 10.1126/science.1077194

Dupin, I., Sakamoto, Y., and Etienne-Manneville, S. (2011). Cytoplasmic intermediate filaments mediate actin-driven positioning of the nucleus. *J. Cell Sci.* 124, 865–872. doi: 10.1242/jcs.076356

Evan, G. I., Lewis, G. K., Ramsay, G., and Bishop, J. M. (1985). Isolation of monoclonal antibodies specific for human c-myc proto-oncogene product. *Mol. Cell. Biol.* 5, 3610–3616. doi: 10.1128/mcb.5.12.3610

Fabricius, V., Lefèbre, J., Geertsema, H., Marino, S. F., and Ewers, H. (2018). Rapid and efficient C-terminal labeling of nanobodies for DNA-PAINT. *J. Phys. Appl. Phys.* 51:474005. doi: 10.1088/1361-6463/aae0e2

Feng, Z., Ning Chen, W., Vee Sin Lee, P., Liao, K., and Chan, V. (2005). The influence of GFP-actin expression on the adhesion dynamics of HepG2 cells on a model extracellular matrix. *Biomaterials* 26, 5348–5358. doi: 10.1016/j.biomaterials.2005.01.069

Fernández-Alfonso, T., Kwan, R., and Ryan, T. A. (2006). Synaptic vesicles interchange their membrane proteins with a large surface reservoir during recycling. *Neuron* 51, 179–186. doi: 10.1016/j.neuron.2006.06.008

Flores, L. R., Keeling, M. C., Zhang, X., Sliogeryte, K., and Gavara, N. (2019). Lifeact-GFP alters F-actin organization, cellular morphology and biophysical behaviour. *Sci. Rep.* 9:3241. doi: 10.1038/s41598-019-40092-w

Flynn, K. C., Pak, C. W., Shaw, A. E., Bradke, F., and Bamburg, J. R. (2009). Growth cone-like waves transport actin and promote axonogenesis and neurite branching. *Dev. Neurobiol.* 69, 761–779. doi: 10.1002/dneu.20734

Francis, R., Xu, X., Park, H., Wei, C.-J., Chang, S., Chatterjee, B., et al. (2011). Connexin43 modulates cell polarity and directional cell migration by regulating microtubule dynamics. *PLoS One* 6:e26379. doi: 10.1371/journal.pone.0026379

Fricker, F. R., Antunes-Martins, A., Galino, J., Paramsothy, R., La Russa, F., Perkins, J., et al. (2013). Axonal neuregulin 1 is a rate limiting but not essential factor for nerve remyelination. *Brain* 136, 2279–2297. doi: 10.1093/brain/awt148

Fuchs, J., Böhme, S., Oswald, F., Hedde, P. N., Krause, M., Wiedenmann, J., et al. (2010). A photoactivatable marker protein for pulse-chase imaging with superresolution. *Nat. Methods* 7, 627–630. doi: 10.1038/nmeth.1477

Gallego-Sandín, S., Rodríguez-García, A., Alonso, M. T., and García-Sancho, J. (2009). The endoplasmic reticulum of dorsal root ganglion neurons contains functional TRPV1 channels. *J. Biol. Chem.* 284, 32591–32601. doi: 10.1074/jbc.M109.019687

Ganguly, A., Tang, Y., Wang, L., Ladt, K., Loi, J., Dargent, B., et al. (2015). A dynamic formin-dependent deep F-actin network in axons. *J. Cell Biol.* 210, 401–417. doi: 10.1083/jcb.201506110

Gao, Y., Anthony, S. M., Yu, Y., Yi, Y., and Yu, Y. (2018). Cargos rotate at microtubule intersections during intracellular trafficking. *Biophys. J.* 114, 2900–2909. doi: 10.1016/j.bpj.2018.05.010

Gokhin, D. S., Nowak, R. B., Khoory, J. A., Piedra Ade, L., Ghiran, I. C., and Fowler, V. M. (2015). Dynamic actin filaments control the mechanical behavior of the human red blood cell membrane. *Mol. Biol. Cell* 26, 1699–1710. doi: 10.1091/mbc.E14-12-1583

Gordon-Weeks, P. R., Burgoyne, R. D., and Gray, E. G. (1982). Presynaptic microtubules: organisation and assembly/disassembly. *Neuroscience* 7, 739–749. doi: 10.1016/0306-4522(82)90079-3

Gould, T. J., Myers, J. R., and Bewersdorf, J. (2011). Total internal reflection STED microscopy. *Opt. Express* 19, 13351–13357. doi: 10.1364/OE.19.013351

Graffe, M., Zenisek, D., and Taraska, J. W. (2015). A marginal band of microtubules transports and organizes mitochondria in retinal bipolar synaptic terminals. *J. Gen. Physiol.* 146, 109–117. doi: 10.1085/jgp.201511396

Grau, M. B., Curto, G. G., Rocha, C., Magiera, M. M., Sousa, P. M., Giordano, T., et al. (2013). Tubulin glycylases and glutamylases have distinct functions in stabilization and motility of ependymal cilia. *J. Cell Biol.* 202, 441–451. doi: 10.1083/jcb.201305041

Grienberger, C., and Konnerth, A. (2012). Imaging calcium in neurons. *Neuron* 73, 862–885. doi: 10.1016/j.neuron.2012.02.011

Groc, L., Heine, M., Cognet, L., Brickley, K., Stephenson, F. A., Lounis, B., et al. (2004). Differential activity-dependent regulation of the lateral mobilities of AMPA and NMDA receptors. *Nat. Neurosci.* 7, 695–696. doi: 10.1038/nn1270

Gubernator, N. G., Zhang, H., Staal, R. G. W., Mosharov, E. V., Pereira, D. B., Yue, M., et al. (2009). Fluorescent false neurotransmitters visualize dopamine release from individual presynaptic terminals. *Science* 324, 1441–1444. doi: 10.1126/science.1172278

Guizetti, J., Schermelleh, L., Mäntler, J., Maar, S., Poser, I., Leonhardt, H., et al. (2011). Cortical constriction during abscission involves helices of ESCRT-III–dependent filaments. *Science* 331, 1616–1620. doi: 10.1126/science.1201847

Gustafsson, M. G. L. (2005). Nonlinear structured-illumination microscopy: wide-field fluorescence imaging with theoretically unlimited resolution. *Proc. Natl. Acad. Sci. U.S A.* 102, 13081–13086. doi: 10.1073/pnas.0406877102

Haas, K. T., Compans, B., Letellier, M., Bartol, T. M., Grillo-Bosch, D., Sejnowski, T. J., et al. (2018). Pre-post synaptic alignment through neuroligin-1 tunes synaptic transmission efficiency. *ELIFE* 7:e31755. doi: 10.7554/eLife.31755

Hambrock, A., Löffler-Walz, C., and Quast, U. (2002). Glibenclamide binding to sulphonylurea receptor subtypes: dependence on adenine nucleotides. *Br. J. Pharmacol.* 136, 995–1004. doi: 10.1038/sj.bjp.0704801

Harata, N. C., Choi, S., Pyle, J. L., Aravanis, A. M., and Tsien, R. W. (2006). Frequency-dependent kinetics and prevalence of kiss-and-run and reuse at hippocampal synapses studied with novel quenching methods. *Neuron* 49, 243–256. doi: 10.1016/j.neuron.2005.12.018

Hauser, M., Yan, R., Li, W., Repina, N. A., Schaffer, D. V., and Xu, K. (2018). The spectrin-actin-based periodic cytoskeleton as a conserved nanoscale scaffold and ruler of the neural stem cell lineage. *Cell Rep.* 24, 1512–1522. doi: 10.1016/j.celrep.2018.07.005

He, J., Zhou, R., Wu, Z., Carrasco, M. A., Kurshan, P. T., Farley, J. E., et al. (2016). Prevalent presence of periodic actin–spectrin-based membrane skeleton in a broad range of neuronal cell types and animal species. *Proc. Natl. Acad. Sci. U.S.A.* 113, 6029–6034. doi: 10.1073/pnas.1605707113

Heilemann, M., Dedecker, P., Hofkens, J., and Sauer, M. (2009). Photoswitches: key molecules for subdiffraction-resolution fluorescence imaging and molecular quantification. *Laser Photonics Rev.* 3, 180–202. doi: 10.1002/lpor.200810043

Hell, S. W. (2007). Far-field optical nanoscopy. *Science* 316, 1153–1158. doi: 10.1126/science.1137395

Hell, S. W., and Wichmann, J. (1994). Breaking the diffraction resolution limit by stimulated emission: stimulated-emission-depletion fluorescence microscopy. *Opt. Lett.* 19, 780–782.

Heller, J. P., Odii, T., Zheng, K., and Rusakov, D. A. (2019). Imaging tripartite synapses using super-resolution microscopy. *Methods* doi: 10.1016/j.ymeth.2019.05.024 [Epub ahead of print].

Heuser, J. E., and Reese, T. S. (1973). Evidence for recycling of synaptic vesicle membrane during transmitter release at the frog neuromuscular junction. *J. Cell Biol.* 57, 315–344. doi: 10.1083/jcb.57.2.315

Hofmann, M., Eggeling, C., Jakobs, S., and Hell, S. W. (2005). Breaking the diffraction barrier in fluorescence microscopy at low light intensities by using reversibly photoswitchable proteins. *Proc. Natl. Acad. Sci. U.S.A.* 102, 17565–17569. doi: 10.1073/pnas.0506010102

Holubcová, Z., Howard, G., and Schuh, M. (2013). Vesicles modulate an actin network for asymmetric spindle positioning. *Nat. Cell Biol.* 15, 937–947. doi: 10.1038/ncb2802

Hoopmann, P., Punge, A., Barysch, S. V., Westphal, V., Bückers, J., Opazo, F., et al. (2010). Endosomal sorting of readily releasable synaptic vesicles. *Proc. Natl. Acad. Sci. U.S.A.* 107, 19055–19060. doi: 10.1073/pnas.1007037107

Hoopmann, P., Rizzoli, S. O., and Betz, W. J. (2012). FM dye photoconversion for visualizing synaptic vesicles by electron microscopy. *Cold Spring Harb. Protoc.* 2012, 84–86. doi: 10.1101/pdb.prot067611

Hopp, T. P., Prickett, K. S., Price, V. L., Libby, R. T., March, C. J., Cerretti, D. P., et al. (1988). A short polypeptide marker sequence useful for recombinant protein identification and purification. *BioTechnology* 6, 1204–1210. doi: 10.1038/nbt1088-1204

Howarth, M., Takao, K., Hayashi, Y., and Ting, A. Y. (2005). Targeting quantum dots to surface proteins in living cells with biotin ligase. *Proc. Natl. Acad. Sci. U.S.A.* 102, 7583–7588. doi: 10.1073/pnas.0503125102

Hoyle, N. P., Seinkmane, E., Putker, M., Feeney, K. A., Krogager, T. P., Chesham, J. E., et al. (2017). Circadian actin dynamics drive rhythmic fibroblast mobilization during wound healing. *Sci. Transl. Med.* 9, eaal2774. doi: 10.1126/scitranslmed.aal2774

Hua, Y., Sinha, R., Martineau, M., Kahms, M., and Klingauf, J. (2010). A common origin of synaptic vesicles undergoing evoked and spontaneous fusion. *Nat. Neurosci.* 13, 1451–1453. doi: 10.1038/nn.2695

Hua, Y., Sinha, R., Thiel, C. S., Schmidt, R., Hüve, J., Martens, H., et al. (2011). A readily retrievable pool of synaptic vesicles. *Nat. Neurosci.* 14, 833–839. doi: 10.1038/nn.2838

Huang, B., Wang, W., Bates, M., and Zhuang, X. (2008). Three-dimensional super-resolution imaging by stochastic optical reconstruction microscopy. *Science* 319, 810–813. doi: 10.1126/science.1153529

Huang, J., Huang, Y., Yu, H., Subramanian, D., Padmanabhan, A., Thadani, R., et al. (2012). Nonmedially assembled F-actin cables incorporate into the actomyosin ring in fission yeast. *J. Cell Biol.* 199, 831–847. doi: 10.1083/jcb.201209044

Inoue, M., Takeuchi, A., Horigane, S., Ohkura, M., Gengyo-Ando, K., Fujii, H., et al. (2015). Rational design of a high-affinity, fast, red calcium indicator R-CaMP2. *Nat. Methods* 12, 64–70. doi: 10.1038/nmeth.3185

Izeddin, I., Specht, C. G., Lelek, M., Darzacq, X., Triller, A., Zimmer, C., et al. (2011). Super-resolution dynamic imaging of dendritic spines using a low-affinity photoconvertible actin probe. *PLoS One* 6:e15611. doi: 10.1371/journal.pone.0015611

Jang, K.-J., Kim, M. S., Feltrin, D., Jeon, N. L., Suh, K.-Y., and Pertz, O. (2010). Two distinct filopodia populations at the growth cone allow to sense nanotopographical extracellular matrix cues to guide neurite outgrowth. *PLoS One* 5:e15966. doi: 10.1371/journal.pone.0015966

Jézéquel, J., Johansson, E. M., Dupuis, J. P., Rogemond, V., Gréa, H., Kellermayer, B., et al. (2017). Dynamic disorganization of synaptic NMDA receptors triggered by autoantibodies from psychotic patients. *Nat. Commun.* 8:1791. doi: 10.1038/s41467-017-01700-3

Johnson, H. W., and Schell, M. J. (2009). Neuronal IP3 3-kinase is an f-actin–bundling protein: role in dendritic targeting and regulation of spine morphology. *Mol. Biol. Cell* 20, 5166–5180. doi: 10.1091/mbc.E09-01-0083

Kahms, M., and Klingauf, J. (2018). Novel pH-sensitive lipid based exo-endocytosis tracers reveal fast intermixing of synaptic vesicle pools. *Front. Cell. Neurosci.* 12:18. doi: 10.3389/fncel.2018.00018

Kaizuka, T., and Takumi, T. (2018). Postsynaptic density proteins and their involvement in neurodevelopmental disorders. *J. Biochem.* 163, 447–455. doi: 10.1093/jb/mvy022

Keller, B.-M., Maier, J., Weldle, M., Segan, S., Traenkle, B., and Rothbauer, U. (2019). A strategy to optimize the generation of stable chromobody cell lines for visualization and quantification of endogenous proteins in living cells. *Antibodies* 8:10. doi: 10.3390/antib8010010

Kellogg, D. R., Mitchison, T. J., and Alberts, B. M. (1988). Behaviour of microtubules and actin filaments in living *Drosophila embryos*. *Dev. Camb. Engl.* 103, 675–686.

Keppler, A., Gendreizig, S., Gronemeyer, T., Pick, H., Vogel, H., and Johnsson, K. (2003). A general method for the covalent labeling of fusion proteins with small molecules in vivo. *Nat. Biotechnol.* 21, 86–99. doi: 10.1038/nbt765

Kerr, J. M., and Blanpied, T. A. (2012). Subsynaptic AMPA receptor distribution is acutely regulated by actin-driven reorganization of the postsynaptic density. *J. Neurosci.* 32, 658–673. doi: 10.1523/JNEUROSCI.2927-11.2012

Kiuchi, T., Higuchi, M., Takamura, A., Maruoka, M., and Watanabe, N. (2015). Multitarget super-resolution microscopy with high-density labeling by exchangeable probes. *Nat. Methods* 12, 743–746. doi: 10.1038/nmeth.3466

Klockow, J. L., Hettie, K. S., and Glass, T. E. (2013). ExoSensor 517: a dual-analyte fluorescent chemosensor for visualizing neurotransmitter exocytosis. *ACS Chem. Neurosci.* 4, 1334–1338. doi: 10.1021/cn400128s

Korobova, F., and Svitkina, T. (2009). Molecular architecture of synaptic actin cytoskeleton in hippocampal neurons reveals a mechanism of dendritic spine morphogenesis. *Mol. Biol. Cell* 21, 165–176. doi: 10.1091/mbc.e09-07-0596

Koskinen, M., and Hotulainen, P. (2014). Measuring F-actin properties in dendritic spines. *Front. Neuroanat.* 8:74. doi: 10.3389/fnana.2014.00074

Kovar, D. R., Harris, E. S., Mahaffy, R., Higgs, H. N., and Pollard, T. D. (2006). Control of the assembly of ATP- and ADP-actin by formins and profilin. *Cell* 124, 423–435. doi: 10.1016/j.cell.2005.11.038

Kraszewski, K., Mundigl, O., Daniell, L., Verderio, C., Matteoli, M., and De Camilli, P. (1995). Synaptic vesicle dynamics in living cultured hippocampal neurons visualized with CY3-conjugated antibodies directed against the lumenal domain of synaptotagmin. *J. Neurosci. Off. J. Soc. Neurosci.* 15, 4328–4342. doi: 10.1523/jneurosci.15-06-04328.1995

Kronlage, C., Schäfer-Herte, M., Böning, D., Oberleithner, H., and Fels, J. (2015). Feeling for filaments: quantification of the cortical actin web in live vascular endothelium. *Biophys. J.* 109, 687–698. doi: 10.1016/j.bpj.2015.06.066

Kuriu, T., Inoue, A., Bito, H., Sobue, K., and Okabe, S. (2006). Differential control of postsynaptic density scaffolds via actin-dependent and -independent mechanisms. *J. Neurosci.* 26, 7693–7706. doi: 10.1523/JNEUROSCI.0522-06.2006

Kuzmenkov, A. I., Nekrasova, O. V., Kudryashova, K. S., Peigneur, S., Tytgat, J., Stepanov, A. V., et al. (2016). Fluorescent protein-scorpion toxin chimera is a convenient molecular tool for studies of potassium channels. *Sci. Rep.* 6:33314. doi: 10.1038/srep33314

Ladepeche, L., Dupuis, J. P., Bouchet, D., Doudnikoff, E., Yang, L., Campagne, Y., et al. (2013). Single-molecule imaging of the functional crosstalk between surface NMDA and dopamine D1 receptors. *Proc. Natl. Acad. Sci. U.S.A.* 110, 18005–18010. doi: 10.1073/pnas.1310145110

Larsson, V. J., Jafferali, M. H., Vijayaraghavan, B., Figueroa, R. A., and Hallberg, E. (2018). Mitotic spindle assembly and γ-tubulin localisation depend on the integral nuclear membrane protein samp1. *J. Cell Sci.* 131:jcs211664. doi: 10.1242/jcs.211664

Lee, S. H., Jin, C., Cai, E., Ge, P., Ishitsuka, Y., Teng, K. W., et al. (2017). Super-resolution imaging of synaptic and Extra-synaptic AMPA receptors with different-sized fluorescent probes. *ELIFE* 6:e27744. doi: 10.7554/eLife.27744

Lei, W., Myers, K. R., Rui, Y., Hladyshau, S., Tsygankov, D., and Zheng, J. Q. (2017). Phosphoinositide-dependent enrichment of actin monomers in dendritic spines regulates synapse development and plasticity. *J. Cell Biol.* 216, 2551–2564. doi: 10.1083/jcb.201612042

Leipold, E., Hansel, A., Olivera, B. M., Terlau, H., and Heinemann, S. H. (2005). Molecular interaction of δ-conotoxins with voltage-gated sodium channels. *FEBS Lett.* 579, 3881–3884. doi: 10.1016/j.febslet.2005.05.077

Lemieux, M. G., Janzen, D., Hwang, R., Roldan, J., Jarchum, I., and Knecht, D. A. (2014). Visualization of the actin cytoskeleton: different F-actin-binding probes tell different stories. *Cytoskeleton* 71, 157–169. doi: 10.1002/cm.21160

Leyton-Puig, D., Kedziora, K. M., Isogai, T., van den Broek, B., Jalink, K., and Innocenti, M. (2016). PFA fixation enables artifact-free super-resolution imaging of the actin cytoskeleton and associated proteins. *Biol. Open* 5, 1001–1009. doi: 10.1242/bio.019570

Li, D., Shao, L., Chen, B.-C., Zhang, X., Zhang, M., Moses, B., et al. (2015). Extended-resolution structured illumination imaging of endocytic and cytoskeletal dynamics. *Science* 349:aab3500. doi: 10.1126/science.aab3500

Li, H., Guo, F., Rubinstein, B., and Li, R. (2008). Actin-driven chromosomal motility leads to symmetry breaking in mammalian meiotic oocytes. *Nat. Cell Biol.* 10, 1301–1308. doi: 10.1038/ncb1788

Lillo, M. P., Cañadas, O., Dale, R. E., and Acuña, A. U. (2002). Location and properties of the taxol binding center in microtubules: a picosecond laser study with fluorescent taxoids. *Biochemistry* 41, 12436–12449. doi: 10.1021/bi0261793

Lin, M. Z., and Schnitzer, M. J. (2016). Genetically encoded indicators of neuronal activity. *Nat. Neurosci.* 19, 1142–1153. doi: 10.1038/nn.4359

Liu, D. S., Loh, K. H., Lam, S. S., White, K. A., and Ting, A. Y. (2013). Imaging trans-cellular neurexin-neuroligin interactions by enzymatic probe ligation. *PLoS One* 8:e52823. doi: 10.1371/journal.pone.0052823

Lopata, A., Hughes, R., Tiede, C., Heissler, S. M., Sellers, J. R., Knight, P. J., et al. (2018). Affimer proteins for F-actin: novel affinity reagents that label F-actin in live and fixed cells. *Sci. Rep.* 8:6572. doi: 10.1038/s41598-018-24953-4

Lorenz, M., DesMarais, V., Macaluso, F., Singer, R. H., and Condeelis, J. (2004). Measurement of barbed ends, actin polymerization, and motility in live carcinoma cells after growth factor stimulation. *Cell Motil.* 57, 207–217. doi: 10.1002/cm.10171

Los, G. V., Encell, L. P., McDougall, M. G., Hartzell, D. D., Karassina, N., Zimprich, C., et al. (2008). HaloTag: a novel protein labeling technology for cell imaging and protein analysis. *ACS Chem. Biol.* 3, 373–382. doi: 10.1021/cb800025k

Lu, H., Fagnant, P. M., Bookwalter, C. S., Joel, P., and Trybus, K. M. (2015). Vascular disease-causing mutation R258C in ACTA2 disrupts actin dynamics and interaction with myosin. *Proc. Natl. Acad. Sci. U.S.A.* 112, E4168–E4177. doi: 10.1073/pnas.1507587112

Lukinavičius, G., Mitronova, G. Y., Schnorrenberg, S., Butkevich, A. N., Barthel, H., Belov, V. N., et al. (2018). Fluorescent dyes and probes for super-resolution microscopy of microtubules and tracheoles in living cells and tissues. *Chem. Sci.* 9, 3324–3334. doi: 10.1039/C7SC05334G

Lukinavičius, G., Reymond, L., D'Este, E., Masharina, A., Göttfert, F., Ta, H., et al. (2014). Fluorogenic probes for live-cell imaging of the cytoskeleton. *Nat. Methods* 11, 731–733. doi: 10.1038/nmeth.2972

Lynch, S. M., Zhou, C., and Messer, A. (2008). An scFv intrabody against the nonamyloid component of alpha-synuclein reduces intracellular aggregation and toxicity. *J. Mol. Biol.* 377, 136–147. doi: 10.1016/j.jmb.2007.11.096

Lysakowski, A., Figueras, H., Price, S. D., and Peng, Y.-Y. (1999). Dense-cored vesicles, smooth endoplasmic reticulum, and mitochondria are closely associated with non-specialized parts of plasma membrane of nerve terminals: implications for exocytosis and calcium buffering by intraterminal organelles. *J. Comp. Neurol.* 403, 378–390. doi: 10.1002/(sici)1096-9861(19990118)403:3<378::aid-cne7>3.0.co;2-x

Mace, E. M., and Orange, J. S. (2012). Dual channel STED nanoscopy of lytic granules on actin filaments in natural killer cells. *Commun. Integr. Biol.* 5, 184–186. doi: 10.4161/cib.18818

MacGillavry, H. D., Song, Y., Raghavachari, S., and Blanpied, T. A. (2013). Nanoscale scaffolding domains within the postsynaptic density concentrate synaptic AMPA receptors. *Neuron* 78, 615–622. doi: 10.1016/j.neuron.2013.03.009

Magliocca, V., Petrini, S., Franchin, T., Borghi, R., Niceforo, A., Abbaszadeh, Z., et al. (2017). Identifying the dynamics of actin and tubulin polymerization in iPSCs and in iPSC-derived neurons. *Oncotarget* 8, 111096–111109. doi: 10.18632/oncotarget.22571

Maidorn, M., Olichon, A., Rizzoli, S. O., and Opazo, F. (2019). Nanobodies reveal an extra-synaptic population of SNAP-25 and Syntaxin 1A in hippocampal neurons. *MABS* 11, 305–321. doi: 10.1080/19420862.2018.1551675

Martens, H., Weston, M. C., Boulland, J.-L., Grønborg, M., Grosche, J., Kacza, J., et al. (2008). Unique luminal localization of VGAT-C terminus allows for selective labeling of active cortical GABAergic synapses. *J. Neurosci.* 28, 13125–13131. doi: 10.1523/JNEUROSCI.3887-08.2008

Matteoli, M., Takei, K., Perin, M. S., Südhof, T. C., and Camilli, P. D. (1992). Exo-endocytotic recycling of synaptic vesicles in developing processes of cultured hippocampal neurons. *J. Cell Biol.* 117, 849–861. doi: 10.1083/jcb.117.4.849

Maupin-Szamier, P., and Pollard, T. D. (1978). Actin filament destruction by osmium tetroxide. *J. Cell Biol.* 77, 837–852. doi: 10.1083/jcb.77.3.837

McCann, C. M., and Lichtman, J. W. (2008). In vivo imaging of presynaptic terminals and postsynaptic sites in the mouse submandibular ganglion. *Dev. Neurobiol.* 68, 760–770. doi: 10.1002/dneu.20621

McDonald, L., Liu, B., Taraboletti, A., Whiddon, K., Shriver, L. P., Konopka, M., et al. (2016). Fluorescent flavonoids for endoplasmic reticulum cell imaging. *J. Mater. Chem. B Mater. Biol. Med.* 4, 7902–7908. doi: 10.1039/c6tb02456d

McGough, A., Pope, B., Chiu, W., and Weeds, A. (1997). Cofilin changes the twist of F-Actin: implications for actin filament dynamics and cellular function. *J. Cell Biol.* 138, 771–781. doi: 10.1083/jcb.138.4.771

McMahon, S. M., and Jackson, M. B. (2018). An inconvenient truth: calcium sensors are calcium buffers. *Trends Neurosci.* 41, 880–884. doi: 10.1016/j.tins.2018.09.005

Merriam, E. B., Millette, M., Lumbard, D. C., Saengsawang, W., Fothergill, T., Hu, X., et al. (2013). Synaptic regulation of microtubule dynamics in dendritic spines by calcium. F-Actin, and Drebrin. *J. Neurosci.* 33, 16471–16482. doi: 10.1523/JNEUROSCI.0661-13.2013

Michalet, X., Pinaud, F. F., Bentolila, L. A., Tsay, J. M., Doose, S., Li, J. J., et al. (2005). Quantum dots for live cells, in vivo imaging, and diagnostics. *Science* 307, 538–544. doi: 10.1126/science.1104274

Mikasova, L., Xiong, H., Kerkhofs, A., Bouchet, D., Krugers, H. J., and Groc, L. (2017). Stress hormone rapidly tunes synaptic NMDA receptor through membrane dynamics and mineralocorticoid signalling. *Sci. Rep.* 7:8053. doi: 10.1038/s41598-017-08695-3

Mikhaylova, M., Cloin, B. M. C., Finan, K., van den Berg, R., Teeuw, J., Kijanka, M. M., et al. (2015). Resolving bundled microtubules using anti-tubulin nanobodies. *Nat. Commun.* 6:7933. doi: 10.1038/ncomms8933

Miller, E. W. (2016). Small molecule fluorescent voltage indicators for studying membrane potential. *Curr. Opin. Chem. Biol.* 33, 74–80. doi: 10.1016/j.cbpa.2016.06.003

Milles, S., Tyagi, S., Banterle, N., Koehler, C., VanDelinder, V., Plass, T., et al. (2012). Click strategies for single-molecule protein fluorescence. *J. Am. Chem. Soc.* 134, 5187–5195. doi: 10.1021/ja210587q

Morales, M., Colicos, M. A., and Goda, Y. (2000). Actin-dependent regulation of neurotransmitter release at central synapses. *Neuron* 27, 539–550. doi: 10.1016/S0896-6273(00)00064-67

Moutel, S., Bery, N., Bernard, V., Keller, L., Lemesre, E., de Marco, A., et al. (2016). NaLi-H1: a universal synthetic library of humanized nanobodies providing highly functional antibodies and intrabodies. *Elife* 5:e16228. doi: 10.7554/eLife.16228

Mundel, P., Heid, H. W., Mundel, T. M., Krüger, M., Reiser, J., and Kriz, W. (1997). Synaptopodin: an actin-associated protein in telencephalic dendrites and renal podocytes. *J. Cell Biol.* 139, 193–204. doi: 10.1083/jcb.139.1.193

Munsie, L. N., Caron, N., Desmond, C. R., and Truant, R. (2009). Lifeact cannot visualize some forms of stress-induced twisted F-actin. *Nat. Methods* 6:317. doi: 10.1038/nmeth0509-317

Nagai, T., Yamada, S., Tominaga, T., Ichikawa, M., and Miyawaki, A. (2004). Expanded dynamic range of fluorescent indicators for Ca2+ by circularly permuted yellow fluorescent proteins. *Proc. Natl. Acad. Sci. U.S.A.* 101, 10554–10559. doi: 10.1073/pnas.0400417101

Nair, D., Hosy, E., Petersen, J. D., Constals, A., Giannone, G., Choquet, D., et al. (2013). Super-resolution imaging reveals that AMPA receptors inside synapses are dynamically organized in nanodomains regulated by PSD95. *J. Neurosci.* 33, 13204–13224. doi: 10.1523/JNEUROSCI.2381-12.2013

Nakai, J., Ohkura, M., and Imoto, K. (2001). A high signal-to-noise Ca 2+ probe composed of a single green fluorescent protein. *Nat. Biotechnol.* 19, 137–141. doi: 10.1038/84397

Neupane, B., Jin, T., Mellor, L. F., Loboa, E. G., Ligler, F. S., and Wang, G. (2015). Continuous-wave stimulated emission depletion microscope for imaging actin cytoskeleton in fixed and live cells. *Sensors* 15, 24178–24190. doi: 10.3390/s150924178

Nicke, A., Wonnacott, S., and Lewis, R. J. (2004). α-Conotoxins as tools for the elucidation of structure and function of neuronal nicotinic acetylcholine receptor subtypes. *Eur. J. Biochem.* 271, 2305–2319. doi: 10.1111/j.1432-1033.2004.04145.x

Nielsen, K. J., Schroeder, T., and Lewis, R. (2000). Structure–activity relationships of ω-conotoxins at N-type voltage-sensitive calcium channels. *J. Mol. Recognit.* 13, 55–70. doi: 10.1002/(sici)1099-1352(200003/04)13:2<55::aid-jmr488>3.0.co;2-o

Nishimune, H., Badawi, Y., Mori, S., and Shigemoto, K. (2016). Dual-color STED microscopy reveals a sandwich structure of bassoon and Piccolo in active zones of adult and aged mice. *Sci. Rep.* 6:27935. doi: 10.1038/srep27935

Okumoto, S., Looger, L. L., Micheva, K. D., Reimer, R. J., Smith, S. J., and Frommer, W. B. (2005). Detection of glutamate release from neurons by genetically encoded surface-displayed FRET nanosensors. *Proc. Natl. Acad. Sci. U.S.A.* 102, 8740–8745. doi: 10.1073/pnas.0503274102

Orth, C. B., Vlachos, A., Turco, D. D., Burbach, G. J., Haas, C. A., Mundel, P., et al. (2005). Lamina-specific distribution of synaptopodin, an actin-associated molecule essential for the spine apparatus, in identified principal cell dendrites of the mouse hippocampus. *J. Comp. Neurol.* 487, 227–239. doi: 10.1002/cne.20539

Oser, M., Yamaguchi, H., Mader, C. C., Bravo-Cordero, J. J., Arias, M., Chen, X., et al. (2009). Cortactin regulates cofilin and N-WASp activities to control the stages of invadopodium assembly and maturation. *J. Cell Biol.* 186, 571–587. doi: 10.1083/jcb.200812176

Paknikar, A. K., Eltzner, B., and Köster, S. (2019). Direct characterization of cytoskeletal reorganization during blood platelet spreading. *Prog. Biophys. Mol. Biol.* 144, 166–176. doi: 10.1016/j.pbiomolbio.2018.05.001

Palay, S. L. (1956). Synapses in the central nervous system. *J. Biophys. Biochem. Cytol.* 2, 193–202.

Pan, L., Yan, R., Li, W., and Xu, K. (2018). Super-resolution microscopy reveals the native ultrastructure of the erythrocyte cytoskeleton. *Cell Rep.* 22, 1151–1158. doi: 10.1016/j.celrep.2017.12.107

Panza, P., Maier, J., Schmees, C., Rothbauer, U., and Söllner, C. (2015). Live imaging of endogenous protein dynamics in zebrafish using chromobodies. *Development* 142, 1879–1884. doi: 10.1242/dev.118943

Paredes, R. M., Etzler, J. C., Watts, L. T., and Lechleiter, J. D. (2008). Chemical calcium indicators. *Methods* 46, 143–151. doi: 10.1016/j.ymeth.2008.09.025

Park, H., Li, Y., and Tsien, R. W. (2012). Influence of synaptic vesicle position on release probability and exocytotic fusion mode. *Science* 335, 1362–1366. doi: 10.1126/science.1216937

Patel, S., Fok, S. Y. Y., Stefen, H., Tomanić, T., Parić, E., Herold, R., et al. (2017). Functional characterisation of filamentous actin probe expression in neuronal cells. *PLoS One* 12:e0187979. doi: 10.1371/journal.pone.0187979

Patrizio, A., Renner, M., Pizzarelli, R., Triller, A., and Specht, C. G. (2017). Alpha subunit-dependent glycine receptor clustering and regulation of synaptic receptor numbers. *Sci. Rep.* 7:10899. doi: 10.1038/s41598-017-11264-3

Pereira, P. M., Albrecht, D., Culley, S., Jacobs, C., Marsh, M., Mercer, J., et al. (2019). Fix your membrane receptor imaging: actin cytoskeleton and CD4 membrane organization disruption by chemical fixation. *Front. Immunol.* 10:675. doi: 10.3389/fimmu.2019.00675

Perkins, G. A., Tjong, J., Brown, J. M., Poquiz, P. H., Scott, R. T., Kolson, D. R., et al. (2010). The micro-architecture of mitochondria at active zones: electron tomography reveals novel anchoring scaffolds and cristae structured for high-rate metabolism. *J. Neurosci.* 30, 1015–1026. doi: 10.1523/JNEUROSCI.1517-09.2010

Pleiner, T., Bates, M., and Görlich, D. (2018). A toolbox of anti–mouse and anti–rabbit IgG secondary nanobodies. *J. Cell Biol.* 217, 1143–1154. doi: 10.1083/jcb.201709115

Plessner, M., Melak, M., Chinchilla, P., Baarlink, C., and Grosse, R. (2015). Nuclear F-actin formation and reorganization upon cell spreading. *J. Biol. Chem.* 290, 11209–11216. doi: 10.1074/jbc.M114.627166

Poot, M., Zhang, Y. Z., Krämer, J. A., Wells, K. S., Jones, L. J., Hanzel, D. K., et al. (1996). Analysis of mitochondrial morphology and function with novel fixable fluorescent stains. *J. Histochem. Cytochem.* 44, 1363–1372. doi: 10.1177/44.12.8985128

Pyle, J. L., Kavalali, E. T., Piedras-Rentería, E. S., and Tsien, R. W. (2000). Rapid reuse of readily releasable pool vesicles at hippocampal synapses. *Neuron* 28, 221–231. doi: 10.1016/s0896-6273(00)00098-2

Qian, Y., Piatkevich, K. D., Mc Larney, B., Abdelfattah, A. S., Mehta, S., Murdock, M. H., et al. (2019). A genetically encoded near-infrared fluorescent calcium ion indicator. *Nat. Methods* 16, 171–174. doi: 10.1038/s41592-018-0294-6

Qu, Y., Hahn, I., Webb, S. E. D., Pearce, S. P., and Prokop, A. (2016). Periodic actin structures in neuronal axons are required to maintain microtubules. *Mol. Biol. Cell* 28, 296–308. doi: 10.1091/mbc.e16-10-0727

Rácz, B. L., and Weinberg, R. J. (2013). Microdomains in forebrain spines: an ultrastructural perspective. *Mol. Neurobiol.* 47, 77–89. doi: 10.1007/s12035-012-8345-y

Rankin, B. R., Kellner, R. R., and Hell, S. W. (2008). Stimulated-emission-depletion microscopy with a multicolor stimulated-Raman-scattering light source. *Opt. Lett.* 33, 2491–2493. doi: 10.1364/OL.33.002491

Rego, E. H., Shao, L., Macklin, J. J., Winoto, L., Johansson, G. A., Kamps-Hughes, N., et al. (2012). Nonlinear structured-illumination microscopy with a photoswitchable protein reveals cellular structures at 50-nm resolution. *Proc. Natl. Acad. Sci. U.S.A.* 109, E135–E143. doi: 10.1073/pnas.1107547108

Revelo, N. H., Kamin, D., Truckenbrodt, S., Wong, A. B., Reuter-Jessen, K., Reisinger, E., et al. (2014). A new probe for super-resolution imaging of membranes elucidates trafficking pathways. *J. Cell Biol.* 205, 591–606. doi: 10.1083/jcb.201402066

Richards, D. A., Guatimosim, C., and Betz, W. J. (2000). Two endocytic recycling routes selectively fill two vesicle pools in frog motor nerve terminals. *Neuron* 27, 551–559. doi: 10.1016/s0896-6273(00)00065-9

Richards, D. A., Rizzoli, S. O., and Betz, W. J. (2004). Effects of wortmannin and latrunculin a on slow endocytosis at the frog neuromuscular junction. *J. Physiol.* 557, 77–91. doi: 10.1113/jphysiol.2004.062158

Richter, K. N., Revelo, N. H., Seitz, K. J., Helm, M. S., Sarkar, D., Saleeb, R. S., et al. (2017). Glyoxal as an alternative fixative to formaldehyde in immunostaining and super-resolution microscopy. *EMBO J.* 37, 139–159. doi: 10.15252/embj.201695709

Riedl, J., Crevenna, A. H., Kessenbrock, K., Yu, J. H., Neukirchen, D., Bista, M., et al. (2008). Lifeact: a versatile marker to visualize F-actin. *Nat. Methods* 5, 605–607. doi: 10.1038/nmeth.1220

Riedl, J., Flynn, K. C., Raducanu, A., Gärtner, F., Beck, G., Bösl, M., et al. (2010). Lifeact mice for studying F-actin dynamics. *Nat. Methods* 7, 168–169. doi: 10.1038/nmeth0310-168

Ries, J., Kaplan, C., Platonova, E., Eghlidi, H., and Ewers, H. (2012). A simple, versatile method for GFP-based super-resolution microscopy via nanobodies. *Nat. Methods* 9, 582–584. doi: 10.1038/nmeth.1991

Rinnerthaler, G., Geiger, B., and Small, J. V. (1988). Contact formation during fibroblast locomotion: involvement of membrane ruffles and microtubules. *J. Cell Biol.* 106, 747–760. doi: 10.1083/jcb.106.3.747

Robison, P., Caporizzo, M. A., Ahmadzadeh, H., Bogush, A. I., Chen, C. Y., Margulies, K. B., et al. (2016). Detyrosinated microtubules buckle and bear load in contracting cardiomyocytes. *Science* 352:aaf0659. doi: 10.1126/science.aaf0659

Rocchetti, A., Hawes, C., and Kriechbaumer, V. (2014). Fluorescent labelling of the actin cytoskeleton in plants using a cameloid antibody. *Plant Methods* 10:12. doi: 10.1186/1746-4811-10-12

Römer, W., Pontani, L.-L., Sorre, B., Rentero, C., Berland, L., Chambon, V., et al. (2010). Actin dynamics drive membrane reorganization and scission in clathrin-independent endocytosis. *Cell* 140, 540–553. doi: 10.1016/j.cell.2010.01.010

Rust, M. J., Bates, M., and Zhuang, X. (2006). Sub-diffraction-limit imaging by stochastic optical reconstruction microscopy (STORM). *Nat. Methods* 3, 793–795. doi: 10.1038/nmeth929

Sanders, T. A., Llagostera, E., and Barna, M. (2013). Specialized filopodia direct long-range transport of SHH during vertebrate tissue patterning. *Nature* 497, 628–632. doi: 10.1038/nature12157

Sankaranarayanan, S., Atluri, P. P., and Ryan, T. A. (2003). Actin has a molecular scaffolding, not propulsive, role in presynaptic function. *Nat. Neurosci.* 6, 127–135. doi: 10.1038/nn1002

Sankaranarayanan, S., De Angelis, D., Rothman, J. E., and Ryan, T. A. (2000). The use of pHluorins for optical measurements of presynaptic activity. *Biophys. J.* 79, 2199–2208. doi: 10.1016/S0006-3495(00)76468-X

Sara, Y., Virmani, T., Deák, F., Liu, X., and Kavalali, E. T. (2005). An isolated pool of vesicles recycles at rest and drives spontaneous neurotransmission. *Neuron* 45, 563–573. doi: 10.1016/j.neuron.2004.12.056

Scaduto, R. C., and Grotyohann, L. W. (1999). Measurement of mitochondrial membrane potential using fluorescent rhodamine derivatives. *Biophys. J.* 76, 469–477. doi: 10.1016/S0006-3495(99)77214-0

Schapitz, I. U., Behrend, B., Pechmann, Y., Lappe-Siefke, C., Kneussel, S. J., Wallace, K. E., et al. (2010). Neuroligin 1 is dynamically exchanged at postsynaptic sites. *J. Neurosci.* 30, 12733–12744. doi: 10.1523/JNEUROSCI.0896-10.2010

Schell, M. J., Erneux, C., and Irvine, R. F. (2001). Inositol 1,4,5-trisphosphate 3-Kinase a associates with f-actin and dendritic spines via its N terminus. *J. Biol. Chem.* 276, 37537–37546. doi: 10.1074/jbc.M104101200

Schenck, S., Kunz, L., Sahlender, D., Pardon, E., Geertsma, E. R., Savtchouk, I., et al. (2017). Generation and characterization of anti-VGLUT nanobodies acting as inhibitors of transport. *Biochemistry* 56, 3962–3971. doi: 10.1021/acs.biochem.7b00436

Schikorski, T., and Stevens, C. F. (1997). Quantitative ultrastructural analysis of hippocampal excitatory synapses. *J. Neurosci.* 17, 5858–5867. doi: 10.1523/jneurosci.17-15-05858.1997

Schoen, M., Reichel, J. M., Demestre, M., Putz, S., Deshpande, D., Proepper, C., et al. (2016). Super-resolution microscopy reveals presynaptic localization of the ALS/FTD related protein fus in hippocampal neurons. *Front. Cell. Neurosci.* 9:496. doi: 10.3389/fncel.2015.00496

Sekhar, A. R., Mallik, B., Kumar, V., and Sankar, J. (2019). A cell-permeant small molecule for the super-resolution imaging of the endoplasmic reticulum in live cells. *Org. Biomol. Chem.* 17, 3732–3736. doi: 10.1039/C9OB00408D

Sekine-Aizawa, Y., and Huganir, R. L. (2004). Imaging of receptor trafficking by using α-bungarotoxin-binding-site-tagged receptors. *Proc. Natl. Acad. Sci. U.S.A.* 101, 17114–17119. doi: 10.1073/pnas.0407563101

Sharonov, A., and Hochstrasser, R. M. (2006). Wide-field subdiffraction imaging by accumulated binding of diffusing probes. *Proc. Natl. Acad. Sci. U.S.A.* 103, 18911–18916. doi: 10.1073/pnas.0609643104

Shimomura, O., Johnson, F. H., and Saiga, Y. (1962). Extraction, purification and properties of aequorin, a bioluminescent protein from the luminous hydromedusan, aequorea. *J. Cell. Comp. Physiol.* 59, 223–239. doi: 10.1002/jcp.1030590302

Shon, K.-J., Stocker, M., Terlau, H., Stühmer, W., Jacobsen, R., Walker, C., et al. (1998). κ-conotoxin pviia is a peptide inhibiting theshaker K+ channel. *J. Biol. Chem.* 273, 33–38. doi: 10.1074/jbc.273.1.33

Shupliakov, O., Bloom, O., Gustafsson, J. S., Kjaerulff, O., Low, P., Tomilin, N., et al. (2002). Impaired recycling of synaptic vesicles after acute perturbation of the presynaptic actin cytoskeleton. *Proc. Natl. Acad. Sci. U.S.A.* 99, 14476–14481. doi: 10.1073/pnas.212381799

Sidenstein, S. C., D'Este, E., Böhm, M. J., Danzl, J. G., Belov, V. N., and Hell, S. W. (2016). Multicolour multilevel STED nanoscopy of actin/spectrin organization at synapses. *Sci. Rep.* 6:26725. doi: 10.1038/srep26725

Small, J. V. (1988). The actin cytoskeleton. *Electron Microsc. Rev.* 1, 155–174.

Smith, A. J., Taneja, T. K., Mankouri, J., and Sivaprasadarao, A. (2007). Molecular cell biology of KATP channels: implications for neonatal diabetes. *Expert Rev. Mol. Med.* 9, 1–17. doi: 10.1017/S1462399407000403

Spacek, J., and Harris, K. M. (1997). Three-dimensional organization of smooth endoplasmic reticulum in hippocampal CA1 dendrites and dendritic spines of the immature and mature rat. *J. Neurosci.* 17, 190–203. doi: 10.1523/jneurosci.17-01-00190.1997

Specht, C. G., Izeddin, I., Rodriguez, P. C., El Beheiry, M., Rostaing, P., Darzacq, X., et al. (2013). Quantitative nanoscopy of inhibitory synapses: counting gephyrin molecules and receptor binding sites. *Neuron* 79, 308–321. doi: 10.1016/j.neuron.2013.05.013

Spracklen, A. J., Fagan, T. N., Lovander, K. E., and Tootle, T. L. (2014). The pros and cons of common actin labeling tools for visualizing actin dynamics during *Drosophila oogenesis*. *Dev. Biol.* 393, 209–226. doi: 10.1016/j.ydbio.2014.06.022

Stepanova, T., Slemmer, J., Hoogenraad, C. C., Lansbergen, G., Dortland, B., De Zeeuw, C. I., et al. (2003). Visualization of microtubule growth in cultured neurons via the use of EB3-GFP (end-binding protein 3-green fluorescent protein). *J. Neurosci.* 23, 2655–2664. doi: 10.1523/jneurosci.23-07-02655.2003

St-Pierre, F., Chavarha, M., and Lin, M. Z. (2015). Designs and sensing mechanisms of genetically encoded fluorescent voltage indicators. *Curr. Opin. Chem. Biol.* 27, 31–38. doi: 10.1016/j.cbpa.2015.05.003

Subach, O. M., Barykina, N. V., Anokhin, K. V., Piatkevich, K. D., and Subach, F. V. (2019). Near-infrared genetically encoded positive calcium indicator based on GAF-FP bacterial phytochrome. *Int. J. Mol. Sci.* 20:E3488. doi: 10.3390/ijms20143488

Südhof, T. C. (2012). The presynaptic active zone. *Neuron* 75, 11–25. doi: 10.1016/j.neuron.2012.06.012

Takahashi, A., Camacho, P., Lechleiter, J. D., and Herman, B. (1999). Measurement of intracellular calcium. *Physiol. Rev.* 79, 1089–1125. doi: 10.1152/physrev.1999.79.4.1089

Tao-Cheng, J.-H., Thein, S., Yang, Y., Reese, T. S., and Gallant, P. E. (2014). Homer is concentrated at the postsynaptic density and does not redistribute after acute synaptic stimulation. *Neuroscience* 266, 80–90. doi: 10.1016/j.neuroscience.2014.01.066

Tardin, C., Cognet, L., Bats, C., Lounis, B., and Choquet, D. (2003). Direct imaging of lateral movements of AMPA receptors inside synapses. *EMBO J.* 22, 4656–4665. doi: 10.1093/emboj/cdg463

Taylor, M. J., Lampe, M., and Merrifield, C. J. (2012). A feedback loop between dynamin and actin recruitment during clathrin-mediated endocytosis. *PLoS Biol.* 10:e1001302. doi: 10.1371/journal.pbio.1001302

Taylor, R. D., Heine, M., Emptage, N. J., and Andreae, L. C. (2018). Neuronal receptors display cytoskeleton-independent directed motion on the plasma membrane. *iScience* 10, 234–244. doi: 10.1016/j.isci.2018.12.001

Testa, I., Urban, N. T., Jakobs, S., Eggeling, C., Willig, K. I., and Hell, S. W. (2012). Nanoscopy of living brain slices with low light levels. *Neuron* 75, 992–1000. doi: 10.1016/j.neuron.2012.07.028

Testa, I., Wurm, C. A., Medda, R., Rothermel, E., von Middendorf, C., Fölling, J., et al. (2010). multicolor fluorescence nanoscopy in fixed and living cells by exciting conventional fluorophores with a single wavelength. *Biophys. J.* 99, 2686–2694. doi: 10.1016/j.bpj.2010.08.012

Theg, D. E. (1964). Cytoplasmic microtubules in different animal cells. *J. Cell Biol.* 23, 265–275. doi: 10.1083/jcb.23.2.265

Thevathasan, J. V., Kahnwald, M., Cieśliński, K., Hoess, P., Peneti, S. K., Reitberger, M., et al. (2019). Nuclear pores as versatile reference standards for quantitative superresolution microscopy. *bioRxiv* 582668. doi: 10.1101/582668

Tiede, C., Bedford, R., Heseltine, S. J., Smith, G., Wijetunga, I., Ross, R., et al. (2017). Affimer proteins are versatile and renewable affinity reagents. *ELIFE* 6:e24903. doi: 10.7554/eLife.24903

Torregrosa-Hetland, C. J., Villanueva, J., Garcia-Martínez, V., Expósito-Romero, G., Francés, M., del, M., et al. (2013). Cortical F-actin affects the localization and dynamics of SNAP-25 membrane clusters in chromaffin cells. *Int. J. Biochem. Cell Biol.* 45, 583–592. doi: 10.1016/j.biocel.2012.11.021

Truckenbrodt, S., Maidorn, M., Crzan, D., Wildhagen, H., Kabatas, S., and Rizzoli, S. O. (2018a). X10 expansion microscopy enables 25-nm resolution on conventional microscopes. *EMBO Rep.* 19:e45836. doi: 10.15252/embr.201845836

Truckenbrodt, S., Viplav, A., Jähne, S., Vogts, A., Denker, A., Wildhagen, H., et al. (2018b). Newly produced synaptic vesicle proteins are preferentially used in synaptic transmission. *EMBO J.* 37:e98044. doi: 10.15252/embj.201798044

Tucker, K. R., Cavolo, S. L., and Levitan, E. S. (2016). Elevated mitochondria-coupled NAD(P)H in endoplasmic reticulum of dopamine neurons. *Mol. Biol. Cell* 27, 3214–3220. doi: 10.1091/mbc.E16-07-0479

Urban, N. T., Willig, K. I., Hell, S. W., and Nägerl, U. V. (2011). STED nanoscopy of actin dynamics in synapses deep inside living brain slices. *Biophys. J.* 101, 1277–1284. doi: 10.1016/j.bpj.2011.07.027

van de Linde, S., Löschberger, A., Klein, T., Heidbreder, M., Wolter, S., Heilemann, M., et al. (2011). Direct stochastic optical reconstruction microscopy with standard fluorescent probes. *Nat. Protoc.* 6, 991–1009. doi: 10.1038/nprot.2011.336

van den Dries, K., Schwartz, S. L., Byars, J., Meddens, M. B., Bolomini-Vittori, M., Lidke, D. S., et al. (2013). Dual-color superresolution microscopy reveals nanoscale organization of mechanosensory podosomes. *Mol. Biol. Cell* 24, 2112–2123. doi: 10.1091/mbc.E12-12-0856

Vassilopoulos, S., Gibaud, S., Jimenez, A., Caillol, G., and Leterrier, C. (2019). Ultrastructure of the axonal periodic scaffold reveals a braid-like organization of actin rings. *bioRxiv* 636217. doi: 10.1101/636217

Vidali, L., Rounds, C. M., Hepler, P. K., and Bezanilla, M. (2009). Lifeact-mEGFP reveals a dynamic apical F-Actin network in tip growing plant cells. *PLoS One* 4:e5744. doi: 10.1371/journal.pone.0005744

Vincke, C., and Muyldermans, S. (2012). Introduction to heavy chain antibodies and derived Nanobodies. *Methods Mol. Biol.* 911, 15–26. doi: 10.1007/978-1-61779-968-6_2

Virant, D., Traenkle, B., Maier, J., Kaiser, P. D., Bodenhöfer, M., Schmees, C., et al. (2018). A peptide tag-specific nanobody enables high-quality labeling for dSTORM imaging. *Nat. Commun.* 9:930. doi: 10.1038/s41467-018-03191-2

Visegrády, B., Lorinczy, D., Hild, G., Somogyi, B., and Nyitrai, M. (2004). The effect of phalloidin and jasplakinolide on the flexibility and thermal stability of actin filaments. *FEBS Lett.* 565, 163–166. doi: 10.1016/j.febslet.2004.03.096

Vishwanath, V. A., and McIntosh, J. M. (2006). Synthesis of fluorescent analogs of α-conotoxin MII. *Bioconjug. Chem.* 17, 1612–1617. doi: 10.1021/bc060163y

Vlachos, A., Korkotian, E., Schonfeld, E., Copanaki, E., Deller, T., and Segal, M. (2009). Synaptopodin regulates plasticity of dendritic spines in hippocampal neurons. *J. Neurosci.* 29, 1017–1033. doi: 10.1523/JNEUROSCI.5528-08.2009

Wang, L., Dumoulin, A., Renner, M., Triller, A., and Specht, C. G. (2016). The role of synaptopodin in membrane protein diffusion in the dendritic spine neck. *PLoS One* 11:e0148310. doi: 10.1371/journal.pone.0148310

Wang, L. L., Lee, K.-T., Jung, K.-W., Lee, D.-G., and Bahn, Y.-S. (2018). The novel microtubule-associated CAP-glycine protein Cgp1 governs growth, differentiation, and virulence of *Cryptococcus neoformans*. *Virulence* 9, 566–584. doi: 10.1080/21505594.2017.1423189

Wegner, W., Ilgen, P., Gregor, C., van Dort, J., Mott, A. C., Steffens, H., et al. (2017). In vivo mouse and live cell STED microscopy of neuronal actin plasticity using far-red emitting fluorescent proteins. *Sci. Rep.* 7:11781. doi: 10.1038/s41598-017-11827-4

Wehland, J., Osborn, M., and Weber, K. (1977). Phalloidin-induced actin polymerization in the cytoplasm of cultured cells interferes with cell locomotion and growth. *Proc. Natl. Acad. Sci. U.S.A.* 74, 5613–5617. doi: 10.1073/pnas.74.12.5613

Westphal, M., Jungbluth, A., Heidecker, M., Mühlbauer, B., Heizer, C., Schwartz, J.-M., et al. (1997). Microfilament dynamics during cell movement and chemotaxis monitored using a GFP–actin fusion protein. *Curr. Biol.* 7, 176–183. doi: 10.1016/s0960-9822(97)70088-5

Whelan, D. R., and Bell, T. D. M. (2015). Image artifacts in single molecule localization microscopy: why optimization of sample preparation protocols matters. *Sci. Rep.* 5:7924. doi: 10.1038/srep07924

Wiederschain, G. Ya. (2011). The molecular probes handbook. A guide to fluorescent probes and labeling technologies. *Biochem. Mosc.* 76, 1276–1276. doi: 10.1134/S0006297911110101

Wienisch, M., and Klingauf, J. (2006). Vesicular proteins exocytosed and subsequently retrieved by compensatory endocytosis are nonidentical. *Nat. Neurosci.* 9, 1019–1027. doi: 10.1038/nn1739

Wildanger, D., Bückers, J., Westphal, V., Hell, S. W., and Kastrup, L. (2009a). A STED microscope aligned by design. *Opt. Express* 17, 16100–16110. doi: 10.1364/OE.17.016100

Wildanger, D., Medda, R., Kastrup, L., and Hell, S. W. (2009b). A compact STED microscope providing 3D nanoscale resolution. *J. Microsc.* 236, 35–43. doi: 10.1111/j.1365-2818.2009.03188.x

Wilhelm, B. G., Mandad, S., Truckenbrodt, S., Kröhnert, K., Schäfer, C., Rammner, B., et al. (2014). Composition of isolated synaptic boutons reveals the amounts of vesicle trafficking proteins. *Science* 344, 1023–1028. doi: 10.1126/science.1252884

Wilkins, M. E., Li, X., and Smart, T. G. (2008). Tracking Cell Surface GABAB receptors using an α-bungarotoxin tag. *J. Biol. Chem.* 283, 34745–34752. doi: 10.1074/jbc.M803197200

Wilson, N. R., Kang, J., Hueske, E. V., Leung, T., Varoqui, H., Murnick, J. G., et al. (2005). Presynaptic regulation of quantal size by the vesicular glutamate transporter VGLUT1. *J. Neurosci.* 25, 6221–6234. doi: 10.1523/JNEUROSCI.3003-04.2005

Winans, A. M., Collins, S. R., and Meyer, T. (2016). Waves of actin and microtubule polymerization drive microtubule-based transport and neurite growth before single axon formation. *ELIFE* 5:e12387. doi: 10.7554/eLife.12387

Woodford, C. R., Frady, E. P., Smith, R. S., Morey, B., Canzi, G., Palida, S. F., et al. (2015). Improved PeT molecules for optically sensing voltage in neurons. *J. Am. Chem. Soc.* 137, 1817–1824. doi: 10.1021/ja510602z

Wulf, E., Deboben, A., Bautz, F. A., Faulstich, H., and Wieland, T. (1979). Fluorescent phallotoxin, a tool for the visualization of cellular actin. *Proc. Natl. Acad. Sci. U.S.A.* 76, 4498–4502. doi: 10.1073/pnas.76.9.4498

Xu, K., Zhong, G., and Zhuang, X. (2013). Actin, spectrin, and associated proteins form a periodic cytoskeletal structure in axons. *Science* 339, 452–456. doi: 10.1126/science.1232251

Xu, L., Rönnlund, D., Aspenström, P., Braun, L. J., Gad, A. K. B., and Widengren, J. (2016). Resolution, target density and labeling effects in colocalization studies - suppression of false positives by nanoscopy and modified algorithms. *FEBS J.* 283, 882–898. doi: 10.1111/febs.13652

Yau, K. W., Schätzle, P., Tortosa, E., Pagès, S., Holtmaat, A., Kapitein, L. C., et al. (2016). Dendrites in vitro and in vivo contain microtubules of opposite polarity and axon formation correlates with uniform plus-end-out microtubule orientation. *J. Neurosci.* 36, 1071–1085. doi: 10.1523/JNEUROSCI.2430-15.2016

Yi, J., Wu, X. S., Crites, T., and Hammer, J. A. (2012). Actin retrograde flow and actomyosin II arc contraction drive receptor cluster dynamics at the immunological synapse in Jurkat T cells. *Mol. Biol. Cell* 23, 834–852. doi: 10.1091/mbc.e11-08-0731

Zarrouk, A., Nury, T., Dauphin, A., Frère, P., Riedinger, J.-M., Bachelet, C.-M., et al. (2015). Impact of C24:0 on actin-microtubule interaction in human neuronal SK-N-BE cells: evaluation by FRET confocal spectral imaging microscopy after dual staining with rhodamine-phalloidin and tubulin tracker green. *Funct. Neurol.* 30, 33–46.

Zenisek, D., Steyer, J. A., and Almers, W. (2000). Transport, capture and exocytosis of single synaptic vesicles at active zones. *Nature* 406, 849–854. doi: 10.1038/35022500

Zenisek, D., Steyer, J. A., Feldman, M. E., and Almers, W. (2002). A membrane marker leaves synaptic vesicles in milliseconds after exocytosis in retinal bipolar cells. *Neuron* 35, 1085–1097. doi: 10.1016/s0896-6273(02)00896-6

Zhang, Q., Li, Y., and Tsien, R. W. (2009). The dynamic control of kiss-and-run and vesicular reuse probed with single nanoparticles. *Science* 323, 1448–1453. doi: 10.1126/science.1167373

Zhao, Y., Araki, S., Wu, J., Teramoto, T., Chang, Y.-F., Nakano, M., et al. (2011). An expanded palette of genetically encoded Ca2+ indicators. *Science* 333, 1888–1891. doi: 10.1126/science.1208592

Zhong, G., He, J., Zhou, R., Lorenzo, D., Babcock, H. P., Bennett, V., et al. (2014). Developmental mechanism of the periodic membrane skeleton in axons. *ELIFE* 3, e04581. doi: 10.7554/eLife.04581

Zhu, Y., and Stevens, C. F. (2008). Probing synaptic vesicle fusion by altering mechanical properties of the neuronal surface membrane. *Proc. Natl. Acad. Sci. U.S.A.* 105, 18018–18022. doi: 10.1073/pnas.0809714105

Zobel, T., and Bogdan, S. (2013). A high resolution view of the fly actin cytoskeleton lacking a functional WAVE complex. *J. Microsc.* 251, 224–231. doi: 10.1111/jmi.12020

Conflict of Interest Statement: The authors declare that the research was conducted in the absence of any commercial or financial relationships that could be construed as a potential conflict of interest.

frontiers in Synaptic Neuroscience

ORIGINAL RESEARCH
published: 15 October 2019
doi: 10.3389/fnsyn.2019.00029

Estimating the Readily-Releasable Vesicle Pool Size at Synaptic Connections in the Neocortex

Natalí Barros-Zulaica[1], John Rahmon[1], Giuseppe Chindemi[1], Rodrigo Perin[2], Henry Markram[1,2], Eilif Muller[1†] and Srikanth Ramaswamy[1*†]*

[1] Blue Brain Project, École Polytechnique Fédérale de Lausanne, Geneva, Switzerland, [2] Laboratory of Neural Microcircuitry, Brain Mind Institute, École Polytechnique Fédérale de Lausanne, Lausanne, Switzerland

Previous studies based on the 'Quantal Model' for synaptic transmission suggest that neurotransmitter release is mediated by a single release site at individual synaptic contacts in the neocortex. However, recent studies seem to contradict this hypothesis and indicate that multi-vesicular release (MVR) could better explain the synaptic response variability observed *in vitro*. In this study we present a novel method to estimate the number of release sites per synapse, also known as the size of the readily releasable pool (N_{RRP}), from paired whole-cell recordings of connections between layer 5 thick tufted pyramidal cell (L5_TTPC) in the juvenile rat somatosensory cortex. Our approach extends the work of Loebel et al. (2009) by leveraging a recently published data-driven biophysical model of neocortical tissue. Using this approach, we estimated N_{RRP} to be between two to three for synaptic connections between L5_TTPCs. To constrain N_{RRP} values for other connections in the microcircuit, we developed and validated a generalization approach using published data on the coefficient of variation (CV) of the amplitudes of post-synaptic potentials (PSPs) from literature and comparing them against *in silico* experiments. Our study predicts that transmitter release at synaptic connections in the neocortex could be mediated by MVR and provides a data-driven approach to constrain the MVR model parameters in the microcircuit.

Keywords: synaptic transmission, quantal analysis, multi vesicular release, neocortex, mathematical model, short-term depression

OPEN ACCESS

Edited by:
Dirk Feldmeyer, Julich Research Centre, Germany

Reviewed by:
Christian Stricker, Australian National University, Australia
Stefan Hallermann, Leipzig University, Germany

****Correspondence:***
Natalí Barros-Zulaica
natali.barroszulaica@epfl.ch
Srikanth Ramaswamy
srikanth.ramaswamy@epfl.ch

[†] Co-senior authors

Received: *30 April 2019*
Accepted: *30 September 2019*
Published: *15 October 2019*

Citation:
Barros-Zulaica N, Rahmon J, Chindemi G, Perin R, Markram H, Muller E and Ramaswamy S (2019) Estimating the Readily-Releasable Vesicle Pool Size at Synaptic Connections in the Neocortex. Front. Synaptic Neurosci. 11:29. doi: 10.3389/fnsyn.2019.00029

INTRODUCTION

Synaptic transmission is the basis for neuronal communication and information processing in the brain. Synaptic communication between neurons is mediated by neurotransmitters contained in presynaptic vesicles that are stochastically released from axonal boutons by incoming action potentials (APs) and diffuse across the synaptic cleft to bind receptors. Synaptic receptors are a class of ion channels which open as a result of transmitter binding, and the resulting transmembrane currents either depolarize or hyperpolarize the postsynaptic membrane, depending on the ion to which the channel is permeable (Mason et al., 1991; Südhof, 2000). Understanding the mechanisms behind vesicle release is crucial to unravel how information propagates between neuron types (Tsodyks and Markram, 1997). Disrupted vesicle release is implicated in pathologies such as Alzheimer's disease or schizophrenia (Waites and Garner, 2011).

In 1954, del Castillo and Katz described the 'Quantal model' of synaptic transmission (Del Castillo and Katz, 1954). This model is characterized by the number of independent release sites (N), the probability of releasing a vesicle in the presynaptic cell followed by an AP (p) and the content of each vesicle, the quantal size (q), which collectively determine the efficacy of synaptic transmission (Del Castillo and Katz, 1954; Tsodyks and Markram, 1997). Previously, it was thought that no more than one vesicle could be released per synaptic contact, leading to the univesicular release hypothesis (UVR), in which N is equal to the number of physical synaptic contacts in a neuronal connection, at least for synapses in the neocortex (Korn et al., 1981, 1994; Silver et al., 2003; Biró et al., 2005). However, evidences as fluctuations of evoked postsynaptic potentials (PSPs) (Tang et al., 1994), large concentration of neurotransmitter in the synaptic cleft (Tong and Jahr, 1994) or a high range variability of receptor-mediated signals of *N*-methyl-D-aspartate (NMDA) and α-amino-3-hydroxy-5-methyl-4-isoxazolepropionic acid (AMPA) receptors (Conti and Lisman, 2003) suggested that transmission at a single synaptic contact could be multiquantal. Consequently, a multivesicular release hypothesis (MVR) was proposed, where several release sites could underlie a synaptic contact in a neuronal connection. In fact, there are evidences showing that MVR occurs in brain regions such as the hippocampus (Tong and Jahr, 1994; Christie and Jahr, 2006), the cerebellum (Auger et al., 1998), the hypothalamus (Gordon, 2005) or the cerebral cortex (Huang et al., 2010; Rudolph et al., 2015; Molnár et al., 2016).

Recent studies in the rodent neocortex support the idea of MVR between pyramidal cells (Loebel et al., 2009; Hardingham et al., 2010; Rollenhagen et al., 2018). It has also been reported that modalities of vesicle release differ across cortical areas. For instance, connections between excitatory neurons in layer 4 exhibit UVR in the primary visual cortex, as against MVR in the primary somatosensory cortex (Huang et al., 2010). By contrast, other studies have reported that connections between layer 4 stellate cells and layer 2/3 pyramidal cells in the rat barrel cortex (Silver et al., 2003), and between pyramidal cells and interneurons in the rat cortex (Molnár et al., 2016) display UVR. A recent study has also reported that connections between pyramidal cells and fast spiking interneurons in the human neocortex exhibit MVR (Molnár et al., 2016). MVR is a complex process that is thought to regulate synaptic transmission and plasticity by increasing the dynamic range of synapses and could, therefore, influence cognitive functions such as learning and memory (Fuhrmann et al., 2004). MVR is also known to directly impact synaptic noise through spontaneous miniature postsynaptic currents (Fatt and Katz, 1950) and synaptic variability resulting in an increase of synaptic strength through larger vesicle pool sizes (Oertner et al., 2002), which could have important implications in the transmission of information between neurons (Fuhrmann et al., 2004).

Theoretical and computational models have enabled a mechanistic understanding of MVR through investigating synaptic processes such as short-term synaptic plasticity (Hennig, 2013). These models account for parameters to model presynaptic processes including the probability of neurotransmitter release and the number of vesicles available for release (Tsodyks and Markram, 1997; Loebel et al., 2009; Hennig, 2013; Zhang and Peskin, 2015). In addition, these models also assume that each synaptic contact has access to a limited amount of releasable neurotransmitter, take into account vesicle depletion and replenishment (Liley and North, 1953), and facilitation mechanisms (Betz, 1970; Varela et al., 1997; Markram et al., 1998). Some models have also demonstrated an important functional role for the number of release sites per synaptic connection in neuronal information coding (Fuhrmann et al., 2002). It has also been reported that the number and frequency of vesicles released is essential for receptor activation (Boucher et al., 2010). Some studies also outline the importance of having a readily releasable pool (N_{RRP}) with more than one vesicle for synaptic plasticity (Nadkarni et al., 2010). Despite the importance of MVR in information transmission and processing between neurons, we lack an understanding of its role in brain regions such as the neocortex, which is the seat of higher order cognitive functions in the mammalian brain.

In this study, we leveraged a rigorously validated data-driven model of neocortical tissue at the cellular and synaptic levels of detail to estimate the average size of the N_{RRP} for individual synaptic contacts between cell-type-specific connections (Markram et al., 2015). To compute the N_{RRP}, we sampled synaptically connected pairs of neurons within the virtual neocortical tissue model and simulated paired whole-cell recordings *in silico*. The properties of *in silico* synaptic connections were constrained by an experimental dataset that characterized the physiology of *in vitro* synaptic connections between layer 5 thick-tufted pyramidal cells (L5_TTPC) in the juvenile rat somatosensory cortex, which are marked by prominent short-term depression (Ramaswamy and Markram, 2015). In particular, we used this dataset to estimate synaptic noise and the MVR free parameter N_{RRP}, extending the work of Loebel and colleges (Loebel et al., 2009). Next, we optimized the N_{RRP}, to reproduce response variability as observed in experiments, which is typically assessed by the coefficient of variation (CV; standard deviation/mean) of PSPs. We further developed an approach to estimate N_{RRP} for both excitatory and inhibitory connection types using published literature that reported the CV of PSPs for synaptic connections in the neocortex. Our study combining *in vitro* experiments and *in silico* computational modeling, predicts that the vast majority of synaptic connections in the neocortex are mediated by MVR, albeit with lower N_{RRP} values than previously reported (Loebel et al., 2009), which suggests that MVR could be a general property of local neocortical connections.

MATERIALS AND METHODS

Slice Preparation and Electrophysiology

Fourteen- to eighteen-day-old Wistar rats were decapitated according to the guidelines of the Swiss Animal Welfare Act, and the Swiss National Institutional and Veterinary office guidelines in the Canton of Vaud on Animal Experimentation for the ethical use of animals. Multiple, simultaneous somatic whole cell patch-clamp recordings from clusters of 6–12 cells were carried out

with Multiclamp 700B amplifiers in current clamp mode. Brain sagittal slices of 300 μM width were cut on an HR2 vibratome (Sigmann Elektronik). Temperature was maintained at 34 ± 1°C in all experiments. The extracellular solution contained 125 mM NaCl, 2.5 mM KCl, 25 mM D-glucose, 25 mM $NaHCO_3$, 1.25 mM NaH2PO4, 2 mM CaCl2, and 1 mM MgCl2 bubbled with 95% O2 and 5% CO2. The intracellular pipette solution contained 110 mM potassium gluconate, 10 mM KCl, 4 mM ATP-Mg, 10 mM phosphocreatine, 0.3 mM GTP, 10 Hepes, and 13 mM biocytin adjusted to pH 7.3–7.4 with 5 M KOH.

Data was acquired through an ITC-1600 board (Instrutech) connected to a PC running a custom-written routine (PulseQ) under IGOR Pro (WaveMetrics, Lake Oswego, OR, United States). L5_TTPCs were selected according to their large soma size (15–25 μm) and their apparent large trunk of the apical dendrite. Cells were visualized by infrared differential interference contrast video microscopy using a VX55 camera (Till Photonics) mounted on an upright BX51WI microscope (Olympus). Sampling rates were 5–10 kHz, and the voltage signal was filtered with a 2-kHz Bessel filter. The resting membrane potential was −65.3 ± 4.3 mV, the input resistance was 59.7 ± 17.1 MΩ and the access resistance was 15.2 ± 3.7 MΩ. The stimulation protocol consisted of pre-synaptic stimulation with eight electric pulses at 20 Hz followed by a single pulse 500 ms later (recovery test), at the sufficient current intensity to generate APs in the presynaptic neuron while the postsynaptic neuron responses were recorded. The protocol was repeated between 20 to 60 times with a time between repetitions of 12 s (**Figure 1A**, top).

Stochastic Model for Short-Term Dynamics and Multi-Vesicular Release

Our model describes the short-term synaptic dynamics defined by a stochastic generalization of the Tsodyks-Markram model (TM-model) (Tsodyks and Markram, 1997; Maass and Markram, 2002) that is known to fit excitatory as well as inhibitory synapses behavior of biological experiments (Markram et al., 1998; Gupta et al., 2000). This model considers that there is a finite number of vesicles ready to be released defined by N_{RRP} that could be in ready or recovery state. In this study we followed the synaptic dynamics described previously that is able to predict the sequence of PSP amplitudes produced by any spike train (Tsodyks and Markram, 1997). This behavior is described by four main synaptic parameters: the absolute synaptic efficacy (A), the fraction of synaptic resources used by a single spike (U), the time constant for recovery from facilitation (F) and the time constant for recovery from depression (D). The PSP amplitudes prediction obeys the following mathematical expressions:

$$A_n = A u_n R_n$$

$$A = 1$$

$$u_1 = U$$

$$R_1 = 1$$

$$u_{n+1} = U + u_n\,(1 - U)\exp\left(-\frac{\Delta t_n}{F}\right)$$

$$R_{n+1} = 1 + (R_n - R_n u_n - 1)\exp(-\frac{\Delta t_n}{D})$$

In short, when the nth spike occurs there is certain fraction of synaptic efficacy modeled by R_n. Accordingly, the product $u_n R_n$ models the fraction of synaptic efficacy used by the nth spike. Combining these terms is possible to describe the fraction of synaptic efficacy available when the next spike arrives at time Δt_n assuming that the synaptic efficacy has an exponential recovery with time constant D. How much fraction of synaptic efficacy (R_{n+1}) is used when ($n + 1$)th spike occurs is defined by u_{n+1} which increases for each subsequent spike from u_n to $U(1–u_n) + u_n$ and goes back to U following an exponential with time constant F (Maass and Markram, 2002).

Thus, if a vesicle is successfully released, these receptors get activated with a conductance g_{max}/N_{RRP} with g_{max} as the maximal conductance.

Fitting Synapse Model Parameters to the Data

We constrained our synaptic model by extracting the parameters U, D and F from *in vitro* connections ($n = 33$; **Figures 3C–E**). To this end, we measured the peak for the excitatory postsynaptic potential (EPSP) amplitudes of each averaged voltage trace (**Figure 3A**). All experimental traces were normalized to their maximum value that allowed us to directly compute the peak value instead of the total amplitude. To perform an accurate computation of the peaks we used an analytical tool for deconvolving the voltage averaged trace (Richardson and Silberberg, 2008), which made it possible to exclude the smoothing effect of the low pass filtering of the cell membrane with a time scale equal to τ_{mem}, so we could extract the peaks from the EPSPs (**Figure 3B**).

To express this process mathematically we used the next equation:

$$R_{input} I_{syn} = \tau_{mem}\frac{dV}{dt} + V$$

The right-hand part of the expression is the voltage deconvolution, while the left hand contains the unfiltered synaptic current. The requirement here is to compute τ_{mem} for each *in vitro* connection by fitting the decay part of the recovery peak (9th EPSP) of the averaged voltage trace to an exponential.

Once the EPSP peaks were extracted from the deconvolved and normalized trace, we introduced them as an input into a genetic algorithm (GA) (Goldberg and Holland, 1988) that creates 500 generations of potential U, D and F within the following ranges U (0–1.0), D (0–1000.0) and F (0–2000.0). According to the mathematical expression of the model, the GA was able to estimate the peaks per different generation. The GA minimized the mean square distance between the original and the estimated peaks giving one solution for the minimum distance. In order to optimize the result, the GA was run 50 times. Then, we considered that the U, D, F generation related with the minimum

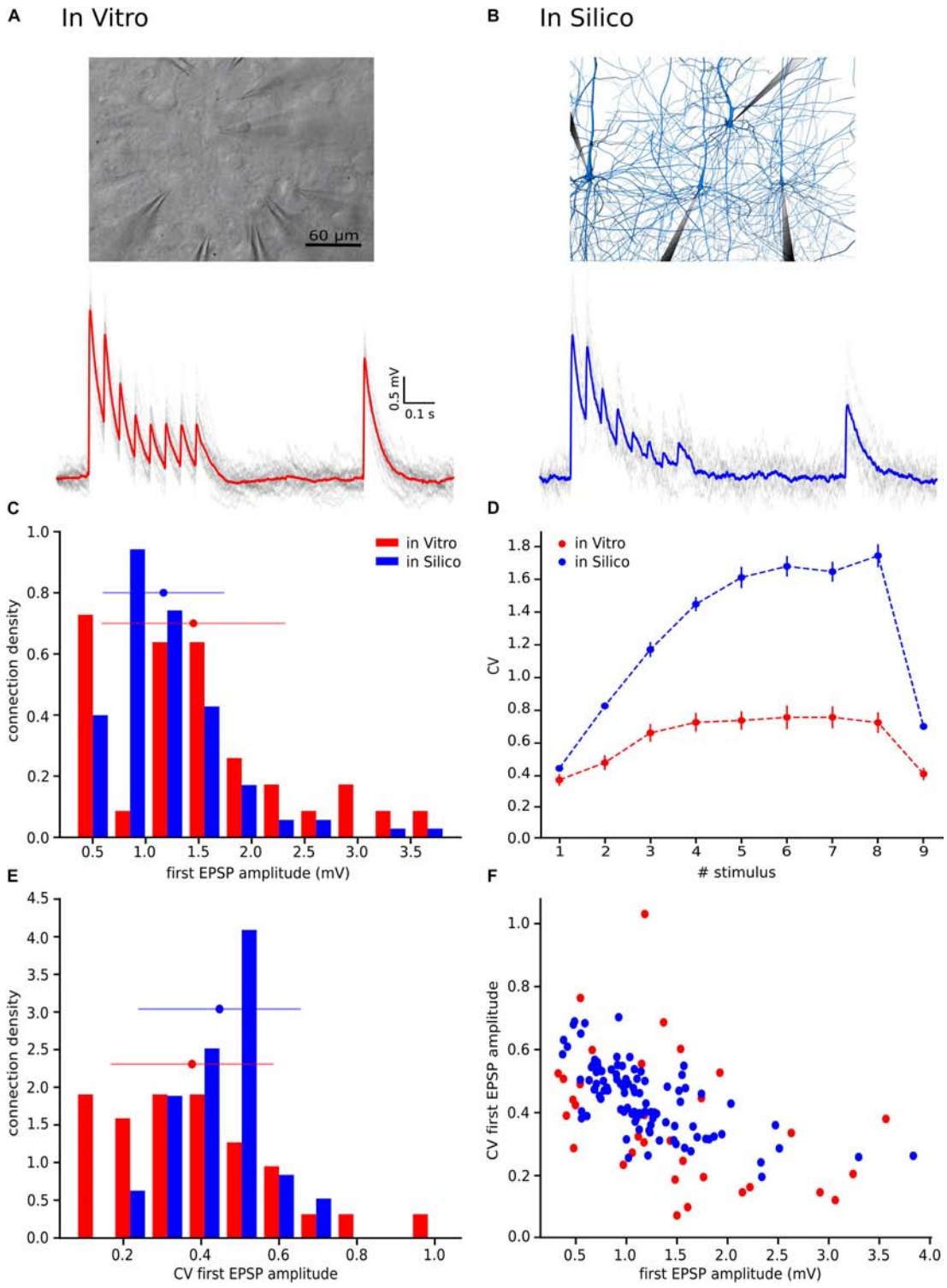

FIGURE 1 | With the UVR hypothesis it was not possible to reproduce the variability observed *in vitro*. **(A)** Example of a multiple whole cell patch-clamp recording in L5_TTPC connections (top). *In vitro* mean voltage trace (bottom; red) of 20 protocol repetitions (gray). **(B)** Illustration of an *in silico* patch-clamp experiment performed on L5_TTPC connections from the data-driven model of the rat cortex microcolumn. *In silico* mean voltage trace (bottom; blue) of 20 protocol repetitions (gray). **(C)** Histogram showing the distribution of the first EPSP amplitude for *in vitro* (red) and for *in silico* (blue) experiments. **(D)** Mean CV profiles for the *in vitro* (red) and the *in silico* (blue) experiments. **(E)** CV distribution of the first EPSP amplitude for *in vitro* (red) and *in silico* (blue) data sets. **(F)** Raster plot of the first EPSP amplitude against the CV of the first EPSP amplitude for *in vitro* (red) and *in silico* (blue) experiments. In the distributions and the CV profile, dots represent the mean and vertical and horizontal bars represent the standard deviation of all the experiments respectively.

distance out of the 50 repetitions was the best solution. We performed that process for each of the *in vitro* connections.

In silico Experiments: The Cortical Microcircuit

For the *in silico* experiments we leveraged a previously published model of juvenile rat somatosensory cortical tissue (Markram et al., 2015). In brief, the tissue model consists of 31,000 morphologically detailed neurons distributed across 6 layers within a volume of 0.29 mm^3 giving rise to 8 million synaptic connections mediated by 37 million synaptic contacts. All the neuronal and synaptic models can be freely obtained through the open-access Neocortical Microcircuit Collaboration (NMC) portal (Ramaswamy et al., 2015).

Having computed the mean and the standard deviation of the synaptic parameters from fitting the *in vitro* data to the TM-model, we updated these parameters in the neocortical tissue model that were implemented as distributions defined by their mean and standard deviation. We also computed by scaling its values until we matched the experimentally measured amplitude of the first EPSP in a train of responses, which determined the *in silico* g_{max} value for a simulated connection. Next, we performed patch-clamp *in silico* experiments (**Figure 1B**, up), under similar conditions to actual *in vitro* paired recordings, with different N_{RRP} values. These values were defined based on the mean of a Poisson distribution shifted one unit to the right, because at least one vesicle had to be released per synaptic site. The range of means of the Poisson distributions varied from 0 to 13 ($1 \leq N_{RRP} \geq 14$) in the case of studying MVR and 0 ($N_{RRP} = 1$) while studying UVR. We decided to set the maximum value to 14 vesicles on average per release site because is already the double of what Loebel and colleges predicted on their research (Loebel et al., 2009), so we considered that no more than 14 vesicles could be released per synaptic contact.

As the next step, we simulated 100 L5_TTPC connections *in silico* with 20 stimulus-response repetitions each. To reproduce *in vitro* experiments as faithfully as possible, we ensured that the U, D and F distributions *in silico* were identical to those extracted from *in vitro* recordings. We then compared the resulting EPSPs of simulated *in silico* connections to ascertain that they were well the range of experimentally measured values, consequently the EPSPs out of the experimental range were eliminated. Therefore, we excluded 15 connections and undertook the study with 85 connections out of 100.

Noise Calibration. Ornstein-Uhlenbeck Process

After simulating *in silico* connections with different N_{RRP} values and selecting a subset where the 1st EPSP amplitude was within the experimentally observed range, we artificially applied voltage fluctuations to *in silico* traces to take into account the membrane noise observed experimentally. This was achieved by implementing an Ornstein-Uhlenbeck process (OU-process), which is a stochastic process that allowed us to simulate small random variability. The OU-process describes the velocity of the movement of a Brownian particle considering the friction and is a stationary Gauss-Markov process (Enrico Bibbona, 2008).

Mathematically the expression used in this work for this process was:

$$X(t+1) = X(t) - \frac{X(t)}{\tau}dt + \sigma\sqrt{\frac{2}{\tau}dt}\ W_t$$

$$X(t_0) = x_0$$

Where τ is the membrane time constant, σ is the standard deviation of the voltage and W_t is a random term coming from the Wiener process. In the case of $\sigma = 0$ the equation will have the solution $X(t) = x_0 e^{-(t-t_0)/\tau}$ so X(t) relaxes exponentially toward 0. In general, X(t) fluctuates randomly, the third term pushes it away from zero, while the second term pulls it back to zero (Bibbona et al., 2008). In Physics this process is used to describe noisy relaxation activity.

In our specific case, we defined σ and τ using the voltage values between the 8th and the 9th EPSPs, 400 ms in total, for each repetition (sweep) in a connection and then we averaged the resulting values (**Figure 4A**). By computing the standard deviation of these points, we obtained one σ per connection ($n = 33$ connections in total). By computing the autocorrelation of this part of the voltage trace and fitting it to an exponential, we obtained one τ per connection (**Figure 4B**), which provided constraints to implement a similar membrane noise for *in silico* traces (**Figure 4C**).

CV Profile Computation. The Jack-Knife Bootstrapping Analysis

In order to compute the CV for the EPSP amplitudes for *in vitro* and *in silico* connections in a comparable way, we implemented the Jack-Knife method (JKK) (Efron and Tibshirani, 1994).

This method consists in excluding one observation at a time from a group of observations. In our specific case, from a set of single traces we computed the average of all but one off the traces each time, obtaining a set of averaged-JKK traces in the end. From each of these averaged-JKK traces we computed the amplitudes for all nine EPSPs in a train of synaptic responses. Through this computation, we were able to compute the EPSP amplitudes more precisely considering that we removed the noise by averaging. Thereafter, we computed the CV profiles for the *in vitro* data set and the *in silico* simulations using the following equations:

$$CV^n = \frac{std^n}{\bar{A}^n}$$

$$\bar{A}^n = \frac{1}{N}\sum_{i=1}^{N} A_i^n$$

$$std^n = \sqrt{(N-1)\sum_{i=1}^{n}(A_i^n - \bar{A}_i^n)}$$

Where n denotes the EPSP index ($n = 1$–9) and N is the number of single traces per connection.

Having two sets of simulations, to study UVR and MVR, we computed the CV profile of EPSP amplitudes using the JKK approach in both cases and compared them with the CV profile measured in the *in vitro* dataset. The EPSP amplitude was computed as the difference between the minimum value within 50 ms before stimulation time and the maximum value within 300 ms after stimulation time. We computed the mean square distance in order to obtain the minimum error between *in vitro* and *in silico* CV profiles (**Figure 5E**). We iterated this procedure 50 times and then we provided the mean and the standard deviation for the N_{RRP} that correspond with the smallest error.

Statistical Analysis

Mean values for the EPSP amplitudes, the CVs and the synaptic parameters were expressed as their respective mean ± their standard deviation. Differences between distributions were measured using the Kruskal-Wallis test which shows a significant difference when $p < 0.05$. In order to compare two dimensional data sets (**Figures 1F**, **6F**) we used the cross validated Kolmogorov-Smirnov test for two-dimensional data that shows significant differences when $p < 0.2$ (Press and Teukolsky, 1988). In order to test the goodness of fit for the fitting of the synaptic parameters we ran a Kolmogorov-Smirnov one sided test for three different distributions – beta, gamma and normal. Out of these three we chose the one with the highest p value and the smallest distance between the real and the expected distributions.

RESULTS

Motivation for Implementing MVR in the Model

To reproduce the synaptic release variability observed *in vitro*, we began by implementing UVR at all synaptic contacts in the neocortical microcircuit model. As a result, the synaptic responses *in silico* were highly variable in comparison against biological data. In order to further investigate the potential causes for this difference in response variability, we undertook whole-cell recordings *in vitro* from 33 pairs of connected L5_TTPCs cells (**Figure 1A**, top) and computed the amplitude and the CV of the amplitudes for each EPSP. **Figure 1** shows exemplar traces *in vitro* (**Figure 1A**, left in red) and *in silico* (**Figure 1B**, right in blue). As it was expected differences in the shape, amplitude and noise of the mean traces can be seen. The *in vitro* trace in red has a higher amplitude than the *in silico* in blue. Is also visible that the shape of the *in silico* mean trace is noisier than the *in vitro*, reflecting larger variability between protocol repetitions.

Next, we compared the distribution profiles of the first EPSP amplitude for the entire *in vitro* dataset ($n = 33$) and a subset of *in silico* connections ($n = 100$). Performing the Kruskal-Wallis test on the distributions of the first EPSP amplitude (**Figure 1C**) between *in vitro* and *in silico* connections revealed no significant difference in the mean values of their distributions (1.46 ± 0.86 mV for *in vitro*; 1.17 ± 0.57 mV for *in silico*; $p = 0.15$). However, a Kruskal-Wallis test between the distributions of the CV for the first EPSP amplitude (**Figure 1E**) revealed a significant difference in the mean values between *in vitro* and *in silico* connections (mean CV values: 0.38 ± 0.21 for *in vitro*; 0.45 ± 0.11 for *in silico*; $p = 0.0092$). Consequently, computing the CV profile for the EPSP amplitudes for every stimulus in a train showed a significant difference between *in vitro* and *in silico* data sets (**Figure 1D**; $p < 10^{-9}$). The distributions (**Figures 1C,E**) were normalized to the respecting sample size such that the sum of products of width and height of each column was equal to the total count of connections (33 for *in vitro*, 100 for *in silico*). This difference was further corroborated through a Kolmogorov-Smirnov test for two-dimensional data (Press and Teukolsky, 1988), which also showed a significant difference between the first EPSP amplitude against the CV of the first EPSP amplitude for *in vitro* and *in silico* datasets (**Figure 1F**; $p = 0.0022$).

This striking difference motivated us to implement the MVR hypothesis, which is known to provide enhance the dynamic range of synapses through higher variability (Wang et al., 2006; Brémaud et al., 2007).

Validating the Method

Before applying our method to an *in vitro* data collection, we wanted to ensure that we were able to achieve the correct N_{RRP} value by using our procedure. For this purpose, we built 3 *in silico* data sets with different averaged N_{RRP}s with mean values around 1, 4 and 10, each of them composed of 30 L5TTPC connections, similarly to the number of connections that is possible to obtain from *in vitro* experiments. Next, we simulated 100 *in silico* L5_TTPC connections with average N_{RRP} values ranging from 1 to 14 (see section "*In silico* Experiments: The Cortical Microcircuit") and compared them against each CV profile computed through the JKK approach obtained from each of the *in silico* data sets (**Figure 2B**). Each *in silico* data set and the corresponding simulations consisted of different pairs of L5_TTPC connections.

In this manner, we obtained N_{RRP}s that characterized each of the three different *in silico* data sets. We computed a minimum error around the correct value of each *in silico* data set (1, 4 and 10) which corresponding N_{RRP}s were 1.01 ± 0.10, 4.07 ± 0.30 and 9.85 ± 0.45, obtaining as results $N_{RRP} = 1.10 \pm 0.31$ (dots), $N_{RRP} = 4.11 \pm 1.75$ (squares) and $N_{RRP} = 10.71 \pm 3.21$ (triangles), respectively (**Figure 2**). By comparing the CV profiles between the *in silico* data sets (black) and the simulations (gray) (**Figure 2B**) we found that they were not significantly different ($p > 0.4$), which validated the efficacy of our method.

Extracting Values for the TM-Model and Noise Calibration

To enable comparison between the *in vitro* and the *in silico* experiments, we used the TM synapse model to extract the U, D, and F parameters from the *in vitro* dataset (see Materials and Methods). These parameters were obtained by the deconvolution of each *in vitro* averaged trace (**Figure 3B**) to extract the values of the peaks from the same voltage level. This resulted in three distributions, one each for U, D, and F, respectively. For U we obtained a normal distribution (goodness of fit: $p = 0.92$; $D = 0.097$) with a mean value of 0.38 ± 0.1 (**Figure 3C**), D fitted a gamma distribution ($p = 0.81$; $D = 0.11$) with a mean value of

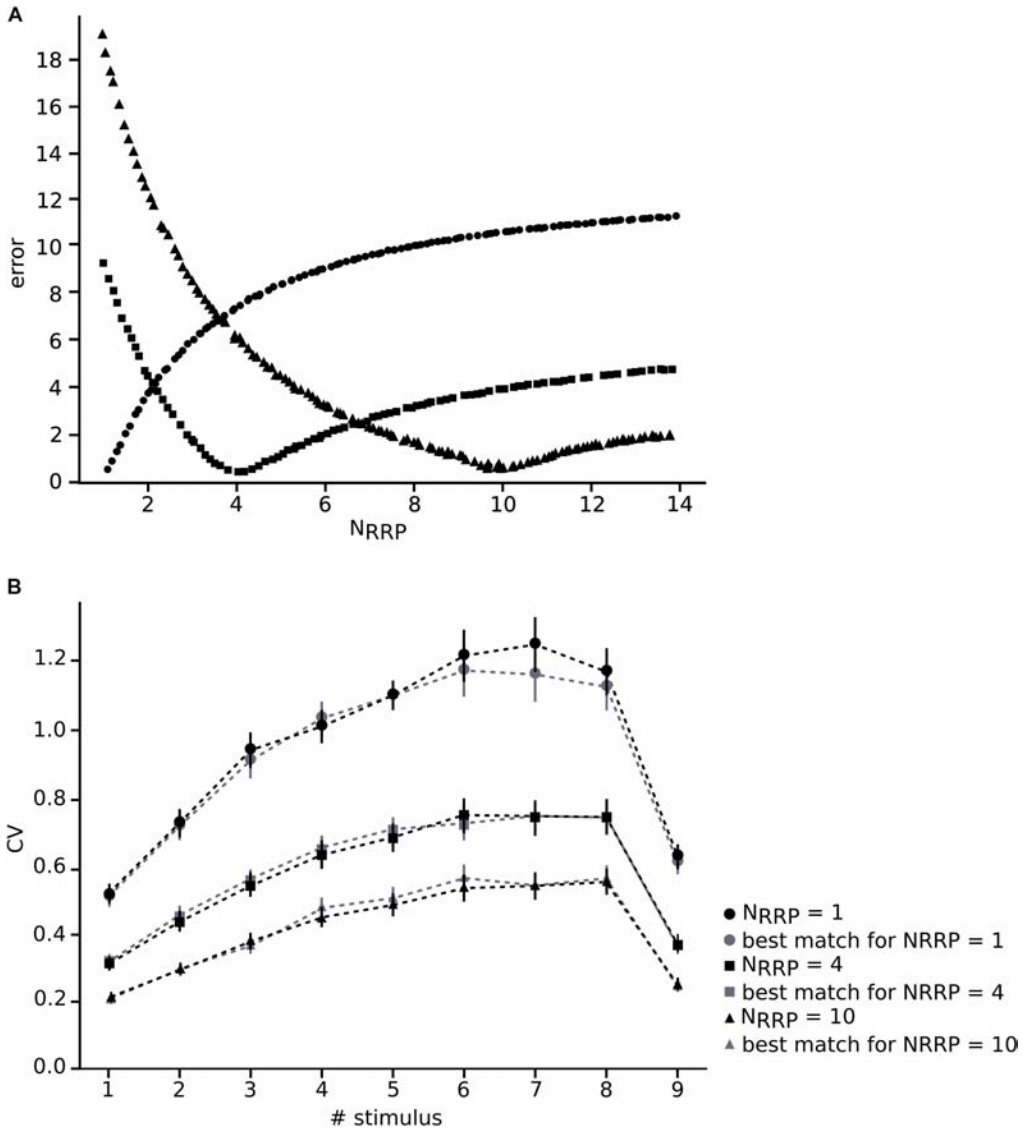

FIGURE 2 | Validating the method. **(A)** Varying N_{RRP} against error for the different *in silico* data sets around the appropriate corresponding N_{RRP} (dots, N_{RRP} = 1; squares, N_{RRP} = 4; triangles, N_{RRP} = 10). **(B)** Mean CV profiles of the three different *in silico* data sets (black) and the simulations (gray). Dots, squares and triangles represent the mean while the error bars show the standard deviation.

365.6 ± 100.15 ms (**Figure 3D**) and F was also fitted to a gamma distribution (p = 0.1; D = 0.21) with mean 25.71 ± 45.87 ms (**Figure 3E**). These values were similar to the values found in previous studies (Tsodyks and Markram, 1997; Wang et al., 2002). As the next step we estimated the g_{max} for connections. We simulated *in silico* connections by tuning an initial g_{max} value until the first EPSP amplitude matched experimental measurements. The resulting g_{max} was 1.54 ± 1.20 nS, which is consistent with previous estimates (Markram et al., 1997, 2015; Ramaswamy and Markram, 2015; Ramaswamy et al., 2015), and enabled the *in silico* reproduction of synaptic physiology between L5_TTPCs connections. We also further calibrated the membrane voltage noise parameter by implementing an OU-process on the *in vitro* dataset (see "Materials and Methods") to obtain σ = 0.22 ± 0.10 mV (**Figure 4B**, top) and τ = 28.2 ± 3.5 ms (**Figure 4B**, bottom). Thus, by prescribing U, D, F and g_{max} parameters, and adding a synthetic membrane voltage noise to each simulated *in silico* connection we captured the biologically observed synaptic variability in L5_TTPC connections.

Optimizing N_{RRP} for L5_TTPC Connections

Having defined the core synaptic parameter set, we next simulated *in silico* L5_TTPC connections as described before, although now we compared them against the CV_{JKK} computed from the *in vitro* data set. We observed a specific relationship between N_{RRP} and the CV for L5_TTPC connections (**Figure 5C**) that fits the power law with amplitude = 0.55 ± 0.015 and

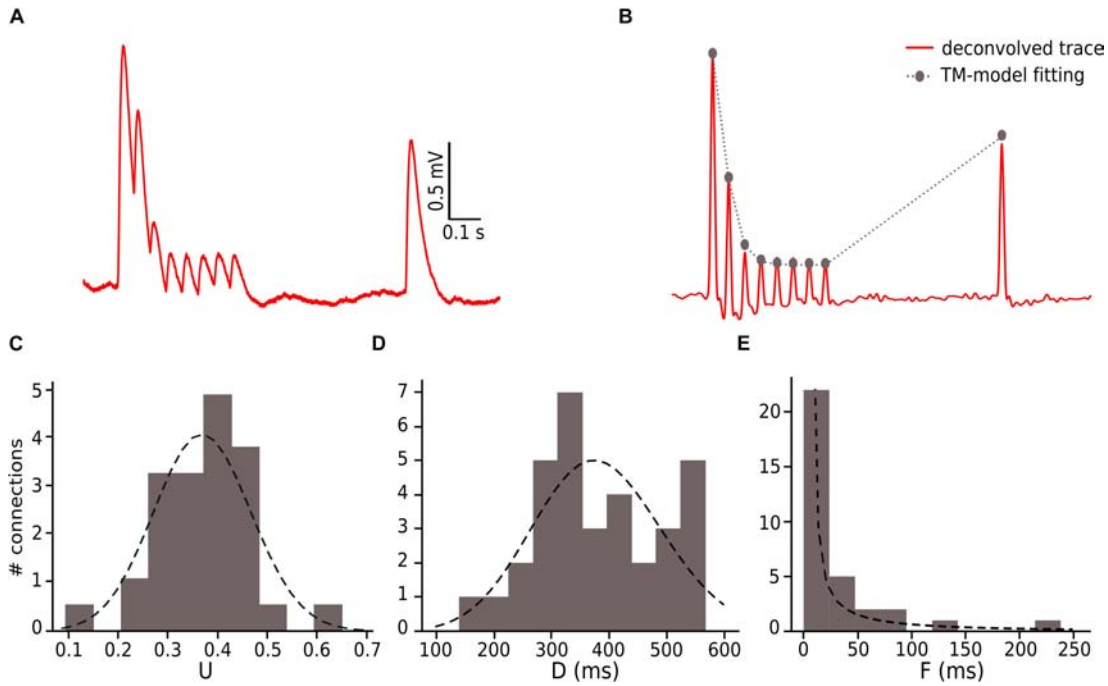

FIGURE 3 | Fitting *in vitro* data to the TM-model. **(A)** Example of an *in vitro* mean voltage trace of L5_TTPC connection. **(B)** Corresponding deconvolved voltage trace (red) with the fit to the deterministic TM-model (gray). **(C)** Distribution of the probability of release parameter (U), **(D)** distribution of the time to recovery from depression (D) and **(E)** distribution of the time to recovery from facilitation (F). Values obtained from the fitting to the TM-model of 33 *in vitro* connections.

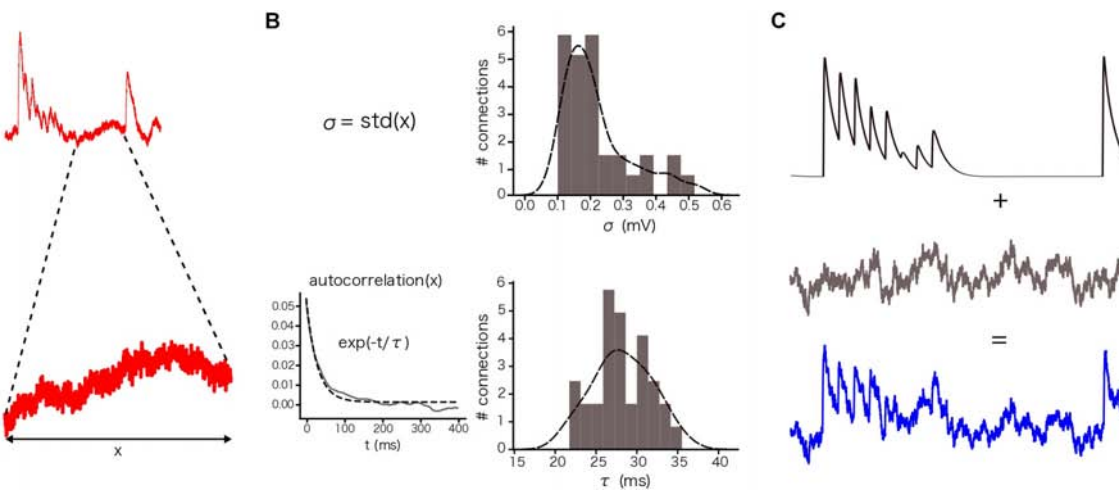

FIGURE 4 | Noise calibration. **(A)** Example of an *in vitro* single protocol repetition (top). Zoom over 400 ms segment used to compute the parameters for noise calibration (bottom). **(B)** Distribution of σ (up) and τ (bottom). σ was computed as the standard deviation of the voltage segment. τ was computed by fitting the voltage segment autocorrelation to an exponential. The distributions show the mean values for the 33 *in vitro* connections. **(C)** (up) Single *in silico* trace without noise, (middle) OU-process generated to be added to the single *in silico* trace and (bottom) the noisy single protocol repetition that is the result of adding the previous two traces.

index = −0.39 ± 0.032. Initially, we observed that the CV for the first EPSP amplitude was higher when N_{RRP} was smaller. Therefore, for UVR-like connections the variability between individual sweeps is larger than for MVR-like connections. This result is in agreement with previous studies (Wang et al., 2006; Brémaud et al., 2007) and is also reflected in the simulated *in silico* connections with N_{RRP} = 1 (**Figures 5A,B**, top) and N_{RRP} = 20 (**Figures 5A,B**, bottom) to illustrate how the variability and voltage profile of EPSPs changes with the number of released vesicles.

In order to determine N_{RRP}, we next computed the CV profiles of the *in silico* connections simulated with different N_{RRP}s and

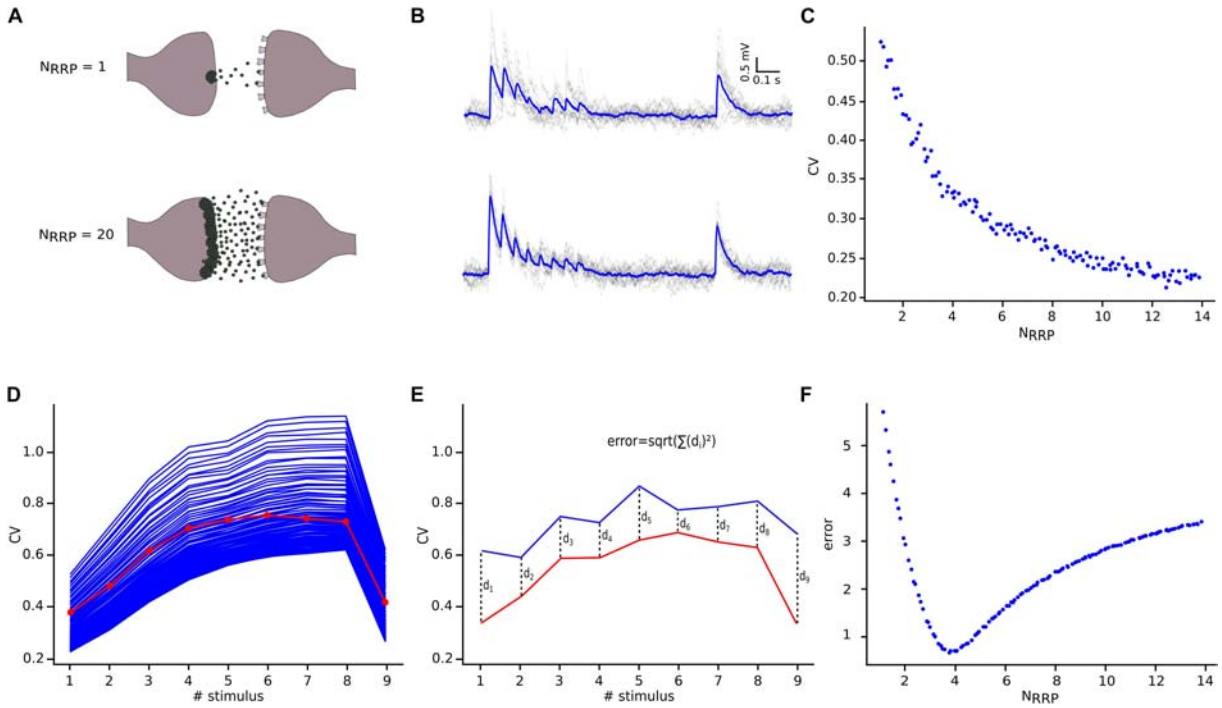

FIGURE 5 | NRRP computation. **(A)** Illustration showing one synaptic connection releasing neuro transmitters from only one vesicle (top) and the same synaptic connection releasing neurotransmitters from twenty vesicles (bottom). **(B)** The corresponding effect of releasing neurotransmitters from one (top) or from twenty (bottom) vesicles reflected on the variability and shape of the *in silico* traces. The mean voltage traces are painted in blue while each protocol repetition is represented in gray. **(C)** Diagram showing the effect of N_{RRP} over the CV. **(D)** Mean CV profile for the *in vitro* (red) and all the *in silico* connections with different N_{RRP} values. **(E)** Diagram explaining the mean square distance computation. **(F)** N_{RRP} against error, showed a clear minimum around the value obtained for this specific connection.

measured their mean square distance (**Figure 5E**) in comparison against the *in vitro* CV profile (**Figure 5D**). We found that for L5_TTPC connections the minimum error was obtained with $N_{RRP} = 3.78 \pm 1.65$ (**Figure 5F**), which demonstrates that our predictions of MVR for these connections is consistent with previous reports (Loebel et al., 2009; Rollenhagen et al., 2018).

Implementing MVR Improved the Variability of the Synapses in the Model

We next sought to test if our hypothesis of MVR between L5_TTPCs could better explain variability in experimental as against UVR (**Figure 1**). Therefore, we computed the distributions for the first EPSP amplitude, the CV of the first EPSP amplitude, and the CV profile of the EPSP amplitudes for all stimuli in a train. We found that the shape and the amplitude a randomly chosen *in silico* connection mediated by MVR (**Figure 6B**) was similar to a randomly chosen *in vitro* trace (**Figure 6A**), in contrast to an *in silico* connection mediated by UVR discussed before (see Motivation for implementing MVR in the model; **Figure 1B**, bottom). The CV profile for the EPSPs of all MVR *in silico* connections (**Figure 6D**, blue) also closely matched the *in vitro* dataset (red) as against UVR *in silico* connections (**Figure 1D**). Although our model has a slightly higher CV for the 6th, 7th, and 8th EPSPs, the Kruskal-Wallis test showed no significant differences between both CV profiles for any of the EPSPs ($p = 0.89$, $p = 0.52$, $p = 0.42$, respectively), demonstrating that the MVR hypothesis improved the synaptic variability of *in silico* connections.

Further results, shown in the distributions for the first EPSP amplitude (**Figure 6C**) and for the CV of the first EPSP amplitude (**Figure 6E**) corroborated the fact that MVR explained the experimentally observed variability better in contrast to UVR. The mean value of both MVR distributions was statistically insignificant compared against experimental data (mean EPSP values: 1.46 ± 0.86 mV for *in vitro*; 1.46 ± 0.95 mV for *in silico*; $p = 0.69$) (mean CV values: 0.38 ± 0.21 for *in vitro*; 0.35 ± 0.13 for *in silico*; $p = 0.86$). The distributions (**Figures 6C,E**) were normalized to the respective sample size such that the sum of products of width and height of each column is equal to the total count (33 for *in vitro*, 85 for *in silico*). In addition, a Kolmogorov-Smirnov test showed no significant difference between the first EPSP amplitude against the CV of the first EPSP amplitude for *in vitro* and *in silico* connections ($p = 0.29$) (**Figure 6F**), conclusively demonstrating that both data sets could, in principle, come from the same population.

N_{RRP} Prediction for Other Cell-Type-Specific Connections

We extended this method to other cell-type-specific connections predicted in the neocortical tissue model (Markram et al.,

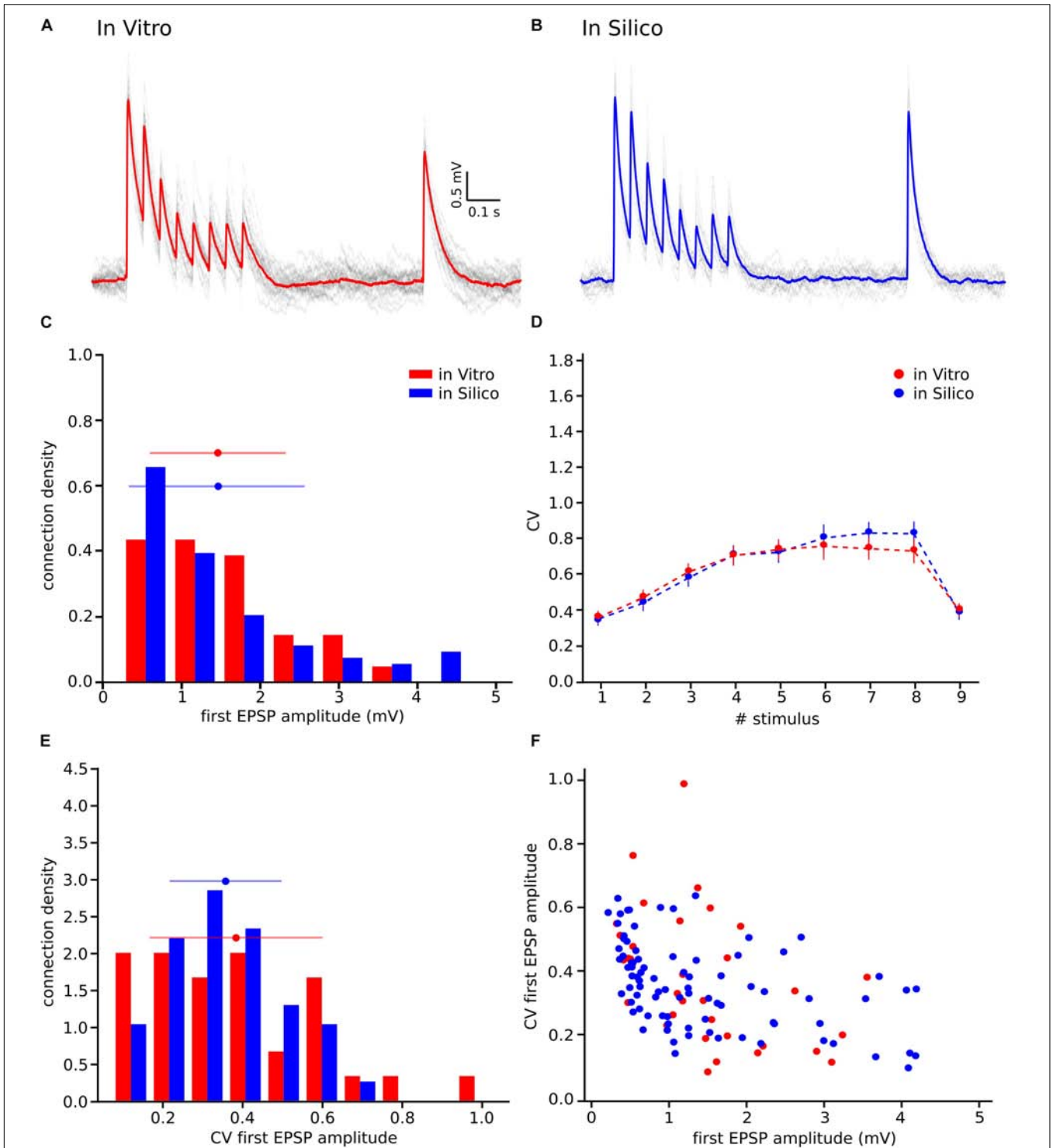

FIGURE 6 | Releasing multiple vesicles improved the variability of the model. **(A)** *In vitro* mean voltage trace (red) of 20 protocol repetitions (gray) (same as in **Figure 1A**). **(B)** *In silico* mean voltage trace (blue) of 20 protocol repetitions (gray). **(C)** Distribution of the first EPSP amplitude for *in vitro* (red) and for the *in silico* (blue) experiments. **(D)** Mean CV profiles for the *in vitro* (red) and the *in silico* (blue) experiments. **(E)** CV Distribution of the first EPSP amplitude for *in vitro* (red) and the *in silico* (blue) data sets. **(F)** Raster plot of the first EPSP amplitude against the CV of the first EPSP amplitude for *in vitro* (red) and *in silico* (blue) experiments. All the *in silico* experiments are done with the N_{RRP} value that produces the minimum error. In the distributions and the CV profile, dots represent the mean and vertical and horizontal bars represent the standard deviation of all the experiments.

2015; Ramaswamy et al., 2015; Reimann et al., 2015) and also independently characterized by other groups (Feldmeyer et al., 2002, 2005, 2006; Wang et al., 2002). Specifically, we computed the amplitudes and CVs of first PSP amplitudes from these published studies due to lack of access to raw experimental data. Synaptic parameter specifications for the different connections in the model are described in the NMC portal (Ramaswamy et al., 2015).

Before computing the CV for different cell-type-specific synaptic connections obtained from the literature, we had to take into account that they were not necessarily computed using the JKK bootstrapping approach. Our previous analyses demonstrate that the CV of the first EPSP computed through the JKK method has a slightly larger value than the CV computed analytically. In the case of L5_TTPC connections the CV_{JKK} was 0.38 ± 0.21 as against the analytical CV of 0.31 ± 0.14 for the *in vitro* data set but the N_{RRP}s computed after 50 iterations in both cases were mostly similar (N_{RRP} without JKK = 2.41 ± 1.08 and N_{RRP} with JKK = 2.73 ± 1.22; p = 0.94; **Figures 7A,B**, respectively). This N_{RRP} obtained by comparing the *in vitro* and the *in silico* CVs for only the first EPSP is smaller than the previous N_{RRP} obtained by comparing the CV for all the EPSPs, but as revealed in the previous analysis we did not match the exact CV value for the 1st pulse, although there were no significant difference.

Knowing that the JKK bootstrapping method provided a more accurate method to compute EPSP amplitudes, we applied a transformation from CV to CV_{JKK} (**Figure 7C**). First, we computed the CV of the first EPSP amplitude without (**Figure 7A**) and with the JKK (**Figure 7B**) method. Second, we represented both CVs in the same plot for the different N_{RRP} values and we performed a linear fit to the mean of 50 repetitions (**Figure 7C**). Next, we determined the corresponding CV value computed with the JKK approach (**Figure 7B**), for this connection (L5_TTPC) we obtained CV_{JKK} = 0.39 ± 0.15 with a correspondent N_{RRP} = 2.84 ± 1.34. We did that for every connection for which we could find data in the literature and our simulation matched the variability (**Table 1**).

The generalized results to five different cell-type-specific connections are summarized in **Table 1**. We further predict

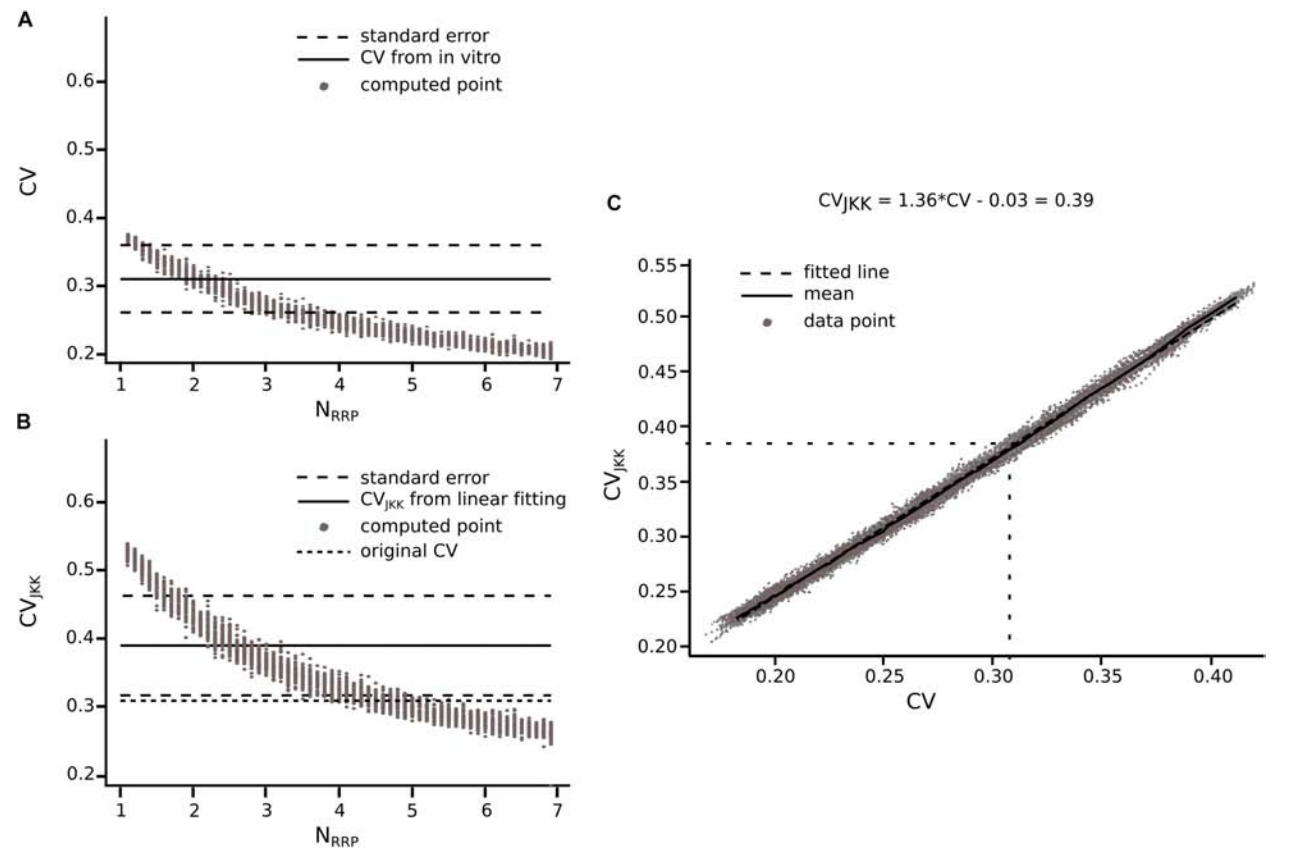

FIGURE 7 | Extension of the method for connections reported in literature.Transformation from CV to CV_{JKK} using L5_TTPC connection as example **(A)** CV computed for different N_{RRP}. Solid black line represents the CV computed for the *in vitro* data. Dotted black lines represent the standard error of the CV. **(B)** CV_{JKK} computed for different N_{RRP}. Solid black line represents the CV_{JKK} obtained from the lineal fitting on **C**. Dotted black lines represent the standard error for this CV_{JKK}. Short dotted black line represents the original CV found in literature. **(C)** CV to CV_{JKK} transformation. Solid black line represents the mean of the 50 iterations and dotted black line represent the linear fitting which equation is at the top of the plot. In **(A,B)** the gray dots show the 50 iterations from which we extract the best N_{RRP} as the one corresponding with the closest CV.

TABLE 1 | Results for connections reported in literature.

Connection type	Literature data	Jack-Knife conversion	Prediction
	CV	CV	N_{RRP}
L23_NBC_LBC-L23_PC	0.40 ± 0.09 (Wang et al., 2002)	0.38 ± 0.21	1.96 ± 0.98
L23_PC-L23_PC	0.33 ± 0.18 (Feldmeyer et al., 2006)	0.48 ± 0.23	2.60 ± 1.28
L4_SSC-L23_PC	0.27 ± 0.13 (Feldmeyer et al., 2002)	0.37 ± 0.09	1.81 ± 0.37
L4_SSC-L5_TPC:C	0.33 ± 0.20 (Feldmeyer et al., 2005)	0.46 ± 0.15	1.26 ± 0.50
L5_TTPC-L5_SBC	0.32 ± 0.08 (Wang et al., 2002)	0.34 ± 0.16	1.82 ± 0.90
L5_TTPC-L5_TTPC	0.31 ± 0.14 (Measured in this study)	0.39 ± 0.15	2.84 ± 1.34

Table summarizing the CV_{JKK} computed for other five cell connections through the collection of data from literature and applying the JKK conversion explained in ***Figure 6****. For the L5_TTPC connection we used the CV computed in this work from our in vitro data set. L23_NBC_LBC: layer 2 and 3 nest and large basket cells; L23_PC: pyramidal cells in layer 2 and 3; L4_SSC: layer 4 spiny stellate cells; L5_TPC:C: thick tuft pyramidal cells that receive projections from thalamus; L5_SBC: small basket cells from layer 5.*

that for connections between layer 4 spiny stellate (L4_SSC) and slender-tufted layer 5 pyramidal cell connections that project across the corpus callosum (L5_TPC:C), synaptic release is mediated by UVR (see **Table 1**; N_{RRP} = 1.26 ± 0.50), while for the remainder of connections the predicted N_{RRP} is between 2 to 3 (see **Table 1**; N_{RRP} = 2.60 ± 1.28 for L23_PC-L23_PC; N_{RRP} = 1.96 ± 0.98 for L23_NBC_LBC-L23_PC; N_{RRP} = 1.81 ± 0.37 for L4_SSC-L23_PC and N_{RRP} = 1.82 ± 0.90 for L5_TTPC-L5_SBC).

Our results predict that synaptic release at most connections in the neocortex are more likely mediated by MVR rather than UVR, supporting the idea that the release of multiple vesicles enhances the response variability of neocortical synapses and augments information transmission.

DISCUSSION

In this work we computed the N_{RRP} building on the previous work of Loebel et al. (2009) but extended it to all individual synaptic contacts in a connection. Our approach is based on the comparison of the amplitudes and CV of EPSPs between cell-type-specific *in vitro* and *in silico* connections with different N_{RRP} values within the framework of a large-scale, data driven tissue level model of juvenile rat neocortical microcircuitry (Markram et al., 2015). The CV of the amplitude distributions reliably reflects the concentration of neurotransmitter in the synaptic cleft and for the postsynaptic receptor occupancy (Faber and Korn, 1991; Auger and Marty, 2000; Neishabouri and Faisal, 2014). For example, a large quantity of presynaptic neurotransmitter release would give rise to a high amplitude EPSP. However, a large fraction of receptors would be occupied as well and consequently it would be more difficult to generate a second EPSP if more neurotransmitter is released. Thus, it is possible to measure the variability of the EPSP amplitude considering that high variability represents a small number of released vesicles.

UVR Cannot Reproduce the Variability Observed Into the Biological Data

Our analysis demonstrates that the UVR hypothesis cannot reproduce the variability observed on the *in vitro* traces, in fact the CV profile for the *in silico* experiments is significantly larger, although the first EPSP amplitude is not statistically different. This result suggests that the MVR hypothesis could be more relevant to explain the response variability in neocortical synapses. On the one hand, this idea differs from previous studies (Redman, 1990; Gulyás et al., 1993; Murphy et al., 2004), which claim that at each active zone in a synapse only one vesicle could be released, suggesting that the biological variability may come from changes in the quantal size. On the other hand, more recent studies validate our MVR hypothesis that better explains biological variability (Brémaud et al., 2007; Loebel et al., 2009; Hardingham et al., 2010; Huang et al., 2010; Rudolph et al., 2015). This discrepancy could be partly attributed to the fact that the studies validating the UVR hypothesis were undertaken in brain regions other than the neocortex, with different experimental protocols, across different species and cell-types.

Before obtaining evidence, which supports the MVR hypothesis, we extracted a core set of synaptic important parameters from an *in vitro* dataset obtained from L5_TTPCs. First, we computed the parameters pertaining to a deterministic model of short-term synaptic depression (Tsodyks and Markram, 1997). To this end, we had to select only those connections whose 1st EPSP amplitude was within the range of the *in vitro* data set and apply the deconvolution for computing the peaks. Then we introduced the peak values on a GA that calculated the synaptic parameters. The values obtained were similar to values found in previous researches (Tsodyks and Markram, 1997; Wang et al., 2006). Second, we calibrated the synaptic noise which represented the synaptic trial-to-trial variability. Many studies support the idea that background synaptic noise is not merely "noise," but an addition of various meaningful mechanisms as channels and receptors dynamics (Azouz and Gray, 1999; Faisal et al., 2008). Synaptic noise is also thought to arise from the spontaneous fusion and release of vesicle (Fatt and Katz, 1950). This noise could not only influence the synaptic variability, but also the transmission of information (Jacobson et al., 2005). Thus, while some studies do not support our hypothesis of the contribution of the number of vesicles in synaptic noise (Mackenzie et al., 2000), several others (Korn et al., 1993; Franks et al., 2003; Faisal et al., 2008; Pulido and Marty, 2017) inspired us to include additional synaptic noise in

our model. Finally, we also validated our method by building three different *in silico* data sets where the mean N_{RRP} was set to 1, 4 and 10, respectively. Although the mean values obtained using the method were slightly larger, no significant differences were found, and therefore, we used the validated method with experimental data sets.

L5_TTPC Synapses Are Driven by Multiple Vesicles

Increasing the N_{RRP} improved the variability of our model, resulting in synapses that more faithfully reproduced the experimentally observed physiology. Consequently, for synaptic connections between L5_TTPCs the predicted N_{RRP} was 3.78 ± 1.65 within a range of 1 to 9 vesicles. Synaptic connections between L5_TTPCs are mediated by about 4 to 8 contacts on average (Markram et al., 1997). We predict that the total number of release sites for pairs synaptic contact between L5_TTPC connections ranges between 4 to 72, which is consistent with two previous studies of that have estimated vesicles in L5_TTPC synaptic contacts to range from 2 to 30 docked vesicles (Rollenhagen and Lübke, 2006), and 7 to 170 vesicles (Loebel et al., 2009). Our predictions are also consistent with a recent study, which estimated that the number of readily releasable vesicles at individual synaptic contacts of L5B PCs ranged from 1.2 to 12.8 with an average of (5.40 ± 1.24) per contact (Rollenhagen et al., 2018). The estimated mean value is slightly larger than what we predict, which could be due to a difference in the developmental age and the cortical area. While our experimental data set was obtained in the non-barrel hind limb somatosensory cortex of juvenile rats, Rollenhagen et al. (2018) investigated synapses between L5B PCs in the barrel cortex of adult rats. Compared to cortical synapses, the neuromuscular junction and the Calyx of Held, which are extensively studied synaptic assemblies, also show MVR with about two, and three vesicles per active zone, respectively (Neher and Sakaba, 2008; Ruiz et al., 2011; Sakaba, 2018). These studies support the idea that MVR occurs in different brain areas within different ranges, suggesting that MVR may be important not only for reliable information transmission, but also a key mechanism for defining synaptic functionality. Is synaptic release in other cell-type-specific connections in the rat neocortex mediated by MVR?

We extended our method to predict the N_{RRP} for L5_TTPC synapses to other cell-type-specific connections in the neocortex reported in the literature. For five different cell-type-specific connections, we predict that the average N_{RRP} is between 2 and 3 (see **Table 1**). Although our predictions are inconsistent with some observations, for connections between L4_SSC and L23_PCs (Silver et al., 2003), they are comparable with other studies that support the notion of MVR as a fundamental property of intra and inter-laminar cortical synapses (Brémaud et al., 2007; Huang et al., 2010).

Due to lack of specific data, we extrapolated synaptic parameters measured in the superficial layers (Wang et al., 2002) to deeper layers, in particular for synaptic connections between L2/3 PCs and basket cells to their counterparts L5 to predict the N_{RRP}. Our data-driven framework is designed in to integrate specific data sets as and when they become available to enable predictions on the N_{RRP} of cortical synapses.

Despite the occurrence of weak *in silico* synaptic connections between L5_TTPCs in the neocortical tissue model, the CV distribution has a lower mean because the subset of *in silico* connections that were sampled to reproduce experimental findings display high EPSP amplitudes. Previous work seems to suggest that weak synaptic connections are necessary to maintain synchronous activity in the cortex (Bruno and Sakmann, 2006; Ren et al., 2017). Therefore, future refinements of this approach should consider how weak connections could impact predictions of N_{RRP}. It should be noted that other parameters relevant to predict the N_{RRP}, such as g_{max} were determined indirectly in our study, which could impact our results. For instance, if g_{max} was underestimated, we would have had obtained a larger N_{RRP} by increasing its value considering the same CV. It is also known that other synaptic mechanisms such as the membrane fusion, receptor saturation, and vesicle recycling directly influence vesicle release (Stevens, 2003; Watanabe et al., 2013; Rizo and Xu, 2015; Rudolph et al., 2015). We propose that future work should consider all these synaptic factors to predict N_{RRP} for cortical connections.

In summary, we described an approach built upon previous work (Loebel et al., 2009) to predict the N_{RRP} per active synaptic contact for neocortical connections. By systematically comparing *in vitro* and *in silico* data on the CV of the EPSP amplitude CV, we could predict the N_{RRP}. Our preliminary results suggest that MVR could serve as a fundamental mechanism in the brain to increase the dynamic range of synapses and their variability.

DATA AVAILABILITY STATEMENT

The raw data supporting the conclusions of this manuscript will be made available by the authors, without undue reservation, to any qualified researcher.

ETHICS STATEMENT

All experiments were performed according to the Swiss national and institutional guidelines.

AUTHOR CONTRIBUTIONS

NB-Z developed and performed the data analysis and the *in silico* experiments, drafted the manuscript, and generated the figures. JR developed and performed the initial data analysis. GC developed and performed some data analysis and some *in silico* experiments. RP designed and performed the *in vitro* experiments. HM contributed to data interpretation and procured funding for the study. SR gathered data from the published literature, contributed to data interpretation, and drafted the manuscript. EM contributed to data interpretation

and an initial draft of the manuscript. SR and EM jointly conceived and supervised the study.

FUNDING

This study was supported by funding to the Blue Brain Project, a research center of the École Polytechnique Fédérale de Lausanne, from the Swiss Government's ETH Board of the Swiss Federal Institutes of Technology.

ACKNOWLEDGMENTS

The authors thank Dr. Michael Reimann and the Blue Brain Project team for insightful discussions.

REFERENCES

Auger, C., Kondo, S., and Marty, A. (1998). Multivesicular release at single functional synaptic sites in cerebellar stellate and basket cells. *J. Neurosci.* 18, 4532–4547. doi: 10.1523/jneurosci.18-12-04532.1998

Auger, C., and Marty, A. (2000). Quantal currents at single-site central synapses. *J. Physiol.* 526(Pt 1), 3–11. doi: 10.1111/j.1469-7793.2000.t01-3-00003.x

Azouz, R., and Gray, C. M. (1999). Cellular mechanisms contributing to response variability of cortical neurons in vivo. *J. Neurosci.* 19, 2209–2223. doi: 10.1523/jneurosci.19-06-02209.1999

Betz, W. J. (1970). Depression of transmitter release at the neuromuscular junction of the frog. *J. Physiol.* 206, 629–644. doi: 10.1113/jphysiol.1970.sp009034

Bibbona, E. (2008). The Ornstein-Uhlenbeck process as a model of a low-pass filtered white noise. *Metrologia* 45, S117–S126.

Bibbona, E., Panfilo, G., and Tavella, P. (2008). The Ornstein–Uhlenbeck process as a model of a low pass filtered white noise. *Metrologia* 45, S117–S126.

Biró, A. A., Holderith, N. B., and Nusser, Z. (2005). Quantal size is independent of the release probability at hippocampal excitatory synapses. *J. Neurosci.* 25, 223–232. doi: 10.1523/jneurosci.3688-04.2005

Boucher, J., Kröger, H., and Sík, A. (2010). Realistic modelling of receptor activation in hippocampal excitatory synapses: analysis of multivesicular release, release location, temperature and synaptic cross-talk. *Brain Struct. Funct.* 215, 49–65. doi: 10.1007/s00429-010-0273-x

Brémaud, A., West, D. C., and Thomson, A. M. (2007). Binomial parameters differ across neocortical layers and with different classes of connections in adult rat and cat neocortex. *Proc. Natl. Acad. Sci. U. S. A.* 104, 14134–14139. doi: 10.1073/pnas.0705661104

Bruno, R. M., and Sakmann, B. (2006). Cortex is driven by weak but synchronously active thalamocortical synapses. *Science* 312, 1622–1627. doi: 10.1126/science.1124593

Christie, J. M., and Jahr, C. E. (2006). Multivesicular release at schaffer collateral-CA1 hippocampal synapses. *J. Neurosci.* 26, 210–216. doi: 10.1523/jneurosci.4307-05.2006

Conti, R., and Lisman, J. (2003). The high variance of AMPA receptor- and NMDA receptor-mediated responses at single hippocampal synapses: evidence for multiquantal release. *Proc. Natl. Acad. Sci. U.S.A.* 100, 4885–4890. doi: 10.1073/pnas.0630290100

Del Castillo, J., and Katz, B. (1954). Quantal components of the end-plate potential. *J. Physiol.* 124, 560–573. doi: 10.1113/jphysiol.1954.sp005129

Efron, B., and Tibshirani, R. J. (1994). *An Introduction to the Bootstrap*. New York, NY: Chapman & Hall.

Faber, D. S., and Korn, H. (1991). Applicability of the coefficient of variation method for analyzing synaptic plasticity. *Biophys. J.* 60, 1288–1294. doi: 10.1016/s0006-3495(91)82162-2

Faisal, A. A., Selen, L. P. J., and Wolpert, D. M. (2008). Noise in the nervous system. *Nat. Rev. Neurosci.* 9, 292–303.

Fatt, P., and Katz, B. (1950). Some observations on biological noise. *Nature* 166, 597–598. doi: 10.1038/166597a0

Feldmeyer, D., Lübke, J., and Sakmann, B. (2006). Efficacy and connectivity of intracolumnar pairs of layer 2/3 pyramidal cells in the barrel cortex of juvenile rats. *J. Physiol.* 575, 583–602. doi: 10.1113/jphysiol.2006.105106

Feldmeyer, D., Lübke, J., Silver, R. A., and Sakmann, B. (2002). Synaptic connections between layer 4 spiny neurone – layer 2/3 pyramidal cell pairs in juvenile rat barrel cortex: physiology and anatomy of interlaminar signalling within a cortical column. *J. Physiol.* 538, 803–822. Pt 3, doi: 10.1113/jphysiol.2001.012959

Feldmeyer, D., Roth, A., and Sakmann, B. (2005). Monosynaptic connections between pairs of spiny stellate cells in layer 4 and pyramidal cells in layer 5A indicate that lemniscal and paralemniscal afferent pathways converge in the infragranular somatosensory cortex. *J. Neurosci.* 25, 3423–3431. doi: 10.1523/jneurosci.5227-04.2005

Franks, K. M., Stevens, C. F., and Sejnowski, T. J. (2003). Independent sources of quantal variability at single glutamatergic synapses. *J. Neurosci.* 23, 3186–3195. doi: 10.1523/jneurosci.23-08-03186.2003

Fuhrmann, G., Cowan, A., Segev, I., Tsodyks, M., and Stricker, C. (2004). Multiple mechanisms govern the dynamics of depression at neocortical synapses of young rats. *J. Physiol.* 557, 415–438. doi: 10.1113/jphysiol.2003.058107

Fuhrmann, G., Segev, I., Markram, H., and Tsodyks, M. (2002). Coding of temporal Information by activity-dependent synapses. *J. Neurophysiol.* 87, 140–148. doi: 10.1152/jn.00258.2001

Goldberg, D. E., and Holland, J. H. (1988). Genetic algorithms and machine learning. *Mach. Learn.* 3, 95–99. doi: 10.1023/A:1022602019183

Gordon, G. R. J. (2005). Noradrenaline triggers multivesicular release at glutamatergic synapses in the hypothalamus. *J. Neurosci.* 25, 11385–11395. doi: 10.1523/jneurosci.2378-05.2005

Gulyás, A. I., Miles, R., Sík, A., Tóth, K., Tamamaki, N., and Freund, T. F. (1993). Hippocampal pyramidal cells excite inhibitory neurons through a single release site. *Nature* 366, 683–687. doi: 10.1038/366683a0

Gupta, A., Wang, Y., and Markram, H. (2000). Organizing principles for a diversity of GABAergic interneurons and synapses in the neocortex. *Science* 287, 273–278. doi: 10.1126/science.287.5451.273

Hardingham, N. R., Read, J. C. A., Trevelyan, A. J., Nelson, J. C., Jack, J. J. B., and Bannister, N. J. (2010). Quantal analysis reveals a functional correlation between presynaptic and postsynaptic efficacy in excitatory connections from rat neocortex. *J. Neurosci.* 30, 1441–1451. doi: 10.1523/JNEUROSCI.3244-09.2010

Hennig, M. H. (2013). Theoretical models of synaptic short term plasticity. *Front. Comput. Neurosci.* 7:45. doi: 10.3389/fncom.2013.00045

Huang, C.-H., Bao, J., and Sakaba, T. (2010). Multivesicular release differentiates the reliability of synaptic transmission between the visual cortex and the somatosensory cortex. *J. Neurosci.* 30, 11994–12004. doi: 10.1523/JNEUROSCI.2381-10.2010

Jacobson, G. A., Diba, K., Yaron-Jakoubovitch, A., Oz, Y., Koch, C., Segev, I., et al. (2005). Subthreshold voltage noise of rat neocortical pyramidal neurones. *J. Physiol.* 564, 145–160. doi: 10.1113/jphysiol.2004.080903

Korn, H., Bausela, F., Charpier, S., and Faber, D. S. (1993). Synaptic noise and multiquantal release at dendritic synapses. *J. Neurophysiol.* 70, 1249–1254. doi: 10.1152/jn.1993.70.3.1249

Korn, H., Sur, C., Charpier, S., Legendre, P., and Faber, D. S. (1994). The one-vesicle hypothesis and multivesicular release. *Adv. Second Messenger Phosphoprotein Res.* 29, 301–322.

Korn, H., Triller, A., Mallet, A., and Faber, D. S. (1981). Fluctuating responses at a central synapse: n of binomial fit predicts number of stained presynaptic boutons. *Science* 213, 898–901. doi: 10.1126/science.6266015

Liley, A. W., and North, K. A. (1953). An electrical investigation of effects of repetitive stimulation on mammalian neuromuscular junction. *J. Neurophysiol.* 16, 509–527. doi: 10.1152/jn.1953.16.5.509

Loebel, A., Silberberg, G., Helbig, D., Markram, H., Tsodyks, M., and Richardson, M. J. E. (2009). Multiquantal release underlies the distribution of synaptic efficacies in the neocortex. *Front. Comput. Neurosci.* 3:27. doi: 10.3389/neuro.10.027.2009

Maass, W., and Markram, H. (2002). Synapses as dynamic memory buffers. *Neural Netw.* 15, 155–161. doi: 10.1016/s0893-6080(01)00144-7

Mackenzie, P. J., Kenner, G. S., Prange, O., and Murphy, T. H. (2000). Vesicle number does not predict postsynaptic measures of miniature synaptic activity frequency in cultured cortical neurons. *Neuroscience* 98, 1–7. doi: 10.1016/s0306-4522(00)00089-0

Markram, H., Lübke, J., Frotscher, M., Roth, A., and Sakmann, B. (1997). Physiology and anatomy of synaptic connections between thick tufted pyramidal neurones in the developing rat neocortex. *J. Physiol.* 500(Pt 2), 409–440. doi: 10.1113/jphysiol.1997.sp022031

Markram, H., Muller, E., Ramaswamy, S., Reimann, M. W., Sanchez, C., Ailamaki, A., et al. (2015). Reconstruction and simulation of neocortical microcircuitry. *Cell* 163, 456–492. doi: 10.1016/j.cell.2015.09.029

Markram, H., Wang, Y., and Tsodyks, M. (1998). Differential signaling via the same axon of neocortical pyramidal neurons. *Proc. Natl. Acad. Sci. U.S.A.* 95, 5323–5328. doi: 10.1073/pnas.95.9.5323

Mason, A., Nicoll, A., and Stratford, K. (1991). Synaptic transmission between individual pyramidal neurons of the rat visual cortex in vitro. *J. Neurosci.* 11, 72–84. doi: 10.1523/jneurosci.11-01-00072.1991

Molnár, G., Rózsa, M., Baka, J., Holderith, N., Barzó, P., Nusser, Z., et al. (2016). Human pyramidal to interneuron synapses are mediated by multi-vesicular release and multiple docked vesicles. *eLife* 5:e18167. doi: 10.7554/eLife.18167

Murphy, G. J., Glickfeld, L. L., Balsen, Z., and Isaacson, J. S. (2004). Sensory neuron signaling to the brain: properties of transmitter release from olfactory nerve terminals. *J. Neurosci.* 24, 3023–3030. doi: 10.1523/jneurosci.5745-03.2004

Nadkarni, S., Bartol, T. M., Sejnowski, T. J., and Levine, H. (2010). Modelling vesicular release at hippocampal synapses. *PLoS Comput. Biol.* 6:e1000983. doi: 10.1371/journal.pcbi.1000983

Neher, E., and Sakaba, T. (2008). Multiple roles of calcium ions in the regulation of neurotransmitter release. *Neuron* 59, 861–872. doi: 10.1016/j.neuron.2008.08.019

Neishabouri, A., and Faisal, A. A. (2014). Axonal noise as a source of synaptic variability. *PLoS Comput. Biol.* 10:e1003615. doi: 10.1371/journal.pcbi.1003615

Oertner, T. G., Sabatini, B. L., Nimchinsky, E. A., and Svoboda, K. (2002). Facilitation at single synapses probed with optical quantal analysis. *Nat. Neurosci.* 5, 657–664. doi: 10.1038/nn867

Press, W. H., and Teukolsky, S. A. (1988). Kolmogorov-Smirnov test for two-dimensional data. *Comput. Phys.* 2:74. doi: 10.1063/1.4822753

Pulido, C., and Marty, A. (2017). Quantal fluctuations in central mammalian synapses: functional role of vesicular docking sites. *Physiol. Rev.* 97, 1403–1430. doi: 10.1152/physrev.00032.2016

Ramaswamy, S., Courcol, J.-D., Abdellah, M., Adaszewski, S. R., Antille, N., Arsever, S., et al. (2015). The neocortical microcircuit collaboration portal: a resource for rat somatosensory cortex. *Front. Neural Circuits* 9:44. doi: 10.3389/fncir.2015.00044

Ramaswamy, S., and Markram, H. (2015). Anatomy and physiology of the thick-tufted layer 5 pyramidal neuron. *Front. Cell. Neurosci.* 9:233. doi: 10.3389/fncel.2015.00233

Redman, S. (1990). Quantal analysis of synaptic potentials in neurons of the central nervous system. *Physiol. Rev.* 70, 165–198. doi: 10.1152/physrev.1990.70.1.165

Reimann, M. W., King, J. G., Muller, E. B., Ramaswamy, S., and Markram, H. (2015). An algorithm to predict the connectome of neural microcircuits. *Front. Comput. Neurosci.* 9:120. doi: 10.3389/fncom.2015.00120

Ren, H.-P., Bai, C., Baptista, M. S., and Grebogi, C. (2017). Weak connections form an infinite number of patterns in the brain. *Sci. Rep.* 7:46472. doi: 10.1038/srep46472

Richardson, M. J., and Silberberg, G. (2008). Measurement and analysis of postsynaptic potentials using a novel voltage-deconvolution method. *J. Neurophysiol.* 99, 1020–1031. doi: 10.1152/jn.00942.2007

Rizo, J., and Xu, J. (2015). The synaptic vesicle release machinery. *Annu. Rev. Biophys.* 44, 339–367. doi: 10.1146/annurev-biophys-060414-034057

Rollenhagen, A., and Lübke, J. H. R. (2006). The morphology of excitatory central synapses: from structure to function. *Cell Tissue Res.* 326, 221–237. doi: 10.1007/s00441-006-0288-z

Rollenhagen, A., Ohana, O., Sätzler, K., Hilgetag, C. C., Kuhl, D., and Lübke, J. H. R. (2018). Structural properties of synaptic transmission and temporal dynamics at excitatory layer 5B synapses in the adult rat somatosensory cortex. *Front. Synaptic Neurosci.* 10:24. doi: 10.3389/fnsyn.2018.00024

Rudolph, S., Tsai, M.-C., von Gersdorff, H., and Wadiche, J. I. (2015). The ubiquitous nature of multivesicular release. *Trends Neurosci.* 38, 428–438. doi: 10.1016/j.tins.2015.05.008

Ruiz, R., Cano, R., Casañas, J. J., Gaffield, M. A., Betz, W. J., and Tabares, L. (2011). Active zones and the readily releasable pool of synaptic vesicles at the neuromuscular junction of the mouse. *J. Neurosci.* 31, 2000–2008. doi: 10.1523/jneurosci.4663-10.2011

Sakaba, T. (2018). Kinetics of transmitter release at the calyx of held synapse. *Proc. Jpn. Acad. Ser. B Phys. Biol. Sci.* 94, 139–152. doi: 10.2183/pjab.94.010

Silver, R. A., Lubke, J., Sakmann, B., and Feldmeyer, D. (2003). High-probability uniquantal transmission at excitatory synapses in barrel cortex. *Science* 302, 1981–1984. doi: 10.1126/science.1087160

Stevens, C. F. (2003). Neurotransmitter release at central synapses. *Neuron* 40, 381–388. doi: 10.1016/s0896-6273(03)00643-3

Südhof, T. C. (2000). The synaptic vesicle cycle revisited. *Neuron* 28, 317–320.

Tang, C. M., Margulis, M., Shi, Q. Y., and Fielding, A. (1994). Saturation of postsynaptic glutamate receptors after quantal release of transmitter. *Neuron* 13, 1385–1393. doi: 10.1016/0896-6273(94)90423-5

Tong, G., and Jahr, C. E. (1994). Multivesicular release from excitatory synapses of cultured hippocampal neurons. *Neuron* 12, 51–59. doi: 10.1016/0896-6273(94)90151-1

Tsodyks, M. V., and Markram, H. (1997). The neural code between neocortical pyramidal neurons depends on neurotransmitter release probability. *Proc. Natl. Acad. Sci. U.S.A.* 94, 719–723. doi: 10.1073/pnas.94.2.719

Varela, J. A., Sen, K., Gibson, J., Fost, J., Abbott, L. F., and Nelson, S. B. (1997). A quantitative description of short-term plasticity at excitatory synapses in layer 2/3 of rat primary visual cortex. *J. Neurosci.* 17, 7926–7940. doi: 10.1523/jneurosci.17-20-07926.1997

Waites, C. L., and Garner, C. C. (2011). Presynaptic function in health and disease. *Trends Neurosci.* 34, 326–337. doi: 10.1016/j.tins.2011.03.004

Wang, Y., Gupta, A., Toledo-Rodriguez, M., Wu, C. Z., and Markram, H. (2002). Anatomical, physiological, molecular and circuit properties of nest basket cells in the developing somatosensory cortex. *Cereb. Cortex* 12, 395–410. doi: 10.1093/cercor/12.4.395

Wang, Y., Markram, H., Goodman, P. H., Berger, T. K., Ma, J., and Goldman-Rakic, P. S. (2006). Heterogeneity in the pyramidal network of the medial prefrontal cortex. *Nat. Neurosci.* 9, 534–542. doi: 10.1038/nn1670

Watanabe, S., Rost, B. R., Camacho-Pérez, M., Davis, M. W., Söhl-Kielczynski, B., Rosenmund, C., et al. (2013). Ultrafast endocytosis at mouse hippocampal synapses. *Nature* 504, 242–247. doi: 10.1038/nature12809

Zhang, C., and Peskin, C. S. (2015). Improved signaling as a result of randomness in synaptic vesicle release. *Proc. Natl. Acad. Sci. U.S.A.* 112, 14954–14959. doi: 10.1073/pnas.1513160112

Conflict of Interest: The authors declare that the research was conducted in the absence of any commercial or financial relationships that could be construed as a potential conflict of interest.

frontiers in Synaptic Neuroscience

REVIEW
published: 20 November 2019
doi: 10.3389/fnsyn.2019.00032

Considerations for Measuring Activity-Dependence of Recruitment of Synaptic Vesicles to the Readily Releasable Pool

*John F. Wesseling**

CSIC/Instituto de Neurociencias, Universidad Miguel Hernández, Alicante, Spain

The connection strength of most chemical synapses changes dynamically during normal use as a function of the recent history of activity. The phenomenon is known as short-term synaptic plasticity or synaptic dynamics, and is thought to be involved in processing and filtering information as it is transmitted across the synaptic cleft. Multiple presynaptic mechanisms have been implicated, but large gaps remain in our understanding of how the mechanisms are modulated and how they interact. One important factor is the timing of recruitment of synaptic vesicles to a readily-releasable pool. A number of studies have concluded that activity and/or residual Ca^{2+} can accelerate the mechanism, but alternative explanations for some of the evidence have emerged. Here I review the methodology that we have developed for isolating the recruitment and the dependence on activity from other kinds of mechanisms that are activated concurrently.

Keywords: RRP, readily-releasable, residual, activity, recruitment, vesicle, pool

OPEN ACCESS

Edited by:
Henrique Prado von Gersdorff, Oregon Health & Science University, United States

Reviewed by:
Steven James Mennerick, Washington University in St. Louis, United States
Wallace B. Thoreson, University of Nebraska Medical Center, United States
Lucia Tabares, University of Seville, Spain

***Correspondence:**
John F. Wesseling
johnfwesseling@gmail.com

Received: *05 July 2019*
Accepted: *06 November 2019*
Published: *20 November 2019*

Citation:
Wesseling JF (2019) Considerations for Measuring Activity-Dependence of Recruitment of Synaptic Vesicles to the Readily Releasable Pool. Front. Synaptic Neurosci. 11:32. doi: 10.3389/fnsyn.2019.00032

1. INTRODUCTION

Presynaptic terminals typically contain hundreds of vesicles laden with neurotransmitter, but, at any given time, only a few per cent are docked at the plasma membrane and are ready to undergo exocytosis on demand. These *readily releasable* vesicles are often described as constituents of a *readily releasable pool* (RRP). High frequency trains of action potentials can deplete the RRP at a broad range of synapse types by driving exocytosis more quickly than replacement vesicles are recruited from reserve stores. The depletion is one of the mechanisms that causes short-term synaptic depression, although not the only one; e.g., inactivation of presynaptic voltage-gated Ca^{2+}-channels and desensitization of postsynaptic neurotransmitter receptors play important additional roles at some types of synapses (Trussell et al., 1993; Otis et al., 1996; Chen et al., 2002; Nanou and Catterall, 2018).

The Ca^{2+} that enters presynaptic terminals during the high frequency trains is cleared slowly during subsequent periods of rest; this is termed *residual* Ca^{2+}. A number of studies have concluded that the residual Ca^{2+} can accelerate how quickly replacement vesicles are recruited to the RRP (Kusano and Landau, 1975; Dittman and Regehr, 1998; Stevens and Wesseling, 1998; von Gersdorff et al., 1998; Wang and Kaczmarek, 1998; Gomis et al., 1999; Wang and Manis, 2008; Babai et al., 2010; Johnson et al., 2017). However, the techniques used to measure the timing of recruitment vary greatly between research groups, and the details matter because some techniques generate estimates that are 10-fold faster than others (discussed in Garcia-Perez and Wesseling, 2008).

Some of the discrepancies may be semantic. For example, RRPs are thought to contain separate slow-releasing and fast-releasing subdivisions; vesicles within slow-releasing subdivisions are

sometimes termed *reluctantly releasable* (Wu and Borst, 1999; Moulder and Mennerick, 2005; Neher, 2017; see Taschenberger et al., 2016 for evidence for a third subdivision). Some models, termed *serial* models, include the premise that vesicles recruited to the fast-releasing subdivision are drawn from vesicles already within the slow-releasing subdivision (Wu and Borst, 1999; Sakaba and Neher, 2001; Hosoi et al., 2007; Lee et al., 2010; Miki et al., 2016). If so, some widely used techniques may measure the transfer of vesicles from the slow-releasing subdivision to the fast-releasing subdivision rather than from entirely outside the RRP to within any of the subdivisions.

Nevertheless, at least two alternative explanations have been proposed for some of the evidence used to conclude that residual Ca^{2+} accelerates recruitment from outside the RRP entirely to within any subdivision, which we term *recruitment to the RRP as a whole*. Here I first describe the underlying caveats and then our own strategy for measuring the timing and why we remain confident that residual Ca^{2+} truly does accelerate the underlying mechanism, at least at excitatory hippocampal synapses.

Note that the concept of recruitment to the RRP as a whole will be equivalent to recruitment to the slow-releasing subdivision if a serial model turns out to be correct. I use the more general terminology here, however, because we remain open to the possibility that slow- and fast-releasing subdivisions may instead operate wholly in parallel. Indeed, results from experiments on calyces of Held indicate that neurotransmitter in both slow- and fast-releasing subdivisions can be released directly with sub-millisecond timing; neurotransmitter in the slow-releasing subdivision is released slowly during trains of action potentials at least partly because the fraction of slow-releasing vesicles that undergo exocytosis directly after each action potential - termed the *probability of release per vesicle* - is low (see Figure 5-figure supplement 1 in Raja et al., 2019). The results do not rule out serial models where slow-releasing vesicles can be recruited to the fast-releasing subdivision in addition to undergoing exocytosis directly, but we believe that our conclusions are equally valid whether or not transfer between subdivisions can occur (Mahfooz et al., 2016).

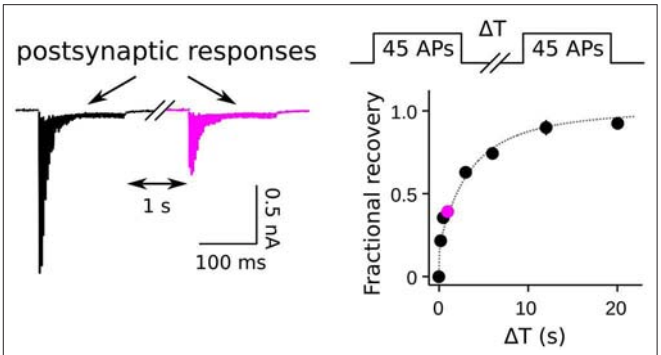

FIGURE 1 | Measurement of RRP replenishment using pairs of trains of presynaptic action potentials. Left panel is an example of postsynaptic responses when the inter-train interval was 1 s at a calyx of Held synapse. Right panel is the time course of recovery extracted from trials where the length of the inter-train interval (ΔT) was varied. The magenta data point corresponds to the example at left. Adapted from Figure 8 of Mahfooz et al. (2016).

2. THE CAVEATS

The caveats for measuring activity-dependence of recruitment to the RRP as a whole both pertain to experiments where the timing of recruitment is estimated from the time course of recovery after inducing short-term depression. In these cases, recovery is mainly measured from synaptic output generated by pairs of stimuli separated by interleaved rest intervals (**Figure 1**). The first stimulus induces the depression, and the second is used to assess the amount of recovery during the rest interval, typically by dividing the aggregate postsynaptic response generated by the second stimulus by the response generated by the first. The full recovery time course is then estimated from the individual trials as a function of the length of the rest interval; if significant recruitment occurs during stimulation, the offset can be estimated from interleaved trials where the rest interval is zero (Wesseling and Lo, 2002). A variety of stimuli have been used, including: single or multiple action potentials in trains; direct depolarization of presynaptic terminals via voltage clamp; indirect depolarization by applying hyperkalemic solution; and even osmotic shocks. All except osmotic shocks drive exocytosis by admitting Ca^{2+} into the presynaptic terminals. Evidence that the Ca^{2+} chelator EGTA lengthens the time course of recovery is interpreted as evidence that the recruitment mechanism is normally accelerated by the residual Ca^{2+} remaining after the first stimulus of each pair. However, the conclusion depends on the assumption that recovery from depression is equivalent to RRP replenishment, and this is not necessarily correct when the stimuli are not sufficient to fully exhaust all subdivisions of the RRP.

2.1. Enhanced Fusogenicity

The first caveat arose from the finding that residual Ca^{2+} activates a mechanism that transiently enhances the fusogenicity of readily releasable vesicles at hippocampal synapses (Stevens and Wesseling, 1999a; Garcia-Perez and Wesseling, 2008; e.g., see **Figure 2**). Enhancement of synaptic strength above baseline is typically masked during intense stimulation because of concurrent depletion of the RRP. However, the mechanism can enhance synaptic strength above baseline when conditions are manipulated to minimize the depletion, and is likely to be at least one of the causes of the classically defined element of short-term enhancement termed *Augmentation* (Magleby, 1979; Regehr, 2012). The role in information processing has not yet been resolved, but the mechanism does transiently sharpen the frequency filtering properties of synaptic transmission on a time scale of seconds.

The amount of enhancement of fusogenicity of individual readily releasable vesicles does not seem to be related to the extent of RRP depletion or subsequent replenishment, even when only recently recruited vesicles are present, suggesting that the mechanism operates independently from recruitment mechanisms (Garcia-Perez and Wesseling, 2008). Even extensive use that depletes the reserve stores and slows the bulk rate

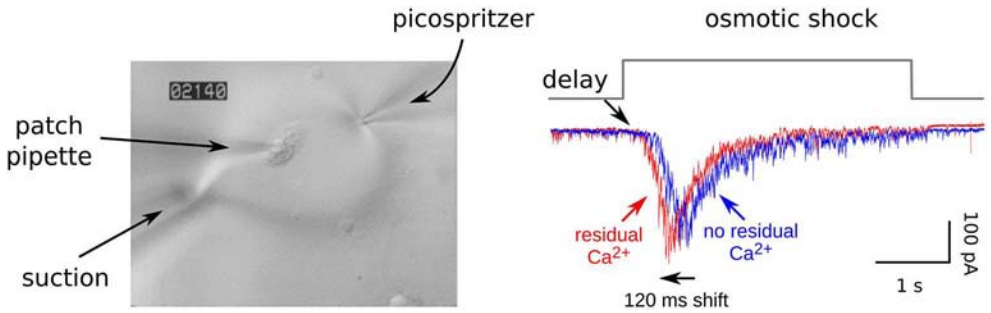

FIGURE 2 | Residual Ca^{2+} accelerates release elicited by osmotic shocks. **Left:** Image of an autapse during a strong osmotic shock. Hypertonic solution was applied with a picospritzer for rapid onset combined with a suction pipette for equally rapid clearance, and was visible via DIC microscopy. **Right:** Postsynaptic responses during osmotic shocks. The leftwards shift after generating residual Ca^{2+} indicates that the Ca^{2+} enhances fusogenicity of readily releasable vesicles by lowering the energy barrier that prevents spontaneous exocytosis. In this experiment, residual Ca^{2+} was generated by firing a train of action potentials ending immediately before the recording begins, and caused 4-fold enhancement in the probability of release; RRP depletion was avoided because the extracellular Ca^{2+} was lowered to 0.25 mM. EGTA blocks the leftwards shift and enhancement of synaptic strength but does not alter the length of the delay in the absence of residual Ca^{2+} (not shown). See Figure 4 of Stevens and Wesseling (1999a) for a more extensive analysis and Figure 8 of Garcia-Perez and Wesseling (2008) for an analogous experiment when the readily releasable vesicles were new recruits.

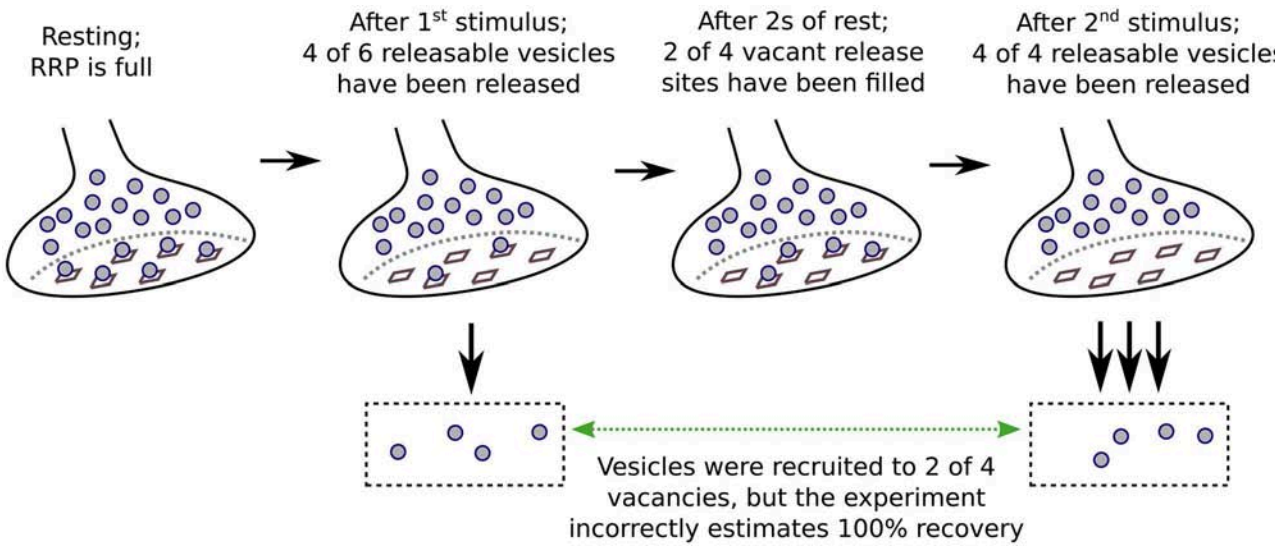

FIGURE 3 | Enhanced fusogenicity can interfere with measurements of RRP replenishment.

of recruitment by a factor of 3—termed *supply-rate depression* (Garcia-Perez et al., 2008)—does not dampen the enhancement for individual vesicles once they have entered the RRP (Garcia-Perez and Wesseling, 2008).

Naturally, the impact of residual Ca^{2+} is largest when the concentration is high. As a consequence, the second stimuli of pairs that fail to completely exhaust the RRP drive exocytosis of a greater fraction of the readily releasable vesicles if applied after short rest intervals, when the RRP has only partially replenished, than after long rest intervals when replenishment is complete but fusogenicity is no longer enhanced because most of the residual Ca^{2+} has been cleared away (**Figure 3**). In this way, responses rebound from depression more quickly than RRP replenishment, and can even transiently overshoot baseline values (Garcia-Perez and Wesseling, 2008). EGTA would be expected to reduce the mismatch between recovery from depression and RRP replenishment by preventing the enhancement of fusogenicity. This would slow recovery even if the recruitment mechanism were not accelerated by Ca^{2+}.

2.2. Fast Replenishment of EGTA-Sensitive Subdivisions

The mechanism that enhances fusogenicity either is not present or does not remain active long enough to influence recovery from depression after short trains of action potentials at calyces of Held (Mahfooz et al., 2016), and possibly other types of synapses. However, Ritzau-Jost et al. (2018) have identified a second caveat that could be equally problematic. In some cases, EGTA is thought to selectively block release of vesicles from the slow-releasing subdivision of the RRP, while leaving release

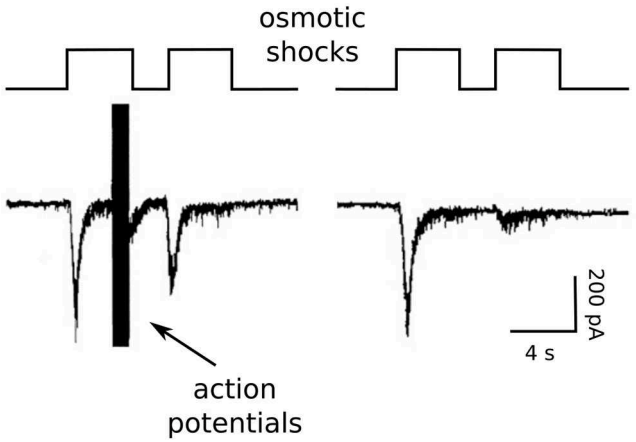

FIGURE 4 | Osmotic shock technique used to assess Ca^{2+}-dependent acceleration of recruitment. Reproduction of Figure 2A of Stevens and Wesseling (1998). The RRP was emptied with a pair of osmotic shocks induced with hypertonic solution. Action potentials were evoked during the end of the first osmotic shock at left, but not at right.

from the fast-releasing subdivision intact, likely owing to details about how quickly the EGTA chelates free Ca^{2+} (Adler et al., 1991; Neher, 1998). When this occurs, treating with EGTA would change the measurement of recovery from a measurement of replenishment of the RRP as a whole to a measurement of replenishment of only the fast-releasing subdivision. This could be problematic because the fast-releasing subdivision is thought to be replenished more slowly than the slow-releasing subdivision at some types of synapses (Wu and Borst, 1999; Sakaba and Neher, 2001; Lee et al., 2013; Ritzau-Jost et al., 2018; but see Garcia-Perez and Wesseling, 2008; Mahfooz et al., 2016). Here again, EGTA could slow recovery without necessarily altering the underlying timing of recruitment of vesicles to the RRP.

3. DETECTING ACCELERATION WITH OSMOTIC SHOCKS

Because of these concerns and concerns that Ca^{2+} channel inactivation might additionally complicate measurements of recovery, we began our studies by measuring RRP replenishment with pairs of strong osmotic shocks in the presence and absence of residual Ca^{2+} (Stevens and Wesseling, 1998; see **Figure 4**).

We accomplished this by exploiting unique features of isolated neurons grown in cell culture on small islands of substrate. The axons of the isolated neurons form synapses onto the dendrites; these are termed *autapses* for auto synapses (Furshpan et al., 1976; Bekkers and Stevens, 1991). The islands can be superfused rapidly with hypertonic solution, allowing osmotic shocks to be induced rapidly (see image in **Figure 2**). The osmotic shocks drive exocytosis without increasing intracellular Ca^{2+} (Rosenmund and Stevens, 1996), allowing one to follow the time course of recovery by measuring the postsynaptic responses to transmitter released by pairs, much like in experiments where transmitter release is instead driven by action potentials (e.g., **Figure 1**), except in the absence of the presynaptic Ca^{2+} admitted by action potentials (right panel in **Figure 4**). Conveniently, the presynaptic terminals of the autapses can be flooded with residual Ca^{2+} by evoking trains of action potentials with the same electrode used to measure postsynaptic responses, additionally allowing measurements of recovery in the presence of residual Ca^{2+} at the same synapses. We found that action potentials evoked during the first osmotic shock of pairs increased the size of the response to the second osmotic shock, indicating that recovery during the interval between shocks was faster (left panel in **Figure 4**). The increase was driven by residual Ca^{2+} because it was blocked by EGTA, and EGTA had no impact in the absence of action potentials/residual Ca^{2+}. A control showing that the action potentials do not alter the sizes of individual quantal events ruled out postsynaptic mechanisms.

4. RESPONSES TO OSMOTIC SHOCKS RELIABLY REPORT RRP REPLENISHMENT

The controls for confirming that osmotic shocks drive transmitter release from the RRP rather than some other source include co-depletion experiments where trains of action potentials largely eliminate the response to strong osmotic shocks and vice versa (Rosenmund and Stevens, 1996; Moulder and Mennerick, 2005; Garcia-Perez et al., 2008). However, although osmotic shocks do not admit Ca^{2+}, they do transiently inhibit Ca^{2+} influx through voltage gated Ca^{2+} channels, which can complicate the interpretation of experiments where osmotic shocks precede trains of action potentials within $\sim$10 s (Rosenmund and Stevens, 1996; Garcia-Perez and Wesseling, 2008). Nevertheless, the amount of neurotransmitter released by strong osmotic shocks seems to be equivalent to the amount released during trains of action potentials that exhaust the RRP (Stevens and Williams, 2007), suggesting that strong osmotic shocks can completely exhaust the RRP.

Although the mechanism by which osmotic shocks drive transmitter release is not known, we suspect that physical torsion of the active zone plays a role. Because of this, we were initially concerned that the first shock of each pair might damage the active zone in a way that would alter the timing of vesicle recruitment. However, the pairs of shocks could be repeated many times in individual preparations with reproducible results (Stevens and Wesseling, 1998). And, the time course of recovery was the same in analogous experiments where the hypertonic solution was replaced with hyperkalemic solution or trains of action potentials that were sufficiently intense to nearly completely exhaust the RRP (Stevens and Tsujimoto, 1995; Wesseling and Lo, 2002); hyperkalemic solutions and trains of action potentials generate residual Ca^{2+}, so the relevant comparison is to the osmotic shock trials where residual Ca^{2+} was present.

Altogether, these studies provide compelling evidence that osmotic shocks can be used to reliably measure the time course of RRP replenishment, and indicate that residual Ca^{2+} truly does accelerate the mechanism underlying vesicle recruitment. The caveats described above are avoided because the osmotic shocks

likely exhaust the RRP. Even if not, we reasoned that the residual Ca^{2+}-dependent increase in fusogenicity that is key for the first caveat could not explain the increased amount of release elicited by the second osmotic shocks of pairs because, otherwise, Ca^{2+} would have additionally increased the amount released during single osmotic shocks initiated when the RRP was full, but this was not seen (Stevens and Wesseling, 1999a; e.g., **Figure 2**). And, the second caveat is avoided because EGTA did not affect the time course of recovery in the absence of residual Ca^{2+}.

Note that the logic for ruling out the first caveat is based on information from experiments where the shocks were induced with rapid, strong hypertonic challenges. The caveat might be problematic for weaker hypertonic challenges that do not exhaust the RRP because residual Ca^{2+} would then be expected to increase the aggregate response even when the RRP is full (Rosenmund and Stevens, 1996; Schotten et al., 2015).

In addition, at least one group has reported evidence for basal intracellular Ca^{2+} levels in cultured neurons that were high enough to accelerate the time course of RRP replenishment without additional stimulation (Liu et al., 2014). The result seems to be at odds with our finding that EGTA had no impact on recruitment or fusogenicity in the absence of action potentials. The neurons in Liu et al. (2014) were not autapses, and the presynaptic axon terminals were not voltage clamped by a second electrode, but there were other methodological differences and the ultimate cause of the discrepancy is not known.

5. RELEVANCE OF AUTAPTIC SYNAPSES TO NATIVE SYNAPSES IN TISSUE

We have not attempted to repeat the osmotic shock experiments at synapses in tissue because of technical difficulties applying and clearing hypertonic solutions rapidly. However, the timing of rate-limiting mechanisms in recruitment to the RRP at autapses—which we grow from dissociated hippocampus—are remarkably similar to at Schaffer collateral synapses in *ex vivo* hippocampal slices. Evidence that recruitment mechanisms are similar in autapses and tissue includes: (1) the time course of RRP replenishment measured with action potentials that matched recovery measured with osmotic shocks above was extracted from experiments at Schaffer collateral synapses; (2) both the use-dependence of induction of supply-rate depression during extended trains of action potentials, and the timing of recovery during subsequent rest intervals, were similar or identical in the two preparations (Stevens and Wesseling, 1999b; Garcia-Perez et al., 2008); (3) the induction of supply-rate depression was selectively accelerated in synapsin knockouts by the same amount in the two preparations (Gabriel et al., 2011); and, finally, (4) the fast rebound in synaptic strength attributed to the transient residual Ca^{2+}-dependent enhancement of fusogenicity that is key for the first caveat was initially characterized in autapses and was later found to be intact at Schaffer collateral synapses (Stevens and Wesseling, 1999a; Garcia-Perez and Wesseling, 2008). Taken together, these results suggest that the autapse preparation is a good model for synapses in *ex vivo* tissue, and by extension, *in vivo*, at least for studying rate-limiting mechanisms involved in synaptic vesicle recruitment to the RRP.

In contrast, we do routinely observe striking differences between autapses and Schaffer collateral synapses in phenomena that are downstream of recruitment, such as more paired-pulse depression and more asynchronous release. Even so, the differences do not necessarily lessen the utility of autapses for investigating principles underlying the downstream events because both phenomena are heavily influenced by subtle changes in experimental conditions such as temperature and/or extracellular Ca^{2+} levels, suggesting that the differences are modulatory rather than at the level of basic mechanism. And indeed, there is substantial heterogeneity among Schaffer collateral synapses (e.g., Dobrunz and Stevens, 1997), and some individuals express as much paired-pulse depression as typical autapses. (We have never attempted to measure the extent of variation in asynchronous release among individual Schaffer collateral synapses).

6. CONTROLS FOR CONFIRMING RRP EXHAUSTION DURING TRAINS OF ACTION POTENTIALS

We are not aware of doubts about the conclusion that Ca^{2+} accelerates recruitment to the RRP as a whole beyond the caveats raised in Garcia-Perez and Wesseling (2008), and Ritzau-Jost et al. (2018). However, there are substantial quantitative discrepancies between our estimates of the timing of RRP replenishment during rest intervals and estimates from other groups. We have confidence in our own estimates because, to our knowledge, the discrepancies can always be traced back to experimental designs where time courses are estimated indirectly from the responses to single action potentials or short trains that do not fully exhaust the RRP, which can overestimate the true speed of vesicle recruitment by a large amount owing to the caveats described above. In contrast, mechanisms that are not related to vesicle recruitment should no longer interfere when recovery is extrapolated from the aggregate response to pairs of stimuli that both fully exhaust the RRP.

It is therefore sometimes critical to verify that a candidate frequency of action potentials is sufficient to exhaust the RRP. However, we have found that experiments demonstrating only that synaptic strength depresses to a low steady state level do not guarantee exhaustion, especially of the slow-releasing subdivision (e.g., Figure 3 of Mahfooz et al., 2016). Instead, we verify RRP exhaustion by inducing abrupt jumps to a higher frequency, and include trials where the extracellular Ca^{2+} level is elevated (Wesseling and Lo, 2002; Garcia-Perez and Wesseling, 2008; Mahfooz et al., 2016). In both cases, the absence of an increase in the amount of release is interpreted as evidence that the RRP is exhausted. For the frequency jump experiments, we verify that the axons can follow at the higher frequencies with matched controls after preventing RRP exhaustion by lowering the extracellular Ca^{2+}.

Note that the frequency of stimulation required for exhausting the RRP depends very much on the type of synapse, and factors that influence probability of release, such as extracellular Ca^{2+}, and must be determined on a case by case basis. For example, 20 Hz was sufficient at Schaffer collateral synapses (Garcia-Perez

and Wesseling, 2008), but even 100 Hz was not enough at calyces of Held (Mahfooz et al., 2016).

7. RESOLVING LIMITS WITH TRAINS OF ACTION POTENTIALS

Although the experiments referenced above showed that vesicle recruitment to the RRP is accelerated by Ca^{2+}, they did not resolve the extent of the acceleration. That is, in our hands, the osmotic shock technique is limited to rest intervals lasting > 500 ms, and so could have failed to detect acceleration driven by residual Ca^{2+} that was cleared from presynaptic terminals more quickly. This was a real concern in 1998 because residual Ca^{2+} was thought to be cleared in hundreds of ms (Wu and Saggau, 1994).

To address this, we analyzed the rate of transmitter release at times when the RRP was maintained in a near-empty steady state by ongoing stimulation with action potentials. We reasoned that ongoing transmitter release while the RRP is maintained in such a state would necessarily equal recruitment because, otherwise, the RRP would replenish during ongoing stimulation. We could then calculate the minuscule fraction of the RRP that was replenished during the short intervals between action potentials simply by dividing the average amount of release after individual action potentials by the size of the RRP when completely full. The result could be extrapolated to predict the full time course of RRP replenishment during long rest intervals, and the prediction could be compared to actual measurements. A mismatch between prediction and measurement would suggest that a component of the Ca^{2+}-dependent acceleration dissipates too quickly to influence the time course of RRP replenishment during subsequent periods of rest.

We did not find any such mismatch for Schaffer collateral synapses beyond the amount already expected from the osmotic shock experiments, indicating that the osmotic shock technique is a reliable tool for measuring the full extent of Ca^{2+}-dependent acceleration of vesicle recruitment to the RRP, at least at hippocampal synapses (Wesseling and Lo, 2002). And, later experiments showed that residual Ca^{2+} is cleared in multiple phases, with a slow component taking tens of seconds in Schaffer collaterals that may be the component that modulates the timing of vesicle recruitment (Brager et al., 2003; Garcia-Perez and Wesseling, 2008).

8. 10-FOLD MISMATCH AT CALYX OF HELD

We obtained a strikingly different result at calyces of Held, where we found a > 10-fold mismatch between prediction and measurement (Mahfooz et al., 2016). We interpret the result as indicating that the effect of activity on the recruitment mechanism reverses much more quickly at calyces of Held. If so, the widely reported observation that RRP replenishment follows a double exponential function after depleting the RRP a single time at calyces of Held does not necessarily indicate that some RRP subdivisions are replenished more quickly than others. Instead, the time course of replenishment is almost always predicted to be closely approximated by a double exponential function when the timing of recruitment quickly decelerates during rest intervals, even when all subdivisions are replenished at the same rate. The mathematical equation for this is:

$$RRP(t) = 1 - e^{-\int \alpha(t)} \quad (1)$$

where $RRP(t)$ is RRP fullness, and $\alpha(t)$ is the unitary rate of recruitment to all subdivisions over time (Wesseling and Lo, 2002; Hosoi et al., 2007; Mahfooz et al., 2016); a unitary rate plays the same role as a rate constant or rate coefficient in standard chemical kinetics, with the difference being that the value of a unitary rate can vary over time.

The conclusion that the effect of activity reverses quickly at calyces of Held is consistent with a role for residual Ca^{2+}, which is thought to be cleared much more quickly at calyces of Held compared to Schaffer collateral synapses (Hosoi et al., 2007; Garcia-Perez and Wesseling, 2008). However, unlike for hippocampal synapses, we have not yet devised a method for confirming that Ca^{2+} is indeed the intermediary. Intriguingly, conceptually similar experiments at ribbon synapses within cone photoreceptors in the retina suggest a similarly large mismatch between the timing of recruitment during ongoing stimulation and during subsequent rest intervals (Thoreson et al., 2016).

Notably, the double exponential time course that is characteristic of RRP replenishment after the induction of supply-rate depression at hippocampal synapses is caused by a completely different type of mechanism likely involving depletion of reserve stores, and does not involve Ca^{2+} (Stevens and Wesseling, 1999b; Gabriel et al., 2011). Supply-rate depression can be easily isolated from residual Ca^{2+}-dependent mechanisms because it is not induced until after exocytosis of the equivalent contents of several RRPs, which takes > 6 s at room temperature when the frequency of stimulation is maximal (Garcia-Perez et al., 2008).

9. CAVEATS RELATED TO ESTIMATING RRP CAPACITY

A variety of procedures have been employed for extracting information about RRP size from synaptic responses evoked by trains of presynaptic action potentials (Wesseling and Lo, 2002; Neher, 2015; Thanawala and Regehr, 2016; Thoreson et al., 2016). In our case, correct estimates were critical for estimating the timing of recruitment during ongoing stimulation. We avoided procedures that are based on the premise that all readily releasable vesicles undergo exocytosis with the same probability following individual action potentials because the premise is not compatible with the concept that RRPs contain both fast- and slow-releasing subdivisions, and can lead to underestimates of the true size when the slow subdivision is large. This was important for our analysis because such methods would have produced order of magnitude sized overestimates of the timing of vesicle recruitment in some cases, at least for calyces of Held where the RRPs in some preparations contained slow-releasing

subdivisions that were almost 10-fold greater than the fast-releasing subdivision (Figure 9 of Mahfooz et al., 2016).

We avoided the premise by first summing up the amount of release during trains of stimulation that fully exhaust the RRP, and then subtracting the fraction of the sum generated by transmitter that was newly recruited during stimulation (Wesseling and Lo, 2002; Mahfooz et al., 2016). The procedure does not depend on assumptions about the distribution of release probabilities among readily releasable vesicles, but does depend on assumptions about mechanisms underlying recruitment that are not yet fully resolved. An evaluation of the full range of possibilities, however, indicated that even extreme assumptions do not alter the estimates by more than 25 % (Figure 7 of Mahfooz et al., 2016), which is not enough to alter the conclusion that recruitment at the calyx of Held is much faster during ongoing stimulation than during subsequent periods of rest.

Even the small range of uncertainty in estimates of RRP size could be largely eliminated by incorporating the premise that RRPs have a fixed capacity for storing vesicles (Mahfooz et al., 2016). The premise is supported by: (1) evidence that intracellular Ca^{2+} does not alter the number of readily releasable vesicles at resting synapses, when the RRP would be full, despite accelerating recruitment of new vesicles when partially empty (Stevens and Wesseling, 1999a); and, (2) a mathematical analysis that found straightforward relationships between the results of frequency jump experiments where the RRP was first driven to a variety of partially full steady state levels using submaximal frequencies for stimulation followed by abrupt jumps to a higher frequency that then exhausted the RRP (Mahfooz et al., 2016; Raja et al., 2019). Experiments demonstrating that RRP size at resting synapses was not altered when synaptic strength was increased 2-fold by increasing extracellular Ca^{2+} ruled out specific alternatives that have been proposed (Wesseling and Lo, 2002; Mahfooz et al., 2016). Thoreson et al. (2016) concluded that RRPs also have a fixed capacity at ribbon type synapses in cone photoreceptors using a largely independent line of reasoning.

The premise of a fixed capacity is particularly relevant because it matches the physical interpretation that the RRP is made up of vesicles that are docked to a stable collection of release sites (e.g., **Figure 3**).

10. PARADIGM LEVEL CONCERNS

The evidence for a fixed capacity is additionally relevant because it addresses concerns about the utility of the very concept of an RRP for understanding the physiology of synaptic transmission (see Pan and Zucker, 2009). For example, endocytosis of spent vesicular membrane occurs by a variety of modes, the fastest of which is termed *kiss-and-run* exo/endocytosis, and may occur in milliseconds (Alabi and Tsien, 2013). At least one study has concluded that vesicles undergoing kiss-and-run can be fully recycled more rapidly than recruitment to the RRP (Pyle et al., 2000). If so, the rapidly recycled vesicles could, in principle, contribute multiple quanta of neurotransmitter to estimates of RRP size even though only one of the quanta would be truly readily-releasable at any given time. However, such a mechanism does not seem to be consistent with the evidence that RRP capacity is not affected by extracellular or intracellular Ca^{2+} because kiss-and-run is modulated by both (Harata et al., 2006; Richards, 2010; Leitz and Kavalali, 2011). Additional observations arguing against a role for kiss-and-run in estimates of RRP size at Schaffer collateral synapses and calyces of Held include evidence that: (1) RRP size is not influenced by the time taken to exhaust the RRP over a large range, extending from 30–1000 ms at calyces of Held (Chen et al., 2015; Mahfooz et al., 2016), whereas very fast recycling would be expected to have more of an impact in experiments where the time taken is longer; (2) the amount of kiss-and-run is less at synapses with higher probability of release, but increasing the probability by deleting synaptophysin family proteins did not alter estimates of RRP capacity (Raja et al., 2019; see Gordon et al., 2011 and Kwon and Chapman, 2011 for evidence that endocytosis is slower in synaptophysin knockouts); and, (3) RRP capacity is consistently similar or less, than the number of docked vesicles measured with morphological techniques (Schikorski and Stevens, 2001; Neher, 2017; see von Gersdorff et al., 1996 for a different result at ribbon synapses). In any case, the maximum speed of vesicle recycling after kiss-and-run continues to be debated, but most estimates seem to be slower or equivalent to recruitment to the RRP (Aravanis et al., 2003; Richards, 2010; Alabi and Tsien, 2013).

11. MOLECULAR EFFECTORS

We have not made much progress toward identifying effectors of residual Ca^{2+} that accelerate vesicle recruitment to the RRP. Part of the difficulty is that the rate-limiting mechanism in recruitment has not yet been identified. Still viable possibilities include: locomotion of vesicles to docking sites in the active zone; a post-docking priming step; or even post-exocytosis reconstitution of release sites (Neher, 2010). At present, it seems that kiss-and-run exo/endocytosis is probably not involved, however, because Ca^{2+} is thought to block rather than accelerate this phenomenon (Harata et al., 2006; Richards, 2010; Leitz and Kavalali, 2011). In any case, we can at least rule out our initial hypothesis that synapsin proteins are involved (Gabriel et al., 2011; see also Gaffield and Betz, 2007).

Liu et al. (2014) reported a Ca^{2+}-dependent component of basal recruitment that was absent in synaptotagmin 7 knockout synapses. The result suggests that synaptotagmin 7 may be involved, but a wide range of other functions for synaptotagmin 7 have been reported by other groups (Bacaj et al., 2013; Jackman et al., 2016; Chen et al., 2017). Notably, although Liu et al. (2014) did use osmotic shocks to monitor RRP replenishment, the experimental design differed from our own in key regards including: enough basal Ca^{2+} to activate the Ca^{2+}-dependent component of recruitment; and hypertonic challenges lasting 10 s, vs. only 3 or 4 in our case, suggesting that the shocks were weaker.

Other groups have concluded that Ca^{2+} accelerates vesicle trafficking at calyces of Held via calmodulin and Munc 13-1 (reviewed in Ritzau-Jost et al., 2018). However, our

understanding has been that the calmodulin pathway is thought to accelerate transfer of vesicles from the slow- to fast-releasing subdivision of the RRP, which would be downstream of vesicle recruitment to the RRP as a whole, and therefore a different category of mechanism (Sakaba and Neher, 2001; Hosoi et al., 2007; but see Van Hook et al., 2014); some other explanation will be required for key results if it turns out that vesicles are recruited to slow- and fast-releasing subdivisions in parallel. In any case, it seems that the Munc 13-1^{W464R} mutation thought to disrupt the calmodulin pathway did not eliminate the mismatch between the timing of vesicle recruitment during ongoing stimulation and during subsequent rest intervals (Lipstein et al., 2013). The steady state response at mutant calyces of Held was not altered (their Figure 7C), but recovery during rest intervals was slower (their Figure 5D3), suggesting that the mutation actually made the mismatch greater. These results support the idea that calmodulin acts downstream of recruitment to the RRP, at least at calyces of Held. If so, the mechanism could have an important impact during light or moderate use that might be superseded as rate-limiting during heavy use by the upstream step whereby vesicles are initially recruited to the RRP as a whole. Myosine light chain kinase has also been implicated in regulating short-term plasticity during light and moderate use without affecting release as much during heavy use (Srinivasan et al., 2008; González-Forero et al., 2012).

12. SUMMARY

Multiple concerns have been raised that could complicate the interpretation of some experiments designed to measure activity and residual Ca^{2+}-dependent acceleration of the mechanism by which vesicles are recruited to the RRP. However, we continue to be confident that residual Ca^{2+} does accelerate the recruitment mechanism, at least at hippocampal synapses, because our own experiments in this area were designed to avoid the underlying caveats. A key methodological point is that multiple aspects of our experimental design depended critically on stimulation protocols that are sufficiently intense to nearly completely exhaust both fast- and slow-releasing subdivisions of the RRP, and that control experiments designed to confirm that both are truly exhausted need to be more sophisticated than simply observing that stimulation drives neurotransmitter release to a low steady state. A second point is that the calmodulin/Munc 13 pathway implicated in modulating vesicle trafficking seems to operate downstream of vesicle recruitment to the RRP, and that the molecules responsible for accelerating recruitment at the upstream step whereby vesicles are recruited to the RRP as a whole remain to be determined. The list of presynaptic protein families with no known function remains long, so there is no shortage of candidates.

AUTHOR CONTRIBUTIONS

The author confirms being the sole contributor of this work and has approved it for publication.

FUNDING

Funding was obtained from the Spanish Ministry of Science (SAF2013-48983R and BFU2016-80918R), a Severo Ochoa Center for Excellence award to the Instituto de Neurociencia de Alicante, and the Consejo Superior de Investigaciones Cientificas of Spain.

ACKNOWLEDGMENTS

I thank Drs. Alexander Walter, Ana Gomis, and Huisheng Liu for insightful suggestions.

REFERENCES

Adler, E. M., Augustine, G. J., Duffy, S. N., and Charlton, M. P. (1991). Alien intracellular calcium chelators attenuate neurotransmitter release at the squid giant synapse. *J. Neurosci.* 11, 1496–1507. doi: 10.1523/JNEUROSCI.11-06-01496.1991

Alabi, A. A., and Tsien, R. W. (2013). Perspectives on kiss-and-run: role in exocytosis, endocytosis, and neurotransmission. *Ann. Rev. Physiol.* 75, 393–422. doi: 10.1146/annurev-physiol-020911-153305

Aravanis, A. M., Pyle, J. L., and Tsien, R. W. (2003). Single synaptic vesicles fusing transiently and successively without loss of identity. *Nature* 423, 643–647. doi: 10.1038/nature01686

Babai, N., Bartoletti, T. M., and Thoreson, W. B. (2010). Calcium regulates vesicle replenishment at the cone ribbon synapse. *J. Neurosci.* 30, 15866–15877. doi: 10.1523/JNEUROSCI.2891-10.2010

Bacaj, T., Wu, D., Yang, X., Morishita, W., Zhou, P., Xu, W., et al. (2013). Synaptotagmin-1 and synaptotagmin-7 trigger synchronous and asynchronous phases of neurotransmitter release. *Neuron* 80, 947–959. doi: 10.1016/j.neuron.2013.10.026

Bekkers, J. M., and Stevens, C. F. (1991). Excitatory and inhibitory autaptic currents in isolated hippocampal neurons maintained in cell culture. *Proc. Natl. Acad. Sci. U.S.A.* 88, 7834–7838.

Brager, D. H., Cai, X., and Thompson, S. M. (2003). Activity-dependent activation of presynaptic protein kinase C mediates post-tetanic potentiation. *Nat. Neurosci.* 6, 551–552. doi: 10.1038/nn1067

Chen, C., Blitz, D. M., and Regehr, W. G. (2002). Contributions of receptor desensitization and saturation to plasticity at the retinogeniculate synapse. *Neuron* 33, 779–788. doi: 10.1016/S0896-6273(02)00611-6

Chen, C., Satterfield, R., Young, S. M., and Jonas, P. (2017). Triple function of synaptotagmin 7 ensures efficiency of high-frequency transmission at central GABAergic synapses. *Cell Reports* 21, 2082–2089. doi: 10.1016/j.celrep.2017.10.122

Chen, Z., Das, B., Nakamura, Y., DiGregorio, D. a., and Young, S. M. (2015). Ca2+ channel to synaptic vesicle distance accounts for the readily releasable pool kinetics at a functionally mature auditory synapse. *J. Neurosci.* 35, 2083–2100. doi: 10.1523/JNEUROSCI.2753-14.2015

Dittman, J. S., and Regehr, W. G. (1998). Calcium dependence and recovery kinetics of presynaptic depression at the climbing fiber to Purkinje cell synapse. *J. Neurosci.* 18, 6147–6162.

Dobrunz, L. E., and Stevens, C. F. (1997). Heterogeneity of release probability, facilitation, and depletion at central synapses. *Neuron* 18, 995–1008.

Furshpan, E. J., MacLeish, P. R., O'Lague, P. H., and Potter, D. D. (1976). Chemical transmission between rat sympathetic neurons and cardiac myocytes developing in microcultures: evidence for cholinergic, adrenergic, and dual-function neurons. *PNAS* 73, 4225–4229.

Gabriel, T., García-Pérez, E., Mahfooz, K., Goñi, J., Martínez-Turrillas, R., Pérez-Otaño, I., et al. (2011). A new kinetic framework for synaptic vesicle trafficking tested in synapsin knock-outs. *J. Neurosci.* 31, 11563–11577. doi: 10.1523/JNEUROSCI.1447-11.2011

Gaffield, M. a., and Betz, W. J. (2007). Synaptic vesicle mobility in mouse motor nerve terminals with and without synapsin. *J. Neurosci.* 27, 13691–13700. doi: 10.1523/JNEUROSCI.3910-07.2007

Garcia-Perez, E., Lo, D. C., and Wesseling, J. F. (2008). Kinetic isolation of a slowly recovering component of short-term depression during exhaustive use at excitatory hippocampal synapses. *J. Neurophysiol.* 100, 781–95. doi: 10.1152/jn.90429.2008

Garcia-Perez, E., and Wesseling, J. F. (2008). Augmentation controls the fast rebound from depression at excitatory hippocampal synapses. *J. Neurophysiol.* 99, 1770–1786. doi: 10.1152/jn.01348.2007

Gomis, A., Burrone, J., and Lagnado, L. (1999). Two actions of calcium regulate the supply of releasable vesicles at the ribbon synapse of retinal bipolar cells. *J. Neurosci.* 19, 6309–6317.

González-Forero, D., Montero, F., García-Morales, V., Domínguez, G., Gómez-Pérez, L., García-Verdugo, J. M., et al. (2012). Endogenous Rho-kinase signaling maintains synaptic strength by stabilizing the size of the readily releasable pool of synaptic vesicles. *J. Neurosci.* 32, 68–84. doi: 10.1523/JNEUROSCI.3215-11.2012

Gordon, S. L., Leube, R. E., and Cousin, M. A. (2011). Synaptophysin is required for synaptobrevin retrieval during synaptic vesicle endocytosis. *J. Neurosci.* 31, 14032–14036. doi: 10.1523/JNEUROSCI.3162-11.2011

Harata, N. C., Choi, S., Pyle, J. L., Aravanis, A. M., and Tsien, R. W. (2006). Frequency-dependent kinetics and prevalence of kiss-and-run and reuse at hippocampal synapses studied with novel quenching methods. *Neuron* 49, 243–256. doi: 10.1016/j.neuron.2005.12.018

Hosoi, N., Sakaba, T., and Neher, E. (2007). Quantitative analysis of calcium-dependent vesicle recruitment and its functional role at the calyx of Held synapse. *J. Neurosci.* 27, 14286–14298. doi: 10.1523/JNEUROSCI.4122-07.2007

Jackman, S. L., Turecek, J., Belinsky, J. E., and Regehr, W. G. (2016). The calcium sensor synaptotagmin 7 is required for synaptic facilitation. *Nature* 529, 88–91. doi: 10.1038/nature16507

Johnson, S. L., Olt, J., Cho, S., von Gersdorff, H., and Marcotti, W. (2017). The coupling between Ca2+ channels and the exocytotic Ca2+ sensor at hair cell ribbon synapses varies tonotopically along the mature cochlea. *J. Neurosci.* 37, 2471–2484. doi: 10.1523/JNEUROSCI.2867-16.2017

Kusano, K., and Landau, E. M. (1975). Depression and recovery of transmission at the squid giant synapse. *J. Physiol.* 245, 13–32.

Kwon, S. E., and Chapman, E. R. (2011). Synaptophysin regulates the kinetics of synaptic vesicle endocytosis in central neurons. *Neuron* 70, 847–854. doi: 10.1016/j.neuron.2011.04.001

Lee, J. S., Ho, W.-K., and Lee, S.-H. (2010). Post-tetanic increase in the fast-releasing synaptic vesicle pool at the expense of the slowly releasing pool. *J. Gen. Physiol.* 136, 259–272. doi: 10.1085/jgp.201010437

Lee, J. S., Ho, W.-K., Neher, E., and Lee, S.-H. (2013). Superpriming of synaptic vesicles after their recruitment to the readily releasable pool. *PNAS* 110, 15079–15084. doi: 10.1073/pnas.1314427110

Leitz, J., and Kavalali, E. T. (2011). Ca(2+) influx slows single synaptic vesicle endocytosis. *J. Neurosci.* 31, 16318–16326. doi: 10.1523/JNEUROSCI.3358-11.2011

Lipstein, N., Sakaba, T., Cooper, B. H., Lin, K.-H., Strenzke, N., Ashery, U., et al. (2013). Dynamic control of synaptic vesicle replenishment and short-term plasticity by Ca(2+)-calmodulin-Munc13-1 signaling. *Neuron* 79, 82–96. doi: 10.1016/j.neuron.2013.05.011

Liu, H., Bai, H., Hui, E., Yang, L., Evans, C. S., Wang, Z., et al. (2014). Synaptotagmin 7 functions as a Ca2+-sensor for synaptic vesicle replenishment. *eLife* 3:e01524. doi: 10.7554/eLife.01524

Magleby, K. L. (1979). Facilitation, augmentation, and potentiation of transmitter release. *Progress Brain Res.* 49, 175–182.

Mahfooz, K., Singh, M., Renden, R., and Wesseling, J. F. (2016). A well-defined readily releasable pool with fixed capacity for storing vesicles at calyx of held. *PLoS Comput. Biol.* 12, 1–39. doi: 10.1371/journal.pcbi.1004855

Miki, T., Malagon, G., Pulido, C., Llano, I., Neher, E., and Marty, A. (2016). Actin- and Myosin-dependent vesicle loading of presynaptic docking sites prior to exocytosis. *Neuron* 91, 808–823. doi: 10.1016/j.neuron.2016.07.033

Moulder, K. L., and Mennerick, S. (2005). Reluctant vesicles contribute to the total readily releasable pool in glutamatergic hippocampal neurons. *J. Neurosci.* 25, 3842–3850. doi: 10.1523/JNEUROSCI.5231-04.2005

Nanou, E., and Catterall, W. A. (2018). Calcium channels, synaptic plasticity, and neuropsychiatric disease. *Neuron* 98, 466–481. doi: 10.1016/j.neuron.2018.03.017

Neher, E. (1998). Vesicle pools and Ca2+ microdomains: new tools for understanding their roles in neurotransmitter release. *Neuron* 20, 389–399.

Neher, E. (2010). What is rate-limiting during sustained synaptic activity: vesicle supply or the availability of release sites. *Front. Synapt. Neurosci.* 2:144. doi: 10.3389/fnsyn.2010.00144

Neher, E. (2015). Merits and limitations of vesicle pool models in view of heterogeneous populations of synaptic vesicles. *Neuron* 87, 1131–1142. doi: 10.1016/j.neuron.2015.08.038

Neher, E. (2017). Some subtle lessons from the calyx of held synapse. *Biophys. J.* 112, 215–223. doi: 10.1016/j.bpj.2016.12.017

Otis, T., Zhang, S., and Trussell, L. O. (1996). Direct measurement of AMPA receptor desensitization induced by glutamatergic synaptic transmission. *J. Neurosci.* 16, 7496–7504.

Pan, B., and Zucker, R. S. (2009). A general model of synaptic transmission and short-term plasticity. *Neuron* 62, 539–554. doi: 10.1016/j.neuron.2009.03.025

Pyle, J. L., Kavalali, E. T., Piedras-Rentería, E. S., and Tsien, R. W. (2000). Rapid reuse of readily releasable pool vesicles at hippocampal synapses. *Neuron* 28, 221–231. doi: 10.1016/S0896-6273(00)00098-2

Raja, M. K., Preobraschenski, J., Del Olmo-Cabrera, S., Martinez-Turrillas, R., Jahn, R., Perez-Otano, I., et al. (2019). Elevated synaptic vesicle release probability in synaptophysin/gyrin family quadruple knockouts. *eLife* 8:e40744. doi: 10.7554/eLife.40744

Regehr, W. G. (2012). Short-term presynaptic plasticity. *Cold Spring Harbor Perspect. Biol.* 4:a005702. doi: 10.1101/cshperspect.a005702

Richards, D. A. (2010). Regulation of exocytic mode in hippocampal neurons by intra-bouton calcium concentration. *J. Physiol.* 588(Pt 24):4927–4936. doi: 10.1113/jphysiol.2010.197509

Ritzau-Jost, A., Jablonski, L., Viotti, J., Lipstein, N., Eilers, J., and Hallermann, S. (2018). Apparent calcium dependence of vesicle recruitment. *J. Physiol.* 596, 4693–4707. doi: 10.1113/JP275911

Rosenmund, C., and Stevens, C. F. (1996). Definition of the readily releasable pool of vesicles at hippocampal synapses. *Neuron* 16, 1197–1207.

Sakaba, T., and Neher, E. (2001). Calmodulin mediates rapid recruitment of fast-releasing synaptic vesicles at a calyx-type synapse. *Neuron* 32, 1119–1131. doi: 10.1016/S0896-6273(01)00543-8

Schikorski, T., and Stevens, C. F. (2001). Morphological correlates of functionally defined synaptic vesicle populations. *Nat. Neurosci.* 4, 391–395. doi: 10.1038/86042

Schotten, S., Meijer, M., Walter, A. M., Huson, V., Mamer, L., Kalogreades, L., et al. (2015). Additive effects on the energy barrier for synaptic vesicle fusion cause supralinear effects on the vesicle fusion rate. *eLife* 4:e05531. doi: 10.7554/eLife.05531

Srinivasan, G., Kim, J. H., and von Gersdorff, H. (2008). The pool of fast releasing vesicles is augmented by myosin light chain kinase inhibition at the calyx of Held synapse. *J. Neurophysiol.* 99, 1810–1824. doi: 10.1152/jn.00949.2007

Stevens, C. F., and Tsujimoto, T. (1995). Estimates for the pool size of releasable quanta at a single central synapse and for the time required to refill the pool. *Proc. Natl. Acad. Sci. U.S.A.* 92, 846–849.

Stevens, C. F., and Wesseling, J. F. (1998). Activity-dependent modulation of the rate at which synaptic vesicles become available to undergo exocytosis. *Neuron* 21, 415–424.

Stevens, C. F., and Wesseling, J. F. (1999a). Augmentation is a potentiation of the exocytotic process. *Neuron* 22, 139–146.

Stevens, C. F., and Wesseling, J. F. (1999b). Identification of a novel process limiting the rate of synaptic vesicle cycling at hippocampal synapses. *Neuron* 24, 1017–1028.

Stevens, C. F., and Williams, J. H. (2007). Discharge of the readily releasable pool with action potentials at hippocampal synapses. *J. Neurophysiol.* 98, 3221–3229. doi: 10.1152/jn.00857.2007

Taschenberger, H., Woehler, A., and Neher, E. (2016). Superpriming of synaptic vesicles as a common basis for intersynapse variability and modulation of synaptic strength. *PNAS* 113, E4548–E4557. doi: 10.1073/pnas.1606383113

Thanawala, M. S., and Regehr, W. G. (2016). Determining synaptic parameters using high-frequency activation. *J. Neurosci. Methods* 264, 136–152. doi: 10.1016/j.jneumeth.2016.02.021

Thoreson, W. B., Van Hook, M. J., Parmelee, C., and Curto, C. (2016). Modeling and measurement of vesicle pools at the cone ribbon synapse: Changes in release probability are solely responsible for voltage-dependent changes in release. *Synapse* 70, 1–14. doi: 10.1002/syn.21871

Trussell, L. O., Zhang, S., and Raman, I. M. (1993). Desensitization of AMPA receptors upon multiquantal neurotransmitter release. *Neuron* 10, 1185–1196.

Van Hook, M. J., Parmelee, C. M., Chen, M., Cork, K. M., Curto, C., and Thoreson, W. B. (2014). Calmodulin enhances ribbon replenishment and shapes filtering of synaptic transmission by cone photoreceptors. *J. Gen. Physiol.* 144, 357–378. doi: 10.1085/jgp.201411229

von Gersdorff, H., Sakaba, T., Berglund, K., and Tachibana, M. (1998). Submillisecond kinetics of glutamate release from a sensory synapse. *Neuron* 21, 1177–1188.

von Gersdorff, H., Vardi, E., Matthews, G., and Sterling, P. (1996). Evidence that vesicles on the synaptic ribbon of retinal bipolar neurons can be rapidly released. *Neuron* 16, 1221–1227.

Wang, L.-Y., and Kaczmarek, L. K. (1998). High-frequency firing helps replenish the readily releasable pool of synaptic vesicles. *Nature* 394, 384–388.

Wang, Y., and Manis, P. B. (2008). Short-term synaptic depression and recovery at the mature mammalian endbulb of Held synapse in mice. *J. Neurophysiol.* 100, 1255–1264. doi: 10.1152/jn.90715.2008

Wesseling, J. F., and Lo, D. C. (2002). Limit on the role of activity in controlling the release-ready supply of synaptic vesicles. *J. Neurosci.* 22, 9708–9720. doi: 10.1523/JNEUROSCI.22-22-09708.2002

Wu, L. G., and Borst, J. G. (1999). The reduced release probability of releasable vesicles during recovery from short-term synaptic depression. *Neuron* 23, 821–832.

Wu, L. G., and Saggau, P. (1994). Presynaptic calcium is increased during normal synaptic transmission and paired-pulse facilitation, but not in long-term potentiation in area CA1 of hippocampus. *J. Neurosci.* 14, 645–654.

Conflict of Interest: The author declares that the research was conducted in the absence of any commercial or financial relationships that could be construed as a potential conflict of interest.

frontiers in Synaptic Neuroscience

ORIGINAL RESEARCH
published: 22 November 2019
doi: 10.3389/fnsyn.2019.00031

Optimizing Optogenetic Activation of Purkinje Cell Axons to Investigate the Purkinje Cell – DCN Synapse

Kim M. Gruver[1,2] *and Alanna J. Watt*[1]*

[1] Department of Biology, McGill University, Montreal, QC, Canada, [2] Integrated Program in Neuroscience, McGill University, Montreal, QC, Canada

Optogenetics is a state-of-the-art tool for interrogating neural circuits. In the cerebellum, Purkinje cells serve as the sole output of the cerebellar cortex where they synapse on neurons in the deep cerebellar nuclei (DCN). To investigate the properties of this synaptic connection, we sought to elicit time-locked single action potentials from Purkinje cell axons. Using optical stimulation of channelrhodopsin-2 (ChR2)-expressing Purkinje cells combined with patch-clamp recordings of Purkinje cells and DCN neurons in acute cerebellar slices, we determine the photostimulation parameters required to elicit single time-locked action potentials from Purkinje cell axons. We show that axons require longer light pulses than somata do to elicit single action potentials and that Purkinje cell axons are also more susceptible to light perturbations. We then demonstrate that these empirically determined photostimulation parameters elicit time-locked synaptic currents from postsynaptic cells in the DCN. Our results highlight the importance of optimizing optogenetic stimulation conditions to interrogate synaptic connections.

Keywords: optogenetics, electrophysiology, Purkinje cells, cerebellum, action potentials, deep cerebellar nuclei, axon

OPEN ACCESS

Edited by:
Mary B. Kennedy, California Institute of Technology, United States

Reviewed by:
Taro Ishikawa, The Jikei University School of Medicine, Japan
Giuseppe Sciamanna, University of Rome Tor Vergata, Italy

***Correspondence:**
Alanna J. Watt
alanna.watt@mcgill.ca

Received: *18 April 2019*
Accepted: *04 November 2019*
Published: *22 November 2019*

Citation:
Gruver KM and Watt AJ (2019) Optimizing Optogenetic Activation of Purkinje Cell Axons to Investigate the Purkinje Cell – DCN Synapse. Front. Synaptic Neurosci. 11:31. doi: 10.3389/fnsyn.2019.00031

INTRODUCTION

Optogenetics is a powerful tool that has transformed the investigation of neural circuits. The ability to genetically target and optically activate distinct cell populations of presynaptic neurons allows for functional circuit mapping which has refined our understanding of the brain (Huber et al., 2008; Cruikshank et al., 2010; Pfeffer et al., 2013). Genetically targeted opsins distribute throughout cell membranes and can be detected in all cellular compartments, including the soma, dendrites, and axons (Nagel et al., 2003; Boyden et al., 2005; Lewis et al., 2009). Light pulses can thus be focused onto subcellular compartments to elicit neuronal activity that originates locally (Petreanu et al., 2007; Jackman et al., 2014). For example, targeting axons with focal optical stimulation can be an effective means by which to probe connectivity, especially in acute slices where presynaptic axons are preserved even if their soma is lesioned. However, this approach raises the question of whether focal stimulation of a neuron's axon requires different conditions than focal stimulation of its soma. This is important to address given that there are several recent reports showing that focal axonal stimulation with inhibitory optogenetic tools paradoxically produces excitation rather than inhibition (Mahn et al., 2016; Messier et al., 2018). These studies highlight the importance of empirically testing conditions for optogenetic experiments.

Cerebellar Purkinje cells carry information from the cerebellar cortex via synapses made onto neurons in the deep cerebellar nuclei (DCN) (Palay and Chan-Palay, 1974; Person and Raman, 2012). Previous studies have demonstrated that this connection can be investigated with Channelrhodopsin-2 (ChR2), since the synaptic responses elicited optogenetically resemble those elicited from extracellular electrical stimulation (Jackman et al., 2014). However, the parameters to elicit action potentials optogenetically can differ with different equipment, for example with a LED versus a laser. To study the synaptic properties of the Purkinje cell – DCN neuron connection optogenetically, we first need to understand how to elicit well-timed single action potentials reliably from Purkinje cell axonal stimulation. Here, we determine the experimental conditions necessary to reliably activate Purkinje cells using a patterned illuminator with a LED light source. We find that focal illumination of Purkinje cell axons requires longer light pulses than somata, and that axons are more susceptible to perturbations from ambient light. Finally, we show that these empirically determined conditions enable us to elicit well-timed synaptic responses in DCN neurons.

MATERIALS AND METHODS

Animals

Transgenic mice hemizygous for Purkinje cell-specific Cre [strain B6.Cg-Tg(Pcp2-cre)3555Jdhu/J; stock number: 010536; *PCP2-Cre*] and mice homozygous for Channelrhodopsin-2/H134R fused with enhanced YFP [strain: B6;129S-Gt(ROSA)26Sor$^{tm32(CAG-COP4*H134R/EYFP)Hze}$/J; stock number 012569; *Ai32*], or ChR2(H134R)-EYFP, were acquired from The Jackson Laboratory (Bar Harbor, ME, United States) and bred to produce hemizygous *PCP2-Cre/Ai32* mice expressing modified ChR2 in Purkinje cells (Jackman et al., 2014). All animal procedures were approved by the McGill Animal Care Committee, in accordance with guidelines established by the Canadian Council on Animal Care.

Acute Slice Preparation

Slices were prepared as described previously (Jayabal et al., 2017; Ady et al., 2018). Male and female mice (P20 to P31) were deeply anesthetized with isoflurane and decapitated. Brains were removed and immediately placed in ice-cold artificial cerebrospinal fluid (ACSF; in mM: 125 NaCl, 2.5 KCl, 2 $CaCl_2$, 1 $MgCl_2$, 1.25 NaH_2PO_4, 25 $NaHCO_3$, and 25 glucose, bubbled with 95% O_2–5% CO_2 to maintain pH at 7.3; osmolality ∼317 mOsm) for Purkinje cell experiments, or partial sucrose replacement slicing solution (in mM: 50 NaCl, 2.5 KCl, 0.5 $CaCl_2$, 10 $MgCl_2$, 1.25 NaH_2PO_4, 25 $NaHCO_3$, 25 glucose, and 111 sucrose bubbled with 95% O2–5% CO_2 to maintain pH at 7.3; osmolality ∼317 mOsm) for DCN experiments. Chemicals were purchased from Sigma-Aldrich (Oakville, ON, Canada) and/or Fisher Scientific (for $CaCl_2$ and $MgCl_2$; Toronto, ON, Canada). Parasagittal slices of cerebellar vermis and paravermis were cut using a Leica VT 1000S vibrating blade microtome at a thickness of 200 μm. All slices were then incubated in ACSF at 37°C for 30–45 min, and subsequently stored at room temperature for up to 6 h. Slices were typically stored in a chamber that minimized light exposure. However, for ambient light experiments, slices were stored in ACSF in a clear glass chamber in a laboratory with bright overhead lights, and were illuminated with a halogen lamp to visualize Purkinje cells in acute slices. In the "ambient light" condition, slices were exposed to a continuous spectrum of white background light.

Imaging

Slices were imaged with a custom two-photon microscope equipped with a Ti:Sapphire laser (MaiTai; Spectra Physics, Santa Clara, CA, United States) tuned to 890 nm and image stacks (1 μm z-step) were acquired with ScanImage running in MATLAB (Mathworks, Natick, MA, United States) (Pologruto et al., 2003). Maximal intensity projections of image stacks were generated in ImageJ (US National Institutes of Health[1]).

Electrophysiology

Borosilicate patch pipettes (2–9 MΩ) were pulled with a P-1000 puller (Sutter Instruments, Novato, CA, United States). For current-clamp experiments in Purkinje cells, the internal solution contained (in mM): 130 potassium gluconate, 0.5 EGTA, 10 HEPES, 4 Mg-ATP, 0.4 Na-GTP, 10 NaCl, 10 KCl, with 286 mOsm and pH 7.3 (adjusted with KOH). For voltage-clamp experiments in DCN neurons, the internal solution contained (in mM): 150 potassium gluconate, 3 KCl, 10 HEPES, 0.5 EGTA, 3 Mg-ATP, 0.5 GTP tris salt, 5 phosphocreatine-(di)tris, with 297 mOsm and pH 7.2 (adjusted with KOH). Recordings were acquired with a Multiclamp 700B amplifier (Molecular Devices, Sunnyvale, CA, United States) on a SliceScope Pro 3000 microscope (Scientifica, Uckfield, United Kingdom) from neurons in slices maintained at a temperature of 34°C ± 1°C and bathed with oxygenated ACSF. Purkinje cells whose resting membrane potential was > −40 mV were excluded from analysis. For voltage-clamp recordings in DCN neurons, cells were voltage-clamped to −60 mV, and R_{in} and resting membrane potential were monitored. Recordings in which the R_{in} changed more than 25% were excluded from analysis. Data acquisition and analyses were performed using custom IGOR Pro acquisition and data analysis software (Sjöström et al., 2001) (Wavemetrics, Portland, OR, United States).

Optical Stimulation

Slices expressing ChR2 were optically stimulated using a Polygon400E patterned spatial illuminator with a 470 nm LED light source (Mightex, Toronto, ON, Canada), through a 60X water-immersion objective (Olympus LUMPLFLN60XW, Tokyo, Japan). Visually identified regions of interest for photostimulation were delineated using PolyScan2 software (Mightex). Photostimulation was induced while patch-clamping the soma of either Purkinje cells or DCN neurons. We used a 40 × 40 μm blue square light pulse with an estimated focal plane power density of 100 mW/mm^2 for both axonal and somatic photostimulation, or in some cases, circular light pulses (∼20 μm diameter) were used for somatic stimulation.

[1]https://imagej.nih.gov/ij/

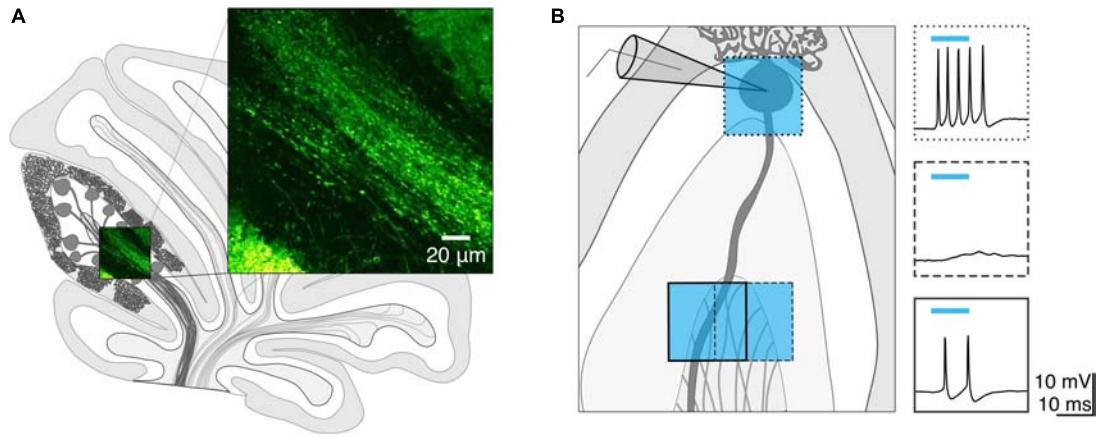

FIGURE 1 | Channelrhodopsin-2 expression in Purkinje cell axons. **(A)** Schematic of sagittal cerebellar slice. Inset is a maximal intensity projection of a two-photon stack showing ChR2(H134R)-EYFP expression (green) in axons in the white matter. **(B)** Left, schematic showing multiple photostimulation regions (blue squares) and somatic recording electrode. Right, representative current-clamp traces show optically evoked action potentials following somatic (box with dotted line outline) and white matter (dashed and solid line outline on boxes) stimulation locations. Shifting the photostimulation location ∼30 μm in the white matter of the cerebellum produced action potentials. Blue bars above traces indicate onset and duration of light pulse.

For axonal photostimulation during Purkinje cell experiments, the area illuminated was 120–200 μm from the Purkinje cell soma. This distance varied due to variation in the thickness of the granule cell layer, but was always in the white matter close to the recorded Purkinje cell. For axonal photostimulation during DCN experiments, the area illuminated was ∼200 μm from the DCN neuron soma, in the white matter adjacent to the DCN. Interstimulus intervals were 15 s for evoking action potentials from Purkinje cell somata or axons and 20 s for eliciting postsynaptic responses in the DCN.

Data Analysis

All electrophysiological data were analyzed using custom Igor Pro data analysis software (Watt et al., 2009). Action potential latency was measured as the time in ms from the onset of the light stimulus to the peak of the action potential. For inhibitory postsynaptic currents (IPSCs), the rise time was measured as the time between 20 – 80% of the peak. For Purkinje cell recordings, jitter was measured as the variability (represented as standard deviation, SD) in time from the beginning of the light pulse to the peak of the action potential. For DCN recordings, jitter in the onset of the postsynaptic response was measured as the variability (SD) in time to reach 20% of the peak IPSC.

Statistics

Mann–Whitney *U* tests were performed using JMP software (SAS, Carey, NC, United States) with the level of significance (α) set at $P < 0.05$. Data are reported as mean ± SEM. For all data, n = number of cells and N = number of mice.

RESULTS

We wondered whether focal photostimulation of Purkinje cells would result in differential effects depending on the targeted subcellular compartment. To address this, we first confirmed that ChR2 is expressed in Purkinje cell axons of ChR2(H134R)-EYFP mice. Consistent with what has been previously reported (Jackman et al., 2014), we observed robust ChR2 expression in Purkinje cell axons located in the white matter of the cerebellum (**Figure 1A**).

We next sought to test whether spatially targeted photostimulation of Purkinje cells can be reliably elicited in axons. While this has been demonstrated by others using short light pulses from a laser (Jackman et al., 2014), to our knowledge this has not been characterized from a LED light source. We made whole-cell current-clamp recordings from Purkinje cell somata and injected negative current until we hyperpolarized the cell to silence spontaneous action potentials. Using a spatial illuminator delivering 470 nm light from a LED, we applied a 40 × 40 μm square light pulse either to the soma or to the cerebellar white matter to stimulate axons and recorded antidromic action potentials. To elicit action potentials in the axon, we photostimulated in the white matter while monitoring the somatic recording for the presence of an elicited action potential(s). If no action potential was evoked in one location, we would then parametrically shift our photostimulation location (in 30–40 μm steps) until action potentials were evoked (**Figure 1B**). If we were unable to elicit action potentials after illuminating multiple stimulation locations, we concluded that the axon of the Purkinje cell was likely cut.

Once we had identified a white matter photostimulation location from which we could elicit action potentials (**Figure 2A**), we tested photostimulus pulses of different durations to explore the conditions required to elicit single action potentials when light was delivered to the soma (**Figures 2B**(left),**C**) and axon (**Figures 2B**(right),**D**). We found that there was variability in the numbers of action potentials elicited at a given light duration across cells (**Figure 2D**).

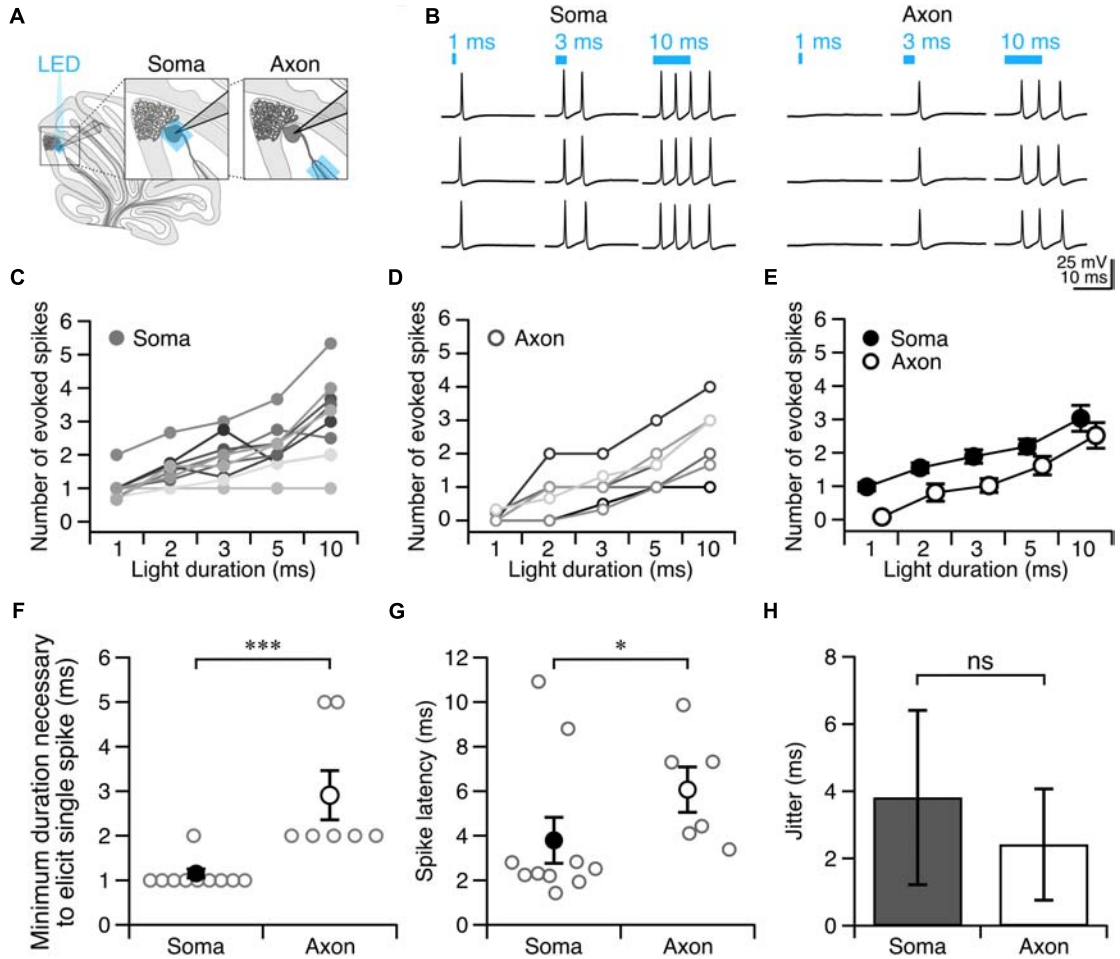

FIGURE 2 | Purkinje cell axons require longer light durations to evoke an action potential than somata. **(A)** Schematic depicting the recording configuration. **(B)** Representative current-clamp traces of optically evoked action potentials evoked following somatic (left) and axonal (right) stimulation. **(C–E)** The number of action potentials evoked for different photostimulus durations. **(C)** Soma, individual cells. **(D)** Axon, individual cells. **(E)** Averages. **(F)** Minimum duration of light stimulus required to elicit a single action potential from each subcellular locus. **(G)** Latency to the first action potential evoked by photostimulus was longer in axons than in soma. **(H)** Jitter of spike latency. Soma: $n = 10$; Axon: $n = 7$. Data represented as mean ± SEM. ns = not significant, $P > 0.05$; *$P < 0.05$; ***$P < 0.001$.

Since our aim was to identify light stimulation conditions that reliably elicit single action potentials across cells, we wanted to avoid eliciting multiple action potentials, although in most cases we were unable to accomplish this without occasional action potential failures (and used a failure cut-off of <33.3%). We found that 1 ms light stimulation reliably elicited single action potentials with somatic illumination (0.98 ± 0.12 spike for 1 ms, 1.55 ± 0.15 spike for 2 ms $n = 10$ cells; $N = 7$ mice; **Figure 2E**), but not with axonal illumination (0.08 ± 0.06 spike for 1 ms, $n = 7$ cells; $N = 6$ mice; **Figure 2E**). The optimal light stimulation duration that elicited single action potentials for axonal stimulation was typically 2 or 3 ms for individual cells (2 ms: 0.81 ± 0.26 spike; 3 ms: 1.02 ± 0.21 spike, **Figure 2E**). We sought to identify the optimal minimal light stimulation to elicit action potentials from the soma and axon for each cell, and found that the average minimal light duration necessary for axons (axon minimal light duration: 2.86 ± 0.55 ms; **Figure 2F**), was significantly longer than for somata (soma minimal light duration = 1.10 ± 0.10 ms, $n = 10$, $N = 7$; $P = 0.0003$; **Figure 2F**). This was also longer than what has previously been reported with a laser light source (Jackman et al., 2014). The latency from light onset to the evoked action potential was also significantly shorter for the soma than for the axon (soma: latency = 3.80 ± 1.03 ms; axon: latency = 6.07 ± 1.02 ms; $P = 0.042$; **Figure 2G**). However, although the latency to fire single action potentials with somatic or axonal photostimulation differed, we found no significant differences in the jitter of evoked spikes (soma: jitter = 3.81 ± 2.59 ms; axon: jitter = 2.42 ± 1.66 ms; $P = 0.46$; **Figure 2H**), suggesting that photostimulation results in consistently time-locked action potentials from both the axon and soma.

Since photostimulation of Purkinje cell axons requires longer light pulses to elicit an action potential than somatic stimulation, we wondered whether axons might be more susceptible to light perturbations, such as exposure to background white

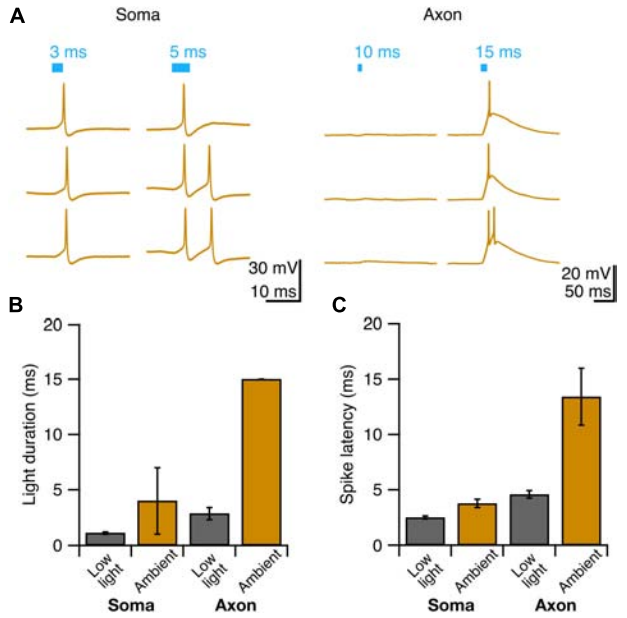

FIGURE 3 | Purkinje cell axons are more vulnerable to suboptimal experimental conditions than cell bodies. **(A)** Representative current-clamp traces of optically evoked action potentials elicited from Purkinje cell somata (left) and axons (right) when exposed to ambient light. **(B)** Axons require longer light durations to elicit single spikes in ambient light than somata. **(C)** The latency to spike after pulse onset for somata and axons exposed to ambient light. Ambient light: Soma: $n = 3$; Axon: $n = 3$.

light that might result in inactivation of ChR2 channels (Lin et al., 2009). To test this, we exposed Purkinje cells to ambient light during slice incubation and recordings, and elicited action potentials as before (**Figure 3A**, see section "Materials and Methods"). We observed an increase in the pulse duration necessary to evoke a single action potential from axons exposed to ambient light compared to what was observed for experiments performed in low light ($P = 0.013$; **Figure 3B**). By comparison, we did not find a difference in the pulse duration necessary to reliably elicit a single action potential from the soma between ambient light and low light conditions ($P = 0.35$; **Figure 3B**). Although the spike latency showed a tendency to increase in the ambient light condition compared to the low light condition for both the soma and axon (**Figure 3C**), these differences were not significant. These results suggest that Purkinje cell axons are more susceptible to ambient light than somata are, perhaps due to the presumed lower density of ChR2 channels in axons rendering them proportionally more sensitive to photo-inactivation.

Having identified conditions that reliably elicit single well-timed action potentials in Purkinje cell axons, we then sought to determine whether this paradigm would allow us to robustly elicit well-timed postsynaptic responses in DCN neurons. After making whole-cell voltage-clamp recordings from DCN neurons (**Figure 4A**), we stimulated Purkinje cell axons with variable light durations in the white matter ~200 μm from the patched cell, and recorded evoked IPSCs (**Figure 4B**). IPSC amplitude increased modestly with increasing photostimulus duration (**Figure 4C**), which may be due to additional action potentials elicited with longer light stimulation durations (**Figures 2D,E**), or from additional presynaptic axons being recruited by longer pulses. Rise times of evoked IPSCs were rapid (0.88 ± 0.06 ms, $n = 7$ cells; $N = 3$ mice, **Figure 4D**), with averages varying <0.2 ms across different stimulation durations, consistent with fast kinetics previously reported for this synapse (Pedroarena and Schwarz, 2003; Pugh and Raman, 2005; Uusisaari and Knöpfel, 2008). The jitter of the onset of postsynaptic response was low for all photostimulus durations, consistent with well-timed action potentials (**Table 1** and **Figure 4E**).

We found that with increasing light duration we saw more instances of multi-peak IPSCs (**Figure 4B**), which is in line with our observation that longer light durations elicit multiple presynaptic action potentials (**Figure 2B**), but may also reflect the recruitment of additional axons with longer pulses. Based on our empirical results above, we conclude that a 2 or 3 ms photostimulation duration is best suited to reliably elicit well-timed single presynaptic action potentials in Purkinje cell axons in order to investigate the Purkinje cell – DCN synapse.

DISCUSSION

We determined the light pulse duration from a 470 nm LED required to elicit well-timed single action potentials in Purkinje cell axons in acute sagittal slices from transgenic mice expressing ChR2 in Purkinje cells. We show that axons require longer pulse durations than somata to elicit the same number of action potentials, and that axonal photostimulation causes longer latencies to spike than somatic photostimulation. We also found that axons are more susceptible to perturbation from background light exposure. Finally, we demonstrate that the conditions we have used elicit well-timed single action potentials from Purkinje cell axonal stimulation allow us to elicit robust time-locked synaptic currents in postsynaptic neurons in the DCN. Since several recent studies using inhibitory optogenetic tools have shown that focal photostimulation of somata and axons yields different results, where stimulation of axons can result in paradoxical effects on activity (Mahn et al., 2016; Messier et al., 2018), we set out to confirm whether the conditions required for axonal photostimulation were similar to those for Purkinje cell somatic stimulation from mice transgenically expressing EYFP-fused ChR2(H134R). We found that we could elicit well-timed action potentials in both the soma and axon with focal photostimulation, although axons required longer light pulses, and displayed longer latencies. These light pulses were longer than what has been previously reported using a laser for photostimulation (Jackman et al., 2014).

Since we measured action potentials with a somatic patch pipette recording, we expected action potential latencies to be shorter when evoked from the soma than from the axon. Purkinje cell axons have been estimated to have a conduction velocity of

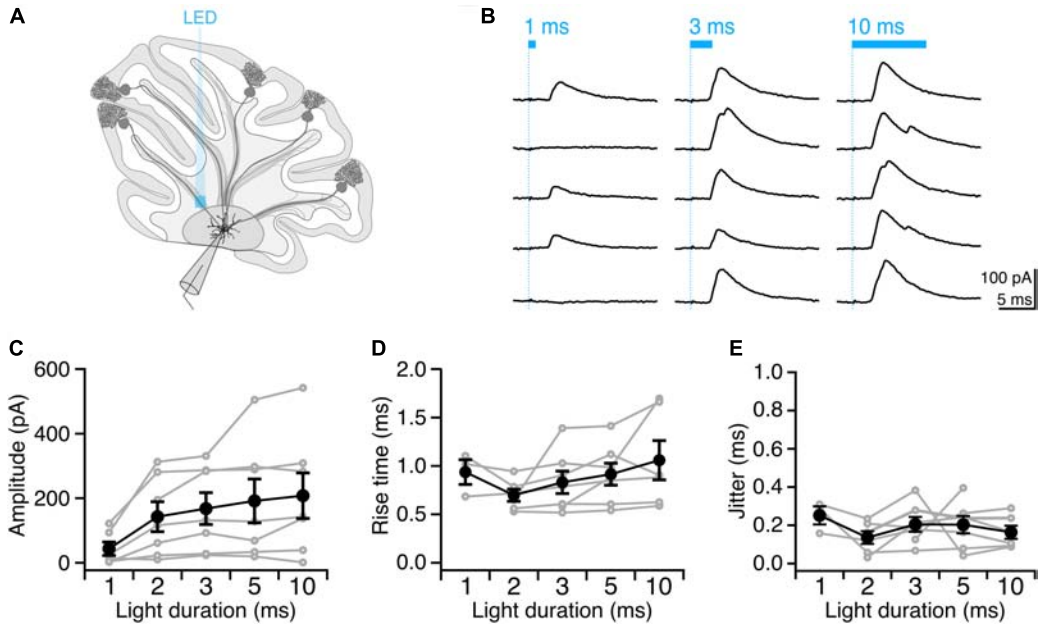

FIGURE 4 | Precisely timed synaptic responses in a DCN neuron with optogenetic Purkinje cell activation. **(A)** Recording configuration. Light pulses were delivered to Purkinje cell axons while performing whole-cell voltage-clamp recordings in DCN neurons. **(B)** Representative traces of IPSCs evoked with durations of light in same location. Blue bar above traces indicates onset and duration of light pulse. **(C)** Average IPSC amplitude across photostimulus durations. **(D)** Average IPSC rise time. **(E)** Jitter of onset of IPSCs. Individual cells, gray. Average, black. *n* = 7.

TABLE 1 | Synaptic properties of evoked IPSCs from DCN neurons.

Duration	1 ms	2 ms	3 ms	5 ms	10 ms
Amplitude (pA)	43.59 ± 20.92	142.80 ± 46.33	168.30 ± 49.18	191.80 ± 67.71	207.90 ± 70.32
Rise time (ms)	0.94 ± 0.13	0.70 ± 0.06	0.83 ± 0.12	0.91 ± 0.11	1.06 ± 0.2
Jitter of onset (ms)	0.25 ± 0.05	0.14 ± 0.03	0.21 ± 0.04	0.20 ± 0.05	0.16 ± 0.03

Amplitude, rise time, and jitter of the onset of the postsynaptic response (time to 20% of the peak) were determined from the average IPSCs evoked for each photostimulus duration. Amplitude analysis includes failures. n = 7.

∼1–10 m/s (Khaliq and Raman, 2005), so given the distances between axonal stimulation location and somatic patch pipette (<200 μm separation), only a small fraction of the increased latency (up to 0.2 ms) should be attributed to the conduction latency arising from the distal site of axonal action potential initiation. Several other factors likely contribute to the increased latency of action potentials arising from axonal stimulation. Purkinje cell axons are myelinated (Ljungberg et al., 2016) and action potentials travel between nodes of Ranvier in the axon. However, given that internodal spacing ranges between 60 and 260 μm (Clark et al., 2005), the area of focal photostimulation is likely to only occasionally overlap with a node of Ranvier. In support of this, internodal spacing of nodes of Ranvier have been shown to be a limiting factor in the induction of action potentials in myelinated axons (Arlow et al., 2013). Since light scattering is increased in lipid-rich tissues such as myelin which is abundant in the cerebellar white matter, lower light intensities likely reach Purkinje cell axons compared to the soma (Mattis et al., 2012). However, although the latency to action potential is longer for axons, the jitter between trials is not significantly different, suggesting that action potentials can be elicited reliably and with high temporal precision following axonal photostimulation.

We observed that Purkinje cell axons required longer light pulses and showed longer latencies than somata do to elicit action potentials, so we then wondered whether they may have heightened sensitivity to light perturbations. To test this, we exposed slices to ambient light and repeated our measurements. Axons required longer light pulses in this condition compared to axons maintained in low light, while there was no significant difference in the light pulse duration necessary to elicit spikes from somata held in either low light or ambient light. These results may be due to a slow recovery from inactivation induced by exposure to ambient light: ChR2(H134R) recovers from desensitization and inactivation more slowly than other engineered ChR2 variants (Lin, 2011). Since transgenically expressed ChR2 is not specifically clustered at nodes of Ranvier in myelinated axons (**Figure 1**; Grubb and Burrone, 2010; Arlow et al., 2013), inactivation of individual ChR2 molecules in a region with an already limited availability may greatly reduce the efficacy of a photostimulus. This axonal sensitivity supports our hypothesis that Purkinje cell axons are more

affected than somata are by light perturbations in optogenetic experiments and suggests that extra care should be taken when photostimulating axons to minimize unnecessary light exposure. Finally, we confirm that the parameters which elicit well-timed single action potentials from Purkinje cell axons allow us to elicit temporally precise synaptic responses in DCN neurons with little trial-to-trial jitter. The parameters we established to best elicit single action potentials from Purkinje cell axons matched well to conditions we observed to best elicit IPSCs in target DCN neurons when focally stimulating a population of presynaptic Purkinje cells (2 or 3 ms). Given the relatively large size of our photostimulation pulse and because Purkinje cell axons bundle together in the white matter, we do not expect to have stimulated single axons, but rather, small subpopulations of Purkinje cell axons. However, further optimization of the size and location of the photostimulation pulse might allow us to reliably photostimulate individual presynaptic axons in the future. Our findings highlight the importance of empirically determining photostimulation parameters from presynaptic neurons to optimize conditions for optogenetic experiments. We expect that some of our findings, such as that axons typically require longer light pulses for similar responses to axons and are more susceptible to background ambient light, are general features that will likely be observed across cell types and recording configurations. However, the major conclusion of this work is that it is important to determine photostimulation parameters empirically when precise temporal control of action potentials is desired for optogenetic experiments.

DATA AVAILABILITY STATEMENT

The datasets generated for this study are available on request to the corresponding author.

ETHICS STATEMENT

All animal procedures were approved by the McGill Animal Care Committee, in accordance with guidelines established by the Canadian Council on Animal Care.

AUTHOR CONTRIBUTIONS

KG performed the experiments and analyzed electrophysiological data. AW conceived of the project, and acquired and analyzed two-photon imaging, and electrophysiological data. Both authors designed the experiments, interpreted the data, wrote the manuscript, and have approved the final version of the manuscript and agreed to be accountable for all aspects of the work.

FUNDING

This work was supported by a Discovery Grant (05118) from the Natural Sciences and Engineering Research Council of Canada, a New Investigator Grant (Nouveau Chercheur; 189153) from the Fonds de Recherche Nature et Technologies de Québec (AW), and an Operating Grant (130570) and Project grant (153150) from the Canadian Institutes of Health Research.

ACKNOWLEDGMENTS

We thank Jesper Sjöström for custom Igor software for data collection and analysis. We thank members of the Watt lab for help and support with this project, and for critical feedback on this manuscript. We also thank Tanya Koch for technical help with maintenance of our transgenic mouse colony.

REFERENCES

Ady, V., Toscano-Márquez, B., Nath, M., Chang, P. K., Hui, J., Cook, A., et al. (2018). Altered synaptic and firing properties of cerebellar purkinje cells in a mouse model of ARSACS. *J. Physiol.* 596, 4253–4267. doi: 10.1113/JP275902

Arlow, R. L., Foutz, T. J., and McIntyre, C. C. (2013). Theoretical principles underlying optical stimulation of myelinated axons expressing channelrhodopsin-2. *Neuroscience* 248, 541–551. doi: 10.1016/j.neuroscience.2013.06.031

Boyden, E. S., Zhang, F., Bamberg, E., Nagel, G., and Deisseroth, K. (2005). Millisecond-timescale, genetically targeted optical control of neural activity. *Nat. Neurosci.* 8, 1263–1268. doi: 10.1038/nn1525

Clark, B. A., Monsivais, P., Branco, T., London, M., and Häusser, M. (2005). The site of action potential initiation in cerebellar purkinje neurons. *Nat. Neurosci.* 8, 137–139. doi: 10.1038/nn1390

Cruikshank, S. J., Urabe, H., Nurmikko, A. V., and Connors, B. W. (2010). Pathway-specific feedforward circuits between thalamus and neocortex revealed by selective optical stimulation of axons. *Neuron* 65, 230–245. doi: 10.1016/j.neuron.2009.12.025

Grubb, M. S., and Burrone, J. (2010). Channelrhodopsin-2 localised to the axon initial segment. *PLoS One* 5:e13761. doi: 10.1371/journal.pone.0013761

Huber, D., Petreanu, L., Ghitani, N., Ranade, S., Hromádka, T., Mainen, Z., et al. (2008). Sparse optical microstimulation in barrel cortex drives learned behaviour in freely moving mice. *Nature* 451, 61–64. doi: 10.1038/nature06445

Jackman, S. L., Beneduce, B. M., Drew, I. R., and Regehr, W. G. (2014). Achieving high-frequency optical control of synaptic transmission. *J. Neurosci.* 34, 7704–7714. doi: 10.1523/JNEUROSCI.4694-13.2014

Jayabal, S., Ljungberg, L., and Watt, A. J. (2017). Transient cerebellar alterations during development prior to obvious motor phenotype in a mouse model of spinocerebellar ataxia type 6. *J. Physiol.* 595, 949–966. doi: 10.1113/JP273184

Khaliq, Z. M., and Raman, I. M. (2005). Axonal propagation of simple and complex spikes in cerebellar purkinje neurons. *J. Neurosci.* 25, 454–463. doi: 10.1523/JNEUROSCI.3045-04.2005

Lewis, T. L., Mao, T., Svoboda, K., and Arnold, D. B. (2009). Myosin-dependent targeting of transmembrane proteins to neuronal dendrites. *Nat. Neurosci.* 12, 568–576. doi: 10.1038/nn.2318

Lin, J. Y. (2011). A user's guide to channelrhodopsin variants: features, limitations and future developments. *Exp. Physiol.* 96, 19–25. doi: 10.1113/expphysiol.2009.051961

Lin, J. Y., Lin, M. Z., Steinbach, P., and Tsien, R. Y. (2009). Characterization of engineered channelrhodopsin variants with improved properties and kinetics. *Biophys. J.* 96, 1803–1814. doi: 10.1016/j.bpj.2008.11.034

Ljungberg, L., Lang-Ouellette, D., Yang, A., Jayabal, S., Quilez, S., and Watt, A. J. (2016). Transient developmental purkinje cell axonal torpedoes in healthy and

ataxic mouse cerebellum. *Front. Cell. Neurosci.* 10:248. doi: 10.3389/fncel.2016.00248

Mahn, M., Prigge, M., Ron, S., Levy, R., and Yizhar, O. (2016). Biophysical constraints of optogenetic inhibition at presynaptic terminals. *Nat. Neurosci.* 19, 554–556. doi: 10.1038/nn.4266

Mattis, J., Tye, K. M., Ferenczi, E. A., Ramakrishnan, C., O'Shea, D. J., Prakash, R., et al. (2012). Principles for applying optogenetic tools derived from direct comparative analysis of microbial opsins. *Nat. Methods* 9, 159–172. doi: 10.1038/nmeth.1808

Messier, J. E., Chen, H., Cai, Z.-L., and Xue, M. (2018). Targeting light-gated chloride channels to neuronal somatodendritic domain reduces their excitatory effect in the axon. *eLife* 7:e38506. doi: 10.7554/eLife.38506

Nagel, G., Szellas, T., Huhn, W., Kateriya, S., Adeishvili, N., Berthold, P., et al. (2003). Channelrhodopsin-2, a directly light-gated cation-selective membrane channel. *Proc. Natl. Acad. Sci. U.S.A.* 100, 13940–13945. doi: 10.1073/pnas.1936192100

Palay, S. L., and Chan-Palay, V. (1974). *The Purkinje Cell in Cerebellar Cortex*. Berlin: Springer.

Pedroarena, C. M., and Schwarz, C. (2003). Efficacy and short-term plasticity at gabaergic synapses between purkinje and cerebellar nuclei neurons. *J. Neurophysiol.* 89, 704–715. doi: 10.1152/jn.00558.2002

Person, A. L., and Raman, I. M. (2012). Purkinje neuron synchrony elicits time-locked spiking in the cerebellar nuclei. *Nature* 481, 502–505. doi: 10.1038/nature10732

Petreanu, L., Huber, D., Sobczyk, A., and Svoboda, K. (2007). Channelrhodopsin-2-assisted circuit mapping of long-range callosal projections. *Nat. Neurosci.* 10, 663–668. doi: 10.1038/nn1891

Pfeffer, C. K., Xue, M., He, M., Huang, Z. J., and Scanziani, M. (2013). Inhibition of inhibition in visual cortex: the logic of connections between molecularly distinct interneurons. *Nat. Neurosci.* 16, 1068–1076. doi: 10.1038/nn.3446

Pologruto, T. A., Sabatini, B. L., and Svoboda, K. (2003). ScanImage: flexible software for operating laser scanning microscopes. *Biomed. Eng. Online* 2:13. doi: 10.1186/1475-925X-2-13

Pugh, J. R., and Raman, I. M. (2005). GABAA receptor kinetics in the cerebellar nuclei: evidence for detection of transmitter from distant release sites. *Biophys. J.* 88, 1740–1754. doi: 10.1529/biophysj.104.055814

Sjöström, P. J., Turrigiano, G. G., and Nelson, S. B. (2001). Rate, timing, and cooperativity jointly determine cortical synaptic plasticity. *Neuron* 32, 1149–1164. doi: 10.1016/S0896-6273(01)00542-6

Uusisaari, M., and Knöpfel, T. (2008). GABAergic synaptic communication in the GABAergic and non-GABAergic cells in the deep cerebellar nuclei. *Neuroscience* 156, 537–549. doi: 10.1016/j.neuroscience.2008.07.060

Watt, A. J., Cuntz, H., Mori, M., Nusser, Z., Sjöström, P. J., and Häusser, M. (2009). Traveling waves in developing cerebellar cortex mediated by asymmetrical purkinje cell connectivity. *Nat. Neurosci.* 12, 463–473. doi: 10.1038/nn.2285

Conflict of Interest: The authors declare that the research was conducted in the absence of any commercial or financial relationships that could be construed as a potential conflict of interest.

frontiers in Synaptic Neuroscience

REVIEW
published: 11 February 2020
doi: 10.3389/fnsyn.2020.00005

Unveiling the Synaptic Function and Structure Using Paired Recordings From Synaptically Coupled Neurons

Guanxiao Qi[1]*, *Danqing Yang*[1], *Chao Ding*[1] and *Dirk Feldmeyer*[1,2,3]

[1] Institute of Neuroscience and Medicine, INM-10, Jülich Research Centre, Jülich, Germany, [2] Department of Psychiatry, Psychotherapy and Psychosomatics, RWTH Aachen University Hospital, Aachen, Germany, [3] Jülich-Aachen Research Alliance, Translational Brain Medicine (JARA Brain), Aachen, Germany

Synaptic transmission between neurons is the basic mechanism for information processing in cortical microcircuits. To date, paired recording from synaptically coupled neurons is the most widely used method which allows a detailed functional characterization of unitary synaptic transmission at the cellular and synaptic level in combination with a structural characterization of both pre- and postsynaptic neurons at the light and electron microscopic level. In this review, we will summarize the many applications of paired recordings to investigate synaptic function and structure. Paired recordings have been used to study the detailed electrophysiological and anatomical properties of synaptically coupled cell pairs within a synaptic microcircuit; this is critical in order to understand the connectivity rules and dynamic properties of synaptic transmission. Paired recordings can also be adopted for quantal analysis of an identified synaptic connection and to study the regulation of synaptic transmission by neuromodulators such as acetylcholine, the monoamines, neuropeptides, and adenosine etc. Taken together, paired recordings from synaptically coupled neurons will remain a very useful approach for a detailed characterization of synaptic transmission not only in the rodent brain but also that of other species including humans.

Keywords: paired recordings, synaptic connection, structure-function analysis, quantal analysis, neuromodulation

OPEN ACCESS

Edited by:
Christiaan P. J. De Kock, Vrije Universiteit Amsterdam, Netherlands

Reviewed by:
Jean-Sébastien Jouhanneau, Helmholtz Association of German Research Centers (HZ), Germany
Srikanth Ramaswamy, École Polytechnique Fédérale de Lausanne, Switzerland

***Correspondence:**
Guanxiao Qi
g.qi@fz-juelich.de

Received: *30 September 2019*
Accepted: *22 January 2020*
Published: *11 February 2020*

Citation:
Qi G, Yang D, Ding C and Feldmeyer D (2020) Unveiling the Synaptic Function and Structure Using Paired Recordings From Synaptically Coupled Neurons. Front. Synaptic Neurosci. 12:5. doi: 10.3389/fnsyn.2020.00005

INTRODUCTION

To understand local neuronal microcircuits in the brain, it is necessary to know the morphological and electrophysiological properties of both the pre- and postsynaptic neurons, the synaptic connection type(s) and their structure-function relationship. However, in many studies of synaptic transmission the identity of the pre- and postsynaptic neuron is not well or not at all characterized. This is because of the relatively unspecific stimulation protocols (e.g., extracellular stimulation) often used to investigate synaptic connectivity, which generally do not allow to determine the structural and functional properties of the presynaptic neuron. Paired recordings together with intracellular staining by markers such as biocytin/neurobiotin and/or fluorescent dyes are better suited for studying local neuronal microcircuits. This technique permits a simultaneous, correlated characterization of the structural and functional properties of a synaptic connection.

Monosynaptic connections between identified neurons have been investigated in both cortical and subcortical brain regions using paired recordings in acute brain slices (Malinow, 1991; Mason et al., 1991; Buhl et al., 1994; Deuchars et al., 1994; Bolshakov and Siegelbaum, 1995; Miles et al., 1996; Stratford et al., 1996; Geiger et al., 1997; Markram et al., 1997a; Thomson and Deuchars, 1997; Feldmeyer et al., 1999; Gupta et al., 2000; Tamas et al., 2000, 2003; Holmgren et al., 2003; Szabadics et al., 2006; Helmstaedter et al., 2008; Olah et al., 2009, for reviews, see Miles and Poncer, 1996; Debanne et al., 2008; Feldmeyer and Radnikow, 2016). Sharp microelectrodes were initially used in these experiments (Mason et al., 1991; Buhl et al., 1994; Deuchars et al., 1994). However, electrophysiological recordings with sharp microelectrodes have several limitations, e.g., the electrical noise is high and the membrane seal poor, the approach is generally blind and thus the inter-somatic distance between pre- and postsynaptic neurons not well controlled (Brette and Destexhe, 2012). Later, patch pipettes were employed in order to measure synaptic responses with a higher signal-to-noise ratio and an improved temporal resolution. A significant advance was the use of infrared differential interference contrast optics (Dodt and Zieglgansberger, 1990) that significantly improved the visual identification of neurons in acute brain slices (Stuart et al., 1993) so that it became possible to obtain recordings from synaptic connections between visually identified neurons.

An advantage of paired recordings is the fact that functional characterization can be combined with the morphological and/or molecular analysis at both the light and electron microscopic level (Deuchars et al., 1994; Markram et al., 1997a, 1998b; Reyes et al., 1998; Feldmeyer et al., 2002, 2006; Silver et al., 2003; Tamas et al., 2003; Kapfer et al., 2007; Silberberg and Markram, 2007; Helmstaedter et al., 2008). After histochemical processing, the expression of specific marker proteins of the synaptically connected neuron pair can be determined, in a subsequent step the somatodendritic and axonal morphologies recovered and then reconstructed in three spatial dimensions. This will allow a quantitative analysis of morphological features such as orientation, branching pattern, spatial length density etc. These parameters could provide a basis for an objective classification of pre- and postsynaptic neurons in a specific synaptic connection. Furthermore, paired recordings also permit the identification of synaptic contacts of unitary synaptic connections using a combination of light and electron microscopy. In addition to this detailed analysis of the synaptic transmission at a defined neuronal microcircuit paired recordings also allow the study of quantal properties of identified synapses and the modulation of synaptic transmission by neurotransmitters such as acetylcholine, noradrenaline, dopamine, serotonin, and adenosine.

ELECTROPHYSIOLOGICAL, MORPHOLOGICAL AND/OR, MOLECULAR CHARACTERIZATION OF SYNAPTIC CONNECTIONS IN LOCAL NEURONAL MICROCIRCUITS

The most crucial step for paired recordings in acute brain slices is to find a sufficiently stable synaptic connection so that a detailed analysis of its structural and functional properties is possible. This step depends on several important factors which will be discussed here in brief (for more details, see Radnikow et al., 2012; Feldmeyer and Radnikow, 2016). First, it is important to determine the optimal procedure for preparing brain slices so that the axo-dendritic branches of both pre- and postsynaptic neuron for the synaptic connection under study is well preserved. A suitable slice thickness needs to be determined depending on the recording configuration (whole-cell with patch pipettes or intracellular with sharp microelectrodes); an increase in the slice thickness may significantly increase the connection probability and the quantification of synapse number per connection (Thomson and Lamy, 2007; Stepanyants et al., 2009). Second, the composition of solutions used during the slicing and incubation needs to be adjusted carefully according to the age of animals and type of species. Several slicing and incubation solutions for adult and senescent animal and human brain tissue are available under http://www.brainslicemethods.com/ (Ting et al., 2014, 2018a,b). Finally, the connection probability of different neuron types is highly variable (from 5 to 70%) depending on both the presynaptic axonal projection and the postsynaptic dendritic arborization (Thomson and Lamy, 2007; Lefort et al., 2009; Fino et al., 2013; Pfeffer et al., 2013; Jiang et al., 2015; Markram et al., 2015; Radnikow et al., 2015; Seeman et al., 2018; Jouhanneau and Poulet, 2019). Therefore, choosing the appropriate strategy, either a random patch or a "searching" protocol (Qi et al., 2015), is critical for the success of paired recordings. Paired recordings from synaptically coupled neurons allow a wide variety of functional and structural analysis. The most relevant issues will be described below.

Electrophysiological Characterization of Local Synaptic Transmission

The synaptic strength (or weight) is a key parameter to characterize the efficacy of a synaptic connection. It reflects whether the synaptic connection has a strong or weak influence on postsynaptic output. It is measured as the peak amplitude of postsynaptic potentials (PSPs) evoked by presynaptic action potentials (APs). For excitatory synaptic connections in the neocortex, the PSP amplitude is not normally distributed but skewed toward lower values ($\sim$0.5 mV) with a long tail with higher values (>2 mV) (**Figures 1A,B**) (Markram et al., 1997a; Feldmeyer et al., 1999, 2002, 2006; Sjostrom et al., 2001; Holmgren et al., 2003; Lefort et al., 2009). It has been shown by theoretical analysis that this synaptic weight distribution can be understood through optimization of information storage in neuronal networks (Brunel et al., 2004; Varshney et al., 2006; Barbour et al., 2007). It has also been suggested that the high-amplitude connections represent rare, strong connections that mediate stimulus-specific response amplification in cortical microcircuits (Cossell et al., 2015).

The time course of postsynaptic response is another important determinant of the computational power of a synaptic connection and significantly affects the synaptic integration in postsynaptic neurons. Long-lasting PSPs show a stronger summation while brief postsynaptic responses are necessary to achieve a high temporal fidelity for repetitive synaptic inputs. Quantitatively, the time course of excitatory or inhibitory PSPs (EPSPs/IPSPs)

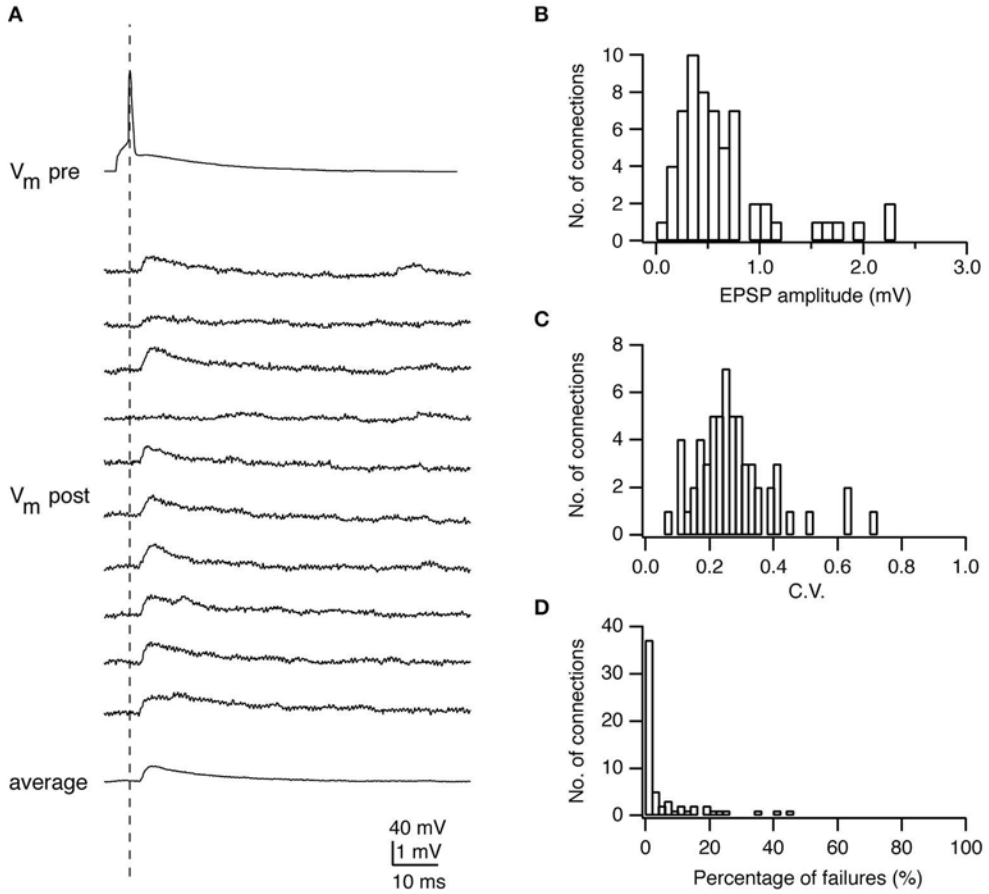

FIGURE 1 | Electrophysiological characterization of synaptic connections using paired recordings. **(A)** Paired recordings from a synaptic connection established between a presynaptic L4 spiny neuron and a postsynaptic L2/3 pyramidal cell. Top, a presynaptic AP; Middle, ten successive EPSPs in response to a presynaptic AP; Bottom, the average EPSP. **(B)** Histogram of the EPSP amplitudes in L4-L2/3 connections ($n = 64$). **(C)** Histogram of the coefficients of variation (C.V.s) of EPSPs in L4-L2/3 connections ($n = 64$). **(D)** Histogram of the failure rate (in %) in L4-L2/3 connections ($n = 64$). Figure has been adapted from Feldmeyer et al. (2002) with permission.

is described by its 20–80% rise time, decay time constant and half-width. It should be noted that the EPSP/IPSP time course is shaped by (low-pass) dendritic filtering due to the distance between the recording site (normally at the soma) and the synapse location (Rall, 1967).

The latency is defined as the time difference between the peak of presynaptic AP and the beginning of the PSP. The size and variation of latencies determines the time window of integration of the synaptic response. Many factors such as the fine structure of the pre- and postsynaptic sites, the release probability of neurotransmitters, and the passive and/or active electrophysiological properties of both pre- and postsynaptic neurons affect the latency in synaptic transmission.

The reliability is an important property of a synaptic connection, which characterizes the extent of the PSP variability. Synaptic reliability and variability are sensitive to recording conditions, e.g., the temperature and Ca^{2+} concentration in the recording solution. The reliability of synaptic transmission increases with the increasing temperature (Hardingham and Larkman, 1998; Volgushev et al., 2004) and Ca^{2+} concentration (Rozov et al., 2001; Silver et al., 2003) due to enhanced transmitter release. To determine this parameter, an AP is elicited in the presynaptic neuron resulting in an EPSP or IPSP in the postsynaptic neuron (**Figures 1A**, **4A**). Between 50 and 100 sweeps are recorded to determine the mean amplitude of the synaptic response (**Figures 1B**, **4B**) and its variance. A frequently used measure for the reliability is the coefficient of variation (CV) which is defined as:

$$CV_{PSP} = \sqrt{(\sigma^2_{PSP} - \sigma^2_{Noise})}/\mu_{PSP}$$

where σ^2_{PSP} is the variance of the PSP amplitude, σ^2_{Noise} the variance of the membrane potential fluctuation, and μ_{PSP} the mean PSP amplitude (**Figure 1C**). The variance of the PSP is corrected by subtracting the membrane potential variance, which includes membrane potential noise (i.e., from random ion channel openings) and electrical noise introduced by the recording equipment. CV_{PSP} is a surrogate measure for the

release probability of transmitters. However, this measure is only indirect and a detailed quantal analysis (see below) is needed to determine its actual value.

The failure rate is defined as the frequency with which a synapse fails to respond to a presynaptic AP (**Figure 1D**). In general, synaptic connections with a low neurotransmitter release probability (e.g., synapses formed by L6A cortico-thalamic pyramidal neurons) (Yang et al., 2019) and/or few synaptic contacts (e.g., synapse formed between parallel fibers from granule cells and Purkinje cell dendrites) (Isope and Barbour, 2002) show a significant number of failures. However, failures may not be apparent despite a relatively low release probability when the number of synaptic contacts is sufficiently large. Under this condition it is likely that vesicle release would occur at least at a small fraction of synaptic contacts; hence, no failures would be observed. This is in accordance with findings in a number of paired recording studies in acute cortical slices that generally report a low failure rate of synaptic transmission (Atzori et al., 2001; Koester and Johnston, 2005; Feldmeyer et al., 2006; Frick et al., 2008; Lefort et al., 2009).

Changes in the strength of the synaptic response are critical for the flexibility and plasticity of synaptic function. For monosynaptic connections, paired recordings have shown that, during the delivery of multiple stimuli at short time intervals, the size of the postsynaptic responses can become either larger or smaller, a phenomenon known as short-term facilitation or depression, respectively. When the release probability is low during the initial presynaptic AP, PSP facilitation is likely to occur. This is likely to results from an increase in the Ca^{2+} concentration in the presynaptic terminal with each successive presynaptic AP which will lead to successively larger PSPs (i.e., an increase in release probability). After some time the release probability and hence the PSP amplitude will decrease again because of a depletion of the readily releasable pool of synaptic vesicles (see below). Short-term synaptic depression, on the other hand, occurs when the initial release probability is high, i.e., when many synaptic vesicles are released during the first presynaptic AP. This then results in a transient depletion of synaptic vesicle from the readily releasable pool (Zucker and Regehr, 2002; Rizzoli and Betz, 2004, 2005). Whether a synaptic connection shows short-term facilitation or depression depends on the pre- and/or postsynaptic neuron identity (Markram et al., 1998b; Reyes et al., 1998; Scanziani et al., 1998; Gupta et al., 2000; Koester and Johnston, 2005; Ma et al., 2012) (**Figure 3**). By eliciting a pair (or train) of APs in the presynaptic neuron at a fixed interval (e.g., 100 ms) and measuring the amplitude of the postsynaptic response, the paired-pulse ratio (PPR) is calculated as PPR $= PSP_2/PSP_1$. The PPR is commonly used to characterize short-term synaptic plasticity and specifies whether the initial release probability is high or low. Although the PPR is widely used, it is not sufficient to unmask the interplay between release, depression and facilitation (Dittman et al., 2000). There is some ambiguity in using the PPR to determine depression/facilitation dynamics in the case of strongly facilitating synapses. In these synapses, PPR might be small for the first two PSPs and gradually becomes larger during repetitive presynaptic stimulation (Markram et al., 1998a). For such cases a train of frequency-dependent APs elicited in the presynaptic neuron is more appropriate to be adopted for measuring the postsynaptic response.

Synaptic function is also affected by retrograde messengers (e.g., glutamate, GABA, endocannabinoid) released from postsynaptic dendrites (Zilberter et al., 2005). Paired recordings between layer 2/3 pyramidal cells and bitufted interneurons showed that the dendritic GABA release depresses excitatory transmission via presynaptic metabotropic $GABA_B$ receptors in the rat neocortex (Zilberter et al., 1999). For the inhibitory transmission, depolarization-induced suppression of inhibition (DSI) was found widely in different cortical areas including the hippocampus (Wilson and Nicoll, 2001), cerebellum (Kreitzer and Regehr, 2001), and neocortex (Trettel and Levine, 2003). DSI has been shown to be caused by the postsynaptic deporalization-induced dendritic release of endocannabinoids, which diffuse retrogradely to presynaptic axonal terminals where they bind to cannabinoid 1 receptors to reduce the GABA release.

It should be noted that there are some differences between *in vitro acute brain slice (or ex vivo)* and *in vivo* recording conditions. Therefore, the property of synaptic transmission studied *in vitro* may be different from that *in vivo* condition. A prominent difference is the extracellular Ca^{2+} concentration which is ∼1.2–1.3 mM free Ca^{2+} in the cerebrospinal fluid (Heinemann et al., 1977; Massimini and Amzica, 2001; Crochet et al., 2005; Borst, 2010) but 2 mM Ca^{2+} compound in a standard extracellular perfusion solution. Because calcium salts do not fully dissociate the free Ca^{2+} concentration in the extracellular fluid will be lower than the absolute $CaCl_2$ concentration [or any other calcium salt this is substituted for $CaCl_2$ (e.g., $Ca(CH_3SO_3)_2$)]. An absolute $CaCl_2$ concentration of 2 mM amounts to 1.7 mM free Ca^{2+} (as can be measured with an ion-selective electrode and/or calculated from the dissociation constant). Thus, compared to the *in vitro* condition, the PSP amplitude and reliability will be lower and the failure rate higher under *in vivo* condition because of the reduced synaptic release probability. In addition, the short-term synaptic plasticity is likely to change from strong depression to no change or weak facilitation. In addition, the membrane conductance of neocortical neurons is high *in vivo* because of the intense synaptic bombardment, which rarely appears under *in vitro* conditions (Destexhe et al., 2003). Therefore, the time course of PSPs recorded *in vivo* is also different from that *in vitro*, e.g., the decay of PSPs is faster *in vivo* than *in vitro* because of enhanced membrane conductances.

Long-term synaptic changes such as long-term potentiation (LTP) and depression (LTD) have been considered as the cellular mechanism of learning and memory (Huganir and Nicoll, 2013). Paired recordings have been widely adopted to investigate the LTP and LTD and uncover their induction conditions and mechanisms (Malinow, 1991; Arancio et al., 1995; Bolshakov and Siegelbaum, 1995; Liao et al., 1995; Markram et al., 1997b; Bi and Poo, 1998; Egger et al., 1999; Montgomery et al., 2001). For example, the postsynaptic insertion of AMPA receptors has been considered to be the molecular basis of LTP induction. Spike-timing-dependent plasticity (STDP) is one Hebbian type of long-term synaptic plasticity. Its induction depends on the precise timing of pre- and postsynaptic AP

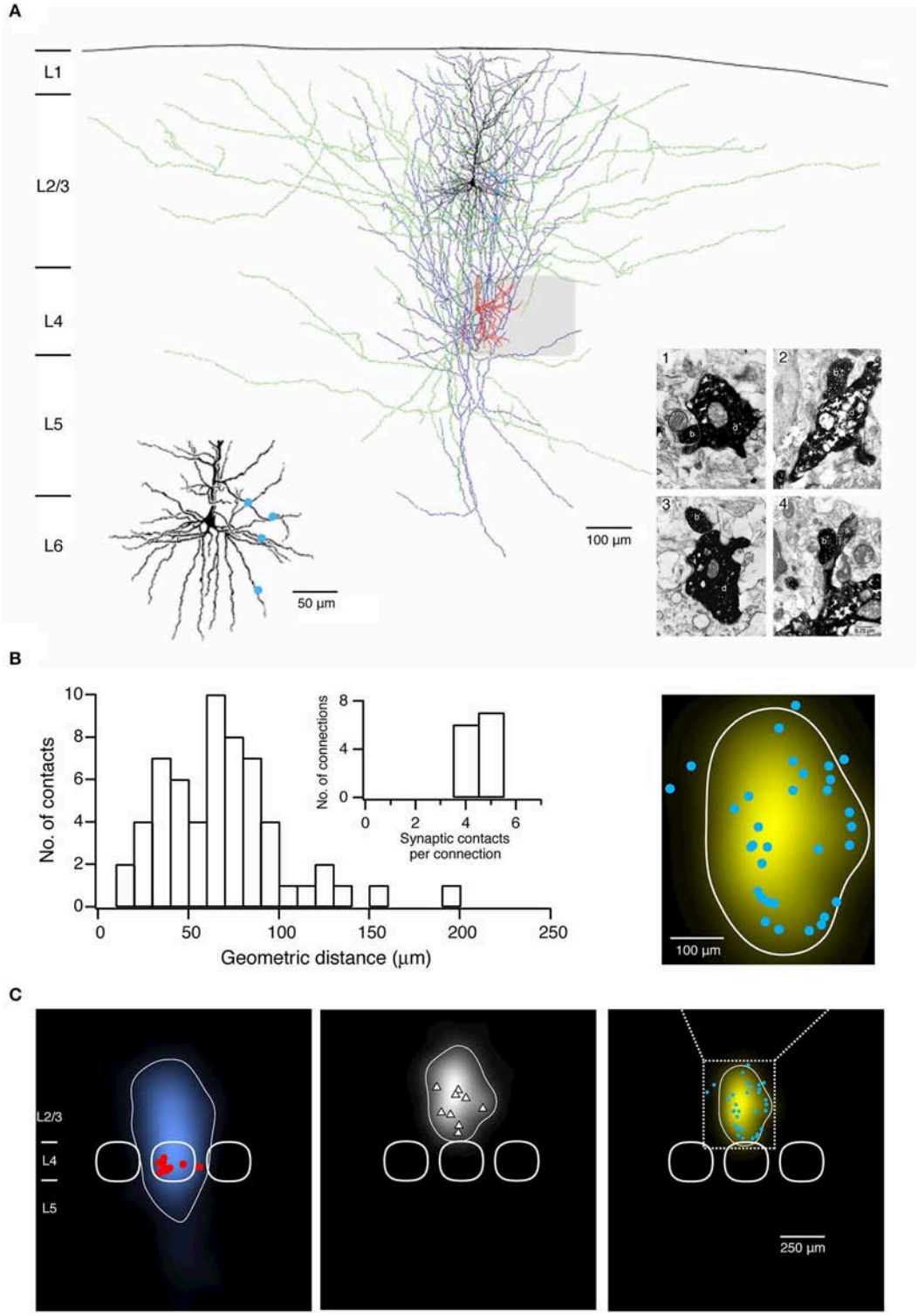

FIGURE 2 | Morphological characterization of synaptic connections using paired recordings in combination with biocytin fillings. **(A)** Morphological reconstruction of a synaptically coupled cell pair between a L4 spiny stellate cell and a L2/3 pyramidal neuron. The somatodendritic and axonal compartments of the presynaptic spiny stellate cell are drawn in red and blue, respectively. The somatodendritic and axonal compartments of the postsynaptic L2/3 pyramidal neuron are drawn in black and green, respectively. The gray square represents the L4 barrel where the spiny stellate cell is located. Left inset, four putative synaptic contacts established by the axon of the L4 spiny stellate cell with the dendrites of the L2/3 pyramidal neuron are marked by blue dots. Right inset, electron micrographs of the synaptic contacts. All

(Continued)

FIGURE 2 | four synaptic contacts which were identified with the light microscope were confirmed at the electron microscopic level. The axonal boutons (b) of the L4 spiny stellate cell established synaptic contacts on dendritic shafts (d) in contacts 1–3 while on a dendritic spine in contact 4 of the L2/3 pyramidal neuron. **(B)** Histogram of the geometric distances from the somata of putative synaptic contacts in 13 L4 spiny neuron-L2/3 pyramidal cell pairs. Inset, distribution of number of synaptic contacts per connection. **(C)** 2D maps of axonal (left) and dendritic (middle) "length density" of synaptically coupled L4 spiny neurons and L2/3 pyramidal cells ($n = 9$), aligned with respect to the barrel center. The predicted innervation domain (right) of L2/3 dendrites by L4 axons is given by the product of the L4 axonal density and the L2/3 dendritic density. Contours (thin lines) enclosing 80% of the integrated density are superimposed. Positions of L4 spiny neuron sonata (red dots), L2/3 pyramidal cell sonata (white triangles), putative synaptic contacts (cyan dots), and outlines of barrels (thick lines) are indicated symbolically. Inset, zoom in the predicted innervation domain superimposed by putative synaptic contacts. **(A,B)** have been adapted from Feldmeyer et al. (2002) with permission and **(C)** from Lubke et al. (2003) with permission.

firing. Paired recordings between layer 5 pyramidal cells showed that if a presynaptic neuron fires earlier (e.g., +10 ms) than its postsynaptic neuron, LTP will be induced. Otherwise, if the presynaptic neuron fires later (e.g., −10 ms) than its postsynaptic neuron, LTD will develop (Markram et al., 1997b; Bi and Poo, 1998, 2001; Abbott and Nelson, 2000). However, this rule does not apply to synaptic connections established between layer 4 spiny neurons. Whether presynaptic neurons fire earlier or later (e.g., ±10 ms) than postsynaptic neurons LTD will always be induced because of presynaptic metabotropic glutamate receptor activation (Egger et al., 1999).

In addition to chemical synapses, synaptic coupling can also occur via electrical synapses or gap junctions, in particular between immature neurons and interneurons of the same type. Paired recordings are also feasible to record from neurons coupled via gap junctions and to characterize their electrical properties such as the coupling coefficient and junctional conductance (Galarreta and Hestrin, 1999; Gibson et al., 1999). When combining with the biocytin labeling, the morphological properties of gap junctions can be studied at both light and electron microscopic levels as described below (Tamas et al., 2000).

Paired (or multiple) recordings allow to study the organization principles of neuronal networks and shed light on their fundamental features. Previous connectivity studies suggest that neuronal networks are not randomly connected but may have a fine-scale specificity of connectivity (Song et al., 2005; Brown and Hestrin, 2009; Yu et al., 2009; Ko et al., 2011; Perin et al., 2011; Jiang et al., 2013; Cossell et al., 2015). For example, it was demonstrated that two excitatory neurons are more likely to be connected if they share a common neighbor, the so-called "common neighbor rule," in neuronal networks of cortical layers 2/3 and 5 (Song et al., 2005; Ko et al., 2011; Perin et al., 2011). The preference of connection formation between two excitatory neurons also depends on their long-range axonal targets (Brown and Hestrin, 2009), developing origins (Yu et al., 2009) and orientation selectivities (Ko et al., 2011).

Morphological and/or Molecular Characterization of Synaptic Connections

For a detailed characterization of the morphological properties of synaptic connections, an optimal biocytin filling and a careful histochemical processing are of major importance. We have optimized these procedures in our laboratory (see Marx et al., 2012; Radnikow et al., 2012; Qi et al., 2015; Feldmeyer and Radnikow, 2016).

Following histochemical processing biocytin-labeled neuronal cell pairs are inspected under the light microscope using a 100× or a 50× oil immersion objective. Oil immersion objectives with a high numerical aperture (= 1.4) have to be used in order to focus throughout the entire slice thickness (∼300 µm). Computer-assisted 3D neuronal reconstructions are made using the Neurolucida® system (Microbrightfield). This is a neuroanatomical reconstruction system for tracing the neuronal somatodendritic and axonal branches in all three dimensions (3D). Tracing is normally done manually; automatic or semi-automatic tracing approaches are often not applicable because of the dense and profuse branching of the dendritic branches and in particular axonal collaterals of the pre- and postsynaptic neurons (**Figure 2A**). Dendrites and axons are traced at high resolution, i.e., with 0.5–1.0 µm step size in z-direction. Furthermore, frequent alignments in the *x*, *y*, and *z*-dimensions of the neurons are required.

To identify synaptic contacts formed between the pre- and postsynaptic neurons a light microscope with the highest magnification [e.g., 1000×, 100× objective (oil immersion) and 10× eyepiece] is used. Putative synaptic contacts are defined as locations where a presynaptic axonal bouton comes near or overlaps with a dendritic spine or shaft of the postsynaptic neuron at the same focus (**Figure 2A**). Then, the spatial distribution of putative synaptic contacts on postsynaptic somatodendritic compartments can be determined (**Figure 2B**). In order to verify putative synaptic contacts identified under a light microscope a subsequent electron microscopic (EM) analysis is required (Markram et al., 1997a; Feldmeyer et al., 2002); under EM pre- and postsynaptic axonal boutons and dendritic spines or shafts, respectively, can be identified unambiguously (**Figure 2A**).

A quantitative morphological analysis of reconstructed neurons can be performed using the Neuroexplorer® (Microbrightfield) software. This software extracts parameters including the length of axonal and dendritic branches, the degree of arborization, the orientation etc., which can be used to classify neuronal cell types, e.g., by using the cluster analysis. Furthermore, morphological data about the axonal and dendritic arborization of the pre- and postsynaptic neurons can be further processed to calculate axonal and dendritic length 'density maps' (**Figure 2C**) (Lubke et al., 2003; Narayanan et al., 2015). These "density maps" could reflect a general pattern of axonal or dendritic length distribution across the layers and columns. By calculating the product of the presynaptic axonal density with the postsynaptic dendritic density, the average 'innervation domains'

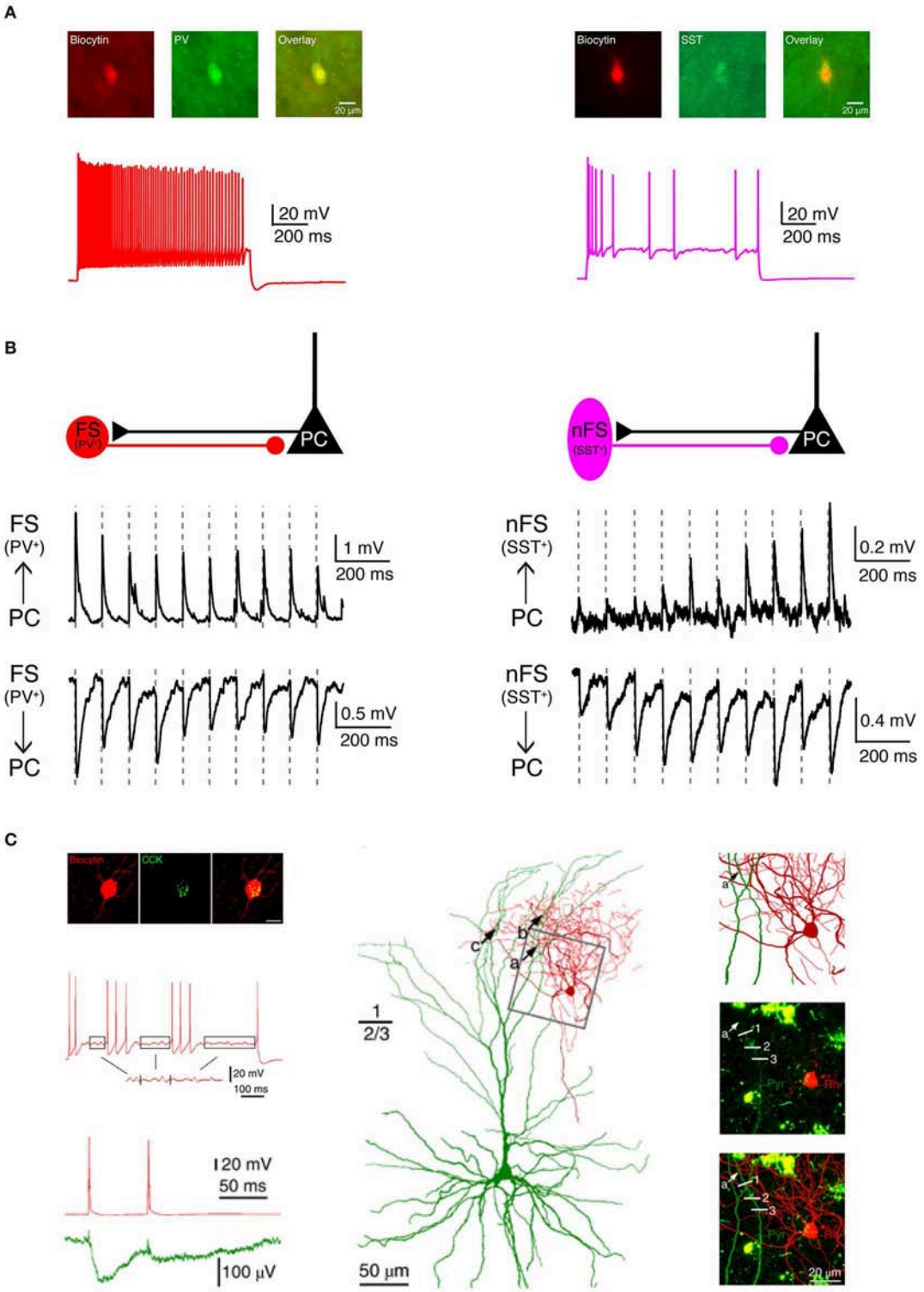

FIGURE 3 | Electrophysiological, morphological and molecular characterization of synaptic connections by combining paired recordings with immuno-fluorescent stainings for specific marker proteins. **(A)** Two main types of GABAergic interneurons in the neocortex are PV^+ fast spiking interneurons (left, red) which express the Ca^{2+}-binding protein parvalbumin (PV) and SST^+ non-fast spiking interneurons (right, violet) which express the neuropeptide somatostatin (SST). **(B)** Two interneuron types form synaptic connections with different characteristics. Left, PV^+ fast spiking interneurons receive initially strong but quickly depressing EPSPs from neighboring excitatory neurons. At the same time, they produce depressing IPSPs in synaptically connected neighboring excitatory neurons. Right, SST^+ non-fast

(Continued)

FIGURE 3 | spiking interneurons, in contrast, receive initially weak and gradually facilitating EPSPs from neighboring excitatory neurons and in turn elicit facilitating IPSPs in their target excitatory neurons. **(C)** Boldog et al. identified a specialized human cortical GABAergic cell type, the so-called L1 rosehip cell (RC). L1 RCs express cholecystokinin (CCK), but not PV, SST, or other molecular markers. L1 RCs exhibit an intermittent non-fast spiking firing pattern with subthreshold membrane potential oscillations (boxed segments). By combining paired recordings with Ca^{2+} imaging the authors were able to demonstrate that L1 RCs establish inhibitory synapses onto apical dendritic tufts of L2/3 pyramidal cells to regulate the AP backpropagation in a segment-specific manner. Electrical signals and morphologies of L1 RCs are in red and those of L2/3 pyramidal cells in green. **(A,B)** have been adapted from Feldmeyer et al. (2018) with permission and **(C)** from Boldog et al. (2018) with permission.

can be determined (**Figure 2C**). Such 'innervation domains' delineate the probability distribution of synaptic contacts for an identified synaptic microcircuit (Lubke et al., 2003; Stepanyants and Chklovskii, 2005).

In addition to biocytin labeling alone, a combination with immunofluorescent staining is also possible, e.g., for specific molecular marker proteins such as Ca^{2+}-binding protein/neuropeptide like parvalbumin, somatostatin, vasoactive intestinal polypeptide (VIP), cholecystokinin (CCK) or transcription factor like Fez2, CTIP2, Foxp2 for different inhibitory and excitatory neuron types, respectively (**Figures 3A,C**). For this, the neuron is filled with biocytin and a biocytin-conjugated fluorescent dye during the electrophysiological recording (e.g., Alexa Fluor 594) so that it is easily distinguished from other neurons after paraformaldehyde fixation. In a second step, immunofluorescent staining is performed after brief period of fixation (<1 day) using a primary antibody for the marker protein and a secondary antibody coupled to a fluorosphore. Finally, the neuron is permanently stained via the biocytin-horseradish peroxidase (HRP) reaction in which diaminobenzidine (DAB) is converted in a dark brownish precipitate. This allows high resolution morphological reconstructions of the labeled neurons (**Figure 3C**). It should be noted, however, that this multiple staining protocol may compromise the efficiency and quality of the biocytin-HRP staining to some extent, especially when the waiting time between fluorescence imaging and DAB processing is too long, making reconstructions of the neuronal morphology less reliable.

UNCOVERING THE QUANTAL PROPERTY OF SYNAPTIC TRANSMISSION BETWEEN IDENTIFIED CORTICAL NEURONS

As described above, postsynaptic responses in postsynaptic neurons induced by presynaptic neuronal firing fluctuate in amplitude with time; in some trials the presynaptic AP may even fail to elicit a PSP. These fluctuations have been interpreted in the framework of the quantal analysis of synaptic transmission. Quantal analysis extracts the basic functional properties of synapses from postsynaptic responses using statistical models based on some assumptions (for review, see Korn and Faber, 1991). It can give an insight into the function of synapses and identify the locus of changes in synaptic strength (Stevens, 1993). Three parameters are adopted to describe the synaptic properties: the number of release sites (N), the release probability (p), and the amplitude of postsynaptic response following a single vesicle release—the quantum (q). The size of postsynaptic response and its variability are determined by these quantal parameters. Presynaptic modulation is related to p (i.e., the release probability), while postsynaptic changes (i.e., in the number of postsynaptic receptors etc.) are related to q. The formation of new contacts would be related to a change in N. In addition, an increase in p from zero at existing release sites in so-called "silent" synapses could also be treated as an increase in N. In the past years, paired recordings in different preparations including the neocortex, hippocampus, striatum, and cerebellum have been extensively used to uncover the values for parameters N, p, and q of synaptic connections (Bekkers and Stevens, 1990; Malinow and Tsien, 1990; Larkman et al., 1991; Gulyas et al., 1993; Isaac et al., 1995; Liao et al., 1995; Scheuss et al., 2002; Silver et al., 2003; Koos et al., 2004; Biro et al., 2005; Saviane and Silver, 2006; Bremaud et al., 2007; Hardingham et al., 2010; Huang et al., 2010; Molnar et al., 2016).

Using the frog neuromuscular junction preparation, del Castillo and Katz (Del Castillo and Katz, 1954) found that several peaks appear in the PSP amplitude histogram. Later, it has been shown that the number of peaks matched the number of anatomical synaptic contacts and the location of peaks is always multiple of that in the miniature PSP amplitude histogram, which led to postulate of the "one-site/one-vesicle" hypothesis (Del Castillo and Katz, 1954; Korn et al., 1981). However, at most synapses the PSP amplitude histogram displays no clear peaks. Therefore, more sophisticated methods have been introduced so that quantal analysis can be applied more generally. Clements and Silver developed the variance-mean (V-M) analysis of synaptic transmission, also called multiple probability fluctuation analysis, MPFA (Clements and Silver, 2000). The variance and mean are calculated from the fluctuation of PSP amplitudes in response to a presynaptic AP. A fundamental feature of this method is that it explores the fluctuation of synaptic responses at different p (induced by altering the extracellular Ca^{2+} concentration) (**Figure 4C**), therefore it can provide more information about the underlying synaptic mechanisms because of multiple points in V-M plot. Assuming that the vesicle release follows a binomial model, a plot of the variance vs. the mean of synaptic responses at different p displays a parabolic relationship. From the V-M plot, the values for N, p, and q can be estimated (**Figure 4D**). Scheuss and Neher further extended the application of the V-M analysis to the synaptic response during a train of APs (Scheuss and Neher, 2001). Instead of changing p by altering extracellular [Ca^{2+}], this method allows to sample from a dynamic p, i.e., the PSP amplitude variation during AP

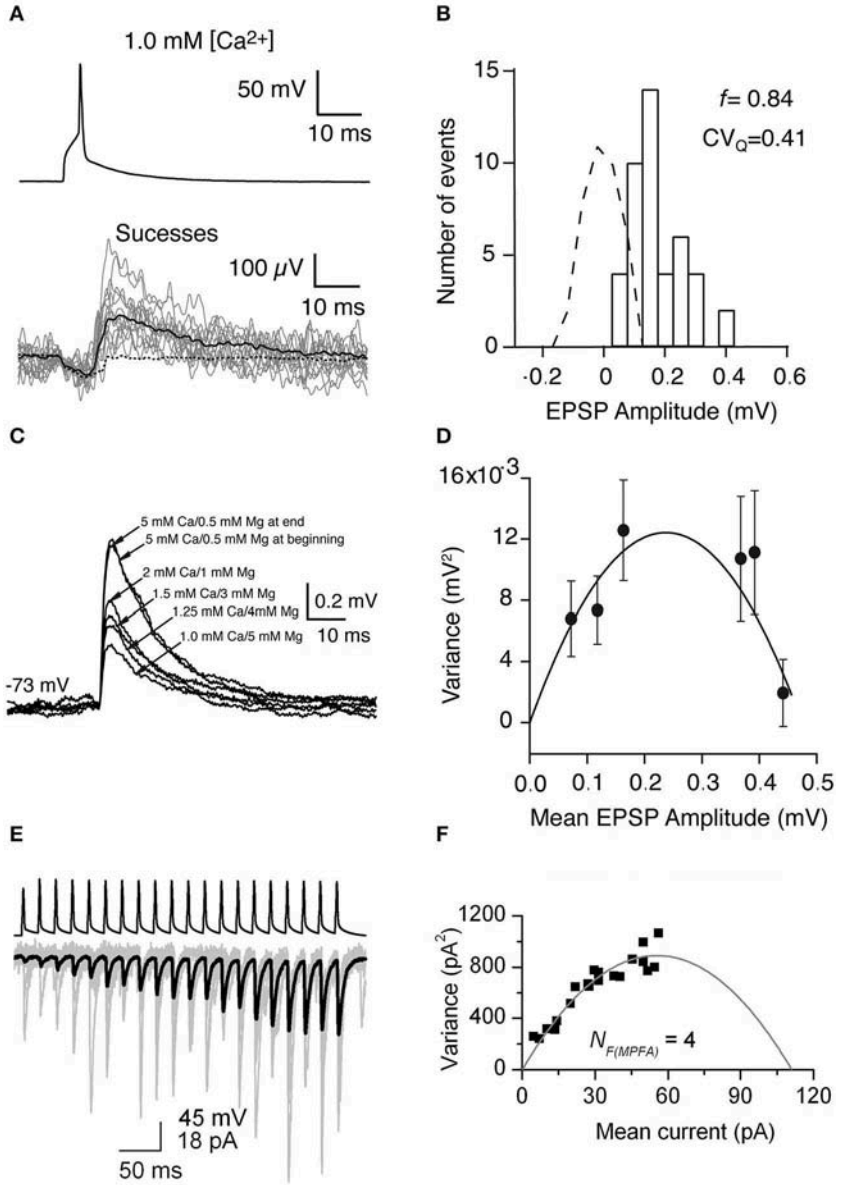

FIGURE 4 | Uncovering quantal properties of synaptic transmission between identified cortical neurons. **(A)** Top, the single AP evoked by a brief suprathreshold depolarizing current pulse. Bottom, 14 individual EPSPs (gray traces), the mean of the 44 EPSP successes (black solid line), and the mean of the 279 failures (black dashed line) recorded at −72 mV in 1 mM [Ca^{2+}] and 5 mM [Mg^{2+}]. **(B)** Histogram of EPSP amplitude and scaled baseline noise (dashed line). For EPSP recordings from this specific synaptic connection, the failure rate (f) is 0.84 and the coefficient of variation of the quantal EPSP amplitude (CV_Q) is 0.41 which was calculated from the background-subtracted variance. **(C)** Mean EPSPs recorded in different extracellular Ca^{2+} and Mg^{2+} concentrations at a postsynaptic membrane potential of −73 mV. **(D)** Relationship between the variance of the EPSP amplitude which was corrected for background variance and mean EPSP amplitude for a synaptically coupled L4-L2/3 cell pair. Each data point shows a different release probability condition. Error bars indicate the theoretical standard error in the estimate of the variance. Solid line shows the fit to a multinomial model with $q = 0.09$ mV, $N_F = 5.25$, and $\alpha = 19{,}800$. **(E)** A brief train of 20 APs (top) in a presynaptic CA1 pyramidal cell evoke facilitating EPSCs in an oriens-alveus interneuron. Individual EPSCs are shown in gray and the averaged EPSC in black. **(F)** Relationship between the variance values of the postsynaptic responses which were calculated at each AP of the train and the mean current. A multinomial quantal model was fitted to the data, resulting in an $N_{F(MPFA)}$ of 4, and a q of 24.7 pA. **(A–D)** have been adapted from Silver et al. (2003) with permission and **(E,F)** from Biro et al. (2005) with permission.

train in the presynaptic neuron (**Figures 4E,F**). In this way, the experimental protocol is simplified because prolonged recordings are not necessary. Therefore, this approach is more readily usable.

In addition to the aforementioned univesicular release hypothesis (UVR), a multivesicular release hypothesis (MVR) has been proposed, where several vesicles are released at a single synaptic site. Recent studies in the neocortex of rodents and humans have supplied controversial evidence regarding uni- and multivesicular release. It has been reported that synaptic connections between layer 4 excitatory neurons and layer 2/3 pyramidal cells in the rat barrel cortex exhibit the UVR (Silver et al., 2003). In contrast, synaptic connections between

layer 4 excitatory neurons exhibit either UVR in the primary visual cortex or MVR in the primary somatosensory cortex of mice (Huang et al., 2010). Synaptic connections between layer 5B pyramidal cells also exhibit MVR in the developing and adult somatosensory cortex of rats (Rollenhagen et al., 2018; Barros-Zulaica et al., 2019). Depending on the species, synaptic connections between pyramidal cells and interneurons exhibit either UVR in the rat neocortex or MVR in the human neocortex (Molnar et al., 2016). Therefore, transmitter release at different synaptic connections can be mediated by UVR or MVR depending on the synapse type, the cortical area and the species.

STUDYING THE REGULATION OF SYNAPTIC TRANSMISSION BY NEUROMODULATORS

Given that synaptic transmission between individual neuron pairs is the basic unit in information processing in the brain, it is crucial to understand how synaptic transmission is dynamically regulated by neuromodulators. Neuromodulator receptors are ubiquitously distributed in the brain and can be found on both dendrites and axon terminals of excitatory and inhibitory neurons (Marder, 2012). Most neuromodulators, such as acetylcholine, norepinephrine, dopamine, serotonin etc., are synthesized by a relatively small population of neurons located in several distinct nuclei in the basal forebrain, midbrain or brainstem. These neuromodulator-releasing neurons have long-range axonal afferents that project to many cortical areas. Once released from their axon terminals, neuromodulators can diffuse over substantial distances and act on receptors remote from their release sites (a mechanism termed "volume transmission") (Zoli et al., 1999; Agnati et al., 2010). Other neuromodulators, such as adenosine and different types of neuropeptides (e.g., VIP, Neuropeptide Y), are locally synthesized and released by neurons and/or glial cells during neuronal network activity. Synaptic transmission between synaptically coupled neurons are constantly under the influence of neuromodulators. The effect of these neuromodulators can change the function and dynamics of cortical microcircuits in a differential way because the receptor types and their distribution may differ in pre- and postsynaptic neurons. The effects of neuromodulators can be studied by bath-application of the specific neuromodulator, their agonists and antagonists. In this way, the exact concentration of applied compounds at equilibrium is known and hence pharmacological approaches, including dose-response relationships can be applied easily to dissect the molecular mechanisms of neuromodulator effects. Bath-application of neuromodulators at different concentrations might correspond to physiological concentrations of neuromodulatory release at different brain states. For example, in the neocortex, the acetylcholine concentration changes dramatically during sleep, wakefulness, arousal and sustained attention (Himmelheber et al., 2000; Teles-Grilo Ruivo et al., 2017). It is worth noting that the concentration of bath-applied agonists needs to be carefully adjusted in the physiologically meaningful range, e.g., 1–10 μM for acetylcholine. Excessive concentrations (>100 μM for acetylcholine) should be avoided in order not to distort the quantification of the synaptic effects of neuromodulators. The effects of neuromodulators can also be studied by local puff-application of the neuromodulator itself or one of its agonists/antagonists; however, with this method the actual concentration of the neuromodulator is not known. In this way transient components of the response can be detected; this is not possible when using bath-application. By combining local puff-application of neuromodulator agonists with bath-application of neuromodulator antagonists, the subtypes of neuromodulator receptors can be determined pharmacologically. Recently, optogenetic stimulation of specific types of neuromodulator afferents (e.g., cholinergic afferents from the basal forebrain) has been applied to detect synaptic responses to the endogenous release of neuromodulators (Hedrick and Waters, 2015; Urban-Ciecko et al., 2018). Below, acetylcholine and adenosine are chosen as examples to illustrate the regulation of synaptic transmission by neuromodulators.

Acetylcholine (ACh) plays an important role in arousal, attention and vigilance. In the neocortex, ACh is released mainly from axonal boutons of neurons located in the nucleus basalis of Meynert in the basal forebrain. Cholinergic afferent terminals are distributed at high density throughout the cortical layers (Kalmbach et al., 2012). It has been proposed that most of the intra-cortical ACh is not released at synaptic contacts but rather diffusely into the extracellular space, i.e., by volume transmission. However, some evidence suggests that phasic release exists ubiquitously in the cortical cholinergic system (Sarter et al., 2009). The effects of ACh in the neocortex are mediated by two types of ACh receptors, the G-protein-coupled muscarinic AChRs (mAChRs) and the nicotinic AChR ion channels (nAChRs). It has been shown that ACh affects excitatory synaptic transmission by causing either a reduction or an increase in the release probability. An ACh-induced reduction in release probability has been shown through paired recordings of excitatory L4-L4 (**Figures 5A,B**) and L4-L2/3 (**Figures 5C,D**) synaptic connections in the rat barrel cortex (Eggermann and Feldmeyer, 2009) which exhibited a decreased EPSP amplitude and increased failure rate, variability and PPR. M_4 mAChRs located in presynaptic L4 axonal terminals caused the suppression of synaptic release probably by decreasing the open probability of presynaptic Ca^{2+} channels. Such a suppressive effect of ACh was also found in excitatory connections established by L2/3 and L5 pyramidal neurons (Levy et al., 2006, 2008). In layer 6, the ACh effect on synaptic transmission depends on the presynaptic neuron type: ACh decreases the synaptic release probability of L6 cortico-cortical pyramidal neurons to other excitatory and inhibitory neurons via activating the presynaptically located M_4 mAChRs. In contrast, ACh enhances the synaptic transmission originating from L6A cortico-thalamic pyramidal neurons via activating the α_4/β_2 nAChRs located at presynaptic axonal terminals (Yang et al., 2019). A similar nicotinic enhancement effect of ACh was found both *in vitro* and *in vivo* at synaptic connections between L2 pyramidal neurons and somatostatin-expressing interneurons (Urban-Ciecko et al., 2018).

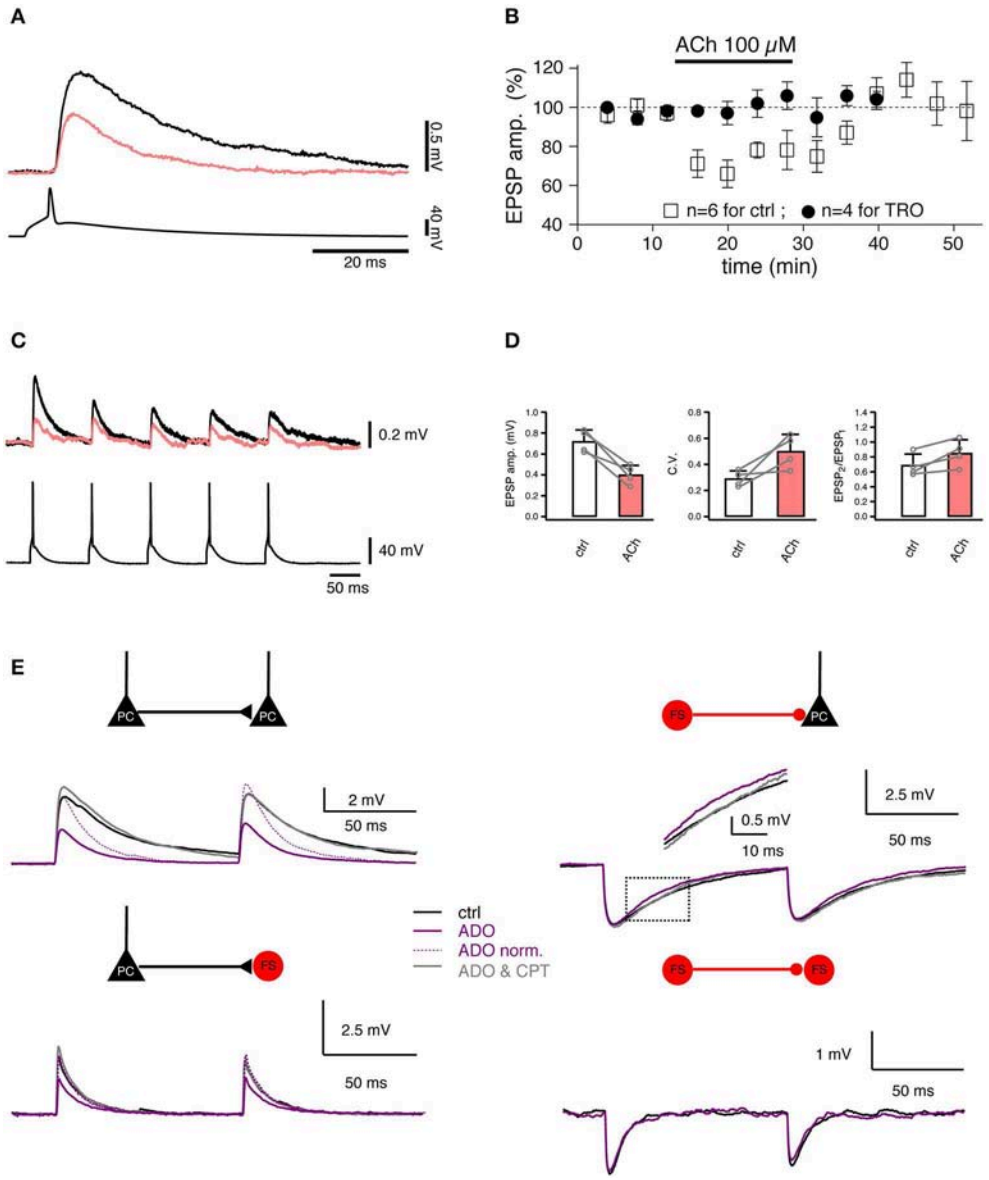

FIGURE 5 | Studying the regulation of synaptic transmission by neuromodulators. **(A)** Paired recordings from a synaptic connection between two L4 spiny neurons. Bath-applied acetylcholine (ACh, 100 μM) reduces the EPSP amplitude (coral trace). **(B)** Time course of the ACh effect on the first EPSP amplitude [open boxes, control; filled circles, in the presence of 1 μM tropicamide (TRO), a selective M_4 muscarinic acetylcholine receptor antagonist]. **(C)** Paired recordings from a synaptic connection between a L4 spiny neuron and a L2/3 pyramidal cell. A train of five APs elicited in a presynaptic L4 spiny neuron (bottom) evoked EPSPs in a postsynaptic L2/3 pyramidal cell (top) in the control condition (black) and in the presence of 100 μM ACh (coral). **(D)** Summary of the effects in L4-to-L2/3 connections ($n = 4$) in the control condition (black open box) and in the presence of 100 μM ACh (coral filled box). Left, the EPSP amplitude. Middle, the coefficient of variation (C.V.). Right, the paired-pulse ratio. Open circles are values for individual connections, connecting lines indicate the direction of change. Error bars indicate the standard deviation. **(E)** Paired recordings from synaptic connections formed between L4 spiny neurons, between L4 spiny neurons and L4 interneurons, and between L4 interneurons show that adenosine (ADO) differentially modulate the excitatory and inhibitory synaptic transmission. Overlay of average EPSPs recorded under three recording conditions: control (black), 100 μM adenosine (purple), and 100 μM adenosine plus 5 μM 8-cyclopentyltheophylline (CPT), a specific adenosine A1 receptor antagonist (gray) are shown for four connection types. **(A–D)** have been adapted from Eggermann and Feldmeyer (2009) with permission and **(E)** from Qi et al. (2017) with permission.

In contrast to ACh, adenosine is an endogenous neuromodulator which is generated during high neuronal activity, e.g., by the intra- and extracellular metabolism of adenosine triphosphate. Adenosine has been suggested to play an important role in the sleep homeostasis (Porkka-Heiskanen et al., 1997, 2000). Recently, the effect of adenosine on synaptic transmission has been assessed using paired recordings (Kerr et al., 2013; Qi et al., 2017). Adenosine induces a suppression of the neurotransmitter release probability at intralaminar L2/3, L4, and L5 and translaminar L4-L2/3 excitatory connections. The adenosine effect is most likely mediated by A_1 adenosine receptors located in presynaptic axonal terminals; they induce a

reduction in the open probability of presynaptic Ca^{2+} channels involved in triggering the release of neurotransmitters. This effect is already apparent at low endogenous concentrations of adenosine (∼1 μM) which are tonically released (Qi et al., 2017). In contrast, adenosine has a much smaller effect on inhibitory synaptic transmission onto excitatory neurons: here, only the IPSP time course is altered due to activation of postsynaptically located A_1 adenosine receptors. There is no effect on inhibitory synaptic transmission onto interneurons (**Figure 5E**).

In addition to ACh and adenosine, a synapse type-dependent neuromodulation has also been found for other neuromodulators such as dopamine. Paired recordings from pyramidal cells and interneurons in ferret prefrontal cortex showed that dopamine depresses excitatory transmission between two pyramidal cells through D_1 receptor actions at a presynaptic site (Gao et al., 2001) but has no effect on excitatory transmission between pyramidal cells and fast-spiking (FS) interneurons (Gao and Goldman-Rakic, 2003). In addition, dopamine differentially modulates inhibition of pyramidal cells from FS vs. non-FS interneurons. Dopamine decreases release of GABA onto pyramidal cells through effects on presynaptic D_1 receptors on axonal terminals of FS interneurons, whereas inhibition from non-FS interneurons onto pyramidal cells is enhanced, presumably owing to a postsynaptic effect (Gao et al., 2003). Similarly, differential modulatory effects of dopamine on different types of synaptic transmission in the medial prefrontal cortex (Dembrow et al., 2010; Dembrow and Johnston, 2014) and neostriatum (Tecuapetla et al., 2007, 2009) have also been found. In summary, the effect of neuromodulators on synaptic transmission depends on the synapse type which is determined by both presynaptic and postsynaptic neuronal identities.

OUTLOOK

Paired recordings from synaptically coupled excitatory and/or inhibitory neurons are a powerful technique to investigate the structure-function relationship of synaptic microcircuits at the subcellular, cellular, and network level. It allows the simultaneous electrophysiological, morphological and/or molecular analysis of both the pre- and postsynaptic neurons in synaptic connections. This is as yet difficult if not impossible for other techniques using extracellular (electrical or optical) stimulation of presynaptic neurons, see e.g., Crochet et al. (2005) and Pala and Petersen (2018). In addition, long-time stable paired recordings permit an in-depth characterization of a defined unitary synaptic connection using, e.g., the quantal analysis. Furthermore, agonist and/or antagonist can be applied readily to neurons in slice preparations (and even spatially focussed), which allows studying the effects of neuromodulators on the synaptic transmission. However, to appreciate the insight obtained from paired recordings in brain slices, one needs to be aware of several shortcomings.

A major disadvantage of slice preparations is the often substantial truncation of axonal branches so that only parts of the axon are reserved in the 300–400 μm-thick brain slice. For some pyramidal cell types, the degree of truncation could be up to 90% when taking into account projections to other cortical or subcortical areas (Stepanyants et al., 2009; Narayanan et al., 2015). Therefore, the slice preparation is not suited for the study of synaptic connections between neurons whose cell bodies are more than >300 μm in the lateral direction. For studying synaptic connections between neurons with inter-soma distances >500 μm within the same column, e.g., translaminar L2/3-to-L5 or L4-to-L6 connections (Reyes and Sakmann, 1999; Qi and Feldmeyer, 2016), paired recordings in the slice preparation is still usable when the slicing procedure is optimized. However, *local* axonal projections, in particular those of interneurons are generally recovered with a relatively low degree of truncation (∼10% or less) (Koelbl et al., 2015; Emmenegger et al., 2018) because of their limited horizontal and vertically projections (see **Movie S1**). Synaptic connections involving these neuron types can therefore be characterized with high accuracy and reliability and their connectivity estimates are largely correct. Except for these local synaptic connections, absolute values for connectivity ratios between two neuron types obtained in slice preparations are highly questionable, in particular for those with large inter-somatic distances such as translaminar or non-local intralaminar synaptic connections. This problem is even more prominent when slicing procedures have not been optimized for a given synaptic connection at a defined developmental stage. Another problem for connectivity estimates is that distal synaptic contacts, e.g., those on the apical tuft dendrites of pyramidal neurons, may escape detection (Williams and Stuart, 2002, 2003). When recorded at the soma the amplitude of their synaptic response is very small and therefore likely to be obscured by electrical noise. However, this type of problem is not confined to the paired recording approach but could also arise in other techniques adopted to study the synaptic connectivity.

In recent years light-induced activation of neurons by photo-release of caged glutamate (Callaway and Katz, 1993) or by activation of channelrhodopsin-2 channels expressed in different neuronal compartments, e.g., soma, dendrites (Boyden et al., 2005), or axonal terminals (Petreanu et al., 2007) has been used to investigate neuronal microcircuits on a larger scale. However, it is so far not possible to identify the detailed structural properties of presynaptic neurons with these optical approaches. Furthermore, the number and location of synaptic contacts for a synaptic connection cannot be identified. Paired recordings, however, allow a detailed characterization of both pre- and postsynaptic neurons and their synaptic contacts in a synaptic connection. This is of paramount importance because many studies have demonstrated that both GABAergic interneurons and glutamatergic excitatory neurons in the neocortex are highly diverse with respect to their morphologies and synaptic properties. Therefore, the identification of both pre- and postsynaptic neurons is necessary for a deep characterization of a synaptic connection.

To enhance the success rate of recording synaptic connections in local neuronal microcircuits, the number of simultaneously recorded neurons (*n*) has been increased from dual (2), triple (3), quadruple (4), octuple (8) up to 12 (Thomson et al., 2002; Song et al., 2005; Kampa et al., 2006; Brown and Hestrin, 2009; Lefort et al., 2009; Yu et al., 2009; Ko et al., 2011; Perin et al.,

2011; Rieubland et al., 2014; Jiang et al., 2015; Guzman et al., 2016; Peng et al., 2017; Hemberger et al., 2019). Multiple ($n > 2$) recordings may yield more synaptic connections because the number of potential synaptic connections (m) established between n neurons increases steeply with increasing n: $m = n \times (n-1)$. However, multiple recordings especially when $n > 4$ have several shortcomings compared to paired recordings. First, the mechanical stability will decrease the more electrodes are placed together in the recordings chamber while the electrical noise of the recording will increase substantially because of capacitive coupling (electrical "cross-talk") in multichannel electrophysiology experiments. This is particularly problematic when the two recorded signals are not of similar amplitude as is the case in paired recordings (presynaptic AP vs. small postsynaptic response) (Nelson et al., 2017). It is likely to decrease the probability of successful, high resolution recordings from a large number of neurons. In addition, the quality of the measured signals (i.e., the signal to-noise ratio of the recordings) will also deteriorate so that the detection of small PSPs (10–20 μV) is severely compromised (Seeman et al., 2018). Furthermore, the time for recording from an individual synaptic connections will be relatively short, i.e., the characterization of this connection limited because of the restricted overall total recording time for all possible synaptic connections. Therefore, a detailed functional characterization of the properties of unitary PSPs (e.g., quantal analysis) is very difficult. Moreover, when biocyin is added to pipettes during multiple recordings, many neurons will be stained in the same slice after the histochemical processing, which makes a reliable and complete reconstruction of neuronal morphology (including both the dendritic and axonal branches) extremely complicated if not impossible, especially when more than two interneurons with a dense axonal plexus are involved. Finally, the estimate of connectivity ratios for all connection types using multiple recordings in the same slice preparation is likely to be unreliable in particular for translaminar or non-local intralaminar synaptic connections because the slicing procedure is optimal only for a few specific connection types (mainly the local ones) but not for the majority. This problem could be overcome in paired recordings through optimizing the slicing procedure for *specific* types of synaptic connections. Despite of aforementioned shortcomings that exist so far, multiple recordings show great promise for future high-throughput analysis of cortical microcircuits in rodent and more precious human brains (Peng et al., 2019).

Not only cortical inhibitory but also excitatory neurons show a high diversity (Zeng and Sanes, 2017). To directly target specific neuronal subpopulations, paired recordings have been conducted in acute brain slices from transgenic animals where one specific or several populations of neurons are labeled by fluorescent groups (e.g., GFP, YFP, tdTomato etc.) as in transgenic, knock-in animals or via viral infection (Pfeffer et al., 2013; Seeman et al., 2018). Paired recordings can be combined easily with other cutting-edge techniques, such as optogenetics, Ca^{2+} imaging, activity-dependent immediate early gene expression and pseudorabies virus retrograde tracing etc. (Wickersham et al., 2007; Yassin et al., 2010; Ko et al., 2011; Jouhanneau et al., 2014; Lee et al., 2014; Cossell et al., 2015; Morgenstern et al., 2016). More recently, the paired recording approach has also been adopted to record from synaptically coupled neurons in the intact brain of anesthetized mice (Jouhanneau et al., 2015, 2018). Paired recordings have also been used to investigate the functional and structural properties of synapses in surgically dissected human brain slices (Molnar et al., 2008; Testa-Silva et al., 2010, 2014; Boldog et al., 2018; Seeman et al., 2018). For human tissue, paired recording in slices is still the only method of choice to study the functional neuronal microcircuits in preparations from human brains. Therefore, paired recordings will remain an important approach for studying neuronal microcircuits in different brain regions and species.

AUTHOR CONTRIBUTIONS

GQ generated the figures. GQ and DF wrote the manuscript with comments and suggestions from DY and CD.

FUNDING

This work was supported by the Helmholtz Society and the European Union's Horizon 2020 Research, Innovation Programme under Grant Agreement No. 785907 (Human Brain Project SGA2; to DF).

ACKNOWLEDGMENTS

We thank Werner Hucko for help with immunohistochemical staining and Valerie Wiener for help with morphological reconstruction.

SUPPLEMENTARY MATERIAL

The Supplementary Material for this article can be found online at: https://www.frontiersin.org/articles/10.3389/fnsyn.2020.00005/full#supplementary-material

Movie S1 | Rotation of a 3D morphologically reconstructed parvalbumin+ (PV+), fast-spiking interneuron in layer 4 of rat barrel cortex. The somatodendritic compartment is shown in red and the axon in cyan. Borders between different layers are also shown.

REFERENCES

Abbott, L. F., and Nelson, S. B. (2000). Synaptic plasticity: taming the beast. *Nat. Neurosci.* 3(Suppl.), 1178–1183. doi: 10.1038/81453

Agnati, L. F., Guidolin, D., Guescini, M., Genedani, S., and Fuxe, K. (2010). Understanding wiring and volume transmission. *Brain Res. Rev.* 64, 137–159. doi: 10.1016/j.brainresrev.2010.03.003

Arancio, O., Kandel, E. R., and Hawkins, R. D. (1995). Activity-dependent long-term enhancement of transmitter release by presynaptic 3',5'-cyclic GMP in cultured hippocampal neurons. *Nature* 376, 74–80. doi: 10.1038/376074a0

Atzori, M., Lei, S., Evans, D. I., Kanold, P. O., Phillips-Tansey, E., Mcintyre, O., et al. (2001). Differential synaptic processing separates stationary from transient inputs to the auditory cortex. *Nat. Neurosci.* 4, 1230–1237. doi: 10.1038/nn760

Barbour, B., Brunel, N., Hakim, V., and Nadal, J. P. (2007). What can we learn from synaptic weight distributions? *Trends Neurosci.* 30, 622–629. doi: 10.1016/j.tins.2007.09.005

Barros-Zulaica, N., Rahmon, J., Chindemi, G., Perin, R., Markram, H., Muller, E., et al. (2019). Estimating the readily-releasable vesicle pool size at synaptic connections in the neocortex. *Front. Synaptic. Neurosci.* 11:29. doi: 10.3389/fnsyn.2019.00029

Bekkers, J. M., and Stevens, C. F. (1990). Presynaptic mechanism for long-term potentiation in the hippocampus. *Nature* 346, 724–729. doi: 10.1038/346724a0

Bi, G., and Poo, M. (2001). Synaptic modification by correlated activity: Hebb's postulate revisited. *Annu. Rev. Neurosci.* 24, 139–166. doi: 10.1146/annurev.neuro.24.1.139

Bi, G. Q., and Poo, M. M. (1998). Synaptic modifications in cultured hippocampal neurons: dependence on spike timing, synaptic strength, and postsynaptic cell type. *J. Neurosci.* 18, 10464–10472. doi: 10.1523/JNEUROSCI.18-24-10464.1998

Biro, A. A., Holderith, N. B., and Nusser, Z. (2005). Quantal size is independent of the release probability at hippocampal excitatory synapses. *J. Neurosci.* 25, 223–232. doi: 10.1523/JNEUROSCI.3688-04.2005

Boldog, E., Bakken, T. E., Hodge, R. D., Novotny, M., Aevermann, B. D., Baka, J., et al. (2018). Transcriptomic and morphophysiological evidence for a specialized human cortical GABAergic cell type. *Nat. Neurosci.* 21, 1185–1195. doi: 10.1038/s41593-018-0205-2

Bolshakov, V. Y., and Siegelbaum, S. A. (1995). Regulation of hippocampal transmitter release during development and long-term potentiation. *Science* 269, 1730–1734. doi: 10.1126/science.7569903

Borst, J. G. (2010). The low synaptic release probability *in vivo*. *Trends Neurosci.* 33, 259–266. doi: 10.1016/j.tins.2010.03.003

Boyden, E. S., Zhang, F., Bamberg, E., Nagel, G., and Deisseroth, K. (2005). Millisecond-timescale, genetically targeted optical control of neural activity. *Nat. Neurosci.* 8, 1263–1268. doi: 10.1038/nn1525

Bremaud, A., West, D. C., and Thomson, A. M. (2007). Binomial parameters differ across neocortical layers and with different classes of connections in adult rat and cat neocortex. *Proc. Natl. Acad. Sci. U.S.A.* 104, 14134–14139. doi: 10.1073/pnas.0705661104

Brette, R., and Destexhe, A. (2012). "Intracellular recording," in *Handbook of Neural Activity Measurement*, eds R. Brette and A. Destexhe (Cambridge: Cambridge University Press), 44–91.

Brown, S. P., and Hestrin, S. (2009). Intracortical circuits of pyramidal neurons reflect their long-range axonal targets. *Nature* 457, 1133–1136. doi: 10.1038/nature07658

Brunel, N., Hakim, V., Isope, P., Nadal, J. P., and Barbour, B. (2004). Optimal information storage and the distribution of synaptic weights: perceptron versus Purkinje cell. *Neuron* 43, 745–757. doi: 10.1016/S0896-6273(04)00528-8

Buhl, E. H., Halasy, K., and Somogyi, P. (1994). Diverse sources of hippocampal unitary inhibitory postsynaptic potentials and the number of synaptic release sites. *Nature* 368, 823–828. doi: 10.1038/368823a0

Callaway, E. M., and Katz, L. C. (1993). Photostimulation using caged glutamate reveals functional circuitry in living brain slices. *Proc. Natl. Acad. Sci. U.S.A.* 90, 7661–7665. doi: 10.1073/pnas.90.16.7661

Clements, J. D., and Silver, R. A. (2000). Unveiling synaptic plasticity: a new graphical and analytical approach. *Trends Neurosci.* 23, 105–113. doi: 10.1016/S0166-2236(99)01520-9

Cossell, L., Iacaruso, M. F., Muir, D. R., Houlton, R., Sader, E. N., Ko, H., et al. (2015). Functional organization of excitatory synaptic strength in primary visual cortex. *Nature* 518, 399–403. doi: 10.1038/nature14182

Crochet, S., Chauvette, S., Boucetta, S., and Timofeev, I. (2005). Modulation of synaptic transmission in neocortex by network activities. *Eur. J. Neurosci.* 21, 1030–1044. doi: 10.1111/j.1460-9568.2005.03932.x

Debanne, D., Boudkkazi, S., Campanac, E., Cudmore, R. H., Giraud, P., Fronzaroli-Molinieres, L., et al. (2008). Paired-recordings from synaptically coupled cortical and hippocampal neurons in acute and cultured brain slices. *Nat. Protoc.* 3, 1559–1568. doi: 10.1038/nprot.2008.147

Del Castillo, J., and Katz, B. (1954). Quantal components of the end-plate potential. *J. Physiol.* 124, 560–573. doi: 10.1113/jphysiol.1954.sp005129

Dembrow, N., and Johnston, D. (2014). Subcircuit-specific neuromodulation in the prefrontal cortex. *Front. Neural Circuits* 8:54. doi: 10.3389/fncir.2014.00054

Dembrow, N. C., Chitwood, R. A., and Johnston, D. (2010). Projection-specific neuromodulation of medial prefrontal cortex neurons. *J. Neurosci.* 30, 16922–16937. doi: 10.1523/JNEUROSCI.3644-10.2010

Destexhe, A., Rudolph, M., and Pare, D. (2003). The high-conductance state of neocortical neurons *in vivo*. *Nat. Rev. Neurosci.* 4, 739–751. doi: 10.1038/nrn1198

Deuchars, J., West, D. C., and Thomson, A. M. (1994). Relationships between morphology and physiology of pyramid-pyramid single axon connections in rat neocortex *in vitro*. *J. Physiol.* 478, 423–435. doi: 10.1113/jphysiol.1994.sp020262

Dittman, J. S., Kreitzer, A. C., and Regehr, W. G. (2000). Interplay between facilitation, depression, and residual calcium at three presynaptic terminals. *J. Neurosci.* 20, 1374–1385. doi: 10.1523/JNEUROSCI.20-04-01374.2000

Dodt, H. U., and Zieglgansberger, W. (1990). Visualizing unstained neurons in living brain slices by infrared DIC-videomicroscopy. *Brain Res.* 537, 333–336. doi: 10.1016/0006-8993(90)90380-T

Egger, V., Feldmeyer, D., and Sakmann, B. (1999). Coincidence detection and changes of synaptic efficacy in spiny stellate neurons in rat barrel cortex. *Nat. Neurosci.* 2, 1098–1105. doi: 10.1038/16026

Eggermann, E., and Feldmeyer, D. (2009). Cholinergic filtering in the recurrent excitatory microcircuit of cortical layer 4. *Proc. Natl. Acad. Sci. U.S.A.* 106, 11753–11758. doi: 10.1073/pnas.0810062106

Emmenegger, V., Qi, G., Wang, H., and Feldmeyer, D. (2018). Morphological and functional characterization of non-fast-spiking GABAergic interneurons in layer 4 microcircuitry of rat barrel cortex. *Cereb. Cortex* 28, 1439–1457. doi: 10.1093/cercor/bhx352

Feldmeyer, D., Egger, V., Lubke, J., and Sakmann, B. (1999). Reliable synaptic connections between pairs of excitatory layer 4 neurones within a single 'barrel' of developing rat somatosensory cortex. *J. Physiol.* 521, 169–190. doi: 10.1111/j.1469-7793.1999.00169.x

Feldmeyer, D., Lubke, J., and Sakmann, B. (2006). Efficacy and connectivity of intracolumnar pairs of layer 2/3 pyramidal cells in the barrel cortex of juvenile rats. *J. Physiol.* 575, 583–602. doi: 10.1113/jphysiol.2006.105106

Feldmeyer, D., Lubke, J., Silver, R. A., and Sakmann, B. (2002). Synaptic connections between layer 4 spiny neurone-layer 2/3 pyramidal cell pairs in juvenile rat barrel cortex: physiology and anatomy of interlaminar signalling within a cortical column. *J. Physiol.* 538, 803–822. doi: 10.1113/jphysiol.2001.012959

Feldmeyer, D., Qi, G., Emmenegger, V., and Staiger, J. F. (2018). Inhibitory interneurons and their circuit motifs in the many layers of the barrel cortex. *Neuroscience* 368, 132–151. doi: 10.1016/j.neuroscience.2017.05.027

Feldmeyer, D., and Radnikow, G. (2016). "Paird recordings from synaptically coupled neurones in acute neocortical slices," in *Neuromethods*, ed A. Korngreen (New York, NY: Humana Press), 171–191.

Fino, E., Packer, A. M., and Yuste, R. (2013). The logic of inhibitory connectivity in the neocortex. *Neuroscientist* 19, 228–237. doi: 10.1177/1073858412456743

Frick, A., Feldmeyer, D., Helmstaedter, M., and Sakmann, B. (2008). Monosynaptic connections between pairs of L5A pyramidal neurons in columns of juvenile rat somatosensory cortex. *Cereb. Cortex* 18, 397–406. doi: 10.1093/cercor/bhm074

Galarreta, M., and Hestrin, S. (1999). A network of fast-spiking cells in the neocortex connected by electrical synapses. *Nature* 402, 72–75. doi: 10.1038/47029

Gao, W. J., and Goldman-Rakic, P. S. (2003). Selective modulation of excitatory and inhibitory microcircuits by dopamine. *Proc. Natl. Acad. Sci. U.S.A.* 100, 2836–2841. doi: 10.1073/pnas.262796399

Gao, W. J., Krimer, L. S., and Goldman-Rakic, P. S. (2001). Presynaptic regulation of recurrent excitation by D1 receptors in prefrontal circuits. *Proc. Natl. Acad. Sci. U.S.A.* 98, 295–300. doi: 10.1073/pnas.98.1.295

Gao, W. J., Wang, Y., and Goldman-Rakic, P. S. (2003). Dopamine modulation of perisomatic and peridendritic inhibition in prefrontal cortex. *J. Neurosci.* 23, 1622–1630. doi: 10.1523/JNEUROSCI.23-05-01622.2003

Geiger, J. R., Lubke, J., Roth, A., Frotscher, M., and Jonas, P. (1997). Submillisecond AMPA receptor-mediated signaling at a principal neuron-interneuron synapse. *Neuron* 18, 1009–1023. doi: 10.1016/S0896-6273(00)80339-6

Gibson, J. R., Beierlein, M., and Connors, B. W. (1999). Two networks of electrically coupled inhibitory neurons in neocortex. *Nature* 402, 75–79. doi: 10.1038/47035

Gulyas, A. I., Miles, R., Sik, A., Toth, K., Tamamaki, N., and Freund, T. F. (1993). Hippocampal pyramidal cells excite inhibitory neurons through a single release site. *Nature* 366, 683–687. doi: 10.1038/366683a0

Gupta, A., Wang, Y., and Markram, H. (2000). Organizing principles for a diversity of GABAergic interneurons and synapses in the neocortex. *Science* 287, 273–278. doi: 10.1126/science.287.5451.273

Guzman, S. J., Schlogl, A., Frotscher, M., and Jonas, P. (2016). Synaptic mechanisms of pattern completion in the hippocampal CA3 network. *Science* 353, 1117–1123. doi: 10.1126/science.aaf1836

Hardingham, N. R., and Larkman, A. U. (1998). Rapid report: the reliability of excitatory synaptic transmission in slices of rat visual cortex *in vitro* is temperature dependent. *J. Physiol.* 507, 249–256. doi: 10.1111/j.1469-7793.1998.249bu.x

Hardingham, N. R., Read, J. C., Trevelyan, A. J., Nelson, J. C., Jack, J. J., and Bannister, N. J. (2010). Quantal analysis reveals a functional correlation between presynaptic and postsynaptic efficacy in excitatory connections from rat neocortex. *J. Neurosci.* 30, 1441–1451. doi: 10.1523/JNEUROSCI.3244-09.2010

Hedrick, T., and Waters, J. (2015). Acetylcholine excites neocortical pyramidal neurons via nicotinic receptors. *J. Neurophysiol.* 113, 2195–2209. doi: 10.1152/jn.00716.2014

Heinemann, U., Lux, H. D., and Gutnick, M. J. (1977). Extracellular free calcium and potassium during paroxsmal activity in the cerebral cortex of the cat. *Exp. Brain Res.* 27, 237–243. doi: 10.1007/BF00235500

Helmstaedter, M., Staiger, J. F., Sakmann, B., and Feldmeyer, D. (2008). Efficient recruitment of layer 2/3 interneurons by layer 4 input in single columns of rat somatosensory cortex. *J. Neurosci.* 28, 8273–8284. doi: 10.1523/JNEUROSCI.5701-07.2008

Hemberger, M., Shein-Idelson, M., Pammer, L., and Laurent, G. (2019). Reliable sequential activation of neural assemblies by single pyramidal cells in a three-layered cortex. *Neuron* 104, 353–369.e5. doi: 10.1016/j.neuron.2019.07.017

Himmelheber, A. M., Sarter, M., and Bruno, J. P. (2000). Increases in cortical acetylcholine release during sustained attention performance in rats. *Brain Res. Cogn. Brain Res.* 9, 313–325. doi: 10.1016/S0926-6410(00)00012-4

Holmgren, C., Harkany, T., Svennenfors, B., and Zilberter, Y. (2003). Pyramidal cell communication within local networks in layer 2/3 of rat neocortex. *J. Physiol.* 551, 139–153. doi: 10.1113/jphysiol.2003.044784

Huang, C. H., Bao, J., and Sakaba, T. (2010). Multivesicular release differentiates the reliability of synaptic transmission between the visual cortex and the somatosensory cortex. *J. Neurosci.* 30, 11994–12004. doi: 10.1523/JNEUROSCI.2381-10.2010

Huganir, R. L., and Nicoll, R. A. (2013). AMPARs and synaptic plasticity: the last 25 years. *Neuron* 80, 704–717. doi: 10.1016/j.neuron.2013.10.025

Isaac, J. T., Nicoll, R. A., and Malenka, R. C. (1995). Evidence for silent synapses: implications for the expression of LTP. *Neuron* 15, 427–434. doi: 10.1016/0896-6273(95)90046-2

Isope, P., and Barbour, B. (2002). Properties of unitary granule cell–>Purkinje cell synapses in adult rat cerebellar slices. *J. Neurosci.* 22, 9668–9678. doi: 10.1523/JNEUROSCI.22-22-09668.2002

Jiang, X., Shen, S., Cadwell, C. R., Berens, P., Sinz, F., Ecker, A. S., et al. (2015). Principles of connectivity among morphologically defined cell types in adult neocortex. *Science* 350:aac9462. doi: 10.1126/science.aac9462

Jiang, X., Wang, G., Lee, A. J., Stornetta, R. L., and Zhu, J. J. (2013). The organization of two new cortical interneuronal circuits. *Nat. Neurosci.* 16, 210–218. doi: 10.1038/nn.3305

Jouhanneau, J. S., Ferrarese, L., Estebanez, L., Audette, N. J., Brecht, M., Barth, A. L., et al. (2014). Cortical fosGFP expression reveals broad receptive field excitatory neurons targeted by POm. *Neuron* 84, 1065–1078. doi: 10.1016/j.neuron.2014.10.014

Jouhanneau, J. S., Kremkow, J., Dorrn, A. L., and Poulet, J. F. (2015). *In vivo* monosynaptic excitatory transmission between layer 2 cortical pyramidal neurons. *Cell. Rep.* 13, 2098–2106. doi: 10.1016/j.celrep.2015.11.011

Jouhanneau, J. S., Kremkow, J., and Poulet, J. F. A. (2018). Single synaptic inputs drive high-precision action potentials in parvalbumin expressing GABA-ergic cortical neurons *in vivo*. *Nat. Commun.* 9:1540. doi: 10.1038/s41467-018-03995-2

Jouhanneau, J. S., and Poulet, J. F. A. (2019). Multiple two-photon targeted whole-cell patch-clamp recordings from monosynaptically connected neurons *in vivo*. *Front. Synaptic Neurosci.* 11:15. doi: 10.3389/fnsyn.2019.00015

Kalmbach, A., Hedrick, T., and Waters, J. (2012). Selective optogenetic stimulation of cholinergic axons in neocortex. *J. Neurophysiol.* 107, 2008–2019. doi: 10.1152/jn.00870.2011

Kampa, B. M., Letzkus, J. J., and Stuart, G. J. (2006). Cortical feed-forward networks for binding different streams of sensory information. *Nat. Neurosci.* 9, 1472–1473. doi: 10.1038/nn1798

Kapfer, C., Glickfeld, L. L., Atallah, B. V., and Scanziani, M. (2007). Supralinear increase of recurrent inhibition during sparse activity in the somatosensory cortex. *Nat. Neurosci.* 10, 743–753. doi: 10.1038/nn1909

Kerr, M. I., Wall, M. J., and Richardson, M. J. (2013). Adenosine A1 receptor activation mediates the developmental shift at layer 5 pyramidal cell synapses and is a determinant of mature synaptic strength. *J. Physiol.* 591, 3371–3380. doi: 10.1113/jphysiol.2012.244392

Ko, H., Hofer, S. B., Pichler, B., Buchanan, K. A., Sjostrom, P. J., and Mrsic-Flogel, T. D. (2011). Functional specificity of local synaptic connections in neocortical networks. *Nature* 473, 87–91. doi: 10.1038/nature09880

Koelbl, C., Helmstaedter, M., Lubke, J., and Feldmeyer, D. (2015). A barrel-related interneuron in layer 4 of rat somatosensory cortex with a high intrabarrel connectivity. *Cereb. Cortex* 25, 713–725. doi: 10.1093/cercor/bht263

Koester, H. J., and Johnston, D. (2005). Target cell-dependent normalization of transmitter release at neocortical synapses. *Science* 308, 863–866. doi: 10.1126/science.1100815

Koos, T., Tepper, J. M., and Wilson, C. J. (2004). Comparison of IPSCs evoked by spiny and fast-spiking neurons in the neostriatum. *J. Neurosci.* 24, 7916–7922. doi: 10.1523/JNEUROSCI.2163-04.2004

Korn, H., and Faber, D. S. (1991). Quantal analysis and synaptic efficacy in the CNS. *Trends. Neurosci.* 14, 439–445. doi: 10.1016/0166-2236(91)90042-S

Korn, H., Triller, A., Mallet, A., and Faber, D. S. (1981). Fluctuating responses at a central synapse: n of binomial fit predicts number of stained presynaptic boutons. *Science* 213, 898–901. doi: 10.1126/science.6266015

Kreitzer, A. C., and Regehr, W. G. (2001). Cerebellar depolarization-induced suppression of inhibition is mediated by endogenous cannabinoids. *J. Neurosci.* 21:RC174. doi: 10.1523/JNEUROSCI.21-20-j0005.2001

Larkman, A., Stratford, K., and Jack, J. (1991). Quantal analysis of excitatory synaptic action and depression in hippocampal slices. *Nature* 350, 344–347. doi: 10.1038/350344a0

Lee, A. T., Gee, S. M., Vogt, D., Patel, T., Rubenstein, J. L., and Sohal, V. S. (2014). Pyramidal neurons in prefrontal cortex receive subtype-specific forms of excitation and inhibition. *Neuron* 81, 61–68. doi: 10.1016/j.neuron.2013.10.031

Lefort, S., Tomm, C., Floyd Sarria, J. C., and Petersen, C. C. (2009). The excitatory neuronal network of the C2 barrel column in mouse primary somatosensory cortex. *Neuron* 61, 301–316. doi: 10.1016/j.neuron.2008.12.020

Levy, R. B., Reyes, A. D., and Aoki, C. (2006). Nicotinic and muscarinic reduction of unitary excitatory postsynaptic potentials in sensory cortex; dual intracellular recording *in vitro*. *J. Neurophysiol.* 95, 2155–2166. doi: 10.1152/jn.00603.2005

Levy, R. B., Reyes, A. D., and Aoki, C. (2008). Cholinergic modulation of local pyramid-interneuron synapses exhibiting divergent short-term dynamics in rat sensory cortex. *Brain Res.* 1215, 97–104. doi: 10.1016/j.brainres.2008.03.067

Liao, D., Hessler, N. A., and Malinow, R. (1995). Activation of postsynaptically silent synapses during pairing-induced LTP in CA1 region of hippocampal slice. *Nature* 375, 400–404. doi: 10.1038/375400a0

Lubke, J., Roth, A., Feldmeyer, D., and Sakmann, B. (2003). Morphometric analysis of the columnar innervation domain of neurons connecting layer 4 and layer 2/3 of juvenile rat barrel cortex. *Cereb. Cortex* 13, 1051–1063. doi: 10.1093/cercor/13.10.1051

Ma, Y., Hu, H., and Agmon, A. (2012). Short-term plasticity of unitary inhibitory-to-inhibitory synapses depends on the presynaptic interneuron subtype. *J. Neurosci.* 32, 983–988. doi: 10.1523/JNEUROSCI.5007-11.2012

Malinow, R. (1991). Transmission between pairs of hippocampal slice neurons: quantal levels, oscillations, and LTP. *Science* 252, 722–724. doi: 10.1126/science.1850871

Malinow, R., and Tsien, R. W. (1990). Presynaptic enhancement shown by whole-cell recordings of long-term potentiation in hippocampal slices. *Nature* 346, 177–180. doi: 10.1038/346177a0

Marder, E. (2012). Neuromodulation of neuronal circuits: back to the future. *Neuron* 76, 1–11. doi: 10.1016/j.neuron.2012.09.010

Markram, H., Lubke, J., Frotscher, M., Roth, A., and Sakmann, B. (1997a). Physiology and anatomy of synaptic connections between thick tufted pyramidal neurones in the developing rat neocortex. *J. Physiol.* 500, 409–440. doi: 10.1113/jphysiol.1997.sp022031

Markram, H., Lubke, J., Frotscher, M., and Sakmann, B. (1997b). Regulation of synaptic efficacy by coincidence of postsynaptic APs and EPSPs. *Science* 275, 213–215. doi: 10.1126/science.275.5297.213

Markram, H., Muller, E., Ramaswamy, S., Reimann, M. W., Abdellah, M., Sanchez, C. A., et al. (2015). Reconstruction and simulation of neocortical microcircuitry. *Cell* 163, 456–492. doi: 10.1016/j.cell.2015.09.029

Markram, H., Pikus, D., Gupta, A., and Tsodyks, M. (1998a). Potential for multiple mechanisms, phenomena and algorithms for synaptic plasticity at single synapses. *Neuropharmacology* 37, 489–500. doi: 10.1016/S0028-3908(98)00049-5

Markram, H., Wang, Y., and Tsodyks, M. (1998b). Differential signaling via the same axon of neocortical pyramidal neurons. *Proc. Natl. Acad. Sci. U.S.A.* 95, 5323–5328. doi: 10.1073/pnas.95.9.5323

Marx, M., Gunter, R. H., Hucko, W., Radnikow, G., and Feldmeyer, D. (2012). Improved biocytin labeling and neuronal 3D reconstruction. *Nat. Protoc.* 7, 394–407. doi: 10.1038/nprot.2011.449

Mason, A., Nicoll, A., and Stratford, K. (1991). Synaptic transmission between individual pyramidal neurons of the rat visual cortex *in vitro*. *J. Neurosci.* 11, 72–84. doi: 10.1523/JNEUROSCI.11-01-00072.1991

Massimini, M., and Amzica, F. (2001). Extracellular calcium fluctuations and intracellular potentials in the cortex during the slow sleep oscillation. *J. Neurophysiol.* 85, 1346–1350. doi: 10.1152/jn.2001.85.3.1346

Miles, R., and Poncer, J. C. (1996). Paired recordings from neurones. *Curr. Opin. Neurobiol.* 6, 387–394. doi: 10.1016/S0959-4388(96)80124-3

Miles, R., Toth, K., Gulyas, A. I., Hajos, N., and Freund, T. F. (1996). Differences between somatic and dendritic inhibition in the hippocampus. *Neuron* 16, 815–823. doi: 10.1016/S0896-6273(00)80101-4

Molnar, G., Olah, S., Komlosi, G., Fule, M., Szabadics, J., Varga, C., et al. (2008). Complex events initiated by individual spikes in the human cerebral cortex. *PLoS Biol.* 6:e222. doi: 10.1371/journal.pbio.0060222

Molnar, G., Rozsa, M., Baka, J., Holderith, N., Barzo, P., Nusser, Z., et al. (2016). Human pyramidal to interneuron synapses are mediated by multi-vesicular release and multiple docked vesicles. *Elife* 5:e18167. doi: 10.7554/eLife.18167.008

Montgomery, J. M., Pavlidis, P., and Madison, D. V. (2001). Pair recordings reveal all-silent synaptic connections and the postsynaptic expression of long-term potentiation. *Neuron* 29, 691–701. doi: 10.1016/S0896-6273(01)00244-6

Morgenstern, N. A., Bourg, J., and Petreanu, L. (2016). Multilaminar networks of cortical neurons integrate common inputs from sensory thalamus. *Nat. Neurosci.* 19, 1034–1040. doi: 10.1038/nn.4339

Narayanan, R. T., Egger, R., Johnson, A. S., Mansvelder, H. D., Sakmann, B., De Kock, C. P., et al. (2015). Beyond columnar organization: cell type- and target layer-specific principles of horizontal axon projection patterns in rat vibrissal cortex. *Cereb. Cortex* 25, 4450–4468. doi: 10.1093/cercor/bhv053

Nelson, M. J., Valtcheva, S., and Venance, L. (2017). Magnitude and behavior of cross-talk effects in multichannel electrophysiology experiments. *J. Neurophysiol.* 118, 574–594. doi: 10.1152/jn.00877.2016

Olah, S., Fule, M., Komlosi, G., Varga, C., Baldi, R., Barzo, P., et al. (2009). Regulation of cortical microcircuits by unitary GABA-mediated volume transmission. *Nature* 461, 1278–1281. doi: 10.1038/nature08503

Pala, A., and Petersen, C. C. (2018). State-dependent cell-type-specific membrane potential dynamics and unitary synaptic inputs in awake mice. *Elife* 7:e35869. doi: 10.7554/eLife.35869.020

Peng, Y., Barreda Tomas, F. J., Klisch, C., Vida, I., and Geiger, J. R. P. (2017). Layer-specific organization of local excitatory and inhibitory synaptic connectivity in the rat presubiculum. *Cereb. Cortex* 27, 2435–2452. doi: 10.1093/cercor/bhx049

Peng, Y., Mittermaier, F. X., Planert, H., Schneider, U. C., Alle, H., and Geiger, J. R. P. (2019). High-throughput microcircuit analysis of individual human brains through next-generation multineuron patch-clamp. *Elife* 8:e48178. doi: 10.7554/eLife.48178.sa2

Perin, R., Berger, T. K., and Markram, H. (2011). A synaptic organizing principle for cortical neuronal groups. *Proc. Natl. Acad. Sci. U.S.A.* 108, 5419–5424. doi: 10.1073/pnas.1016051108

Petreanu, L., Huber, D., Sobczyk, A., and Svoboda, K. (2007). Channelrhodopsin-2-assisted circuit mapping of long-range callosal projections. *Nat. Neurosci.* 10, 663–668. doi: 10.1038/nn1891

Pfeffer, C. K., Xue, M., He, M., Huang, Z. J., and Scanziani, M. (2013). Inhibition of inhibition in visual cortex: the logic of connections between molecularly distinct interneurons. *Nat. Neurosci.* 16, 1068–1076. doi: 10.1038/nn.3446

Porkka-Heiskanen, T., Strecker, R. E., and Mccarley, R. W. (2000). Brain site-specificity of extracellular adenosine concentration changes during sleep deprivation and spontaneous sleep: an *in vivo* microdialysis study. *Neuroscience* 99, 507–517. doi: 10.1016/S0306-4522(00)00220-7

Porkka-Heiskanen, T., Strecker, R. E., Thakkar, M., Bjorkum, A. A., Greene, R. W., and Mccarley, R. W. (1997). Adenosine: a mediator of the sleep-inducing effects of prolonged wakefulness. *Science* 276, 1265–1268. doi: 10.1126/science.276.5316.1265

Qi, G., and Feldmeyer, D. (2016). Dendritic target region-specific formation of synapses between excitatory layer 4 neurons and layer 6 pyramidal cells. *Cereb. Cortex* 26, 1569–1579. doi: 10.1093/cercor/bhu334

Qi, G., Radnikow, G., and Feldmeyer, D. (2015). Electrophysiological and morphological characterization of neuronal microcircuits in acute brain slices using paired patch-clamp recordings. *J. Vis. Exp.* 95:e52358. doi: 10.3791/52358

Qi, G., Van Aerde, K., Abel, T., and Feldmeyer, D. (2017). Adenosine differentially modulates synaptic transmission of excitatory and inhibitory microcircuits in layer 4 of rat barrel cortex. *Cereb. Cortex* 27, 4411–4422. doi: 10.1093/cercor/bhw243

Radnikow, G., Gunter, R. H., Marx, M., and Feldmeyer, D. (2012). "Morpho-functional mapping of cortical networks in brain slice preparations using paired electrophysiological recordings," in *Neuronal Network Analysis Neuromethods*, Vol. 67, eds T. Fellin and M. Halassa (New York, NY: Humana Press), 405–431.

Radnikow, G., Qi, G., and Feldmeyer, D. (2015). "Synaptic microcircuits in the barrel cortex," in *Sensorimotor Integration in the Whisker System,* eds *P. Krieger and A. Groh. (New York, NY: Springer),* 59–108.

Rall, W. (1967). Distinguishing theoretical synaptic potentials computed for different soma-dendritic distributions of synaptic input. *J. Neurophysiol.* 30, 1138–1168. doi: 10.1152/jn.1967.30.5.1138

Reyes, A., Lujan, R., Rozov, A., Burnashev, N., Somogyi, P., and Sakmann, B. (1998). Target-cell-specific facilitation and depression in neocortical circuits. *Nat. Neurosci.* 1, 279–285. doi: 10.1038/1092

Reyes, A., and Sakmann, B. (1999). Developmental switch in the short-term modification of unitary EPSPs evoked in layer 2/3 and layer 5 pyramidal neurons of rat neocortex. *J. Neurosci.* 19, 3827–3835. doi: 10.1523/JNEUROSCI.19-10-03827.1999

Rieubland, S., Roth, A., and Hausser, M. (2014). Structured connectivity in cerebellar inhibitory networks. *Neuron* 81, 913–929. doi: 10.1016/j.neuron.2013.12.029

Rizzoli, S. O., and Betz, W. J. (2004). The structural organization of the readily releasable pool of synaptic vesicles. *Science* 303, 2037–2039. doi: 10.1126/science.1094682

Rizzoli, S. O., and Betz, W. J. (2005). Synaptic vesicle pools. *Nat. Rev. Neurosci.* 6, 57–69. doi: 10.1038/nrn1583

Rollenhagen, A., Ohana, O., Satzler, K., Hilgetag, C. C., Kuhl, D., and Lubke, J. H. R. (2018). Structural properties of synaptic transmission and temporal dynamics at excitatory layer 5B synapses in the adult rat somatosensory cortex. *Front. Synaptic. Neurosci.* 10:24. doi: 10.3389/fnsyn.2018.00024

Rozov, A., Burnashev, N., Sakmann, B., and Neher, E. (2001). Transmitter release modulation by intracellular Ca^{2+} buffers in facilitating and depressing nerve terminals of pyramidal cells in layer 2/3 of the rat neocortex indicates a target cell-specific difference in presynaptic calcium dynamics. *J. Physiol.* 531, 807–826. doi: 10.1111/j.1469-7793.2001.0807h.x

Sarter, M., Parikh, V., and Howe, W. M. (2009). Phasic acetylcholine release and the volume transmission hypothesis: time to move on. *Nat. Rev. Neurosci.* 10, 383–390. doi: 10.1038/nrn2635

Saviane, C., and Silver, R. A. (2006). Fast vesicle reloading and a large pool sustain high bandwidth transmission at a central synapse. *Nature* 439, 983–987. doi: 10.1038/nature04509

Scanziani, M., Gahwiler, B. H., and Charpak, S. (1998). Target cell-specific modulation of transmitter release at terminals from a single axon. *Proc. Natl. Acad. Sci. U.S.A.* 95, 12004–12009. doi: 10.1073/pnas.95.20.12004

Scheuss, V., and Neher, E. (2001). Estimating synaptic parameters from mean, variance, and covariance in trains of synaptic responses. *Biophys. J.* 81, 1970–1989. doi: 10.1016/S0006-3495(01)75848-1

Scheuss, V., Schneggenburger, R., and Neher, E. (2002). Separation of presynaptic and postsynaptic contributions to depression by covariance analysis of successive EPSCs at the calyx of Held synapse. *J. Neurosci.* 22, 728–739. doi: 10.1523/JNEUROSCI.22-03-00728.2002

Seeman, S. C., Campagnola, L., Davoudian, P. A., Hoggarth, A., Hage, T. A., Bosma-Moody, A., et al. (2018). Sparse recurrent excitatory connectivity in the microcircuit of the adult mouse and human cortex. *Elife* 7:e37349. doi: 10.7554/eLife.37349.032

Silberberg, G., and Markram, H. (2007). Disynaptic inhibition between neocortical pyramidal cells mediated by Martinotti cells. *Neuron* 53, 735–746. doi: 10.1016/j.neuron.2007.02.012

Silver, R. A., Lubke, J., Sakmann, B., and Feldmeyer, D. (2003). High-probability uniquantal transmission at excitatory synapses in barrel cortex. *Science* 302, 1981–1984. doi: 10.1126/science.1087160

Sjostrom, P. J., Turrigiano, G. G., and Nelson, S. B. (2001). Rate, timing, and cooperativity jointly determine cortical synaptic plasticity. *Neuron* 32, 1149–1164. doi: 10.1016/S0896-6273(01)00542-6

Song, S., Sjostrom, P. J., Reigl, M., Nelson, S., and Chklovskii, D. B. (2005). Highly nonrandom features of synaptic connectivity in local cortical circuits. *PLoS Biol.* 3:e68. doi: 10.1371/journal.pbio.0030068

Stepanyants, A., and Chklovskii, D. B. (2005). Neurogeometry and potential synaptic connectivity. *Trends Neurosci.* 28, 387–394. doi: 10.1016/j.tins.2005.05.006

Stepanyants, A., Martinez, L. M., Ferecsko, A. S., and Kisvarday, Z. F. (2009). The fractions of short- and long-range connections in the visual cortex. *Proc. Natl. Acad. Sci. U.S.A.* 106, 3555–3560. doi: 10.1073/pnas.0810390106

Stevens, C. F. (1993). Quantal release of neurotransmitter and long-term potentiation. *Cell* 72(Suppl), 55–63. doi: 10.1016/S0092-8674(05)80028-5

Stratford, K. J., Tarczy-Hornoch, K., Martin, K. A., Bannister, N. J., and Jack, J. J. (1996). Excitatory synaptic inputs to spiny stellate cells in cat visual cortex. *Nature* 382, 258–261. doi: 10.1038/382258a0

Stuart, G. J., Dodt, H. U., and Sakmann, B. (1993). Patch-clamp recordings from the soma and dendrites of neurons in brain slices using infrared video microscopy. *Pflugers Arch.* 423, 511–518. doi: 10.1007/BF00374949

Szabadics, J., Varga, C., Molnar, G., Olah, S., Barzo, P., and Tamas, G. (2006). Excitatory effect of GABAergic axo-axonic cells in cortical microcircuits. *Science* 311, 233–235. doi: 10.1126/science.1121325

Tamas, G., Buhl, E. H., Lorincz, A., and Somogyi, P. (2000). Proximally targeted GABAergic synapses and gap junctions synchronize cortical interneurons. *Nat. Neurosci.* 3, 366–371. doi: 10.1038/73936

Tamas, G., Lorincz, A., Simon, A., and Szabadics, J. (2003). Identified sources and targets of slow inhibition in the neocortex. *Science* 299, 1902–1905. doi: 10.1126/science.1082053

Tecuapetla, F., Carrillo-Reid, L., Bargas, J., and Galarraga, E. (2007). Dopaminergic modulation of short-term synaptic plasticity at striatal inhibitory synapses. *Proc. Natl. Acad. Sci. U.S.A.* 104, 10258–10263. doi: 10.1073/pnas.0703813104

Tecuapetla, F., Koos, T., Tepper, J. M., Kabbani, N., and Yeckel, M. F. (2009). Differential dopaminergic modulation of neostriatal synaptic connections of striatopallidal axon collaterals. *J. Neurosci.* 29, 8977–8990. doi: 10.1523/JNEUROSCI.6145-08.2009

Teles-Grilo Ruivo, L. M., Baker, K. L., Conway, M. W., Kinsley, P. J., Gilmour, G., Phillips, K. G., et al. (2017). Coordinated acetylcholine release in prefrontal cortex and hippocampus is associated with arousal and reward on distinct timescales. *Cell. Rep.* 18, 905–917. doi: 10.1016/j.celrep.2016.12.085

Testa-Silva, G., Verhoog, M. B., Goriounova, N. A., Loebel, A., Hjorth, J., Baayen, J. C., et al. (2010). Human synapses show a wide temporal window for spike-timing-dependent plasticity. *Front. Synaptic. Neurosci.* 2:12. doi: 10.3389/fnsyn.2010.00012

Testa-Silva, G., Verhoog, M. B., Linaro, D., De Kock, C. P., Baayen, J. C., Meredith, R. M., et al. (2014). High bandwidth synaptic communication and frequency tracking in human neocortex. *PLoS Biol.* 12:e1002007. doi: 10.1371/journal.pbio.1002007

Thomson, A. M., and Deuchars, J. (1997). Synaptic interactions in neocortical local circuits: dual intracellular recordings *in vitro*. *Cereb. Cortex* 7, 510–522. doi: 10.1093/cercor/7.6.510

Thomson, A. M., and Lamy, C. (2007). Functional maps of neocortical local circuitry. *Front. Neurosci.* 1, 19–42. doi: 10.3389/neuro.01.1.1.002.2007

Thomson, A. M., West, D. C., Wang, Y., and Bannister, A. P. (2002). Synaptic connections and small circuits involving excitatory and inhibitory neurons in layers 2–5 of adult rat and cat neocortex: triple intracellular recordings and biocytin labelling *in vitro*. *Cereb. Cortex* 12, 936–953. doi: 10.1093/cercor/12.9.936

Ting, J. T., Daigle, T. L., Chen, Q., and Feng, G. (2014). Acute brain slice methods for adult and aging animals: application of targeted patch clamp analysis and optogenetics. *Methods Mol. Biol.* 1183, 221–242. doi: 10.1007/978-1-4939-1096-0_14

Ting, J. T., Kalmbach, B., Chong, P., De Frates, R., Keene, C. D., Gwinn, R. P., et al. (2018a). A robust *ex vivo* experimental platform for molecular-genetic dissection of adult human neocortical cell types and circuits. *Sci. Rep.* 8:8407. doi: 10.1038/s41598-018-26803-9

Ting, J. T., Lee, B. R., Chong, P., Soler-Llavina, G., Cobbs, C., Koch, C., et al. (2018b). Preparation of acute brain slices using an optimized N-Methyl-D-glucamine protective recovery method. *J. Vis. Exp.* 132:e53825. doi: 10.3791/53825

Trettel, J., and Levine, E. S. (2003). Endocannabinoids mediate rapid retrograde signaling at interneuron right-arrow pyramidal neuron synapses of the neocortex. *J. Neurophysiol.* 89, 2334–2338. doi: 10.1152/jn.01037.2002

Urban-Ciecko, J., Jouhanneau, J. S., Myal, S. E., Poulet, J. F. A., and Barth, A. L. (2018). Precisely timed nicotinic activation drives SST inhibition in neocortical circuits. *Neuron* 97, 611–625 e615. doi: 10.1016/j.neuron.2018.01.037

Varshney, L. R., Sjostrom, P. J., and Chklovskii, D. B. (2006). Optimal information storage in noisy synapses under resource constraints. *Neuron* 52, 409–423. doi: 10.1016/j.neuron.2006.10.017

Volgushev, M., Kudryashov, I., Chistiakova, M., Mukovski, M., Niesmann, J., and Eysel, U. T. (2004). Probability of transmitter release at neocortical synapses at different temperatures. *J. Neurophysiol.* 92, 212–220. doi: 10.1152/jn.01166.2003

Wickersham, I. R., Lyon, D. C., Barnard, R. J., Mori, T., Finke, S., Conzelmann, K. K., et al. (2007). Monosynaptic restriction of transsynaptic tracing from single, genetically targeted neurons. *Neuron* 53, 639–647. doi: 10.1016/j.neuron.2007.01.033

Williams, S. R., and Stuart, G. J. (2002). Dependence of EPSP efficacy on synapse location in neocortical pyramidal neurons. *Science* 295, 1907–1910. doi: 10.1126/science.1067903

Williams, S. R., and Stuart, G. J. (2003). Role of dendritic synapse location in the control of action potential output. *Trends Neurosci.* 26, 147–154. doi: 10.1016/S0166-2236(03)00035-3

Wilson, R. I., and Nicoll, R. A. (2001). Endogenous cannabinoids mediate retrograde signalling at hippocampal synapses. *Nature* 410, 588–592. doi: 10.1038/35069076

Yang, D., Gunter, R. H., Qi, G., Radnikow, G., and Feldmeyer, D. (2019). Cell type-Specific modulation of layer 6A excitatory microcircuits by acetylcholine in rat barrel Cortex. *BioRxiv.* 701318. doi: 10.1101/701318

Yassin, L., Benedetti, B. L., Jouhanneau, J. S., Wen, J. A., Poulet, J. F., and Barth, A. L. (2010). An embedded subnetwork of highly active neurons in the neocortex. *Neuron* 68, 1043–1050. doi: 10.1016/j.neuron.2010.11.029

Yu, Y. C., Bultje, R. S., Wang, X., and Shi, S. H. (2009). Specific synapses develop preferentially among sister excitatory neurons in the neocortex. *Nature* 458, 501–504. doi: 10.1038/nature07722

Zeng, H., and Sanes, J. R. (2017). Neuronal cell-type classification: challenges, opportunities and the path forward. *Nat. Rev. Neurosci.* 18, 530–546. doi: 10.1038/nrn.2017.85

Zilberter, Y., Harkany, T., and Holmgren, C. D. (2005). Dendritic release of retrograde messengers controls synaptic transmission in local neocortical networks. *Neuroscientist* 11, 334–344. doi: 10.1177/1073858405275827

Zilberter, Y., Kaiser, K. M., and Sakmann, B. (1999). Dendritic GABA release depresses excitatory transmission between layer 2/3 pyramidal and bitufted neurons in rat neocortex. *Neuron* 24, 979–988. doi: 10.1016/S0896-6273(00)81044-2

Zoli, M., Jansson, A., Sykova, E., Agnati, L. F., and Fuxe, K. (1999). Volume transmission in the CNS and its relevance for neuropsychopharmacology. *Trends Pharmacol. Sci.* 20, 142–150. doi: 10.1016/S0165-6147(99)01343-7

Zucker, R. S., and Regehr, W. G. (2002). Short-term synaptic plasticity. *Annu. Rev. Physiol.* 64, 355–405. doi: 10.1146/annurev.physiol.64.092501.114547

Conflict of Interest: The authors declare that the research was conducted in the absence of any commercial or financial relationships that could be construed as a potential conflict of interest.

frontiers in Synaptic Neuroscience

ORIGINAL RESEARCH
published: 14 February 2020
doi: 10.3389/fnsyn.2020.00006

Monosynaptic Tracing Success Depends Critically on Helper Virus Concentrations

*Thomas K. Lavin, Lei Jin, Nicholas E. Lea and Ian R. Wickersham**

McGovern Institute for Brain Research, Massachusetts Institute of Technology, Cambridge, MA, United States

Monosynaptically-restricted transsynaptic tracing using deletion-mutant rabies virus (RV) has become a widely used technique in neuroscience, allowing identification, imaging, and manipulation of neurons directly presynaptic to a starting neuronal population. Its most common implementation is to use Cre mouse lines in combination with Cre-dependent "helper" adeno-associated viral vectors (AAVs) to supply the required genes to the targeted population before subsequent injection of a first-generation (ΔG) rabies viral vector. Here we show that the efficiency of transsynaptic spread and the degree of nonspecific labeling in wild-type control animals depend strongly on the concentrations of these helper AAVs. Our results suggest practical guidelines for achieving good results.

Keywords: rabies, virus, monosynaptic tracing, AAV (adeno-associated virus), circuit tracing

INTRODUCTION

Rabies virus (RV) has proven useful for neuroscience, because of its natural behavior of spreading between synaptically-connected neurons [although both the mechanism of transsynaptic spread and the true degree of its synaptic specificity remain unclear (Luo et al., 2018; Beier, 2019)] in an apparently exclusively retrograde direction (in the central nervous system, whereas in primary sensory neurons it appears to be bidirectional (Bauer et al., 2014; Zampieri et al., 2014). This has allowed it to serve as a useful tool for mapping synaptic connections, usually in the context of "monosynaptic tracing," which refers to the use of a modified RV to label neurons that are, putatively, directly presynaptic to a targeted population of neurons (Wickersham et al., 2007b). It relies on the use of a RV to which two modifications have been made. First, in order to render it incapable of spread between neurons without assistance, one (or more) of its genes has been deleted; in first-generation vectors, this is the glycoprotein gene, denoted "G" (Wickersham et al., 2007a). Second, in order to allow selective targeting of the initial infection to the group of neurons of interest, the viral particles are coated with the envelope protein of a different virus (the avian-endemic retrovirus "ASLV-A"; the envelope protein of which is called "EnvA"), rendering the virus incapable of infecting mammalian neurons without assistance (Wickersham et al., 2007b). In the targeted neuronal population, two exogenous proteins must be expressed before injection of the RV: the receptor for EnvA [a quail cell surface protein called "TVA" (Bates et al., 1993)], to allow the modified RV to infect the starting cells, and the deleted viral gene(s) [G, in the case of first-generation ("ΔG") vectors]. While this can be achieved by single-cell transfection techniques (Marshel et al., 2010; Rancz et al., 2011; Wertz et al., 2015; Rompani et al., 2017), the much more accessible and widely used implementation is to use Cre (Sauer and Henderson, 1988)-dependent adeno-associated viral vectors ("AAVs"; Atasoy et al., 2008; Wall et al., 2010; Watabe-Uchida et al., 2012; Kohara et al., 2014; Beier et al., 2015; Liu et al., 2017; Ährlund-Richter et al., 2019; Szonyi et al., 2019; Zhang et al., 2019) in combination with a Cre mouse line, in order to map inputs to

OPEN ACCESS

Edited by:
Dirk Feldmeyer, Julich Research Centre, Germany

Reviewed by:
Francesco Ferraguti, Innsbruck Medical University, Austria
Edward M. Callaway, Salk Institute for Biological Studies, United States

***Correspondence:**
Ian R. Wickersham
wickersham@mit.edu

Received: *20 August 2019*
Accepted: *23 January 2020*
Published: *14 February 2020*

Citation:
Lavin TK, Jin L, Lea NE and Wickersham IR (2020) Monosynaptic Tracing Success Depends Critically on Helper Virus Concentrations. Front. Synaptic Neurosci. 12:6. doi: 10.3389/fnsyn.2020.00006

a Cre-expressing group of neurons (see **Figure 1**). This approach has been used in a large number of studies and contributed considerably to our understanding of the organization of many circuits within the mammalian nervous system.

Within this basic paradigm of using Cre-dependent "helper" AAVs to provide the genes required for monosynaptic tracing, many variations are possible. A major consideration in design of such experiments is the mismatch between the minuscule amount of TVA required for successful initial infection of the starting cells, because of the high sensitivity of the EnvA-TVA interaction (Federspiel et al., 1994; Seidler et al., 2008), and the high levels of G that appear to be required for efficient spread of the virus from the starting cells to the putatively presynaptic cells. This causes a problem: to achieve acceptable levels of transsynaptic spread, a high concentration of AAV may be found to be necessary; however, because it appears that all putatively Cre-dependent AAVs "leak" because of spontaneous recombination of some fraction of virions' genomes, even at the plasmid DNA stage [Kimberly Ritola, personal communication; unpublished results from our laboratory; and see also a very recent article on this issue (Fischer et al., 2019)], a high concentration of an AAV expressing TVA can result in an unacceptably high level of "background" labeling of cells by the RV in wild-type mice. Different groups have taken different approaches to dealing with this, including using two separate Cre-dependent AAVs so that G is expressed at a presumably higher level than TVA (Watabe-Uchida et al., 2012) and/or using a low-affinity mutant of TVA (Miyamichi et al., 2013; Sakurai et al., 2016).

Our current approach is to use a mixture of two AAVs, described first in Liu et al. (2017), which are coupled with the tetracycline transactivator system (Gossen and Bujard, 1992). The first AAV is Cre-dependent and expresses, in Cre-expressing cells, TVA (transmembrane isoform; Bates et al., 1993; Young et al., 1993; Jha et al., 2011), EGFP (Cormack et al., 1996), and the tetracycline transactivator ("tTA"); the second is not directly Cre-dependent but simply expresses both G (SAD B19 strain; Conzelmann et al., 1990) and the blue fluorophore mTagBFP2 (Subach et al., 2011) under the control of the tetracycline response element. Expression of tTA from the first AAV drives expression of G from the second AAV in the same cells. Note that this uses the "TET-OFF" system so that no tetracycline (or doxycycline, etc.) needs to be added in order to make the system work.

The use of this combination has several intended advantages. First, the use of a two-AAV combination allows the concentrations of the vectors encoding TVA and G to be independently titrated. Second, the tTA-TRE system should provide amplification of the level of G expression with respect to the level of expression of the genes in the first AAV, so that

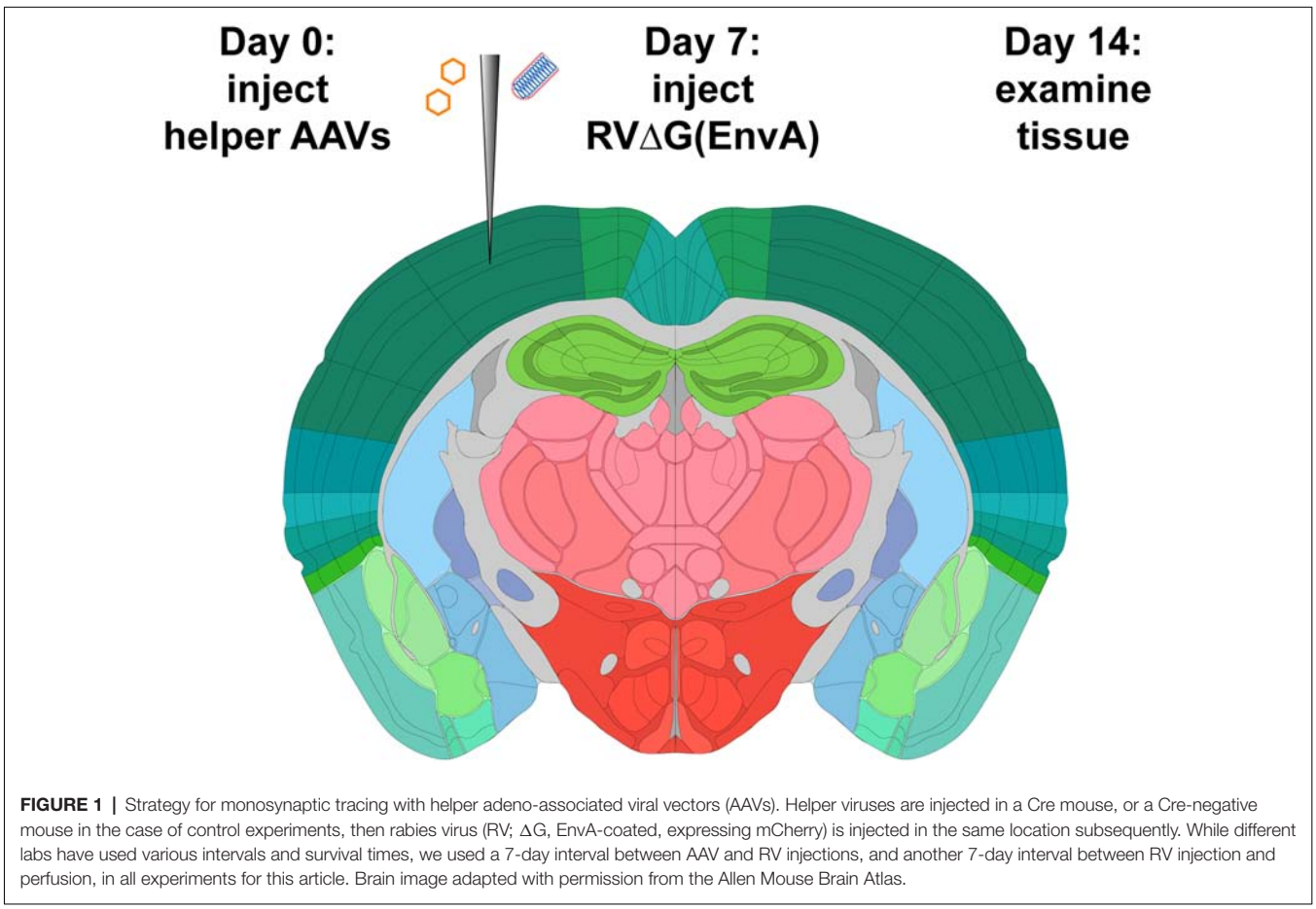

FIGURE 1 | Strategy for monosynaptic tracing with helper adeno-associated viral vectors (AAVs). Helper viruses are injected in a Cre mouse, or a Cre-negative mouse in the case of control experiments, then rabies virus (RV; ΔG, EnvA-coated, expressing mCherry) is injected in the same location subsequently. While different labs have used various intervals and survival times, we used a 7-day interval between AAV and RV injections, and another 7-day interval between RV injection and perfusion, in all experiments for this article. Brain image adapted with permission from the Allen Mouse Brain Atlas.

the TVA/EGFP/tTA virus can be titrated down to very low concentration to result in low background labeling in wild-type mice but with the G expression level still high enough to result in plentiful transsynaptic spread of the RV. Third, the use of the tet transactivator system can also allow the expression of G (and mTagBFP2) to be turned off (or potentially titrated) by administration of doxycycline after transsynaptic spread has taken place, in order to mitigate toxicity to the starting cells, although we have not done this in any of the work presented in this article.

We have recently published a detailed step-by-step protocol for monosynaptic tracing using these viruses for monosynaptic tracing with Cre mice (Lavin et al., 2019b). Here we present results of our titration experiments to test the effects of using different dilutions of the helper viruses, to show the reasons for the specific concentrations that we recommend. We found that the two-helper combination described above and in Liu et al. (2017) gives much better results than the simpler single AAV which we described earlier (Kohara et al., 2014), which did not allow independent optimization of transsynaptic tracing efficiency and minimization of background labeling in Cre-negative mice. We also found that *excessively high* titers of the helper viruses gave very poor results, suggesting that preventing toxicity due to overly high expression of the helper virus genes [or perhaps simply due to either direct toxicity of the AAVs or an immune reaction to them (Hirsch et al., 2011; Bockstael et al., 2012; Flotte and Büning, 2018; Hinderer et al., 2018; Hordeaux et al., 2018a,b; Rabinowitz et al., 2019)] is as minuscule as ensuring sufficient expression of them. Finally, and most practically, we suggest specific concentrations of the helper viruses that gave best results in the Cre line in which we performed the titration and that should serve either as a likely choice of parameters for end-users or as a promising starting point for much more limited titration series to be done as pilot experiments when targeting other cell types in other Cre lines.

MATERIALS AND METHODS

All experiments involving animals were conducted according to NIH guidelines and approved by the MIT Committee for Animal Care. Mice were housed 1–5 per cage under a normal light/dark cycle for all experiments.

Viruses

Cloning of AAV genome plasmids pAAV-synP-FLEX-splitTVA-EGFP-B19G (Addgene 52473), pAAV-syn-FLEX-splitTVA-EGFP-tTA (Addgene 100798), and pAAV-TREtight-mTagBFP2-B19G (Addgene 100799) has been described (Kohara et al., 2014; Liu et al., 2017). These genomes were packaged in serotype 1 AAV capsids by, and are available for purchase from, Addgene (catalog numbers 52473-AAV1, 100798-AAV1, and 100799-AAV1). The titers of the AAVs, as determined by Addgene by qPCR, were as follows:

- AAV1-synP-FLEX-splitTVA-EGFP-B19G (lot #v14715): 2.4×10^{13} gc/ml
- AAV1-syn-FLEX-splitTVA-EGFP-tTA (lot #v15287): 1.7×10^{13} gc/ml
- AAV1-TREtight-mTagBFP2-B19G (lot #v14716): 3.2×10^{13} gc/ml.

Cloning of pRVΔG-4FLPo (Matsuyama et al., 2019; Addgene 122050) and pRVΔG-4mCherry (Weible et al., 2010; Addgene 52488) have been described. Production of EnvA-enveloped RV RVΔG-4mCherry(EnvA) (Kohara et al., 2014) was done as described previously (Wickersham et al., 2010; Wickersham and Sullivan, 2015; Chatterjee et al., 2018) but using helper plasmids pCAG-B19N (Addgene #59924), pCAG-B19P (Addgene #59925), pCAG-B19G (Addgene #59921), pCAG-B19L (Addgene #59922), and pCAG-T7pol (Addgene #59926) for the rescue step (Chatterjee et al., 2018). The final titers were 5.82×10^9 infectious units/ml for RVΔG-4FLPo(EnvA) and 1.70×10^{10} infectious units/ml for RVΔG-4mCherry(EnvA), as determined by infection of TVA-expressing cells as described previously (Wickersham et al., 2010; Matsuyama et al., 2019).

Helper AAVs were diluted in Dulbecco's phosphate-buffered saline (DPBS; Fisher, 14-190-250) by the desired dilution factors (see main text). In the case of AAV-syn-FLEX-splitTVA-EGFP-tTA and AAV-TREtight-mTagBFP2-B19G, the two viruses were combined (after dilution, when applicable) in a 50/50 ratio by volume before injection.

Mouse Strains

Adult mice of both sexes were used. For compatibility with other projects in the laboratory, the PV-Cre (Jackson 017320) and DAT-Cre (Jackson 006660) used were also heterozygous for the FLP-dependent tdTomato reporter line Ai65F (Daigle et al., 2018); obtained in this case by crossing the Cre− and FLP-dependent tdTomato double-reporter line Ai65D (Madisen et al., 2015; Jackson Laboratory 021875) to the Cre deleter line Meox2-Cre (Tallquist and Soriano, 2000; Jackson Laboratory 003755), then breeding out the Meox2-Cre allele, resulting in a reporter line for which only FLP is required for expression of tdTomato). For those mice in which RVΔG-4FLPo was used, the reporter allele was necessary for reporting RV activity; for those in which RVΔG-4mCherry was used, the presence of this reporter allele was irrelevant. For Cre-negative control injections using RVΔG-4FLPo, the Ai65F line was used. For Cre-negative control injections using RVΔG-4mCherry, either Ai65F or the Cre-dependent reporter line Ai14 (Madisen et al., 2010) was used; in these cases, the presence of the reporter alleles was again irrelevant.

Stereotaxic Injections

For pilot studies (**Figures 2–4**), we injected 300 nl of helper AAV solution into primary somatosensory cortex (coordinates with respect to bregma: AP = −0.58 mm, LM = 3.00 mm, DV = −1.00 mm) of anesthetized adult mice as described (Lavin et al., 2019b), using a stereotaxic instrument (Stoelting Co., 51925) and custom injection apparatus consisting of a hydraulic manipulator (Narishige, MO-10) with head-stage coupled *via* custom adaptors to a wire plunger advanced through pulled glass capillaries (Drummond, Wiretrol II) back-filled with mineral oil and front-filled with viral vector solution. Seven days after

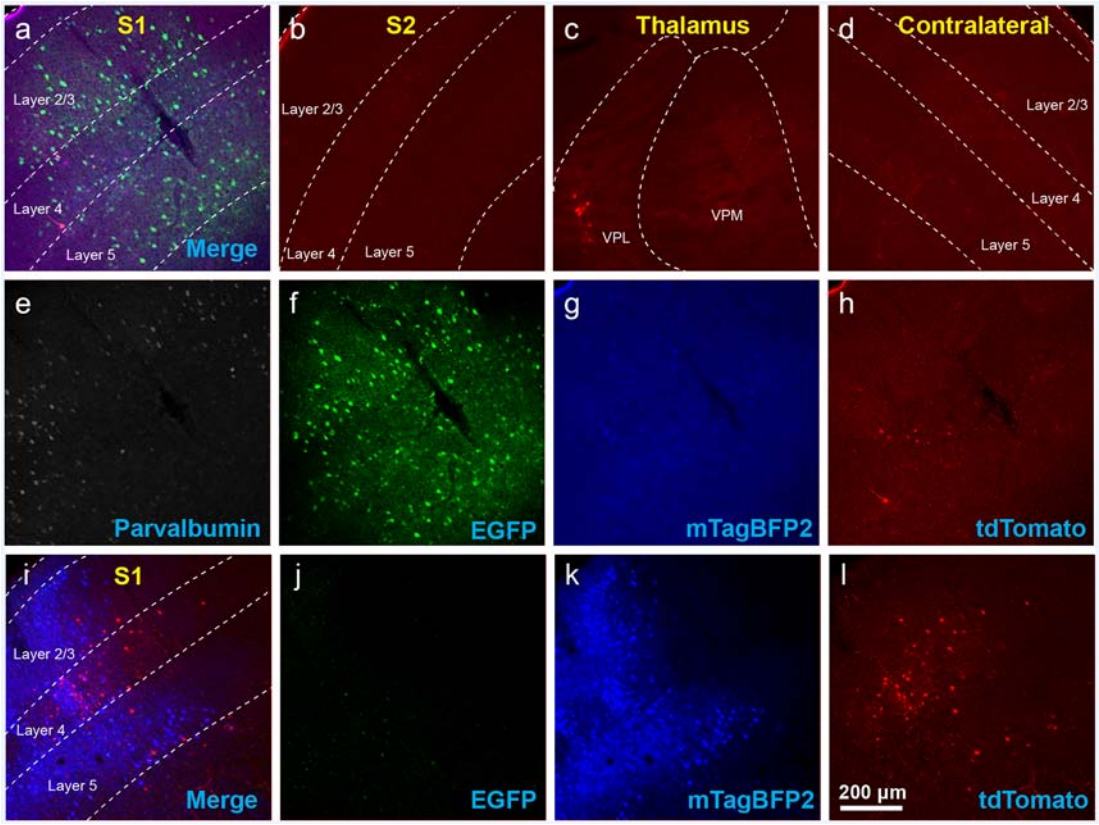

FIGURE 2 | Use of helper viruses at excessive concentrations can result in near-complete failure of monosynaptic tracing. The two-AAV combination described in Liu et al. (2017; AAV1-synP-FLEX-splitTVA-EGFP-B19G mixed with AAV1-TREtight-mTagBFP2-B19G) was injected in the somatosensory cortex of PV-Cre × Ai65F (FLPo-dependent tdTomato reporter) mice, followed by RVΔG-4FLPo(EnvA) 7 days later. **(A–H)** Very poor results were obtained when using new preparations of these AAVs undiluted. **(A)** Injection site in S1. Green = anti-EGFP staining, blue = mTagBFP2, red = tdTomato. Individual channels from this field are shown in panels **(E–H)**. **(B)** No labeled neurons were found in the ipsilateral secondary somatosensory cortex (S2). **(C)** Very few labeled neurons were found in ipsilateral thalamus (VPL and VPM). **(D)** No labeled neurons were found in contralateral S1. **(E–H)** Individual channels from the field shown in panel **(A)**. **(E)** Anti-parvalbumin staining (not shown in panel **A**). **(F)** Anti-EGFP staining, indicating expression from the first, Cre-dependent AAV. **(G)** mTagBFP2, indicating expression from the second, tTA-dependent AAV. **(H)** tdTomato, reporting activity of the FLPo-encoding RV. **(I**,**L)** Injection site after using undiluted viruses in two-helper combination in Cre-negative animal: many labeled cells are seen. **(I)** Overlay of **(J–L)**. **(J)** Anti-EGFP staining, **(K)** mTagBFP2 signal, **(L)** tdTomato marking RV labeling. Scale bar in **(A)**: 200 μm, applies to all panels.

AAV injection, 100 nl of RVΔG-FLPo(EnvA) was injected in the same site.

For subsequent experiments in PV-Cre (**Figures 5**–**7**), 200 nl of helper AAV solution was injected, followed by 100 nl of RVΔG-4mCherry(EnvA) 7 days later. For DAT-Cre mice (**Figure 8**), 200 nl of helper AAV solution was injected (AP = −3.00 mm, LM = 1.50 mm, DV = −4.20 mm), followed by 500 nl of RVΔG-FLPo(EnvA) 7 days later. Two mice were used for each condition ($n = 2$).

Perfusions and Histology

Seven days after injection of the RV, mice were transcardially perfused with 4% paraformaldehyde in phosphate-buffered saline. Brains were postfixed in 4% paraformaldehyde overnight on a shaker at 4°C and cut into 50 μm coronal sections on a vibrating microtome (Leica, VT-1000S), with sections collected into six tubes (containing cryoprotectant solution as described; Lavin et al., 2019b) each, so that each tube contained a series of every sixth section through the sectioned region of the brain. For confocal imaging, sections were immunostained as described previously (Shima et al., 2016) with the following antibodies (as applicable) at the following respective dilutions: chicken anti-GFP (Aves Labs GFP-1020) 1:1,000, guinea pig anti-parvalbumin (Synaptic Systems 195004) 1:1,000, sheep anti-tyrosine hydroxylase (TH; Millipore AB1542) 1:1,000, with secondary antibodies donkey anti-chicken Alexa Fluor 488 (Jackson Immuno 703-545-155) 1:200, donkey anti-guinea pig, AlexaFluor 647 conjugated (Jackson Immuno 706-605-148) 1:200, and donkey anti-sheep, AlexaFluor 647 conjugated (Jackson Immuno 713-605-147) 1:200. Sections were mounted with Prolong Diamond Antifade mounting medium (Thermo Fisher P36970) and imaged on a confocal microscope (Zeiss, LSM 710). For counts, every other series (i.e., either series 1, 3, and 5 or series 2, 4, and 6) of each brain was mounted, so that 50% of the sections from each brain were mounted and examined.

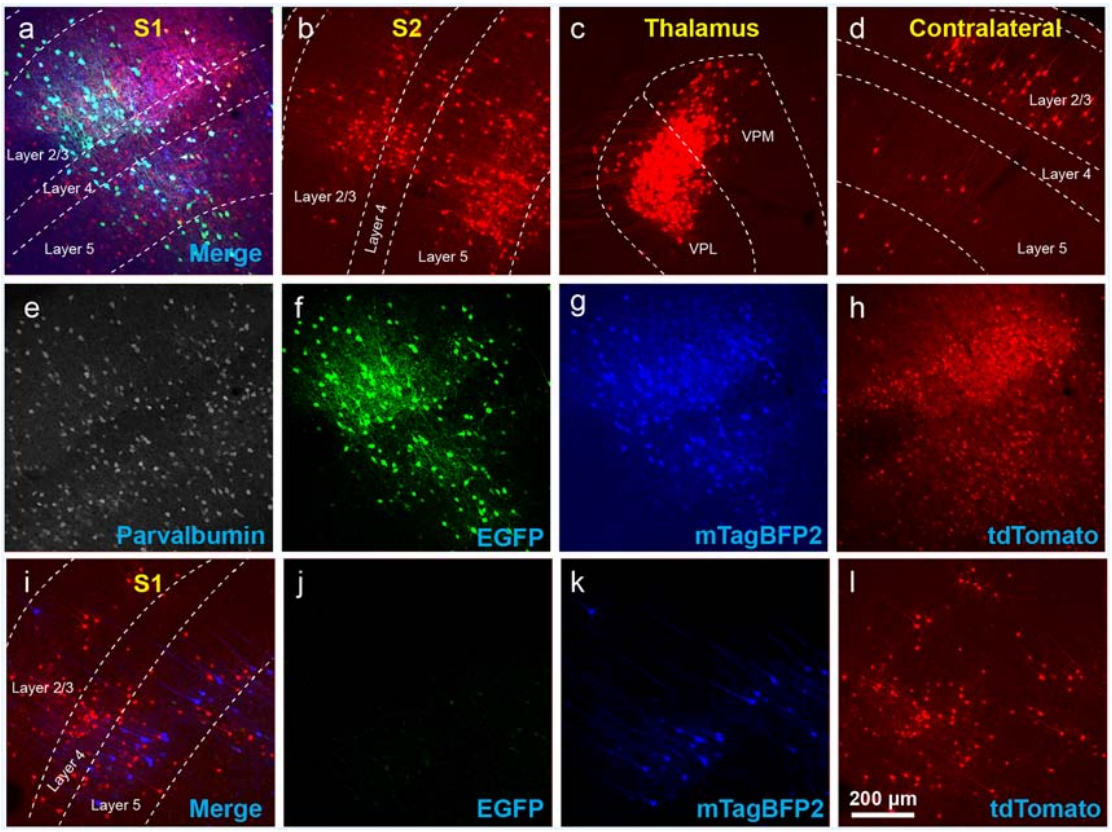

FIGURE 3 | The use of insufficiently-diluted helper viruses results in excessive background labeling in Cre-negative animals. **(A–H)** Diluting the helper viruses to concentrations matching previously used preparations gave much better results. **(A)** Injection site in S1; individual channels from this field are shown in panels **(E–H)**. **(B–D)** Many labeled presynaptic neurons were found in ipsilateral secondary somatosensory cortex **(B)**, ipsilateral thalamus (VPL and VPM; **C**), and contralateral S1 **(D)**. **(E)** Anti-parvalbumin staining (not shown in panel **A**). **(F)** Anti-EGFP staining, indicating expression from the first, Cre-dependent AAV. **(G)** mTagBFP2, indicating expression from the second, G-encoding AAV. **(H)** tdTomato, reporting activity of the FLPo-encoding RV. **(I–L)** Even with the AAVs diluted to match the titers of previous batches, excessive background labeling is seen at the injection site. **(I)** Overlay of **(J–L)**. **(J)** Anti-EGFP staining, **(K)** mTagBFP2 signal, **(L)** tdTomato marking RV labeling. Scale bar in **(A)**: 200 µm, applies to all panels.

Counts

Neurons labeled with either tdTomato or mCherry in contralateral cortex in PV-Cre mice (crossed with Ai65F reporter mice; see Mouse Strains) and at the injection site in Cre-negative (Ai65F reporter) mice were counted manually by examining every other 50 µm section (i.e., 50% of the sections) on an epifluorescence microscope (Zeiss, Imager.Z2). Counts of cells in the contralateral cortex were restricted to those in the sectioned anterior-posterior region common to all sectioned brains. This encompassed the sections between 1.2 mm and −3.0 mm relative to Bregma (Paxinos and Franklin, 2013).

RESULTS

Having previously found Addgene's Viral Service[1] to be an excellent source of high-quality AAVs, we authorized them to package and distribute three of our published Cre-dependent helper AAVs: the standalone helper virus AAV-syn-FLEX-splitTVA-EGFP-B19G from Kohara et al. (2014; referred to below as the "tricistronic" helper virus) and the two viruses to be used in combination as described in Liu et al. (2017): AAV-syn-FLEX-splitTVA-EGFP-tTA and AAV-TREtight-mTagBFP2-B19G. Although the resulting preparations, all with serotype 1 capsids, had much higher titers than earlier batches that we had previously used successfully for similar experiments, we nonetheless first tried using them "straight": undiluted except insofar as, for the two-helper-virus combination, the two viruses were combined in a 50/50 mixture by volume (see "Materials and Methods" section). We injected either AAV1-syn-FLEX-splitTVA-EGFP-B19G or the two-virus mixture into the primary somatosensory cortex of either the PV-Cre (expressing Cre from the parvalbumin locus; Hippenmeyer et al., 2005) mouse line crossed with the Ai65F reporter line (FLP-dependent tdTomato; Shaner et al., 2004; Daigle et al., 2018) or, for Cre-negative controls, the Ai65F reporter line without a Cre allele. Seven days after AAV injection, we injected RVΔG-4FLPo (EnvA) (Lavin et al., 2019b; expressing FLPo

[1]www.addgene.org/viral-service/aav-prep

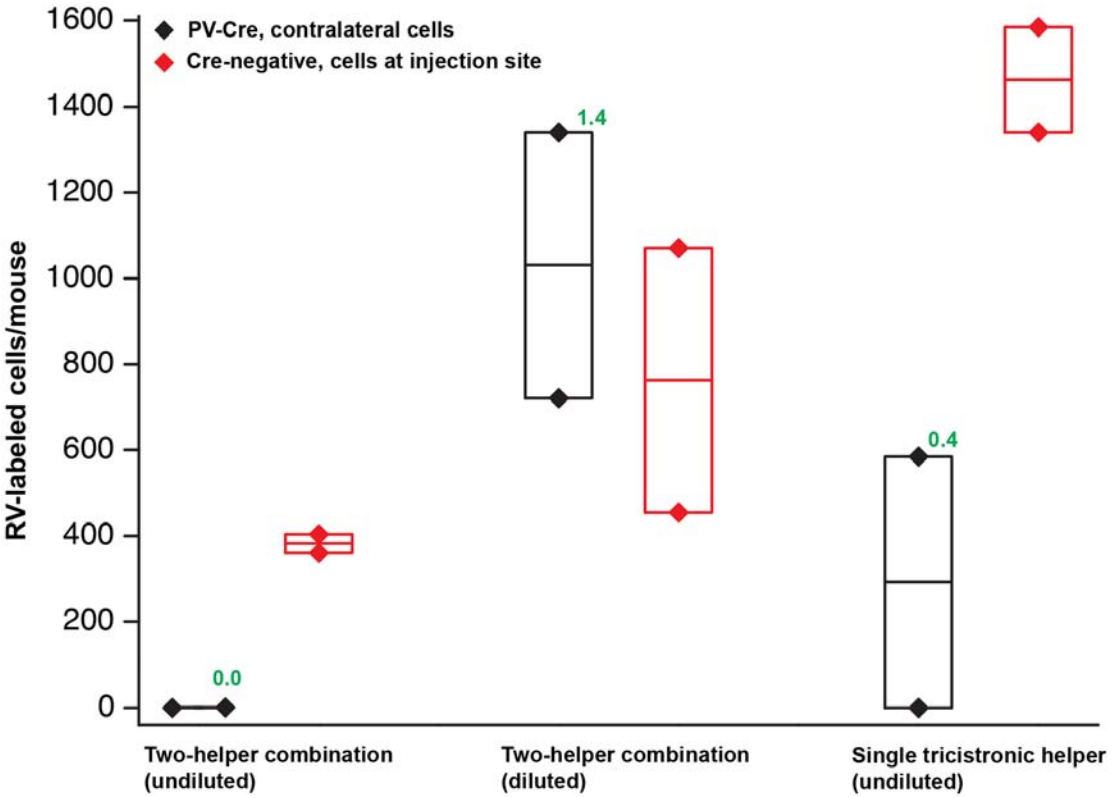

FIGURE 4 | Quantification of results in PV-Cre and Cre-negative mice: a pilot study with helper viruses either undiluted or diluted to titers used in previous work. Black depicts numbers of neurons labeled by RV in the contralateral cortex (in every other 50 μm section) in PV-Cre mice; red depicts numbers of RV-labeled neurons in the vicinity of the injection site, i.e., in ipsilateral cortex (in every other 50 μm section) in Cre-negative mice for all conditions. Diamonds represent cell counts from individual mice; the middle lines in the boxes represent the average count for each condition. Numbers in green represent the ratio of contralateral neurons in Cre+ mice to ipsilateral neurons in Cre− mice. "Diluted" here means diluted to the titers of other batches used previously in our laboratory; see main text for details. Excessive concentrations of helper viruses gave very poor results. Source numbers are provided in **Supplementary Table S1**.

recombinase; Raymond and Soriano, 2007) and perfused the mice 7 days after that.

The results were surprisingly bad. **Figures 2A–H** show example results using the two-helper combination without dilution. While many cells were well-labeled with EGFP, blue fluorescence was barely visible, and there were few tdTomato-labeled cells at the injection site and almost none elsewhere (see **Figure 4** for quantification). Furthermore, matched control injections of the same viruses in Cre-negative mice resulted in undesirably large numbers of RV-labeled neurons at the injection site (**Figures 2I–L**). This was evidently not the fault of the RV preparation: in control-animals injected only with RV, with no helper viruses, we found very few RV-labeled cells at the injection site or otherwise (**Supplementary Figure S1**; cell counts are given in **Supplementary Table S1**), suggesting that the likely cause is "leaky" expression of TVA from the AAV helper virus, even in Cre-negative neurons. While results using the undiluted single tricistronic helper virus looked better in PV-Cre mice, they were still unimpressive, and the problem of a label in Cre-negative mice was far worse (see **Figure 4** for quantification; example images not shown in these cases).

On the assumption that the poor results in Cre mice were due to toxicity resulting from excessive concentration, we diluted the new preparations to the same titers as those of the batches that we had been using previously: namely, we diluted AAV1-syn-FLEX-splitTVA-EGFP-tTA by a factor of 17.96 (to 9.47×10^{11} gc/ml, based on the titer reported by Addgene) and AAV1-TREtight-mTagBFP2-B19G by a factor of 19.98 (to 1.60×10^{12} gc/ml, based on the titer reported by Addgene).

Using these diluted helper viruses gave us much better results, with large numbers of RV-labeled neurons found in upstream regions including secondary somatosensory cortex, thalamus, and contralateral cortex (**Figures 3A–H** show example results; see **Figure 4** for quantification). However, in mice not expressing Cre, even using the diluted AAVs resulted in unreasonably-high numbers of RV-labeled neurons (red; **Figures 3I–L**, with quantification in **Figure 4**), as well as bright blue (but no visible green, even with immunostaining) labeling indicative of leaky expression from the helper viruses in the absence of recombinase.

We, therefore, embarked on a systematic set of experiments testing a range of dilutions for each helper virus, in order to find a set of dilutions for both the two-helper combination and the

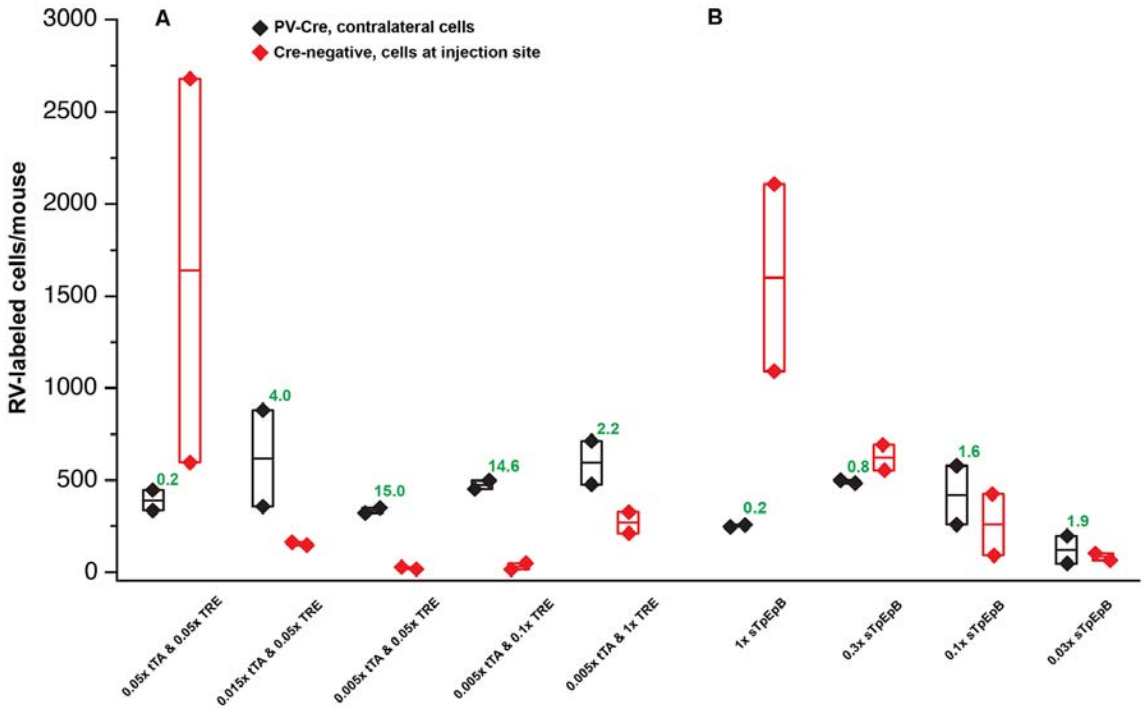

FIGURE 5 | Quantification of results in PV-Cre and Cre-negative mice: systematic dilution series. **(A)** Results of varying the concentrations of the two helper viruses in the tTA-TRE combination system. The highest ratio of contralateral neurons in Cre+ mice to ipsilateral neurons in Cre− mice was obtained with a 1:200 dilution of AAV1-syn-FLEX-splitTVA-EGFP-tTA and a 1:20 dilution of AAV1-TREtight-mTagBFP2-B19G ("0.005 × tTA and 0.05 × TRE" in the figure). **(B)** Results of varying the concentration of the single helper virus AAV1-syn-FLEX-splitTVA-EGFP-B19G. Higher dilutions (out to 1:33.3) give higher ratios of contralateral neurons in Cre+ mice to ipsilateral neurons in Cre− mice, but results with the single-helper approach were nowhere near as good as with the two-helper combination. $n = 2$ for all conditions. Diamonds represent cell counts from individual mice; the middle lines in the boxes represent the average count for each condition. Source numbers are provided in **Supplementary Table S2**.

single helper that would result in efficient transsynaptic label in Cre mice but low background label in Cre-negative mice. For these experiments, the RV used was RVΔG-4mCherry(EnvA) (Kohara et al., 2014), expressing mCherry (Shaner et al., 2004) rather than FLPo, to correspond most closely with the kind of experimental design used by typical users (the use of the FLP/FRT system in the pilot experiments described above was because those were originally intended to be controls for a different project). The results of these experiments are quantified in **Figure 5**, with source numbers given in **Supplementary Table S2**.

For the two-helper combination (**Figure 5A**), we were able to find dilutions that resulted in good transsynaptic label in Cre mice with little label at the injection site of Cre-negative mice. We began with 1:20 dilutions of both AAV1-syn-FLEX-splitTVA-EGFP-tTA and AAV1-TREtight-mTagBFP2-B19G, approximating (with simplification) the 1:17.96 and 1:19.98 dilutions used for used for **Figures 2–4**. Holding the concentration of the TRE AAV constant, we compared dilutions of the FLEX AAV of 1:20, 1:66.67, and 1:200 (labeled in panel A as "0.05×," "0.015×," and "0.005×," respectively). Of these, we found that the most extreme dilution tested, 1:200, worked best, with the numbers of labeled cells in contralateral cortex in Cre mice almost as high as for the 1:20 dilution but with the numbers of labeled cells at the injection site in Cre-negative mice drastically reduced. Holding the concentration of the FLEX AAV constant at 1:200, we then tried increasing the concentration of the TRE AAV, comparing the 1:20 dilution to 1:10 and to undiluted stock. Interestingly, while these two additional conditions resulted in somewhat higher numbers of labeled contralateral cells in PV-Cre mice, they also greatly increased the numbers of cells labeled at the injection site in Cre-negative mice (compare "0.005 × tTA and 0.05 × TRE" to "0.005 × tTA and 1 × TRE" in **Figure 5A**). Because the amount of TVA was not changed across these latter conditions, we assume that the additional labeled cells in Cre-negative mice were due to leaky G expression [presumably primarily from leaky tTA expression driving G expression, but also potentially from the TRE-tight promoter itself being leaky (Shima et al., 2016)] being sufficient to allow limited transsynaptic spread of the RV from the initially-infected cells.

The best condition tested was therefore AAV1-syn-FLEX-splitTVA-EGFP-tTA 1:200 (for a final titer of 8.5×10^{10} gc/ml) and AAV1-TREtight-mTagBFP2-B19G 1:20 (for a final titer of 1.6×10^{12} GC/ml). Example images of results using this combination are shown in **Figures 6A–H**, for Cre mice and **Figures 6I–L**, for Cre-negative mice.

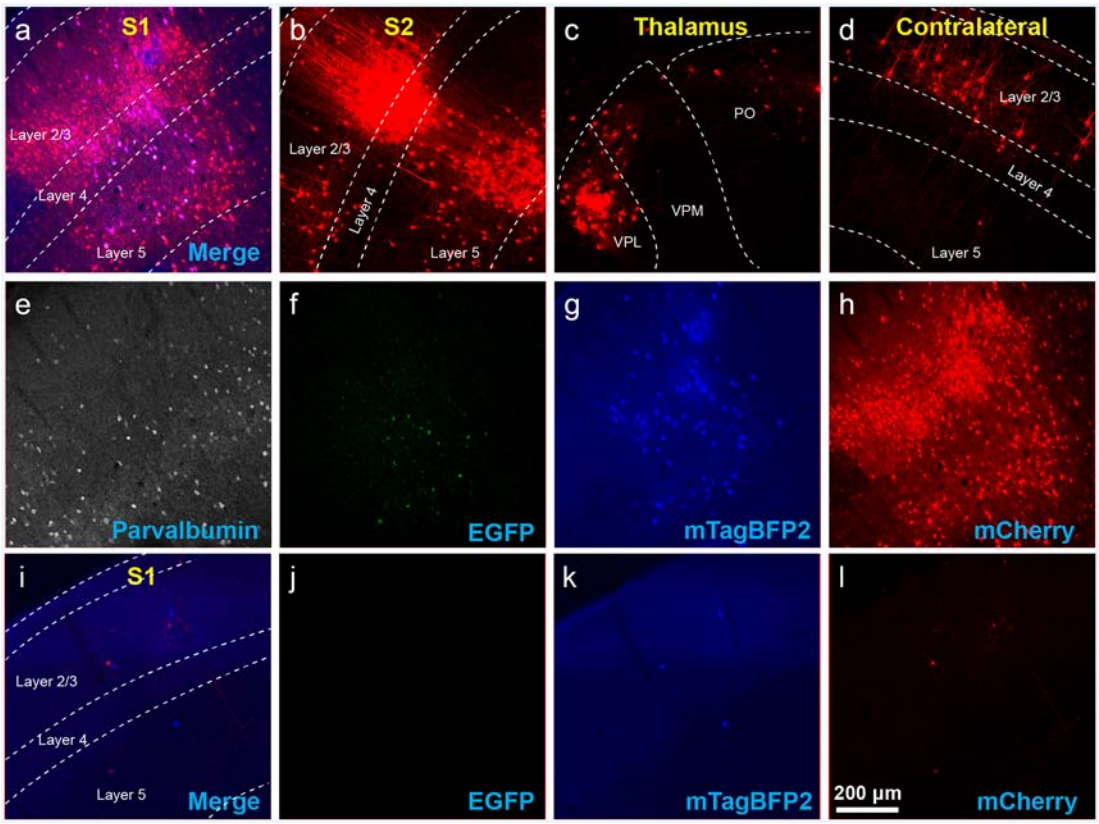

FIGURE 6 | Example results using recommended dilutions of two-helper combination. **(A–H)** Use of the two-AAV combination at 1:200 and 1:20 dilutions (see main text) labeled many presynaptic neurons. **(A)** Injection site in S1. Green = anti-EGFP staining, blue = mTagBFP2, red = mCherry. Individual channels from this field are shown in panels **(E–H)**. **(B)** Many labeled neurons were found in ipsilateral S2. **(C)** Many labeled neurons were found in ipsilateral thalamus (VPL, VPM, and Po). **(D)** Many labeled neurons were found in contralateral S1. **(E–H)** Individual channels from the field shown in panel **(A)**. **(E)** Anti-parvalbumin staining (not shown in panel **A**). **(F)** Anti-EGFP staining, indicating expression from the first, Cre-dependent AAV. Note that, at this dilution, the EGFP signal is quite dim even with immune amplification. **(G)** mTagBFP2, indicating expression from the second, tTA-dependent AAV. **(H)** mCherry, indicating the presence of the ΔG RV. **(I–L)** Injection site after using two-helper combination at 1:200 and 1:20 (see main text): few mCherry-labeled cells are seen. **(I)** Overlay of **(J–L)**. **(J)** Anti-EGFP staining: no signal is visible, even with amplification. **(K)** mTagBFP2 signal. A few blue cells are seen even at these dilutions. **(L)** mCherry expressed by RV. Scale bar in **(A)**: 200 μm, applies to all panels.

For the single tricistronic helper AAV1-syn-FLEX-splitTVA-EGFP-B19G, we compared undiluted ("1×" in **Figure 5B**) to 1:3.33, 1:10, and 1:33.3 dilutions ("0.3×," "0.1×," and "0.03×" in the figure). While all the diluted versions improved matters over the undiluted version, none of the dilutions gave particularly good results, with even the highest dilution still resulting in much higher numbers of labeled cells at the injection site in Cre-negative animals than were found with the optimized two-helper combination, but with far fewer transsynaptically labeled cells in Cre mice. Example images of results using the 1:10 dilution are shown in **Figures 7A–G**, for Cre mice and **Figures 7H–J**, for Cre-negative mice.

Finally, to determine whether the dilutions for the two-virus combination that worked best in PV-Cre mice also worked well in another Cre line, we performed a similar experiment in DAT-Cre mice (Backman et al., 2006), with 1:200 AAV1-syn-FLEX-splitTVA-EGFP-tTA and 1:20 AAV1-TREtight-mTagBFP2-B19G followed by RVΔG-4FLPo(EnvA) a week later. As shown in **Figures 8A–H** for Cre mice and **Figures 8I–L** for Cre-negative mice, there were abundant labeled cells in striatum and cortex, suggesting that these helper virus dilutions may work well with other starting cell populations.

DISCUSSION

Our results demonstrate that the success of monosynaptic tracing depends strongly on the complementation strategy (using the two tTA-TRE coupled helper viruses worked much better than the single helper virus expressing TVA, EGFP, and G) and on the concentrations of the helper viruses.

We have done these titration experiments with cortical injections in PV-Cre or Cre-negative mice. Results with other injection sites and Cre lines will presumably vary depending on the tropism of AAV1 for the targeted cell type and the other cells in the vicinity of the injection site. However, the fact that the parameters that we found to work best in PV-Cre, namely the two-helper combination with dilutions of 1:200 and 1:20, respectively, also gave good results in DAT-Cre mice

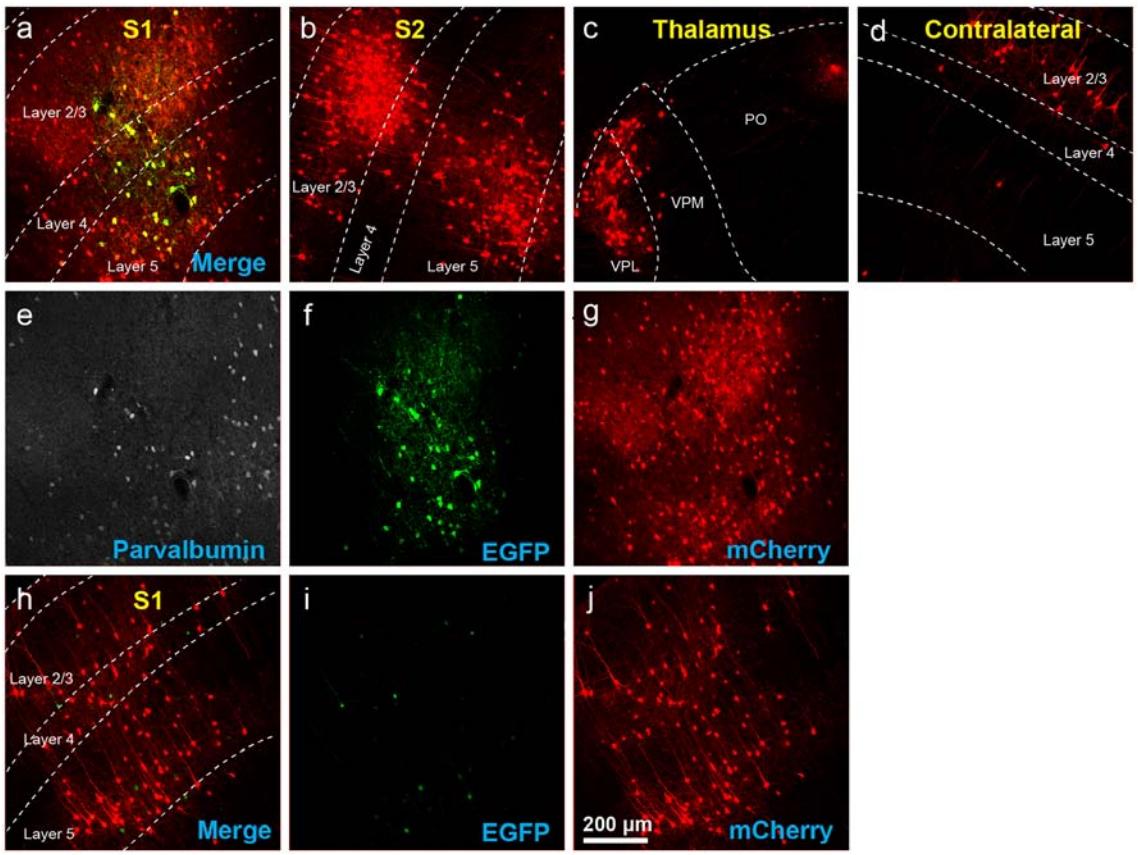

FIGURE 7 | Results using recommended dilutions of the single tricistronic helper. **(A–G)** Use of the single tricistronic helper AAV at 1:10 dilution (see main text) also labeled many presynaptic neurons (but see **Figure 7**). **(A)** Injection site in S1; individual channels from this field are shown in panels **(E–G)**. **(B)** Labeled neurons in ipsilateral S2. **(C)** Labeled neurons in ipsilateral thalamus (VPL, VPM, and Po). **(D)** Labeled neurons in contralateral S1. **(E)** Anti-parvalbumin staining (not shown in panel **A**). **(F)** Anti-EGFP staining, indicating expression from the first, Cre-dependent AAV. **(G)** mCherry, indicating the presence of the ΔG RV. **(H–J)** Injection site after using a single tricistronic helper: many mCherry-labeled neurons are present. **(H)** Overlay of **(I,J)**. **(I)** Anti-EGFP staining: the significant signal is seen even in these Cre-negative mice. **(J)** mCherry expressed by RV. Scale bar in **(A)**: 200 μm, applies to all panels.

(**Figure 8**) may indicate that these could be good general-purpose parameters for most Cre lines; at the very least, they should serve as a good starting point for a much more limited set of titration experiments than we have undertaken here.

Importantly, for all of the experiments presented here, we held the interval between AAV and RV injection constant at 7 days. There is no reason to think that a different interval (e.g., 2 weeks) would not also work fine, but this would presumably necessitate a different dilution of each of the helper viruses (i.e., if given more time to express, the AAVs would presumably need to be diluted even more).

It may also be possible to further improve the design of the helper AAVs in order to minimize the leaky TVA/tTA expression and concomitant off-target RV infection. In a recent article, Fischer et al. (2019) systematically examined factors leading to a "leak" expression from FLEX AAVs. While the FLEX AAV we have used here already contains the "ATG-out" design that is one of Fischer et al.'s (2019) primary recommendations, it also uses the usual (Atasoy et al., 2008) combination of loxP and lox2272 instead of versions that may be more resistant to spontaneous recombination. Any reduction in leak expression would allow higher AAV concentrations to be used, which could increase the efficiency of the transsynaptic spread of the RV, most obviously by increasing expression of G but also potentially by increasing expression of TVA itself (see Miyamichi et al., 2013) for evidence that the amount of TVA-mediated RV entry correlates with the amount of transsynaptic label).

Beyond the specifics of the particular helper viruses and experimental parameters presented here, our findings underscore that monosynaptic tracing results should not be taken as a complete delineation of the set of cells presynaptic to a targeted starting cell group, given that the number of false negatives (unlabeled cells that are actually presynaptic to the starting cells) clearly depends on the experimental parameters.

DATA AVAILABILITY STATEMENT

All datasets generated for this study are included in the article/**Supplementary Material**.

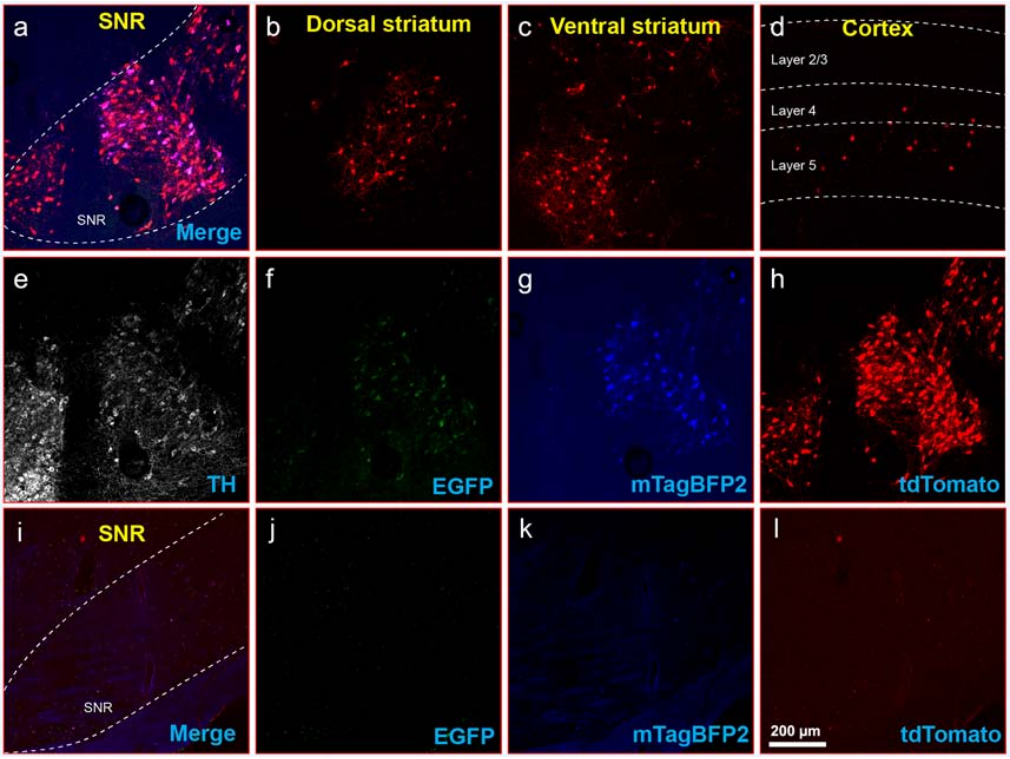

FIGURE 8 | Inputs to midbrain dopaminergic cells using recommended dilutions of two-helper combination. **(A–H)** Results in DAT-Cre mice. **(A)** Injection site in substantial nigra reticulata (SNR): overlay of panels **(F–H)**. **(B)** RV-labeled cells in the dorsal striatum. **(C)** RV-labeled cells in ventral striatum. **(D)** RV-labeled cells in the cortex. **(E)** Anti-tyrosine hydroxylase (TH) staining (not shown in panel **A**). **(F)** Anti-EGFP staining, indicating expression from the first, Cre-dependent AAV. **(G)** mTagBFP2, indicating expression from the second, tTA-dependent AAV. **(H)** tdTomato, reporting activity of the FLPo-encoding RV. **(I–L)** Results in Cre-negative mice (injection site shown). **(I)** Overlay of **(J–L)**. **(J)** anti-EGFP staining: no signal is visible, even with immunostaining. **(K)** mTagBFP2 signal. no signal is visible, even with amplification. **(L)** tdTomato, reporting activity of the FLPo-encoding RV. Only one labeled cell is visible. Scale bar in **(A)**: 200 μm, applies to all panels.

ETHICS STATEMENT

The animal study was reviewed and approved by MIT Committee on Animal Care.

AUTHOR CONTRIBUTIONS

All authors participated in designing experiments. TL, LJ, and NL performed experiments. TL, LJ, and IW wrote the manuscript.

FUNDING

Research reported in this publication was supported by BRAIN Initiative awards U01MH106018, U01MH114829, and U19MH114830 from the National Institute of Mental Health. This manuscript has been released as a preprint at bioRxiv (Lavin et al., 2019a).

ACKNOWLEDGMENTS

We thank Kimberly Ritola of Janelia Research Campus for helpful discussions regarding the important issue of leaky FLEX viruses as well as Melina Fan and Karen Guerin of Addgene for helpful discussions and for producing the helper AAVs and providing them to our laboratory and to the worldwide neuroscience community.

SUPPLEMENTARY MATERIAL

The Supplementary Material for this article can be found online at: https://www.frontiersin.org/articles/10.3389/fnsyn.2020.00006/full#supplementary-material.

FIGURE S1 | Results with rabies virus injection only without helper virus. S1 cortex of two animals were injected with 100 nl RVΔG-4FLPo(EnvA) virus only, without a previous AAV injection. Very few tdTomato-labeled cells were found. Scale bar in a: 100 μm, applies to all panels.

TABLES S1, S2 | Counts of labeled cells in PV-Cre and Cre-negative mice. Numbers of labeled neurons in the contralateral cortex of PV-Cre mice and at the injection site of Cre-negative mice for the various helper virus conditions. Each number in the "# cells" column indicates the total number of labeled cells found in the examined region (either the vicinity of the injection site or the contralateral cortex) across all 50 μm sections in that series of every sixth section (see "Materials and Methods" section). The total number of labeled neurons counted for a given mouse was the sum of the total labeled neurons in each of the three examined series for that mouse (i.e., the total found in every other section). The means of the total numbers of labeled neurons and individual count for each condition are graphed in **Figure 4** (**Supplementary Table S1**) and **Figure 5** (**Supplementary Table S2**).

REFERENCES

Ährlund-Richter, S., Xuan, Y., van Lunteren, J. A., Kim, H., Ortiz, C., Pollak Dorocic, I., et al. (2019). A whole-brain atlas of monosynaptic input targeting four different cell types in the medial prefrontal cortex of the mouse. *Nat. Neurosci.* 22, 657–668. doi: 10.1038/s41593-019-0354-y

Atasoy, D., Aponte, Y., Su, H. H., and Sternson, S. M. (2008). A FLEX switch targets Channelrhodopsin-2 to multiple cell types for imaging and long-range circuit mapping. *J. Neurosci.* 28, 7025–7030. doi: 10.1523/JNEUROSCI.1954-08.2008

Backman, C. M., Malik, N., Zhang, Y., Shan, L., Grinberg, A., Hoffer, B. J., et al. (2006). Characterization of a mouse strain expressing Cre recombinase from the 3' untranslated region of the dopamine transporter locus. *Genesis* 44, 383–390. doi: 10.1002/dvg.20228

Bates, P., Young, J. A., and Varmus, H. E. (1993). A receptor for subgroup A Rous sarcoma virus is related to the low density lipoprotein receptor. *Cell* 74, 1043–1051. doi: 10.1016/0092-8674(93)90726-7

Bauer, A., Nolden, T., Schröter, J., Römer-Oberdörfer, A., Gluska, S., Perlson, E., et al. (2014). Anterograde glycoprotein-dependent transport of newly generated rabies virus in dorsal root ganglion neurons. *J. Virol.* 88, 14172–14183. doi: 10.1128/jvi.02254-14

Beier, K. T. (2019). Hitchhiking on the neuronal highway: mechanisms of transsynaptic specificity. *J. Chem. Neuroanat.* 99, 9–17. doi: 10.1016/j.jchemneu.2019.05.001

Beier, K. T., Steinberg, E. E., DeLoach, K. E., Xie, S., Miyamichi, K., Schwarz, L., et al. (2015). Circuit architecture of VTA dopamine neurons revealed by systematic input-output mapping. *Cell* 162, 622–634. doi: 10.1016/j.cell.2015.07.015

Bockstael, O., Melas, C., Pythoud, C., Levivier, M., McCarty, D., Samulski, R. J., et al. (2012). Rapid transgene expression in multiple precursor cell types of adult rat subventricular zone mediated by adeno-associated type 1 vectors. *Hum. Gene Ther.* 23, 742–753. doi: 10.1089/hum.2011.216

Chatterjee, S., Sullivan, H. A., MacLennan, B. J., Xu, R., Hou, Y., Lavin, T. K., et al. (2018). Nontoxic, double-deletion-mutant rabies viral vectors for retrograde targeting of projection neurons. *Nat. Neurosci.* 21, 638–646. doi: 10.1038/s41593-018-0091-7

Conzelmann, K. K., Cox, J. H., Schneider, L. G., and Thiel, H. J. (1990). Molecular cloning and complete nucleotide sequence of the attenuated rabies virus SAD B19. *Virology* 175, 485–499. doi: 10.1016/0042-6822(90)90433-r

Cormack, B. P., Valdivia, R. H., and Falkow, S. (1996). FACS-optimized mutants of the green fluorescent protein (GFP). *Gene* 173, 33–38. doi: 10.1016/0378-1119(95)00685-0

Daigle, T. L., Madisen, L., Hage, T. A., Valley, M. T., Knoblich, U., Larsen, R. S., et al. (2018). A suite of transgenic driver and reporter mouse lines with enhanced brain-cell-type targeting and functionality. *Cell* 174, 465.e22–480.e22. doi: 10.1016/j.cell.2018.06.035

Federspiel, M. J., Bates, P., Young, J. A., Varmus, H. E., and Hughes, S. H. (1994). A system for tissue-specific gene targeting: transgenic mice susceptible to subgroup A avian leukosis virus-based retroviral vectors. *Proc. Natl. Acad. Sci. U S A* 91, 11241–11245. doi: 10.1073/pnas.91.23.11241

Fischer, K. B., Collins, H. K., and Callaway, E. M. (2019). Sources of off-target expression from recombinase-dependent AAV vectors and mitigation with cross-over insensitive ATG-out vectors. *Proc. Natl. Acad. Sci. U S A* 116, 27001–27010. doi: 10.1073/pnas.1915974116

Flotte, T. R., and Büning, H. (2018). Severe toxicity in nonhuman primates and piglets with systemic high-dose administration of adeno-associated virus serotype 9-like vectors: putting patients first. *Hum. Gene Ther.* 29, 283–284. doi: 10.1089/hum.2018.021

Gossen, M., and Bujard, H. (1992). Tight control of gene expression in mammalian cells by tetracycline-responsive promoters. *Proc. Natl. Acad. Sci. U S A* 89, 5547–5551. doi: 10.1073/pnas.89.12.5547

Hinderer, C., Katz, N., Buza, E. L., Dyer, C., Goode, T., Bell, P., et al. (2018). Severe toxicity in nonhuman primates and piglets following high-dose intravenous administration of an adeno-associated virus vector expressing human SMN. *Hum. Gene Ther.* 29, 285–298. doi: 10.1089/hum.2018.015

Hippenmeyer, S., Vrieseling, E., Sigrist, M., Portmann, T., Laengle, C., Ladle, D. R., et al. (2005). A developmental switch in the response of DRG neurons to ETS transcription factor signaling. *PLoS Biol.* 3:e159. doi: 10.1371/journal.pbio.0030159

Hirsch, M. L., Fagan, B. M., Dumitru, R., Bower, J. J., Yadav, S., Porteus, M. H., et al. (2011). Viral single-strand DNA induces p53-dependent apoptosis in human embryonic stem cells. *PLoS One* 6:e27520. doi: 10.1371/journal.pone.0027520

Hordeaux, J., Hinderer, C., Goode, T., Katz, N., Buza, E. L., Bell, P., et al. (2018a). Toxicology study of intra-cisterna magna adeno-associated virus 9 expressing human α-L-iduronidase in rhesus macaques. *Mol. Ther. Methods Clin. Dev.* 10, 79–88. doi: 10.1016/j.omtm.2018.06.003

Hordeaux, J., Wang, Q., Katz, N., Buza, E. L., Bell, P., and Wilson, J. M. (2018b). The neurotropic properties of AAV-PHP.B are limited to C57BL/6J mice. *Mol. Ther.* 26, 664–668. doi: 10.1016/j.ymthe.2018.01.018

Jha, N. K., Latinovic, O., Martin, E., Novitskiy, G., Marin, M., Miyauchi, K., et al. (2011). Imaging single retrovirus entry through alternative receptor isoforms and intermediates of virus-endosome fusion. *PLoS Pathog.* 7:e1001260. doi: 10.1371/journal.ppat.1001260

Kohara, K., Pignatelli, M., Rivest, A. J., Jung, H. Y., Kitamura, T., Suh, J., et al. (2014). Cell type-specific genetic and optogenetic tools reveal hippocampal CA2 circuits. *Nat. Neurosci.* 17, 269–279. doi: 10.1038/nn.3614

Lavin, T. K., Jin, L., Lea, N. E., and Wickersham, I. (2019a). Monosynaptic tracing success depends critically on helper virus concentrations. *bioRxiv* [Preprint]. doi: 10.1101/736017

Lavin, T. K., Jin, L., and Wickersham, I. R. (2019b). Monosynaptic tracing: a step-by-step protocol. *J. Chem. Neuroanat.* 102:101661. doi: 10.1016/j.jchemneu.2019.101661

Liu, K., Kim, J., Kim, D. W., Zhang, Y. S., Bao, H., Denaxa, M., et al. (2017). Lhx6-positive GABA-releasing neurons of the zona incerta promote sleep. *Nature* 548, 582–587. doi: 10.1038/nature23663

Luo, L., Callaway, E. M., and Svoboda, K. (2018). Genetic dissection of neural circuits: a decade of progress. *Neuron* 98:865. doi: 10.1016/j.neuron.2018.05.004

Madisen, L., Garner, A. R., Shimaoka, D., Chuong, A. S., Klapoetke, N. C., Li, L., et al. (2015). Transgenic mice for intersectional targeting of neural sensors and effectors with high specificity and performance. *Neuron* 85, 942–958. doi: 10.1016/j.neuron.2015.02.022

Madisen, L., Zwingman, T. A., Sunkin, S. M., Oh, S. W., Zariwala, H. A., Gu, H., et al. (2010). A robust and high-throughput Cre reporting and characterization system for the whole mouse brain. *Nat. Neurosci.* 13, 133–140. doi: 10.1038/nn.2467

Marshel, J. H., Mori, T., Nielsen, K. J., and Callaway, E. M. (2010). Targeting single neuronal networks for gene expression and cell labeling *in vivo*. *Neuron* 67, 562–574. doi: 10.1016/j.neuron.2010.08.001

Matsuyama, M., Jin, L., Lavin, T. K., Sullivan, H. A., Hou, Y., Lea, N. E., et al. (2019). "Self-inactivating" rabies viruses are just first-generation, ΔG rabies viruses. *bioRxiv* [Preprint]. doi: 10.1101/550640

Miyamichi, K., Shlomai-Fuchs, Y., Shu, M., Weissbourd, B. C., Luo, L., and Mizrahi, A. (2013). Dissecting local circuits: parvalbumin interneurons underlie broad feedback control of olfactory bulb output. *Neuron* 80, 1232–1245. doi: 10.1016/j.neuron.2013.08.027

Paxinos, G., and Franklin, B. J. (2013). *Paxinos and Franklin's The Mouse Brain in Stereotaxic Coordinates.* Amsterdam: Elsevier/AP.

Rabinowitz, J., Chan, Y. K., and Samulski, R. J. (2019). Adeno-associated virus (AAV) versus immune response. *Viruses* 11:E102. doi: 10.3390/v11020102

Rancz, E. A., Franks, K. M., Schwarz, M. K., Pichler, B., Schaefer, A. T., and Margrie, T. W. (2011). Transfection *via* whole-cell recording *in vivo*: bridging single-cell physiology, genetics and connectomics. *Nat. Neurosci.* 14, 527–532. doi: 10.1038/nn.2765

Raymond, C. S., and Soriano, P. (2007). High-efficiency FLP and PhiC31 site-specific recombination in mammalian cells. *PLoS One* 2:e162. doi: 10.1371/journal.pone.0000162

Rompani, S. B., Müllner, F. E., Wanner, A., Zhang, C., Roth, C. N., Yonehara, K., et al. (2017). Different modes of visual integration in the lateral geniculate nucleus revealed by single-cell-initiated transsynaptic tracing. *Neuron* 93:1519. doi: 10.1016/j.neuron.2017.03.009

Sakurai, K., Zhao, S., Takatoh, J., Rodriguez, E., Lu, J., Leavitt, A. D., et al. (2016). Capturing and manipulating activated neuronal ensembles with

CANE delineates a hypothalamic social-fear circuit. *Neuron* 92, 739–753. doi: 10.1016/j.neuron.2016.10.015

Sauer, B., and Henderson, N. (1988). Site-specific DNA recombination in mammalian cells by the Cre recombinase of bacteriophage P1. *Proc. Natl. Acad. Sci. U S A* 85, 5166–5170. doi: 10.1073/pnas.85.14.5166

Seidler, B., Schmidt, A., Mayr, U., Nakhai, H., Schmid, R. M., Schneider, G., et al. (2008). A Cre-loxP-based mouse model for conditional somatic gene expression and knockdown *in vivo* by using avian retroviral vectors. *Proc. Natl. Acad. Sci. U S A* 105, 10137–10142. doi: 10.1073/pnas.0800487105

Shaner, N. C., Campbell, R. E., Steinbach, P. A., Giepmans, B. N., Palmer, A. E., and Tsien, R. Y. (2004). Improved monomeric red, orange and yellow fluorescent proteins derived from Discosoma sp. red fluorescent protein. *Nat. Biotechnol.* 22, 1567–1572. doi: 10.1038/nbt1037

Shima, Y., Sugino, K., Hempel, C. M., Shima, M., Taneja, P., Bullis, J. B., et al. (2016). A Mammalian enhancer trap resource for discovering and manipulating neuronal cell types. *Elife* 5:e13503. doi: 10.7554/eLife.13503

Subach, O. M., Cranfill, P. J., Davidson, M. W., and Verkhusha, V. V. (2011). An enhanced monomeric blue fluorescent protein with the high chemical stability of the chromophore. *PLoS One* 6:e28674. doi: 10.1371/journal.pone.0028674

Szonyi, A., Sos, K. E., Nyilas, R., Schlingloff, D., Domonkos, A., Takács, V. T., et al. (2019). Brainstem nucleus incertus controls contextual memory formation. *Science* 364:eaaw0445. doi: 10.1126/science.aaw0445

Tallquist, M. D., and Soriano, P. (2000). Epiblast-restricted Cre expression in MORE mice: a tool to distinguish embryonic vs. extra-embryonic gene function. *Genesis* 26, 113–135. doi: 10.1002/(sici)1526-968x(200002)26:2<113::aid-gene3>3.0.co;2-2

Wall, N. R., Wickersham, I. R., Cetin, A., De La Parra, M., and Callaway, E. M. (2010). Monosynaptic circuit tracing *in vivo* through Cre-dependent targeting and complementation of modified rabies virus. *Proc. Natl. Acad. Sci. U S A* 107, 21848–21853. doi: 10.1073/pnas.1011756107

Watabe-Uchida, M., Zhu, L., Ogawa, S. K., Vamanrao, A., and Uchida, N. (2012). Whole-brain mapping of direct inputs to midbrain dopamine neurons. *Neuron* 74, 858–873. doi: 10.1016/j.neuron.2012.03.017

Weible, A. P., Schwarcz, L., Wickersham, I. R., Deblander, L., Wu, H., Callaway, E. M., et al. (2010). Transgenic targeting of recombinant rabies virus reveals monosynaptic connectivity of specific neurons. *J. Neurosci.* 30, 16509–16513. doi: 10.1523/JNEUROSCI.2442-10.2010

Wertz, A., Trenholm, S., Yonehara, K., Hillier, D., Raics, Z., Leinweber, M., et al. (2015). PRESYNAPTIC NETWORKS. Single-cell-initiated monosynaptic tracing reveals layer-specific cortical network modules. *Science* 349, 70–74. doi: 10.1126/science.aab1687

Wickersham, I. R., Finke, S., Conzelmann, K. K., and Callaway, E. M. (2007a). Retrograde neuronal tracing with a deletion-mutant rabies virus. *Nat. Methods* 4, 47–49. doi: 10.1038/nmeth999

Wickersham, I. R., Lyon, D. C., Barnard, R. J., Mori, T., Finke, S., Conzelmann, K. K., et al. (2007b). Monosynaptic restriction of transsynaptic tracing from single, genetically targeted neurons. *Neuron* 53, 639–647. doi: 10.1016/j.neuron.2007.01.033

Wickersham, I. R., and Sullivan, H. A. (2015). Rabies viral vectors for monosynaptic tracing and targeted transgene expression in neurons. *Cold Spring Harb. Protoc.* 2015, 375–385. doi: 10.1101/pdb.prot072389

Wickersham, I. R., Sullivan, H. A., and Seung, H. S. (2010). Production of glycoprotein-deleted rabies viruses for monosynaptic tracing and high-level gene expression in neurons. *Nat. Protoc.* 5, 595–606. doi: 10.1038/nprot.2009.248

Young, J. A., Bates, P., and Varmus, H. E. (1993). Isolation of a chicken gene that confers susceptibility to infection by subgroup A avian leukosis and sarcoma viruses. *J. Virol.* 67, 1811–1816. doi: 10.1128/jvi.67.4.1811-1816.1993

Zampieri, N., Jessell, T. M., and Murray, A. J. (2014). Mapping sensory circuits by anterograde transsynaptic transfer of recombinant rabies virus. *Neuron* 81, 766–778. doi: 10.1016/j.neuron.2013.12.033

Zhang, Z., Zhong, P., Hu, F., Barger, Z., Ren, Y., Ding, X., et al. (2019). An excitatory circuit in the perioculomotor midbrain for non-REM sleep control. *Cell* 177, 1293.e16–1307.e16. doi: 10.1016/j.cell.2019.03.041

Conflict of Interest: The authors declare that the research was conducted in the absence of any commercial or financial relationships that could be construed as a potential conflict of interest.

frontiers in Synaptic Neuroscience

METHODS
published: 27 March 2020
doi: 10.3389/fnsyn.2020.00011

A Practical Guide to Using CV Analysis for Determining the Locus of Synaptic Plasticity

*Jennifer A. Brock[1,2], Aurore Thomazeau[1], Airi Watanabe[1,2], Sally Si Ying Li[3] and P. Jesper Sjöström[1]**

[1] Centre for Research in Neuroscience, Brain Repair and Integrative Neuroscience Program, Department of Medicine, The Research Institute of the McGill University Health Centre, Montreal General Hospital, Montreal, QC, Canada, [2] Integrated Program in Neuroscience, McGill University, Montreal, QC, Canada, [3] Solomon H. Snyder Department of Neuroscience, Johns Hopkins University School of Medicine, Baltimore, MD, United States

Long-term synaptic plasticity is widely believed to underlie learning and memory in the brain. Whether plasticity is primarily expressed pre- or postsynaptically has been the subject of considerable debate for many decades. More recently, it is generally agreed that the locus of plasticity depends on a number of factors, such as developmental stage, induction protocol, and synapse type. Since presynaptic expression alters not just the gain but also the short-term dynamics of a synapse, whereas postsynaptic expression only modifies the gain, the locus has fundamental implications for circuits dynamics and computations in the brain. It therefore remains crucial for our understanding of neuronal circuits to know the locus of expression of long-term plasticity. One classical method for elucidating whether plasticity is pre- or postsynaptically expressed is based on analysis of the coefficient of variation (CV), which serves as a measure of noise levels of synaptic neurotransmission. Here, we provide a practical guide to using CV analysis for the purposes of exploring the locus of expression of long-term plasticity, primarily aimed at beginners in the field. We provide relatively simple intuitive background to an otherwise theoretically complex approach as well as simple mathematical derivations for key parametric relationships. We list important pitfalls of the method, accompanied by accessible computer simulations to better illustrate the problems (downloadable from GitHub), and we provide straightforward solutions for these issues.

Keywords: long-term plasticity, long-term potentiation, long-term depression, spike-timing-dependent plasticity, paired recordings, monosynaptic connections, electrophysiology

OPEN ACCESS

Edited by:
Maxim Volgushev, University of Connecticut, United States

Reviewed by:
Dmitri A. Rusakov, University College London, United Kingdom
Mario Treviño, Universidad de Guadalajara, Mexico

***Correspondence:**
P. Jesper Sjöström
jesper.sjostrom@mcgill.ca

Received: *02 December 2019*
Accepted: *04 March 2020*
Published: *27 March 2020*

Citation:
Brock JA, Thomazeau A, Watanabe A, Li SSY and Sjöström PJ (2020) A Practical Guide to Using CV Analysis for Determining the Locus of Synaptic Plasticity. Front. Synaptic Neurosci. 12:11. doi: 10.3389/fnsyn.2020.00011

INTRODUCTION

Synapses transform and transmit information between neurons in a dynamic manner. This activity-dependent capacity to modify the strength of connections between neurons—termed synaptic plasticity—is widely believed to underlie information storage (Bliss and Collingridge, 1993; Malenka and Bear, 2004; Nabavi et al., 2014) as well as circuit remapping during development (Katz and Shatz, 1996; Cline, 1998; Song and Abbott, 2001).

There has been considerable disagreement regarding the locus of expression of long-term plasticity, that is whether the long-term modifications that underpin enduring changes in synaptic efficacy are primarily located presynaptically—through alterations to neurotransmitter release

properties—or postsynaptically—through modifications to the number and/or responsiveness of postsynaptic receptors (Lisman, 2003; MacDougall and Fine, 2014; Padamsey and Emptage, 2014). Much of this earlier divisiveness stemmed from the difficulty in analyzing central synapses (Bliss, 1990; Redman, 1990; Korn and Faber, 1991) using classical methods that were developed in the context of the neuromuscular junction (Del Castillo and Katz, 1954). For brevity, the structural and functional differences between the neuromuscular junction and central synapses are not stated here, as they have been reviewed in detail before (Bliss, 1990; Redman, 1990; Sanes and Lichtman, 1999).

After decades of debate, it is now generally accepted that either pre- or postsynaptic mechanisms can support the expression of long-term plasticity (Sheng and Kim, 2002; Malenka and Bear, 2004; Castillo, 2012). In fact, there is also evidence for both pre- and postsynaptic involvement in certain cases (Kullmann and Nicoll, 1992; Sjöström et al., 2007; Loebel et al., 2013; Costa et al., 2015). Generally, the locus of expression depends on factors such as animal age, induction protocol, and synapse type (Isaac et al., 1997; Corlew et al., 2007; Larsen and Sjöström, 2015). Indeed, there appears to be tremendous diversity in the cellular mechanisms that contribute to the expression of long-term potentiation (LTP) and depression (LTD) at central synapses (Malenka and Bear, 2004; Sjöström et al., 2008; Castillo, 2012). This diversity likely helps ensure the proper functioning of information storage by way of redundancy (Malenka and Bear, 2004; Murphy and Corbett, 2009). Despite this overwhelming diversity, the functional consequences of the locus of expression are actually quite poorly understood. Only a handful of recent theoretical studies show computational benefits from pre- and postsynaptic expression, such as memory savings and improved receptive field discriminability (Costa et al., 2015, 2017).

The locus of expression may thus hold distinct implications for neural coding and is therefore an important variable to resolve. For example, by modifying release probability, presynaptic expression not only affects the synaptic weight but also the reliability (Otmakhov et al., 1993) and short-term synaptic dynamics of neurotransmission (Markram and Tsodyks, 1996; Sjöström et al., 2007). Synaptic dynamics, such as short-term facilitation or depression, describe changes in synaptic strength that occur over the course of milliseconds to minutes (Zucker and Regehr, 2002; Abbott and Regehr, 2004; Fujisawa et al., 2008; Regehr, 2012). Such changes of synaptic efficacy have been proposed to underpin functionalities such as promotion of stability (Seeholzer et al., 2019), adaptation (Chance et al., 1998), decorrelation and burst detection (Lisman, 1997; Goldman et al., 2002), dynamic gain control (Abbott et al., 1997), detection of temporal coherence (Tsodyks and Markram, 1997), and working memory (Fujisawa et al., 2008; Costa et al., 2017). Postsynaptic expression, on the other hand, typically changes only the gain of synaptic transmission (Pananceau et al., 1998; Selig et al., 1999) (although see Poncer and Malinow, 2001), which in turn may affect signal to noise (Otmakhov et al., 1993). Whether long-term plasticity alters short-term plasticity thus has important computational implications. The locus of plasticity expression therefore matters.

The primary source of noise in synaptic transmission is derived from the probabilistic nature of neurotransmitter release (Otmakhov et al., 1993; Costa et al., 2017). As the coefficient of variation (CV) serves as a handy metric of noise due to synaptic release, changes in the CV due to e.g., the induction of long-term plasticity therefore imply presynaptic expression of plasticity (Bekkers and Stevens, 1990; Malinow and Tsien, 1990; Faber and Korn, 1991; Costa et al., 2017). Using CV analysis, it is therefore possible to resolve the locus of plasticity expression at central synapses. Here we provide basic instructions for how to carry out CV analysis, including tips and tricks for circumventing shortcomings and avoiding pitfalls.

MATERIALS AND EQUIPMENT

Animals and Ethics Statement

The animal study was reviewed and approved by the Montreal General Hospital Facility Animal Care Committee (The MGH FACC), and adhered to the guidelines of the Canadian Council on Animal Care (CCAC). P11-16 C57BL/6J mice were anesthetized with isoflurane and sacrificed once the hind-limb withdrawal reflex was lost. Every attempt was made to ensure minimum discomfort to the animals.

Acute Slice Electrophysiology

After decapitation, the brain was removed and placed in ice-cold (∼4°C) artificial cerebrospinal fluid (ACSF), containing in mM: 125 NaCl, 2.5 KCl, 1 $MgCl_2$, 1.25 NaH_2PO_4, 2 $CaCl_2$, 26 $NaHCO_3$, and 25 glucose, bubbled with 95% O_2/5% CO_2. Osmolarity of the ACSF was adjusted to 338 mOsm with glucose. Oblique coronal 300-μm-thick acute brain slices were prepared using a Campden Instruments 5000 mz^{-2} vibratome (Lafayette Instrument, Lafayette, IN, United States). Brain slices were kept at ∼33°C in oxygenated ACSF for ∼15 min and then allowed to cool at room temperature for at least one hour before we started the recordings. We carried out experiments with ACSF heated to 32–34°C with a resistive inline heater (Scientifica Ltd.), with temperature recorded and verified offline. Recordings were truncated or not used if outside this range.

We patched neurons with pipettes (4–6 MΩ) pulled from medium-wall capillaries using a P-1000 electrode puller (Sutter Instruments, Novato, CA, United States), and filled with a gluconate-based current-clamp solution containing (in mM): 5 KCl, 115 K-gluconate, 10 K-HEPES, 4 Mg-ATP, 0.3 Na-GTP, 10 Na_2-phosphocreatine, adjusted to pH 7.2–7.4 with KOH. For 2-photon microscopy (see below), internal solution was supplemented with 10 μM Alexa Fluor 594 (Life Technologies, Carlsbad, CA, United States). Osmolarity of internal solution was adjusted to 310 mOsm with sucrose (Abrahamsson et al., 2016; Lalanne et al., 2016). Whole-cell recordings were amplified with BVC-700A amplifiers (Dagan Corporation, Minneapolis, MN, United States) or Multiclamp 700B amplifiers (Molecular Devices, San Jose, CA, United States). Voltage signals were first filtered at 5 kHz and then digitized at 10 kHz using PCI-6229 boards (National Instruments, Austin, TX, United States) controlled by custom software (Sjöström et al., 2001) running in

Igor Pro 8 (Wavemetrics Inc., Lake Oswego, OR, United States) on a SuperLogics (Natick, MA, United States) computer.

Neurons were patched at 400× magnification with infrared video Dodt contrast (built in-house from Thorlabs parts) on a custom-modified SliceScope microscope (Scientifica Ltd., Uckfield, United Kingdom) (Abrahamsson et al., 2017). Primary visual cortex was identified by the presence of layer 4. Layer-5 (L5) pyramidal cells (PCs) were then targeted based on their large somata, thick apical dendrites, and distinctive triangular shape. We verified cell morphology using 2-photon microscopy (**Figures 2A,B**, **5Dii**).

To compensate for their sparse connectivity (Song et al., 2005; Abrahamsson et al., 2017), connected L5 PC pairs were targeted for recording by the quadruple whole-cell recording approach, enabling us to test for 12 possible connections simultaneously (Abrahamsson et al., 2016; Lalanne et al., 2016). Seals were formed with four cells and then quickly and successively broken through to avoid plasticity washout. To find connections, we evoked in each cell five spikes at 30 Hz by current injections (5 ms duration; 1.3 nA amplitude) every 20 s for 10–20 repetitions. Spikes in different cells were separated by >700 ms to ensure that long-term plasticity was not accidentally induced (Sjöström et al., 2003; Lalanne et al., 2016). If no EPSPs were found, all four recordings were interrupted, and another four nearby cells were patched with fresh pipettes. If at least one sufficiently large connection was found (>∼0.3 mV, to ensure good signal-to-noise ratio), the baseline of the experiment was started. Perfusion temperature, input resistance, resting membrane potential or holding current, and EPSP amplitude were continuously monitored online and reassessed offline. Series resistance was not compensated. Liquid junction potential (10 mV) was not accounted for. As quality selection criteria, we required that input resistance change less than 30% and resting membrane potential less than 8 mV over the time course of the experiment, and that baseline period was stable as measured with a *t*-test of Pearson's *r* (Sjöström et al., 2003, 2007; Buchanan et al., 2012; Abrahamsson et al., 2017). If these measures were stable over a 15-min-long period, LTD or LTP was elicited by repeated pre- and postsynaptic spike pairings. The LTD induction consisted on five spikes evoked in both pre- and postsynaptic cells at 20 Hz, repeated 15 times every 10 s, displaced by $\Delta t = 25$ ms pre- relative to postsynaptic spike. Similarly, LTP induction consisted of five spikes evoked in pre- and postsynaptic cells at 50 Hz, repeated 15 times every 10 s, displaced by $\Delta t = 10$ ms. In the post-pairing period, the spike bursts were continued up to 180 repetitions, for a total of 75 min.

Two-Photon Laser-Scanning Microscopy

Two-photon laser-scanning microscopy was performed with an imaging workstation custom-built from a SliceScope (Scientifica Ltd., United Kingdom) microscope (Buchanan et al., 2012). Detectors were Scientifica 2PIMS-2000 or custom-built based on R3896 bialkali photomultipliers (Hamamatsu, Bridgewater, NJ, United States) and scanners were 6215H 3-mm galvanometric mirrors (Cambridge Technology, Bedford, MA, United States). Two-photon excitation was achieved using a MaiTai HP (Spectraphysics, Santa Clara, CA, United States) titanium-sapphire laser tuned to 820 nm to excite Alexa Fluor 594 fluorescence. Lasers were gated with SH05/SC10 (Thorlabs) shutters, and manually attenuated with a polarizing beam splitter in combination with a half-lambda plate (Thorlabs GL10-B and AHWP05M-980). Laser output was monitored with a power meter (Newport 1916-R with 818-SL). Fluorescence was collected with Semrock (FF665, FF01-680/SP-25) and Chroma filters (t565lpxr, ET630/75m, ET525/50m). Laser-scanning Dodt contrast was achieved by collecting the laser light after the spatial filter with an amplified diode (Thorlabs PDA100A-EC). Imaging data were acquired using customized variants of ScanImage version 3.7 (Pologruto et al., 2003) running in MATLAB (The MathWorks, Natick, MA, United States) via PCI-6110 boards (National Instruments).

After each whole-cell recording, L5 PC morphologies were acquired as stacks of 512-by-512-pixel slices (∼1.5 pixels/μm), with each slice spaced by 1 μm. Each slice was an average of 3 red-channel frames acquired at 2 ms per line. Morphologies shown (**Figures 2A,B**, **5Dii**) are pseudo-colored maximum-intensity projections of such 3D stacks compiled with ImageJ (NIH, United States).

Statistics

Unless otherwise noted, results are reported as the mean ± standard error of the mean (SEM). Significance levels are denoted using asterisks ($^{*}p < 0.05$, $^{**}p < 0.01$, $^{***}p < 0.001$). All pairwise comparisons were carried out using a two-tailed Student's *t*-test for equal means. If an equality of variances *F* test gave $p < 0.05$, we employed the unequal variances *t*-test. Wilcoxon–Mann–Whitney's non-parametric test was always used in parallel to the *t*-test, with similar outcome. Statistical tests were performed in Igor Pro (Wavemetrics Inc.).

Simulations

Coefficient of variation analysis simulations were Monte-Carlo based with 150 repetitions of individual long-term plasticity experiments, carried out in Igor Pro. Each experiment was simulated with a baseline period consisting of 60 responses and a post-induction baseline of 240 responses. In real life, this would correspond to a 10-min baseline with an inter-stimulus interval of 10 s, followed by a 40-min-long post-pairing baseline, which is representative of our actual experiments (Sjöström et al., 2001, 2003; Abrahamsson et al., 2017). The number of release sites was fixed to $n = 5$, which is representative of a typical L5 PC-to-PC monosynaptic connection (Markram et al., 1997). To illustrate presynaptically expressed LTD (Sjöström et al., 2003, 2007), the probability of release was initially set to $p_{\mathrm{release}} = 0.55$, and was reduced to $p_{\mathrm{release}} = 0.4$ after the induction (which are representative values, e.g., see Costa et al., 2015), while the quantal amplitude was fixed at q = 0.35 mV.

Individual responses were simulated by drawing from a binomial distribution. Noise due to background activity, the amplifier, etc., was drawn from a zero-mean normal distribution with a standard deviation of 0.1 mV, which is representative of our experiments. Background noise was fixed and did not change throughout the simulated experiments.

For the outlier simulations, a single response in the baseline period was systematically increased by adding $0.1e^{-3} \times 2^{j}$mV, where $j = \{0, \ldots, 5\}$, of which three steps are shown in **Figures 4Ci–iii**, with 150 simulation reruns for each step. The *z*-score, also known as the standard score, was calculated analytically from the binomial distribution parameters.

For the baseline trend simulations, a line with slope $0.6e^{-6} \times 2^{j}\mu$V/min and zero mean was added to the simulated baseline responses, where $j = \{0, \ldots, 5\}$. As an illustration, three slopes are shown in **Figures 5Ci–iii**, each with 150 simulation reruns.

A simplified, accessible version of the simulation code is possible to download in Igor Procedure File format from GitHub: https://github.com/pj-sjostrom/Sim_CV_analysis. This code was created with a minimum number of user-modifiable parameters, to be pedagogical and relatively easy to experiment with for somebody who is new to the concept of CV analysis. This code includes the LTD simulations shown in **Figures 4**, **5**, but extends to other scenarios, including LTP.

BOX 1 | Assumptions underlying the binomial release model.
Using the binomial distribution as a model of neurotransmitter release implies that several key assumptions were made. Here, we highlight several of these assumptions.

1. The release probability, *p*, of one quantal unit is uniform across all *n* release sites (Johnson and Wernig, 1971; McLachlan, 1978; Redman, 1990; Faber and Korn, 1991; Quastel, 1997). There is some evidence that this is in fact the case, for e.g., in the neocortex (Koester and Johnston, 2005) and hippocampus (Branco et al., 2008) (although see Walmsley et al., 1988).
2. The quantal size, *q*, is uniform across all *n* release sites and over a given epoch (McLachlan, 1978; Korn et al., 1987; Redman, 1990; Faber and Korn, 1991; Quastel, 1997). This requirement seems less biologically plausible. For example, because synaptic contacts are distributed in the dendritic arbor (Markram et al., 1997), dendritic cable filtering (Sjöström et al., 2008; Maheux et al., 2016) would likely ensure that the quantal size, *q*, varies from release site to release site. Although there is some evidence for mechanisms normalizing synaptic weights across the dendritic arbor (Magee, 2000; Magee and Cook, 2000; Häusser, 2001), there is also evidence to the contrary (Williams and Stuart, 2002; Nevian et al., 2007).
3. Each of the *n* release sites may secrete at most one quantum per action potential (Triller and Korn, 1982; Korn et al., 1987; Korn and Faber, 1991; Quastel, 1997), which is known as the "one vesicle hypothesis" (Korn and Faber, 1991; Quastel, 1997) (although see Tong and Jahr, 1994; Auger et al., 1998; Oertner et al., 2002; Lisman, 2009; Jensen et al., 2019). Considering that the neurotransmitter contents of one quantum is likely sufficient to saturate postsynaptic receptors (Redman, 1990; Lisman and Harris, 1993), it follows that—to satisfy the requirement for linear summation—uniquantal release from central synapses is thought to occur across multiple, spatially segregated release sites (Lisman and Harris, 1993).
4. Release is independent across all *n* sites (Johnson and Wernig, 1971; McLachlan, 1978; Quastel, 1997). This implies that there is no interaction or correlation of release events across adjacent sites and that released quanta summate linearly (Quastel, 1997).
5. The number of *n* release sites remains constant. This is probably true for early LTP in many cases, although new synaptic contacts are likely to be formed in late LTP (2–3 h after induction) (Geinisman et al., 1993; Bolshakov et al., 1997; Korn and Faber, 1998; Loebel et al., 2013). But *n* can also be affected by so-called "AMPAfication" of silent NMDA-only synapses, which occurs in very early development (Isaac et al., 1995, 1996; Liao et al., 1995; Kerchner and Nicoll, 2008)

Whether or not all five points hold true for all synapses is thus not always clear. As an example, the majority of Schaefer collateral inputs to hippocampal CA1 PCs are thought to feature a single active zone, yet multi-vesicular release has been suggested at these connections (Tong and Jahr, 1994; Oertner et al., 2002; Jensen et al., 2019). Either multiple vesicles can be released from one release site, or each active zone hosts multiple release sites. Either way, both points 3 and 4 above may thus be violated, calling into question the validity of the binomial release model. Having said that, the CV analysis method may still work, even if e.g., a Poisson rather than a binomial model of release should be employed (Korn and Faber, 1998), it is just that the analytical treatment becomes considerably more complex if e.g., multivesicular release occurs. It is furthermore possible to test experimentally for uni-vesicular versus multi-vesicular release (Saviane and Silver, 2007).

THE QUANTAL THEORY OF SYNAPTIC RELEASE

Synaptic Release Is Quantized

Even in the absence of nervous impulses, single neurotransmitter-containing vesicles spontaneously fuse with specialized release sites in the presynaptic terminal, releasing their contents into the synaptic cleft through exocytosis (Südhof, 2013). In result, miniature postsynaptic potentials are generated, which represent the postsynaptic response due to the neurotransmitter contained in one vesicle (Fatt and Katz, 1952). This is the smallest unit of neurotransmission, which is known as a "quantum" (Fatt and Katz, 1952; Del Castillo and Katz, 1954). A synaptic bouton may contain multiple active zones or release sites (Korn et al., 1987; Korn and Faber, 1991; Maass and Zador, 1999), each of which are capable of probabilistically secreting a single quantum of neurotransmitter in response to an action potential (Isaacson and Walmsley, 1995; Korn and Faber, 1998; Maass and Zador, 1999). Although the release of multiple quanta has been documented many times (Tong and Jahr, 1994; Auger et al., 1998; Oertner et al., 2002; Lisman, 2009; Jensen et al., 2019), evoked responses are typically assumed to be due to the linear summation of single quanta released across multiple sites. Release at single sites has thus long been thought to be uniquantal as opposed to multiquantal (Lisman and Harris, 1993), even though recent studies suggest otherwise (Jensen et al., 2019). This assumption is central to the use of the binomial release model in CV analysis (see below and **Box 1**).

Stochastic Release Is a Useful Source of Noise

The stochastic properties of neurotransmitter release result in fluctuations of the postsynaptic response (Otmakhov et al., 1993; Neher and Sakaba, 2003; Saviane and Silver, 2007), which are a prominent source of noise (Otmakhov et al., 1993; Neher and Sakaba, 2003). In contrast to experimental noise, which an investigator aims to reduce (Neher and Sakaba, 2003), the pattern of response noise fluctuations recorded from a neuronal connection provides insight into the molecular regulation of synaptic transmission (Katz and Miledi, 1972; Neher and Sakaba, 2003). This response noise is examined as part of fluctuation and quantal analysis to determine parameters governing synaptic efficacy (Scheuss and Neher, 2001) and has long been used for

determining the pre- versus postsynaptic site of modification (Bekkers and Stevens, 1990; Bliss, 1990; Redman, 1990).

Another source of noise are membrane potential fluctuations produced by e.g., release from other synapses. As opposed to the experimental noise, this source of noise is intrinsic to the cell and cannot be reduced. It is possible, however, to subtract both these sources of background noise (see below) (Faber and Korn, 1991).

Quantal Theory

The quantal theory of neurotransmitter release and the notion of a "quantum" was first described by Del Castillo and Katz (1954) at the neuromuscular junction in order to describe parameters influencing synaptic function and efficacy. Through their seminal recordings of the amphibian neuromuscular junction, it was observed that evoked potentials in a muscle fiber randomly fluctuate between integer multiples of the spontaneous miniature potential or basic quantal unit, q (Del Castillo and Katz, 1954; Korn and Faber, 1991, 1998). This finding has since been replicated at other synapse types (Redman and Walmsley, 1983; Korn et al., 1987; Isaacson and Walmsley, 1995). Quantal analysis relies on the pattern of fluctuations in evoked responses to calculate presynaptic factors influencing neurotransmitter release and postsynaptic factors influencing synaptic responsiveness, thereby allowing the locus of plasticity expression to be determined (Malinow and Tsien, 1990; Redman, 1990; Isaac et al., 1996; Reid and Clements, 1999; Enoki et al., 2009).

Quantal Analysis Relies on Response Fluctuations

In quantal statistical models of neurotransmitter release, the mean synaptic response, μ, and its variance, σ^2, depend on: (1) the probability that one quantum will be released, p, from the readily releasable pool of vesicles at the nerve terminal; (2) the total number of active release sites, n; and (3) the amplitude of the synaptic response produced by one quantum, q (Del Castillo and Katz, 1954; Martin, 1966; Korn et al., 1986). If a binomial distribution of responses is assumed (**Box 1**), the mean and variance are the expected value, $E[X]$, and the variance, $Var[X]$, of the response statistic X:

$$E[X] = \mu = npq \quad (1)$$

$$Var[X] = \sigma^2 = np(1-p)q^2 \quad (2)$$

In this view, the parameter n corresponds to the number of active zones (Triller and Korn, 1982; Faber and Korn, 1991) or independent functional release sites (Bekkers and Stevens, 1990; Bliss, 1990; Korn and Faber, 1991). However, some debate still remains surrounding this definition (Scheuss and Neher, 2001). For example, n has alternatively been proposed to represent the maximum number of quanta available for evoked release at a given synapse (Redman, 1990; Isaacson and Walmsley, 1995), i.e., the number of docked vesicles or the size of the readily releasable pool (Kaeser and Regehr, 2017). Here, we are adhering to the more common view that n corresponds to the number of release sites.

Changes in p and q Reveal the Locus of Expression

Presynaptic expression of plasticity is mediated by changes to the properties of vesicular release, typically the probability of release, p (Bekkers and Stevens, 1990; Chen and Regehr, 1997; Enoki et al., 2009) (reviewed by Castillo, 2012). Classically, the number of active release sites, n, was also considered to be a presynaptic parameter (Bekkers and Stevens, 1990; Faber and Korn, 1991). However, n has also been shown to be affected by postsynaptic events such as the unsilencing of AMPA receptors, which occurs more commonly in early development (Isaac et al., 1995, 1996; Liao et al., 1995; Kerchner and Nicoll, 2008). Furthermore, changes in n likely occur during the protein synthesis-dependent phase of late LTP (Geinisman et al., 1993; Bolshakov et al., 1997; Korn and Faber, 1998; Loebel et al., 2013). Here, we consider n to be stable for the duration of our experiments (~1 h; **Box 1**). A presynaptic locus is then assumed to be mediated by changes in p (**Box 2**).

Conversely, postsynaptic expression of plasticity is reflected as a change in the regulation, turnover, or responsiveness of postsynaptic receptors (Sheng and Kim, 2002; MacDougall and Fine, 2014; Costa et al., 2017). The quantal size, q, depends upon the number and properties of postsynaptic receptors activated by a quantum as well as by the amount of transmitter contained in one vesicle (Korn and Faber, 1998). Although q may thus in principle be influenced by both pre- and postsynaptic factors, the quantal size is commonly assumed to relate to postsynaptic mechanisms. In other words, vesicle size and transmitter loading are assumed to be both stereotyped and not plastic (Bliss, 1990; Faber and Korn, 1991; Korn and Faber, 1998).

Statistical Models Are Used to Estimate Synaptic Parameters

According to Del Castillo and Katz (1954) and many others (Johnson and Wernig, 1971; McLachlan, 1978; Korn et al., 1987; Bekkers and Stevens, 1990; Redman, 1990), the frequency distribution of evoked postsynaptic responses due to probabilistic presynaptic release follows binomial statistics. Poisson statistics may be more realistic in certain cases, for example in low Ca^{2+}-to-Mg^{2+} conditions when p is very low (Del Castillo and Katz, 1954; Martin, 1966). However, binomial statistics are assumed in the majority of studies of release.

The choice of release statistics comes with inherent assumptions. When the binomial model is relied upon, it is for example implicitly assumed that the release probability, p, and quantal size, q, are uniform across all n release sites (**Box 1**). These assumptions have the added benefit of simplifying the relationships between the synaptic parameters n, p, and q (McLachlan, 1978; Redman, 1990; Faber and Korn, 1991; Korn and Faber, 1991; Costa et al., 2017). Another useful consequence is the binomial model provides a simple theoretical framework for identifying the locus of expression of long-term plasticity by analysis of the CV (**Box 2**; Bekkers and Stevens, 1990; Malinow and Tsien, 1990; Faber and Korn, 1991). However, even if the constraints for the binomial release model

BOX 2 | What is the point of using $1/CV^2$ instead of CV?

It may seem counterintuitive and unnecessarily cumbersome to plot $1/CV^2$, normalized, versus the normalized amplitude in CV analysis. The rationale for this practice stems from the fact that—if you assume a binomial model of vesicular release—the probability of release, p, is proportional to $1/CV^2$. In other words, you can to a first approximation read off the change in release probability, p, from the y-axis when the CV analysis is represented in this manner, which is a handy advantage.

To show that $p \propto 1/CV^2$, we combine the expected value $E[X]$ (Eq. 1) and the variance $Var[X]$ of the binomial distribution (Eq. 2), and plug these into the expression for the CV, which is the standard deviation over the mean.

$$\begin{cases} CV = \dfrac{\sigma}{\mu} \\ E[X] = npq = \mu \\ Var[X] = np(1-p)q^2 = \sigma^2 \end{cases}$$

$$\Rightarrow CV^2 = \left(\frac{\sigma}{\mu}\right)^2 = \frac{np(1-p)}{(np)^2} = \frac{1-p}{np}$$

Here, the scaling resulting from the quantal amplitude, q, vanishes. Solving for p gives:

$$p = \frac{1}{nCV^2 + 1}$$

So, if we assume that the number of release sites, n, does not change after the induction of plasticity, it follows that:

$$\therefore p \propto \frac{1}{CV^2}$$

Although the number of release sites, n, may change in late LTP by growth of new synaptic connections (Geinisman et al., 1993; Bolshakov et al., 1997; Korn and Faber, 1998; Loebel et al., 2013), it is reasonable to assume that n does not change in early LTP (**Box 1**). This assumption, however, is a key caveat of assuming the binomial distribution in CV analysis.

What is special about the diagonal?

One additional advantage of plotting $1/CV^2$ versus the mean is that the diagonal line, $\Delta y/\Delta x = 1$, can be used as a demarcation line to determine whether expression is pre- or postsynaptic (**Figure 1**). To show this, we again use the expressions for the expected value, $E[X]$, and the variance, $Var[X]$, of the binomial distribution (Eqs 1 and 2), and combine these with the expression for the CV.

$$\begin{cases} CV = \dfrac{\sigma}{\mu} \\ E[X] = npq = \mu \\ Var[X] = np(1-p)q^2 = \sigma^2 \end{cases}$$

$$\Rightarrow CV^2 = \left(\frac{\sigma}{\mu}\right)^2 = \frac{np(1-p)}{(np)^2} = \frac{1-p}{np}$$

We solve for $1/CV^2$ and normalize with respect to the initial probability of release, p_0. We also define a presynaptic change in synaptic strength due to altering the probability of release, $c_{pre} = p/p_0$, to explore what happens when expression is only presynaptic. In this scenario, the y coordinate in the CV analysis plot is:

$$\frac{1}{CV^2}_{norm} = \frac{p}{1-p}\frac{1-p_0}{p_0} = \frac{c_{pre}(1-p_0)}{1-c_{pre}p_0}$$

Here, it is useful to note that this above expression does not depend on the quantal amplitude, q. Similarly, the x coordinate, μ_{norm}, in the CV analysis plot is:

$$\mu_{norm} = \frac{npq}{n_0 p_0 q_0} = c_{pre}c_{post}$$

where

$$\begin{cases} n = n_0 \\ c_{pre} = \frac{p}{p_0} \\ c_{post} = \frac{q}{q_0} \end{cases}$$

(Continued)

BOX 2 | Continued

As before, we assume that the number of release sites, n, remains unaltered. In the scenario where plasticity is solely presynaptic, c_{post} reduces to 1, so we are left with $\mu_{norm} = c_{pre}$. Here, the end coordinate becomes:

$$\left(c_{pre}, \frac{c_{pre}(1-p_0)}{1-c_{pre}p_0}\right)$$

Therefore, the slope of an imagined line from the starting coordinate (1, 1) to this end point is:

$$\frac{\Delta y}{\Delta x} = \frac{\frac{c_{pre}(1-p_0)}{1-c_{pre}p_0} - 1}{c_{pre} - 1} = \frac{1}{1-c_{pre}p_0}$$

Since both c_{pre} and p_0 are positive, non-zero numbers, it follows that $\Delta y/\Delta x > 1$. Ergo, presynaptically expressed plasticity gives rise to data points above the unitary diagonal line $\Delta y/\Delta x = 1$ for LTP. In the case of LTD, the scenario is the inverse; presynaptically expressed plasticity gives rise to data points below the diagonal (**Figure 1**).

In the case where plasticity is solely postsynaptically expressed, we are left with $\mu_{norm} = c_{post}$, so the final CV coordinate is now:

$$\left(c_{post}, \frac{c_{pre}(1-p_0)}{1-c_{pre}p_0}\right) = \left(c_{post}, \frac{1-p_0}{1-p_0}\right) = (c_{post}, 1)$$

which implies a line parallel to the x-axis:

$$\frac{\Delta y}{\Delta x} = \frac{1-1}{c_{post} - 1} = 0$$

This finding is in effect trivial, since we already observed above that $1/CV^2_{norm}$ did not depend on the quantal amplitude, q. It is also consistent with the above observation that $p \propto 1/CV^2$ since a line parallel to the x-axis implies that the probability of release p remains unaltered as the mean μ is increased or decreased.

In practice, since CV analysis relies on a finite number of data points in the baseline and post-induction period, the slope of the line between the coordinate (1, 1) and the end point will suffer from inaccuracy, due to the noise inherent in the stochasticity of release. This means pre- and postsynaptically expressed plasticity will not always give rise to data points on opposite sides of the diagonal demarcation line (e.g., see **Figures 4** and **5**), especially for experiments with baseline period with relatively few responses. Plasticity can of course also be expressed as a mixture of pre- and postsynaptic mechanisms (Sjöström et al., 2007; Costa et al., 2015), in which case data points may consistently end up on or close to the diagonal line.

are not met, CV analysis may still work adequately (**Box 1**; Faber and Korn, 1991).

PRINCIPLES OF CV ANALYSIS

The Basis for CV Analysis in Intuitive Terms

In probability theory and statistics, the CV—which is defined as the standard deviation σ divided by the mean μ—is a general standardized measure of dispersion of a probability or frequency distribution. The CV is, in other words, an experimentally useful measure of noise, or normalized overall variability (Abdi, 2010). For this reason, the CV is also known as the relative standard deviation. Since the majority of the noise at a synapse is due to the stochastic nature of quantal neurotransmitter release (Otmakhov et al., 1993; Costa et al., 2017), changes in noise as indicated by alterations in the CV are useful, since such changes suggest

a presynaptic locus of that change, i.e., due to a change in p (Bekkers and Stevens, 1990; Malinow and Tsien, 1990; Faber and Korn, 1991). Conversely, an on-average alteration in synaptic strength without a concomitant change in the CV would by the same line of reasoning appear to be due to postsynaptic changes in q, e.g., by regulation of AMPA receptors (Kauer et al., 1988; Isaac et al., 1995; Liao et al., 1995; Barria et al., 1997; Nicoll and Malenka, 1999). This latter observation, however, assumes that vesicle neurotransmitter loading is fixed and stereotyped (**Box 1**). In summary, an overall intuitive understanding of CV analysis should thus be based on the observation that changes in synaptic noise are primarily due to presynaptic expression. Conversely, no changes in noise during long-term plasticity suggests that expression is postsynaptic.

Binomial Release Statistics

In the context of neurotransmission, the CV is represented by the standard deviation, σ, of a set of evoked synaptic responses divided by their mean, μ, taken over a given time period (Bekkers and Stevens, 1990; Malinow and Tsien, 1990; Faber and Korn, 1991; Costa et al., 2017):

$$CV = \frac{\sigma}{\mu} \tag{3}$$

To extract specific synaptic release parameters, it is useful to apply a specific statistical model. A typical choice is the binomial release model (**Box 1**), although it is important to understand that the CV is a general measure of noise and that the CV is not in and of itself linked to any particular statistical model.

In terms of binomial statistics, μ is the mean synaptic efficacy given by the expected value of the random variable X, which is $E[X] = \mu = npq$ (Eq. 1), and the standard deviation is derived from the variance (Eq. 2) as $\sigma = \sqrt{Var[X]} = \sqrt{np(1-p)q^2}$. These mathematical relationships have been described many times in greater detail in the previous literature, and we refer the reader to these papers for a more in-depth treatment (Johnson and Wernig, 1971; McLachlan, 1978; Faber and Korn, 1991).

Typically, $1/CV^2$ rather than CV is plotted in most studies (**Figure 1**). This perhaps counterintuitive practice can be explained by the fact that $1/CV^2$ is proportional to the probability of release (**Box 2**). This practice is furthermore justified by the observation that the unitary diagonal line in a $1/CV^2$ versus μ plot (**Figure 1**) is a handy demarcation line between pre- and postsynaptic expression (**Box 2**). In this context, it is worth noting that the analytical expression for the CV is independent of the quantal size, q (Bliss, 1990; Malinow and Tsien, 1990; Faber and Korn, 1991; Korn and Faber, 1991; Costa et al., 2017), as derived from Eqs 1–3:

$$CV = \left(\frac{\sigma}{\mu}\right) = \sqrt{\frac{1-p}{np}}$$

This fact reflects the observation in the above intuitive introduction to CV analysis that postsynaptic changes should not affect synaptic noise levels. Again, this is because the variation at individual release sites predominately stems from the stochastic nature of neurotransmitter release (Otmakhov et al., 1993; Costa et al., 2017) and the CV is a metric of noise (Abdi, 2010; Costa et al., 2017).

To ensure that the CV reflects synaptic noise, characteristic of stochastic release, it has been argued that it should be corrected for the background noise (Faber and Korn, 1991):

$$\sigma^2 = \sigma^2_{measured} - \sigma^2_{background}$$

In practice, we find that subtracting the background noise has little or no impact on the locus of expression, as long as the background noise is stable across recordings.

RESULTS

Expected Outcomes

Coefficient of variation analysis compares the relative change of synaptic parameters before and after induction of plasticity (Faber and Korn, 1991), which in practical terms means we work with normalized values of CV and mean synaptic strength, μ. In the standard CV analysis plot (**Figure 1**), the normalized change in synaptic strength, μ(norm), thus indicates

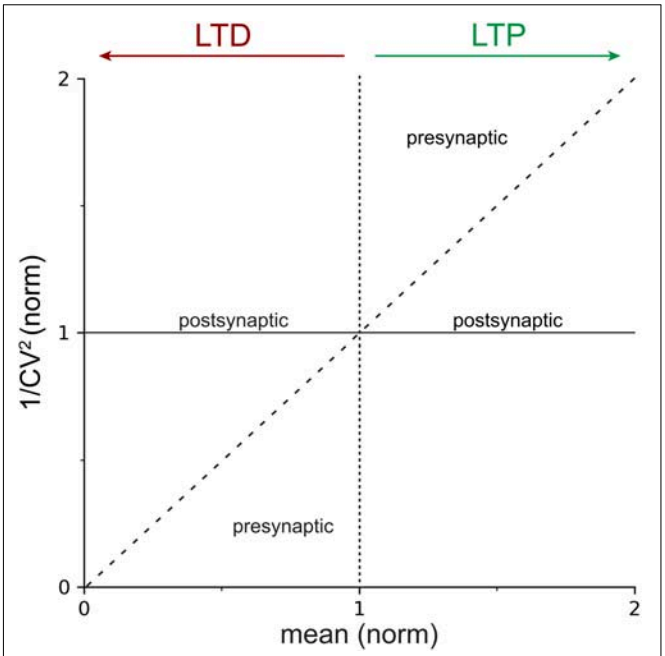

FIGURE 1 | Locus of expression areas in the CV analysis plot. Normalized $1/CV^2$, a proxy for the probability of release p (**Box 2**), is plotted against the normalized mean μ(norm), which is a measure of synaptic strength. The solid horizontal line at $y = 1$ indicates 100% $1/CV^2$(norm), or no change in p. The dotted vertical line at $x = 1$ delineates LTP (to the right) from LTD (to the left). The dashed diagonal line with slope $\Delta y/\Delta x = 1$ demarcates presynaptic from postsynaptic expression of plasticity (**Box 2**). In other words, data that falls on or close to the continuous horizontal line should be considered to be postsynaptically expressed, whereas data that is above the dashed diagonal for LTP, or below it for LTD, should be considered presynaptically expressed. Mixtures of pre- and postsynaptic expression is also possible (Sjöström et al., 2007), which results in data points scattered between the dashed diagonal and the continuous horizontal lines.

whether LTP or LTD took place, while appreciable changes in $1/CV^2$(norm) serve as a proxy for modifications in presynaptic release (Bekkers and Stevens, 1990; Malinow and Tsien, 1990; Faber and Korn, 1991; Costa et al., 2017), as outlined above. Whether a change in $1/CV^2$(norm) is appreciable or not is determined by comparing the outcome to the diagonal line (**Figure 1** and **Box 2**; Sjöström et al., 2003, 2007; Buchanan et al., 2012; Abrahamsson et al., 2017).

If $1/CV^2$(norm) changes at least to the same degree as the mean synaptic efficacy, μnorm, this supports a presynaptic locus of plasticity expression (**Figure 1**). On the contrary, if $1/CV^2$(norm) remains relatively unaffected as the mean response μ(norm) changes, this is evidence to support a postsynaptic locus of plasticity expression (**Figure 1**; Korn and Faber, 1991; Reid and Clements, 1999). Of course, forms of plasticity may involve both pre- and postsynaptic modifications (Kullmann and Nicoll, 1992; Sjöström et al., 2007; Loebel et al., 2013; Costa et al., 2015).

Overall, CV analysis provides an estimate of the locus of plasticity expression without having to resolve precise changes in *n*, *p*, or *q* (Costa et al., 2017). This is useful, because quantifying changes in *n*, *p*, or *q*—known as quantal analysis—is labor intensive and typically requires specific experimental conditions (Larkman et al., 1992, 1997a,b). Another approach for directly quantifying changes in *n*, *p*, or *q*, known as variance-mean analysis, requires sequential changes in cation composition (Clements and Silver, 2000; Clements, 2003). However, CV analysis can readily be performed following plasticity experiments without prior preparation (**Figure 2A**), but this relative simplicity comes at the cost of not knowing the precise changes in *n*, *p*, and *q*. The two sample paired-recording experiments show how both LTP (**Figure 2A**) and LTD (**Figure 2B**) at L5 PC-PC connections are presynaptically expressed according to CV analysis (**Figure 2C**), in agreement with our prior findings (Sjöström et al., 2003, 2007).

To be able to draw robust conclusions about the locus of plasticity, it is essential to repeat across several long-term plasticity experiments (**Figure 3**). Here, the statistical significance of CV analysis can be assessed by comparing the angle φ of the outcome relative to the diagonal (**Figure 3C** and **Box 2**), as we have done before (Sjöström et al., 2003, 2007; Buchanan et al., 2012; Abrahamsson et al., 2017).

In summary, CV analysis is a straightforward method for estimating the locus of expression that can easily be implemented following a standard plasticity experiment without the need for any special preparations (Bekkers and Stevens, 1990; Malinow and Tsien, 1990; Sjöström et al., 2003, 2007). It is important, however, to be aware of the assumptions of the binomial distribution (**Box 1**) as well as several experimental pitfalls associated with CV analysis (see below).

Caveats of CV Analysis

Like any other method, CV analysis comes with caveats (Faber and Korn, 1991; Korn and Faber, 1991; Costa et al., 2017). As a consequence, CV analysis may be misleading in some cases

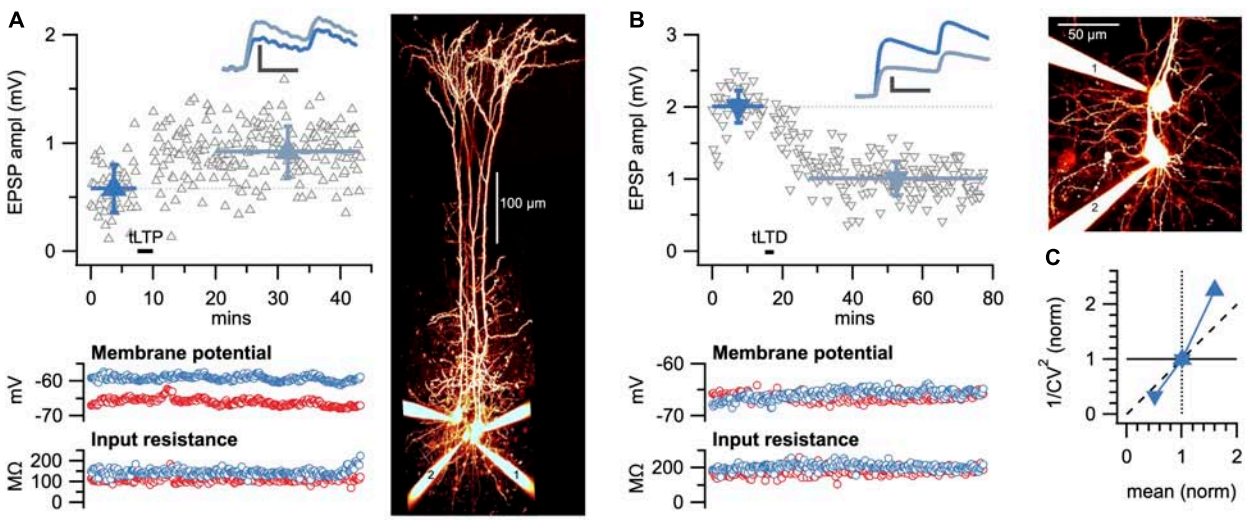

FIGURE 2 | Sample LTP and LTD experiments show presynaptic expression. **(A)** Sample spike-timing-dependent plasticity experiment with $\Delta t = 10$ ms temporal difference between pre- and postsynaptic spike trains evoked at 50 Hz (Sjöström et al., 2001) for which LTP was evoked (EPSP before, dark blue: 0.58 ± 0.03 mV versus after, light blue: 0.92 ± 0.02 mV, $p < 0.001$). Inset: average EPSP traces showed a change in paired-pulse ratio suggesting presynaptic expression (Sjöström et al., 2007). Scale bars: 0.5 mV, 20 ms. Bottom: membrane potential and input resistance of pre- and postsynaptic PCs were stable (red and blue, respectively). Right: flattened 2-photon imaging stack of Alexa-594-filled cells verified PC identity, with pre- and postsynaptic PCs denoted by 1 and 2, respectively. **(B)** Sample spike-timing-dependent plasticity experiment with $\Delta t = -25$ms temporal difference between pre- and postsynaptic spike trains evoked at 20 Hz (Sjöström et al., 2001, 2003) for which LTD was elicited (before: 2.0 ± 0.04 mV versus after: 1.0 ± 0.02 mV, $p < 0.001$. Inset: change in paired-pulse ratio suggested presynaptic expression (Sjöström et al., 2003, 2007). Scale bars: 0.5 mV, 20 ms. Bottom: membrane potential and input resistance of pre- and postsynaptic PCs were stable (red and blue, respectively). Right: pre- and postsynaptic PCs are indicated by 1 and 2, respectively. **(C)** Coefficient of variation analysis of LTP (right-side-up triangle) and LTD experiments (upside-down triangle) in **(A,B)** both indicated a presynaptic locus of expression, in keeping with prior findings (Markram and Tsodyks, 1996; Sjöström et al., 2003, 2007).

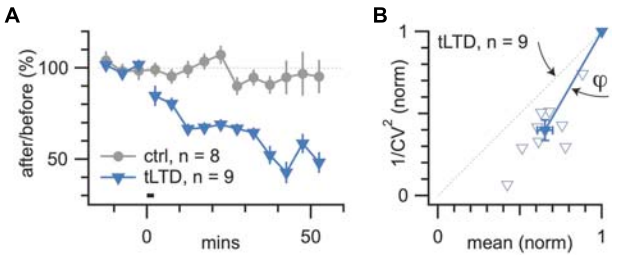

FIGURE 3 | Neocortical LTD in L5 PCs is presynaptically expressed. **(A)** LTD expression at 20 Hz with $\Delta t = -25$ ms like in **Figure 2B** was robust across paired recordings, while no-induction controls were stable (LTD, blue triangles; 65 ± 5%, $n = 9$ versus control, gray circles; 97 ± 2%, $n = 8$, $p < 0.001$). **(B)** Coefficient of variation analysis consistently suggested a presynaptic locus of LTD expression, as all paired recordings gave rise to data points below the diagonal (angle $\varphi = 16° \pm 2°$, $n = 9$, $p < 0.001$; see **Figure 1**).

(Faber and Korn, 1991). Here, we show how to anticipate and circumvent some of the key shortcomings.

The Number of Activated Inputs Should Remain Constant

A constant number of afferents should be activated within and across trials (Redman, 1990; Faber and Korn, 1991; Saviane and Silver, 2007). Although it is possible to conduct CV analysis on synaptic responses evoked with extracellular stimulation (Bekkers and Stevens, 1990; Malinow and Tsien, 1990), there is with extracellular stimulation the potential for loss or gain of afferent fibers throughout the recording, which may complicate CV analysis by requiring corrections (Faber and Korn, 1991; Costa et al., 2017). This potential problem is not specific to CV analysis *per se*, but also applies to e.g., quantal analysis and variance-mean analysis. Furthermore, recordings that show evidence of polysynaptic connectivity violate the simple binomial model (McLachlan, 1978) and therefore complicate the interpretation of quantal parameters by precluding CV analysis (Faber and Korn, 1991; Korn and Faber, 1991; Costa et al., 2017) and require statistical adjustments (Faber and Korn, 1991; Reid and Clements, 1999).

Avoiding these problems can be achieved by interrogating monosynaptic connections using paired recordings (Korn and Faber, 1998; Saviane and Silver, 2007), which have been carried out e.g., in neocortex (**Figure 2**; Sjöström et al., 2003, 2007; Song et al., 2005; Lalanne et al., 2016) and hippocampus (Sayer et al., 1989; Bekkers and Stevens, 1990; Malinow, 1991; Debanne et al., 1999). However, identifying monosynaptic connections is technically challenging and time consuming, especially for synapse types with low connectivity rates. To alleviate this problem, multiple whole-cell recordings may be employed to increase the yield of identified monosynaptic connections (**Figures 2**, **3**), as previously described by us (Sjöström et al., 2003, 2007; Song et al., 2005; Lalanne et al., 2016) and others (Perin et al., 2011; Perin and Markram, 2013; Peng et al., 2019).

It is also possible to circumvent the problem of accidental loss or gain of afferent inputs by using more direct optical methods such as 2-photon glutamate uncaging (Ellis-Davies, 2019; Mitchell et al., 2019) or optical quantal analysis (Oertner et al., 2002; Emptage et al., 2003; MacDougall and Fine, 2019; Padamsey et al., 2019). However, even with paired recordings or these more direct optical methods, it is still possible for the number of release sites n to change (**Box 1**).

Outlier Synaptic Responses Distort CV Analysis

The variation at single synaptic contacts—primarily driven by the stochastic and probabilistic nature of presynaptic release (Otmakhov et al., 1993; Costa et al., 2017)—significantly influences the overall observed variability i.e., fluctuations in evoked potentials between neuronal connections in the brain (Otmakhov et al., 1993; Crochet et al., 2005). This makes the CV an excellent proxy for presynaptic changes in release (Malinow and Tsien, 1990; Faber and Korn, 1991; Costa et al., 2017). However, it also indicates that the CV is sensitive to the variation and stability of synaptic parameters at each release site and is therefore vulnerable to measurement error in the presence of additional sources of variation (Faber and Korn, 1991; Korn and Faber, 1991).

Extraneous sources of variation—for e.g., outliers due to stimulus failure or electrical artifacts (Oleskevich et al., 2000) and baseline trends and/or rundown (Reid and Clements, 1999)—significantly affect the CV and may mask the true locus of expression (**Figures 4**, **5**). A straightforward solution to this caveat is to carefully inspect experiments for outlier responses and then individually exclude them from the CV analysis (**Figures 4D,E**). However, careful selection criteria for removing data points should be applied, otherwise bias will certainly be introduced. For example, electrical artifacts or spurious spiking (**Figure 4D**) are quite striking and useful selection criteria for identifying outliers. In other words, outliers should not be removed merely on the basis of being an outlier. Outliers should only be removed based on evidence for a cause of it being an outlier, such as spurious spiking (**Figure 4D**). Nevertheless, bias is a concern so removal of data points should be rare.

Unstable Baseline Distorts CV Analysis

Recordings should be evaluated for any trends resulting from rundown or instability, which may inflate estimates of the standard deviation, σ (McLachlan, 1978; Scheuss and Neher, 2001). The effect of baseline drift is illustrated in **Figure 5**; note that it is quite substantial even for relatively small baseline trends. Such trends can arise from gradual changes in cell input resistance, resting membrane potential, et cetera (**Figure 5Di**). It is therefore important to continuously monitor such parameters throughout long-term plasticity experiments (**Figures 2A,B**).

One solution to this problem is to systematically eliminate experiments above a threshold trend value, using a numerical selection criterion based on e.g., linear regression or bisection of the baseline period (Lalanne et al., 2016). By applying the same selection criteria to condition as well as control experiments (e.g., **Figure 3**), bias is avoided. We advise against detrending data, as it may introduce bias depending on the assumptions underlying the detrending algorithm. It is possible, however, to remove a portion

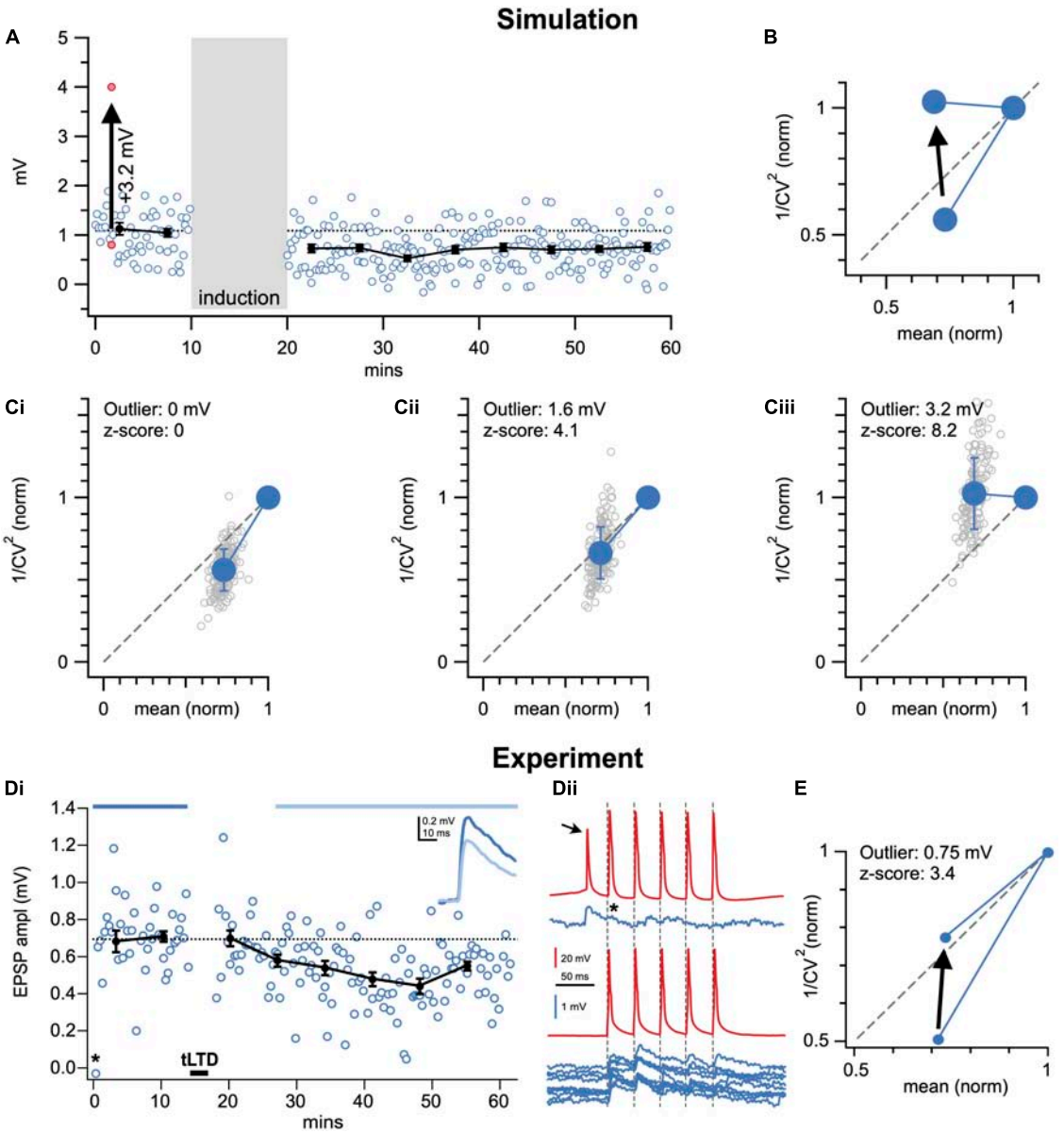

FIGURE 4 | A single outlier response may corrupt CV analysis. **(A)** Sample Monte-Carlo simulation of an individual presynaptically expressed LTD experiment in which a single EPSP was shifted by 3.2 mV (*z*-score: 8.2) to produce a striking outlier (red dots). To enable comparison with experimental data (**Figures 2**, **3**), the number of EPSPs, interstimulus intervals, background noise levels, amount of LTD, initial EPSP amplitude, et cetera were set to representative values (see section "Materials and Equipment"). **(B)** With a single outlier in the baseline period (*z*-score 8.2 as in **A**), CV analysis of LTD was on average biased to erroneously indicate post-instead of presynaptic expression (arrow). In the case of LTP, CV analysis would instead be biased toward presynaptic expression (not shown, but possible to simulate in downloadable code, see section "Materials and Equipment"), because the outlier would still artificially elevate the *y*-axis coordinate, just as for LTD. However, if the outlier is in the post-induction period, the bias is in the opposite direction. **(C)** As in **(A)**, 150 individual simulations (gray circles) were systematically repeated for single outliers of increasing *z*-score values (0, 4.1, and 8.2 shown in **Ci–iii**). The increasing outlier values systematically biased outcome toward a postsynaptic interpretation (summarized in **B**). **(D)** Sample LTD experiment (**Di**, $\Delta t = -25$ms and 20 Hz as in **Figures 2**, **3**) for which a spurious presynaptic spike (arrow, **Dii**, top red trace) resulted in undesirable short-term depression of subsequent EPSP (* in **Dii**, compare top to bottom blue sample traces), leading to an outlier EPSP in the time course (* in **Di**). **(E)** By including the outlier (* in **Di,ii**), CV analysis was biased toward postsynaptic interpretation (arrow). Here, this pitfall was avoided by removing the outlier (arrow starting point).

of the baseline period that is unstable (**Figure 5D**), especially if doing so is supported by some independent selection criterion such as change in input resistance, resting membrane potential, or similar (Lalanne et al., 2016).

Gradual trends in variance or mean may also be addressed by binning $1/CV^2$ over time (Scheuss and Neher, 2001). For simplicity, we do not show this here, but we have relied on this approach before (Sjöström et al., 2003).

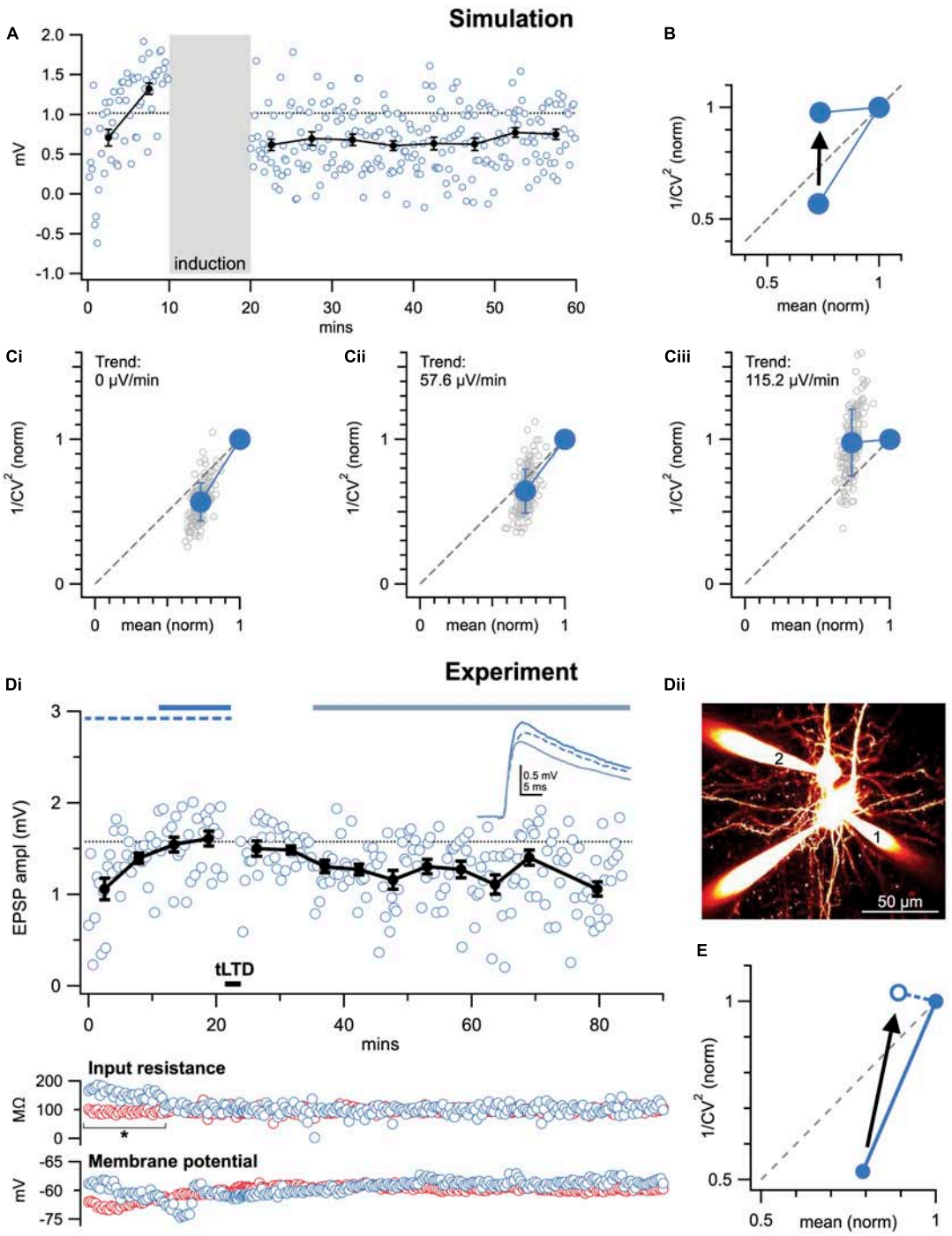

FIGURE 5 | Baseline trends may corrupt CV analysis. **(A)** Sample Monte-Carlo simulation of an individual presynaptically expressed LTD experiment that was suffering from a strong baseline run-up (115.2 μV/min, see section "Materials and Equipment"). **(B)** With baseline trend (115.2 μV/min as in **A**), CV analysis was on average biased to erroneously indicate post-instead of presynaptic expression (arrow). In the case of LTP, CV analysis would instead be biased toward presynaptic expression (not shown, but possible to simulate in downloadable code, see section "Materials and Equipment"), because the baseline trend artificially elevates the *y*-axis coordinate. However, if the baseline trend is in the post-induction period, the bias is in the opposite direction. **(C)** As in **(A)**, 150 individual simulations (gray circles) were systematically repeated for different baseline trends (0, 57.6, and 115.2 μV/min shown in **Ci–iii**). The increasing baseline trend systematically biased outcome toward a postsynaptic interpretation (summarized in **B**). **(D)** Sample LTD experiment (**Di**, $\Delta t = -25$ms and 20 Hz as in **Figures 2**, **3**) at PC1 → PC2 connection **(Dii)** that suffered from an increasing baseline trend, coincident with a significant change in postsynaptic input resistance (bottom: blue circles, asterisk). Presynaptic input resistance and membrane potential are indicated in red. **(E)** By including the entire baseline period, CV analysis was biased toward postsynaptic interpretation (arrow). Here, this pitfall was avoided by removing the unstable baseline period, which was further supported by a significant change in input resistance (* in **Di**).

Alternative Interpretations Are Possible

Even under the best of circumstances, the results of CV analysis should be interpreted while considering the structure and function of the synapse type under investigation (Costa et al., 2017). To illustrate this point, consider NMDA-receptor-dependent LTP in hippocampal area CA1. Some studies have found that this form of plasticity is expressed as an increase in the probability of release, p, suggesting a presynaptic locus (Kullmann and Nicoll, 1992). However, this apparent change in the release probability may in fact be achieved postsynaptically by the conversion of silent to functional synapses (Glasgow et al., 2019). In this scenario, postsynaptic insertion of AMPA receptors may be erroneously interpreted as a presynaptic increase in the probability of release (Isaac et al., 1995, 1996; Liao et al., 1995; Kerchner and Nicoll, 2008). Synaptic unsilencing at the neuromuscular junction, on the other hand, is a mechanistically distinct presynaptic phenomenon (Wojtowicz et al., 1994).

In summary, alternative interpretations are often possible. This pitfall, however, is not limited to CV analysis as such but is a general caveat. Nevertheless, this means CV analysis should generally be supported by other methods for localizing the expression locus, such as analysis of failure rate (Malinow and Tsien, 1990; Faber and Korn, 1991), paired-pulse ratio (**Figures 2A,B**; Poncer and Malinow, 2001; Sjöström et al., 2007; Abrahamsson et al., 2017), NMDA:AMPA ratio (Watt et al., 2004; Sjöström et al., 2007), FM1-43 dye loading (Murthy et al., 1997; Zakharenko et al., 2001), spontaneous release (changes in frequency versus amplitude; Malgaroli and Tsien, 1992; Manabe et al., 1992; Abrahamsson et al., 2017), etc. Of these approaches, evaluating the paired-pulse ratio is likely the most straightforward option, as it can be readily performed in parallel with CV analysis, provided the experiments were carried out with paired pulses (**Figures 2A,B**). Since it relies on two responses rather than one as for CV analysis, paired-pulse ratio analysis is furthermore mathematically independent from CV analysis. Failure-rate and CV analyses, however, are essentially relying on the same theoretical framework and so are not independent methods, which means the corroborative power is limited. For further information regarding these techniques, we invite the reader to the review by Glasgow et al. (2019) in this research topic. Furthermore, modern techniques enable more direct measurements of locus of expression, e.g., using 2-photon glutamate uncaging (Ellis-Davies, 2019; Mitchell et al., 2019), optical glutamate sensors (Jensen et al., 2017, 2019; Durst et al., 2019), or optical quantal analysis (Oertner et al., 2002; Emptage et al., 2003; MacDougall and Fine, 2019; Padamsey et al., 2019). These more advanced methods may however require expensive specialized equipment.

DISCUSSION

We have provided a practical guide to using CV analysis for the purposes of investigating the locus of expression of long-term plasticity. We primarily directed this guide to beginners in the field, so we have tried to simplify key concepts to make them more accessible. We acknowledge that others have delved into the mathematical background with greater detail and rigor than we have here (McLachlan, 1978; Faber and Korn, 1991; Quastel, 1997); this was intentional.

Binomial statistics have been successfully applied to the study of quantal release at peripheral and central synapses for decades (Johnson and Wernig, 1971; McLachlan, 1978; Korn et al., 1987; Bekkers and Stevens, 1990; Malinow and Tsien, 1990). Nonetheless, the simplifying assumptions inherent in this model may not hold in all cases. Therefore, if resolving precise changes in synaptic parameters is required, it is possible to use alternative albeit more laborious approaches to accommodate potential non-uniformities in p and q (Silver et al., 1998; Reid and Clements, 1999; Saviane and Silver, 2007). However, it appears that the locus of plasticity expression can be reliably and easily estimated with CV analysis—using alternative methods such as analysis of NMDA:AMPA ratio, paired-pulse ratio, or quantal analysis in parallel with CV analysis generally give rise to the same interpretation (Reid and Clements, 1999; Sjöström et al., 2007). Modern and more direct methods based on optical activation or readout are especially attractive alternatives (Jensen et al., 2017, 2019; Durst et al., 2019; Ellis-Davies, 2019; MacDougall and Fine, 2019; Mitchell et al., 2019; Padamsey et al., 2019), since they in many cases are virtually free of assumptions. Still, all methods come with their own advantages and caveats, e.g., analysis of paired-pulse ratio may erroneously suggest presynaptic expression for NMDA-only silent synapses that undergo postsynaptic expression (Poncer and Malinow, 2001), glutamate uncaging can necessarily only explore postsynaptic expression, and dyes used with optical methods may distort plasticity mechanisms by buffering calcium (MacDougall and Fine, 2019). It therefore remains important to use several methods in parallel. Classical CV analysis is one method that is both straightforward and inexpensive to use.

Here, we have listed a set of key pitfalls and shortcomings of the CV analysis method, which we have also illustrated in the form of simple downloadable computer simulations (see GitHub link in section "Materials and Equipment"). We have also provided a number of straightforward solutions for the most obvious issues. From this simple guide, it should be clear that CV analysis is a powerful and easy-to-use method, especially when combined with other approaches such as analysis of paired-pulse ratio or NMDA:AMPA ratio (Watt et al., 2000, 2004; Sjöström et al., 2007).

DATA AVAILABILITY STATEMENT

The raw data supporting the conclusions of this article will be made available by the authors, without undue reservation, to any qualified researcher.

ETHICS STATEMENT

The animal study was reviewed and approved by the Montreal General Hospital Faculty Animal Care Committee (MGH FACC).

AUTHOR CONTRIBUTIONS

JB and AW carried out the experiments. SL carried out the mathematical derivations. PS wrote the custom software. JB, PS, and AT wrote the manuscript with input from AW.

FUNDING

This work was supported by CFI LOF 28331 (PS), CIHR OG 126137 (PS), CIHR NIA 288936 (PS), FRSQ CB 254033 (PS), NSERC DG 418546-2 (PS), NSERC DG 2017-04730 (PS), and NSERC DAS 2017-507818 (PS). JB was in receipt of the McGill University Max Stern Recruitment Award and the McGill University Integrated Program in Neuroscience (IPN) Recruitment Award. AW was supported by the McGill University Grad Excellence Award, the Research Institute of the McGill University Health Centre (RI-MUHC) Studentship, and the Healthy Brains, Healthy Lives (HBHL) Master's Fellowship. The funders had no role in study design, data collection and interpretation, or the decision to submit the work for publication.

ACKNOWLEDGMENTS

We thank Alanna Watt and members of the Sjöström Lab for help and useful discussions. We are also grateful for the constructive feedback from the reviewers.

REFERENCES

Abbott, L. F., and Regehr, W. G. (2004). Synaptic computation. *Nature* 431, 796–803.

Abbott, L. F., Varela, J. A., Sen, K., and Nelson, S. B. (1997). Synaptic depression and cortical gain control. *Science* 275, 220–224.

Abdi, H. (2010). "Coefficient of variation," in *Encyclopedia of Research Design*, 1 Edn, ed. N. J. Salkind (Thousand Oaks, CA: SAGE Publications, Inc).

Abrahamsson, T., Chou, C. Y. C., Li, S. Y., Mancino, A., Costa, R. P., Brock, J. A., et al. (2017). Differential regulation of evoked and spontaneous release by presynaptic NMDA receptors. *Neuron* 96, 839.e–855.e. doi: 10.1016/j.neuron.2017.09.030

Abrahamsson, T., Lalanne, T., Watt, A. J., and Sjöström, P. J. (2016). *In vitro* investigation of synaptic plasticity. *Cold Spring Harb. Protoc.* 2016:pdb.top087262. doi: 10.1101/pdb.top087262

Auger, C., Kondo, S., and Marty, A. (1998). Multivesicular release at single functional synaptic sites in cerebellar stellate and basket cells. *J. Neurosci.* 18, 4532–4547. doi: 10.1523/jneurosci.18-12-04532.1998

Barria, A., Muller, D., Derkach, V., Griffith, L. C., and Soderling, T. R. (1997). Regulatory phosphorylation of AMPA-type glutamate receptors by CaM-KII during long-term potentiation. *Science* 276, 2042–2045. doi: 10.1126/science.276.5321.2042

Bekkers, J. M., and Stevens, C. F. (1990). Presynaptic mechanism for long-term potentiation in the hippocampus. *Nature* 346, 724–729. doi: 10.1038/346724a0

Bliss, T. V. (1990). Maintenance is presynaptic. *Nature* 346, 698–699. doi: 10.1038/346698a0

Bliss, T. V., and Collingridge, G. L. (1993). A synaptic model of memory: long-term potentiation in the hippocampus. *Nature* 361, 31–39. doi: 10.1038/361031a0

Bolshakov, V. Y., Golan, H., Kandel, E. R., and Siegelbaum, S. A. (1997). Recruitment of new sites of synaptic transmission during the cAMP-dependent late phase of LTP at CA3-CA1 synapses in the hippocampus. *Neuron* 19, 635–651. doi: 10.1016/s0896-6273(00)80377-3

Branco, T., Staras, K., Darcy, K. J., and Goda, Y. (2008). Local dendritic activity sets release probability at hippocampal synapses. *Neuron* 59, 475–485. doi: 10.1016/j.neuron.2008.07.006

Buchanan, K. A., Blackman, A. V., Moreau, A. W., Elgar, D., Costa, R. P., Lalanne, T., et al. (2012). Target-specific expression of presynaptic NMDA receptors in neocortical microcircuits. *Neuron* 75, 451–466. doi: 10.1016/j.neuron.2012.06.017

Castillo, P. E. (2012). Presynaptic LTP and LTD of excitatory and inhibitory synapses. *Cold Spring Harb. Perspect. Biol.* 4:a005728. doi: 10.1101/cshperspect.a005728

Chance, F. S., Nelson, S. B., and Abbott, L. F. (1998). Synaptic depression and the temporal response characteristics of V1 cells. *J. Neurosci.* 18, 4785–4799. doi: 10.1523/jneurosci.18-12-04785.1998

Chen, C., and Regehr, W. G. (1997). The mechanism of cAMP-mediated enhancement at a cerebellar synapse. *J. Neurosci.* 17, 8687–8694. doi: 10.1523/jneurosci.17-22-08687.1997

Clements, J. D. (2003). Variance-mean analysis: a simple and reliable approach for investigating synaptic transmission and modulation. *J. Neurosci. Methods* 130, 115–125. doi: 10.1016/j.jneumeth.2003.09.019

Clements, J. D., and Silver, R. A. (2000). Unveiling synaptic plasticity: a new graphical and analytical approach. *Trends Neurosci.* 23, 105–113. doi: 10.1016/s0166-2236(99)01520-9

Cline, H. T. (1998). Topographic maps: developing roles of synaptic plasticity. *Curr. Biol.* 8, R836–R839.

Corlew, R., Wang, Y., Ghermazien, H., Erisir, A., and Philpot, B. D. (2007). Developmental switch in the contribution of presynaptic and postsynaptic NMDA receptors to long-term depression. *J. Neurosci.* 27, 9835–9845. doi: 10.1523/jneurosci.5494-06.2007

Costa, R. P., Froemke, R. C., Sjöström, P. J., and van Rossum, M. C. (2015). Unified pre- and postsynaptic long-term plasticity enables reliable and flexible learning. *eLife* 4:e09457. doi: 10.7554/eLife.09457

Costa, R. P., Mizusaki, B. E., Sjöström, P. J., and van Rossum, M. C. (2017). Functional consequences of pre- and postsynaptic expression of synaptic plasticity. *Philos. Trans. R. Soc. Lond. B Biol. Sci.* 372:20160153. doi: 10.1098/rstb.2016.0153

Crochet, S., Chauvette, S., Boucetta, S., and Timofeev, I. (2005). Modulation of synaptic transmission in neocortex by network activities. *Eur. J. Neurosci.* 21, 1030–1044. doi: 10.1111/j.1460-9568.2005.03932.x

Debanne, D., Gähwiler, B. H., and Thompson, S. M. (1999). Heterogeneity of synaptic plasticity at unitary CA3-CA1 and CA3-CA3 connections in rat hippocampal slice cultures. *J. Neurosci.* 19, 10664–10671. doi: 10.1523/jneurosci.19-24-10664.1999

Del Castillo, J. K., and Katz, B. (1954). Quantal components of the end-plate potential. *J. Physiol.* 124, 560–573. doi: 10.1113/jphysiol.1954.sp005129

Durst, C. D., Wiegert, J. S., Helassa, N., Kerruth, S., Coates, C., Schulze, C., et al. (2019). High-speed imaging of glutamate release with genetically encoded sensors. *Nat. Protoc.* 14, 1401–1424. doi: 10.1038/s41596-019-0143-9

Ellis-Davies, G. C. R. (2019). Two-photon uncaging of glutamate. *Front. Synaptic Neurosci.* 10:48. doi: 10.3389/fnsyn.2018.00048

Emptage, N. J., Reid, C. A., Fine, A., and Bliss, T. V. (2003). Optical quantal analysis reveals a presynaptic component of LTP at hippocampal Schaffer-associational synapses. *Neuron* 38, 797–804. doi: 10.1016/s0896-6273(03)00325-8

Enoki, R., Hu, Y. L., Hamilton, D., and Fine, A. (2009). Expression of long-term plasticity at individual synapses in hippocampus is graded, bidirectional, and mainly presynaptic: optical quantal analysis. *Neuron* 62, 242–253. doi: 10.1016/j.neuron.2009.02.026

Faber, D. S., and Korn, H. (1991). Applicability of the coefficient of variation method for analyzing synaptic plasticity. *Biophys. J.* 60, 1288–1294. doi: 10.1016/s0006-3495(91)82162-2

Fatt, P., and Katz, B. (1952). Spontaneous subthreshold activity at motor nerve endings. *J. Physiol.* 117, 109–128.

Fujisawa, S., Amarasingham, A., Harrison, M. T., and Buzsaki, G. (2008). Behavior-dependent short-term assembly dynamics in the medial prefrontal cortex. *Nat. Neurosci.* 11, 823–833. doi: 10.1038/nn.2134

Geinisman, Y., Detoledo-Morrell, L., Morrell, F., Heller, R. E., Rossi, M., and Parshall, R. F. (1993). Structural synaptic correlate of long-term potentiation: formation of axospinous synapses with multiple, completely partitioned transmission zones. *Hippocampus* 3, 435–445. doi: 10.1002/hipo.450030405

Glasgow, S. D., Mcphedrain, R., Madranges, J. F., Kennedy, T. E., and Ruthazer, E. S. (2019). Approaches and limitations in the investigation of synaptic transmission and plasticity. *Front. Synaptic Neurosci.* 11:20. doi: 10.3389/fnsyn.2019.00020

Goldman, M. S., Maldonado, P., and Abbott, L. F. (2002). Redundancy reduction and sustained firing with stochastic depressing synapses. *J. Neurosci.* 22, 584–591. doi: 10.1523/jneurosci.22-02-00584.2002

Häusser, M. (2001). Synaptic function: dendritic democracy. *Curr. Biol.* 11, R10–R12.

Isaac, J. T., Crair, M. C., Nicoll, R. A., and Malenka, R. C. (1997). Silent synapses during development of thalamocortical inputs. *Neuron* 18, 269–280. doi: 10.1016/s0896-6273(00)80267-6

Isaac, J. T., Nicoll, R. A., and Malenka, R. C. (1995). Evidence for silent synapses: implications for the expression of LTP. *Neuron* 15, 427–434. doi: 10.1016/0896-6273(95)90046-2

Isaac, J. T., Oliet, S. H., Hjelmstad, G. O., Nicoll, R. A., and Malenka, R. C. (1996). Expression mechanisms of long-term potentiation in the hippocampus. *J. Physiol. Paris* 90, 299–303. doi: 10.1016/s0928-4257(97)87901-6

Isaacson, J. S., and Walmsley, B. (1995). Counting quanta: direct measurements of transmitter release at a central synapse. *Neuron* 15, 875–884. doi: 10.1016/0896-6273(95)90178-7

Jensen, T. P., Zheng, K., Cole, N., Marvin, J. S., Looger, L. L., and Rusakov, D. A. (2019). Multiplex imaging relates quantal glutamate release to presynaptic Ca^{2+} homeostasis at multiple synapses in situ. *Nat. Commun.* 10:1414. doi: 10.1038/s41467-019-09216-8

Jensen, T. P., Zheng, K., Tyurikova, O., Reynolds, J. P., and Rusakov, D. A. (2017). Monitoring single-synapse glutamate release and presynaptic calcium concentration in organised brain tissue. *Cell Calcium* 64, 102–108. doi: 10.1016/j.ceca.2017.03.007

Johnson, E. W., and Wernig, A. (1971). The binomial nature of transmitter release at the crayfish neuromuscular junction. *J. Physiol.* 218, 757–767. doi: 10.1113/jphysiol.1971.sp009642

Kaeser, P. S., and Regehr, W. G. (2017). The readily releasable pool of synaptic vesicles. *Curr. Opin. Neurobiol.* 43, 63–70. doi: 10.1016/j.conb.2016.12.012

Katz, B., and Miledi, R. (1972). The statistical nature of the acetycholine potential and its molecular components. *J. Physiol.* 224, 665–699. doi: 10.1113/jphysiol.1972.sp009918

Katz, L. C., and Shatz, C. J. (1996). Synaptic activity and the construction of cortical circuits. *Science* 274, 1133–1138. doi: 10.1126/science.274.5290.1133

Kauer, J. A., Malenka, R. C., and Nicoll, R. A. (1988). A persistent postsynaptic modification mediates long-term potentiation in the hippocampus. *Neuron* 1, 911–917. doi: 10.1016/0896-6273(88)90148-1

Kerchner, G. A., and Nicoll, R. A. (2008). Silent synapses and the emergence of a postsynaptic mechanism for LTP. *Nat. Rev. Neurosci.* 9, 813–825. doi: 10.1038/nrn2501

Koester, H. J., and Johnston, D. (2005). Target cell-dependent normalization of transmitter release at neocortical synapses. *Science* 308, 863–866. doi: 10.1126/science.1100815

Korn, H., Burnod, Y., and Faber, D. S. (1987). Spontaneous quantal currents in a central neuron match predictions from binomial analysis of evoked responses. *Proc. Natl. Acad. Sci. U.S.A.* 84, 5981–5985. doi: 10.1073/pnas.84.16.5981

Korn, H., and Faber, D. S. (1991). Quantal analysis and synaptic efficacy in the CNS. *Trends Neurosci.* 14, 439–445. doi: 10.1016/0166-2236(91)90042-s

Korn, H., and Faber, D. S. (1998). Quantal analysis and long-term potentiation. *C. R. Acad. Sci. III* 321, 125–130.

Korn, H., Faber, D. S., and Triller, A. (1986). Probabilistic determination of synaptic strength. *J. Neurophysiol.* 55, 402–421. doi: 10.1152/jn.1986.55.2.402

Kullmann, D. M., and Nicoll, R. A. (1992). Long-term potentiation is associated with increases in quantal content and quantal amplitude. *Nature* 357, 240–244. doi: 10.1038/357240a0

Lalanne, T., Abrahamsson, T., and Sjöström, P. J. (2016). Using Multiple Whole-Cell Recordings to Study Spike-Timing-Dependent Plasticity in Acute Neocortical Slices. *Cold Spring Harb. Protoc.* 2016:db.rot091306. doi: 10.1101/pdb.prot091306

Larkman, A., Hannay, T., Stratford, K., and Jack, J. (1992). Presynaptic release probability influences the locus of long-term potentiation. *Nature* 360, 70–73. doi: 10.1038/360070a0

Larkman, A. U., Jack, J. J., and Stratford, K. J. (1997a). Assessment of the reliability or amplitude histograms from excitatory synapses in rat hippocampal CA1 in vitro. *J. Physiol.* 505(Pt. 2), 443–456. doi: 10.1111/j.1469-7793.1997.443bb.x

Larkman, A. U., Jack, J. J., and Stratford, K. J. (1997b). Quantal analysis of excitatory synapses in rat hippocampal CA1 in vitro during low-frequency depression. *J. Physiol.* 505(Pt. 2), 457–471. doi: 10.1111/j.1469-7793.1997.457bb.x

Larsen, R. S., and Sjöström, P. J. (2015). Synapse-type-specific plasticity in local circuits. *Curr. Opin. Neurobiol.* 35, 127–135. doi: 10.1016/j.conb.2015.08.001

Liao, D., Hessler, N. A., and Malinow, R. (1995). Activation of postsynaptically silent synapses during pairing-induced LTP in CA1 region of hippocampal slice. *Nature* 375, 400–404. doi: 10.1038/375400a0

Lisman, J. (2003). Long-term potentiation: outstanding questions and attempted synthesis. *Philos. Trans. R. Soc. Lond. B Biol. Sci.* 358, 829–842. doi: 10.1098/rstb.2002.1242

Lisman, J. E. (1997). Bursts as a unit of neural information: making unreliable synapses reliable. *Trends Neurosci.* 20, 38–43. doi: 10.1016/s0166-2236(96)10070-9

Lisman, J. E. (2009). The pre/post LTP debate. *Neuron* 63, 281–284. doi: 10.1016/j.neuron.2009.07.020

Lisman, J. E., and Harris, K. M. (1993). Quantal analysis and synaptic anatomy–integrating two views of hippocampal plasticity. *Trends Neurosci.* 16, 141–147. doi: 10.1016/0166-2236(93)90122-3

Loebel, A., Le Be, J. V., Richardson, M. J., Markram, H., and Herz, A. V. (2013). Matched pre- and post-synaptic changes underlie synaptic plasticity over long time scales. *J. Neurosci.* 33, 6257–6266. doi: 10.1523/JNEUROSCI.3740-12.2013

Maass, W., and Zador, A. M. (1999). Dynamic stochastic synapses as computational units. *Neural Comput.* 11, 903–917. doi: 10.1162/089976699300016494

MacDougall, M. J., and Fine, A. (2014). The expression of long-term potentiation: reconciling the preists and the postivists. *Philos. Trans. R. Soc. Lond. B Biol. Sci.* 369, 20130135. doi: 10.1098/rstb.2013.0135

MacDougall, M. J., and Fine, A. (2019). Optical Quantal Analysis. *Front. Synaptic Neurosci.* 11:8. doi: 10.3389/fnsyn.2019.00008

Magee, J. C. (2000). Dendritic integration of excitatory synaptic input. *Nat. Rev. Neurosci.* 1, 181–190. doi: 10.1038/35044552

Magee, J. C., and Cook, E. P. (2000). Somatic EPSP amplitude is independent of synapse location in hippocampal pyramidal neurons. *Nat. Neurosci.* 3, 895–903. doi: 10.1038/78800

Maheux, J., Froemke, R., and Sjöström, P. J. (2016). "Functional plasticity at dendritic synapses," in *Dendrites*, 3rd Edn, eds G. Stuart, N. Spruston, and M. Häusser (Oxford, UK: Oxford University Press), 505–556. doi: 10.1093/acprof:oso/9780198745273.003.0018

Malenka, R. C., and Bear, M. F. (2004). LTP and LTD: an embarrassment of riches. *Neuron* 44, 5–21.

Malgaroli, A., and Tsien, R. W. (1992). Glutamate-induced long-term potentiation of the frequency of miniature synaptic currents in cultured hippocampal neurons. *Nature* 357, 134–139. doi: 10.1038/357134a0

Malinow, R. (1991). Transmission between pairs of hippocampal slice neurons: quantal levels, oscillations, and LTP. *Science* 252, 722–724. doi: 10.1126/science.1850871

Malinow, R., and Tsien, R. W. (1990). Presynaptic enhancement shown by whole-cell recordings of long-term potentiation in hippocampal slices. *Nature* 346, 177–180. doi: 10.1038/346177a0

Manabe, T., Renner, P., and Nicoll, R. A. (1992). Postsynaptic contribution to long-term potentiation revealed by the analysis of miniature synaptic currents. *Nature* 355, 50–55. doi: 10.1038/355050a0

Markram, H., Lübke, J., Frotscher, M., Roth, A., and Sakmann, B. (1997). Physiology and anatomy of synaptic connections between thick tufted pyramidal neurones in the developing rat neocortex. *J. Physiol.* 500(Pt. 2), 409–440. doi: 10.1113/jphysiol.1997.sp022031

Markram, H., and Tsodyks, M. (1996). Redistribution of synaptic efficacy between neocortical pyramidal neurons. *Nature* 382, 807–810. doi: 10.1038/382807a0

Martin, A. R. (1966). Quantal nature of synaptic transmission. *Physiol. Rev.* 46, 51–66. doi: 10.1152/physrev.1966.46.1.51

McLachlan, E. M. (1978). The statistics of transmitter release at chemical synapses. *Int. Rev. Physiol.* 17, 49–117.

Mitchell, D. E., Martineau, É, Tazerart, S., and Araya, R. (2019). Probing single synapses via the photolytic release of neurotransmitters. *Front. Synaptic Neurosci.* 11:19. doi: 10.3389/fnsyn.2019.00019

Murphy, T. H., and Corbett, D. (2009). Plasticity during stroke recovery: from synapse to behaviour. *Nat. Rev. Neurosci.* 10, 861–872. doi: 10.1038/nrn2735

Murthy, V. N., Sejnowski, T. J., and Stevens, C. F. (1997). Heterogeneous release properties of visualized individual hippocampal synapses. *Neuron* 18, 599–612. doi: 10.1016/s0896-6273(00)80301-3

Nabavi, S., Fox, R., Proulx, C. D., Lin, J. Y., Tsien, R. Y., and Malinow, R. (2014). Engineering a memory with LTD and LTP. *Nature* 511, 348–352. doi: 10.1038/nature13294

Neher, E., and Sakaba, T. (2003). Combining deconvolution and fluctuation analysis to determine quantal parameters and release rates. *J. Neurosci. Methods* 130, 143–157. doi: 10.1016/j.jneumeth.2003.09.020

Nevian, T., Larkum, M. E., Polsky, A., and Schiller, J. (2007). Properties of basal dendrites of layer 5 pyramidal neurons: a direct patch-clamp recording study. *Nat. Neurosci.* 10, 206–214. doi: 10.1038/nn1826

Nicoll, R. A., and Malenka, R. C. (1999). Expression mechanisms underlying NMDA receptor-dependent long-term potentiation. *Ann. N. Y. Acad. Sci.* 868, 515–525. doi: 10.1111/j.1749-6632.1999.tb11320.x

Oertner, T. G., Sabatini, B. L., Nimchinsky, E. A., and Svoboda, K. (2002). Facilitation at single synapses probed with optical quantal analysis. *Nat. Neurosci.* 5, 657–664. doi: 10.1038/nn867

Oleskevich, S., Clements, J., and Walmsley, B. (2000). Release probability modulates short-term plasticity at a rat giant terminal. *J. Physiol.* 524(Pt. 2), 513–523. doi: 10.1111/j.1469-7793.2000.00513.x

Otmakhov, N., Shirke, A. M., and Malinow, R. (1993). Measuring the impact of probabilistic transmission on neuronal output. *Neuron* 10, 1101–1111. doi: 10.1016/0896-6273(93)90058-y

Padamsey, Z., and Emptage, N. (2014). Two sides to long-term potentiation: a view towards reconciliation. *Philos. Trans. R. Soc. Lond. B Biol. Sci.* 369, 20130154. doi: 10.1098/rstb.2013.0154

Padamsey, Z., Tong, R., and Emptage, N. (2019). Optical Quantal analysis using Ca^{2+} indicators: a robust method for assessing transmitter release probability at excitatory synapses by imaging single glutamate release events. *Front. Synaptic Neurosci.* 11:5. doi: 10.3389/fnsyn.2019.00005

Pananceau, M., Chen, H., and Gustafsson, B. (1998). Short-term facilitation evoked during brief afferent tetani is not altered by long-term potentiation in the guinea-pig hippocampal CA1 region. *J. Physiol.* 508(Pt. 2), 503–514. doi: 10.1111/j.1469-7793.1998.503bq.x

Peng, Y., Mittermaier, F. X., Planert, H., Schneider, U. C., Alle, H., and Geiger, J. R. P. (2019). High-throughput microcircuit analysis of individual human brains through next-generation multineuron patch-clamp. *eLife* 8:e48178. doi: 10.7554/eLife.48178

Perin, R., Berger, T. K., and Markram, H. (2011). A synaptic organizing principle for cortical neuronal groups. *Proc. Natl. Acad. Sci. U.S.A.* 108, 5419–5424. doi: 10.1073/pnas.1016051108

Perin, R., and Markram, H. (2013). A computer-assisted multi-electrode patch-clamp system. *J. Vis. Exp.* 80:e50630.

Pologruto, T. A., Sabatini, B. L., and Svoboda, K. (2003). ScanImage: flexible software for operating laser scanning microscopes. *Biomed. Eng. Online* 2:13. doi: 10.1186/1475-925X-2-13

Poncer, J. C., and Malinow, R. (2001). Postsynaptic conversion of silent synapses during LTP affects synaptic gain and transmission dynamics. *Nat. Neurosci.* 4, 989–996. doi: 10.1038/nn719

Quastel, D. M. (1997). The binomial model in fluctuation analysis of quantal neurotransmitter release. *Biophys. J.* 72, 728–753. doi: 10.1016/s0006-3495(97)78709-5

Redman, S. (1990). Quantal analysis of synaptic potentials in neurons of the central nervous system. *Physiol. Rev.* 70, 165–198. doi: 10.1152/physrev.1990.70.1.165

Redman, S., and Walmsley, B. (1983). Amplitude fluctuations in synaptic potentials evoked in cat spinal motoneurones at identified group Ia synapses. *J. Physiol.* 343, 135–145. doi: 10.1113/jphysiol.1983.sp014885

Regehr, W. G. (2012). Short-term presynaptic plasticity. *Cold Spring Harb. Perspect. Biol.* 4:a005702. doi: 10.1101/cshperspect.a005702

Reid, C. A., and Clements, J. D. (1999). Postsynaptic expression of long-term potentiation in the rat dentate gyrus demonstrated by variance-mean analysis. *J. Physiol.* 518, 121–130. doi: 10.1111/j.1469-7793.1999.0121r.x

Sanes, J. R., and Lichtman, J. W. (1999). Development of the vertebrate neuromuscular junction. *Annu. Rev. Neurosci.* 22, 389–442. doi: 10.1146/annurev.neuro.22.1.389

Saviane, C., and Silver, R. A. (2007). Estimation of quantal parameters with multiple-probability fluctuation analysis. *Methods Mol. Biol.* 403, 303–317. doi: 10.1007/978-1-59745-529-9_19

Sayer, R. J., Redman, S. J., and Andersen, P. (1989). Amplitude fluctuations in small EPSPs recorded from CA1 pyramidal cells in the guinea pig hippocampal slice. *J. Neurosci.* 9, 840–850. doi: 10.1523/jneurosci.09-03-00840.1989

Scheuss, V., and Neher, E. (2001). Estimating synaptic parameters from mean, variance, and covariance in trains of synaptic responses. *Biophys. J.* 81, 1970–1989. doi: 10.1016/s0006-3495(01)75848-1

Seeholzer, A., Deger, M., and Gerstner, W. (2019). Stability of working memory in continuous attractor networks under the control of short-term plasticity. *PLoS Comput. Biol.* 15:e1006928. doi: 10.1371/journal.pcbi.1006928

Selig, D. K., Nicoll, R. A., and Malenka, R. C. (1999). Hippocampal long-term potentiation preserves the fidelity of postsynaptic responses to presynaptic bursts. *J. Neurosci.* 19, 1236–1246. doi: 10.1523/jneurosci.19-04-01236.1999

Sheng, M., and Kim, M. J. (2002). Postsynaptic signaling and plasticity mechanisms. *Science* 298, 776–780. doi: 10.1126/science.1075333

Silver, R. A., Momiyama, A., and Cull-Candy, S. G. (1998). Locus of frequency-dependent depression identified with multiple-probability fluctuation analysis at rat climbing fibre-Purkinje cell synapses. *J. Physiol.* 510(Pt. 3), 881–902. doi: 10.1111/j.1469-7793.1998.881bj.x

Sjöström, P. J., Rancz, E. A., Roth, A., and Häusser, M. (2008). Dendritic excitability and synaptic plasticity. *Physiol. Rev.* 88, 769–840. doi: 10.1152/physrev.00016.2007

Sjöström, P. J., Turrigiano, G. G., and Nelson, S. B. (2001). Rate, timing, and cooperativity jointly determine cortical synaptic plasticity. *Neuron* 32, 1149–1164. doi: 10.1016/s0896-6273(01)00542-6

Sjöström, P. J., Turrigiano, G. G., and Nelson, S. B. (2003). Neocortical LTD via coincident activation of presynaptic NMDA and cannabinoid receptors. *Neuron* 39, 641–654. doi: 10.1016/s0896-6273(03)00476-8

Sjöström, P. J., Turrigiano, G. G., and Nelson, S. B. (2007). Multiple forms of long-term plasticity at unitary neocortical layer 5 synapses. *Neuropharmacology* 52, 176–184. doi: 10.1016/j.neuropharm.2006.07.021

Song, S., and Abbott, L. F. (2001). Cortical development and remapping through spike timing-dependent plasticity. *Neuron* 32, 339–350. doi: 10.1016/s0896-6273(01)00451-2

Song, S., Sjöström, P. J., Reigl, M., Nelson, S., and Chklovskii, D. B. (2005). Highly nonrandom features of synaptic connectivity in local cortical circuits. *PLoS Biol.* 3:e68. doi: 10.1371/journal.pbio.0030068

Südhof, T. C. (2013). Neurotransmitter release: the last millisecond in the life of a synaptic vesicle. *Neuron* 80, 675–690. doi: 10.1016/j.neuron.2013.10.022

Tong, G., and Jahr, C. E. (1994). Multivesicular release from excitatory synapses of cultured hippocampal neurons. *Neuron* 12, 51–59. doi: 10.1016/0896-6273(94)90151-1

Triller, A., and Korn, H. (1982). Transmission at a central inhibitory synapse. III. Ultrastructure of physiologically identified and stained terminals. *J. Neurophysiol.* 48, 708–736. doi: 10.1152/jn.1982.48.3.708

Tsodyks, M. V., and Markram, H. (1997). The neural code between neocortical pyramidal neurons depends on neurotransmitter release probability. *Proc. Natl. Acad. Sci. U.S.A.* 94, 719–723. doi: 10.1073/pnas.94.2.719

Walmsley, B., Edwards, F. R., and Tracey, D. J. (1988). Nonuniform release probabilities underlie quantal synaptic transmission at a mammalian excitatory central synapse. *J. Neurophysiol.* 60, 889–908. doi: 10.1152/jn.1988.60.3.889

Watt, A. J., Sjöström, P. J., Häusser, M., Nelson, S. B., and Turrigiano, G. G. (2004). A proportional but slower NMDA potentiation follows AMPA potentiation in LTP. *Nat. Neurosci.* 7, 518–524. doi: 10.1038/nn1220

Watt, A. J., van Rossum, M. C., Macleod, K. M., Nelson, S. B., and Turrigiano, G. G. (2000). Activity coregulates quantal AMPA and NMDA currents at neocortical synapses. *Neuron* 26, 659–670. doi: 10.1016/s0896-6273(00)81202-7

Williams, S. R., and Stuart, G. J. (2002). Dependence of EPSP efficacy on synapse location in neocortical pyramidal neurons. *Science* 295, 1907–1910. doi: 10.1126/science.1067903

Wojtowicz, J. M., Marin, L., and Atwood, H. L. (1994). Activity-induced changes in synaptic release sites at the crayfish neuromuscular junction. *J. Neurosci.* 14, 3688–3703. doi: 10.1523/jneurosci.14-06-03688.1994

Zakharenko, S. S., Zablow, L., and Siegelbaum, S. A. (2001). Visualization of changes in presynaptic function during long-term synaptic plasticity. *Nat. Neurosci.* 4, 711–717. doi: 10.1038/89498

Zucker, R. S., and Regehr, W. G. (2002). Short-term synaptic plasticity. *Annu. Rev. Physiol.* 64, 355–405.

Conflict of Interest: The authors declare that the research was conducted in the absence of any commercial or financial relationships that could be construed as a potential conflict of interest.

frontiers in Synaptic Neuroscience

METHODS
published: 30 April 2020
doi: 10.3389/fnsyn.2020.00018

Autaptic Cultures: Methods and Applications

*John M. Bekkers**

Eccles Institute of Neuroscience, The John Curtin School of Medical Research, The Australian National University, Canberra, ACT, Australia

Neurons typically form daisy chains of synaptic connections with other neurons, but they can also form synapses with themselves. Although such self-synapses, or autapses, are comparatively rare *in vivo*, they are surprisingly common in dissociated neuronal cultures. At first glance, autapses in culture seem like a mere curiosity. However, by providing a simple model system in which a single recording electrode gives simultaneous access to the pre- and postsynaptic compartments, autaptic cultures have proven to be invaluable in facilitating important and elegant experiments in the area of synaptic neuroscience. Here, I provide detailed protocols for preparing and recording from autaptic cultures (also called micro-island or microdot cultures). Variations on the basic procedure are presented, as well as practical tips for optimizing the outcomes. I also illustrate the utility of autaptic cultures by reviewing the types of experiments that have used them over the past three decades. These examples serve to highlight the power and elegance of this simple model system, and will hopefully inspire new experiments for the interrogation of synaptic function.

Keywords: autapse, culture, methods, review, synapse

OPEN ACCESS

Edited by:
Dirk Feldmeyer, Helmholtz Association of German Research Centers (HZ), Germany

Reviewed by:
Michael Beierlein, University of Texas Health Science Center at Houston, United States
Kimberly M. Huber, University of Texas Southwestern Medical Center, United States

***Correspondence:**
John M. Bekkers
john.bekkers@anu.edu.au

Received: *21 December 2019*
Accepted: *01 April 2020*
Published: *30 April 2020*

Citation:
Bekkers JM (2020) Autaptic Cultures: Methods and Applications. Front. Synaptic Neurosci. 12:18. doi: 10.3389/fnsyn.2020.00018

INTRODUCTION

The brain achieves its astonishing feats of information processing in part because of the complexity of its synaptic connections. Many synaptic circuit motifs have been elucidated, including feedforward, feedback, recurrent and lateral inhibition and excitation (Douglas and Martin, 2007; Yuste, 2015). Perhaps surprisingly, one of the most simple circuit motifs of all—that in which a neuron makes a synaptic connection with itself—was relatively late to come to the attention of neuroscientists. The term "autapse" entered the neuroscience lexicon only in 1972 when it was first coined to describe putative self-synapses on Golgi-stained pyramidal neurons in rabbit neocortex (Van der Loos and Glaser, 1972). Since then, both anatomical and physiological evidence for autapses *in vivo* has accumulated steadily (Karabelas and Purpura, 1980; Park et al., 1980; Peters and Proskauer, 1980; Preston et al., 1980; Lübke et al., 1996; Cobb et al., 1997; Tamás et al., 1997; Pouzat and Marty, 1998, 1999; Pawelzik et al., 2003; Bacci and Huguenard, 2006; Connelly and Lees, 2010; Manseau et al., 2010; Jiang et al., 2012, 2015; Yin et al., 2018; Deleuze et al., 2019). Today there is no question that autapses exist in the brain, albeit in much smaller numbers than (hetero-) synapses. However the importance of autapses for the normal operation of neural circuits remains a matter for speculation (Bekkers, 1998, 2003, 2009; White et al., 1998; Li et al., 2010; Connelly, 2014; Deleuze et al., 2014; Guo et al., 2016; Wiles et al., 2017).

In parallel with these discoveries about autapses in intact brain tissue, it was found that, under the right conditions, autapses in neuronal cultures are surprisingly common. When constrained to grow in isolation on "microislands" or "microdots" a few tens of microns across (Furshpan et al., 1976, 1986; Landis, 1976), cultured neurons readily form autapses (Segal and Furshpan, 1990; Bekkers and Stevens, 1991). The presence of two or more neurons on the microisland does not seem to curtail autapse formation (Tarsa and Goda, 2002; Wierda and Sørensen, 2014), suggesting that neurons are just as likely to form autapses as synapses when given the opportunity. It is possible that the 2-dimensional geometry of cultures, with the greater likelihood that an axon will encounter its dendrites, is an important reason why autapses are so prevalent in culture (Ikeda and Bekkers, 2006).

Although initially a curiosity, autaptic cultures have proven to be a valuable model system for addressing a range of important questions in cellular neuroscience. By providing a homogeneous population of synaptic contacts on a single, isolated neuron, autaptic cultures offer the ultimate in synaptic reductionism. Their functional simplicity has enabled many important and elegant experiments that would not have been possible in more complex systems.

The goals of this article are, first, to show how to prepare and utilize these cultures and, second, to give an overview of their many applications, with an emphasis on neurophysiological experiments. An alternative method for studying single neurons in isolation is to use very-low-density cultures, which have been described in detail elsewhere (e.g., Goslin et al., 1998; Ventimiglia and Lindsay, 1998; Fath et al., 2009); I will not be discussing this approach here. I will also not be discussing the use of similar cultures to study neurite growth on patterned substrates, which is of interest to the design of brain-machine interfaces (e.g., Jang et al., 2016; Gautam et al., 2017).

METHODS FOR PREPARING AUTAPTIC CULTURES

Autaptic cultures are prepared in essentially the same way as conventional dissociated primary cultures ("mass cultures"), the main difference being the preparation of the culture plates. Several excellent articles about preparing autaptic cultures have been published (Segal et al., 1998; Allen, 2006; Fasano et al., 2008; Rost et al., 2010; Burgalossi et al., 2012; Lu et al., 2016) and the guidance below draws upon all of these, as well as my own experience (Bekkers and Stevens, 1991; Bekkers, 2005). It should be kept in mind that cell culture is often laced with superstition. The best advice is to start simple and elaborate only if necessary.

The methods presented here will focus on general-purpose hippocampal or cortical cultures prepared from newborn mice or rats. Others have described how to prepare cultures from embryos (Fath et al., 2009; Lu et al., 2016), older tissue (Ogata and Tatebayashi, 1991; Brewer, 1997; Allen, 2006) and other brain areas (Johnson, 1994; Shi and Rayport, 1994; Sulzer et al., 1998; Michel and Trudeau, 2000; Moechars et al., 2006). There is even a protocol for preparing autaptic cultures from human induced pluripotent stem cells (Fenske et al., 2019). Whatever the tissue source, it goes without saying that all procedures must be approved by the local ethics committee.

Overview of the Procedure

Figure 1 shows the basic steps in preparing autaptic cultures, and the detailed requirements are listed in **Tables 1–4**. Briefly, the key initial step is to prepare coverslips with spots of permissive growth substrate (e.g., collagen, poly-D-lysine) dispersed across a coating of non-permissive substrate (agarose). Dissociated primary neurons are then added to the coverslips, usually (but not always) after first growing a monolayer of glial cells (astrocytes) on the spots to provide trophic support for the neurons. Autaptic neurons are typically ready for use after 1–2 weeks *in vitro*. The entire procedure will take at least 2–3 weeks, depending on the exact method used.

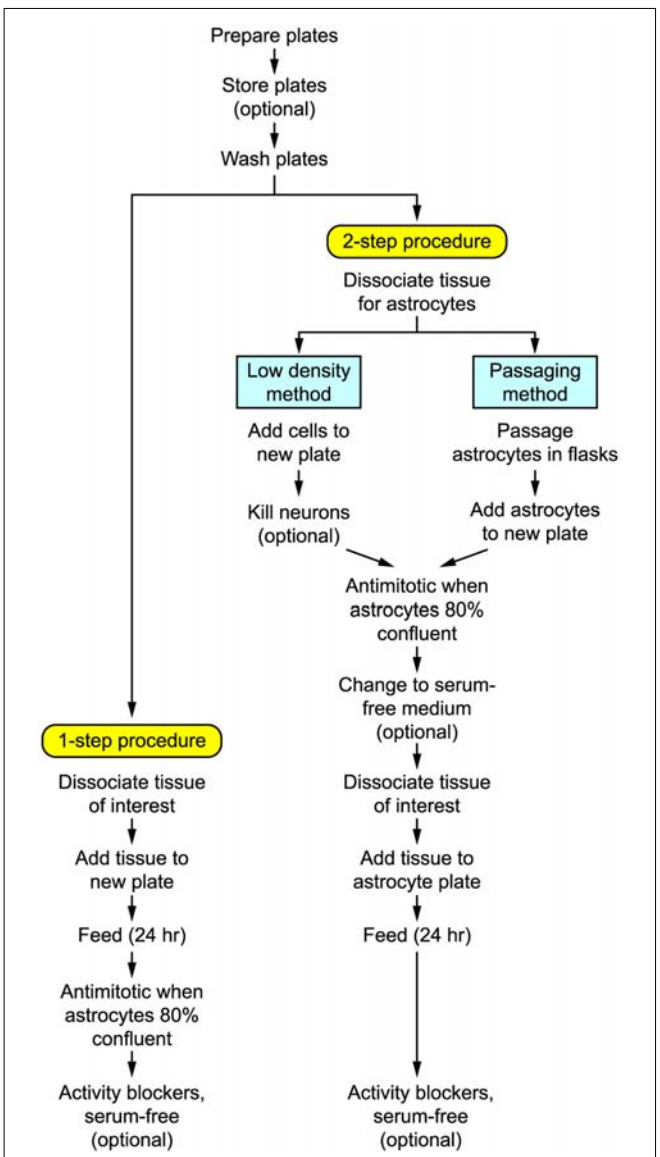

FIGURE 1 | Flow diagram summarizing the steps involved in preparing autaptic cultures.

TABLE 1 | Solutions for preparing plates.

Permissive coating solution

Stock solutions:
- 5 mg/ml poly-D-lysine in sterile dH_2O
- Collagen as assayed by the supplier

To prepare 1 ml of permissive coating solution:
- Aim for final concentrations of ∼0.1 mg/ml poly-D-lysine and ∼0.5 mg/ml collagen
- Dilute the collagen to 0.5 mg/ml in 1 ml of sterile dH_2O
- Add 20 μl of poly-D-lysine stock to the 1 ml of diluted collagen

Keep the coating solution for several weeks at 4°C.

Quantity	Name	Supplier	Catalog number
5 mg	Poly-D-lysine hydrobromide 30-70K	Sigma–Aldrich	P7280
20 ml	Rat tail collagen	Thermo Fisher	A1048301
		Sigma–Aldrich	C3867
5 g	Agarose, Type II-A: medium EEO	Sigma–Aldrich	A9918

Notes: 1. Poly-L-lysine, and either the hydrobromide or hydrochloride salt, should work as well, but some experimentation may be required. 2. Some investigators recommend preparing the poly-D/L-lysine stock in borate buffer (1.24 g of boric acid, 1.9 g of sodium tetraborate, 400 ml of H_2O).

TABLE 2 | Solutions for tissue dissociation.

Dissection solution

This can be standard mammalian Ringer containing (in mM): 125 NaCl, 3 KCl, 2 $CaCl_2$, 1 $MgCl_2$, 25 HEPES @ pH 7.4 adjusted with NaOH, 10 glucose, 25 sorbitol to give 315 mOsm/kg, 0.22 μm filtered to sterilize.

Enzyme solution

Mix in a 15 ml tube:
- 5 ml Hank's Balanced Salt Solution (BSS; divalent-free, with phenol red)
- 50 μl 50 mM EDTA stock
- 75 μl 100 mM $CaCl_2$
- ∼1 mg cysteine
- 100 units papain suspension

Add about 10 μl of 1 M NaOH to adjust pH to about 7 (i.e., a pale pink color).

Keep in 37°C bath for 10–15 min to dissolve papain, then 0.22 μm filter into another sterile 15 ml tube and return the tube to the 37°C bath until required.

Quantity	Name	Supplier	Catalog number
500 ml	Hank's BSS, divalent-free, with phenol red	Thermo Fisher	14170112
100 g	EDTA	Sigma–Aldrich	E6758
5 g	L-cysteine, HCl monohydrate	Sigma–Aldrich	C7889
100 mg	Papain, suspension	Worthington	LS 003126
		Sigma–Aldrich	P3125

Preparation of Plates

(1) *Clean the coverslips*. We use 24-well culture plates and grow the cells on 12–13 mm diameter No. 1 circular glass coverslips, one per well, which routinely provides 1–5 isolated single neurons per coverslip, i.e., up to this number of autapse experiments per well. Larger coverslips may be more convenient in some situations (see Step 5). Clean the coverslips by swirling them for 5 min in 10 N nitric or hydrochloric acid. This is intended to make the glass more hydrophilic for the agarose coating, but simply cleaning with ethanol also works (Lu et al., 2016). Rinse thoroughly in tap water, followed by distilled water then 100% ethanol, and store in a glass bottle under 100% ethanol. A large number can be cleaned at the same time and used for months.

(2) *Place coverslips in culture plates*. Using forceps and working in a sterile hood, flame the coverslips dry one at a time by passing them through a gas flame. Place the coverslips in the culture plates, one per well. Center the coverslip in each well and press down gently to "stick" it in position.

(3) *Coat coverslips with agarose*. Prepare 0.15–0.2% agarose in dH_2O. This can be done by weighing 15–20 mg of agarose into 10 ml of dH_2O in a 15 ml centrifuge tube. The tube, with its cap loosened, is microwaved or placed in boiling water for 2–5 min until the agarose is dissolved. Using a 200 μl pipette, spread a thin layer of the agarose solution on each coverslip then suck off the excess (It helps to first stick down the coverslip by placing a drop of solution at the edge of the coverslip so it runs underneath). It is important that the whole coverslip is covered with an agarose solution; any gaps can allow astrocytes or neurons to grow on the glass, compromising the required isolation of microislands. Sometimes the glass does not wet well; in this case, you need to add more agarose solution so a large drop completely covers the glass. Allow the plate to dry in the hood. We usually prepare 4 or 5 plates like this at once then store them at room temperature for several months (Burgalossi et al., 2012).

TABLE 3 | Culture media.

Classic serum-containing medium

To prepare 100 ml:

- 2 ml of 1 M stock glucose in MEM with Earle's Salts
- 5 ml of heat-inactivated Fetal Bovine Serum (FBS)
- 1 ml of 5,000 units/ml stock Penicillin-Streptomycin
- MEM, Earle's salts, top-up to 100 ml
- 100 μl Serum Extender

Filter (0.22 μm) into a sterile bottle. Keep in the dark at 4°C for about 2 weeks.

Quantity	Name	Supplier	Catalog number
1,000 ml	Minimal Essential Medium (MEM) with Earle's Salts, without glutamine	Sigma–Aldrich	51412C
100 ml	FBS	Various	
100 ml	Penicillin-Streptomycin	Thermo Fisher	15070063
1 vial	MITO+ Serum Extender	Corning	355006

Alternative serum-containing medium

To prepare 100 ml:

- 50 ml DMEM with HEPES: Weigh out 870 mg Dulbecco's Modified Eagle's Medium (DMEM) with high glucose (powder), add <50 ml distilled water (dH_2O) while stirring. Make up to 50 ml with dH_2O.
- Mix the 50 ml prepared in step 1 with 50 ml of DMEM with high glucose (liquid).
- 2 ml B-27 supplement.
- 1 ml of 5,000 units/ml stock Penicillin-Streptomycin.
- 5 ml heat-inactivated FBS.
- Add about 350 μl 1 M NaOH to adjust pH to about 7.5.

Filter (0.22 μm) into a sterile bottle. Keep in the dark at 4°C for about 2 weeks.

Quantity	Name	Supplier	Catalog number
For 10 L	Dulbecco's Modified Eagle's Medium with high glucose (powder)	Sigma–Aldrich	D1152
100 ml	Dulbecco's Modified Eagle's Medium with high glucose (liquid)	Sigma–Aldrich	D0422
10 ml	B-27 Supplement (50×)	Thermo Fisher	17504044
100 ml	Penicillin-Streptomycin	Thermo Fisher	15070063
100 ml	FBS	Various	

Complete Neurobasal medium (serum-free)

To prepare 100 ml, mix aseptically:

- 98 ml of Neurobasal or Neurobasal Plus medium
- 2 ml of B-27 or B-27 Plus Supplement
- 250 μl of GlutaMAX-I Supplement

Keep in the dark at 4°C for about 2 weeks.

Quantity	Name	Supplier	Catalog number
500 ml	Neurobasal Medium	Thermo Fisher	21103049
	Neurobasal Plus medium		A3582901
10 ml	B-27 Supplement (50×)	Thermo Fisher	17504044
	B-27 Plus Supplement (50×)		A3582801
100 ml	GlutaMAX-I Supplement	Thermo Fisher	A1286001

Notes: 1. To heat-inactivate FBS, heat @ 56°C for 30 min in a water bath. 2. MEM without phenol red may be preferred for cultures that will be used for imaging experiments to minimize background fluorescence. 3. For suppressing the overgrowth of glial cells, prepare a 2.5 mM stock solution of cytosine arabinoside, free base (Sigma–Aldrich, C-1768) in dH_2O and store the stock at −20°C. Dilute this in warmed culture medium to achieve a final concentration of 5 μM in the culture plate after feeding. 4. Glial cells grow more readily in medium supplemented with FBS, so an alternative for suppressing glial growth, particularly if plating onto an astrocyte feeder layer, is to replace the FBS with twice the concentration of horse serum.

(4) *Prepare the permissive substrate*. Prepare about 1 ml of permissive substrate solution. We normally use a mixture of poly-D-lysine and rat tail collagen (**Table 1**) because cells attach better to poly-D-lysine (Segal et al., 1998) but collagen adds viscosity that may help with the spotting (next step); however, either could be used on its own. The mixture keeps for several weeks at 4°C. Possible alternatives are poly-L-lysine and poly-D,L-ornithine (Segal et al., 1998).

(5) *Apply spots of permissive substrate*. The next step—dispersing small spots of poly-D-lysine/collagen on the agarose coating—is critical. The original method uses a micro atomizer or airbrush to spray a mist of permissive substrate onto the agarose-coated coverslips, which requires judgment and experience to achieve a satisfactory distribution of small, discrete spots (Segal and Furshpan, 1990; Bekkers and Stevens, 1991; Fasano et al., 2008). A more recent method is to fabricate a stamping tool that imprints a regular pattern of permissive substrate solution onto the coverslips (Moulder et al., 2007; Sgro et al., 2011; Burgalossi et al., 2012; Ricoult et al., 2012).

(i) *Microatomizer method*. Obtain a small glass reagent sprayer or artist's airbrush (see **Table 4** for suggested

TABLE 4 | Other requirements.

13 mm round glass coverslips, No. 1 (0.13–0.17 mm thickness), cleaned as described
24 well culture plates
56 mm sterile culture dish (for coarse dissection of tissue)
35 mm sterile culture dish (for fine dissection of tissue, if required)
15 ml sterile plastic centrifuge tubes (for preparing solutions, incubating in enzyme, trituration)
50 ml sterile plastic centrifuge tubes (for working aliquots of culture medium)
0.22 μm pore 25 mm diameter sterile syringe filters (for sterilizing solutions)
10 ml syringes (for use with syringe filters)
10 ml sterile pipettes (for dispensing medium and adding cell suspension to plates)
Sterile Pasteur pipettes plugged at the wide end with cotton wool (for dispensing solutions during dissection and doing trituration)
Hemocytometer and access to a microscope (for counting cells)
Dissection instruments: e.g., dissection scope, medium scissors for decapitation, small scissors for opening the skull, small flat spatula for removing the brain and doing coarse dissection, one pair fine forceps, one scalpel blade for mincing tissue
80% v/v ethanol in distilled water (for sterilizing the dissection instruments and work area)
Sterile bottles (for storing the culture medium and solutions used in the preparation)
Small atomizer (for spraying the culture plates). We have the most experience with a small glass reagent sprayer (e.g., Kimble 5 ml thin layer chromatography sprayer, kimble-chase.com) but a small recycled perfume spray bottle might work as well, or an artist's airbrush (e.g., Aztec airbrush from www.testors.com). See "Preparation of Plates" section for more details.
Stamping tool for applying spots of permissive substrate. This is an alternative to the atomizer. The stamping tool yields more reproducible microislands but the tool needs to be fabricated. See "Preparation of Plates" section for more details.

Notes: 1. Quantities depend on the number of cultures. We find that one newborn animal is sufficient to yield enough hippocampal neurons for one or two 24-well plates. 2. The composition of the glass used in the coverslips may affect the health of the cultures. Be prepared to test coverslips from different suppliers.

sources). A small perfume bottle may also work. Sterilize the sprayer by spraying 80% ethanol and allowing it to dry in the culture hood. Load the substrate solution into the atomizer and spray the coating solution onto the dry agarose-coated plates. The spraying pressure, spraying duration, and distance from the plate need to be optimized so that small, discrete spots (∼200 μm diameter) of the substrate solution settle on the coverslip. Here are some tips to guide mastery of this critical step (see also "Troubleshooting" section below).

- Hold the culture plate vertically (the coverslips should not fall out if they have been stuck down with agarose) against a dark surface for better visibility then apply a brief burst of spray from about 15 cm away to cover each half of the plate.
- Alternatively, place the plates on a horizontal surface and spray from ∼50 cm away, allowing the mist to settle on the plates (Fasano et al., 2008).
- Higher pressure in the atomizer tends to produce smaller spots, but the spraying time needs to be brief to avoid producing too many spots that merge.
- The spattering can be practiced by spraying an uncoated coverslip with a test solution in which a dye (e.g., Trypan blue) is added to the normal coating solution (to have the right viscosity). The distribution and sizes of the spots can be observed under a dissecting scope immediately after spraying, then the spots can then be wiped off and another attempt made.
- The spots may vary markedly in size, which is acceptable; you only need ∼10–20 spots on the coverslip that have the preferred size (∼200 μm).

(ii) *Stamping tool method*. This method requires the fabrication of a special "microstamp" but yields much more reproducible microislands and, hence, a higher yield of isolated autaptic neurons (Moulder et al., 2007; Rost et al., 2010; Sgro et al., 2011; Burgalossi et al., 2012; Ricoult et al., 2012). The stamp can be made using photolithography and microcontact printing techniques. A typical pattern might be an array of squares or circles, 150–200 μm across, spaced at 400–500 μm intervals (Sgro et al., 2011; Burgalossi et al., 2012). The permissive substrate solution is loaded onto the stamp then transferred to the agarose-coated coverslips with gentle pressure. The key precaution with this method is to avoid under- or overloading the stamp with substrate solution (Moulder et al., 2007; Burgalossi et al., 2012).

(6) *Sterilize and store the prepared plates*. Allow the plates to dry in the hood, which should only take a few minutes. It is advisable to sterilize the plates by placing them under a UV lamp in the culture hood for 20–30 min. Prepared plates can then be covered and kept at room temperature for several weeks before use. Indeed, doing so has been reported to result in healthier cultures (Sgro et al., 2011), although others state that the plates should be prepared just before use (Fath et al., 2009).

(7) *Wash the plates*. The day before the cell preparation, add a few drops of culture medium to each well—just enough to cover the coverslip—and keep the plates in an incubator overnight. This "washes" the substrate and seems to improve the survival of cells. Just before adding the cell suspension to the plates the washing medium is sucked out and discarded.

A variation on the above is to use the "sandwich" method, in which the coverslip containing the neurons is opposed to and separate from an astrocyte feeder culture that provides diffusible growth factors to the medium (Brewer and Cotman, 1989). A simple way to prepare plates for this method is to simply scratch the bottom of each well with a needle (Lu et al., 2016). This raises small protuberances of plastic that will hold the coverslip just above the bottom of the well. Another method is to briefly touch the bottom of each well in three places with a hot soldering iron, raising small plastic welts. The coverslips for "sandwich" cultures are prepared by first distributing them in large (e.g., 60 mm) culture dishes. They are then coated with agarose and sprayed with a permissive substrate, as described above for the standard method. Finally, they are sterilized and stored in the large culture dishes until needed for the cell preparation. See "Alternative Plating Method" section below for further details.

Plating Procedure

Broadly speaking, primary neuronal cultures can be prepared in two different ways (**Figure 1**):

(i) *One-step procedure*. Neural tissue is enzymatically dissociated and the single-cell suspension is plated at a high enough density that the neurons will survive while the astrocytes become sufficiently numerous to provide longer-term trophic support for the neurons. This method works best with rats or embryonic tissue.

(ii) *Two-step procedure*. A monolayer "lawn" of astrocytes without neurons is prepared first, then the neurons are plated on top of the astrocytes 1–3 weeks later. This method works well for both rat and mouse postnatal tissue and tends to give a more consistent yield of autaptic neurons (Pyott and Rosenmund, 2002). The astrocytic lawn can be prepared in two ways.

   (a) *Low-density*: The dissociated cell suspension is directly added to the microisland plates at a low enough density that only the astrocytes survive.

   (b) *Passaging*: The astrocytes are grown and passaged separately before adding them to the microisland plates.

For both the one-step and two-step procedures the cultures are more likely to be successful when prepared from embryonic or newborn tissue, e.g., from rodents aged between embryonic day 16 (E16) and postnatal days 0–3 (P0–3). If cultures need to be prepared from older animals, more elaborate procedures are required (Kay and Wong, 1986; Kaneda et al., 1988; Ogata and Tatebayashi, 1991; Brown et al., 1993; Magistretti et al., 1996; Brewer, 1997; Allen, 2006). The steps presented below assume that newborn rodent tissue is being used. Methods for using embryonic tissue are described elsewhere (Goslin et al., 1998; Fath et al., 2009).

Unless otherwise stated, all of the following steps are done in a sterile laminar flow hood.

(1) *Prepare instruments and solutions*. Assemble the dissection instruments (**Table 4**) in the hood and sterilize them with 80% ethanol. Prepare the enzyme solution (**Table 2**), chill the dissection solution (**Table 2**) and warm the culture medium (**Table 3**). Papain is most commonly used in the enzyme solution because it is regarded as gentler than trypsin for dissociating fragile neural tissue (Goslin et al., 1998). However, if preparing astrocytes for passaging (see Step 8 below) then trypsin is suitable and more economical. The choice of the culture medium is critical. For growing neurons under defined conditions, serum-free medium (e.g., Neurobasal medium; **Table 3**) is preferred. On the other hand, astrocytes grow better in serum-containing medium (**Table 3**, Rost et al., 2010; Burgalossi et al., 2012). Thus, unless the neurons are being plated onto a confluent monolayer of astrocytes (see Steps 6 and 8 below), it is advisable to start with a serum-containing medium to promote astrocyte division. If desired, the culture can be switched to a serum-free medium after the astrocytes have reached confluence. A disadvantage of using serum is that there may be batch-to-batch variability in the properties of the serum, and so it may be advisable to test small amounts of different batches before placing a larger order.

(2) *Extract the tissue*. One newborn rat or mouse pup provides enough hippocampal or cortical cells for one or two 24-well plates. Sacrifice the pup using an approved method of euthanasia and remove the brain into ice-cold dissection solution. Dissect out the hippocampi or cortical tissue, if possible peel off the meninges (enclosing membrane), then cut the tissue into roughly 1 mm square blocks.

(3) *Incubate the tissue in enzyme*. Using a sterile pipette, transfer the tissue pieces, with as little of the dissection solution as possible, to the sterile 15 ml centrifuge tube containing the enzyme solution. Place the tube in a 37°C water bath with agitator and leave it gently agitating for 30 min. Alternatively, gentle manual agitation for a few seconds every 10 min will suffice. While the tissue is incubating, prepare a plugged sterile glass Pasteur pipette by gently melting the tip of the pipette in a burner flame in the hood. You want to smoothen the sharp edges of the pipette tip without making the tip much narrower.

(4) *Dissociate the tissue*. At the end of the incubation, move the tube with tissue back to the laminar flow hood and (optionally) add 50–100 μl of 10 mg/ml DNAse I stock solution and wait for about 30 s. This breaks down DNA from damaged cells and reduces clumping during the subsequent trituration. Using the smoothed Pasteur pipette, suck off as much as possible of the supernatant enzyme solution and add 1–2 ml of warmed culture medium. After allowing the tissue to settle, suck off and discard the supernatant. Repeat this 3–4 times to completely wash out the enzyme. Add a milliliter or so of culture medium and very gently triturate the tissue 3–4 times. Wait for the pieces to settle, then save the supernatant (which should appear a little cloudy due to the suspension of dissociated cells) to another sterile 15 ml tube. Repeat this process 6–8 times, each time triturating slightly more vigorously (but still very gently) and saving the supernatant until the tissue is mostly dissociated. Ensure that no air bubbles get into the solution at any

stage during this procedure. Being very gentle and careful is the key to success. You should finish with 6–10 ml of single-cell suspension.

(5) *Count the cells*. Counting is done using a hemocytometer on a phase-contrast microscope. A good preparation is one that contains many phase-bright neurons with the stumps of processes visible. However, we count all phase-bright cells, including ones without obvious processes. Typically we get a yield of about 15–25 $\times$ 10^4 cells ml^{-1} from the CA1 regions of two hippocampi. Possible remedies for a low yield are given in the "Troubleshooting" section.

(6) *Determine the dilutions*. **Table 5** gives suggested cell counts and volumes for different types of cultures. When using the two-step procedure we typically prepare two 24-well plates during each culture preparation: one in which we prepare a low-density astrocyte culture using a new culture plate (*C* or *D* in **Table 5**), and one in which we plate neurons on top of a low-density astrocyte culture that was prepared 2–3 weeks previously and which is now a confluent monolayer (*E* or *F* in **Table 5**). Note that, when plating on top of an astrocyte monolayer (*E* or *F*), the suspension of neurons is simply added to the 0.5 ml of the medium that is already in each well. The low-density astrocyte cultures (*C* and *D* in **Table 5**) typically grow to confluency over 2–3 weeks with little contamination from surviving neurons. However, if neurons do remain, they can usually be lysed by simply removing the plate from the incubator for 30–60 min. Alternatively, the neurons can be killed by adding 0.2–1 mM glutamate to the culture medium for several hours, then rinsing and refeeding with fresh culture medium (Segal et al., 1998; Harms et al., 2005). Note that cell plating densities are advisory, and experimentation will be required to find densities that suit your particular conditions. In general, higher plating density leads to more surviving neurons with greater synaptic connectivity (Ivenshitz and Segal, 2010), but this may be a disadvantage if the aim is to maximize the number of microdots occupied by a single neuron. Further comments on plating density are made in the sections "Troubleshooting" and "Electrophysiological Recordings From Autapses."

(7) *Incubate the culture plates*. Place the culture plate(s) into an incubator at 37°C, 5% CO_2. The neurons should settle and stick to the substrate within an hour or two. They should begin to extend processes within 24 h, or sooner if plated on astrocytes.

(8) *Passaging method for preparing astrocyte monolayers*. Passaging provides an ample supply of pure astrocytes that can be plated out on new culture dishes at a higher density than in Step 6 above, which means that a confluent astrocytic "lawn" will grow more quickly. On the other hand, this approach is more complex. Briefly, neural tissue is dissociated as in Steps 1–4 above, except that harsher enzymes (e.g., trypsin) and more vigorous trituration are used to favor the more hardy astrocytes over neurons. The cells are grown in culture flasks under conditions that suit astrocytes and are passaged until required (Ullian et al., 2001).

TABLE 5 | Cell dilutions.

Type of culture	Final cell density ($\times 10^4$ ml^{-1})	Volume per well (24-well plate; ml)
A: 1-step procedure, rat	7–9	0.5
B: 1-step procedure, mouse	12–15	0.5
C: 2-step procedure, rat, to prepare a low-density astrocyte culture	3–5	0.5
D: 2-step procedure, mouse, to prepare a low-density astrocyte culture	3–5	0.5
E: 2-step procedure, rat, plating on an astrocyte monolayer	6–10	0.1
F: 2-step procedure, mouse, plating on an astrocyte monolayer	10–15	0.1

Feeding

Following the plating of neurons, it is normal for significant neuronal death and accumulation of debris to occur over the first 24 h. The debris should be removed as much as possible by feeding the culture the day after the dissociation. If using 24-well plates, this is done by removing 0.15 ml of the old medium from each well (i.e., about 1/3 the well volume) and adding the same quantity of fresh, warmed medium.

A general rule of thumb is that autaptic cultures do better with minimal feeding, say, once every 1–2 weeks using the 0.15 ml off/on protocol above. However, there are several important exceptions to this rule.

(i) *When astrocytes approach confluence (one-step procedure)*. About 4–5 days after plating with the one-step procedure the astrocytes should be about 80% confluent. To prevent overgrowth of the neurons by astrocytes, the cultures should be treated with an antimitotic drug, e.g., cytosine arabinoside (araC, 5 μM final concentration; see **Table 3**, Notes), administered using the one-third off/on method above. The cultures are then fed again 1–3 days later with drug-free medium. Both of these feeds, as well as subsequent ones, can be done using a serum-free medium if desired, provided the transition is done slowly to avoid shock to the neurons.

(ii) *When astrocytes approach confluence (two-step procedure, preparing an astrocyte culture)*. Again, treatment with antimitotic should be done when the astrocytes reach about 80% confluence. In this case, the switch to a serum-free medium could be made by exchanging all of the medium at once, taking advantage of the greater robustness of astrocytes. However, it is important not to change the medium too soon (e.g., <2 days) before neurons are plated onto the astrocytes; the astrocytes need to be given time to "condition" the medium with trophic factors that aid neuron survival. The antimitotic should be left in place until after the neuronal suspension is added, to prevent mitosis of the newly added astrocytes.

(iii) *When the culture medium becomes acidic*. If the medium contains phenol red, acidity is apparent as a shift to a pale

yellow color, indicative of an accumulation of acidic waste products. This change is often seen in older, denser cultures. If this occurs, feeding should be done more frequently to minimize damage to the neurons.

Particularly in older cultures, it may help to add blockers of synaptic transmission to the culture medium to reduce excitotoxicity. For example, after 7–10 days *in vitro* we sometimes add kynurenic acid (1 mM final concentration in each well), CNQX or DNQX (10 μM) to inhibit non-NMDA ionotropic glutamate receptors, or D, L-APV (40 μM) to inhibit NMDA receptors. We find that cultures typically survive much better for longer periods (>3–4 weeks) in the presence of one of these blockers. However, it should be kept in mind that chronic blockade of excitatory synaptic transmission may affect synapse maturation (Murthy et al., 2001).

Alternative Plating Method

The "sandwich" culture is an elegant method for exposing neurons to astrocyte-conditioned medium without physical contact with the astrocytes (Brewer and Cotman, 1989; Goslin et al., 1998; Lu et al., 2016). Because the autaptic neurons are resting on coated glass rather than an astrocytic lawn, the quality of the optics is improved, which is beneficial for certain experiments. In this method, dissociated cells are plated in wells that do not contain coverslips but which have small plastic protuberances on the bottom, as described in the "Preparation of Plates" section. After 1–2 weeks a confluent mixed neuron-glia feeder culture is obtained. At this time another dissociation is done and the isolated cells are plated onto coverslips that had previously been agarose-coated and sprayed in large culture dishes (see "Preparation of Plates" section and Goslin et al., 1998). These large culture dishes are placed in the incubator for a few hours to allow the neurons to settle and attach, then each coverslip is taken out, inverted, and placed neuron side down in each well in the plate containing the feeder culture. The plastic protuberances hold the coverslip and adherent neurons just above the glia, allowing access to secreted growth factors without direct contact.

Troubleshooting

(1) *Agarose does not stick to the glass coverslips*. Make sure the coverslips have been thoroughly washed in concentrated acid and just as thoroughly rinsed in water. We have found that it helps to store the coverslips under 100% ethanol. If the ethanol contains too much water, the glass seems to be less easily wetted by agarose.

(2) *Problems with obtaining a suitable archipelago of microislands*. When using the spray technique, it is unnecessary to be too fussy about getting uniform spot sizes. It is normal to have a wide variety of sizes and shapes, provided that the spots are at least a few tens of microns apart and there is a reasonable number of spots (∼10–20 per coverslip) that are roughly 200 μm in diameter. The challenge is to find the optimum parameter settings for the sprayer being used. Parameters to vary include airflow, spray burst duration, distance of sprayer from the coverslips, and size of the spray nozzle. For example, with our glass microatomizer (Kimble-Chase; see **Table 4**) we use airflow (from a reticulated air supply) at 3–4 L min^{-1}, burst duration 0.5–1 s and spray distance ∼10–15 cm.

(3) *Poor yield of cells following tissue dissociation*. The dissociation is the critical step for obtaining good autaptic cultures and, indeed, any dissociated cultures. Three factors seem key to achieving a good yield of healthy neurons, these being in the order of decreasing importance: (i) the age of the animal; (ii) the care in trituration; and (iii) the choice of dissociation enzyme. In general, the younger the animal the better the yield of neurons and, hence, the better the quality of the culture. Even a single day can make a difference: in our experience, P0 pups provide better neurons than P1 or P2 animals. For the best neuronal yield, embryos (e.g., E16–18) can be used, but this comes at the cost of more challenging surgery and the loss of the mother (Fath et al., 2009). Trituration is another important factor and requires you to be slow, gentle and patient. Each stroke of the trituration should, for example, take several seconds. The supernatant containing the cell suspension should be collected after every 3–4 strokes to avoid exposing isolated cells to unnecessary additional trauma. The tip of the Pasteur pipette used for trituration should be carefully fire-polished in the flame of a gas burner. Some researchers recommend using two Pasteur pipettes with wider and narrower polished openings; the narrower tip is used later in the trituration process (Fath et al., 2009). Finally, the type and activity of the enzyme are important. We find that papain is best for P0–1 rat tissue, but the suitability of alternative enzymes for other tissues (e.g., trypsin; Allen, 2006; Fath et al., 2009) needs to be determined empirically. Be aware also that the assayed activity of an enzyme can decline with time in storage.

(4) *Excessive neuronal death a few days after plating*. As noted in the "Feeding" section some loss of neurons is normal within a day or two of plating, particularly if not plating on astrocytes. It is important to remove the debris by feeding the day after plating because the debris seems to have an inhibitory effect on the survival of the remaining cells. Subsequent excessive neuronal death could be due to a multitude of factors that can be time-consuming to track down. For convenience, it is best to troubleshoot these factors using mass cultures rather than microdots. Three key factors to explore are: (i) the substrate; (ii) the astrocyte feeder layer; and (iii) the culture medium (Goslin et al., 1998). Substrate problems might include the properties or cleanliness of the glass coverslips, or the freshness of the permissive coating solution. These can be tested by plating directly on the coated or uncoated bottom of plastic culture dishes, which are generally optimized for good cell survival. If the neurons survive better on plastic, test the coating solution on different coverslips. Anecdotally, problems have been traced back to the type of glass used in different brands of coverslips, although this is less likely to be an issue for autaptic cultures where the glass is covered with agarose.

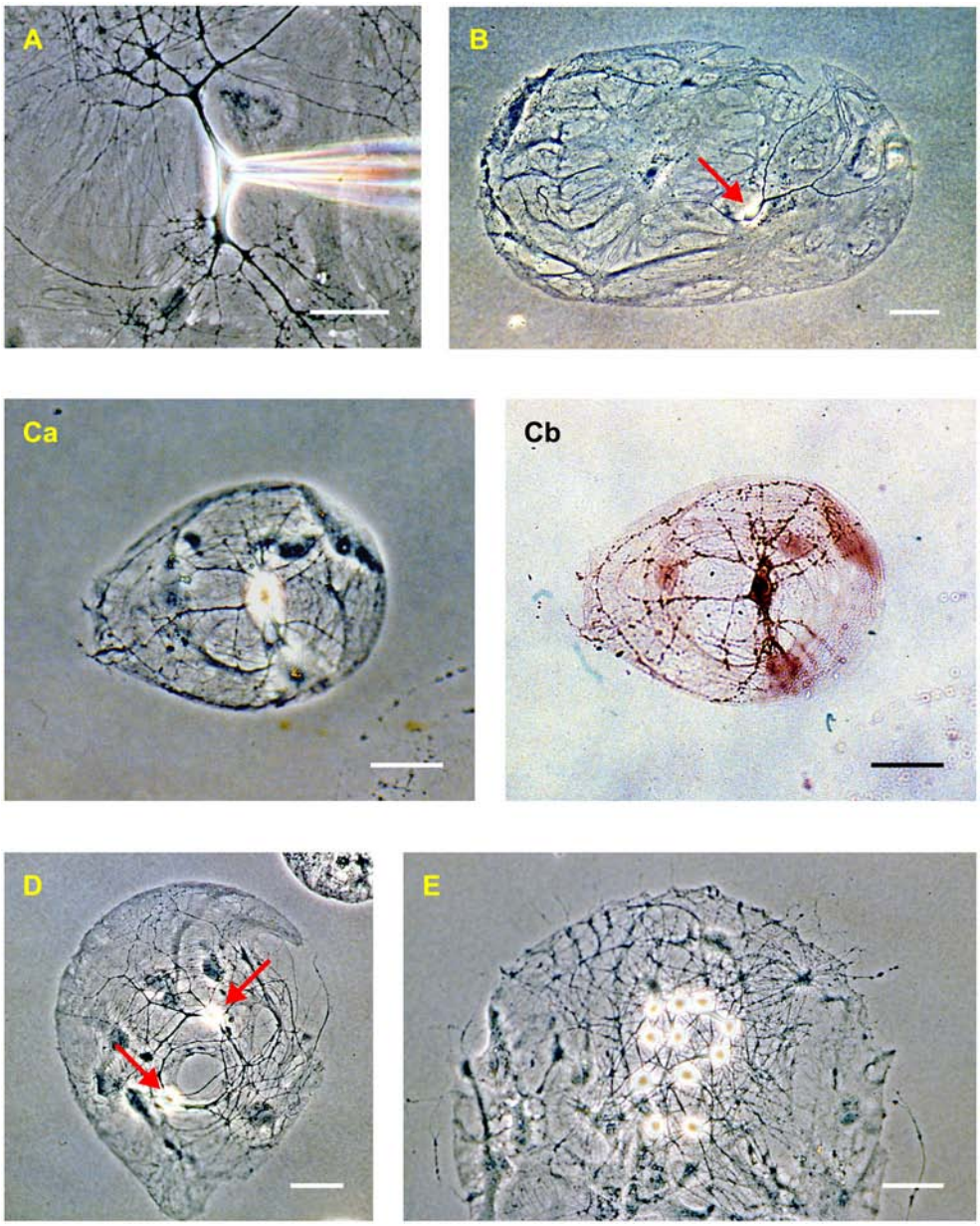

FIGURE 2 | Rat hippocampal neurons in dissociated culture (2–3 weeks *in vitro*). **(A)** Phase-contrast image of an isolated neuron in a mass culture showing the phase-bright soma, thick tapering dendrites, and thin untapered axons. Confluent astrocytes are visible beneath the neuron. A patch electrode, entering from the right, is positioned on the soma. **(B)** "Microdot" or "microisland" of astrocytes occupied by a single neuron (red arrow). This is a comparatively large island. **(C)** A microisland of more typical size, occupied by a single neuron imaged using phase contrast **(Ca)** and bright-field **(Cb)** microscopy after processing with a synapsin antibody to reveal autapses (dark spots on the processes in **Cb**). **(D)** Example of a microisland occupied by two neurons (red arrows). **(E)** Example of a microisland with multiple neurons. The scale bar in all panels is 50 μm.

If the neurons still die on plastic, they may require an astrocyte feeder layer, particularly if using mouse tissue or tissue from older (e.g., >P5) animals. Ideally, the astrocyte feeder layer should form a homogeneous extent of flat cells without too many gaps or overgrowth (e.g., **Figure 2A**). This is normally achieved by treating with an antimitotic agent (e.g., araC) as they approach confluence. The astrocyte cultures should also not be too old. We find that <3–4 weeks is preferred. Finally, the culture medium is probably the most important determinant of healthy cultures. Commercially available formulations are constantly evolving and some experimentation may be required to find the optimum for your application. Generally speaking, the serum-containing medium is better for growing astrocytes but it may be

compromised by unpredictable variability between different lots of serum. Serum-free medium has the advantage of greater consistency but not all cell types may thrive in the absence of serum. Whatever the choice of medium, a universal precaution is that it should be fresh, sterile and adjusted to the correct pH and osmolarity.

ELECTROPHYSIOLOGICAL RECORDINGS FROM AUTAPSES

In this section, I will give tips for performing the most basic kind of electrophysiology experiment with autaptic cultures, i.e., a whole-cell patch-clamp recording of autaptic current from a single, isolated neuron under physiological conditions. These techniques are readily extended to more elaborate experiments of the kind that are summarized in later sections.

Choosing a Neuron

Broadly speaking, cultures can be used for electrophysiology experiments after ∼7 days *in vitro* (DIV), although autaptic currents are expected to be small at that stage (Gomperts et al., 2000). Longer time in culture typically leads to a greater number of autaptic connections and larger currents per neuron (Gomperts et al., 2000), but there is also a progressive loss of neurons with culture age. We find that ∼14–21 DIV is a good compromise for measuring large autaptic currents from healthy rodent neurons.

It is common to perform autaptic culture experiments in a HEPES-buffered bath solution at room temperature without bubbling or perfusion (e.g., Bekkers, 2005). Other standard bath solutions could also be used, for example, a perfused, carbogen-bubbled, bicarbonate-buffered bath solution warmed to physiological temperature, as in slice experiments (e.g., Ikeda et al., 2018). A phase-contrast microscope provides the best optics for observing neurites in culture (**Figure 2**). This may be important if one wishes to ensure, for example, that axons are not crossing the space between microislands. However, other types of contrast enhancement, such as differential interference contrast (DIC) or Hoffman modulation contrast, are acceptable for most studies with autaptic cultures.

After placing a whole coverslip in the chamber, the entire coverslip should be scanned at low magnification (e.g., 10× objective) to find potential microislands occupied by a single neuron. The shapes and sizes of these islands can be very diverse (**Figure 2**). In many cases it is unambiguous that a single neuron is present; in other cases, the identification is less clear. For example, glial overgrowth may obscure the view, or the soma of a glial cell (e.g., an oligodendrocyte) might be mistaken for that of a neuron. At other times the putative single neuron may occupy a very small island and it can be difficult to know if another neuron is hidden underneath the first. In these cases, the electrophysiology must be called upon to provide a definitive answer (see next section).

Identification of the type of neuron (e.g., glutamatergic, GABAergic, subtypes of these) can be inconclusive if simply based upon morphology. Dendritic morphology is often altered in culture, and in any case, the confinement of a neuron to a small island can make its dendrites hard to see. The best strategy is to prepare cultures from transgenic tissue in which the neurons of interest are fluorescently labeled (e.g., Ikeda et al., 2008).

During this initial scan, it is important to establish the health of the culture. The underlying layer of astrocytes should uniformly cover the islands of the permissive substrate, and the larger islands on the plate should be occupied by significant numbers of healthy-looking neurons (e.g., **Figure 2E**). There should be no sign of detachment of the astrocytes from the substrate, or of the agarose coating (which looks like a thin, transparent membrane) from the glass. If the culture contains clumps of many neuronal somata, perhaps extending thick fascicles of neurites between the clumps, then the plating density was too high. If there are healthy astrocytes but few neurons, then the plating density may have been too low.

Incidentally, cultures sometimes contain cells with vigorously waving cilia. These are ependymal cells from the meninges. They do not seem to interfere with experiments.

Whole-Cell Patch-Clamp

Standard patch-clamp techniques can be used with autaptic cultures, with a few precautions that are discussed below. After obtaining a stable whole-cell recording from the soma of an isolated neuron, the cell is voltage-clamped at a hyperpolarized holding potential (e.g., −60 mV) and a 1 ms-long depolarizing voltage-clamp step to 0 mV is applied (**Figure 3A**; this shows a hyperpolarizing test pulse followed by two depolarizing steps in succession). Each depolarizing step produces, in sequence, an outward capacitance transient (labeled *1* in **Figure 3B**), an inward "action current" (unclamped action potential; *2* in **Figure 3B**) and an inward capacitance transient (*3* in **Figure 3B**). The action current escapes into the axon as a propagating action potential and, if autapses are present, a voltage-clamped autaptic current appears after a delay (*4* in **Figure 3B**). In this example the neuron is glutamatergic and a fast inward excitatory autaptic current is observed. This autaptic current is selectively blocked by an inhibitor of AMPA receptors (**Figure 3B**, cyan trace). A similar experiment with an isolated GABAergic neuron shows an inhibitory autaptic current with slower kinetics, as expected for a current mediated by $GABA_A$ receptors (**Figure 3C**; in this example the pipette solution contained high Cl^-).

Experiments can also be performed in current-clamp mode, in which case autaptic potentials would be recorded (Bekkers and Stevens, 1991). However, voltage-clamp recordings are generally more convenient because the repeated firing of self-exciting neurons can generally be more effectively controlled; thus, most investigators use voltage clamp.

This basic autapse experiment illustrates some precautions to keep in mind when measuring autaptic currents. First, the internal solution should allow the neuron to fire brief action potentials, i.e., it should typically be a high-K^+ solution to enable rapid spike repolarization. This is necessary to ensure the presynaptic action potential and the postsynaptic autaptic response are temporally dissociated, given that both are recorded in the same electrode (**Figure 3**). An internal solution that blocks K^+ channels, such as a high-Cs^+ solution of the kind commonly

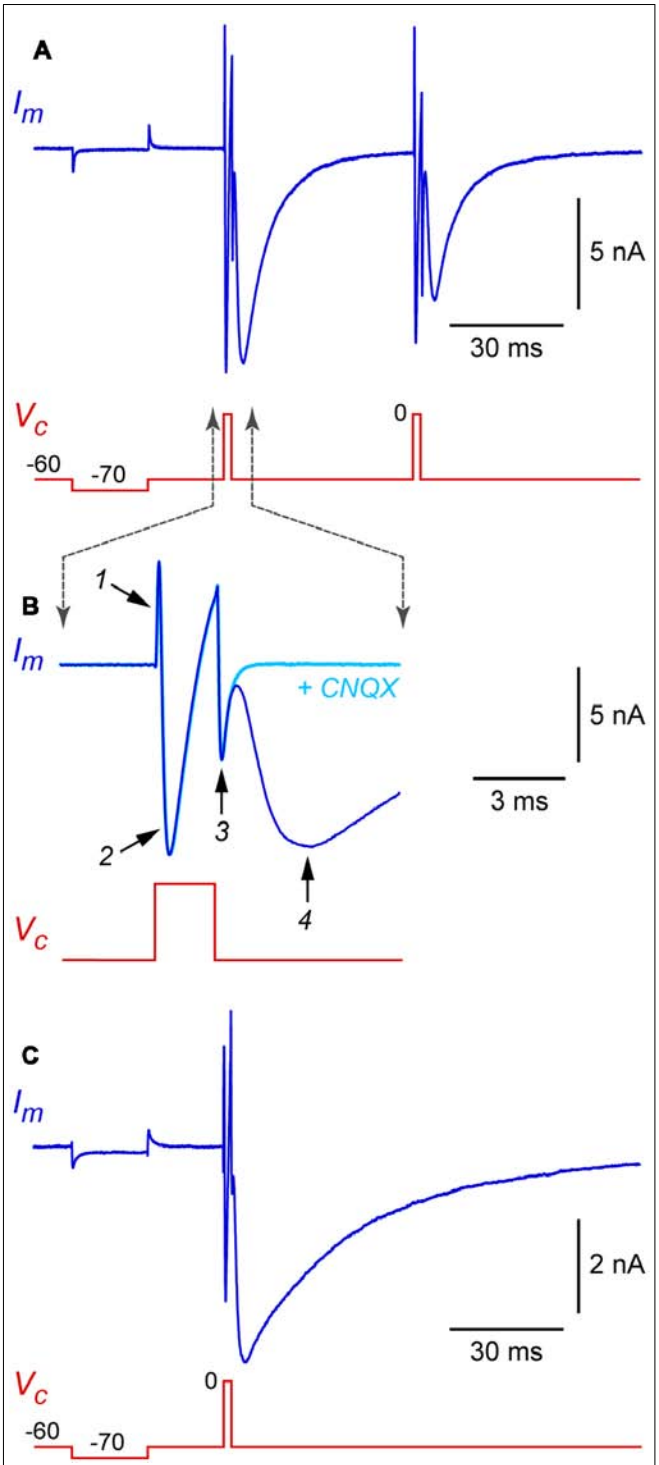

FIGURE 3 | Example autaptic postsynaptic currents recorded from isolated rat hippocampal neurons. **(A)** Membrane current (I_m, blue trace) recorded in response to a voltage clamp command (V_c, red trace) in an isolated glutamatergic neuron. In this example, two depolarizing stimuli (each a 2 ms-long step from −60 mV holding potential to 0 mV) were applied at a 50 ms interval. A hyperpolarizing test pulse (20 ms-long step from −60 to −70 mV) preceded the depolarizing stimuli. **(B)** Same data shown on an expanded time scale to illustrate the phases of the I_m response. Also shown (*Continued*)

FIGURE 3 | Continued
(cyan trace) is I_m from the same cell immediately after switching to a flow pipe containing 20 μM CNQX (6-cyano-7-nitroquinoxaline-2,3-dione) to block the excitatory postsynaptic current (EPSC). Labeled traces are (*1*) "on" capacitance transient, (*2*) action current (I_{Na} and I_K), (*3*) "off" capacitance transient, and (*4*) autaptic EPSC. **(C)** Similar recording from an isolated GABAergic interneuron, showing an autaptic inhibitory postsynaptic current (autaptic IPSC) in response to a single stimulus. Same time scale as in panel **(A)**; note the slower kinetics. In this experiment the pipette solution contained high Cl^-, giving an inward current at −60 mV holding potential. Experiments in this figure were done at room temperature without series resistance compensation.

chosen to improve voltage clamp at depolarized potentials, should not be used.

A second precaution is that care must be taken to minimize voltage clamp errors. Autaptic currents can be large (up to 10 nA) and voltage escape could lead to uncontrolled action potentials and a reverberating feedback response in the neuron (Segal and Furshpan, 1990; Segal, 1991). Lower-resistance patch electrodes should generally be selected (e.g., <3–4 MΩ) to facilitate the achievement of low (<10–15 MΩ) electrode series resistance (R_s). In addition to improving voltage control, low R_s enables fast whole-cell capacitance transients (labeled *1* and *3* in **Figure 3B**) which are less likely to merge with and obscure the closely following autaptic current. If merging does occur and is a concern, a workaround is to pharmacologically isolate the transients and action current by briefly superfusing a blocker of postsynaptic receptors (e.g., CNQX for glutamatergic autapses; **Figure 3B**, cyan trace), then digitally subtracting the blocked trace from the unblocked trace. This procedure should yield the pure autaptic current with minimal contamination from transients. In any case, electronic series resistance compensation should generally be used when measuring autaptic currents to minimize voltage clamp errors (Williams, 2004). Some investigators further reduce voltage clamp errors by applying a low concentration of blocker of postsynaptic receptors to reduce the amplitude of the autaptic current (Otsu et al., 2004).

A related precaution is to ensure that R_s remains as stable as possible throughout the experiment. It is common for R_s to increase steadily over time, which destabilizes the R_s compensation and causes an apparent rundown in the amplitude of the autaptic current. We have found that this increase in R_s can be much reduced by using internal solutions with a higher osmolarity (e.g., 330 mOsm/kg *cf* 310 mOsm/kg for the external solution; Bekkers, 2005). Higher internal osmolarity causes the neuron to swell slightly, possibly reducing a tendency of intracellular organelles to block the electrode tip.

Finally, autaptic currents sometimes exhibit delayed peaks without a preceding action current. This is often a sign that there is more than one neuron on the microdot, giving rise to a polysynaptic circuit. For some kinds of experiments, the delayed polysynaptic currents may not be a concern, particularly if the early autaptic current dominates. Another strategy, if the second neuron is visible, is to destroy the first neuron using the patch electrode (e.g., by aspirating the soma) then lower a new electrode

to record from the second neuron. This strategy is only useful if the presence on the second neuron of remnant synapses from the first neuron is not a concern.

APPLICATIONS OF AUTAPTIC CULTURES

In this section, I will illustrate the utility of autaptic cultures by giving an overview of studies that have made use of them over the past three decades. I will organize my survey to highlight the unique technical advantages of autapses while paying less attention to the specific research questions being addressed. Most of the examples will be electrophysiology experiments using hippocampal and neocortical cultures, but some use autaptic cultures from other brain areas, including the thalamus (Moechars et al., 2006), basal forebrain (Allen, 2006), nucleus accumbens (Shi and Rayport, 1994), raphé nucleus (Johnson, 1994) and ventral tegmental area (Sulzer et al., 1998; Michel and Trudeau, 2000). First, I will make general comments about the advantages and disadvantages of autaptic cultures.

Advantages

Like any dissociated culture model, autaptic cultures provide the convenience of a simplified two-dimensional structure: easy access to individual cells for making electrical recordings, and excellent visibility for imaging experiments. Also, however, autaptic cultures offer unique advantages (**Figure 4**).

(1) *The convenience of recording an unambiguous monosynaptic connection with a single electrode* (**Figure 4A**). Because of the ease of recording, autaptic cultures provide a simple assay system for studying factors that determine synaptic strength.
(2) *The ability to study a single axon and all its synaptic connections* (**Figure 4A**). A single axon means that the properties of a defined population of synaptic boutons can be studied, with no ambiguity about the origin of evoked or spontaneous synaptic events.
(3) *Access to a homogeneous population of modified synapses* (**Figure 4A**). Genetic modification of an isolated neuron ensures that all inputs onto the neuron are modified identically, providing an ideal testbed for structure-function studies.
(4) *Complete control over the extracellular environment of a neuron and all its synapses* (**Figure 4B**). Because all of their processes are restricted to a small area, autaptic cultures allow the rapid, homogeneous application of solutions or optical stimuli to an entire neuron, facilitating useful assays.
(5) *The ability to define the neighborhood of a neuron and study intercellular interactions* (**Figures 4C,D**). By selecting microislands occupied by different types or numbers of neurons or glia, interactions between these cell types can be explored in a simple system.

Examples of studies that explicitly draw upon these advantages are given in later sections.

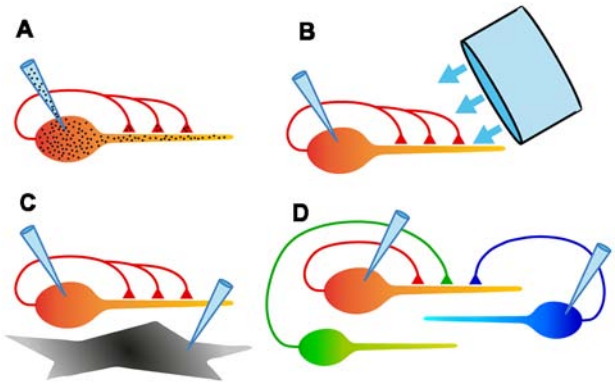

FIGURE 4 | Schematic diagrams summarizing some of the experimental configurations possible with autaptic cultures. **(A)** Electrical recording from assured monosynaptic connections in a homogeneous set of autapses using a single electrode, and control of both pre- and postsynaptic intracellular solutions using a single electrode. **(B)** Ability to rapidly and uniformly apply extracellular solutions or light stimulation to all autaptic connections received by that neuron. **(C)** Study of signaling between a neuron and an underlying astrocyte, using two recording electrodes. **(D)** Study of competition between two or more neurons confined to a microisland. This also allows simultaneous comparison of synaptic and autaptic responses in the same neuron.

Disadvantages

Autaptic cultures are susceptible to disadvantages that apply to culture models in general. For instance, cultured neurons commonly lose the dendritic and axonal morphologies that characterize their appearance *in vivo*. Their intrinsic functional properties might also be modified, and this must be checked or stated as a proviso (see next section). In addition to these general concerns about cultures, however, autaptic cultures have some specific disadvantages. Because the same neuron provides both the presynaptic and postsynaptic compartment, it may be impossible to separate processes that occur both pre- and postsynaptically. For example, Ca^{2+} signals that originate from the presynaptic action potential and the postsynaptic response may be entangled because of dendritic backpropagation (Otsu and Murphy, 2004). It is also difficult to depolarize the postsynaptic membrane without affecting presynaptic excitability (Bekkers and Stevens, 1991). When performing whole-cell patch-clamp experiments, one must be aware of the possibility of "washout" of key intracellular components, which might be a greater concern for autaptic cultures because both pre- and postsynaptic components could be vulnerable. That said, stable autaptic responses can generally be obtained, provided the electrode series resistance and other recording conditions are carefully controled (see "Whole-Cell Patch-Clamp" section). Lastly, the setting up of autaptic cultures is more fickle and labor intensive than that of conventional cell cultures, chiefly because more elaborate substrate preparation is required.

Comparison of Autapses With Synapses in Other Model Systems

As a prelude to discussing the applications of autaptic cultures, I will briefly comment on comparisons between the electrical properties of autapses and synapses in two other widely-used model systems, mass cultures, and acute brain slices.

Comparison With Interneuronal Synapses in Mass Cultures

The basic biophysical features of autapses and synapses in mass cultures are reported to be the same (Bekkers and Stevens, 1991) or similar (Shi and Rayport, 1994; Mennerick et al., 1995; Liu et al., 2009, 2013). Autaptic EPSCs have somewhat larger amplitudes and readily-releasable vesicle pool sizes than their mass-culture counterparts (Mennerick et al., 1995; Liu et al., 2013), and differences in short-term plasticity have also been reported (Liu et al., 2013). Overall, however, autapses and interneuronal synapses in culture appear to function similarly.

Comparison With Synapses in Acute Slices

Dissociated cultures—including autaptic cultures—are less able to preserve the synaptic "microenvironment" than are more intact preparations, like acute slices, and this raises questions about the wider applicability of findings made in the culture setting. Nevertheless, many experimental findings made with autapses have translated well to the intact brain. For example, detailed molecular studies of the synaptic vesicle cycle at autapses (see "A Homogeneous Population of Modified Synapses" section) have been confirmed more generally (Chamberland and Tóth, 2016; Dittman and Ryan, 2019). Certain types of synaptic plasticity that have been studied in slices are also faithfully replicated in autaptic cultures. For instance, depolarization-induced suppression of excitation (DSE; Straiker and Mackie, 2009) and inhibition (DSI; Straiker and Mackie, 2005; Kellogg et al., 2009) are present at autapses, as is long-term depression (LTD; Goda and Stevens, 1996; Tong et al., 1996; Kumura et al., 2000). Cultured dentate granule cells form autapses that resemble mossy fiber inputs to CA3 pyramidal cells, including expression of a presynaptic form of long-term potentiation (Rost et al., 2010). On the other hand, studies have also highlighted the potential risks of using cultures. For example, reports on the co-release of neurotransmitters (Hnasko and Edwards, 2012) and the efficacy of neuromodulators (Bekkers et al., 1996) show that the exact experimental conditions in culture can have an impact on the findings. All of this reinforces the point that, as for any model system, effective use of autaptic cultures must balance convenience and caution.

I will now turn to a survey of applications of autaptic cultures, organized under the five major advantages listed above in the "Advantages" section.

Examples of Applications

The Convenience of a Single Electrode

By providing access to large, monosynaptic currents that can be stably measured with a single electrode, autaptic cultures have been used in many key experiments on the biophysics of synaptic transmission. Early examples include studies of multivesicular release at glutamatergic synapses (Tong and Jahr, 1994b), how transporters shape neurotransmission (Tong and Jahr, 1994a; Diamond and Jahr, 1997), and how the kinetics of EPSCs are determined by asynchronous vesicle release and temperature (Diamond and Jahr, 1995; Pyott and Rosenmund, 2002). The role of presynaptic Ca^{2+} in determining neurotransmission has also been examined using autapses (Reid et al., 1998; Lee et al., 2000; Ikeda et al., 2008).

A different application has been to use autaptic cultures to study neuromodulation, again taking advantage of their convenience as an assay system. Modulators that have been characterized with autapses include histamine (Bekkers, 1993), adrenoceptor agonists (Raman et al., 1996), calcineurin (Tong et al., 1995), somatostatin (Boehm and Betz, 1997), clozapine (Michel and Trudeau, 2000), cyclic AMP (Gekel and Neher, 2008), amyloid α protein (Ripoli et al., 2013) and GABA acting *via* $GABA_B$ receptors (Valente et al., 2016). Several reports have also used autaptic cultures to examine short-term synaptic plasticity and its modulation (Mennerick and Zorumski, 1995a; Brody and Yue, 2000; Straiker and Mackie, 2007; Straiker et al., 2018). Lastly, autapses have been used as a convenient testbed for developing new molecular tools for the study of synaptic function (e.g., pHoenix, Rost et al., 2015).

A Single Axon

An autaptic neuron in culture is innervated by a single afferent (from itself) and thus provides access to a uniquely homogeneous population of presynaptic terminals—reliably stimulated—that can be used for the study of neurotransmitter release (Otsu and Murphy, 2004). For example, autaptic cultures have been utilized to measure the nonuniform probability of glutamate release from different boutons on the same axon (Rosenmund et al., 1993), the variable distribution of presynaptic Ca channel subtypes on a single afferent (Reid et al., 1997), and the differential invasion of glutamate-releasing terminals by action potentials (Prakriya and Mennerick, 2000). Autapses are also convenient for studying the synaptic vesicle cycle, for example, by using pharmacological approaches to count the number of releasable vesicles (Ikeda and Bekkers, 2009) or optical methods based on the styryl dyes (e.g., FM1–43) to follow vesicles through the cycle (Murthy et al., 1997; Murthy and Stevens, 1998). Experiments that load "false" neurotransmitters into synaptic vesicles have also been used to probe vesicle dynamics at autapses (Pan et al., 1993; Bekkers, 2005).

Another kind of experiment that relies on having a single axon takes advantage of the fact that both evoked and spontaneous postsynaptic currents originate from the same population of autaptic terminals, removing the ambiguity that typifies other kinds of synaptic circuits. For example, autaptic cultures been used to identify presynaptically silent synapses that give spontaneous but not evoked transmitter release (Kimura et al., 1997), and postsynaptically silent synapses that express only NMDA receptors (Gomperts et al., 1998). Autapses also allow the unambiguous study of phasic and asynchronous release from the same population of boutons (Otsu et al., 2004; Chang and Mennerick, 2010).

Lastly, the presence of a single axon enables definitive experiments showing the co-release of neurotransmitters from one neuron. For instance, autaptic cultures have been used to demonstrate the co-release of glutamate and serotonin from raphé neurons (Johnson, 1994) and of glutamate

and dopamine from neurons in the ventral tegmental area (Sulzer et al., 1998).

A Homogeneous Population of Modified Synapses

Perhaps the most widely used application of autaptic cultures has been in structure-function studies, which take advantage of the ability to genetically modify a single isolated neuron and to examine the consequences of that modification for synaptic transmission, secure in the knowledge that all autapses received by that neuron are identically modified. The use of this culture system also enables the study of mutations that are postnatal lethal.

Genetically-modified autaptic cultures have been used to answer fundamental questions about the SNARE proteins, including SNAP-25 and SNAP-23 (Delgado-Martínez et al., 2007; Weber et al., 2014), syntaxin-1 (Gerber et al., 2008) and synaptobrevin-1 (Young, 2005; Zimmermann et al., 2014). Key experiments on the presynaptic Ca^{2+} sensor, synaptotagmin, have also been performed using autapses. For example, mutational analyses of synaptotagmin-1 (Fernández-Chacón et al., 2001; Stevens and Sullivan, 2003; Han et al., 2004; Nishiki and Augustine, 2004; Schupp et al., 2016; Chang et al., 2018) and synaptotagmin-4 (Ting et al., 2006) have elaborated details of the Ca^{2+} binding and synaptic vesicle fusion processes. The roles of many other presynaptic auxiliary proteins have been explored at autapses, including Munc13 (Augustin et al., 1999; Rosenmund et al., 2002; Varoqueaux et al., 2002; Junge et al., 2004; Basu et al., 2007), Munc18 (Meijer et al., 2015), synapsin (Gitler et al., 2004, 2008; Baldelli et al., 2007), bassoon (Altrock et al., 2003), synaptic vesicle protein 2 (Custer et al., 2006), RIM1α (Calakos et al., 2004), snapin (Thakur et al., 2004) and Rab3 (Schlüter et al., 2004). A number of these experiments took advantage of another convenient feature of autaptic cultures—the ability to completely superfuse a single neuron—to look for changes in the size of the readily-releasable pool (RRP) of synaptic vesicles. This feature will be further discussed in the next section.

Other researchers have used autapses and molecular genetic approaches to study the involvement of vesicular glutamate transporters in synaptic transmission (Fremeau et al., 2004; Wojcik et al., 2004; Zimmermann et al., 2015), as well as the properties of presynaptic voltage-gated Ca^{2+} channels (Few et al., 2012; Nanou et al., 2016). Lastly, a variety of disease models have been explored using this strategy. For example, genetic models of Alzheimer's disease (Pratt et al., 2011), autism (Weston et al., 2014) and epilepsy (Heeroma et al., 2009) have been implemented and studied in autaptic cultures.

Control Over the Extracellular Environment

The ability to uniformly perfuse extracellular solution over an isolated autaptic neuron brings obvious advantages in pharmacological experiments, like the neuromodulation studies mentioned earlier ("The Convenience of a Single Electrode" section). However, uniform perfusion also enables other kinds of experiments that are difficult or impossible to achieve using other systems. Two main types of such experiments have been performed: measurements of synaptic vesicle pools using the application of hypertonic sucrose solution, and studies that disentangle subsynaptic (strictly, "sub-autaptic") and extrasynaptic receptors by exploiting the unique configuration of autaptic cultures.

Sucrose experiments depend on the classical finding that hypertonic solution causes the direct release of synaptic vesicles without electrical stimulation (Fatt and Katz, 1952). By applying pulses of sucrose solution to the entire dendritic arbor of an isolated neuron on a small island, all presynaptic vesicle pools can be identically stimulated with a hypertonic challenge and the resulting postsynaptic electrical response can be recorded at the soma. Critically, spontaneous or electrically-evoked release from those same pools can also be recorded, allowing a comparison between the postsynaptic responses to the different release mechanisms. For example, by measuring the total charge carried by the (multi-vesicle) sucrose-evoked response, then dividing this by the mean charge of the (single-vesicle) spontaneous "miniature" synaptic response measured in the same neuron, one can estimate the total size of the RRP of synaptic vesicles across all release sites on that neuron (Rosenmund and Stevens, 1996; Stevens and Williams, 2007).

This method has been widely used to measure changes in the RRP size following genetic mutations, as mentioned in the previous section ("A Homogeneous Population of Modified Synapses"). The approach has also been used to study changes in RRP size following different kinds of plasticity, for example, long-term depression (Goda and Stevens, 1998), short-term depression (Stevens and Wesseling, 1998, 1999b) and augmentation (Stevens and Wesseling, 1999a; Garcia-Perez and Wesseling, 2008), as well as other factors that alter the RRP size at autapses (Stevens and Sullivan, 1998; Moulder et al., 2004; Moulder and Mennerick, 2005).

The second main type of experiment that exploits the ease of autapse superfusion is a method for distinguishing subsynaptic and extrasynaptic NMDA receptors. This experiment depends on the fact that electrical stimulation (e.g., *via* a whole-cell electrode at the soma) selectively activates subsynaptic NMDA receptors, whereas superfusing the entire neuron with glutamate activates both sub- and extrasynaptic NMDA receptors. Hence, by comparing these two responses one can infer the distinct properties of both pools of NMDA receptors (Tovar and Westbrook, 1999). In an elegant variation on this experiment, subsynaptic NMDA receptors are "tagged" by blocking them with an activity-dependent antagonist (MK-801) while electrically stimulating at the soma; the subsequent response to whole-cell application of glutamate must then be entirely due to unblocked extrasynaptic NMDA receptors (Tovar and Westbrook, 2002).

This approach has been used in several interesting studies. For example, the mobility and turnover of the different pools of NMDA receptors have been measured (Li et al., 2002; Tovar and Westbrook, 2002), as well as their subunit composition (Tovar and Westbrook, 1999; Thomas et al., 2006), pharmacology (Xia et al., 2010; Vyklicky et al., 2016) and desensitization properties (Li et al., 2003).

Lastly, the compact dendritic arbor of autaptic cultures facilitates the use of optical techniques for the study of synaptic function. For example, autaptic cultures permit the uniform

elevation of intracellular Ca^{2+} in calcium uncaging experiments (Burgalossi et al., 2012). However, optogenetic techniques have not been used with autaptic cultures and provide an opportunity for interesting experiments in the future.

A Defined Neighborhood

The applications described so far have highlighted the isolation of autaptic neurons, but this final application takes advantage of microislands as a useful model for studying intercellular interactions in the local neighborhood. These experiments fall into two broad classes: signaling between an autaptic neuron and the underlying glial cells, and competition between neurons on microislands occupied by two or more neurons.

Neuron/glia signaling has been studied by making dual whole-cell recordings from an isolated autaptic neuron and an underlying glial cell (Mennerick and Zorumski, 1994, 1995a; Mennerick et al., 1996). These experiments have shown, for example, how transporters in the glia modulate the timecourse of the autaptic EPSC in the neuron (Mennerick and Zorumski, 1995b; Mennerick et al., 1999), and how autaptic neurons grown without glial contact exhibit more asynchronous neurotransmitter release (Sobieski et al., 2015). Culturing without contact with glia has also been shown to reduce the number of autapses that form (Ullian et al., 2001).

For studying interactions between neurons, microislands with two or more neurons are selected (**Figure 4D**). Early work used microislands with small numbers of neurons to study epileptiform activity, which tends to be very strong when neurons are spatially constrained in this way (Segal and Furshpan, 1990; Segal, 1991, 1994). More recent work, however, has tended to focus on two-neuron microislands for "mix and match" experiments. For example, it has been shown that chronically silencing one of a pair of isolated excitatory neurons leads to characteristic changes in the postsynaptic AMPA receptor subunit composition in each neuron (Harms et al., 2005). Other work has explored the competition between glutamatergic and GABAergic neurons when grown as mixed or homotypic pairs (Rao et al., 2000; Chang et al., 2014; Wierda and Sørensen, 2014), or between wildtype and mutant neurons that lack presynaptic proteins involved in transmitter release (Tarsa and Goda, 2002; García-Pérez et al., 2015). Finally, two-cell microislands with different combinations of striatal, cortical and thalamic neurons have been used to examine the effect of glutamatergic input on refining striatal output (Paraskevopoulou et al., 2019).

CONCLUSION

Autaptic cultures provide the ultimate in synaptic simplicity: a one-neuron circuit. Despite a current tendency to study complex and preferably *in vivo* neural networks, autaptic cultures still have an important place in the toolbox of cellular neuroscientists because they enable straightforward, elegant experiments that address fundamental questions about synaptic transmission. The examples of applications given in this review provide a taste of the diversity of experiments that are possible with autaptic cultures, and will hopefully inspire novel applications, perhaps involving new-generation optical technologies. Of course, like all model systems, autaptic cultures have advantages and disadvantages, and these must be carefully weighed up when deciding whether autapses are the right tool for the job. It is hoped that this review has provided enough information to make that decision easier, and will assist in the implementation of autaptic culture experiments with the minimum pain and maximum prospect of success.

DATA AVAILABILITY STATEMENT

The datasets generated for this study are available on request to the corresponding author.

AUTHOR CONTRIBUTIONS

JB wrote the manuscript and prepared the figures.

FUNDING

This work was supported by Project Grant 1128320 from the National Health and Medical Research Council of Australia and Discovery Project Grant DP 180101034 from the Australian Research Council.

ACKNOWLEDGMENTS

I thank Jane Sullivan for comments on the manuscript. I also thank the reviewers for helpful suggestions.

REFERENCES

Allen, T. G. (2006). Preparation and maintenance of single-cell micro-island cultures of basal forebrain neurons. *Nat. Protoc.* 1, 2543–2550. doi: 10.1038/nprot.2006.394

Altrock, W. D., tom Dieck, S., Sokolov, M., Meyer, A. C., Sigler, A., Brakebusch, C., et al. (2003). Functional inactivation of a fraction of excitatory synapses in mice deficient for the active zone protein bassoon. *Neuron* 37, 787–800. doi: 10.1016/s0896-6273(03)00088-6

Augustin, I., Rosenmund, C., Südhof, T. C., and Brose, N. (1999). Munc13–1 is essential for fusion competence of glutamatergic synaptic vesicles. *Nature* 400, 457–461. doi: 10.1038/22768

Bacci, A., and Huguenard, J. R. (2006). Enhancement of spike-timing precision by autaptic transmission in neocortical inhibitory interneurons. *Neuron* 49, 119–130. doi: 10.1016/j.neuron.2005.12.014

Baldelli, P., Fassio, A., Valtorta, F., and Benfenati, F. (2007). Lack of synapsin I reduces the readily releasable pool of synaptic vesicles at central inhibitory synapses. *J. Neurosci.* 27, 13520–13531. doi: 10.1523/JNEUROSCI.3151-07.2007

Basu, J., Betz, A., Brose, N., and Rosenmund, C. (2007). Munc13–1 C1 domain activation lowers the energy barrier for synaptic vesicle fusion. *J. Neurosci.* 27, 1200–1210. doi: 10.1523/JNEUROSCI.4908-06.2007

Bekkers, J. M. (1993). Enhancement by histamine of NMDA-mediated synaptic transmission in the hippocampus. *Science* 261, 104–106. doi: 10.1126/science.8391168

Bekkers, J. M. (1998). Are autapses prodigal synapses? *Curr. Biol.* 8, R52–R55. doi: 10.1016/s0960-9822(98)70033-8

Bekkers, J. M. (2003). Synaptic transmission: functional autapses in the cortex. *Curr. Biol.* 13, R433–R435. doi: 10.1016/s0960-9822(03)00363-4

Bekkers, J. M. (2005). Presynaptically silent GABA synapses in hippocampus. *J. Neurosci.* 25, 4031–4039. doi: 10.1523/JNEUROSCI.4969-04.2005

Bekkers, J. M. (2009). Synaptic transmission: excitatory autapses find a function? *Curr. Biol.* 19, R296–R298. doi: 10.1016/j.cub.2009.02.010

Bekkers, J. M., and Stevens, C. F. (1991). Excitatory and inhibitory autaptic currents in isolated hippocampal neurons maintained in cell culture. *Proc. Natl. Acad. Sci. U S A* 88, 7834–7838. doi: 10.1073/pnas.88.17.7834

Bekkers, J. M., Vidovic, M., and Ymer, S. (1996). Differential effects of histamine on the N-methyl-D-aspartate channel in hippocampal slices and cultures. *Neuroscience* 72, 669–677. doi: 10.1016/0306-4522(95)00586-2

Boehm, S., and Betz, H. (1997). Somatostatin inhibits excitatory transmission at rat hippocampal synapses *via* presynaptic receptors. *J. Neurosci.* 17, 4066–4075. doi: 10.1523/JNEUROSCI.17-11-04066.1997

Brewer, G. J. (1997). Isolation and culture of adult rat hippocampal neurons. *J. Neurosci. Methods* 71, 143–155. doi: 10.1016/s0165-0270(96)00136-7

Brewer, G. J., and Cotman, C. W. (1989). Survival and growth of hippocampal neurons in defined medium at low density: advantages of a sandwich culture technique or low oxygen. *Brain Res.* 494, 65–74. doi: 10.1016/0006-8993(89)90144-3

Brody, D. L., and Yue, D. T. (2000). Relief of G-protein inhibition of calcium channels and short-term synaptic facilitation in cultured hippocampal neurons. *J. Neurosci.* 20, 889–898. doi: 10.1523/JNEUROSCI.20-03-00889.2000

Brown, L. D., Kim, K.-M., Nakajima, Y., and Nakajima, S. (1993). The role of G protein in muscarinic depolarization near resting potential in cultured hippocampal neurons. *Brain Res.* 612, 200–209. doi: 10.1016/0006-8993(93)91661-b

Burgalossi, A., Jung, S., Man, K. N., Nair, R., Jockusch, W. J., Wojcik, S. M., et al. (2012). Analysis of neurotransmitter release mechanisms by photolysis of caged Ca^{2+} in an autaptic neuron culture system. *Nat. Protoc.* 7, 1351–1365. doi: 10.1038/nprot.2012.074

Calakos, N., Schoch, S., Sudhof, T. C., and Malenka, R. C. (2004). Multiple roles for the active zone protein RIM1$\propto$ in late stages of neurotransmitter release. *Neuron* 42, 889–896. doi: 10.1016/j.neuron.2004.05.014

Chamberland, S., and Tóth, K. (2016). Functionally heterogeneous synaptic vesicle pools support diverse synaptic signalling. *J. Physiol.* 594, 825–835. doi: 10.1113/jp270194

Chang, C. L., Trimbuch, T., Chao, H. T., Jordan, J. C., Herman, M. A., and Rosenmund, C. (2014). Investigation of synapse formation and function in a glutamatergic-GABAergic two-neuron microcircuit. *J. Neurosci.* 34, 855–868. doi: 10.1523/JNEUROSCI.0229-13.2014

Chang, C. Y., and Mennerick, S. (2010). Dynamic modulation of phasic and asynchronous glutamate release in hippocampal synapses. *J. Neurophysiol.* 103, 392–401. doi: 10.1152/jn.00683.2009

Chang, S., Trimbuch, T., and Rosenmund, C. (2018). Synaptotagmin-1 drives synchronous Ca^{2+}-triggered fusion by C_2B-domain-mediated synaptic-vesicle-membrane attachment. *Nat. Neurosci.* 21, 33–40. doi: 10.1038/s41593-017-0037-5

Cobb, S. R., Halasy, K., Vida, I., Nyiri, G., Tamás, G., Buhl, E. H., et al. (1997). Synaptic effects of identified interneurons innervating both interneurons and pyramidal cells in the rat hippocampus. *Neuroscience* 79, 629–648. doi: 10.1016/s0306-4522(97)00055-9

Connelly, W. M. (2014). Autaptic connections and synaptic depression constrain and promote γ oscillations. *PLoS One* 9:e89995. doi: 10.1371/journal.pone.0089995

Connelly, W. M., and Lees, G. (2010). Modulation and function of the autaptic connections of layer V fast spiking interneurons in the rat neocortex. *J. Physiol.* 588, 2047–2063. doi: 10.1113/jphysiol.2009.185199

Custer, K. L., Austin, N. S., Sullivan, J. M., and Bajjalieh, S. M. (2006). Synaptic vesicle protein 2 enhances release probability at quiescent synapses. *J. Neurosci.* 26, 1303–1313. doi: 10.1523/JNEUROSCI.2699-05.2006

Deleuze, C., Bhumbra, G. S., Pazienti, A., Lourenco, J., Mailhes, C., Aguirre, A., et al. (2019). Strong preference for autaptic self-connectivity of neocortical PV interneurons facilitates their tuning to γ-oscillations. *PLoS Biol.* 17:e3000419. doi: 10.1371/journal.pbio.3000419

Deleuze, C., Pazienti, A., and Bacci, A. (2014). Autaptic self-inhibition of cortical GABAergic neurons: synaptic narcissism or useful introspection? *Curr. Opin. Neurobiol.* 26, 64–71. doi: 10.1016/j.conb.2013.12.009

Delgado-Martínez, I., Nehring, R. B., and Sørensen, J. B. (2007). Differential abilities of SNAP-25 homologs to support neuronal function. *J. Neurosci.* 27, 9380–9391. doi: 10.1523/JNEUROSCI.5092-06.2007

Diamond, J. S., and Jahr, C. E. (1995). Asynchronous release of synaptic vesicles determines the time course of the AMPA receptor-mediated EPSC. *Neuron* 15, 1097–1107. doi: 10.1016/0896-6273(95)90098-5

Diamond, J. S., and Jahr, C. E. (1997). Transporters buffer synaptically released glutamate on a submillisecond time scale. *J. Neurosci.* 17, 4672–4687. doi: 10.1523/JNEUROSCI.17-12-04672.1997

Dittman, J. S., and Ryan, T. A. (2019). The control of release probability at nerve terminals. *Nat. Rev. Neurosci.* 20, 177–186. doi: 10.1038/s41583-018-0111-3

Douglas, R. J., and Martin, K. A. (2007). Mapping the matrix: the ways of neocortex. *Neuron* 56, 226–238. doi: 10.1016/j.neuron.2007.10.017

Fasano, C., Thibault, D., and Trudeau, L. E. (2008). Culture of postnatal mesencephalic dopamine neurons on an astrocyte monolayer. *Curr. Protoc. Neurosci.* Chapter 3:Unit 3.21. doi: 10.1002/0471142301.ns0321s44

Fath, T., Ke, Y. D., Gunning, P., Götz, J., and Ittner, L. M. (2009). Primary support cultures of hippocampal and substantia nigra neurons. *Nat. Protoc.* 4, 78–85. doi: 10.1038/nprot.2008.199

Fatt, P., and Katz, B. (1952). Spontaneous subthreshold activity at motor nerve endings. *J. Physiol.* 117, 109–128.

Fenske, P., Grauel, M. K., Brockmann, M. M., Dorrn, A. L., Trimbuch, T., and Rosenmund, C. (2019). Autaptic cultures of human induced neurons as a versatile platform for studying synaptic function and neuronal morphology. *Sci. Rep.* 9:4890. doi: 10.1038/s41598-019-41259-1

Fernández-Chacón, R., Königstorfer, A., Gerber, S. H., García, J., Matos, M. F., Stevens, C. F., et al. (2001). Synaptotagmin I functions as a calcium regulator of release probability. *Nature* 410, 41–49. doi: 10.1038/35065004

Few, A. P., Nanou, E., Watari, H., Sullivan, J. M., Scheuer, T., and Catterall, W. A. (2012). Asynchronous Ca^{2+} current conducted by voltage-gated Ca^{2+} (Ca_V)-2.1 and Ca_V2.2 channels and its implications for asynchronous neurotransmitter release. *Proc. Natl. Acad. Sci. U S A* 109, E452–E460. doi: 10.1073/pnas.1121103109

Fremeau, R. T. Jr., Kam, K., Qureshi, T., Johnson, J., Copenhagen, D. R., Storm-Mathisen, J., et al. (2004). Vesicular glutamate transporters 1 and 2 target to functionally distinct synaptic release sites. *Science* 304, 1815–1819. doi: 10.1126/science.1097468

Furshpan, E. J., Landis, S. C., Matsumoto, S. G., and Potter, D. D. (1986). Synaptic functions in rat sympathetic neurons in microcultures. I. Secretion of norepinephrine and acetylcholine. *J. Neurosci.* 6, 1061–1079. doi: 10.1523/JNEUROSCI.06-04-01061.1986

Furshpan, E. J., MacLeish, P. R., O'Lague, P. H., and Potter, D. D. (1976). Chemical transmission between rat sympathetic neurons and cardiac myocytes developing in microcultures: evidence for cholinergic, adrenergic, and dual-function neurons. *Proc. Natl. Acad. Sci. U S A* 73, 4225–4229. doi: 10.1073/pnas.73.11.4225

García-Pérez, E., Mahfooz, K., Covita, J., Zandueta, A., and Wesseling, J. F. (2015). Levetiracetam accelerates the onset of supply rate depression in synaptic vesicle trafficking. *Epilepsia* 56, 535–545. doi: 10.1111/epi.12930

Garcia-Perez, E., and Wesseling, J. F. (2008). Augmentation controls the fast rebound from depression at excitatory hippocampal synapses. *J. Neurophysiol.* 99, 1770–1786. doi: 10.1152/jn.01348.2007

Gautam, V., Naureen, S., Shahid, N., Gao, Q., Wang, Y., Nisbet, D., et al. (2017). Engineering highly interconnected neuronal networks on nanowire scaffolds. *Nano Lett.* 17, 3369–3375. doi: 10.1021/acs.nanolett.6b05288

Gekel, I., and Neher, E. (2008). Application of an Epac activator enhances neurotransmitter release at excitatory central synapses. *J. Neurosci.* 28, 7991–8002. doi: 10.1523/JNEUROSCI.0268-08.2008

Gerber, S. H., Rah, J. C., Min, S. W., Liu, X., de Wit, H., Dulubova, I., et al. (2008). Conformational switch of syntaxin-1 controls synaptic vesicle fusion. *Science* 321, 1507–1510. doi: 10.1126/science.1163174

Gitler, D., Cheng, Q., Greengard, P., and Augustine, G. J. (2008). Synapsin IIa controls the reserve pool of glutamatergic synaptic vesicles. *J. Neurosci.* 28, 10835–10843. doi: 10.1523/JNEUROSCI.0924-08.2008

Gitler, D., Takagishi, Y., Feng, J., Ren, Y., Rodriguiz, R. M., Wetsel, W. C., et al. (2004). Different presynaptic roles of synapsins at excitatory and inhibitory synapses. *J. Neurosci.* 24, 11368–11380. doi: 10.1523/JNEUROSCI.3795-04.2004

Goda, Y., and Stevens, C. F. (1996). Long-term depression properties in a simple system. *Neuron* 16, 103–111. doi: 10.1016/s0896-6273(00)80027-6

Goda, Y., and Stevens, C. F. (1998). Readily releasable pool size changes associated with long term depression. *Proc. Natl. Acad. Sci. U S A* 95, 1283–1288. doi: 10.1073/pnas.95.3.1283

Gomperts, S. N., Carroll, R., Malenka, R. C., and Nicoll, R. A. (2000). Distinct roles for ionotropic and metabotropic glutamate receptors in the maturation of excitatory synapses. *J. Neurosci.* 20, 2229–2237. doi: 10.1523/JNEUROSCI.20-06-02229.2000

Gomperts, S. N., Rao, A., Craig, A. M., Malenka, R. C., and Nicoll, R. A. (1998). Postsynaptically silent synapses in single neuron cultures. *Neuron* 21, 1443–1451. doi: 10.1016/s0896-6273(00)80662-5

Goslin, K., Asmussen, H., and Banker, G. (1998). "Rat hippocampal neurons in low-density culture," in *Culturing Nerve Cells*, *2nd Edn.* eds G. Banker and K. Goslin (Cambridge, MA: MIT Press), 339–370.

Guo, D., Wu, S., Chen, M., Perc, M., Zhang, Y., Ma, J., et al. (2016). Regulation of irregular neuronal firing by autaptic transmission. *Sci. Rep.* 6:26096. doi: 10.1038/srep26096

Han, W., Rhee, J. S., Maximov, A., Lao, Y., Mashimo, T., Rosenmund, C., et al. (2004). N-glycosylation is essential for vesicular targeting of synaptotagmin 1. *Neuron* 41, 85–99. doi: 10.1016/s0896-6273(03)00820-1

Harms, K. J., Tovar, K. R., and Craig, A. M. (2005). Synapse-specific regulation of AMPA receptor subunit composition by activity. *J. Neurosci.* 25, 6379–6388. doi: 10.1523/JNEUROSCI.0302-05.2005

Heeroma, J. H., Henneberger, C., Rajakulendran, S., Hanna, M. G., Schorge, S., and Kullmann, D. M. (2009). Episodic ataxia type 1 mutations differentially affect neuronal excitability and transmitter release. *Dis. Model. Mech.* 2, 612–619. doi: 10.1242/dmm.003582

Hnasko, T. S., and Edwards, R. H. (2012). Neurotransmitter corelease: mechanism and physiological role. *Annu. Rev. Physiol.* 74, 225–243. doi: 10.1146/annurev-physiol-020911-153315

Ikeda, K., and Bekkers, J. M. (2006). Autapses. *Curr. Biol.* 16:R308. doi: 10.1016/j.cub.2006.03.085

Ikeda, K., and Bekkers, J. M. (2009). Counting the number of releasable synaptic vesicles in a presynaptic terminal. *Proc. Natl. Acad. Sci. U S A* 106, 2945–2950. doi: 10.1073/pnas.0811017106

Ikeda, K., Suzuki, N., and Bekkers, J. M. (2018). Sodium and potassium conductances in principal neurons of the mouse piriform cortex: a quantitative description. *J. Physiol.* 596, 5397–5414. doi: 10.1113/jp275824

Ikeda, K., Yanagawa, Y., and Bekkers, J. M. (2008). Distinctive quantal properties of neurotransmission at excitatory and inhibitory autapses revealed using variance-mean analysis. *J. Neurosci.* 28, 13563–13573. doi: 10.1523/JNEUROSCI.3350-08.2008

Ivenshitz, M., and Segal, M. (2010). Neuronal density determines network connectivity and spontaneous activity in cultured hippocampus. *J. Neurophysiol.* 104, 1052–1060. doi: 10.1152/jn.00914.2009

Jang, M. J., Kim, W. R., Joo, S., Ryu, J. R., Lee, E., Nam, Y., et al. (2016). Cell-type dependent effect of surface-patterned microdot arrays on neuronal growth. *Front. Neurosci.* 10:217. doi: 10.3389/fnins.2016.00217

Jiang, M., Yang, M., Yin, L., Zhang, X., and Shu, Y. (2015). Developmental reduction of asynchronous GABA release from neocortical fast-spiking neurons. *Cereb. Cortex* 25, 258–270. doi: 10.1093/cercor/bht236

Jiang, M., Zhu, J., Liu, Y., Yang, M., Tian, C., Jiang, S., et al. (2012). Enhancement of asynchronous release from fast-spiking interneuron in human and rat epileptic neocortex. *PLoS Biol.* 10:e1001324. doi: 10.1371/journal.pbio.1001324

Johnson, M. D. (1994). Synaptic glutamate release by postnatal rat serotonergic neurons in microculture. *Neuron* 12, 433–442. doi: 10.1016/0896-6273(94)90283-6

Junge, H. J., Rhee, J. S., Jahn, O., Varoqueaux, F., Spiess, J., Waxham, M. N., et al. (2004). Calmodulin and Munc13 form a Ca^{2+} sensor/effector complex that controls short-term synaptic plasticity. *Cell* 118, 389–401. doi: 10.1016/j.cell.2004.06.029

Kaneda, M., Nakamura, H., and Akaike, N. (1988). Mechanical and enzymatic isolation of mammalian CNS neurons. *Neurosci. Res.* 5, 299–315. doi: 10.1016/0168-0102(88)90032-6

Karabelas, A. B., and Purpura, D. P. (1980). Evidence for autapses in the substantia nigra. *Brain Res.* 200, 467–473. doi: 10.1016/0006-8993(80)90935-x

Kay, A. R., and Wong, R. K. S. (1986). Isolation of neurons suitable for patch-clamping from adult mammalian central nervous systems. *J. Neurosci. Methods* 16, 227–238. doi: 10.1016/0165-0270(86)90040-3

Kellogg, R., Mackie, K., and Straiker, A. (2009). Cannabinoid CB_1 receptor-dependent long-term depression in autaptic excitatory neurons. *J. Neurophysiol.* 102, 1160–1171. doi: 10.1152/jn.00266.2009

Kimura, F., Otsu, Y., and Tsumoto, T. (1997). Presynaptically silent synapses: spontaneously active terminals without stimulus-evoked release demonstrated in cortical autapses. *J. Neurophysiol.* 77, 2805–2815. doi: 10.1152/jn.1997.77.5.2805

Kumura, E., Kimura, F., Taniguchi, N., and Tsumoto, T. (2000). Brain-derived neurotrophic factor blocks long-term depression in solitary neurones cultured from rat visual cortex. *J. Physiol.* 524, 195–204. doi: 10.1111/j.1469-7793.2000.t01-2-00195.x

Landis, S. C. (1976). Rat sympathetic neurons and cardiac myocytes developing in microcultures: correlation of the fine structure of endings with neurotransmitter function in single neurons. *Proc. Natl. Acad. Sci. U S A* 73, 4220–4224. doi: 10.1073/pnas.73.11.4220

Lee, S.-H., Rosenmund, C., Schwaller, B., and Neher, E. (2000). Differences in Ca^{2+} buffering properties between excitatory and inhibitory hippocampal neurons from the rat. *J. Physiol.* 525, 405–418. doi: 10.1111/j.1469-7793.2000.t01-3-00405.x

Li, B., Chen, N., Luo, T., Otsu, Y., Murphy, T. H., and Raymond, L. A. (2002). Differential regulation of synaptic and extra-synaptic NMDA receptors. *Nat. Neurosci.* 5, 833–834. doi: 10.1038/nn912

Li, B., Otsu, Y., Murphy, T. H., and Raymond, L. A. (2003). Developmental decrease in NMDA receptor desensitization associated with shift to synapse and interaction with postsynaptic density-95. *J. Neurosci.* 23, 11244–11254. doi: 10.1523/JNEUROSCI.23-35-11244.2003

Li, Y., Schmid, G., Hänggi, P., and Schimansky-Geier, L. (2010). Spontaneous spiking in an autaptic Hodgkin-Huxley setup. *Phys. Rev. E Stat. Nonlin. Soft Matter. Phys.* 82:061907. doi: 10.1103/physreve.82.061907

Liu, H., Chapman, E. R., and Dean, C. (2013). "Self" versus "non-self" connectivity dictates properties of synaptic transmission and plasticity. *PLoS One* 8:e62414. doi: 10.1371/journal.pone.0062414

Liu, H., Dean, C., Arthur, C. P., Dong, M., and Chapman, E. R. (2009). Autapses and networks of hippocampal neurons exhibit distinct synaptic transmission phenotypes in the absence of synaptotagmin I. *J. Neurosci.* 29, 7395–7403. doi: 10.1523/JNEUROSCI.1341-09.2009

Lu, Z., Piechowicz, M., and Qiu, S. (2016). A simplified method for ultra-low density, long-term primary hippocampal neuron culture. *J. Vis. Exp.* 109:e53797. doi: 10.3791/53797

Lübke, J., Markram, H., Frotscher, M., and Sakmann, B. (1996). Frequency and dendritic distribution of autapses established by Layer 5 pyramidal neurons in the developing rat neocortex: comparison with synaptic innervation of adjacent neurons of the same class. *J. Neurosci.* 16, 3209–3218. doi: 10.1523/JNEUROSCI.16-10-03209.1996

Magistretti, J., de Curtis, M., Vescovi, A., Galli, R., and Gritti, A. (1996). Long-term survival of cortical neurones from adult guinea-pig maintained in low-density cultures. *Neuroreport* 7, 1559–1564. doi: 10.1097/00001756-199607080-00005

Manseau, F., Marinelli, S., Mendez, P., Schwaller, B., Prince, D. A., Huguenard, J. R., et al. (2010). Desynchronization of neocortical networks by asynchronous release of GABA at autaptic and synaptic contacts from fast-spiking interneurons. *PLoS Biol.* 8:e1000492. doi: 10.1371/journal.pbio.1000492

Meijer, M., Cijsouw, T., Toonen, R. F., and Verhage, M. (2015). Synaptic effects of Munc18–1 alternative splicing in excitatory hippocampal neurons. *PLoS One* 10:e0138950. doi: 10.1371/journal.pone.0138950

Mennerick, S., Benz, A., and Zorumski, C. F. (1996). Components of glial responses to exogenous and synaptic glutamate in rat hippocampal microcultures. *J. Neurosci.* 16, 55–64. doi: 10.1523/JNEUROSCI.16-01-00055.1996

Mennerick, S., Que, J., Benz, A., and Zorumski, C. F. (1995). Passive and synaptic properties of hippocampal neurons grown in microcultures and in mass cultures. *J. Neurophysiol.* 73, 320–332. doi: 10.1152/jn.1995.73.1.320

Mennerick, S., Shen, W., Xu, W., Benz, A., Tanaka, K., Shimamoto, K., et al. (1999). Substrate turnover by transporters curtails synaptic glutamate transients. *J. Neurosci.* 19, 9242–9251. doi: 10.1523/JNEUROSCI.19-21-09242.1999

Mennerick, S., and Zorumski, C. F. (1994). Glial contributions to excitatory neurotransmission in cultured hippocampal cells. *Nature* 368, 59–62. doi: 10.1038/368059a0

Mennerick, S., and Zorumski, C. F. (1995a). Paired-pulse modulation of fast excitatory synaptic currents in microcultures of rat hippocampal neurons. *J. Physiol.* 488, 85–101. doi: 10.1113/jphysiol.1995.sp020948

Mennerick, S., and Zorumski, C. F. (1995b). Presynaptic influence on the time course of fast excitatory synaptic currents in cultured hippocampal cells. *J. Neurosci.* 15, 3178–3192. doi: 10.1523/JNEUROSCI.15-04-03178.1995

Michel, F. J., and Trudeau, L. E. (2000). Clozapine inhibits synaptic transmission at GABAergic synapses established by ventral tegmental area neurones in culture. *Neuropharmacology* 39, 1536–1543. doi: 10.1016/s0028-3908(99)00239-7

Moechars, D., Weston, M. C., Leo, S., Callaerts-Vegh, Z., Goris, I., Daneels, G., et al. (2006). Vesicular glutamate transporter VGLUT2 expression levels control quantal size and neuropathic pain. *J. Neurosci.* 26, 12055–12066. doi: 10.1523/JNEUROSCI.2556-06.2006

Moulder, K. L., Jiang, X., Taylor, A. A., Shin, W., Gillis, K. D., and Mennerick, S. (2007). Vesicle pool heterogeneity at hippocampal glutamate and GABA synapses. *J. Neurosci.* 27, 9846–9854. doi: 10.1523/JNEUROSCI.2803-07.2007

Moulder, K. L., Meeks, J. P., Shute, A. A., Hamilton, C. K., de Erausquin, G., and Mennerick, S. (2004). Plastic elimination of functional glutamate release sites by depolarization. *Neuron* 42, 423–435. doi: 10.1016/s0896-6273(04)00184-9

Moulder, K. L., and Mennerick, S. (2005). Reluctant vesicles contribute to the total readily releasable pool in glutamatergic hippocampal neurons. *J. Neurosci.* 25, 3842–3850. doi: 10.1523/JNEUROSCI.5231-04.2005

Murthy, V. N., Sejnowski, T. J., and Stevens, C. F. (1997). Heterogeneous release properties of visualized individual hippocampal synapses. *Neuron* 18, 599–612. doi: 10.1016/s0896-6273(00)80301-3

Murthy, V. N., Schikorski, T., Stevens, C. F., and Zhu, Y. (2001). Inactivity produces increases in neurotransmitter release and synapse size. *Neuron* 32, 673–682. doi: 10.1016/s0896-6273(01)00500-1

Murthy, V. N., and Stevens, C. F. (1998). Synaptic vesicles retain their identity through the endocytic cycle. *Nature* 392, 497–501. doi: 10.1038/33152

Nanou, E., Sullivan, J. M., Scheuer, T., and Catterall, W. A. (2016). Calcium sensor regulation of the $Ca_V2.1$ Ca^{2+} channel contributes to short-term synaptic plasticity in hippocampal neurons. *Proc. Natl. Acad. Sci. U S A* 113, 1062–1067. doi: 10.1073/pnas.1524636113

Nishiki, T., and Augustine, G. J. (2004). Synaptotagmin I synchronizes transmitter release in mouse hippocampal neurons. *J. Neurosci.* 24, 6127–6132. doi: 10.1523/JNEUROSCI.1563-04.2004

Ogata, N., and Tatebayashi, H. (1991). Primary culture of neurons derived from the adult mammalian brain. *Brain Res. Bull.* 27, 747–750. doi: 10.1016/0361-9230(91)90058-r

Otsu, Y., and Murphy, T. H. (2004). Optical postsynaptic measurement of vesicle release rates for hippocampal synapses undergoing asynchronous release during train stimulation. *J. Neurosci.* 24, 9076–9086. doi: 10.1523/JNEUROSCI.2060-04.2004

Otsu, Y., Shahrezaei, V., Li, B., Raymond, L. A., Delaney, K. R., and Murphy, T. H. (2004). Competition between phasic and asynchronous release for recovered synaptic vesicles at developing hippocampal autaptic synapses. *J. Neurosci.* 24, 420–433. doi: 10.1523/JNEUROSCI.4452-03.2004

Pan, Z. Z., Tong, G., and Jahr, C. E. (1993). A false transmitter at excitatory synapses. *Neuron* 11, 85–91. doi: 10.1016/0896-6273(93)90273-t

Paraskevopoulou, F., Herman, M. A., and Rosenmund, C. (2019). Glutamatergic innervation onto striatal neurons potentiates GABAergic synaptic output. *J. Neurosci.* 39, 4448–4460. doi: 10.1523/JNEUROSCI.2630-18.2019

Park, M. R., Lighthall, J. W., and Kitai, S. T. (1980). Recurrent inhibition in the rat neostriatum. *Brain Res.* 194, 359–369. doi: 10.1016/0006-8993(80)91217-2

Pawelzik, H., Hughes, D. I., and Thomson, A. M. (2003). Modulation of inhibitory autapses and synapses on rat CA1 interneurones by $GABA_A$ receptor ligands. *J. Physiol.* 546, 701–716. doi: 10.1113/jphysiol.2002.035121

Peters, A., and Proskauer, C. C. (1980). Synaptic relationships between a multipolar stellate cell and a pyramidal neuron in the rat visual cortex. A combined Golgi-electron microscope study. *J. Neurocytology* 9, 163–183. doi: 10.1007/bf01205156

Pouzat, C., and Marty, A. (1998). Autaptic inhibitory currents recorded from interneurones in rat cerebellar slices. *J. Physiol.* 509, 777–783. doi: 10.1111/j.1469-7793.1998.777bm.x

Pouzat, C., and Marty, A. (1999). Somatic recording of GABAergic autoreceptor current in cerebellar stellate and basket cells. *J. Neurosci.* 19, 1675–1690. doi: 10.1523/JNEUROSCI.19-05-01675.1999

Prakriya, M., and Mennerick, S. (2000). Selective depression of low-release probability excitatory synapses by sodium channel blockers. *Neuron* 26, 671–682. doi: 10.1016/s0896-6273(00)81203-9

Pratt, K. G., Zhu, P., Watari, H., Cook, D. G., and Sullivan, J. M. (2011). A novel role for γ-secretase: selective regulation of spontaneous neurotransmitter release from hippocampal neurons. *J. Neurosci.* 31, 899–906. doi: 10.1523/JNEUROSCI.4625-10.2011

Preston, R. J., Bishop, G. A., and Kitai, S. T. (1980). Medium spiny neuron projection from the rat striatum: an intracellular horseradish peroxidase study. *Brain Res.* 183, 253–263. doi: 10.1016/0006-8993(80)90462-x

Pyott, S. J., and Rosenmund, C. (2002). The effects of temperature on vesicular supply and release in autaptic cultures of rat and mouse hippocampal neurons. *J. Physiol.* 539, 523–535. doi: 10.1113/jphysiol.2001.013277

Raman, I. M., Tong, G., and Jahr, C. E. (1996). β-adrenergic regulation of synaptic NMDA receptors by cAMP-dependent protein kinase. *Neuron* 16, 415–421. doi: 10.1016/s0896-6273(00)80059-8

Rao, A., Cha, E. M., and Craig, A. M. (2000). Mismatched appositions of presynaptic and postsynaptic components in isolated hippocampal neurons. *J. Neurosci.* 20, 8344–8353. doi: 10.1523/JNEUROSCI.20-22-08344.2000

Reid, C. A., Bekkers, J. M., and Clements, J. D. (1998). N- and P/Q-type Ca^+ channels mediate transmitter release with a similar cooperativity at rat hippocampal autapses. *J. Neurosci.* 18, 2849–2855. doi: 10.1523/JNEUROSCI.18-08-02849.1998

Reid, C. A., Clements, J. D., and Bekkers, J. M. (1997). Nonuniform distribution of Ca^{2+} channel subtypes on presynaptic terminals of excitatory synapses in hippocampal cultures. *J. Neurosci.* 17, 2738–2745. doi: 10.1523/JNEUROSCI.17-08-02738.1997

Ricoult, S. G., Goldman, J. S., Stellwagen, D., Juncker, D., and Kennedy, T. E. (2012). Generation of microisland cultures using microcontact printing to pattern protein substrates. *J. Neurosci. Methods* 208, 10–17. doi: 10.1016/j.jneumeth.2012.04.016

Ripoli, C., Piacentini, R., Riccardi, E., Leone, L., Li Puma, D. D., Bitan, G., et al. (2013). Effects of different amyloid β-protein analogues on synaptic function. *Neurobiol. Aging* 34, 1032–1044. doi: 10.1016/j.neurobiolaging.2012.06.027

Rosenmund, C., Clements, J. D., and Westbrook, G. L. (1993). Nonuniform probability of glutamate release at a hippocampal synapse. *Science* 262, 754–757. doi: 10.1126/science.7901909

Rosenmund, C., Sigler, A., Augustin, I., Reim, K., Brose, N., and Rhee, J.-S. (2002). Differential control of vesicle priming and short-term plasticity by Munc13 isoforms. *Neuron* 33, 411–424. doi: 10.1016/s0896-6273(02)00568-8

Rosenmund, C., and Stevens, C. F. (1996). Definition of the readily releasable pool of vesicles at hippocampal synapses. *Neuron* 16, 1197–1207. doi: 10.1016/s0896-6273(00)80146-4

Rost, B. R., Breustedt, J., Schoenherr, A., Grosse, G., Ahnert-Hilger, G., and Schmitz, D. (2010). Autaptic cultures of single hippocampal granule cells of mice and rats. *Eur. J. Neurosci.* 32, 939–947. doi: 10.1111/j.1460-9568.2010.07387.x

Rost, B. R., Schneider, F., Grauel, M. K., Wozny, C., Bentz, C., Blessing, A., et al. (2015). Optogenetic acidification of synaptic vesicles and lysosomes. *Nat. Neurosci.* 18, 1845–1852. doi: 10.1038/nn.4161

Schlüter, O. M., Schmitz, F., Jahn, R., Rosenmund, C., and Sudhof, T. C. (2004). A complete genetic analysis of neuronal Rab3 function. *J. Neurosci.* 24, 6629–6637. doi: 10.1523/JNEUROSCI.1610-04.2004

Schupp, M., Malsam, J., Ruiter, M., Scheutzow, A., Wierda, K. D., Sollner, T. H., et al. (2016). Interactions between SNAP-25 and synaptotagmin-1 are involved in vesicle priming, clamping spontaneous and stimulating evoked neurotransmission. *J. Neurosci.* 36, 11865–11880. doi: 10.1523/JNEUROSCI.1011-16.2016

Segal, M. M. (1991). Epileptiform activity in microcultures containing one excitatory hippocampal neuron. *J. Neurophysiol.* 65, 761–770. doi: 10.1152/jn.1991.65.4.761

Segal, M. M. (1994). Endogenous bursts underlie seizurelike activity in solitary excitatory hippocampal neurons in microcultures. *J. Neurophysiol.* 72, 1874–1884. doi: 10.1152/jn.1994.72.4.1874

Segal, M. M., Baughman, R. W., Jones, K. A., and Huettner, J. E. (1998). "Mass cultures and microislands of neurons from postnatal rat brain," in *Culturing Nerve Cells*, 2nd Edn. eds G. Banker and K. Goslin (Cambridge, MA: MIT Press), 309–338.

Segal, M. M., and Furshpan, E. J. (1990). Epileptiform activity in microcultures containing small numbers of hippocampal neurons. *J. Neurophysiol.* 64, 1390–1399. doi: 10.1152/jn.1990.64.5.1390

Sgro, A. E., Nowak, A. L., Austin, N. S., Custer, K. L., Allen, P. B., Chiu, D. T., et al. (2011). A high-throughput method for generating uniform microislands for autaptic neuronal cultures. *J. Neurosci. Methods* 198, 230–235. doi: 10.1016/j.jneumeth.2011.04.012

Shi, W.-X., and Rayport, S. (1994). GABA synapses formed *in vitro* by local axon collaterals of nucleus accumbens neurons. *J. Neurosci.* 14, 4548–4560. doi: 10.1523/JNEUROSCI.14-07-04548.1994

Sobieski, C., Jiang, X., Crawford, D. C., and Mennerick, S. (2015). Loss of local astrocyte support disrupts action potential propagation and glutamate release synchrony from unmyelinated hippocampal axon terminals *in vitro*. *J. Neurosci.* 35, 11105–11117. doi: 10.1523/JNEUROSCI.1289-15.2015

Stevens, C. F., and Sullivan, J. M. (1998). Regulation of the readily releasable vesicle pool by protein kinase C. *Neuron* 21, 885–893. doi: 10.1016/s0896-6273(00)80603-0

Stevens, C. F., and Sullivan, J. M. (2003). The synaptotagmin C2A domain is part of the calcium sensor controlling fast synaptic transmission. *Neuron* 39, 299–308. doi: 10.1016/s0896-6273(03)00432-x

Stevens, C. F., and Wesseling, J. F. (1998). Activity-dependent modulation of the rate at which synaptic vesicles become available to undergo exocytosis. *Neuron* 21, 415–424. doi: 10.1016/s0896-6273(00)80550-4

Stevens, C. F., and Wesseling, J. F. (1999a). Augmentation is a potentiation of the exocytotic process. *Neuron* 22, 139–146. doi: 10.1016/s0896-6273(00)80685-6

Stevens, C. F., and Wesseling, J. F. (1999b). Identification of a novel process limiting the rate of synaptic vesicle cycling at hippocampal synapses. *Neuron* 24, 1017–1028. doi: 10.1016/s0896-6273(00)81047-8

Stevens, C. F., and Williams, J. H. (2007). Discharge of the readily releasable pool with action potentials at hippocampal synapses. *J. Neurophysiol.* 98, 3221–3229. doi: 10.1152/jn.00857.2007

Straiker, A., and Mackie, K. (2005). Depolarization-induced suppression of excitation in murine autaptic hippocampal neurones. *J. Physiol.* 569, 501–517. doi: 10.1113/jphysiol.2005.091918

Straiker, A., and Mackie, K. (2007). Metabotropic suppression of excitation in murine autaptic hippocampal neurons. *J. Physiol.* 578, 773–785. doi: 10.1113/jphysiol.2006.117499

Straiker, A., and Mackie, K. (2009). Cannabinoid signaling in inhibitory autaptic hippocampal neurons. *Neuroscience* 163, 190–201. doi: 10.1016/j.neuroscience.2009.06.004

Straiker, A., Dvorakova, M., Zimmowitch, A., and Mackie, K. (2018). Cannabidiol inhibits endocannabinoid signaling in autaptic hippocampal neurons. *Mol. Pharmacol.* 94, 743–748. doi: 10.1124/mol.118.111864

Sulzer, D., Joyce, M. P., Lin, L., Geldwert, D., Haber, S. N., Hattori, T., et al. (1998). Dopamine neurons make glutamatergic synapses *in vitro*. *J. Neurosci.* 18, 4588–4602. doi: 10.1523/JNEUROSCI.18-15-06057.1998

Tamás, G., Buhl, E. H., and Somogyi, P. (1997). Massive autaptic self-innervation of GABAergic neurons in cat visual cortex. *J. Neurosci.* 17, 6352–6364. doi: 10.1523/JNEUROSCI.17-16-06352.1997

Tarsa, L., and Goda, Y. (2002). Synaptophysin regulates activity-dependent synapse formation in cultured hippocampal neurons. *Proc. Natl. Acad. Sci. U S A* 99, 1012–1016. doi: 10.1073/pnas.022575999

Thakur, P., Stevens, D. R., Sheng, Z. H., and Rettig, J. (2004). Effects of PKA-mediated phosphorylation of Snapin on synaptic transmission in cultured hippocampal neurons. *J. Neurosci.* 24, 6476–6481. doi: 10.1523/JNEUROSCI.0590-04.2004

Thomas, C. G., Miller, A. J., and Westbrook, G. L. (2006). Synaptic and extrasynaptic NMDA receptor NR2 subunits in cultured hippocampal neurons. *J. Neurophysiol.* 95, 1727–1734. doi: 10.1152/jn.00771.2005

Ting, J. T., Kelley, B. G., and Sullivan, J. M. (2006). Synaptotagmin IV does not alter excitatory fast synaptic transmission or fusion pore kinetics in mammalian CNS neurons. *Adv. Exp. Med. Biol.* 26, 372–380. doi: 10.1523/JNEUROSCI.3997-05.2006

Tong, G., and Jahr, C. E. (1994a). Block of glutamate transporters potentiates postsynaptic excitation. *Neuron* 13, 1195–1203. doi: 10.1016/0896-6273(94)90057-4

Tong, G., and Jahr, C. E. (1994b). Multivesicular release from excitatory synapses of cultured hippocampal neurons. *Neuron* 12, 51–59. doi: 10.1016/0896-6273(94)90151-1

Tong, G., Malenka, R. C., and Nicoll, R. A. (1996). Long-term potentiation in cultures of single hippocampal granule cells: a presynaptic form of plasticity. *Neuron* 16, 1147–1157. doi: 10.1016/s0896-6273(00)80141-5

Tong, G., Shepherd, D., and Jahr, C. E. (1995). Synaptic desensitization of NMDA receptors by calcineurin. *Science* 267, 1510–1512. doi: 10.1126/science.7878472

Tovar, K. R., and Westbrook, G. L. (1999). The incorporation of NMDA receptors with a distinct subunit composition at nascent hippocampal synapses *in vitro*. *J. Neurosci.* 19, 4180–4188. doi: 10.1523/JNEUROSCI.19-10-04180.1999

Tovar, K. R., and Westbrook, G. L. (2002). Mobile NMDA receptors at hippocampal synapses. *Neuron* 34, 255–264. doi: 10.1016/s0896-6273(02)00658-x

Ullian, E. M., Sapperstein, S. K., Christopherson, K. S., and Barres, B. A. (2001). Control of synapse number by glia. *Science* 291, 657–660. doi: 10.1126/science.291.5504.657

Valente, P., Orlando, M., Raimondi, A., Benfenati, F., and Baldelli, P. (2016). Fine tuning of synaptic plasticity and filtering by GABA released from hippocampal autaptic granule cells. *Cereb. Cortex* 26, 1149–1167. doi: 10.1093/cercor/bhu301

Van der Loos, H., and Glaser, E. M. (1972). Autapses in neocortex cerebri: synapses between a pyramidal cell's axon and its own dendrites. *Brain Res.* 48, 355–360. doi: 10.1016/0006-8993(72)90189-8

Varoqueaux, F., Sigler, A., Rhee, J. S., Brose, N., Enk, C., Reim, K., et al. (2002). Total arrest of spontaneous and evoked synaptic transmission but normal synaptogenesis in the absence of Munc13-mediated vesicle priming. *Proc. Natl. Acad. Sci. U S A* 99, 9037–9042. doi: 10.1073/pnas.122623799

Ventimiglia, R., and Lindsay, R. M. (1998). "Rat striatal neurons in low-density, serum-free culture," in *Culturing Nerve Cells*, 2nd Edn. eds G. Banker and K. Goslin (Cambridge, MA: MIT Press), 371–393.

Vyklicky, V., Smejkalova, T., Krausova, B., Balik, A., Korinek, M., Borovska, J., et al. (2016). Preferential inhibition of tonically over phasically activated NMDA receptors by pregnane derivatives. *J. Neurosci.* 36, 2161–2175. doi: 10.1523/JNEUROSCI.3181-15.2016

Weber, J. P., Toft-Bertelsen, T. L., Mohrmann, R., Delgado-Martinez, I., and Sørensen, J. B. (2014). Synaptotagmin-7 is an asynchronous calcium sensor for synaptic transmission in neurons expressing SNAP-23. *PLoS One* 9:e114033. doi: 10.1371/journal.pone.0114033

Weston, M. C., Chen, H., and Swann, J. W. (2014). Loss of mTOR repressors Tsc1 or Pten has divergent effects on excitatory and inhibitory synaptic transmission in single hippocampal neuron cultures. *Front. Mol. Neurosci.* 7:1. doi: 10.3389/fnmol.2014.00001

White, J. A., Chow, C. C., Ritt, J., Soto-Trevino, C., and Kopell, N. (1998). Synchronization and oscillatory dynamics in heterogeneous, mutually inhibited neurons. *J. Comput. Neurosci.* 5, 5–16. doi: 10.1023/a:1008841325921

Wierda, K. D., and Sørensen, J. B. (2014). Innervation by a GABAergic neuron depresses spontaneous release in glutamatergic neurons and unveils

the clamping phenotype of synaptotagmin-1. *J. Neurosci.* 34, 2100–2110. doi: 10.1523/JNEUROSCI.3934-13.2014

Wiles, L., Gu, S., Pasqualetti, F., Parvesse, B., Gabrieli, D., Bassett, D. S., et al. (2017). Autaptic connections shift network excitability and bursting. *Sci. Rep.* 7:44006. doi: 10.1038/srep44006

Williams, S. R. (2004). Spatial compartmentalization and functional impact of conductance in pyramidal neurons. *Nat. Neurosci.* 7, 961–967. doi: 10.1038/nn1305

Wojcik, S. M., Rhee, J. S., Herzog, E., Sigler, A., Jahn, R., Takamori, S., et al. (2004). An essential role for vesicular glutamate transporter 1 (VGLUT1) in postnatal development and control of quantal size. *Proc. Natl. Acad. Sci. U S A* 101, 7158–7163. doi: 10.1073/pnas.0401764101

Xia, P., Chen, H. S., Zhang, D., and Lipton, S. A. (2010). Memantine preferentially blocks extrasynaptic over synaptic NMDA receptor currents in hippocampal autapses. *J. Neurosci.* 30, 11246–11250. doi: 10.1523/JNEUROSCI.2488-10.2010

Yin, L., Zheng, R., Ke, W., He, Q., Zhang, Y., Li, J., et al. (2018). Autapses enhance bursting and coincidence detection in neocortical pyramidal cells. *Nat. Commun.* 9:4890. doi: 10.1038/s41467-018-07317-4

Young, S. M. Jr. (2005). Proteolysis of SNARE proteins alters facilitation and depression in a specific way. *Proc. Natl. Acad. Sci. U S A* 102, 2614–2619. doi: 10.1073/pnas.0409656102

Yuste, R. (2015). From the neuron doctrine to neural networks. *Nat. Rev. Neurosci.* 16, 487–497. doi: 10.1038/nrn3962

Zimmermann, J., Herman, M. A., and Rosenmund, C. (2015). Co-release of glutamate and GABA from single vesicles in GABAergic neurons exogenously expressing VGLUT3. *Front. Synaptic Neurosci.* 7:16. doi: 10.3389/fnsyn.2015.00016

Zimmermann, J., Trimbuch, T., and Rosenmund, C. (2014). Synaptobrevin 1 mediates vesicle priming and evoked release in a subpopulation of hippocampal neurons. *J. Neurophysiol.* 112, 1559–1565. doi: 10.1152/jn.00340.2014

Conflict of Interest: The author declares that the research was conducted in the absence of any commercial or financial relationships that could be construed as a potential conflict of interest.

Advantages of publishing in Frontiers

OPEN ACCESS
Articles are free to read for greatest visibility and readership

FAST PUBLICATION
Around 90 days from submission to decision

HIGH QUALITY PEER-REVIEW
Rigorous, collaborative, and constructive peer-review

TRANSPARENT PEER-REVIEW
Editors and reviewers acknowledged by name on published articles

Frontiers
Avenue du Tribunal-Fédéral 34
1005 Lausanne | Switzerland

Visit us: www.frontiersin.org
Contact us: info@frontiersin.org | +41 21 510 17 00

REPRODUCIBILITY OF RESEARCH
Support open data and methods to enhance research reproducibility

DIGITAL PUBLISHING
Articles designed for optimal readership across devices

FOLLOW US
@frontiersin

IMPACT METRICS
Advanced article metrics track visibility across digital media

EXTENSIVE PROMOTION
Marketing and promotion of impactful research

LOOP RESEARCH NETWORK
Our network increases your article's readership